

City Research Online

City, University of London Institutional Repository

Citation: Ogrodniczak, P. (2024). Numerical investigation of non-equilibrium flash boiling of organic fluids for power generation. (Unpublished Doctoral thesis, City St George's, University of London)

This is the accepted version of the paper.

This version of the publication may differ from the final published version.

Permanent repository link: https://openaccess.city.ac.uk/id/eprint/36080/

Link to published version:

Copyright: City Research Online aims to make research outputs of City, University of London available to a wider audience. Copyright and Moral Rights remain with the author(s) and/or copyright holders. URLs from City Research Online may be freely distributed and linked to.

Reuse: Copies of full items can be used for personal research or study, educational, or not-for-profit purposes without prior permission or charge. Provided that the authors, title and full bibliographic details are credited, a hyperlink and/or URL is given for the original metadata page and the content is not changed in any way.

City Research Online: http://openaccess.city.ac.uk/ publications@city.ac.uk



City, University of London
School of Science & Technology
Department of Mechanical Engineering & Aeronautics

Numerical investigation of non-equilibrium flash boiling of organic fluids for power generation

Pawel Ogrodniczak

Supervisors:

Dr Martin White

Prof Abdulnaser Sayma

Submitted for the degree of Doctor of Philosophy - December 2024

Declaration

I declare that this thesis, entitled *Numerical investigation of non-equilibrium flash boiling of organic fluids for power generation*, is the result of my own independent research. It has not been submitted for any degree or diploma at any other institution.

All sources of information and assistance used during the research have been fully and appropriately cited.

Signed,

Pawel Ogrodniczak

16 December 2024

Abstract

The organic Rankine cycle is a suitable technology for heat-to-power conversion from thermal sources at temperatures between 80 and 380 °C. However, the simple organic Rankine cycle poses some limitations when it comes to the effective utilisation of open sensible heat sources, which is mainly related to isothermal evaporation. Two-phase expansion has been proposed as a means of improving cycle performance, but, efficient expanders that can tolerate wet conditions are required. Using certain molecularly complex fluids it is theoretically possible to design a so-called wet-to-dry cycle, in which the fluid transitions from a two-phase state to a superheated vapour regime in a process known as flash boiling. Previous studies indicate that the wet-to-dry cycle can potentially generate 30 % more power from heat sources at temperatures between 150 and 250 °C. Since the fluid can hypothetically escape the two-phase dome during expansion, existing turboexpander architectures can be employed so long as the wet portion of the expansion is confined to the turbine nozzle to avoid erosion of the rotor blades.

The key characteristic of a two-phase turboexpander designed for the wet-to-dry cycle is the nozzle, which has to facilitate complete mixture vapourisation in an efficient manner. Due to the lack of relevant experimental data, the concept of the proposed two-phase turboexpander must be assessed with the aid of numerical tools. To this day, numerical studies focused on the wet-to-dry expansion have either neglected non-equilibrium effects or oversimplified the expansion by assuming an inviscid one-dimensional flow. The main objective of this work is to numerically investigate flash boiling in a passage representative of a turboexpander nozzle designed for the wet-to-dry cycle and to assess the feasibility of designing a nozzle that can achieve complete mixture vapourisation under relevant operating conditions. To this end, a suitable non-equilibrium flash-boiling model is implemented to conduct numerical simulations that account for non-equilibrium effects, two-dimensional flow variations, effects of turbulence and viscosity, as well as the influence of drag, lift and turbulent dispersion forces. The model is applied to simulate the wet-to-dry expansion of the siloxane MM in a converging-diverging nozzle for a range of inlet pressures from 500 to 1250 kPa, inlet vapour qualities from 0.1 to 0.5, and for a range of droplet sizes.

The research presented in this thesis give insight into the underlying physics of wet-to-dry expansion under a range of operating conditions relevant to the wet-to-dry cycle. The phase-change process, extent of non-equilibrium effects, spatial distribution of phases as well as flow uniformity are assessed. Nozzle geometries designed with a non-equilibrium tool are investigated to evaluate the importance of incorporating non-equilibrium effects in the nozzle design routine. Lastly, an optimisation study is carried out, which aimed at maximising the vapourisation rate in the nozzle, while maintaining an efficient expansion.

The results indicate that the droplet diameter has the greatest impact on the two-phase expansion, and it is generally difficult to achieve complete mixture vapourisation when droplets are too large. The wet-to-dry transition can be more readily accomplished at high operating pressures but these conditions are associated with reduced cycle performance. Droplet breakup has been found to be significant and suitable methods for accounting for these effects have been proposed. Including non-equilibrium effects in the nozzle design tool is important and can potentially help generate better-performing nozzles with an enhanced vapourisation rate. Finally, the vapourisation rate can be enhanced by means of optimisation techniques but simultaneous consideration of expansion efficiency is essential.

This thesis contributes to a better understanding of flash boiling of organic fluids in passages designed for high-speed two-phase flows. This research also highlights the important challenges that are likely to accompany the design of a two-phase turboexpander for the wet-to-dry cycle, providing a step forward towards developing a turbine prototype.

Contents

1 Introduction **1**
- 1.1 Organic Rankine cycle . . . 1
- 1.2 Limitations of the simple organic Rankine cycle . . . 3
- 1.3 Wet-to-dry cycle . . . 4
- 1.4 Wet-to-dry expansion . . . 5
- 1.5 Scope of research . . . 8
- 1.6 Thesis outline . . . 9
- 1.7 Publications . . . 11

2 Background and motivation **13**
- 2.1 Introduction . . . 13
- 2.2 Rankine cycle . . . 14
- 2.3 Organic Rankine cycle . . . 15
- 2.4 Limitations of simple organic Rankine cycle . . . 18
- 2.5 Alternative cycle architectures . . . 22
  - 2.5.1 Transcritical cycle . . . 23
  - 2.5.2 Zeotropic mixtures . . . 23
  - 2.5.3 Trilateral flash cycle . . . 24
  - 2.5.4 Partially-evaporated cycle . . . 26
  - 2.5.5 Potential and challenges of alternative cycle architectures . . . 27
- 2.6 Two-phase expanders . . . 28
  - 2.6.1 Single-phase expanders . . . 29
    - 2.6.1.1 Turboexpanders . . . 29
    - 2.6.1.2 Volumetric expanders . . . 31
  - 2.6.2 Review of two-phase expanders . . . 34
    - 2.6.2.1 Two-phase volumetric expanders . . . 34
    - 2.6.2.2 Two-phase turboexpanders . . . 39
    - 2.6.2.3 Summary of two-phase expanders . . . 48
- 2.7 Wet-to-dry cycle . . . 50
- 2.8 Conclusions . . . 56

3 Modelling flash boiling **57**
- 3.1 Introduction . . . 57
- 3.2 Modelling frameworks . . . 57
  - 3.2.1 Eulerian-Lagrangian framework . . . 58

3.2.2 Eulerian-Eulerian framework . . . 60
3.3 Flash-boiling models . . . 61
3.3.1 Homogeneous-equilibrium model . . . 62
3.3.2 Inhomogeneous equilibrium models . . . 63
3.3.3 Non-equilibrium phase-change . . . 64
3.3.4 Nucleation process . . . 69
3.3.5 Non-equilibrium two-fluid model . . . 74
3.4 Simulating wet-to-dry expansion . . . 78
3.5 Scope of research . . . 85

4 Two-fluid model **86**
4.1 Introduction . . . 86
4.2 Governing equations . . . 86
4.2.1 Interphase exchange terms . . . 88
4.3 Phase coupling . . . 89
4.3.1 Interfacial area . . . 89
4.3.2 Mass and heat transfer . . . 94
4.3.3 Interfacial heat-transfer rate . . . 95
4.3.4 Momentum exchange . . . 99
4.3.5 Summary of interphase models . . . 103
4.4 Turbulence modelling . . . 103
4.5 Metastability and fluid properties . . . 105
4.6 Numerical implementation . . . 108
4.7 Validation study . . . 109
4.7.1 Solver setup . . . 110
4.7.2 Mesh independence study . . . 111
4.7.3 Comparison with experimental and numerical data . . . 112
4.8 Conclusions . . . 116

5 Non-equilibrium simulation of the wet-to-dry expansion **119**
5.1 Introduction . . . 119
5.2 Nozzle design . . . 119
5.3 Investigated operating conditions . . . 123
5.4 Computational fluid dynamics setup . . . 128
5.5 Mesh independence study . . . 131
5.6 Three-dimensional and transient effects . . . 134
5.7 Sensitivity to interphase models . . . 136
5.7.1 Baseline model . . . 137
5.7.2 Alternative interphase models . . . 137
5.7.3 Sensitivity to momentum-transfer models . . . 138
5.7.4 Sensitivity to heat-transfer models . . . 142
5.7.5 Summary of the sensitivity study . . . 145
5.8 Parametric study results . . . 149
5.8.1 Mixture vapourisation . . . 149
5.8.2 Significance of droplet size . . . 154

5.8.3 Design and simulated expansions . . . 155
5.8.4 Significance of non-equilibrium effects . . . 159
5.8.5 Flow uniformity . . . 162
5.8.6 Comment on the initial conditions . . . 164
5.8.7 Droplet breakup . . . 165
5.9 Effect of scale . . . 166
5.10 Conclusions . . . 170

6 Importance of non-equilibrium effects in the nozzle design 172
6.1 Introduction . . . 172
6.2 Nozzle design methodology . . . 172
6.3 Nozzle wall profile discontinuity . . . 173
6.4 Investigated expansions . . . 175
6.5 Influence on vapourisation rate . . . 176
6.6 Influence on mixture velocity . . . 181
6.7 Nozzle shape and pressure distribution . . . 182
6.8 Non-equilibrium effects . . . 184
6.9 Two-dimensional flow patterns . . . 185
6.10 Summary of the performance of non-equilibrium nozzles . . . 190
6.11 Droplet breakup effects . . . 191
6.12 Conclusions . . . 195

7 Nozzle optimisation 197
7.1 Introduction . . . 197
7.2 Overview and literature review . . . 198
7.3 Modelling breakup in the CFD solver . . . 199
7.4 Mesh independence study . . . 202
7.5 One-dimensional optimisation . . . 205
7.5.1 Operating points for optimisation . . . 205
7.5.2 Comparison of nozzle design tool against CFD simulations . . . 207
7.5.3 One-dimensional optimisation results . . . 209
7.6 CFD-based shape optimisation . . . 215
7.6.1 Optimisation setup . . . 215
7.6.2 Shape optimisation results . . . 220
7.6.3 Effect of other geometrical parameters . . . 221
7.7 Effect of droplet size decrease . . . 223
7.8 Conclusions . . . 225

8 Conclusions and recommendations for future work 228
8.1 Introduction . . . 228
8.2 Non-equilibrium flashing model . . . 229
8.3 Numerical simulations . . . 230
8.4 Non-equilibrium nozzle design . . . 232
8.5 Nozzle optimisation . . . 234
8.6 Final remarks . . . 235

8.7 Recommendations for future work . . . 236
8.7.1 Flow modelling . . . 236
8.7.2 Design and optimisation methods . . . 237
8.7.3 Applications . . . 237
8.7.4 Experimentation . . . 238

A Implementation of custom interphase models **260**
A.1 User-defined expressions implemented in the CFD solver . . . 260
A.2 Droplet breakup implementation . . . 262

List of Figures

1.1 Schematic diagram (left) and temperature-entropy diagram (right) of the simple organic Rankine cycle. . . . 2
1.2 The range of applicability of ORC systems compared to other power generation technologies (figure retrieved from [5]) . . . 2
1.3 Wet-to-dry organic Rankine cycle . . . 5

2.1 Schematic of the steam Rankine cycle . . . 14
2.2 Temperature-entropy diagram of a simple organic Rankine cycle; the positive slope of the saturated-vapour curve ensures condensation-free expansion. . . . 16
2.3 The cycle architecture that generates the maximum amount of work with a variable-temperature heat source. . . . 19
2.4 Theoretical cycle satisfying the maximum power condition under the assumption of non-isothermal heat-sink. . . . 20
2.5 Temperature-entropy diagram of the simple organic Rankine cycle; the shaded area represents the exergy loss due to heat-transfer over a finite temperature difference. . . . 21
2.6 Alternative organic Rankine cycle architectures . . . 25
2.7 Schematic diagram of axial (left) and radial-inflow (right) turbines [66] . . . 30
2.8 Schematic diagram of a radial-outflow turbine [71] . . . 31
2.9 Principle of operation of a scroll expander; the figure illustrates the evolution of entrapped volume of high-pressure fluid during expansion [76]. . . . 32
2.10 Principle of operation of a screw expander [66] . . . 33
2.11 Expansion process in a single-stage turboexpander; the effect of nozzle-rotor interspace is neglected. . . . 40
2.12 Schematic of a two-phase rotary separator turbine (figure retrieved from Hays [98]) . . . 41
2.13 a) Schematic drawing of a radial-outflow turbine; b) Radial-outflow turbine rotor installed in a Kalina cycle plant in Bruchsal (figures retrieved from [101]) 42
2.14 Schematic of the rotating radial-outflow turbine (figure retrieved from Li et al. [105]) . . . 43
2.15 A single-stage impulse axial turbine integrated with a single two-phase nozzle (figure retrieved from Hays & Brasz. [103]) . . . 44
2.16 Schematic of the Pelton-type turbine (image retrieved from Prodanovic et al.[108]) . . . 46

2.17 A cryogenic two-phase radial-inflow turbine developed by Elliot Group (image retrieved from Patel & Kimmel [114]) 47
2.18 Temperature-entropy diagram of the wet-to-dry organic Rankine cycle 52
2.19 Saturation curves of the most promising fluids identified by White [8] for the wet-to-dry cycle. 53
2.20 The effect of inlet vapour quality and degree of reaction on the wet-to-dry cycle power output (a) and turbine total-to-static efficiency (b); the power output was normalised by the corresponding single-phase ORC power output to demonstrate the relative advantage of two-phase expansion. 54

3.1 The comparison of Eulerian-Lagrangian and Eulerian-Eulerian methods for modelling dispersed droplet flows. In the Eulerian-Lagrangian framework individual droplets are tracked through the flow-field, while the Eulerian-Eulerian framework treats both phases as interpenetrating continua with a volume fraction α_L used to represent the concentration of liquid in each cell. The shades of blue represent concentration of liquid according to the number of droplets occupying the cell. 58
3.2 Different categories of flash-boiling models divided based on the treatment of non-equilibrium effects; u_L and u_V represent liquid and vapour velocities, while T_L and T_V denote temperatures of the two phases respectively. 62
3.3 Different approaches to modelling the nucleation process in flash-boiling of subcooled liquids. The area denoted by I, II, III and IV represent subcooled liquid, superheated (metastable) liquid, nucleation and equilibrium zones (figure retrieved from Liao and Lucas [132]). 70
3.4 Two-dimensional variation of vapour quality and Mach number in radial-inflow turbine stator designed for the wet-to-dry cycle. The contours were obtained using a homogenous-equilibrium model applied to a two-phase expansion of the siloxane MM from an inlet pressure of 500 kPa and inlet vapour quality of 0.3 (figure retrieved from White [8]). 79
3.5 The graph illustrates the streamwise variation of pressure, nozzle diameter, vapour quality and velocity of liquid and vapour estimated with a one-dimensional inhomogeneous equilibrium model applied to a wet-to-dry expansion of toluene from an inlet pressure of 2847 kPa and inlet vapour quality of 0.01 (figure retrieved from Elliot [28]). 81
3.6 Streamwise variation of pressure, void fraction (α), temperatures and velocities of vapour and liquid obtained by White [43] using a quasi-1D inviscid two-fluid model and non-equilibrium CFD simulations for the two-phase expansion of R1233zd(E). Three different droplet numbers were considered in the study, ranging from 10^8 to 10^{12} droplets per unit volume (figure retrieved from White [43]). 83
3.7 Streamwise variation in nozzle half-height obtained by White [43] using a homogeneous-equilibrium model (HEM) and a non-equilibrium one-dimensional code for liquid Nusselt number of 6 and 12. The dot represents the location of the wet-to-dry transition, while the value q_{out} gives the vapour quality at the nozzle outlet (figure retrieved from White [43]). 84

4.1 Relationship between the inlet void fraction and inlet vapour quality for different inlet pressure relevant to the wet-to-dry cycle. 90
4.2 Streamwise variation of void fraction and vapour mass fraction predicted using a non-equilibrium one-dimensional code applied to the expansions from an inlet total pressure of 1000 and 1250 kPa and an inlet vapour quality of 0.1; the dotted lines denote the streamwise location where the void fraction exceeded 0.7. 91
4.3 Schematic of an evaporating droplet in the wet-to-dry expansion; the phase change is assumed to occur due to interphase heat transfer which is estimated using the two-resistance model. 94
4.4 Suitability of various heat-transfer models for predicting the average Nusselt number of fully contaminated spherical bubbles: (a) $Re_b = 0.1$, $Pr_L = 1-104$. (b) $Re_b = 1 - 150$, $Pr_L = 2$. (figure retrieved from Liao & Lucas [228]) . . . 97
4.5 Streamwise variation of droplet Reynolds number and Péclet number obtained using a non-equilibrium one-dimensional code for four inlet pressure and an inlet vapour quality of 0.3. 98
4.6 Interfacial forces relevant to two-phase droplet flows; U_{slip} represents velocity slip resulting from a difference in vapour and liquid velocities ($U_V - U_L$). . . 99
4.7 The illustration explaining metastable, unstable and stable states. 105
4.8 The illustration metastability of liquid and vapour phases on temperature-volume diagram (figure retrieved from de Lorenzo [241]). 106
4.9 Deviation in the estimated nozzle flow area between the Span Wagner Helmholtz and the cubic Peng-Robinson equations of state; the results were obtained with a one-dimensional non-equilibrium code for various wet-to-dry expansions of the siloxane MM and the assumption of a fixed droplet number density N_D (figure retrieved from White [43]). 107
4.10 Schematic of the BNL nozzle 110
4.11 BNL309 mesh (389 thousand-elements mesh displayed) 111
4.12 The variation of static pressure and vapour volume fraction along the centre line of the BNL nozzle; comparison between the experimental trends, current study, and the other numerical studies of Liao & Lucas [206] and Rane & He [41]. 113
4.13 The variation of vapour volume fraction across the BNL nozzle - comparison between Rane & He [41] study (top contour) and the current study (bottom contour) 113
4.14 Streamwise variation of static pressure inside the BNL nozzle estimated for four experimental runs; the figure also illustrates the experimental measurements and the prediction of the Liao and Lucas [206] model. 115
4.15 Streamwise variation of vapour volume fraction inside the BNL nozzle estimated for four experimental runs; the figure also illustrates the experimental measurements and the prediction of the Liao and Lucas [206] model. 116

5.1 A simplified schematic of a radial-inflow turbine. 120

5.2 Normalised baseline nozzle pressure profile constructed using a Bezier curve with five control points; the red asterisks (*) show the location of the Bezier curve control points. 122
5.3 Wet-to-dry nozzle design routine based on the assumption of quasi-1D isentropic homogeneous-equilibrium flow; *EoS* stands for the equation of state, while y represents the passage height. 124
5.4 The temperature-entropy diagram of the twelve simulated expansion cases; the depicted expansions define the boundary conditions used in the nozzle design and CFD simulations, and are generated under the assumption of isentropic homogeneous-equilibrium flow. 125
5.5 Nozzle geometry for the expansion from 500 kPa and inlet quality of 0.3; although the figure illustrates a three-dimensional geometry, the subsequent analysis used a thin slab in the z direction to perform quasi-2D simulations. 126
5.6 The relationship between the nozzle loss coefficient (ζ_n) and the width of of a radial-inflow turbine nozzle designed for the wet-to-dry cycle. The CFD results were obtained using a homogeneous-equilibrium model. The presented correlations were obtained using b_4 divided by the corresponding unit of length to derive the correlations presented in the figure (figure retrieved from White [8]). 127
5.7 The effect of viscosity on average streamwise variation of static pressure and mixture velocity. The results were obtained for a fixed inlet vapour quality of 0.3 and a droplet density number of 10^{12}. 132
5.8 Average streamwise variation of vapour mass fraction and mixture velocity for different grid sizes. 134
5.9 The structure of the grid generated with an element size of 0.4 mm; the enlarged section illustrates the grid topology in the throat area. 135
5.10 Streamwise variation of average vapour mass fraction, mixture velocity, velocity slip and temperature difference predicted by two-dimensional steady, two-dimensional transient and three-dimensional steady solvers. 135
5.11 Streamwise variation of average vapour mass fraction x_V and average mixture velocity u_{Mix} obtained using alternative drag models. The plot shows two expansion cases: the expansions from 500 and 1000 kPa with a fixed inlet vapour quality of 0.3. 140
5.12 Streamwise variation of average vapour mass fraction x_V and average mixture velocity u_{Mix} obtained using alternative lift models. The plot shows two expansion cases: the expansion from 500 and 1000 kPa with inlet quality of 0.3. 141
5.13 Two-dimensional contours of vapour mass fraction x_V obtained using alternative lift models. The contours illustrate the expansions from 500 kPa (left) and 1000 kPa (right), with an inlet quality of 0.3 and a droplet number of 10^{11}. 142
5.14 Streamwise variation of average vapour mass fraction x_V and average mixture velocity u_{Mix} obtained using alternative turbulent dispersion models. The plot shows two expansion cases: the expansion from 500 and 1000 kPa with inlet quality of 0.3. 143

5.15 Streamwise variation of average vapour mass fraction x_V obtained using alternative models for predicting heat-transfer rate on the liquid side of the interface. The plot shows two expansion cases: the expansion from 500 and 1000 kPa with a fixed inlet vapour quality of 0.3 and a droplet number of 10^{11}. 144
5.16 Two-dimensional contours of vapour mass fraction x_V obtained using different approach to modelling heat transfer between liquid droplets and the liquid-vapour interface. The contours illustrate the expansions from 500 kPa (left) and 1000 kPa (right), with an inlet quality of 0.3 and a droplet number of 10^{11}; Nu denotes Nusselt number on the liquid side of the interface. The values $x_{V,out}$ reported in the figure denote the average vapour quality calculated at the nozzle outlet. 145
5.17 Streamwise variation of liquid and vapour temperatures obtained using alternative models for predicting heat-transfer rate on the liquid side of the interface. The plot shows two expansion cases: the expansion from 500 and 1000 kPa with a fixed inlet vapour quality of 0.3 and a droplet number of 10^{11}. 146
5.18 Streamwise variation of average vapour mass fraction x_V obtained using alternative models for predicting heat-transfer rate on the vapour side of the interface. The plot shows two expansion cases: the expansion from 500 and 1000 kPa with a fixed inlet vapour quality of 0.3. 147
5.19 Streamwise variation of liquid and vapour temperatures obtained using alternative models for predicting heat-transfer rate on the vapour side of the interface. The plot shows two expansion cases: the expansion from 500 and 1000 kPa with a fixed inlet vapour quality of 0.3 and a droplet number of 10^{11}. 148
5.20 Streamwise variation of average vapour mass fraction x_V for the wet-to-dry expansion pressure from an inlet pressure of 500 kPa, and from three different vapour inlet qualities: 0.1, 0.3 and 0.5. The variation of x_V for each expansion case has been shown for three different droplet density numbers N_d: 10^{11}, 10^{12} and 10^{13}. 150
5.21 Streamwise variation of average vapour mass fraction x_V for the wet-to-dry expansion pressure from an inlet pressure of 750 kPa, and from three different vapour inlet qualities: 0.1, 0.3 and 0.5. The variation of x_V for each expansion case has been shown for three different droplet density numbers N_d: 10^{11}, 10^{12} and 10^{13}. 151
5.22 Streamwise variation of average vapour mass fraction x_V for the wet-to-dry expansion pressure from an inlet pressure of 1000 kPa, and from three different vapour inlet qualities: 0.1, 0.3 and 0.5. The variation of x_V for each expansion case has been shown for three different droplet density numbers N_d: 10^{11}, 10^{12} and 10^{13}. 152
5.23 Streamwise variation of average vapour mass fraction x_V for the wet-to-dry expansion pressure from an inlet pressure of 1250 kPa, and from three different vapour inlet qualities: 0.1, 0.3 and 0.5. The variation of x_V for each expansion case has been shown for three different droplet density numbers N_d: 10^{11}, 10^{12} and 10^{13}. 153
5.24 The relationship between the inlet droplet diameter $D_{d,in}$ and the outlet void fraction $\alpha_{V,out}$. 153

5.25 Streamwise variation of the ratios of droplet diameter square and liquid superheat; the lines represent the ratios of the values obtained with $N_d = 10^{11}$ to the values obtained with $N_d = 10^{13}$ for the expansions from 500 and 1000 kPa and inlet quality of 0.3. 155
5.26 The comparison between the design and simulated pressure and mixture velocity profiles generated for the expansion from 500 and 1000 kPa and an inlet quality of 0.3. 156
5.27 The relationship between the inlet droplet diameter $D_{d,in}$ and the β parameters; β_p is the ratio of the pressure drop to the design pressure drop, while β_u is the ratio of the mixture outlet velocity to the design outlet velocity. 157
5.28 The relationship between the mass-flow rate obtained in the original CFD simulations ($\dot{m}$) and the mass-flow rate obtained with the outlet pressure reduced by a factor of 2 ($\dot{m}_{P_{out}/2}$). The black solid line represents the equality line where the mass-flow rates are identical, which indicates that the nozzle is choked. 157
5.29 The relationship between the inlet droplet diameter $D_{d,in}$ and the mass-flow rate $\dot{m}$ obtained using the CFD model. The estimated mass-flow rate was multiplied by the ratio of the design nozzle width to the thickness of the thin slab applied to perform two-dimensional simulations. The dashed line represents the design-mass flow rate. 159
5.30 Streamwise variation of average relative velocity slip ($u_{slip,rel}$) and average thermal non-equilibrium ($T_L - T_V$) in the expansions from 500 kPa and 1000 kPa, with three inlet qualities $x_{V,in}$ of 0.1, 0.3 and 0.5 and three different droplet density number N_d of 10^{11}, 10^{12} and 10^{13}; $u_{slip,rel}$ is the velocity slip normalised by the mixture velocity, while $T_L - T_V$ is temperature difference between the liquid and vapour phases. 160
5.31 Two-dimensional variations of vapour mass fraction and mixture velocity within the nozzles designed for the expansions from 500 and 1000 kPa and inlet vapour quality of 0.3. 163
5.32 The relationship between the inlet droplet diameter and normalised standard deviations of vapour mass fraction (σ_{x_V}) and mixture velocity ($\sigma_{u_{Mix}}$) across the nozzle outlet; the standard deviations were normalised by mean outlet values of x_V and u_{mix}. 164
5.33 The streamwise variation of the ratio of the average Weber number to the critical Weber number; droplet breakup is expected to occur if the ratio We/We_{cr} exceeds unity (denoted by the black dotted line). The mixture was expanded from inlet quality of 0.3 for each presented case. 167
5.34 Streamwise variation of the vapour mass fraction and mixture velocity obtained in the nozzles designed for the mass-flow rates of 0.12 and 0.50 kg/s. The results were generated for the expansion from 500 and 1000 kPa and a fixed inlet vapour quality of 0.3. 168
5.35 Two-dimensional variations of vapour vapour quality obtained in the nozzles designed for the mass-flow rates of 0.12 and 0.50 kg/s. The results were generated for the expansions from 500 and 1000 kPa and a fixed inlet vapour quality of 0.3. The larger nozzles were scaled down for comparison purposes. 169

6.1 Streamwise variation of mixture density ρ_{mix} predicted by the non-equilibrium design tool two inlet pressure of 500 and 1000 kPa, and a fixed inlet vapour quality of 0.3. The droplet size was estimated using a constant droplet number density that varied between 10^{11} and 10^{13}. 174
6.2 The effect of fitting a spline between the two-phase and superheated nozzle section for the expansions from an inlet total pressure of 500 (top) and 1000 (bottom) kPa and an inlet vapour quality of 0.3. 174
6.3 The temperature-entropy diagram of two expansion cases considered for the assessment of including non-equilibrium effects in the nozzle design process. The illustrated expansions refer to an ideal isentropic flow. 176
6.4 Streamwise variation of average vapour mass fraction x_V in nozzles generated by the non-equilibrium and homogeneous-equilibrium design tools; the plot illustrates the design profiles and CFD predictions for the expansion from an inlet pressure of 500 and 1000 kPa, fixed inlet vapour quality of 0.3 and three droplet density numbers N_d of 10^{11}, 10^{12} and 10^{13}. 177
6.5 Streamwise variation of average interfacial area density, liquid heat-transfer coefficient, liquid superheat level and interphase mass-transfer rate in the nozzle designed by the non-equilibrium tool for the expansion from an inlet pressure of 1000 kPa and inlet vapour quality of 0.3; the figure shows the variations for the droplet numbers N_d of 10^{11}, 10^{12} and 10^{13}. 179
6.6 Streamwise variation of average interfacial area density, liquid heat-transfer coefficient, liquid superheat level and interphase mass-transfer rate in the nozzle designed by the non-equilibrium tool for the expansion from an inlet pressure of 500 kPa and inlet vapour quality of 0.3; the figure shows the variations for the droplet numbers N_d of 10^{11}, 10^{12} and 10^{13}. 180
6.7 Streamwise variation of average mixture velocity u_{mix} in nozzles generated by the non-equilibrium and homogeneous-equilibrium design tools; the plot illustrates the design profiles and CFD predictions for the expansion from an inlet pressure of 500 and 1000 kPa, fixed inlet vapour quality of 0.3 and three droplet density numbers N_d of 10^{11}, 10^{12} and 10^{13}. 183
6.8 The effect of droplet density number on the shape of nozzle generated by the non-equilibrium design tool for the expansions from an inlet pressure of 500 (top) and 1000 kPa (bottom). 184
6.9 Streamwise variation of static pressure P in nozzles generated by the non-equilibrium and homogeneous-equilibrium design tools; the plot illustrates the design profiles and CFD predictions for the expansion from an inlet pressure of 500 and 1000 kPa, fixed inlet vapour quality of 0.3 and three droplet density numbers N_d: 10^{11}, 10^{12} and 10^{13}. 185
6.10 Streamwise variation of average relative velocity slip ($u_{slip,rel}$) and average thermal non-equilibrium ($T_L - T_V$) in the nozzles generated by the non-equilibrium (TFM) and homogeneous-equilibrium (HEM) design tools for the expansions from inlet pressure of 500 and 1000 kPa, a fixed inlet vapour quality of 0.3 and three droplet density numbers N_d: 10^{11}, 10^{12} and 10^{13}; $u_{slip,rel}$ is the velocity slip normalised by the mixture velocity, while $T_L - T_V$ is temperature difference between the liquid and vapour phases. 186

6.11 Two-dimensional variation of vapour quality in the nozzles generated by the non-equilibrium (TFM) and homogeneous-equilibrium (HEM) design tools for the expansions from inlet pressure of 500 and 1000 kPa, a fixed inlet vapour quality of 0.3 and three droplet density numbers N_d: 10^{11}, 10^{12} and 10^{13}. . . 187
6.12 Two-dimensional variation of mixture velocity in the nozzles generated by the non-equilibrium and homogeneous-equilibrium design tools for the expansions from inlet pressure of 500 and 1000 kPa, a fixed inlet vapour quality of 0.3 and three droplet density numbers N_d: 10^{11}, 10^{12} and 10^{13}. 188
6.13 The variation of mixture velocity and vapour quality along the centreline of the non-equilibrium nozzle designed for the expansion from an inlet pressure of 1000 kPa, inlet vapour quality of 0.3 and droplet number of 10^{11}; the dotted lines represent the streamwise location corresponding to a rapid flow acceleration. 189
6.14 Vapour and liquid velocity fields in the nozzles generated by the non-equilibrium and homogeneous-equilibrium design tools for the expansions from inlet pressure of 500 and 1000 kPa, a fixed inlet vapour quality of 0.3, and a fixed droplet density number of 10^{12} 189
6.15 The relationship between the inlet droplet diameter $D_{d,in}$ and outlet vapour mass fraction $x_{V,out}$, outlet mixture velocity $u_{mix,out}$, β and σ parameters. The β parameters represent the flow's capability to reach the design outlet conditions, while the σ parameters represent flow's uniformity at the nozzle outlet. The plot has been generated using CFD data obtained in the equilibrium and non-equilibrium nozzles. 191
6.16 The streamwise variation of the ratio of the average Weber number to the critical Weber number in the non-equilibrium nozzles; droplet breakup is expected to occur if the ratio We/We_{cr} exceeds unity (denoted by the black dotted line). The mixture was expanded from inlet quality of 0.3 for each presented case. 192
6.17 The streamwise variation of average vapour mass fraction (x_V), mixture velocity (u_{mix}), droplet diameter (D_d) and the ratio of average to critical Weber number (We/We_{cr}) in the expansion from an inlet pressure between 500 and 1250 kPa and a fixed inlet vapour quality of 0.3. The results were obtained using the non-equilibrium design tool and the CFD model. Droplet size in the non-equilibrium design tool was estimated based on the critical Weber number. The CFD model relied on the droplet diameter profile predicted by the design tool. 194

7.1 The breakup zone in the baseline (top) and 1D-optimised (bottom) nozzles expanding the two-phase mixture from 550 kPa and inlet quality of 0.3; the blue and orange stripes represent the control volumes used to approximate the breakup, which signify the location of breakup. 201
7.2 The relationship between the width of the volumes used to model the breakup and the streamwise variation of the average droplet diameter; the two plots correspond to the baseline (left) and 1D-optimised (right) nozzles expanding the two-phase mixture from 550 kPa and inlet quality of 0.3. 203

7.3 Streamwise variation of mass flow-averaged entropy for various grid sizes (left) and absolute difference in average entropy between the consecutive grids (right). 204
7.4 Three operating points investigated in the optimisation study; the expansions shown under the isentropic flow assumption 206
7.5 Baseline nozzle geometry for the expansion from 550 kPa. 207
7.6 Comparison of average streamwise variation of pressure between the quasi-1D design tool and CFD; the box in the top right presents a close-up of the variations near the nozzle outlet. 208
7.7 Comparison of average streamwise variation of vapour mass fraction (left) and velocity slip (right) between the quasi-1D design tool and CFD; the dotted lines represent the throat location. 209
7.8 The effect of the location of the Bezier control points location on the nozzle pressure profile. 210
7.9 Optimised pressure profiles (left); comparison of average streamwise variation of vapour mass fraction x_V predicted by the quasi-1D tool and CFD in the optimised geometries (right). 211
7.10 Comparison of CFD predictions of average streamwise variation of vapour mass fraction (left) and mass-flow average entropy (right) for the baseline and optimized (optm) pressure profiles; dotted lines represent nozzle sections with the most sudden entropy increase. 212
7.11 Two-dimensional contours of vapour quality in the baseline and optimised geometries; dotted lines correspond to the location of the most sudden entropy increase. 212
7.12 Liquid streamlines plotted for the baseline nozzle designed for the expansion from an inlet pressure of 550 kPa and an inlet vapour quality of 0.3. 213
7.13 Liquid streamlines in the proximity of the nozzle throat predicted by the baseline CFD model (left) and a CFD model with the lift force turned off (right); the figure was plotted for the baseline nozzle designed for the expansion from an inlet pressure of 550 kPa and an inlet vapour quality of 0.3. 214
7.14 Two-dimensional contours of static pressure in the baseline and optimised geometries. 215
7.15 Two alternative pressure profiles with the expansion shifted upstream and downstream respectively. The profiles were obtained by horizontally shifting the control points of the 1D-optimised pressure profile for the expansion from an inlet pressure of 550 kPa and an inlet vapour quality of 0.3. 216
7.16 Two-dimensional variation in vapour quality predicted in the 1D-optimised nozzle (middle) and two modified nozzle geometries with the nozzle throat shifted upstream (top) and downstream (bottom). The pressure profiles used to design the nozzle were very similar which results in nearly identical wall profile downstream of the throat. The nozzles were designed for the expansion from 550 kPa and an inlet vapour quality of 0.3. 217
7.17 The parametrisation of the nozzle used in shape optimisation. 217
7.18 Double inflection in the nozzle wall profile (top) due to an insufficiently high c_1 constant and excessive wall curvature (bottom) due to very high value of c_2. 219

7.19 Two-dimensional contours of vapour quality in the 1D-optimised and 2D-optimised geometries. 221
7.20 The Pareto front obtained in the multi-objective optimisation; the red circle denotes the optimal point. 222
7.21 Discretisation of the flow domain for implementing the combined droplet breakup and droplet number approach; the blue and orange stripes represent the control volumes used to approximate the breakup and droplet size decrease due to vapourisation under a constant droplet number density. The nozzle represents the CFD-optimised geometry designed for the expansion from an inlet pressure of 550 kPa and an inlet vapour quality of 0.3. 223
7.22 The comparison between droplet diameter and vapour mass fraction variation between the droplet breakup and a method combining droplet breakup with the droplet number approach. The results were obtained for the CFD-optimised nozzle designed for the expansion from 550 kPa and an inlet vapour quality of 0.3. 225

List of Tables

2.1 Main challenges in the design of alternative organic Rankine cycle architectures 28
2.2 The summary of performance of experimental and commercial units of two-phase volumetric expanders; VCR, CHP and RC stand for vapour compression refrigeration, combined heat and power and Rankine steam cycle respectively 49
2.3 The summary of performance of experimental and commercial units of two-phase turboexpanders; GTH and CRG stand for geothermal and cryogenic application respectively . . . 50
2.4 Critical properties and environmental indices of potentially suitable fluids for the wet-to-dry cycle. . . . 53

4.1 The summary of potentially suitable interphase models for simulating the wet-to-dry expansion. . . . 103
4.2 BNL309 boundary conditions . . . 110
4.3 BNL309 mesh independence study results . . . 112
4.4 Comparison of average mass outflow between the current study, other numerical studies and experimental data for the BNL309 run . . . 112
4.5 Additional BNL experimental runs simulated in the validation study. . . . 114

5.1 Geometrical features of each investigated converging-diverging nozzle. . . . 128
5.2 Sensitivity of the solution to the resolution of the look-up tables; the simulated expansion had an inlet pressure of 500 kPa and inlet vapour quality of 0.3. . 130
5.3 Mesh independence study results . . . 133
5.4 The summary of interphase models employed in the baseline two-fluid model setup. . . . 137
5.5 The summary of the interphase models considered for the sensitivity study. . 139
5.6 Geometrical features of the nozzles designed for the mass-flow rates of 0.12 and 0.50 kg/s. . . . 167

7.1 Mesh independence study results performed for the 1D-optimised nozzle. . . 204
7.2 Outlet vapour mass fraction predicted by the non-equilibrium design tool for different nozzle length to throat height ratios (L/o_{th}). . . . 206
7.3 Geometrical features of each investigated converging-diverging nozzle. . . . 207

7.4 The influence of the throat axial position on the average vapour mass fraction at the nozzle outlet ($x_{V,out}$) and nozzle efficiency (η_N). The results were obtained for the expansion from 550 kPa and an inlet vapour quality of 0.3. The alternative throat axial positions (X_{th}) were obtained by manipulating the 1D-optimised pressure profile. Baseline geometry results were included as a reference. 216
7.5 The results of the shape optimisation study; Run 1 corresponds to the multi-objective optimisation that aims to maximise the vapour generation rate and nozzle efficiency, while Run 2 corresponds to the single-objective optimisation that aims to maximise nozzle efficiency while satisfying the constraint: $x_{V,out} \geq 0.934$. 221
7.6 The effect of nozzle width and length on the average outlet vapour mass fraction ($x_{V,out}$) and nozzle efficiency (η_N). The results were obtained by modifying the width and length of the CFD-optimised nozzle geometry, while maintaining the same wall profile in the throat area. 222

A.1 The summary of user-defined expressions implemented in the simulation of the wet-to-dry expansion. 261
A.2 The summary of user-defined expressions implemented in the simulation of the breakup process in the the wet-to-dry expansion. 265

Acknowledgments

I would like to begin by expressing my gratitude towards my Lord Jesus Christ, for He has provided me with his grace and strength to complete this piece of work. Without Him, I would not be where I am today, and to Him I give all the glory for anything I can accomplish.

This research work would surely be impossible to complete without the support and guidance that I have received from my supervisor, Dr Martin White. What started as a summer internship under his supervision during my undergraduate studies turned into a great and exciting four-year PhD journey. I am so grateful that you have introduced me to the world of academic research and guided me throughout my doctoral candidature, ensuring that I will make it to the finish line without getting stuck halfway down the road. Thank you for all the regular meetings we have had in the past four years and all the valuable insights you have shared with me. You have truly been an example and an inspiration to me and have greatly contributed to my development as an independent researcher. I am also thankful to have been able to build on the foundations you have laid on the topic of two-phase expansion of organic fluids. Having had such a positive experience, I am approaching this finish line feeling inspired to explore new research frontiers and eager to pursue my career in academia.

I would also like to thank my other supervisor, Prof Abdulnaser Sayma, for his continuous support throughout my studies. I greatly appreciate every insightful discussion and advice that I have received from you in the last few years. Thank you for ensuring that I have always been well supported throughout this time.

I would like to express my gratitude to City, University of London for allowing me to complete these postgraduate studies and providing me with financial support in the form of a doctoral scholarship. At this point point, I would also like extend my gratitude to all my fellow doctoral students with whom I have shared this journey together.

Last but not least, my heartfelt thanks go to my family, who have encouraged and supported me through this often challenging time. In particular, I would like to thank my wife, Karolina, who made many sacrifices, especially after the birth of our son, to enable me to bring this research to completion. I am forever grateful.

Chapter 1

Introduction

1.1 Organic Rankine cycle

According to a recent report of the International Energy Agency, global energy-related emissions of CO_2 in 2022 was estimated to be approximately 36.8 Gt, with the electricity and heat generation alone accounting for around 40 % of these emissions [1]. The energy sector remains one of the primary contributors to the ongoing climate crisis. In an effort to address this problem, multiple countries have implemented strategies to move towards greater environmental sustainability, with the UK being one of the first major economies to set official targets to reach net-zero emissions by 2050 [2]. An important part of this transition is the utilisation of low-grade thermal energy, which represents heat sources at temperatures below 350 °C and/or sources with lower capacity below 1 MW_{th}. These sources may include certain renewable sources, such as geothermal reservoirs, solar energy, or biomass. There is also a substantial amount of low-grade heat that is wasted in fossil-fuel or nuclear power plants, as well as in various industrial processes [3–5]. The Rankine steam cycle applied in conventional power plants has been found unsuitable for low-temperature and small-scale applications, which is primarily related to the feasibility of designing a steam turbine under such conditions [6]. However, if the water is replaced by a suitable organic fluid, it is possible to design a cycle that has a relatively simple layout and an inexpensive expansion machine, extending the application of the Rankine cycle to lower temperatures and smaller power scales. Such a modification of the Rankine cycle is commonly known as an organic Rankine cycle (ORC) and relies on the working principle of conventional steam cycles.
Figure 1.1 illustrates the schematic of the simple organic Rankine cycle and the corresponding temperature-entropy diagram. First, the liquid is pressurised by a pump and passed through a primary heat exchanger, where it absorbs heat from the source and turns into a superheated vapour. High-temperature pressurised vapour is then passed through an expander where it generates useful mechanical work. Finally, the fluid leaving the expander is cooled and turned back into the liquid state. A recuperator is commonly incorporated in the cycle to recover heat from the expander exhaust and raise thermal efficiency of the plant. Because of the ability to select a working fluid from a wide range of available organic compounds, the cycle can be tailored to the application, offering high flexibility in terms of temperature level and power capacity. Figure 1.2 shows the range of application of ORC systems in terms

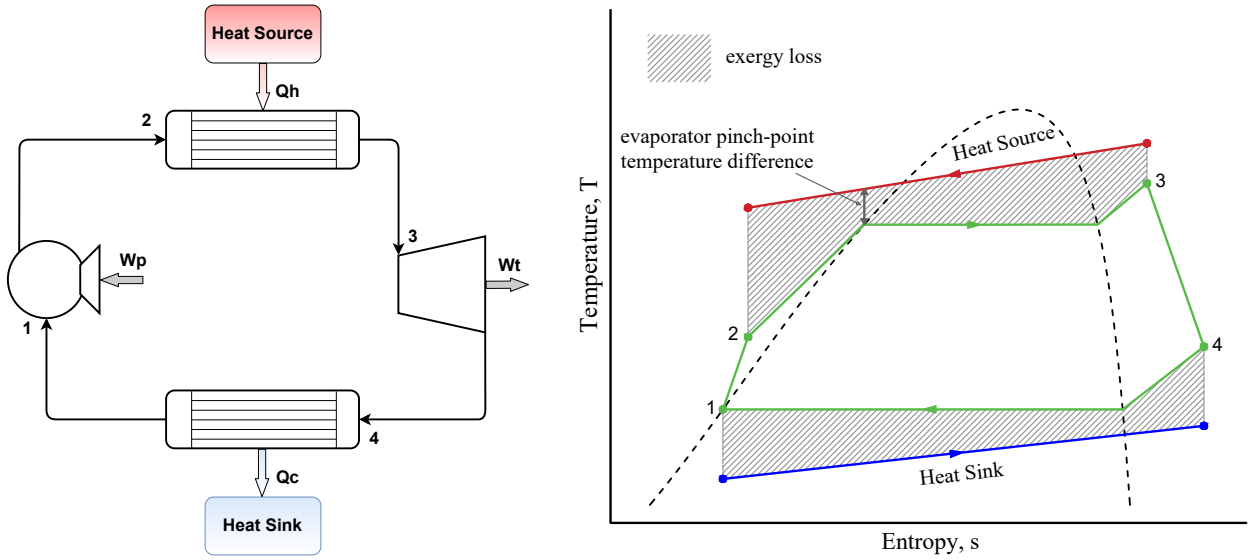


Figure 1.1: Schematic diagram (left) and temperature-entropy diagram (right) of the simple organic Rankine cycle.

of temperature level and power scale compared to other technologies. The organic Rankine cycle closes an important technological gap, providing a viable means of generating power from heat sources at a temperature between 80 and 400 °C and a power output that typically ranges from tens of kW to tens of MW [5]. With first commercial units commissioned in the 1970s and a total installed capacity estimated to exceed 4.5 GW [7], the technology has reached a moderate level of maturity. ORC systems have recently experienced an increased commercial uptake providing a viable means of exploiting low-temperature thermal sources.

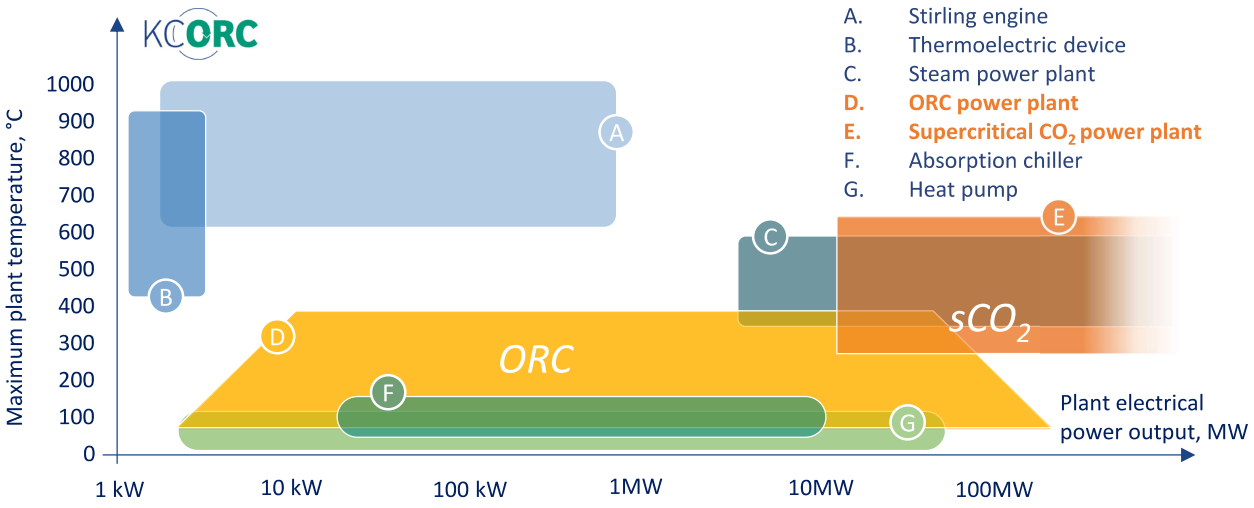


Figure 1.2: The range of applicability of ORC systems compared to other power generation technologies (figure retrieved from [5])

1.2 Limitations of the simple organic Rankine cycle

Although the simple ORC benefits from a simple system layout and has been implemented on a commercial scale, the cycle architecture poses some limitations when applied to certain types of energy sources. Taking for example a sensible (single-phase) open heat source and assuming that the heat stream does not serve a secondary purpose, such as heating of facilities, the optimal heat-source outlet temperature is typically unconstrained and the source can theoretically be cooled down to the environment temperature. In such applications, the emphasis is placed on maximising the net power output, which does not necessarily coincide with the highest thermal efficiency, as it only relates the generated power to the heat absorbed by the cycle and does not provide a direction indication as to how effectively all the available heat is being utilised. In such instances, it can be helpful to resort to exergy efficiency, which can be defined as the ratio of power output ($\dot{W}_{\text{out}}$) to the exergy of the heat source ($\dot{X}_{\text{src}}$):

$$\eta_{\text{ex}} = \frac{\dot{W}_{\text{out}}}{\dot{X}_{\text{src}}} \tag{1.1}$$

where $\dot{X}_{\text{src}}$ denotes the maximum work that can be produced from a given heat source as it is brought to equilibrium with the environment, taking into account the second law of thermodynamics. For a sensible heat source with a varying temperature, $\dot{X}_{\text{src}}$ is given as:

$$\dot{X}_{\text{src}} = \int \left(1 - \frac{T_0}{T_{\text{src}}}\right) d\dot{Q}_{\text{h}} \tag{1.2}$$

where $\dot{Q}_{\text{h}}$ is the heat exchanged between the source and the cycle within the integration interval, while T_{src} and T_0 represent heat source and environment temperatures. It can be readily shown that for an isothermal heat sink at equilibrium with the environment, the maximum exergy efficiency and thus the maximum power output is achieved when the heat source is cooled down to the temperature of the environment. In practice, the heat sink will usually have a finite heat capacity and variable temperature, but the optimum heat source outlet temperature will likely remain close to the heat sink inlet temperature [8]. Referring back to the temperature-entropy diagram from Fig. 1.1, it becomes apparent that the extent of heat source cooling in the simple ORC is limited by the cycle architecture and the pinch-point temperature difference in the evaporator (the minimum temperature difference between the heat source and the working fluid during heat addition). Consequently, the heat source leaving the heat exchanger may have a significant amount of useful exergy that is being wasted. Furthermore, the heat exchange in the evaporator is accompanied by a relatively large temperature difference between the heat source and the working fluid, which is a source of significant irreversibility and exergy loss as indicated in Fig. 1.1. In fact, previous thermodynamic analysis demonstrated that the evaporator is the major contributor to exergy destruction in organic Rankine cycles [9–12].

To overcome these limitations and mitigate the issues surrounding the isothermal evaporation, several alternative cycle architectures have been proposed, which include transcritical and trilateral flash cycles [13]. In the transcritical cycle, the heat addition takes place at

a pressure greater than the critical value and the working fluid transitions directly from a subcooled liquid to a superheated state, omitting the two-phase region. The heat addition in the trilateral flash cycle occurs at a sub-critical pressure, but the working fluid is only heated up to the saturated liquid state, where it undergoes a two-phase expansion. Both cycles aim at minimising the mean temperature difference between the working fluid and the heat source, which can potentially lead to greater heat-source utilisation and higher power outputs [14–17]. Zeotropic mixtures have also been considered due to the possibility of achieving non-isothermal evaporation and condensation, which leads to reduced exergy destruction in the heat exchangers [18–20].

Beside the need for larger heat changers stemming from increased amount of heat absorbed, each cycle presents its own challenges. High operating pressures requires stronger system components and may affect the capital cost of transcritical cycles [21]. Trilateral flash cycles require an expander that can tolerate two-phase conditions, while matching the efficiency of single-phase machines. This can be particularly challenging given the large density difference between the saturated liquid at the expander inlet and two-phase mixture at the expander outlet, which implies large volumetric expansion ratios [22]. The phenomena of composition shift and mixture fractionating can limit the attainable temperature glide and affect thermal performance of cycles based on zeotropic mixtures.

1.3 Wet-to-dry cycle

More recently, a novel type of organic Rankine cycle has been explored, which relies on partial evaporation of the working fluid prior to the expansion. Since it is a subcritical type of cycle, it does not typically require as high operating pressures as the transcritical cycle, while partial evaporation can mitigate the issue of excessive volumetric expansion ratios typical of the trilateral flash cycle. Theoretical and experimental studies indicate that partial evaporation can provide a means of increasing exergy efficiency and power generation from low-temperature heat sources [23–26]. Despite reduced volumetric expansion ratio with respect to expansion from a saturated liquid state, designing an efficient two-phase expander remains a challenge. Volumetric expander have traditionally been considered suitable for wet expansions, however, due to limited built-in volume ratio of these machines, their application is typically restricted to low-temperatures, up to the limit of 150 °[27]. On the other hand, turboexpanders can achieve higher expansion ratios, but the presence of liquid is likely to lead to blade erosion, performance deterioration and increased rate of wear. For this reason, two-phase flow in turbomachinery has generally been avoided.

Within an array of available organic compounds, there exist fluids of high molecular complexity that can have a positive slope of the saturated vapour curve when viewed on the temperature-entropy diagram (Fig. 1.3). Employing such fluids, it is theoretically possible to design a partially-evaporated cycle in which the the expanding fluid transitions from a two-phase state to a superheated vapour regime as indicated on the temperature-entropy diagram shown in Fig. 1.3. Such a cycle architecture was first proposed by Elliot in 1982 [28], and it is referred to as a wet-to-dry cycle.

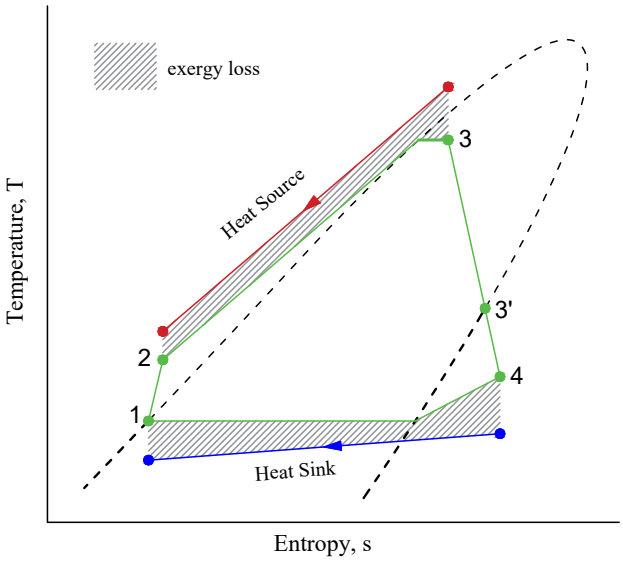


Figure 1.3: Wet-to-dry organic Rankine cycle

In terms of thermodynamic performance, the wet-to-dry cycle can offer similar advantages to the partially-evaporated ORC. It lowers the mean temperature difference in the primary heat exchanger, allowing to absorb more heat from the source and consequently generate more power. Owing to the wet-to-dry transition, the cycle may benefit from greater flexibility concerning the expander selection. Namely, turboexpanders, which have traditionally been discarded due to erosion concerns, could potentially be used so long as the wet portion of the expansion (3-3' in Fig. 1.3) is confined to the turbine nozzle. Having a turbine that could accept two-phase inlet conditions could also be an advantage in off-design operation of ORC systems [29]. The first cycle study was performed by Elliot in the 1980s [28], who found that the wet-to-dry cycle using toluene could offer considerably higher utilisation efficiencies (ratio of the power output to the available heat) compared to conventional single-phase ORC. The concept has only been recently revisited by White [8], who demonstrated that using suitable organic fluids, such as the siloxane MM, the wet-to-dry cycle can potentially generate up to 30% more power from open heat sources at temperatures between 150 and 250 °C.

1.4 Wet-to-dry expansion

Prior research suggests that the wet-to-dry cycle may outperform the single-phase ORC when it comes to power generation from low-temperature open heat sources. Since the fluid can theoretically escape the two-phase dome during expansion, turbomachines can potentially be used, extending the application range of two-phase cycles to temperatures above 150 °C, where the volumetric expanders may struggle due to a limited built-in volume ratio. The critical component of a turbine designed for the wet-to-dry cycle is the nozzle (also referred to as the stator), which must facilitate a complete mixture vapourisation to avoid presence of liquid droplets within the rotor, thus eliminating the erosion concerns. The nozzle should

also deliver a uniform vapour flow in an efficient manner to ensure high performance of the entire machine.

The process in which the working fluid transitions from a two-phase mixture to a superheated vapour in the wet-to-dry cycle is known as flash boiling or simply flashing. It occurs when a liquid, or as in this case, a two-phase mixture, is subjected to a sudden depressurisation, such that its pressure drops below the saturation level. In case of the wet-to-dry cycle, the cause of fluid depressurisation is the rapid acceleration of the two-phase mixture in the turbine nozzle. Existing research has mostly revolved around flash boiling of subcooled or saturated liquids, which is of direct relevance to a variety of technical scenarios, such as flows through cracks and restricted areas (e.g. orifices, valves) or liquid expansion through nozzles and injectors. It has been extensively studied both experimentally and numerically in the context of nuclear safety analysis [30]; specifically in the context of loss of coolant accidents [31], flow-induced instabilities in passive containment cooling systems [32], and flows through pressure relief valves [33] and nozzles [34, 35]. Flashing can also occur in two-phase ejectors designed to replace throttle valves in refrigerations systems [36–38]. In the context of power generations systems, flash boiling has been studied in two-phase geothermal turbines designed for expansion of water [39–42].

Although, the phase-change process taking place in a nozzle designed for the wet-to-dry turbine can be classified as flash boiling, the process differs from the majority of previously investigated flashing flows. Conventional flashing refers to the vapourisation of bulk liquid as it undergoes a sudden depressurisation. Since in the wet-to-dry nozzle, flashing begins with a partially evaporated mixture, where the secondary phase is likely to be in the form of dispersed droplets, flashing refers to the vapourisation of these discrete liquid droplets. In contrast to conventional flashing, where the process involves formation of vapour bubbles in superheated liquid (nucleation process), nucleation is not part of the wet-to-dry expansion. As such, existing nucleation models cannot be directly applied to simulate the formation of the dispersed phase. Furthermore, most of prior research has been devoted to flash boiling of water, whereas this study is concerned with flash boiling of molecularly complex fluids, such as the siloxane MM, which can display significant non-ideal behaviour. As such, any fine-tuned empirical coefficients that have previously been developed to simulate flash boiling of water (e.g. relaxation factors) should be applied with caution. These empirical coefficients define the rate of phase change and influence the distribution of phase volume fraction within the nozzle, consequently affecting the characteristics of the two-phase expansion. Therefore, the application of such empirical constants derived for water may carry significant uncertainty when applied to molecularly complex fluids, such as the siloxane MM. The combination of all these factors makes the wet-to-dry expansion a substantially different process from most studied flashing flows.

To the best of the author's knowledge, there exist no suitable experimental data that could be used to assess the feasibility of designing a wet-to-dry nozzle. Therefore, the concept is currently being assessed with the aid of numerical tools. Numerical modelling of flashing flows is a complex task that requires a simultaneous simulation of mass, momentum, and energy exchange between the two phases. Owing to the density difference, the liquid and

vapour phases may develop a disparity in their velocities, while a finite rate of interphase heat transfer can lead to thermal non-equilibrium with the possibility of both phases entering metastable states (superheated liquid or subcooled vapour), deviating from the local saturation temperature. The disparity in velocity and temperatures is referred to as non-equilibrium effects, which can significantly affect the phase change process and add to the complexity of modelling such flows. In the case of wet-to-dry cycle, the non-equilibrium effects are particularly relevant due to rapid flow acceleration to supersonic speeds within a relatively short channel, which implies small time scales for interphase exchange of momentum and heat.

In summary, modelling flashing flows is a complex task and has frequently been approximated with simplified approaches that either assume a one-dimensional flow or neglect the non-equilibrium effects. The first known study on the wet-to-dry expansion in a converging-diverging nozzle was conducted by Elliot [28], who used a one-dimensional code accounting for the velocity slip but assuming thermal equilibrium between the phases (saturated conditions). The author simulated an expansion of toluene from an inlet temperature of 289 °C (2847 kPa) and vapour quality of 1% to an outlet temperature of 70 °C (27.19 kPa) in a converging–diverging nozzle. The results seem promising as complete mixture vapourisation was predicted, while the nozzle efficiency was estimated to be in the order of 98%. White [8] carried out three-dimensional CFD simulations of the wet-to-dry expansion of the siloxane MM in a radial-inflow turbine stator designed for expansion from an inlet pressure of 500 kPa and vapour quality of 0.3. Although the CFD model predicted complete mixture vapourisation within the stator with efficiencies more than 90%, non-equilibrium effects were ignored. In a subsequent study [43], the author developed a non-equilibrium model one-dimensional code to investigate two-phase expansion of the siloxane MM in a converging-diverging nozzle under a range of operating conditions relevant to the wet-to-dry cycle. The presence of non-equilibrium effect generally delayed the phase change, which in some cases, led to incomplete vapourisation. The delay in the phase-change process translates to higher liquid content at a given streamwise location inside the nozzle, which generally affects the compressibility of the flow. In flash boiling of subcooled water in converging-diverging nozzle, the phase-change delay associated with non-equilibrium effects generally led to increased mass-flow rates [44]. This is due to the fact that even limited vapourisation brings a significant increase in vapour volume fraction, which increases the compressibility of the two-phase mixture and consequently reduces the speed of sound. This effect may be less pronounced in the wet-to-dry expansion because the mixture is already partially evaporated at the nozzle inlet. Nevertheless, the phase-change delay still affects the distribution of phases inside the nozzle, leading to modified pressure, velocity and temperature fields compared to equilibrium flows. This points to the necessity of including non-equilibrium effects in a realistic assessment of the wet-to-dry expansion.

Although the recent study of White [43] considered the non-equilibrium effects, the two-phase expansion was substantially simplified by assuming an inviscid one-dimensional flow. As a consequence of the simplifications, the multidimensional effects could not be assessed. These effects include internal phase separation occurring due to a large difference in phase densities and the associated high relaxation times of heavier liquid droplets. The spatial

distribution of the droplets could also be affected by certain interfacial forces, such as lift and turbulent dispersion forces. The influence of viscosity and turbulence was also ignored. Beside those limitations, no prior study is known to have explored the effect of nozzle shape on the wet-to-dry expansion. Shape optimisation techniques, such as metamodel-assisted optimisation algorithms could potentially be applied to optimise the two-phase nozzle and provide further insight into the feasibility of achieving the wet-to-dry transition in practical nozzles.

1.5 Scope of research

Previous research endeavours dedicated to simulating the wet-to-dry expansion in converging-diverging channels were either simplified by neglecting the non-equilibrium effects or by assuming an inviscid one-dimensional flow. A comprehensive numerical assessment that simultaneously accounts for the non-equilibrium effects, multidimensional effects as well as the influence of viscosity and turbulence is currently missing. Moreover, no form of optimisation is known to have been previously applied to such two-phase nozzles. Given these research gaps, further research is deemed necessary to evaluate the concept of designing a two-phase turboexpander for the wet-to-dry cycle.

In the light of the above, the primary aim of this work is to assess the feasibility of designing a two-phase nozzle that would facilitate complete mixture vapourisation in an efficient manner under conditions relevant to the wet-to-dry cycle. To achieve this aim, the two main objectives are set as follows:

1. Investigate the flash boiling in a converging-diverging nozzle under a range of operating conditions relevant to the wet-to-dry cycle and provide insight into the phase-change characteristics, considering the non-equilibrium effects, multidimensional flow variations and the effects of viscosity and turbulence.

2. Optimise the two-phase nozzle and investigate the influence of nozzle shape on the phase change process and the performance of the nozzle.

Fulfilling the two objectives outlined above will require completing several specific tasks:

- Implement and validate a non-equilibrium flash-boiling model in a suitable CFD solver to perform multidimensional viscous simulations of the wet-to-dry expansion.

- Apply the CFD model to conduct a parametric study to assess the influence of operating conditions on the wet-to-dry expansion of the siloxane MM in a converging-diverging nozzle.

- Study the effect of including non-equilibrium effects in the nozzle design process.

- Apply a previously developed non-equilibrium nozzle design tool to optimise the nozzle pressure profile, aiming at maximising the vapourisation rate.

- Conduct CFD-based shape optimisation study to directly optimise the nozzle shape, aiming at maximising the vapourisation rate and nozzle efficiency.

1.6 Thesis outline

This thesis is composed of eight chapters. Following the introduction, Chapters 2 and 3 provide relevant background and literature review, while the research methodology is presented in Chapter 4. The results of non-equilibrium CFD simulations are reported in Chapters 5 and 6, while the results of the optimisation study are described in Chapter 7. The thesis is concluded with Chapter 8 that summarises the conducted research, presents the main conclusions and gives recommendations for future work. A more detailed breakdown of the thesis is given below.

Chapter 2 covers the fundamentals of the organic Rankine cycle, outlining the primary limitations of the single-phase cycle architecture applied in such systems. The potential and challenges of alternative cycle architectures for improved power generation from open heat sources is discussed. With an efficient two-phase expander identified as the main challenge in the design of two-phase organic Rankine cycles, the chapter follows with a review of two-phase expansion machines. The performance of previously tested two-phase volumetric expanders and two-phase turboexpanders is reviewed, revealing the challenge of designing an efficient two-phase expander for temperatures greater than 150 °C. The chapter is concluded with an introduction of the wet-to-dry cycle as an alternative to the simple organic Rankine cycle for improved power generation from open heat sources. The concept of two-phase turboexpander is proposed, which relies on complete mixture vapourisation in the nozzle component, thereby removing the main concern surrounding the blade erosion.

The key characteristic of the proposed two-phase turboexpander is a nozzle that has to facilitate complete mixture vapourisation. Due to a lack of directly relevant experimental data, the concept is assessed using numerical tools. In Chapter 3, potentially applicable numerical methods for simulating the wet-to-dry expansion in a converging-diverging nozzles are discussed. Two-phase flow modelling frameworks, including the Eulerian-Lagrangian and Eulerian-Eulerian frameworks are covered. Several flash-boiling models are discussed with the aim of identifying the most suitable technique for the current problem. The challenges concerning the simulation of the wet-to-dry expansion are explained, followed by a summary of the scope of this work.

In Chapter 4, the research methodology is outlined, which is mainly focused around the two-fluid model, which is deemed a suitable modelling technique for the wet-to-dry expansion. A detailed description of the two-fluid model is included, covering the governing equations and the interphase models that are applied to simulate the exchange of mass, momentum and energy between the liquid and vapour phases. Numerical implementation in a commercial CFD code is discussed followed by a validation study based on available empirical data taken for flash boiling of water in a converging-diverging nozzle. The selected CFD simulation platform provides a framework for implementing the two-fluid model that has been applied to simulate non-equilibrium flashing in this work. Within that framework, separate mass, momentum and energy conservation are solved, while an array of built-in functions is available for predicting interfacial forces as well as the heat transfer rate between the two

phases. A built-in thermal phase-change model allows the vapourisation rate to be calculated based on the interphase heat transfer rate. The solver also includes built-in models for modelling turbulence in each phase. Most of the employed models were already available in the solver, however some parameters, such as liquid-side heat-transfer coefficient and turbulent dispersion coefficient had to be modelled using user-defined expressions. Thermodynamic properties of the vapour and liquid phases were evaluated using look-up tables generated using REFPROP 10.0, which were coupled with the solver.

The first part of the current analysis concerning the wet-to-dry expansion in converging-diverging nozzles is documented in Chapter 5, beginning with the description of the nozzle design method that is based on an assumption of a homogenous-equilibrium flow. Prior to conducting further analysis, a sensitivity study is performed, aimed at assessing the influence of the interphase models on the two-phase expansion. More specifically, several potentially applicable models for estimating drag, lift and turbulent dispersion effects are investigated alongside alternative models for evaluating the heat-transfer rate between the two phases. Following the sensitivity analysis, the parametric study is undertaken, where the two-phase expansion of the siloxane MM is simulated under a range of thermodynamic conditions relevant to the wet-to-dry cycle. Inlet pressures varying between 500 and 1250 kPa are considered, while inlet vapour qualities between 0.1 and 0.5 are assessed. A constant number of droplet per unit volume is assumed, which ranges from 10^{11} to 10^{13}. At this point it is worth noting that assuming a constant number of droplets per unit volume is a certain simplification as the potential effects of breakup or coalescence cannot be accounted for. It is known that some authors investigating flashing of liquids implemented a transport equation for the bubble number density or the interfacial area. Such transport equations are typically applied in conjunction with nucleation models to predict the birth rate and size of the dispersed vapour bubbles. Additionally, breakup and coalescence mechanisms can be included. Since the current work is concerned with flashing of partially evaporated mixtures, the nucleation models cannot be directly applied to predict the number of liquid droplets. Although, the breakup mechanism may remain important, the first part of study is focused on assessing the general phase-change characteristics under a range of relevant thermodynamic conditions. As such, an assumption of a constant number of droplets in the range of 10^{11} to 10^{13} droplets per unit volume was deemed adequate for the parametric study. The bottom limit of this range has been decided based on droplet breakup consideration, while the upper limit corresponds to conditions that begin to resemble a homogeneous-equilibrium flow. The results of the parametric study help understand the physics of the wet-to-dry expansion in various operating conditions. Streamwise profiles of vapour mass fraction are analysed to investigate the vapourisation rate, while the significance of non-equilibrium effects is assessed through average velocity slip and temperature difference between the phases. The performance of the nozzle design tool based on the homogenous-equilibrium tool is evaluated by comparing the design and simulated expansions. Furthermore, two-dimensional variations of vapour quality and mixture velocity are studied, revealing the uniformity of the two-phase flow. Finally, preliminary droplet breakup analysis is conducted to assess the possible breakup effects. The results reported in Chapter 5 help understand the physics of the wet-to-dry expansion and provide a link between the phase change process, thermodynamic conditions and droplet size. The relationship between optimal cycle operating conditions and possibility

of achieving complete mixture vapourisation is identified.

The nozzles analysed in Chapter 5 were designed based on the assumption of a homogenous-equilibrium flow. Considering the substantial disparity in the velocity and temperature of liquid and vapour phases, it is reasonable to suspect that including the non-equilibrium effects in the nozzle design process may considerably affect the two-phase flow characteristics. This is addressed in Chapter 6, where a previously developed non-equilibrium nozzle design tool is employed to generate nozzle geometries for a parametric study similar to the one reported in Chapter 5. An overview of the design tool is provided and the main differences between the equilibrium and non-equilibrium nozzles are identified. Similar to the parametric study, the vapourisation rate, mixture velocity profiles, the significant of non-equilibrium effects, the flow capability to expand to the design outlet conditions and the flow uniformity are assessed in the nozzles designed with the non-equilibrium tool. These are compared against the simulations performed for the equilibrium nozzles to evaluate the importance of including the non-equilibrium effects at the design stage.

The nozzle optimisation study is undertaken in Chapter 7. The optimisation study is carried out in two stages. First, the non-equilibrium design tool investigated in Chapter 6 is applied to perform one-dimensional optimisation. The main objective of the one-dimensional optimisation is to maximise the vapourisation rate by optimising the nozzle pressure profile imposed during the design process. The optimised nozzles are analysed using non-equilibrium CFD simulations to verify the optimisation results. In the second stage, the optimisation is performed directly using the CFD solver. A novel approach is proposed for modelling breakup in two- and three-dimensional numerical simulations. The nozzle wall is parametrised and shape optimisation is carried out using a metamodel-assisted genetic algorithm, aiming to maximise the vapourisation rate and nozzle efficiency.

The thesis is concluded with Chapter 8, which summarises the main findings and conclusions from each research section. Lastly, recommendations are provided for future research dedicated to the wet-to-dry expansion.

1.7 Publications

The following list summarises journal publications and conference presentations related to the content of this thesis.

1. Ogrodniczak, P., Sayma, A., & White, M. T. (2024). Optimisation of a converging-diverging nozzle for the wet-to-dry expansion of the siloxane MM. *Applied Thermal Engineering*, 260, 124870. DOI: 10.1016/j.applthermaleng.2024.124870.

2. Westpfel, C., Ogrodniczak, P., & White, M. T. (2024). Design of a Two-Phase Blowdown Test Facility. In *5th International Seminar on Non-Ideal Compressible Fluid Dynamics*, 30-31st October, Lyon, France.

3. Ogrodniczak, P., & White, M. T. (2023). Non-equilibrium CFD simulation of the wet-to-dry expansion of the siloxane MM in a converging–diverging nozzle. *Applied Thermal Engineering*, 234, 121158. DOI: 10.1016/j.applthermaleng.2023.121158.

4. Ogrodniczak, P., Sayma, A., & White, M. T. (2023). Pressure profile optimisation of a nozzle for wet-to-dry expansion. In 7^{th} *International Seminar on ORC Power Systems*, 4-6$^{\text{th}}$ September, Seville, Spain.

5. Ogrodniczak, P., White, M.T. (2023). Numerical Validation of a Two-Phase Nozzle Design Tool Based on the Two-Fluid Model Applied to Wet-to-Dry Expansion of Organic Fluids. In: White, M., El Samad, T., Karathanassis, I., Sayma, A., Pini, M., Guardone, A. (eds) *Proceedings of the 4^{th} International Seminar on Non-Ideal Compressible Fluid Dynamics for Propulsion and Power. NICFD 2022*. ERCOFTAC Series, 29, pp.103-113. Springer, Cham. DOI: 10.1007/978-3-031-30936-6_11.

Chapter 2

Background and motivation

2.1 Introduction

In 2015, more than 190 countries signed the Paris Agreement, a legally binding treaty that seeks to address the climate change crisis and limit global warming to below 2 °C (compared to pre-industrial levels) by the end of the 21st century [45]. Since scientists anticipate that exceeding the average temperature by 1.5 °C may bring adverse weather changes, such as extreme heats, floods, and droughts, multiple countries have decided to pursue additional efforts to limit global warming to 1.5 °C, with the UK being one of the first major economies to set official targets to reach net zero emission of greenhouse gases by 2050 [2]. According to the most recent report of the International Energy Agency, the energy sector has the highest share of global CO_2 emissions, having reached an annual emission of 14.65 Gt of CO_2 in 2022, which is more than 39 % of total global emissions [1]. The traditional method of generating electricity and heat, which is based on burning fossil fuels, produces large amounts of CO_2 and other greenhouse gases. Reducing dependence on fossil fuels is therefore essential in mitigating the current climate crisis.

Since there are a variety of renewable or renewable-equivalent energy sources available at temperatures between 80 and 400 °C [6], the development of technologies suitable for utilisation of such low-temperature sources plays an important role in the global transition of the energy sector towards greater environmental sustainability. The energy sources available within this temperature range include geothermal reservoirs, solar energy, and biomass resources [6]. In addition to renewable energy sources, there is great potential in utilising waste heat from various industrial processes, such as the production of iron, steel, nonferrous materials, cement and glass, as well as chemical and petrochemical processes [3, 4]. Waste heat coming from existing power plants could also be utilised to raise the efficiency of these plants (e.g. bottoming cycles). According to the recent report of the Knowledge Center on Organic Rankine Cycle technology, there could be as much as 150 TWh of electricity generated from industrial waste heat in Europe, which amounts to approximately 5% of the total electricity demand in the EU [5]. More than 68% of that waste heat is estimated to be at temperatures below 500 °C. Although waste heat could be reused directly (e.g. heating of facilities), this strongly depends on current demand, and it may not be an effective solution on all occa-

sions. On the other hand, electricity can be easily transported and used for a wide variety of applications, making it a more versatile and flexible form of energy. Therefore, cost-effective and efficient technologies for generating electricity from low-temperature heat sources can contribute substantially to the global shift toward an environmentally friendly energy sector.

2.2 Rankine cycle

The power cycle commonly applied in fossil-fuel power plant is the steam Rankine cycle. Figure 2.1 shows a schematic of a steam Rankine cycle. The cycle consists of four basic components: a pump, an evaporator, an expander, and a condenser. Water first enters the pump as a subcooled or saturated liquid, where its pressure is raised to the required level (1 to 2). It then travels through the evaporator, where it absorbs heat Q_h from the heat source (2 to 3). Once the liquid is fully vapourised, it is often superheated before entering the expander to limit condensation during expansion process. The high-temperature pressurised vapour is then passed through the expander (3 to 4), where usable mechanical power W_t is generated, which can be used to drive a generator and generate electricity. The fluid leaving the expander flows through the condenser (4 to 1), where it rejects excess heat Q_c to the heat sink and turns back into a saturated or subcooled liquid. The working fluid is then ready to be admitted back to the pump, and the cycle repeats. Figure 2.1 also shows each cycle process on a temperature-entropy diagram, which is helpful for describing and visualising thermodynamic cycles.

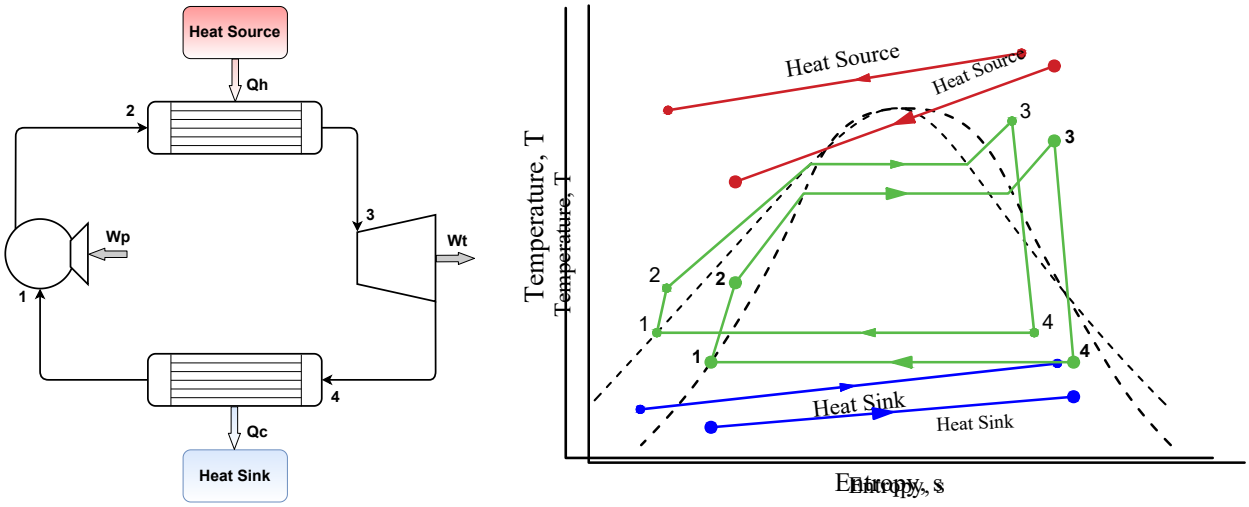


Figure 2.1: Schematic of the steam Rankine cycle

Owing to the simple plant layout and comparatively high thermal efficiency, the Rankine cycle has been the preferred power cycle in applications with moderate temperature levels, between 400 and 600 °C. However, for temperatures below 400 °C, which frequently corresponds to the temperature level of renewable or waste-heat sources, the design of the steam

Rankine cycle poses certain technical difficulties, which can affect its techno-economic viability for such applications. It is also not the best technology for smaller power scales, below several MW, which can often be encountered in waste-heat recovery systems. Therefore, electricity generation technologies for such decentralised energy systems must be technically and economically viable at low capacities and temperatures. The unsuitability of steam cycles at low temperatures (<400 °C) and/or small power outputs (<1 MW) is mainly related to the issues surrounding the design of the steam turbine. Water is characterised by comparatively high enthalpy drops and pressure ratios across the expansion process [46]. If a single-stage steam turbine is to be used under such conditions, it is likely that supersonic conditions in the rotor will develop accompanied by extremely high blade speeds and volumetric expansion ratios [6]. Therefore, the design of a steam turbine for lower-temperature applications would require more complex and costly multi-stage architectures. If it were to be constructed for smaller power scales, below 1 MW, high enthalpy drops could imply very small mass flow rates, requiring partial admission architectures and/or very high rotational speeds [6]. Water having a negative slope of the saturated vapour curve as viewed on the temperature-entropy diagram (Fig. 2.1) tends to condensate during expansion; an effect more pronounced at low temperatures. Liquid formation during expansion raises erosion concerns within the expander and can lead to performance deterioration. Moreover, low vapour pressure of water at low temperatures can lead to excessively large condenser sizes [47]. The combination of all these factors makes water an unsuitable working fluid for exploiting heat sources at temperatures below 400 °C.

2.3 Organic Rankine cycle

The unsuitability of the steam Rankine cycle for the exploitation of low-temperature thermal sources has been discussed in the previous section. However, water can be replaced with organic fluids that are typically characterised by significantly lower specific enthalpy drops across the expansion process, allowing inexpensive single-stage turbine designs. Moreover, higher mass flow rates can be achieved for low power outputs, which extends the design feasibility to small-scale applications [48]. If certain organic fluids with a positive slope of the saturated-vapour curve are employed, condensation-free expansions can be achieved at low temperatures, eliminating the concerns related to wet expansion (see Fig. 2.2). Thus, if water is replaced by an organic compound, a simple plant layout with an inexpensive expander can be designed, making the utilisation of low grade thermal energy sources feasible and more economical [6]. Such a modification of the Rankine cycle is called an organic Rankine cycle (ORC) and it has the same operating principle and system components as the Rankine cycle illustrated in Fig. 2.1.

An advantage of organic Rankine cycles is the possibility of selecting the working fluid from a wide range of organic compounds, such that it can be tailored from a thermodynamic and technical point of view for a given application. Figure 1.2 [5] provides an illustration of how the organic Rankine cycle fills a technological gap, being capable of generating power from heat sources at temperatures between 80 and 400 °C. The ORC systems are also flexible in terms of power capacity, which ranges from micro several-kilowatt applications to large-

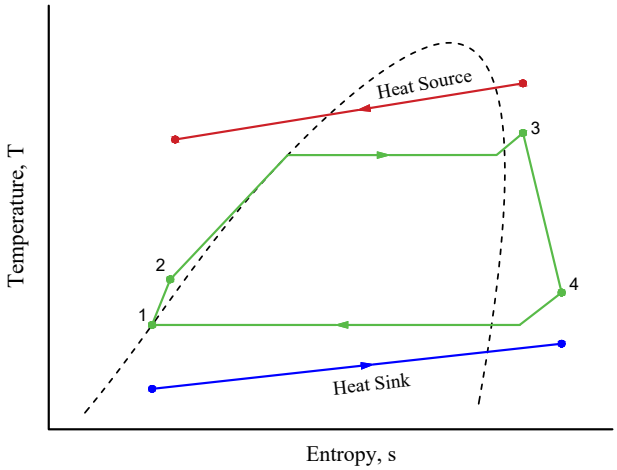


Figure 2.2: Temperature-entropy diagram of a simple organic Rankine cycle; the positive slope of the saturated-vapour curve ensures condensation-free expansion.

scale multi-megawatt installations. Thanks to its flexibility in terms of temperature level and power capacity, the ORC is one of the most suitable technology for power generation from low-temperature heat sources [47]. With the first commercial units commissioned in the 1970s, ORC technology has reached a moderate level of maturity [49]. The potential of ORC systems is reflected in the recent increased commercial uptake of these systems. A recent market survey by Wieland et al. [7] estimates a 40% rise in the installed capacity of ORC systems between 2016 and 2020, with a total installed capacity of around 4.07 GW as of 2020 [7]. Two of the most developing areas of application of ORC systems include geothermal and waste-heat sources, with the first having the largest installed capacity share and the latter the highest number of newly commissioned units.

Despite the increasing share in the green energy sector and promising future forecasts, there remains several factors that may hinder wider adoption of the ORC systems. The first challenge becomes apparent when the Carnot efficiency (Eq. 2.1) is analysed, which sets the upper limit to the efficiency of a heat engine operating between two heat reservoirs.

$$\eta_{Carnot} = 1 - \frac{T_c}{T_h} \tag{2.1}$$

The Carnot efficiency is a useful measure to estimate the potential performance of a heat engine operating with a given heat source. It is clear that the difference in temperature between the heat source T_h and the heat sink T_c should be as large as possible to maximise thermal efficiency. In most systems, the cooling medium is one available in the surroundings of the plant (e.g. ambient air or water reservoir). Therefore, in practice, there is little control over T_c, and the Carnot efficiency will be determined by the temperature of the available heat source. Since the ORC is to be applied to low-temperature sources (low T_h), this is inherently related to low cycle efficiencies. For instance, if the ORC is to utilise a thermal source at 200 °C, the maximum theoretical efficiency is limited to about 38 %, assuming isothermal heat sink at 20 °C. On the other hand, the Carnot efficiency for a large-scale

coal-fired power plant, operating with heat-source temperature in the range of 540-600 °C [50], is in the range of 63 to 66 %. The actual cycle efficiencies will be significantly lower than the theoretical upper limits, but the comparison indicates that for a fixed amount of absorbed heat, a much smaller fraction can be transformed into useful mechanical power in the case of low-temperature ORC systems. This has obvious implications for the ratio of the heat exchanger size to the net power output, which in turn translates to higher relative system component costs. Furthermore, unlike the Rankine steam cycle, the power required to run the feed pump in ORCs may account for a significant fraction of the gross power output due to lower latent heat of vapourisation of organic fluids compared to steam [51]. Low cycle efficiency combined with relatively large heat exchangers and high feed-pump power requirements often makes it more challenging to achieve satisfactory economic performance. In other words, the investment cost per one kilowatt of generated power can be too high to be commercially attractive.

Generally, the lower the temperature of the heat source, the more difficult it is for the system to be economically viable. For example, previous analyses of the potential of organic Rankine cycle for waste-heat recovery excluded heat sources at temperatures below 250 °C when economic aspects, such as energy prices and system installation costs, were taken into account [5]. On the other hand, a significant fraction of total industrial waste heat is estimated to be at temperatures below 200 °C [52]. One of the characteristics of alternative energy sources is their diversity in thermal energy capacity. Taking the example of industrial waste heat, the thermal energy load can be highly dependent on the size of the facility and the type of industrial process. Hence, the power capacity of such systems can significantly differ from one application to another, ranging from tens of kilowatts to multi-megawatt installations. Therefore, in areas such as waste-heat recovery, it would be desirable for the ORC systems to be a viable technical solution for a wide range of power capacities. Tocci et al. [53] compared the investment cost of various power generation technologies on a power scale ranging from 5 to 1000 kW. Although the trend varies from technology to technology, the cost of the system per kilowatt of generated power generally decreases with installed capacity. For example, the investment cost per kW of generated power of a 50 kW system is expected to be around 30% higher than that of a 500 kW system [53]. Hence, the payback periods for smaller-scale systems are likely to be considerably longer, and such systems could be less attractive to investors. In their recent review on ORC systems, Wieland et al. [13] identified the payback periods to be one of obstacles in the broader commercial adoption of ORC technology in waste-heat recovery, which necessitates further research to improve the techno-economic performance of these systems.

In summary, organic Rankine cycles are proven to be a suitable technology for heat-to-power conversion from thermal sources at temperatures between 80 and 380 °C. Despite their potential, there are still challenges and limitations to overcome to make ORC systems economically attractive, especially at temperatures below 200°C and smaller power scales in the order of a few hundreds of kilowatts. For this reason, further research efforts are needed to improve the performance of ORC systems and allow for wider commercialisation. The following sections will elaborate on the primary limitations of the simple organic Rankine cycles and possible alternative cycle architectures that could offer significant performance

advantages.

2.4 Limitations of simple organic Rankine cycle

A performance metric traditionally used in the analysis of thermodynamic cycles is the thermal efficiency, expressed as the ratio of net power output to the amount of heat absorbed by the cycle.

$$\eta_{th} = \frac{\dot{W}_{out}}{\dot{Q}_h} \tag{2.2}$$

Although it provides an indication as to how effectively the cycle transforms the absorbed heat to mechanical power, it may not be the best performance indicator in all cases. For instance, if there is a sensible (single-phase) open heat source that serves no secondary purpose such as facility heating, the emphasis is placed on maximising the net power output. Such a scenario could be encountered in waste-heat recovery applications, where the heat stream has no constraint on the outlet temperature and is rejected to the environment once provided the heat to the cycle. In such cases, a cycle architecture that ensures the maximum cycle efficiency may not be the optimal solution. This is because a cycle could be highly efficient, while absorbing only a small fraction of all the available heat leading to significant amount of available heat being wasted. On the other hand, a different cycle architecture could exhibit lower cycle efficiency but absorbs larger amount of heat and consequently generates more power. In other words, the thermal efficiency and the amount of heat absorbed are not independent in practical applications. This is why exergy efficiency is often employed in thermodynamic analysis of power cycles to help evaluate the relative cycle performance in terms of the generated power.

In the context of heat engines, exergy of the heat source denotes the maximum amount of work that an engine can produce as the heat source is brought to equilibrium with the surroundings, taking into consideration the second-law of thermodynamics. Exergy efficiency is defined as the ratio of power output ($\dot{W}_{out}$) to the maximum theoretical power output defined as exergy ($\dot{X}_{src}$):

$$\eta_{ex} = \frac{\dot{W}_{out}}{\dot{X}_{src}} \tag{2.3}$$

Knowing that the maximum theoretical conversion of heat to work would be achieved by the Carnot engine, the exergy is defined as:

$$\dot{X}_{src} = \int \eta_{Carnot}\ d\dot{Q}_h = \int \left(1 - \frac{T_0}{T_h}\right)\ d\dot{Q}_h \tag{2.4}$$

where $d\dot{Q}_h$ is the heat exchanged with the cycle within the integration interval. For an isothermal heat-source, the maximum amount of work would be generated by the well-known Carnot cycle. For a variable-temperature heat source, the maximum amount of work would be generated by a cycle that is composed of infinitesimal number of Carnot cycles [54] as shown in Fig. 2.3. It is apparent that the cycle that generates maximum amount of work

from a sensible heat source resembles a triangular cycle, wherein the heat source is cooled down to the environment temperature.

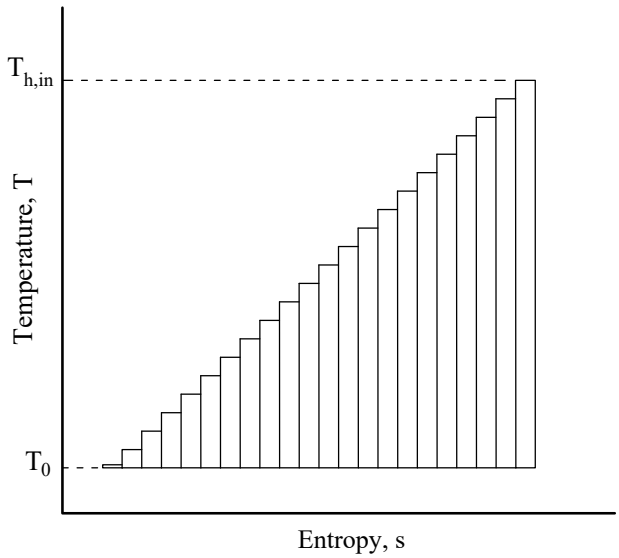


Figure 2.3: The cycle architecture that generates the maximum amount of work with a variable-temperature heat source.

A similar conclusion can be reached through a more analytical approach applied to a more realistic cycle with a non-isothermal heat sink. Dividing the heat addition process into a number of infinitesimal intervals and assuming that in each interval the heat absorbed is converted into work with the Carnot efficiency determines the amount of power an ideal cycle can generate for a given heat-source temperature drop: $T_{hi} - T_{ho}$.

$$\dot{W}_{out,ideal} = (\dot{m}c_p)_h \int_{T_{hi}}^{T_{ho}} (1 - \left(\frac{T_c}{T_h}\right) dT_h \tag{2.5}$$

The heat sink temperature, T_c, is not independent of T_h and the relationship between these two can be derived assuming that under isentropic compression and expansion, the increase in entropy during heat addition will be equal to the decrease in entropy during heat rejection. Since the entropy generation is quantified by the integral of dQ/dT, this leads to:

$$\int_{T_h}^{T_{hi}} \frac{(\dot{m}c_p)_h}{T_h} dT_h = \int_{T_{ci}}^{T_c} \frac{(\dot{m}c_p)_c}{T_c} dT_c \tag{2.6}$$

The solution of equation 2.6 gives the following relationship for the heat sink temperature:

$$T_c = \left(\frac{T_{hi}}{T_h}\right)^{\tau} - T_{ci} \tag{2.7}$$

where τ is the ratio of the heat sink to the heat source capacity rates: $(\dot{m}c_p)_c/(\dot{m}c_p)_h$. Inserting Eq. 2.7 into Eq. 2.5 and integrating gives:

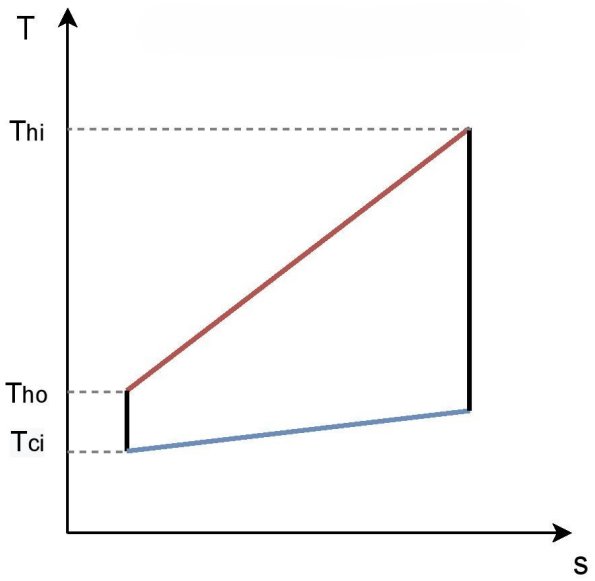


Figure 2.4: Theoretical cycle satisfying the maximum power condition under the assumption of non-isothermal heat-sink.

$$\dot{W}_{out,ideal} = (\dot{m}c_p)_h \left[(T_{hi} - T_{ho}) - \tau T_{ci} \left(\left(\frac{T_{hi}}{T_{ho}} \right)^{\frac{1}{\tau}} - 1 \right) \right] \tag{2.8}$$

Equation 2.8 correlates the power output of an ideal cycle operating with a variable-temperature heat source with the ratio of heat capacity rates (τ), the inlet and outlet temperatures of the heat source and the inlet temperature of the heat sink. In order to find the heat-source outlet conditions that ensure the maximum power output Eq. 2.8 can be differentiated with respect to T_{ho}:

$$T_{ho}\Big|_{W_{out,max}} = \left(T_{ci}\, T_{hi}^{\frac{1}{\tau}} \right)^{\frac{1}{1+\frac{1}{\tau}}} \tag{2.9}$$

Looking at Equation 2.9, it can be seen that the optimal heat source outlet temperature, resulting in the highest power output, will depend on both the heat source and the heat sink inlet temperatures, as well as the heat capacity ratio τ. As the heat capacity ratio, τ, approaches infinity, which can be thought of as an isothermal sink case, the optimal T_{ho} approaches T_{ci}, and the cycle begins to resemble the triangular cycle shown in Fig. 2.4. For more realistic operating conditions and a non-isothermal heat sink, the optimal T_{ho} is expected to remain relatively close to T_{ci} [8]. A theoretical cycle that would satisfy the maximum power output condition under the assumption of a non-isothermal heat sink is shown Fig. 2.4.

Figure 2.5 illustrates the temperature-entropy diagram of a simple organic Rankine cycle. According to the above analysis, the heat-source should be allowed to fall close the the heat-sink inlet temperature to maximise the power output. However as indicated in Fig. 2.4,

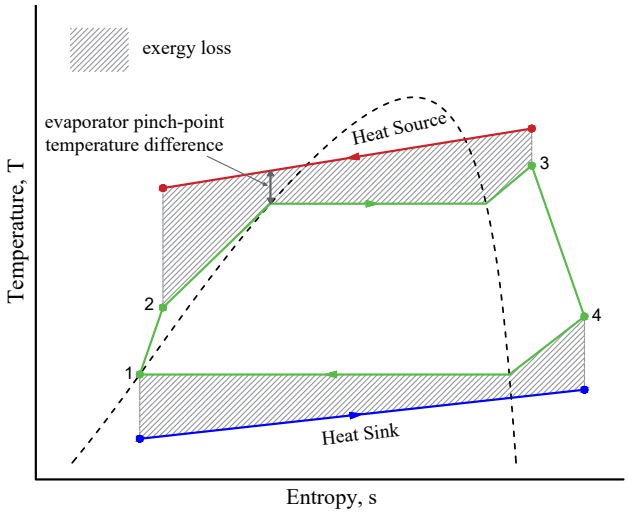


Figure 2.5: Temperature-entropy diagram of the simple organic Rankine cycle; the shaded area represents the exergy loss due to heat-transfer over a finite temperature difference.

the extent to which heat-source can be cooled down in the simple ORC is limited by the presence of pinch-point temperature difference in the evaporator. Moreover, the isothermal evaporation process causes the heat transfer to occur at a relatively large temperature difference, which is a source of irreversibility and exergy destruction in the cycle. In simple terms, the area enclosed by the heat-source and heat-sink curves designates the potential for useful work, thus the greater the temperature difference in the heat exchange between the working fluid and the source the greater the loss in that potential.

The literature includes numerous accounts of exergy analysis of organic Rankine cycle systems, which gives insight into the extent of irreversibility occurring in each cycle component, contributing to the overall loss of cycle performance. Li et al. [55] performed an exergy analysis on an experimental ORC system with a heat source temperature varying between 70 and 100°C and found that the evaporator was the largest contributor to the exergy destruction. Exergy loss in the heat exchangers represented more than 70% of the total exergy loss in the experimental tests. Mago et al. [56] carried out exergy analysis on theoretical models of simple and regenerative ORC systems. The results indicate that majority of exergy destruction occurred in the evaporator, which was responsible for about 77% of the total exergy loss in the simple ORC. An exergy analysis conducted by El-Emam & Dincer [9] on a regenerative ORC operating with geothermal sources with temperature between 160 and 175°C showed that the evaporator and condenser accounted for approximately 75% of the total exergy destruction. Safarian & Aramoun [10] investigated a simple ORC and three modified ORC systems and found that the evaporator had the largest share in the total exergy loss in each investigated cycle architecture. Chen et al. [11] analysed the performance of an experimental ORC unit and also found that the largest part of the exergy loss belonged to the evaporator. The authors highlighted that majority of the exergy destruction occurring in the evaporator was unavoidable due to certain technical limitations inherent to the architecture of the simple organic Rankine cycle. These limitations are related to

the minimum pinch-point temperature difference in the evaporator and a relatively large temperature difference between the working fluid and the heat source associated with the isothermal evaporation process. Similar was found by Dibazar et al. [12] who studied simple and regenerative ORC systems and found that a large fraction of that exergy loss in the evaporator is unavoidable due to limitations given above.

To summarise, the simple organic Rankine cycle has been successfully applied in various applications because of the simple system layout, and relatively high thermal efficiency given the low temperature levels. However, when applied to sensible open heat sources, the cycle architecture presents certain limitations related to the isothermal evaporation process, which limits the attainable power output and exergy efficiency. This emphasises the need for investigating alternative cycle architectures that would help overcome these limitations and allow for further performance improvements.

2.5 Alternative cycle architectures

There are two primary categories of ORCs, single-pressure and multi-pressure level cycles. Multi-pressure level cycles have the advantage of being able to heat up the working fluid at several different pressure levels. This enables better temperature matching between the working fluid and the heat source, leading to improved cycle performance. However, this type of arrangement requires a more complicated system layout and more expensive equipment; therefore, it is only adopted when the increased complexity and cost can be justified by the importance of the power conversion efficiency or when the cost of the power block is much lower than the cost of the entire installation such as in some geothermal systems [57]. In single-pressure level ORCs, the working fluid undergoes the heat addition process at a single-pressure level. Owing to the simple plant layout and attainable efficiencies, the single-pressure level configuration is often the layout of choice for a variety of applications, including geothermal and solar energy, waste heat recovery, and biomass combustion [57]. The most commonly adopted single-level ORC is the one in which the maximum pressure does not exceed the critical value (subcritical cycle), and the working fluid enters the expander as a saturated or superheated vapour. This cycle architecture is referred to as simple organic Rankine cycle and has been discussed in detail in the preceding sections. The main limitation of the simple ORC is related to the isothermal evaporation process, which is associated with significant exergy destruction and limited power output. Although, recuperation is commonly incorporated in the simple ORC as a means of improving thermal efficiency of the plant, preheating the working fluid using expander exhaust does not directly lead to an increased power output. Furthermore, in the recuperated cycle the preheated working fluid enters the primary heat exchanger at a higher temperature, which may affect the minimum heat source outlet temperature. This, in turn, may lead to reduced utilisation of the available heat stream, with larger amount of heat being discarded to the environment [8]. In order to alleviate the issues surrounding the isothermal evaporation, improve the exergy efficiency and allow for higher power outputs, researches have investigated several new cycle architectures.

2.5.1 Transcritical cycle

One of the cycle architectures that alleviates these issues is a transcritical organic Rankine cycle. In the transcritical cycle, the working fluid is pressurised to a level that exceeds the critical pressure of the fluid. It is then heated and turned directly from subcooled liquid to supercritical fluid, omitting the two-phase region (Fig. 2.6a). Since the isothermal boiling process, which accounts for a large part of the total exergy destruction, is completely removed, the cycle has the potential to achieve higher exergy efficiencies and consequently higher power outputs.

Guo et al. [21] compared the transcritical ORC working with CO_2 and subcritical ORC working with R245fa, for geothermal applications with a heat source temperature in the range of 80-120°C. In general, the thermal efficiency of the transcritical ORC was found to be lower than that of the simple ORC, but the transcritical cycle demonstrated the potential of generating more power. However, the transcritical cycle also required larger heat exchangers, with the need for stronger materials due to high operating pressures. Shengjun et al. [58] studied subcritical and transcritical ORCs for low-temperature geothermal sources, considering a variety of organic fluids. It was found that the transcritical cycles could recover much more of the available heat and offer higher net power outputs, but enhanced source utilisation was also associated with the need for larger heat exchangers. The authors also performed a preliminary economic analysis, demonstrating the best performing cycle was a subcritical ORC, while transcritical ORCs operating with the highest pressures exhibited the worst economic performance due to the higher cost of the heat exchangers, which, as the authors noted, may increase substantially with operating pressure. Astolfi et al. [14] investigated different ORC architectures for geothermal applications, with a source temperature varying between 120 and 180°C. The authors found that the transcritical ORC outperformed the simple ORC in most cases, but also required larger heat exchangers, which may affect the overall economic performance of the plant. Lecompte et al.[15] performed techno-economic optimisation of subcritical and transcritical ORCs applied for recovery of waste heat at 180 °C. From the thermodynamic standpoint, the transcritical cycle clearly outperformed the subcritical cycle, delivering over 30% higher power output. However, the estimated cost per kWh was over 70% higher than that of the subcritical one. Li et al. [59] studied the performance of subcritical and transcritical ORCs applied to power generation from hot water with a temperature ranging from 100 to 200°C. The authors found that transcritical ORC outperformed the subcritical cycle at temperature above 160°C, with the highest advantage at 200°C. Oyewunmi et al. [60] performed a techno-economic evaluation of subcritical and transcritical ORCs for waste-heat recovery from a stream of flue gas. The transcritical cycle showed a better thermodynamic performance in terms of thermal efficiency and power output, whereas the simple ORC was more attractive economically.

2.5.2 Zeotropic mixtures

Another alternative to improve the temperature match between the working fluid and the heat source is replacing pure fluids with zeotropic mixtures. Zeotropic mixtures offer the

advantage of non-isothermal evaporation and condensation, which reduces the mean temperature difference in the heat-exchange processes (Fig.2.6b), which can potentially reduce the exergy loss not only in the evaporator but also in the condenser.

Chys et al. [18] examined the potential of using zeotropic mixtures in a subcritical and found that zeotropic mixtures could offer an increase of up to 20% in the generated power, when the heat source temperature was at 150 °C. Lecompte et al. [19] carried out an exergy analysis in a subcritical ORC using zeotropic mixtures and pure fluids. With a heat source inlet temperature set to 150°C, 7.1 to 14.2% higher exergy efficiencies could be achieved when zeotropic mixtures were used. The potential benefit of using zeotropic mixtures has also been confirmed by Dong et al. [20], who found that zeotropic mixtures could generate more power from a heat source at 150°C. However, the economic evaluation demonstrated an increased cost due to the need for larger heat exchangers. Based on the analysis of the existing theoretical and experimental studies, Abadi & Kim [61] confirmed the potential thermodynamic benefits of using zeotropic mixtures in ORCs. The authors also discussed the challenges related to the use of zeotropic mixtures, which include lower heat-transfer coefficients in relation to pure fluids, which may result in larger heat-transfer area. The composition shift during operation may worsen the thermodynamic performance, while fractionating (two-phase state in which the vapour phase consists mainly of one fluid; phenomenon caused by a large difference in the boiling points of fluids making up the mixture) limits the attainable temperature glide. The authors also pointed to the issue of reliable prediction of the thermodynamic properties of zeotropic mixtures. Recently, Xu et al. [62] summarised 94 theoretical and experimental studies on the use of zeotropic mixtures in organic Rankine cycle, providing a comprehensive discussion of thermodynamic as well as economic aspects of zeotropic ORC. In summary, the studies confirmed the potential increase in exergy efficiency when zeotropic mixtures are used. As for the economic aspects, it was difficult to provide a clear judgement, however, the application of zeotropic mixtures generally led to larger heat exchangers size. Similar to Abadi & Kim [61], the authors pointed out to the issues of lower heat-transfer coefficients and composition shifting that essentially worsen the cycle thermodynamic performance.

2.5.3 Trilateral flash cycle

Ian Smith proposed a trilateral flash cycle and carried out extensive research on this topic at City, University of London. The motivation is the same, namely to recover more heat from the heat source, reduce the mean temperature difference between the source and the working fluid, and consequently increase the exergy efficiency and attainable power outputs. The liquid is pressurised and heated up only up to the saturated liquid point. The saturated liquid undergoes flash boiling, changing to a two-phase mixture (Fig.2.6c) during expansion.

Smith [16] showed that if the two-phase expander has an efficiency of at least 75%, the trilateral cycle can generate up to 80% more power from hot liquid streams in the temperature range of 100-200 °C, compared to Rankine steam cycles. Fisher [17] compared the trilateral cycle that used water as the working fluid with an optimised ORC for heat source temperature varying between 150 to 350 °C. The trilateral cycle could achieve 14 to 29% higher exergy efficiency within the investigated temperature range, with a greater advantage toward

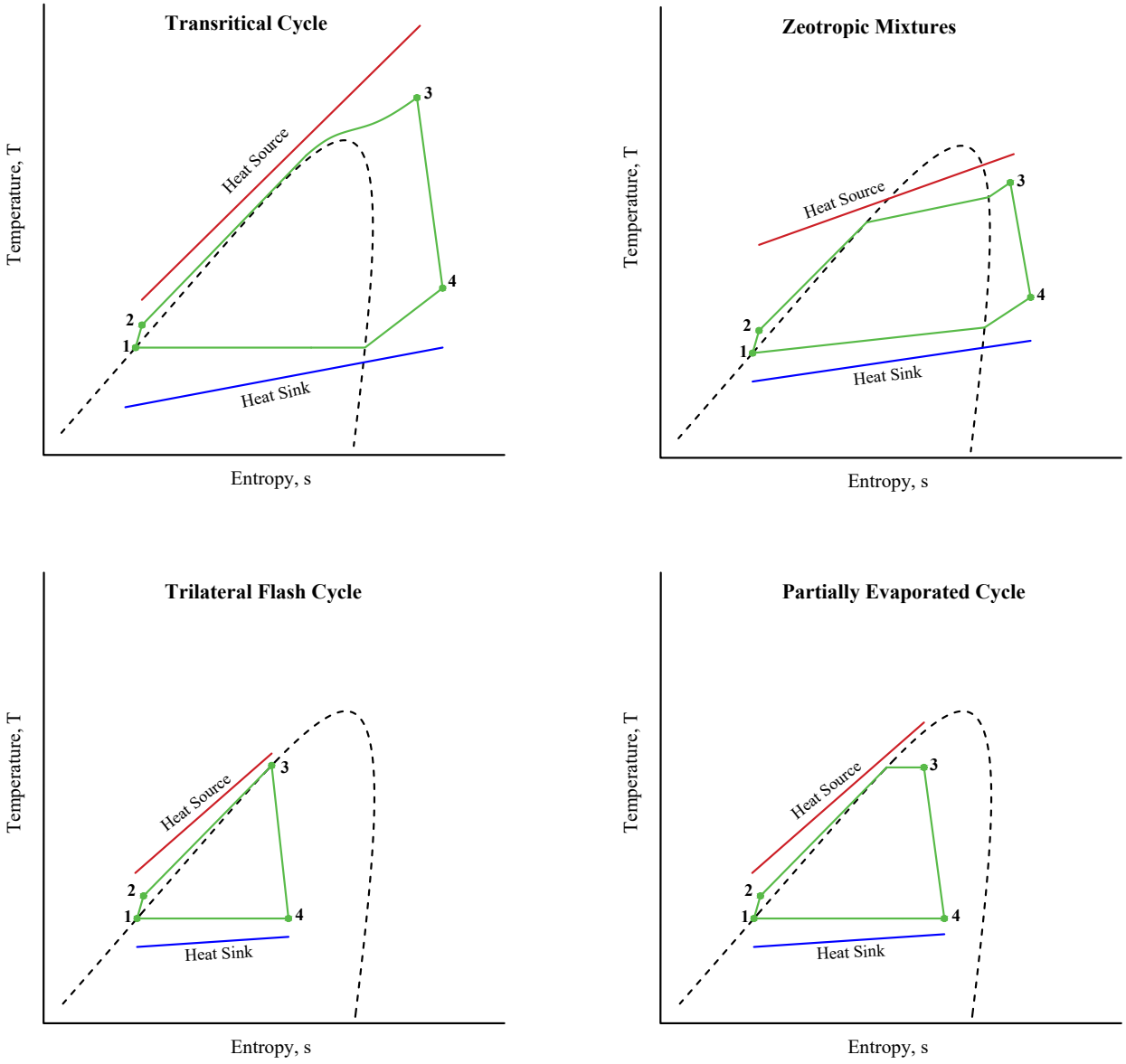


Figure 2.6: Alternative organic Rankine cycle architectures

the lower limit of the considered temperature range (150 °C). Despite the clear advantage of the trilateral cycle, volumetric flow rate could be very high at the expander outlet due to extremely low water vapour pressure at low temperatures. The use of light hydrocarbons has thus been recommended in place of water in this type of cycles. Recently, Lai et al. [63] compared the trilateral flash cycle and ORC for power generation from a thermal source at 80 °C, demonstrating that the trilateral cycle could potentially deliver 30% more power, under the assumption of constant expander efficiency fixed at 75%. The authors pointed out that the required feed-pump work was considerably higher in trilateral flash cycles. Iqbal et al. [64] also compared trilateral and simple organic Rankine cycles for low-temperature applications. The authors found that for a heat source temperature just below 100°C, the trilateral cycle could generate approximately 50% more power compared to the simple ORC. Similar to the study of Lai et al. [63], the authors found that the trilateral cycle required higher feed-pump power and larger heat exchangers, which can influence economics.

The common feature of the trilateral flash cycle is the increased power consumption of the feed pump, which is mainly due to two factors. First, comparing the temperature-entropy diagrams of the simple ORC and the trilateral cycle shown in Fig. 2.5 and Fig. 2.6, it can be noticed that the evaporation temperature in the simple ORC is visibly lower than the heat source inlet temperature. On the other hand, the heat source inlet temperature in the trilateral cycle is much closer to the evaporation temperature. As such, cycles such as the trilateral flash cycles will inevitably need higher evaporation pressures, and consequently higher feed-pump power requirement. The second factor leading to higher feed-pump power consumption is the increased mass-flow rate of the working fluid. Expanding the working fluid from a saturated liquid state reduces the enthalpy drop across the expander, which translates to lower specific power outputs when compared to the expansion from superheated vapour. Having said that, the amount of heat absorbed in two-phase cycles is greater, which means that the mass-flow rate of the working fluid can be increased for a given temperature change. Therefore, despite the lower enthalpy drop, the increase in mass-flow rate leads to higher power outputs, but also entails higher feed-pump power consumption.

2.5.4 Partially-evaporated cycle

Partially-evaporated organic Rankine cycle can be thought of as a blend between the trilateral flash cycle and the simple ORC. The working fluid is only partially evaporated before it is admitted to the expander (Fig. 2.6d). Although such a modification will likely increase exergy loss due to partial isothermal evaporation, and decrease the amount of absorbed heat, some studies suggest that the feed-pump power requirement in partially-evaporated cycles may be lower than in the trilateral flash cycles, which can result in an increased net power output. Such an architecture can also offer technical advantages, such as lower volume expansion ratios as a result of partially evaporated liquid at the expander inlet, which could be beneficial from the standpoint of designing an efficient expander.

Lecompte et al. [23] optimised a partially-evaporated ORC system, varying vapour inlet quality at the expander inlet and the evaporation pressure to maximise the power output. Under the assumption of fixed expander efficiency (70 %) and heat source at 140°C, the

maximum power output was achieved with an inlet vapour quality of 23%. The corresponding feed-pump power consumption was reduced by 24%. In subsequent studies [24], the authors compared the subcritical, transcritical and partially-evaporated ORCs for heat source with temperature varying between 100 and 350°C. Among the three architectures, the partially-evaporated cycle had the highest exergy efficiency within the entire temperature range, with the most pronounced advantage at low temperatures. With heat source at 100°C, the partially-evaporated ORC had approximately 20% higher exergy efficiency than the transcritical cycle, which gradually diminished to about 4% at 350°C. Zhou et al. [25] investigated the thermodynamic performance of a partially-evaporated ORC, using R245fa and R227ea, and their zeotropic mixtures. For the fixed heat source temperature at 120°C, the partially-evaporated ORC had the highest net power output, outperforming the trilateral and simple organic Rankine cycles. Dawo et al. [26] experimentally compared ORC and partially-evaporated cycles for heat source temperature varying between 110°C and 140°C. The cycles were compared on the basis of net system efficiency, which is defined as a ratio of net power output to the available heat. The authors found that the partial evaporation could offer up to 80% increase in net system efficiency compared to the conventional single-phase ORC.

One of the difficulties in designing an efficient expander for trilateral flash cycles is associated with high volumetric expansion ratios, resulting from a large difference in densities between the saturated liquid at the expander inlet and the two-phase mixture at the expander outlet. This can be mitigated to some extent by partially evaporating the fluid prior to expansion. Lai et al. [22] investigated how partial evaporation can influence the volumetric expansion ratio for a heat source at 80°C. Partial evaporation could effectively reduce the volume ratio across the expansion to below 10. However, it should be noted that the study was concerned with temperatures near the lower limit of the range considered for ORC applications (see Fig.1.2). As such, even when the fluid was expanded from the saturated liquid point, the volumetric expansion ratio was below 40 for any of the investigated fluids. Assuming a constant condensation temperature, the volumetric expansion ratio will increase with the heat source temperature; this affects the design of the two-phase expander or even limit the applicability of certain expanders. This issue will be further discussed in the subsequent section on two-phase expanders.

2.5.5 Potential and challenges of alternative cycle architectures

Several alternative architectures have been proposed with the aim of increasing exergy efficiency and power output of ORC systems. Transcritical, zeotropic mixtures-based, and trilateral flash cycles are among the most studied alternative configurations. More recently, a partially-evaporated cycle has also been proposed due to potential thermodynamic and technical benefits. The alternative cycles are more effective in utilising the available heat and thereby can achieve higher power outputs. Higher degree of heat source utilisation are, however, associated with the need for larger heat exchangers, which could contribute to higher installation costs. Furthermore, each cycle presents some specific challenges, which could affect the techno-economic feasibility of the cycles.

Table 2.1: Main challenges in the design of alternative organic Rankine cycle architectures

Cycle architecture	Main challenges
Transcritical	High operating pressures High feed-pump power consumption
Zeotropic mixtures	Composition shift Mixture fractionating Lower heat-transfer coefficients
Two-phase cycles	Efficient two-phase expanders High feed-pump power consumption High volumetric expansion ratios

Transcritical cycles typically operate at substantially higher pressures, which contributes to higher feed-pump power requirement and higher cost of the cycle components, as stronger materials are required. The use of zeotropic mixtures may be associated with gradual performance loss due to a mixture composition shift, whereas the attainable temperature glide may be limited by the fractionating phenomenon. Additional issues are related to lower heat-transfer coefficients and the difficulty in predicting thermodynamic properties of mixtures, making the cycle design process more challenging. The main challenge in the design of the trilateral flash cycle is the availability of efficient two-phase expanders, which is caused not only by the presence of two-phase conditions but also due to high volumetric expansion ratios. Partial evaporation of the saturated liquid can significantly reduce the volumetric expansion ratio, possibly allowing for more feasible expander designs. Another advantage of partial evaporation is the reduced power consumption of the feed pump, which in effect can lead to increased net power outputs. The combination of these factors makes the partially-evaporated cycles a particularly attractive cycle architecture, which may outperform other contenders at low-to-medium temperatures. Having said that, the challenge of designing an efficient two-phase expander remains. Table 2.1 summarises the specific challenges related to each discussed cycle architecture. Two-phase cycles refer to both trilateral flash and partially-evaporated cycles despite some of those issues being more significant in one cycle than the other (e.g. feed-pump power consumption).

2.6 Two-phase expanders

The literature contains sufficient evidence that expanding the working fluid from a two-phase state can improve the performance of organic Rankine cycles. Although two-phase cycles promise to deliver higher power outputs, they also require larger heat exchangers, which can contribute to increased installation cost. Therefore, it is critical to have a high-performing two-phase expansion machine with efficiency that matches that of single-phase expanders. Otherwise, the thermodynamic advantage could be offset by the low performance of the expander. This section will first summarise the available single-phase expander architectures

and then review the performance of experimental prototypes and commercial units of two-phase expanders.

2.6.1 Single-phase expanders

As the device responsible for power generation, the expander is arguably the most critical component in the ORC systems. It greatly affects the performance, power control ability and the total cost of the plant [48]. Furthermore, due to relatively low cycle efficiencies, the overall performance of an ORC is highly sensitive to the performance of the expander. In general, there are two primary types of expansion machines: turboexpanders and volumetric expanders.

2.6.1.1 Turboexpanders

Turboexpanders are devices that extract energy from a continuous flow of a fluid by a dynamic action of moving blade rows [65]. The turboexpander consists of a sequence of stages, each comprised of static (stator) and moving (rotor) blade rows. A pressurised fluid of high enthalpy first enters the stator, where it is being accelerated through partial expansion before admission to the rotor. High-speed fluid entering the rotor is then further expanded and deflected along the rotor blade passage, exchanging momentum with the rotor blades. The rotor is integrated with a rotating shaft, which in turn can be connected to a generator to produce electricity. Depending on the direction of flow with respect to the shaft axis, three main types of turboexpanders can be distinguished: axial, radial-inflow and radial-outflow (centrifugal) turbines. Turboexpanders are typically applied for power outputs ranging from around 100 kW to hundreds of megawatts.

Radial-inflow and axial turbines
The most commonly used types of turboexpanders in ORC systems are radial-inflow and axial turbines. The fundamental difference between these two architectures is the flow direction in relation to the shaft axis. In axial turbines, the flow remains parallel to the shaft axis (axial flow), while in radial-inflow turbines, the flow enters the turbine radially (perpendicular to the shaft axis), gets deflected by 90 °and leaves the turbine axially, i.e. parallel to the shaft axis (Figure 2.7). The choice of the turbine type depends primarily on the operating conditions and scale of the system.

Axial turbines can handle larger volumetric flow rates, which makes them more suitable for large-scale applications. For smaller-scale systems, the axial turbines may become inefficient due to extremely small blades and the need for partial admission (in partial admission some of the stator passages are shut down at decreased mass flow rate in order to sustain design point operation and avoid a drop in efficiency at variable power outputs) [57]. Another drawback of axial turbines is related to the span-wise enlargement which negatively affects the performance of the turbine and can cause an increase in the stress levels. Consequently, the maximum expansion ratios per single stage in axial turbines is limited [67]. In contrast, radial-inflow turbines can be effectively used for lower flow rates and can achieve much higher pressure ratios per stage due to the ability to considerably reduce the mean radius

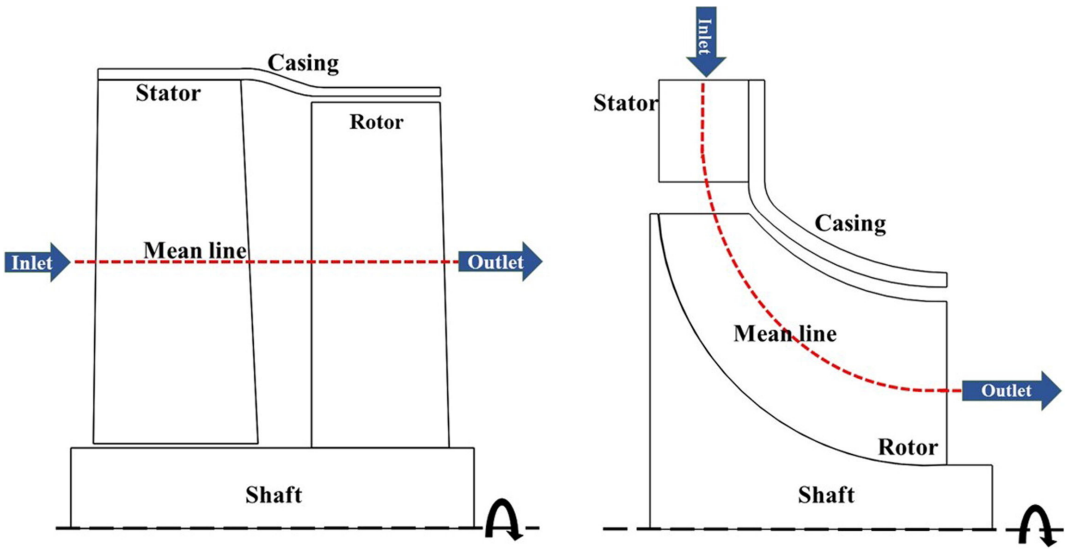


Figure 2.7: Schematic diagram of axial (left) and radial-inflow (right) turbines [66]

along the rotor blade passage (see Figure 2.7). The reduction in mean radius is associated with increased enthalpy drops and consequently higher pressure ratios per stage [66]. This translates to a compact design and high power-to-weight ratios. Hence, radial-inflow turbines are preferred in small-to-medium scale applications with smaller mass-flow rates and high-pressure ratios typical of many ORC systems.

Despite being able to handle small flow rates with high-pressure ratios in a single-stage arrangement, radial-inflow turbines have several other advantages that make them attractive expanders for smaller-scale applications; these were summarized by several authors [66–70]. Many of those advantages stem from the fact that the rotor of a radial-inflow turbine can be manufactured from a single piece of metal through casting or forging. This is associated with increased robustness under high loads, better dynamic stability as well as reduced cost and ease of manufacture. The performance of the radial-inflow turbine is less sensitive to blade profile and can maintain high efficiency at decreased size, where very high manufacturing precision could be expensive. Due to the geometry of radial-inflow turbine and flow direction, tip clearance is not as critical as opposed to small-scale axial turbines. The combination of these factors make the radial-inflow turbine preferred type of turboexpander in smaller-scale applications.

Radial-outflow turbines

A less common turboexpander architecture is one in which the fluid is introduced axially to the turbine, and then expands radially outward through a number of stator-rotor cascades as shown in Figure 2.8.

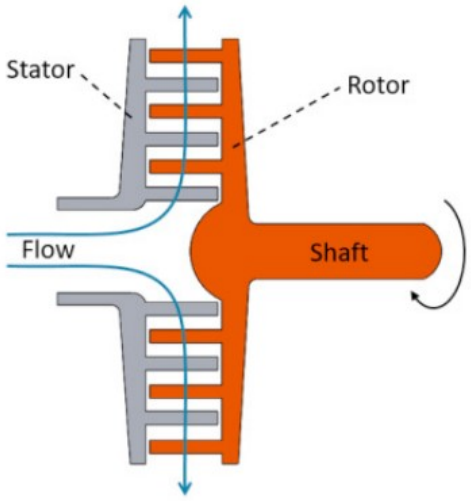


Figure 2.8: Schematic diagram of a radial-outflow turbine [71]

Radial-outflow turbines were first introduced by Parsons-Siemens and Ljungstrom in the early years of the 20th century [72] for steam applications. However, steam is characterised by large enthalpy drops for a given pressure ratio. Radial-outflow turbines have an increasing mean radius along the expansion process, which contributes to lower realisable enthalpy drops per stage. For this reason, the radial-outflow architecture was not effective in steam applications due to very high number of stages required. However, organic fluids are characterised by lower enthalpy drops due to higher molecular weight, which opens up a way of implementing radial-outflow turbines in ORC systems [72]. The radial-outflow turbine is currently being used in commercial ORC systems installed by Exergy [73].

Such a design has certain advantages over the traditional ORC turbines. Unlike the axial turbines, the radial-outflow turbines can accommodate multiple stages on the same rotor disk, which minimizes vibrations as well as the dynamic load on the bearings, and increases the overall number of stages that can be installed in the overhung position. The inherent cross-sectional area increase along the expansion path allows to facilitate higher volumetric expansion ratios, which are common in ORC systems [72, 74]. For a more detailed discussion on radial-outflow turbines, the reader is referred to [75].

2.6.1.2 Volumetric expanders

The design of an efficient turboexpander for power outputs smaller than 50-100kW is very challenging. For such small power outputs, volumetric expanders (also referred to as positive displacement machines) can outperform conventional turbines [57]. Unlike the turboexpanders, power generation in volumetric expanders does not rely on flow velocity. A volume of fluid is first trapped in a sealed chamber. The volume of the chamber is then allowed to gradually increase under the high pressure of the trapped fluid. The volumetric expanders are constructed such that the expanding fluid cause a rotation of the attached shaft. The presence of liquid droplets within high-speed rotating blades of a turboexpander would lead to erosion and a shorter lifetime of the machine. In volumetric expanders, the expansion action

does not rely on the dynamic action but rather volume increase, which makes them more suitable for wet expansions. The characteristic feature of volumetric expanders is a fixed built-in volume ratio, which may pose a problem to an efficient operation at off-design conditions. If the volume ratio is different than the design one, under-expansion or over-expansion of the fluid may occur, considerably reducing the efficiency of the expander. Moreover, the limited built-in volume ratio of the volumetric machines may restrict their use to low-temperature applications characterised by smaller volumetric expansion ratios. Among various types of volumetric expanders, scroll and screw expanders are most frequently selected for ORC applications. These expansion machines are commonly derived from refrigeration compressors and operated in reverse.

Scroll expanders
Scroll expanders consist of two identical spiral components. One of the spirals is fixed, while the other spiral is mobile. The mobile part is offset by 180 °in relation to the fixed part and slightly shifted off centre. The mobile spiral orbits around the centre of the stationary one in a way that an enclosed space is created by the two components. The space enclosed by the two spirals forms a chamber, which gradually increases in volume as the fluid travels from the suction side towards the discharge of the expander. The designed change in chamber volume (built-in volume ratio) allows the high-pressure fluid to expand and generate mechanical power. The schematic of the operation of a scroll expander is shown in Figure 2.9.

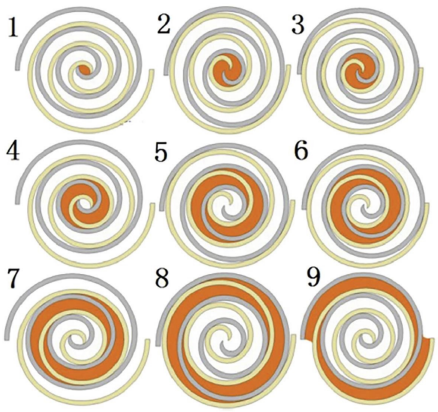


Figure 2.9: Principle of operation of a scroll expander; the figure illustrates the evolution of entrapped volume of high-pressure fluid during expansion [76].

An attractive feature of scroll expanders is low part count, which translates to lower noise level, highly reliable operation and low cost. Furthermore, scroll expanders do not require inlet and exhaust valves, which also has a positive effect on the noise level and expander lifetime [67, 70]. The main limitation of scroll expanders is the operating temperature. Working at high temperatures may cause excessive material expansion and consequently increased internal leakage of the machine. Current high-temperature scroll expanders operate at temperatures up to around 215° [77]. The built-in volume ratio of scroll expanders is typically between 3.5 and 5 [77]. Primary sources of energy loss in these machines include friction, supply pressure drop and internal leakage [46]. Due to low rotational speed, scroll

expanders are usually preferred in micro-scale applications, where power output does not exceed 10 kW [67].

Twin-screw expanders
The most common type of screw expander is a twin-screw expander, which consists of a pair of meshing helical rotors enclosed in a casing [77]. The operation of twin-screw expanders can be divided into three phases: intake, expansion and exhaust. First, high-pressure fluid is admitted to the space between the rotors through the inlet port. The rotors start to rotate due to the high pressure of the enclosed fluid. Thanks to the precisely-profiled structure of the screws, the volume of fluid gradually increases as the screws revolve, which permits the fluid to expand and generate mechanical work. In the last stage of operation, the low-pressure fluid is being exhausted through the port located at the other end of the expander [66]. The principle of operation of twin-screw expanders is illustrated in Figure 2.10.



Figure 2.10: Principle of operation of a screw expander [66]

Screw expanders can achieve relatively high rotational speeds and can achieve power outputs in the order of several hundreds of kilowatts (some studies report theoretical power outputs up to several megawatts). Very small rotor clearance, below 50μm, results in reduced internal leakage. On the other hand, such tight tolerances require very precise and expensive machining. Operation with wet fluids may be beneficial as the liquid phase can act as a sealant, while for operation with dry fluids screw expanders require additional seals that could significantly raise the cost of the machine [69]. The built-in volume ratio can vary between 2 and 8, while the power output could theoretically vary from a few kilowatts up to about one megawatt [67]. With that being said, the design of screw expanders for power ratings below 25 kW becomes more challenging due to high sensitivity of performance to the helical screw profile, which necessitates keeping extremely low tolerances achieved with costly high-precision manufacturing techniques [78].

Other types of volumetric expanders
Scroll and screw expanders have been predominantly considered for ORC systems, however other volumetric expanders have also been investigated. Reciprocating piston expanders can operate under high temperatures and high pressures. They can achieve relatively high built-in volume ratios, in the range of 6-14, which extends the application of these expanders to

higher pressure ratios. For this reason, they have been often considered for transcritical CO_2 cycles [78]. The main challenges surrounding piston expanders include a complex design with accurately timed inlet and exhaust valves, a high number of moving parts with associated balancing problems, and significant friction losses due to numerous interacting surfaces [69]. Piston expanders are also less adapted to two-phase flows than screw or scroll expanders, and, as experimental data report, they may suffer low performance [78]. Generally speaking, piston expanders are more suited to to small-scale applications [67].

Rotary vane expanders benefit from their simple structure, ease of manufacture, and low cost. They are also characterised by relatively high volumetric expansion ratios (up to 10), low noise, and the ability to expand two-phase flows [69]. Vane expanders usually demonstrate low efficiency due to high friction and leakage losses [78]. They are also limited to operation under around 140 °C, because higher temperatures could cause excessive material expansion and associated friction loss, or even locking of the vanes. The inertia caused by the rotor offset limits the rotational speed to about 4000 rpm [77]. Vane expanders have relatively low power capacity and are suitable for micro-scale applications, being capable of generating power ranging from a few watts to several kilowatts [78].

2.6.2 Review of two-phase expanders

Although this work is concerned with two-phase expansion in the context of power cycles, two-phase expanders have also been considered for other applications. Considerable amount of research has been conducted on the use of two-phase expanders for replacing throttle valves in vapour compression refrigeration cycles. In this way, additional energy can be retrieved from compressed-vapour expansion, which would otherwise be wasted in the throttling process. This power can then be used to drive the main compressor, raising the coefficient of performance of these systems [79]. Since entropy generation is generally lower in two-phase expanders than in throttle valves, the expansion process is associated with reduced vapour formation, which in turn increases the cooling capacity. Two-phase expanders have also been investigated for throttle valve replacement in cryogenic processes, such as natural gas liquefaction and air separation plants. The following review focuses mainly on experimental prototypes and commercial units of two-phase expanders, wherein the performance of these units, described in terms of power outputs and machine efficiency, was documented.

2.6.2.1 Two-phase volumetric expanders

Two-phase screw expanders

Much of the early progress on the development of two-phase screw expanders can be attributed to an extensive research programme undertaken at City, University of London between the 1980s and early 2000s with Ian Smith being the lead researcher. Smith et al. [80] investigated twin-screw expanders as two-phase expansion machines for the trilateral flash cycle. The experimental results demonstrated that a twin-screw expander with a rotor diameter of 204 mm and a built-in volume ratio between 3 and 6 could achieve adiabatic efficiencies of more than 70%, generating around 25 kW of power from the expansion of satu-

rated liquid or low-quality vapour of refrigerant R113, having an inlet temperature of 90-120 °C and a rotational speed approximately in the range of 1800 to 3600 rpm. The authors also developed and validated an analytical model based on the one-dimensional homogeneous model to simulate the two-phase expansion occurring in screw expanders. The model was then applied to simulate the performance of a two-stage screw expander integrated in a trilateral flash cycle model applied to power generation from water at a temperature of 150 °C. The model estimated that adiabatic efficiencies of the order of 80% are possible for a machine that generates several megawatts of power. It is also worth mentioning that screw expanders showed much lower performance when applied to two-phase expansion of pressurised water due to higher volumetric expansion ratios and the resulting underexpansion issues.

For an efficient operation in two-phase mode, screw expanders cannot contain a high fraction of lubrication oil to maintain near-equilibrium state between the two phases [81]. Oil-free machines require high-precision timing gears and internal sealing and tend to be much more expensive compared to their oil-flooded counterparts. In an effort to improve the performance and economics of two-phase screw expanders, Smith et al. [81] developed a new rotor profile, a so-called 'N' profile, which reduces contact stresses, providing almost pure rolling motion between the rotors. Therefore, the need for oil lubrication was reduced, such that the process fluid itself could be used as a lubricant, allowing for simpler and cheaper expander designs.

The authors conducted experimental tests on the improved screw expander, which was designed to replace the throttle valve in a 500-ton chiller. The demonstration unit had a rotor diameter of 127.5 mm and a built-in volume ratio of 2.85. It was applied to two-phase expansion of R113 from inlet pressure and temperature of 8.45 bar and 126 °; the outlet pressure and temperature were 3.76 bar and 93 °C respectively. The machine demonstrated an adiabatic efficiency of over 70% at a shaft speed between 2000 and 3000 rpm, while generating 10-15 kW. In later studies [82], the authors investigated the performance of the same expander, but focusing on the feasibility of the use of twin-screw expanders in trilateral flash cycles. The same working fluid, R113, was used, however, the exact operating conditions were not reported. The expander reached a maximum adiabatic efficiency of 76%, generating 10-20 kW of power at a shaft speed between 2500 to 3600 rpm.

Having experimentally proven the potential of two-phase screw expanders, the authors followed up with a numerical assessment of the applicability of screw expanders in trilateral flash systems [27]. Using an empirically-validated model [80], the performance of two-phase screw expanders was studied for power generation from geothermal brine with temperature varying between 100 and 140 °C. The model predicted a declining trend in expander efficiency with increasing difference between the heat source and condensation temperatures. This was related to the elevated volumetric expansion ratio and an insufficiently high built-in volume ratio of the expander, which for screw expanders is typically limited to 5-10. For instance, when brine temperature was fixed at 140°C, the condensation temperature could not be lower than 34°C for the efficiency to remain above 75%, which was considered to be the minimum efficiency level required for the trilateral cycle to compete against the single-phase ORC. Hence, if the screw expanders were to be used at higher temperatures, above 150 °C,

multi-stage architectures would most likely be required to handle the high expansion ratios and maintain high efficiencies. This is why Smith proposed a novel cycle architecture [54] for temperatures greater greater than 170 °C. In the cycle, the expansion is realised in two stages. In the first stage, saturated liquid is expanded to a certain intermediate pressure level; the authors proposed a radial-inflow turbine as the first-stage expander, reporting that then manufacturers assured efficiencies of over 75% provided that the volumetric expansion ratio remains below 25. The partially evaporated liquid, leaving the first expander, would then enter a separator, out of which, the vapour would be further expanded in a screw expander, while the liquid would be mixed with the working fluid in between two pumps, reducing the overall feed-pump power requirement.

Another empirical study carried out at City, University of London focused on the use of twin-screw expander in two-phase organic Rankine cycles. Smith et al. [83] designed a small-scale two-phase ORC demonstration unit working with R124 to generate power from hot water available at 90 °C, while cooling water was available at 15 °C. Oil-flooded compressor having the improved "N" profile and a rotor diameter of 102 mm was used in an expander mode. Shaft speed was set constant at 1800 rpm, so that the expander could be directly connected to a generator. The screw expander reached the maximum efficiency of 74%, expanding wet vapour with an inlet quality of 95%, and generating 22 kW of power. A more recent study at City, University of London was conducted by Read et al. [84], who developed a multi-variable optimisation program to optimise geometry and operating conditions of a twin-screw expander applied to the expansion of wet steam in the context of power generation from low-temperature sources. A prototype of the optimised expander having a rotor diameter of 145.57 mm was tested for pressure ratios ranging from 1 to 12 bar. With the shaft speed set to 4500 rpm, the power output varied between 5 and 140 kW during testing, while the measured adiabatic efficiency was around 70% close to the design point corresponding to a pressure difference between 3 and 6 bar, and shaft power output between 30 and 70 kW. The maximum measured adiabatic efficiency was approximately 78%. Although the absolute pressure values were not reported, assuming that the discharge pressure was close to the atmospheric pressure, the inlet pressure could be around 2 to 13 bar and the corresponding saturation temperature would then be between 120 and 190 °C.

More recently, Bianchi et al. [85–88] conducted an extensive numerical investigation focused on the use of two-phase twin-screw expanders in trilateral flash cycles applied to waste heat recovery from sources at temperatures below 100 °C. A chamber model based on the assumption of one-dimensional homogeneous-equilibrium flow was developed and applied to study two-phase expansion of R245fa from an inlet pressure of 5 bar to an outlet pressure of 1.32 bar. The estimated expander efficiency for the expansion from saturated liquid conditions was 37.6%, while generating around 16 kW of power at a revolution speed of 3750 rpm. Increasing the inlet vapour quality to 0.1 resulted in a remarkable rise in the estimated efficiency, which reached about 83.1% at a power output of 15.1 kW. The results indicate that even little evaporation prior to the the expansion can bring a considerable reduction in the volumetric expansion ratio and consequently help mitigate the underexpansion issue, which was the primary reason for the poor expander performance. Raising the inlet vapour quality further above 0.1 had a limited effect on the expander efficiency, while significantly

reducing the power output.

In subsequent studies [87, 88], the authors modelled the entire trilateral flash cycle with an integrated twin-screw expander, having a rotor diameter of 204 mm and a built-in volume ratio of 5. Two machines working in parallel were simulated to handle mass flow rate of 25 kg/s of R245fa. The expander having a rotational speed of 4500 rpm and generating 110 kW of power, had an estimated efficiency of 74%. Off-design analysis demonstrated that increasing the expander speed could have a detrimental effect on the expander efficiency and power output, which means that raising the rotational speed to increase the mass-flow rate through the machine may be associated with performance loss. Therefore, to handle larger mass-flow rates, larger machines would have to be used if the efficiency is to remain high. This could have its own implications, such as an increased production cost or the need for multiple machines working in parallel. Further analysis showed that a machine with a lower built-in volume ratio could achieve higher volumetric efficiency and had a higher capability of handling larger mass-flow rates for a given pressure ratio. However, reducing the built-in volume ratio from 5.06 to 2.63 caused a simultaneous drop in efficiency from 82 to 63%, which was related to underexpansion issues.

Two-phase scroll expanders
Although screw expanders have been identified as suitable two-phase expansion machines, presenting efficiencies of the order of 70% and a relatively high flexibility in terms of power capacity, other types of volumetric expander have also been investigated for two-phase applications. Fukuta et al. [89] performed both theoretical and experimental studies on a two-phase scroll expander for replacing a throttle valve in transcritical CO_2 refrigeration system. First the authors estimated that a two-phase scroll expander, having a leakage gap of 10 µm and rotational speed of 3600 rpm can achieve an efficiency of 60%. In the experimental part of the study, a scroll expander having an inlet chamber volume of 1.54 cm^3/rev and a built-in volume ratio of 2.18 was tested. The inlet pressure and temperature during testing were set to 9 MPa and 40°C respectively, the outlet pressure was fixed at 4 MPa, while the rotational speed varied between 2000 and 4000 rpm. The scroll expander reached a maximum efficiency of 55%. Kohsokabe et al. [90] also investigated the performance of a two-phase scroll expander prototype designed for CO_2 refrigeration systems. The expander had an inlet volume of 2.8 cm^3/rev and a built-in volume ratio of 2, while the expander rated power output was 0.7 kW. The maximum measured isentropic efficiency was found to be around 83% at a rotational speed of 2655 rpm. The corresponding inlet and outlet pressures were 8.3 MPa and 4.21 MPa respectively.

Scroll expanders have also been considered as two-phase expansion machines in power generation systems using water. Kim et al. [91] conducted an experiment on a 15 kW two-phase scroll expander applied to two-phase expansion of steam from an inlet pressure of around 1.2-1.3 MPa and an inlet temperature between 139 and 145 °C. The shaft speed ranged from 1000 to 1400 rpm, while the outlet pressure was fixed at around 0.4 MPa. The expander demonstrated a similar efficiency in all the undertaken tests, which was around 33.8%. The authors identified the main reason for the poor performance to be the large clearance between the fixed and orbiting scrolls. According to the theoretical analysis, the efficiency

could potentially be raised to 65% if the clearance was reduced from 64 to 30 µm. ECR International proposed a liquid-injected co-generation system for domestic heat and power applications [92]. In the system, pressurised heated water was flashed using a two-phase scroll expander, generating electricity and providing a lower-pressure high-quality vapour flow used for air or water heating. The laboratory tests demonstrated that a prototype of the two-phase scroll expander was capable of generating 2.4 kW of power at an isentropic efficiency of 45%. In subsequent tests, ECR designed and manufactured three other prototypes of scroll expanders using different types of materials. Initial tests demonstrated that one of the expanders, having a revolution speed limited to 1800 rpm, was capable of generating 1.4 kW of power at an isentropic efficiency of around 40%. The power output increased to 1.9 kW, when the shaft speed was increased to 2800 rpm, however, the corresponding efficiency value was not reported. A three idler crank design was also considered with an isentropic efficiency, predicted based on previous prototype tests, to be in the range of 50 to 60%, while generating 2.5 kW at a speed between 3000 and 3600 rpm.

Two-phase vane expanders

Fukuta et al. [93] conducted an experiment on a rotary vane expander designed to expand CO_2 from a supercritical to a two-phase state. The prototype tested had 10 trays, an inlet chamber volume of 64 mm^3, and a built-in volume ratio of 2. The inlet pressure was set to 9.1 MPa, while the inlet temperature varied between 35 and 45 °C. The outlet pressure was 4.1 MPa and the expander rotated at a speed of 1000 to 2500 rpm. The expander efficiency was typically between 50 and 60% under these operating conditions. Yang et al. [94] also carried out tests on a rotary vane expander designed to replace the throttle valve in a transcritical CO_2 refrigeration cycle. In order to mitigate leakage issues, the expander had springs installed within the vanes, ensuring tight contact between the vanes and the cylinder wall and better sealing between the inlet and discharge ports. The tested prototype had a rotor diameter of 46 mm. The pressure on the suction side was in the range of 7.5 to 9 MPa, while the temperature varied between 32.4 and 44.3 °C. The discharge pressure was in the range of 4.8 to 6.4 MPa. The maximum isentropic efficiency was around 23% at a speed of 800 rpm. Although the springs installed in the slots of the vanes ensured a tight fit of the vanes within the cylinder, they were found to be prone to fatigue and caused more significant friction losses.

Jia et al. [95] conducted experimental tests on a prototype of a two-phase CO_2 scroll expander that used injected high-pressure gas to maintain small clearances while reducing friction losses and fatigue problems surrounding the in-vane springs. The results of two experimental tests were presented; inlet pressure and temperature were at 9 MPa and 42°C in the first test, and at 8 MPa and 34 °C in the second test. The rotational speed ranged from approximately 800 to 1800 rpm in each test. The results indicate that the design with high-pressure injected gas gives significantly better performance compared to the spring-based design. The expander achieved a maximum isentropic efficiency of around 45% at a speed of 1000 to 1500 rpm. The corresponding power output for the higher pressure case was between 0.9 and 0.98 kW, and between 0.65 and 0.67 kW for the lower pressure expansion.

Other two-phase volumetric expanders

Dumont et al. [96] experimentally compared three types of volumetric expanders: scroll, piston, and screw expanders for small-scale ORC systems. The results of the tests should be treated with caution because the expanders were not designed or sized to the operating conditions and working fluid present in the test. However, the authors were able to draw general conclusions and give some recommendations. Both scroll and screw expanders are suitable for two-phase expansion. The scroll expanders are recommended for micro-scale applications, with power outputs below several kilowatts, while the screw expanders are preferred when the power output is in the range of tens of kilowatts. Piston expanders were recommended in applications with high pressure and high temperature inlet conditions. They can also achieve higher built-in volume ratios; however, the authors suggest that they can only handle limited wet expansions, which indicates that they may not be suitable for certain two-phase power cycles. The scroll expander had the highest measured efficiency of more than 80%, while the screw and piston expanders demonstrated an efficiency slightly above 50%. However, it should be reiterated that the expanders may not have been working under their nominal conditions. Dumont et al. [97] performed a techno-economic optimization of three different ORC architectures: wet, simple subcritical and trans-critical, designed for waste heat recovery from a 500kW biomass power plant. The inlet temperature of the waste heat was fixed at 300 °C. Several common ORC working fluids were studied, and both volumetric expanders and turbines were considered. Realistic technical constraints for the expanders were implemented in the optimization. For the considered application, the wet cycle was not feasible due to the twin-screw expander limitations. The ratio of the volumetric flow rate at the expander outlet to the shaft power was found to be too high and was considered unfeasible. Since only the screw expander was considered as a viable option for a two-phase expansion machine, the wet ORC was deemed unsuitable for the studied application. However, the authors suggested that if another expander such as radial-inflow or radial-outflow turbines could be integrated with the two-phase ORC, the panel of solution could have been extended.

2.6.2.2 Two-phase turboexpanders

Due to dynamic action of high-speed blades, and the surrounding erosion issues, turboexpanders have often been ruled out for two-phase applications. Nevertheless, several types of two-phase turbines have been proposed and investigated, with some reaching commercialisation stage. Hays [98] presented a history and overview of two-phase turbines, reporting the available performance data of units that had been tested prior to 1999. The authors distinguished three types of two-phase turbines: drag, reaction and impulse turbines. All of these turbines feature an integrated set of two-phase nozzles designed to accelerate the mixture prior to entering the rotor. The author reported that previous experimental studies had demonstrated that two-phase nozzles can reach efficiencies of the order of 85-90%.

Figure 2.11 illustrates the expansion in a single-stage turboexpander, which is a common representation used when describing the performance of turbomachines. The diagram illustrates the actual expansion occurring in the nozzle (1-2) and rotor (2-3) of the turbine alongside ideal isentropic processes and total states at each station in the turbine. The effect of nozzle-rotor interspace was neglected, which is why there is one thermodynamic state at

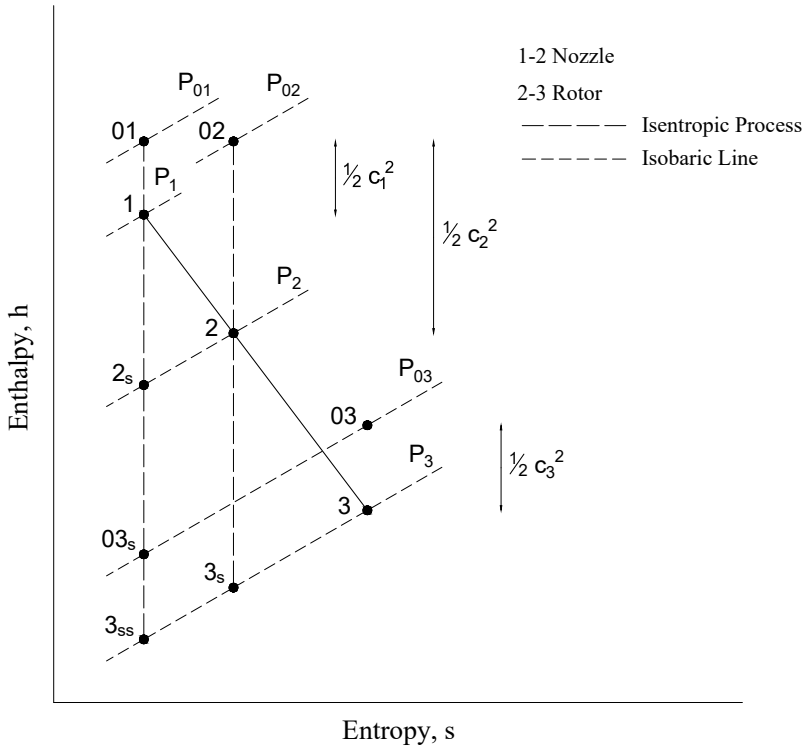


Figure 2.11: Expansion process in a single-stage turboexpander; the effect of nozzle-rotor interspace is neglected.

station 2, which simultaneously represents the nozzle outlet and rotor inlet. The performance of the turbine can be defined comparing the actual and isentropic (ideal) expansions. There are two definitions commonly used to describe the performance of the turboexpander. These include total-to-total (η_{tt}) and a total-to-static efficiencies. The former is more adequate when the kinetic energy of the fluid leaving the rotor outlet is assumed to be recovered.

$$\eta_{tt} = \frac{h_{01} - h_{03}}{h_{01} - h_{03s}} \tag{2.10a}$$

$$\eta_{ts} = \frac{h_{01} - h_{03}}{h_{01} - h_{3ss}} \tag{2.10b}$$

When it comes to performance of the nozzle (η_N) and rotor (η_R), these can also be defined in terms of enthalpy values.

$$\eta_N = \frac{h_1 - h_2}{h_1 - h_{2s}} \tag{2.11a}$$

$$\eta_R = \frac{h_{02} - h_{03}}{h_{02} - h_{3s}} \tag{2.11b}$$

If the kinetic energy is recovered at the rotor outlet, it may be more appropriate to refer to the total isentropic enthalpy, h_{03s}, in the denominator of Eq. 2.11b. For the nozzle, the

efficiency can alternatively be determined by comparing the rise in kinetic energy of the fluid to the enthalpy drop occurring under isentropic flow conditions.

$$\eta_N = \frac{\frac{1}{2}\left(c_2^2 - c_1^2\right)}{h_1 - h_{2s}} \tag{2.12}$$

Since in two-phase expansions, liquid and vapour can develop a velocity slip, mass-flow averaged velocity can be applied to determine nozzle efficiency.

Referring back to the review presented by Hays [98], in the drag turbine shown in Fig. 2.12, also called a rotary separator turbine, a two-phase jet is directed tangentially onto a cylindrical surface of the separator rotor. Due to the centrifugal force, the liquid phase accumulates at the wall of the cylinder, separating it from the gas phase. As a result of friction between the liquid and the separator surface, the kinetic energy of the liquid is converted into a rotational movement of the separator, which, in turn, can be connected to a generator to generate electricity. The kinetic energy of the separated gas can be transformed into useful mechanical work by passing it through a row of rotor blades. The reaction turbine on the other hand accelerates the fluid radially outwards, rotating the turbine wheel due to the reaction force. As for impulse-type turbines, the two-phase jet is released directly onto a row or multiple rows of rotor blades.

Rotary separator

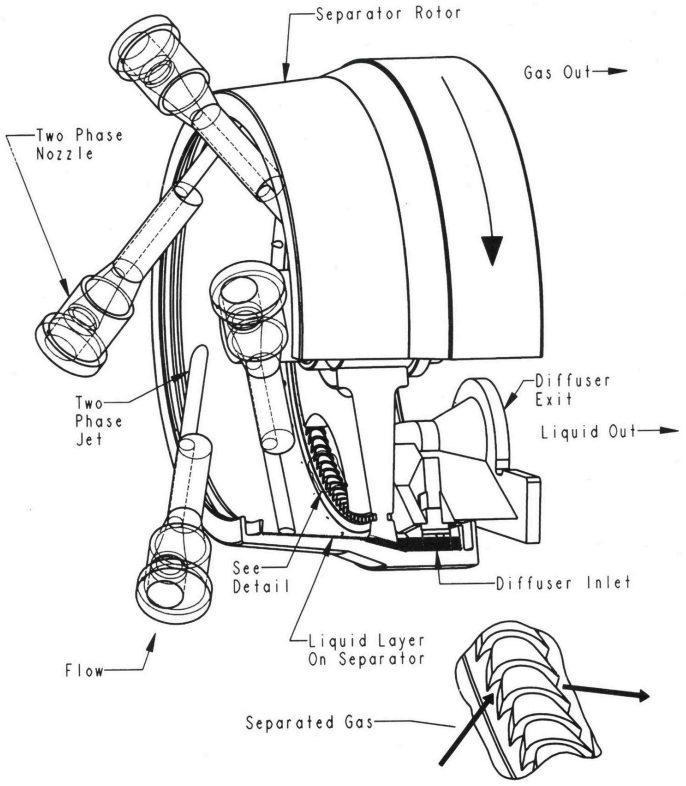


Figure 2.12: Schematic of a two-phase rotary separator turbine (figure retrieved from Hays [98])

to boiling (1a) and then entirely boils in the vaporizer (1b) and the vapor is subsequently superheated (2). The superheated vapor is expanded through a turbine (3) and is then condensed (3a and 3b) and subcooled (4), at which point it is pressurized in the refrigerant pump to close the cycle.

The ORC creates a pinch point between (1a) and the cooling geothermal flow that limits the geothermal water return temperature. The ideal thermodynamic cycle would eliminate this boiling pinch point to recover more heat from the geothermal resource while efficiently converting the recovered heat into electricity. Until now, turbine technology has been a barrier to usage of improved cycles.

Euler Turbine

Pressure reducing valve (PRV) stations are a large source of wasted potential energy in steam systems, converting pressure energy into heat produced by frictional dissipation. The Euler Turbine was designed to capture the energy in steam and gas expansions. Commercial units are operating with single-stage isentropic efficiencies above 80%. Previous state-of-the-art commercial steam turbines of comparable power have isentropic efficiencies of 50% or less.

The Euler Turbine is a radial-outflow reaction turbine consisting of a stator row of converging-diverging nozzles and a rotor row of blades. Figure 3 shows the flow-path through the turbine. Vapor enters axially and is turned radially outward before entering the nozzle row. The flow is accelerated as the pressure drops to an intermediate pressure at the



Figure 2. Euler Turbine package in parallel with a PRV station.

Figure 3. Euler Turbine flow path.

The Euler Turbine was designed to handle saturated steam at the turbine inlet, which can result in as high as 10% moisture at the rotor exit. Unlike radial inflow turbines, centrifugal forces in the Euler Turbine pull moisture and contaminants away from the nozzle-rotor interface. Thus the design is inherently erosion resistant, enabling its wide use with expansions that drop into the wet region. The Euler Turbine utilizes two-dimensional vane and blade profiles, giving stout, strong blades and simple, low-cost construction (Figure 4). Another benefit of the radial outflow design is a reduction in operating speed to approximately half that of comparable radial inflow machines, reducing the size and losses

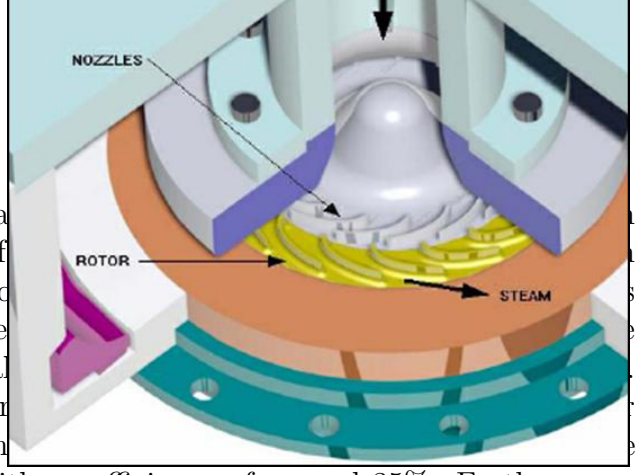


Figure 3. Euler Turbine flow path.



Figure 4. Euler Turbine rotor.



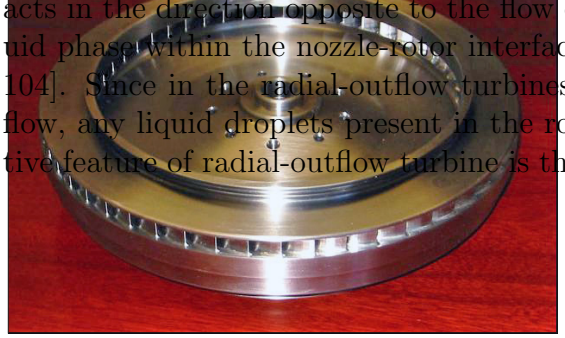


Figure 4. Euler Turbine rotor.

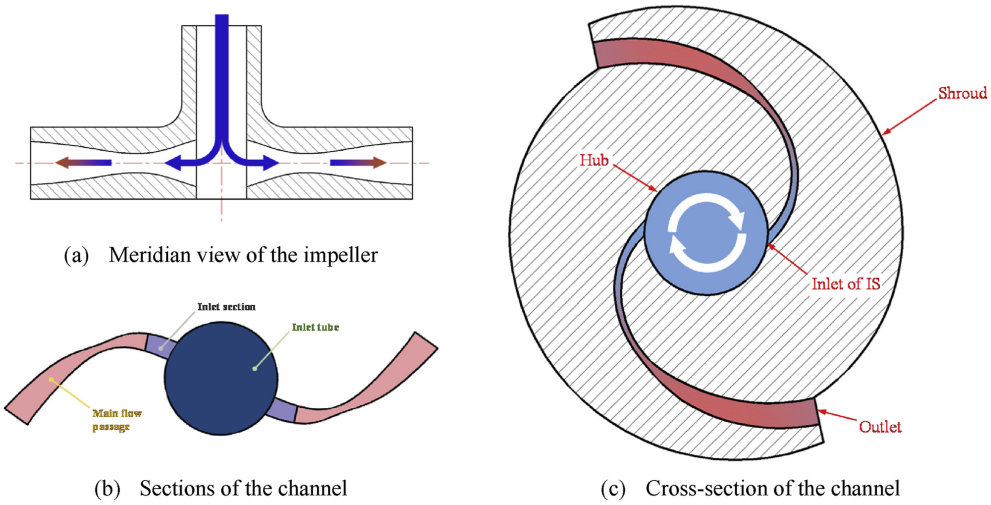
A first demonstration unit of the rotary separa… brine and steam mixtures at a temperature of … had a diameter of 762 mm, generated 21 kW … of the demonstration unit was followed by the … drag turbine power recovery from geothermal … The prototype separator rotor had a diameter … from brines at a temperature of 227 °C. Th… similar to that of the demonstration unit, with an efficiency of around 35%. Furthermore, no signs of erosion within the turbine were found during a 4000-hour endurance test, despite the impinging two-phase jet having a speed of up to 305 m/s. To increase the efficiency of the turbine, subsequent designs used a rotor disk along the separator to use the kinetic energy of the separated gas flow, which had previously been discarded [100]. The incorporation of steam blades increased the efficiency of a 42 kW unit from 35 to 46%. Similar to previous tests, no measurable erosion was found after 700 hours of operation. The rotary separator … d gas sector, as an effective separator, where, for … g inert gases and crude oil [98].

Figure 2.13: a) Schematic drawing of a radial-outflow turbine; b) Radial-outflow turbine rotor installed in a Rankine cycle plant in Bruchsal (figures retrieved from [101])

Radial-outflow turbines

Figure 2.13 a) presents a schematic drawing of a two-phase Euler type reaction turbine developed and tested by Energent Corporation [102]. The turbine was designed to expand saturated vapour flows radially outward, while being capable of handling limited condensation, with up to 10% of liquid mass fraction at the turbine exit [101]. One issue surrounding the use of radial-inflow turbines in two-phase flow applications, is that the centrifugal force acts in the direction opposite to the flow direction. This may cause accumulation of the liquid phase within the nozzle-rotor interface, leading to erosion and vibration problems [103, 104]. Since in the radial-outflow turbines, the centrifugal force acts in the direction of the flow, any liquid droplets present in the rotor are forced out of the turbine. Another attractive feature of radial-outflow turbine is that the flow area increases during expansion, which

helps to facilitate high volumetric expansion ratios characteristic of two-phase expansions. The radial-outflow turbine designed by Energent Corporation was installed in a Kalina cycle applied to geothermal sources in Bruchsal in Germany [101]. The turbine rotor, depicted in Fig. 2.13 b), had a rotor with a diameter of 254 mm and rotated at 28,000 rpm. At the design point, the turbine had a shaft power of 610.5 kW, expanding ammonia-water mixture from 20 bar and 115.3 °C, with an efficiency of 82.4%. The vapour quality at the turbine exit was 96%. Another type of reaction turbine investigated for two-phase flows is one that consists of two curved converging-diverging nozzle channels that guide and accelerate the fluid from the centre of the turbine towards its periphery where the fluid is ejected. The outlets of the two nozzle channels are positioned in such a way that the reaction force of the exiting two-phase jest propels the turbine (Fig.2.14). Recent numerical and experimental studies [39, 40, 105] indicate that this type of two-phase turbine is characterized by rather low performance with an efficiency typically between between 5 and 25%. Rane and He [42] modified the architecture of the rotating two-phase turbine by including an intermediate stator row between the inlet and the rotating channels. Numerical simulations showed that the modified architecture performed better than the baseline geometry, however, the estimated efficiency did not exceed 25%.



(a) Meridian view of the impeller

(b) Sections of the channel

(c) Cross-section of the channel

Figure 2.14: Schematic of the rotating radial-outflow turbine (figure retrieved from Li et al. [105])

Impulse turbines

The most common type of an impulse turbine that has been used in two-phase applications is an axial impulse turbine. A cut-away drawing of an axial impulse with a single integrated two-phase nozzle is shown in Fig. 2.15. In case of flashing flows, the two-phase nozzle would facilitate the phase change, accelerate mixture, and admit it to the rotor at a design angle. Many researchers considered this type of turbine architecture to be more suitable for two-phase flows than radial-inflow turbine due to aforementioned issues concerning the centrifugal force acting in the direction counter to the flow direction and the resulting erosion issues. Nevertheless, the centrifugal force in an axial turbine acts towards the shroud, which may lead to accumulation of the heavier liquid phase on the shroud. This was actually an issue recognised in one of the following studies, where it was found through visual inspection,

Figure 2. Schematic of Two-Phase Jet Interaction with Axial Blading

A key feature of the impulse turbine design is the provision of an axial path for the two-phase flow. As discussed previously radial inflow machinery will centrifuge liquid in a direction counter to the flow. This liquid can collect between the nozzles and rotor blades producing severe erosion. In the axial design the bulk of the liquid leaves the rotor with a swirl to enable collection on the casing wall. The small fraction that is centrifuged is collected on a shroud, which also directs the flow to the casing wall.

that a fraction of the liquid phase is ejected at the shroud [106].

An axial flow two-phase turbine having a single nozzle was also designed and tested for a high lift heat pump application using R-134a. A schematic drawing of this unit is shown in figure 3.

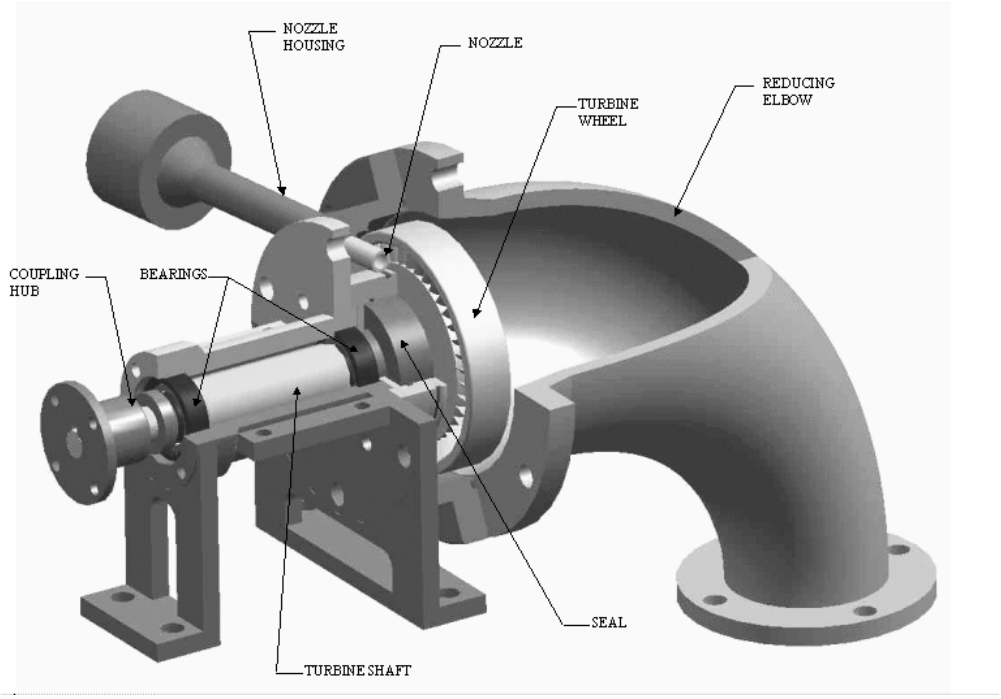


Figure 3. Cut-away Drawing of Two-Phase Axial flow Turbine for Heat Pump

Figure 2.15: A single-stage impulse axial turbine integrated with a single two-phase nozzle (figure retrieved from Hays & Brasz. [103])

International Compressor Engineering Conference at Purdue, July 12-15, 2004

Elliot [28] carried out tests on single- and two-stage axial impulse turbines for the two-phase expansion of water-nitrogen mixtures and R22. A two-phase nozzle was used, which accelerated the gas-liquid mixture that impinges on the turbine blades, exchanging momentum and producing useful mechanical work. The single-stage turbine was tested for the expansion of water-nitrogen and two-phase R22 mixture with a similar rotor diameter of 263 and 261 mm respectively. The expansion of water-nitrogen mixture was expanded from an inlet temperature and pressure of 22°C and 2000 kPa. The turbine generated 9.9 kW, revolving at a speed between 700-2250 rpm, with peak efficiency of 47.5 % at 1652 rpm. The R22 mixture was expanded from 18.6 °C and pressure of 875 kPa. The maximum efficiency of 52.4% was reached at a shaft speed of 1880 rpm; the corresponding power output was 6.34 kW. When it comes to two-stage turbine test, only water-nitrogen mixture expanded from the same thermodynamic conditions as in the single-stage test. The rotational speed of the first stage and second stage were 2200 and 678 rpm respectively, and the turbine achieved a peak efficiency of 50.7%, generating 10.57 kW of power. The authors also pointed out to the issue of possible erosion in this type of two-phase turbines, resulting from direct impingement of droplet onto the rotor blades. Erosion may contribute to the deterioration of machine performance, increased wear rate or even to the eventual failure of the machine.

Hays and Brasz [106] analysed the performance of a 15 kW two-phase impulse turbine designed to replace a throttle valve in a commercial 500-ton chiller operating with R134a. The authors first compared the theoretical predictions of the performance of a two-phase

nozzle working with R134a to the corresponding experimental measurements. Theoretical predictions were obtained using a one-dimensional model that accounted for the interphase exchange of heat and momentum, as well as droplet breakup and wall friction effects. Close agreement was found between the theoretical and experimental results, with a nozzle efficiency measured at approximately 84% at the design point. However, the measured efficiency of the whole turbine was significantly lower than what the model predicted; between 50 and 55%, compared to the predicted 75%. The two-phase turbine has been installed in more than 100 commercial chillers. The authors further investigated the two-phase turbine, highlighting three possible sources of losses that could be responsible for poor rotor performance. These include liquid reflection of the leading edge of the rotor blades, stagnation of liquid at the shroud, and non-optimum flow incidence angle due to incorporating straight blades (fixed angle at a given streamwise position). To further investigate the energy losses, a test facility was constructed in which a representative flow of air-water mixture through the rotor was visually examined. The inspection revealed that 10% of the total flow was reflected off the leading edge of the blades, while about 4% stagnated on the shroud. Based on the findings, the authors improved the rotor design to alleviate the undesirable effects and increase the efficiency of the rotor. The laboratory test conducted on the improved design demonstrated an increase of turbine efficiency which reached 64% [104]. In the following studies, the authors [103] proposed a turbine-compressor unit for transcritical CO_2 refrigeration cycles. The authors reported experimental test results that had previously been taken for expansion of two-phase R134a through a single-stage axial impulse turbine. The rotor of that turbine had 71.1 mm, and revolved at 12,800 rpm, generating 0.31 kW of power at a peak efficiency of 56 %.

Energent Corporation [107] proposed a variable phase cycle, which is essentially a trilateral flash cycle, integrated with a single-stage impulse turbine, as a means of recovering waste heat in geothermal fields. To confirm the potential of the proposed technology, a one-megawatt demonstration plant was constructed at the Terra -Gen BLM East power plant, at Coso Geothermal Resource, California [107]. The cycle was to generate power from liquid brines separated in the steam flash cycle used in the fields. The separated liquid brine was available at a temperature of approximately 110 °C, while the cycle working fluid was selected as R134a. The impulse turbine used consisted of 10 supersonic converging-diverging nozzles and a titanium single-stage axial rotor with a diameter of 406 mm. The rotational speed of the turbine was fixed at 3600 rpm, so that it could be directly connected to the generator. The turbine reached an efficiency of 73% at a maximum shaft power output of 1242 kW. The impulse-type axial turbine has also been used in the variable phase cycle applied to recover waste heat from a marine diesel engine [107]. The waste heat came from hot compressed air that had to be cooled before being fed into the engine. The working fluid was R245fa, while the hot air inlet temperature varied between 190 and 210 °C. The turbine was designed to generate 200 kW of power. The turbine operated with an efficiency of 74% and 65% in two experimental tests; the corresponding power output was 172 and 227 kW respectively [104].

Elliot Group has recently developed a two-phase cryogenic impulse turbine [109], which can handle a higher vapour generation, of the order 30% of outlet vapour quality. The efficiency of these units designed for power outputs between 300 kW and 2.2 MW appears is in the order

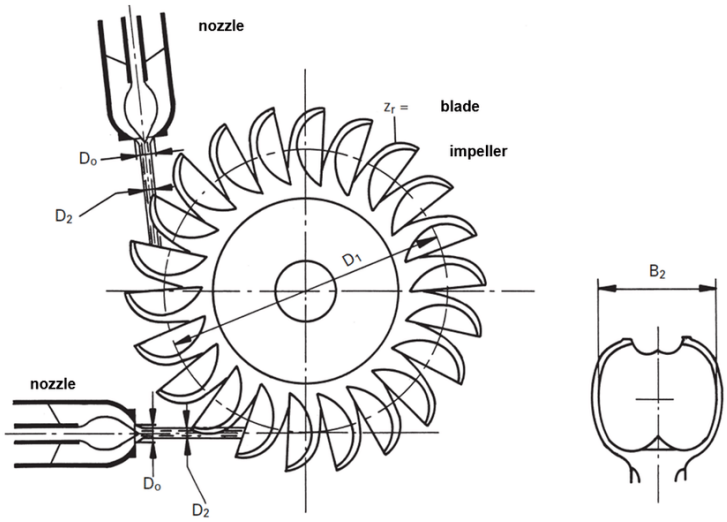


Figure 2.16: Schematic of the Pelton-type turbine (image retrieved from Prodanovic et al.[108])

of 60-70%. Another type of impulse turbine considered for two-phase expansion is a Pelton-type turbine (Fig.2.16) [108]. Iqbal et al. [110] constructed a complete trilateral flash cycle experimental rig, using the Pelton-type expander with a stationary converging-diverging two-phase nozzle. The researchers reported relatively low turbine efficiency (around 25%), which was partly caused by the high jet speeds, for which the turbine buckets were not designed. However, even for lower jet speeds, the turbine efficiency did not exceed 40%. Based on the experimental results, the authors suggested that the Pelton-type impulse turbine is not suitable for trilateral flash cycle systems. He et al. [111] designed and manufactured a Pelton-type impulse turbine for throttle valve replacement in domestic refrigeration systems that use R-410A as the working fluid. The Pelton turbine demonstrated a stable operation during two-phase operation for rotational speeds up to 26,500 rpm, however, the maximum efficiency was only around 32%.

Two-phase radial-inflow turbines

A modified radial-inflow turbine has been developed by Elliot Group, a subsidiary of Ebara Corportation [112], which is the primary developer and manufacturer of two-phase expander for cryogenic applications. The turbine produced by Elliot Group was recently reviewed by Karakas & Stasenko [113], who provided a detailed description of the turbine and its operation. The main components of the turbine can be seen in Fig. 2.17. The subcooled liquid is first accelerated in the static nozzle, and then it enters the rotor component. The fluid remains in the liquid state within the nozzle-rotor stage, which eliminates the issue surrounding the erosion highlighted by other researchers discussing the two-phase radial-inflow turbines. Phase change (flashing) occurs downstream of the rotor exit in a part called exducer, specifically designed for that purpose. The exducer is essentially a rotating axial outflow turbine, wherein the fluid accelerates due to phase change, imparting its momentum to the rotating shaft. The two-phase mixture leaving the exducer travels to the condensation cone, which acts as a diffuser to recover static pressure of the flow. In the second part of the work, the authors used actual site performance data to perform thermodynamic analysis to

quantify the benefit of using the two-phase turbine instead of the throttle valve, as well as to assess the performance of the expander in single- and two-phase operation [113]. Thermodynamic analysis showed that replacing the throttle valve with the two-phase turbine resulted in a 1.7% increase in the mass flow rate of liquefied natural gas, while generating 80 kW of power at a mass flow rate of 27.5 kg/s. The corresponding isentropic efficiency was 82.1 %, while the vapour quality at the exducer outlet (the condensation cone was not included in the design) reached 5.9%. The expander speed varied between 2200 and 3800 RPM. As for two-phase expansion, the turbine efficiency is remarkably high, however, it should be borne in mind that flashing was rather limited with the vapour quality reaching only 5.9% at the exducer outlet. Since the nozzle and rotor components are designed for single-phase operation, the authors suspect that the overall capability of the turbine to handle two-phase flows is rather limited.

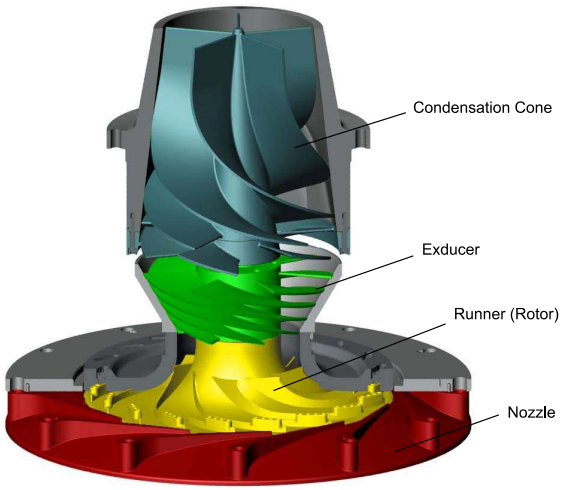


Figure 2.17: A cryogenic two-phase radial-inflow turbine developed by Elliot Group (image retrieved from Patel & Kimmel [114])

Niu et al. [115] conducted experimental tests on a two-phase cryogenic radial-inflow turbine with the aim of measuring the liquid fraction at the turbine exit and its effect on performance. The radial-inflow turbine was integrated within an industrial air separation plant to carry out the tests. An electric heater was installed at the turbine outlet to determine the outlet vapour quality based on the applied heat balance. Five two-phase tests were recorded, with the outlet vapour quality varying between 98.85 and 94.98%. Additional five single-phase (superheated vapour) tests were performed to quantify performance deterioration as a result of condensation (wetness loss). The radial-inflow turbine had a rotor diameter of 56 mm and a degree of reaction of 0.5. The inlet temperature and pressure varied between -174 and -157 °C, and between 3.58 and 4.27 bar, respectively. The pressure ratio varied between 2.63 and 3.30, while the turbine speed was between 50,000 and 55,000 rpm. The two-phase turbine generated between 3.2 and 4.4 kW in the two-phase operation, while having an efficiency in proximity of 86%. As the outlet vapour quality fell from 98.85 to 94.98 %, the corresponding drop in efficiency increased from 1.5 to 2.6%, compared to the single-phase operation. Zhang et al. [116] recognised that the use of two-phase volumetric expander can be justified

in CO_2 refrigeration system due to limited volumetric expansion ratios. For example, the volumetric expansion ratio in CO_2 refrigeration systems was typically between 2 and 3, while it could get as high as 22 when R22 or R134a were used. For such high expansion ratios, it is difficult to construct an efficient single-stage volumetric expander, which motivated the authors to investigate the use of radial-inflow turbines in these systems. A prototype of the turbine, working with R22, was tested, showing very poor performance, with the maximum isentropic efficiency as low as 10.4%. The poor performance can be attributed to a very simplistic nozzle design (a simple diverging bore). Furthermore, an existing rotor component was used, which could be far from optimal under the investigated operating conditions, while the rotational speed was much lower than in standard radial-inflow turbines.

Tesla turbines
Apart from the turboexpanders described above, a less conventional bladeless type of expansion machine, invented by Nikola Tesla [117], was also considered for two-phase applications. In the Tesla turbine, a pressurized fluid is being accelerated through a single or several nozzles. The high-speed fluid is passed through very narrow gaps between stacked rotor disks, which are being rotated due to friction between the fluid and the disks. The bladeless expander was originally considered for air and steam applications. Renuke et al. [118] summarized the experimental tests conducted on Tesla turbine prototypes revealed that the tested prototypes demonstrated relatively low performance, with a peak efficiency typically between 30 and 40%. Recently, Talluri et al. [119] proposed the Tesla turbine as an ORC expander for micro-scale applications with power ratings of up to several kilowatts. They carried out some experimental studies using R1233zd(E) as the working fluid. The maximum adiabatic efficiency of the turbine was about 30%, while the turbine shaft efficiency was below 10%. Talluri et al. [120] extended the analysis of the Tesla turbine to two-phase flows. The authors applied an analytical model for two-phase expansion in the turbine and proposed a prototype model. However, no experimental two-phase tests have yet been conducted.

2.6.2.3 Summary of two-phase expanders

Tables 2.2 and 2.3 present the summary of the reviewed experimental prototypes and commercial units of two-phase volumetric and turboexpanders. The tables include information about the size of the expander (D), and in case of volumetric expanders, built-in volume ratio (BVR) was also included. The operating conditions were summarised in terms of inlet temperature (T_{in}) and pressure (P_{in}), while the performance of the expander was described in terms of shaft speed (N), power output ($\dot{W}$) and peak efficiency (η_{max}).

Looking at the summary of volumetric expanders, it can be seen the screw expanders achieved efficiencies over 70% at power output between 10 and 70 kW with the shaft speed typically between 1800 and 3600 rpm. These were mainly applied to low temperature expansions with the inlet temperature between 90 and 120 °C. The size of the machines range from around 100 to 200 mm, while offering built-in volume ratio of up to 6. Although experimental units generated power in the order of tens of kW, numerical studies indicate that two-phase screw expanders could also be used in larger-scale applications. On the other hand scroll and vane expanders are more suitable for micro-scale applications with power outputs up to several

Table 2.2: The summary of performance of experimental and commercial units of two-phase volumetric expanders; VCR, CHP and RC stand for vapour compression refrigeration, combined heat and power and Rankine steam cycle respectively

Ref	Type	App.	Fluid	$D\,(mm)$	BVR	$T_{in}\,(°C)$	$P_{in}\,(bar)$	$N\,(rpm)$	$\dot{W}\,(kW)$	$\eta_{max}\,(\%)$
[80]		TFC	R113	204	3-6	90-120	sat.	1800-3600	25	70
[81]		VCR	R113	127.5	2.85	126	8.45	2000-3000	10-15	70
[82]	Screw	TFC	R113	127.5	2.85	-	-	2500-3600	10-20	76
[83]		ORC	R124	102	-	90	-	1800	22	74
[84]		RC	Water	145.6	-	120-190	2-13	4500	30-70	78
[89]		VCR	CO_2	-	2.18	40	90	2500	-	55
[91]		RC	Water	-	2.00	-	83	2655	0.7	83
[90]	Scroll	RC	Water	-	2.00	-	83	2655	0.7	83
[92]		CHP	Water	-	-	-	-	1800	2.4	45
[92]		CHP	Water	-	-	-	-	1800	1.4	40
[89]		VCR	CO_2	-	2.00	35-45	91	1000-2500	-	50-60
[94]	Vane	VCR	CO_2	46	-	32-44	75-90	800	-	23
[95]		VCR	CO_2	-	-	34-42	80-90	1000-1500	0.65-0.98	45

kilowatts. In fact the power output of the reviewed experimental units did not exceed 2.4 kW. Scroll expanders generally showed to be capable of high efficiencies, of the order of 80%, with the rotational speed of 1800-2600 rpm. Vane expanders suffer from significant friction losses, which limits their efficiency to about 50-60%. Both, scroll and vane expanders, had a low built-in volume of around 2. Although, reciprocating piston expanders could be in theory applied to two-phase expansion, previous studies indicate they are less suited to wet conditions that other volumetric expanders.

When it comes to two-phase turboexpanders, both rotary separator and Pelton-type turbines demonstrated rather unsatisfactory performance, with a maximum efficiency below 45%. The most frequently used two-phase turbine was the axial impulse turbine. Small units, applied in refrigeration cycles were capable of achieving efficiencies of 50-55%, while generating as little as 15 kW of power. The efficiency of larger units with power output between 170 and 2200 kW demonstrated higher efficiencies, typically between 60 and 70%. The highest recorded efficiency of 74% was achieved by an impulse turbine applied to waste heat recovery from a marine diesel engine. Although radial-outflow and radial-inflow turbines demonstrated remarkably good performance, with peak efficiencies exceeding 80%, it should be reiterated that these expanders have been designed for rather limited wet conditions, with the mass fraction of the liquid phase below 10%. Hence, they resembled more closely the operation of single-phase rather than two-phase machines, which is why they are characterised by such high efficiencies.

Table 2.3: The summary of performance of experimental and commercial units of two-phase turboexpanders; GTH and CRG stand for geothermal and cryogenic application respectively

Ref	Type	App.	Fluid	$D\,(mm)$	$T_{in}\,(°C)$	$P_{in}\,(bar)$	$N\,(rpm)$	$\dot{W}\,(kW)$	$\eta_{max}\,(\%)$
[98]	Rotary separator	GTH	Brine-steam	762	<177.8	-	-	21	35
[98]				1372	227	27.6	-	1569	35
[100]				305	-	8.1	-	42	46
[101]	Radial-outflow	Kalina	NH3-water	254	115.3	20	28,000	610.5	82.4
[28]	One-stage axial impulse	-	Water-nitrogen	263	22	20	1652	9.90	47.5
[28]		-	R22	261	18.6	8.75	1880	6.34	52.4
[106]		VCR	R134a	-				15	55
[104]		VCR	R134a	-				15	64
[103]		VCR	R134a	71.1	-	-	12,800	0.31	56
[107]		GTH	R134a	406	112.8	-	3600	1242	73
[104, 107]		WHR	R245fa	-	190-210	-		172	74
[104, 107]		WHR	R245fa	-	190-210	-		227	65
[121]		CRG	LNG	-	-	-		300-2200	60-70
[28]	Two-stage axial impulse	-	Water-nitrogen	261	22	20	2200 (1st), 678 (2nd)	10.57	50.7
[89]	Pelton	TFC	-	-	-		-	-	25-40
[94]		VCR	R410A	-	-		26,500	-	32
[113, 121]	Radial-inflow	CRG	LNG	-	-120	44.68	2200-3800	80	82.1
[115]		CRG	Air	56	-174 to -157	3.58-4.27	50,000-55,000	3.2-4.4	86
[116]		VCR	R22	-	-		-	-	10.4

2.7 Wet-to-dry cycle

The main advantage of two-phase cycles is the capability to absorb more heat from the heat source and consequently generate more power. However, if the two-phase expander has low efficiency, the advantage over the conventional single-phase cycles may become insignificant

as a fraction of the extra-absorbed energy would be wasted due to the inefficiency of the expander. Moreover, the additional cost related to the larger heat exchangers size and higher feed-pump power requirement may completely outweigh any benefits that the two-phase expansion can bring. Hence, an efficient two-phase expander is a critical component in any two-phase cycle. Previous studies on trilateral flash cycles indicate that the two-phase expander should have an efficiency of at least 75% for the cycle to be a viable alternative to single-phase architectures. It has been showed that screw and scroll expander can reach that level of efficiency, with the first having an advantage of wider power scale, while the latter is more suitable for micro-scale applications. The main limitation of these machines lies in their limited built-in volume ratio, which leads to lower efficiencies at higher expansion ratios. This effectively confines the use of the volumetric expanders to low-temperature applications (around 100-150 °C). On the other hand turboexpanders can facilitate much higher volumetric expansion ratio per stage, however the reviewed experimental studies indicate that these often exhibit lower performance than their single-phase counterparts, and may struggle to reach the 75% efficiency threshold. Certain two-phase turboexpanders demonstrated efficiencies in excess of 80%, but these were designed to handle limited two-phase conditions, effectively resembling the operation of single-phase machines. Furthermore, certain turbine architectures, such as radial-inflow turbine, which have often been the turbine of choice in small-to-medium scale applications, had been discarded due to erosion problems. To conclude, there is currently lack of efficient two-phase machines that could be applied in two-phase power cycles above 150 °C, which could facilitate substantial phase change, while achieving efficiency greater than 75% efficiency.

It is apparent that the design of an efficient two-phase expander for heat sources with temperatures above 150°C is a challenging task. One of the advantages of organic Rankine cycles is the freedom to choose a working fluid from a wide range of organic compounds. There exist fluids that have a positive slope of the saturated-vapour curve when viewed on the temperature-entropy diagram. These fluids are often referred to as dry fluids. They theoretically allow for an expansion that would begin under the two-phase dome and end in the superheated vapour region. Such a cycle architecture has been illustrated on the T-s diagram in Figure 2.18; it is essentially a partially-evaporated organic Rankine cycle with the wet-to-dry transition during expansion. The cycle will be referred to as a wet-to-dry cycle in the current work.

The phase change during expansion is the result of rapid depressurisation which drives the fluid vapourisation - a process referred to as flash boiling or simply flashing. The transition from a two-phase mixture to superheated vapour opens up the possibility of employing the existing turboexpander architectures, while eliminating the issues surrounding the presence of two-phase flow in the rotor of the turbine. The idea is to perform the first part of the expansion, where the transition from two-phase mixture to dry vapour occurs, within the stator of the turbine. This would then make the rotor work in dry conditions, avoiding liquid droplets collision with the high-speed rotor blades, leading to a more efficient erosion-free operation. One of the limitations of two-phase volumetric expander is the limited built-in volume ratio, which essentially means that at higher temperatures either multi-stage expanders or more complex cycles, such as the one proposed by Smith et al. [54], are required.

Since the turboexpanders can facilitate significantly higher volumetric expansion ratios, the wet-to-dry cycle could be applied at temperatures above 150 °C, while maintaining simple system layout with a single-stage expansion machine.

Elliott [28] was the first to discuss the concept of the wet-to-dry cycle. The author carried out some preliminary study on the wet-to-dry expansion of toluene in a converging-diverging nozzle. The results of the simulation seem promising, as complete vapourisation was predicted with nozzle reaching an efficiency as high as 98 %. Although the details concerning the model used to simulate the two-phase expansions were not included in the report, it appears that the authors used a one-dimensional code which only account for the velocity slip between the phases, while neglecting the thermal non-equilibrium effects.

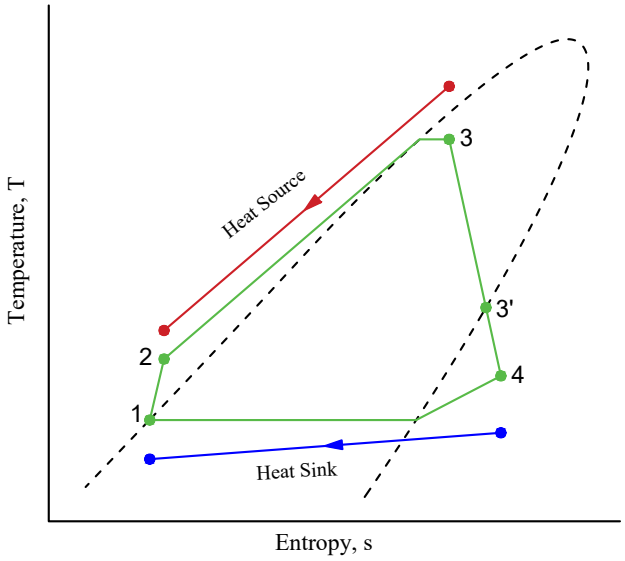


Figure 2.18: Temperature-entropy diagram of the wet-to-dry organic Rankine cycle

This concept was recently revisited by White [8], who identified the most suitable fluids and operating conditions for the cycle. The author also carried out preliminary design of the radial-inflow turbine and CFD simulations of the two-phase expansion within the turbine stator. With heat source temperature varying between 150 and 250 °C, the wet-to-dry cycle was capable of generating between 28 to 3% more power than the single-phase ORC with greater advantage towards the lower limit of the considered temperature range.

White [8] identified several promising fluids for the application in the wet-to-dry cycle. Figure 2.19 illustrates the saturation curves of these fluids on the temperature-entropy diagram, while their critical properties and important environmental indices are shown in Table 2.4. All the fluids are characterised by very low global warming potential (GWP $\leq$ 5) and zero or near-zero ozone depletion potential (ODP). The siloxanes and Novec fluids feature the most favourable shape of the saturation curve, allowing to theoretically expand the fluid from low inlet vapour quality to superheated vapour regime. The cycle optimisation study demonstrated that for heat-temperature in the range of 150 to 250 °C, the greatest ther-

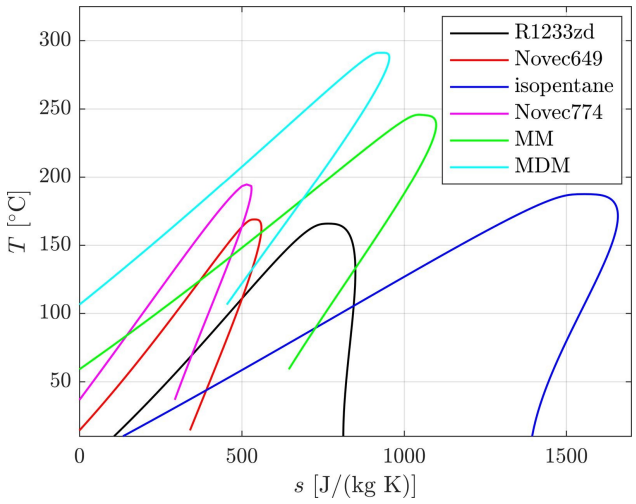


Figure 2.19: Saturation curves of the most promising fluids identified by White [8] for the wet-to-dry cycle.

modynamic advantage of two-phase expansion was achieved using the siloxanes MM and MDM [8]. However, using MDM was associated with very high pressure ratios (over 100) and near-vacuum condensation conditions. Therefore, the siloxane MM was chosen as the optimal working fluid, due to improved technical feasibility of the turbine design, and only slightly worse thermodynamic performance in relation to the siloxane MDM.

Table 2.4: Critical properties and environmental indices of potentially suitable fluids for the wet-to-dry cycle.

Fluid	T_{cr} [°C]	P_{cr} [bar]	GWP	ODP
R1233zd [122, 123]	165.8	35.7	~ 3.8	≤ 0.0004
iso-pentane [124, 125]	187.3	33.8	5	0
Novec649 [126]	168.8	18.7	~ 1	0
Novec774 [127]	195.4	17.1	~ 1	0
Siloxane MM [128, 129]	245.7	19.4	0.48	0
Siloxane MDM [130, 131]	291.1	14.2	0.33	0

With the siloxane MM as the working fluid, and the heat source set to 200 °C, the author carried out a preliminary design of the radial-inflow turbine, based on the meanline-model approach and a set of loss model for predicting the turbine efficiency. Since the rotor would work in dry vapour conditions if the wet-to-dry transition is successfully achieved in the stator, the existing rotor loss correlation were deemed applicable. On the hand, the flow within the stator transitions from a two-phase mixture to a superheated vapour, which casts doubts on the applicability of the existing loss models developed for single-phase expansions. To address this issue, the author derived a dedicated nozzle loss correlation based on a set of CFD simulations performed for several stator geometries. Using the loss models and the cycle model, the author analysed the dependence of cycle and turbine performance on key parameters, such as the inlet vapour quality and the degree of reaction. The former strongly

affects the thermodynamic performance of two-phase cycles, while the latter has a significant influence on turbine performance. Defining the fraction of total expansion taking place in the nozzle, the degree of reaction is also of particular importance as far as the wet-to-dry transition is concerned. The effect of these two parameters on cycle and turbine performance is shown in Fig. 2.20.

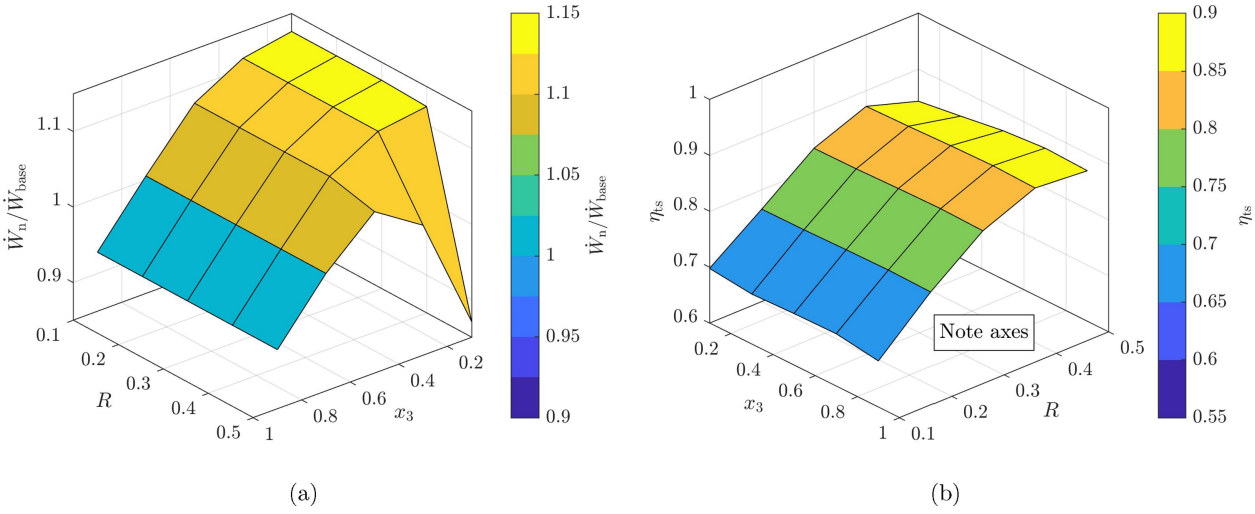


Figure 2.20: The effect of inlet vapour quality and degree of reaction on the wet-to-dry cycle power output (a) and turbine total-to-static efficiency (b); the power output was normalised by the corresponding single-phase ORC power output to demonstrate the relative advantage of two-phase expansion.

If one refers to the temperature-entropy diagram of the wet-to-dry cycle shown in Fig. 2.18, the higher the degree-of-reaction, the further the fluid can expand into the super-heated vapour region. This indicates that having a low degree-of-reaction could increased the chances of achieving dry vapour flow at the rotor inlet. However, the optimisation results suggest that lowering the degree-of-reaction can be limited in practical turboexpanders. It was found that as the degree of reaction was reduced below 0.4, the turbine performance rapidly deteriorated. On the other hand, the inlet vapour quality had no significant effect on the turbine performance but strongly affected the cycle performance, with the lowest quality corresponding to the highest power output. With that being said, it was later shown that low inlet qualities are generally associated with higher volumetric expansion ratios which can affect the turbine design and performance. In summary, the results indicate that higher degree-of-reaction and lower inlet vapour qualities are desired as far the cycle performance and turbine efficiency are concerned. The total-to-static turbine efficiency at an optimal point corresponding to the degree of reaction of 0.4 and an inlet vapour quality of 0.1, was estimated to be above 87%, with the rotor working in subsonic conditions.

Lastly, the author conducted a CFD simulation of the two-phase expansion occurring in the turbine stator. An assessment of the flow field indicates a successful wet-to-dry transition at about two thirds of the streamwise distance, pointing to the feasibility of a wet-to-dry turboexpander concept. Nevertheless, the simulations were performed using a homogeneous-equilibrium model, which assumes that both phases instantaneously exchange momentum

and heat, maintaining identical velocities and temperatures throughout the expansion. This is a significant oversimplification of the phase change process and such a model may not be adequate given the rapid mixture acceleration and the resulting small time scales for momentum and heat exchange. This issue will be further elaborated on in the next chapter, when discussing suitable modelling techniques for the wet-to-dry expansion.

There are several types of turboexpanders that could potentially be used in the wet-to-dry cycle. The first candidate is the radial-inflow turbine, which was investigated by White [8]. Generally speaking, radial-inflow turbines are often the turbine of choice for small-to-medium scale applications due to reasons described in Section 2.6.1.1. They proved to be highly efficient as long as single-phase rotor conditions were maintained [113, 115]. However, due to centrifugal force acting in the direction opposite to the flow direction at the rotor inlet, severe erosion problems could arise in case incomplete vapourisation in the nozzle [103]. Therefore, for successful operation of the radial-inflow turbine in the wet-to-dry cycle, complete mixture vapourisation has to be ensured. An alternative turbine architecture is the radial-outflow turbine, which as discussed before, has several advantages when it comes to two-phase applications. One significant advantage is that it can better tolerate wet conditions, as any liquid present in the rotor will be centrifuged toward the turbine exit. The other advantage is the increasing cross-sectional area in the streamwise direction, which helps facilitate higher volumetric expansion ratios within fewer number of stages. Another potentially suitable candidate are impulse axial turbines, which demonstrated efficiencies close to 70% under two-phase conditions. Welch & Boyle [101] pointed out that the rotor efficiency in these turbines is strongly affected by the vapour quality of the two-phase jet leaving the nozzle. Since in the wet-to-dry cycle it is possible to fully vapourise the fluid within the nozzle, it is expected that these machines could achieve higher efficiencies than those reported in Table 2.3. Furthermore, the impulse axial turbine may benefit from the two-phase nozzles having a straight centreline (non-deflecting nozzle), which could help prevent phase separation and achieve uniform flow conditions at the rotor inlet.

Independently of the type of selected turboexpander, the critical component in the wet-to-dry turbine is the nozzle, which has to facilitate complete vapourisation of the two-phase mixture and deliver dry vapour flow to the rotor in an efficient manner. Provided this is accomplished successfully, the rotor would only work in dry conditions thus making the application of well-established design and analysis methods justified. In the current absence of directly relevant experimental data, the feasibility of designing such a nozzle must be assessed by means of numerical tools. Preliminary CFD simulations conducted by White [8] seem promising, suggesting that a high-efficiency stator can be designed that facilitates the complete wet-to-dry transition, while maintaining efficiency in the order of 90%. Nevertheless, these preliminary CFD results were obtained with an oversimplified phase-change model that may be inadequate under the conditions present in wet-to-dry nozzles. This issue is discussed in the next chapter that outlines the summary of numerical methods applicable to simulating wet-to-dry expansion. The next chapter also highlights the knowledge gap related to simulating wet-to-dry expansion and provides the context to the current work.

2.8 Conclusions

Organic Rankine cycles have been identified as a viable means of exploiting low-grade thermal energy sources. Owing to their flexibility in terms of temperature level and power scale, ORC systems are an attractive power-generation technology for a variety of applications including renewable energy and waste-heat recovery. It has been shown that the main factor restricting further improvement of these systems is the isothermal evaporation process, which is associated with limited power outputs and substantial exergy losses.

Several alternative cycle architecture have been proposed to mitigate the issue of isothermal evaporation, improve the performance of ORC and consequently aid broader commercialisation. A promising alternative cycle architecture, is one in which the fluid is only partially evaporated prior to expansion. The main challenge surrounding the design of this type of cycles is the availability of efficient two-phase expanders. Volumetric expanders were proven to be capable of operating under the the two-phase regime, however, limited built-in volume ratios make them suitable only for temperatures up to approximately 150 °C.

Using certain molecularly-complex fluids it is possible to design a wet-to-dry cycle, wherein the working fluid can transition from a two-phase mixture to superheated vapour state during expansion. Such a cycle architecture can potentially generate up to 30% more power from heat sources at temperatures between 150 and 250 °C, compared single-phase organic Rankine cycle. The fact that the fluid can transition from a two-phase to a superheated vapour state opens a way to employ existing turboexpanders. In comparison with volumetric expanders, turboexpanders can accommodate much higher volumetric expansion ratios, which can effectively extended the application of two-phase organic Rankine cycle to temperatures above 150 °C. This, however, requires the wet portion of the expansion to be confined within the nozzle/stator of the turbine. to ensure efficient erosion-free operation.

Due to lack of directly relevant experimental data, the feasibility of designing a turboexpander for the wet-to-dry cycle is currently being assessed numerically. Preliminary CFD studies indicate that it is possible to design high-efficiency radial-inflow turbine with a subsonic rotor and a stator that facilitates a complete wet-to-dry transition of the two-phase mixture. Nevertheless, these results were obtained using an oversimplified homogeneous-equilibrium model for predicting the phase change process taking place in the stator, which may be inadequate under the conditions of interest. This necessitates further research and application of more realistic models for predicting the wet-to-dry expansion.

Chapter 3

Modelling flash boiling

3.1 Introduction

The two-phase mixture entering the wet-to-dry nozzle begins to evaporate in a process referred to as flash boiling or simply flashing. It is a phenomenon that occurs when a liquid is subjected to depressurisation such that its pressure drops below the saturation level, which initiates the phase change process. In the wet-to-dry nozzle, flashing is associated with a sudden fluid acceleration in the streamwise direction and the simultaneous pressure drop. Flashing is similar in nature to cavitation, but it typically occurs at higher pressures and temperatures with the phase-change process assumed to be dominated by the interphase heat transfer, whereas the effect of pressure non-equilibrium is deemed negligible [30, 132]. Flashing is present in various technical scenarios, such as flows through cracks and restricted areas (e.g., orifices, valves) or liquid expansion through nozzles and injectors. It has been extensively studied both experimentally and numerically in the context of nuclear safety analysis [30]; specifically, in the context of loss of coolant accidents [31], flow-induced instabilities in passive containment cooling systems [32], and flows through pressure relief valves [33] and nozzles [34, 35]. Flashing can also be present in refrigeration systems (e.g. flashing in two-phase ejectors that replace the throttle valve) [36–38], two-phase geothermal turbines [39–42] and the proposed wet-to-dry cycle [8, 43]. In this chapter, relevant literature concerning the simulation of flashing flows is reviewed in an attempt to select a suitable modelling technique for simulating the wet-to-dry expansion in a converging-diverging nozzle. Previous studies of the wet-to-dry expansions are reviewed, and important research gaps are identified. This helps to define the scope of the current work, which is discussed at the end of the chapter.

3.2 Modelling frameworks

When modelling two-phase flows, one first has to select a suitable framework, which depends on factors such as multiphase flow regime, the simulated physical phenomenon, and the primary purpose of analysis. This study is concerned with simulating two-phase expansion of partially evaporated liquids. Due to liquid density being approximately two orders of mag-

nitude higher than that of vapour, even low-quality mixtures are likely to have the liquid volume fraction below 30% at the nozzle inlet, which will further diminish as the vapourisation takes place. Therefore, it is reasonable to assume a droplet flow regime when analysing the wet-to-dry expansion. For such dispersed two-phase flows, the two primary frameworks that can be potentially be applied include the Eulerian-Lagrangian and Eulerian-Eulerian approaches. The two frameworks differ in the approach to modelling the dispersed liquid droplets as illustrated in Fig. 3.1. In the Eulerian-Lagrangian framework, the individual droplets are tracked through the flow-field and can interact with the surrounding vapour. Eulerian-Eulerian framework treats both phases as interpenetrating continua. Instead of resolving the flow of individual droplets, the concentration of droplets in particular domain

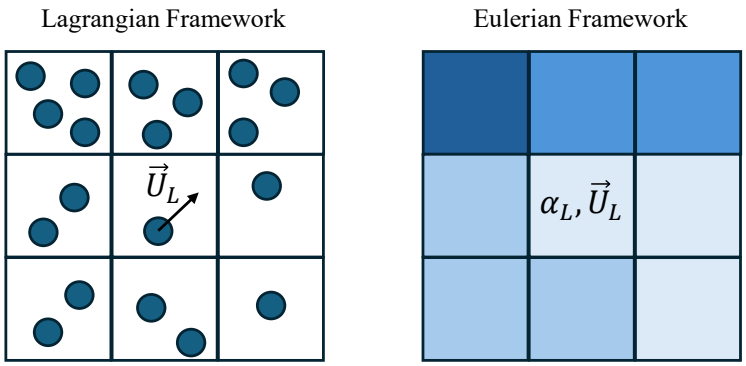


Figure 3.1: The comparison of Eulerian-Lagrangian and Eulerian-Eulerian methods for modelling dispersed droplet flows. In the Eulerian-Lagrangian framework individual droplets are tracked through the flow-field, while the Eulerian-Eulerian framework treats both phases as interpenetrating continua with a volume fraction α_L used to represent the concentration of liquid in each cell. The shades of blue represent concentration of liquid according to the number of droplets occupying the cell.

3.2.1 Eulerian-Lagrangian framework

The Eulerian-Lagrangian framework, often referred to as the *Particle Tracking Model*, is suitable for modelling continuous-dispersed type of two-phase flows. The dispersed phase is modelled as a set of discrete particles, bubbles or droplets, which are tracked as they travel through the continuous medium. Since the model follows the particles through the flow-field, it is particularly useful when exact trajectories and distribution of the dispersed phase is of interest or certain dynamics effects such as droplet breakup and coalescence are to be resolved. The Eulerian-Lagrangian can also account for the heat and mass transfer between the continuous and dispersed phases, making it suitable for simulating problems involving phase change.

When it comes simulating flash boiling, the Eulerian-Lagrangian model has mostly been applied to flash atomisation problems. It occurs when a liquid is injected into a low-pressure environment, causing it to undergo a rapid flash evaporation and breakup into small droplets.

It has previously been recognised that the presence of flashing can significantly alter the atomisation process and the resulting spray patterns. Compared to conventional methods, flash atomisation can potentially generate more homogeneous sprays with smaller droplets for a given pressure ratio applied across the injection nozzle [133, 134]. Moreover, sprays generated under flash-boiling conditions are typically characterised by wider cone angles and reduced penetration lengths [133, 134]. Flash atomisation may play an important role in a variety of applications that rely on injection systems. Some examples include combustion, spray cooling, coating industry and spray drying [134].

A number of authors have employed the Eulerian-Lagrangian framework to simulate flash atomisation inside cylinders of direct-injection internal combustion engines. Flash-boiling conditions within the engine cylinders can have either a beneficial or detrimental effect on the combustion efficiency, depending on factors such as liquid superheat level [135, 136]. In such problems, the emphasis is placed on assessing the spray formation process, hence, the Lagrangian treatment of fuel drops is preferred as it allows for estimating the trajectories of droplets, accounting for droplet dynamics effects and simultaneous flash evaporation. Price et al. [137] followed the Eulerian-Lagrangian approach to investigate fuel spray formation under flash boiling conditions, using the RANS approach with k-epsilon/RNG turbulence model. Suitable models for superheated droplet vapourisation, aerodynamic breakup and droplet-droplet collisions were applied. The model was able to predict key spray characteristics and the simulations results agreed relatively well with the experimental data. In subsequent CFD studies [136], the authors coupled the Eulerian-Lagrangian model with a reduced-order nucleation model for assessing the effect of flashing occurring inside the nozzle, prior to the injection. The model was able to predict important spray features such as spray collapse, plume merging and droplet recirculation for various types of injectors and operating conditions. Beside the aerodynamic breakup, nucleation and sudden growth of bubbles inside the fuel droplets can cause them to shatter and burst outward, leading to cone angle widening near the nozzle exit. This effect was successfully simulated within the Eulerian-Lagrangian framework in the following study of Price et al. [138]. Duronio et al. [139] also employed the Eulerian-Lagrangian framework to conduct CFD simulations of fuel spray formation, accounting for primary and secondary breakup, droplet collisions and droplet vapourisation under flashing conditions. The predicted shape of the spray and the penetration length agreed well with the experimental data. The authors later [140] improved the model by coupling it with Eulerian-Eulerian CFD solver used for simulating flashing inside the injection nozzle to provide a more accurate initialisation for the Eulerian-Lagrangian simulations. A similar approach was taken in the former studies, where the Eulerian-Eulerian framework was employed to simulate in-nozzle flashing [141]. Various spray characteristics predicted by the coupled model were compared with the experimental data demonstrating a good agreement.

Although, most of numerical studies on flashing sprays revolved around internal combustion engines, the Eulerian-Lagrangian model has also been applied to other applications. Bi et al. [142] employed the Eulerian-Lagrangian framework to perform CFD simulation of flash atomisation taking place inside a two-phase ejector. The authors studied the effects of vapourisation rate and physical properties of liquid droplets on the atomisation process.

Owing to high heat-transfer rates and efficient heat dissipation, spray cooling has been considered for cooling of electronic devices as an alternative to air cooling [143]. Chen et al. [144] used the Eulerian-Lagrangian model to investigate the performance of flash spray cooling in the context of spacecraft applications. The authors conducted CFD study to simulate droplets impingement onto a rectangular plate, which was the object of cooling. The results allowed to evaluate the heat-transfer process and the influence of operating conditions and nozzle geometry on cooling performance.

In summary, flash atomisation can be present in a variety of technical applications, with internal combustion engines being the most studied area. Numerical simulation of flash atomisation is a complex task that requires adequate models for predicting droplet dynamics effects as well as flash evaporation occurring due to low-pressure injection environment. The Eulerian-Lagrangian framework, being capable of predicting trajectory and behaviour of individual droplets, has frequently been the model of choice in this type of problems. The studies cited above indicate that the CFD simulations implemented within the Eulerian-Lagrangian framework were able to reproduce spray patterns in flash-boiling conditions under various operating conditions with a reasonable accuracy compared with experimental data. For a more comprehensive review on flash-atomisation problem, an interested reader is referred to the reviews conducted by Sher et al. [133] and Bar-Kohany & Levy [134].

3.2.2 Eulerian-Eulerian framework

The Eulerian-Lagrangian framework requires solving the governing equations for all individual particles or representative parcels of particles, which means that the simulation can be very computationally demanding in case of high volume fraction of the dispersed phase [145]. Moreover, the complexity of the simulation increases with volume fraction of the dispersed phase due to more frequent particle-particle interactions. Therefore, the Eulerian-Lagrangian method is typically limited to low volume fraction, below 10% [146].

In contrast to the Eulerian-Lagrangian model, the Eulerian-Eulerian model assumes that the two-phase flow is composed of two interpenetrating continua with conservation equations solved for each phase. As such, the Eulerian-Eulerian approach is more versatile and can be applied to both continuous-continuous and continuous-dispersed two-phase flows. In the latter case, instead of tracking individual particles, the dispersed phase is represented by a volume fraction, which defines the concentration of the dispersed phase in a given control volume. Average phase properties (velocity, temperature etc.) are determined in each control volume rather than on a individual particle basis. The Eulerian-Eulerian model is applicable to multiphase flows with a wide spectrum of volume fractions, benefiting from low computational cost for flows with high concentration of the dispersed phase. This is why in simulating flash-boiling sprays, some authors resorted to the Eulerian-Eulerian approach to account for flashing occurring inside the nozzle prior to the injection, which involves liquid phase turning into a two-phase mixture [140, 141]. Since individual particles (droplets or bubbles) are not followed through the flow field, the Eulerian-Eulerian approach provides a less-detailed description of the dispersed particles. However, when predicting the exact trajectory and behaviour of individual particles is not of primary importance, the Eulerian-

Eulerian model can be sufficiently accurate, providing a more qualitative description of the two-phase flow with local concentration of the dispersed phase represented by the volume fraction.

The current research is concerned with simulating a wet-to-dry expansion inside nozzle channels, wherein the fluid transitions from a two-phase mixture to a superheated vapour. The quality of mixture entering the nozzle can be as low as 10%, which means that the volume fraction of the dispersed phase can be significantly higher than 10%. This combined with the fact that the main interest lies in investigating the overall phase change process rather than tracking individual droplets, the Eulerian-Eulerian framework is deemed more suitable for this type of analysis. This framework has been frequently adopted in most of former CFD studies on flash boiling in confined channels, conducted by Liao et al. [30, 132] and Ortego Sampedro et al. [147] will also be applied in the current work to simulate the wet-to-dry expansion.

3.3 Flash-boiling models

In the previous section, two-phase flow modelling frameworks have been discussed, highlighting the suitability of the Eulerian-Eulerian approach for simulating the wet-to-dry expansion inside the nozzle channel. Having selected the Eulerian-Eulerian approach, one has to choose an appropriate model for simulating the flash-boiling process itself. Numerical modelling of flashing is a complex task as the two phases simultaneously exchange mass, momentum, and energy throughout the expansion. Realistic flows are characterised by finite rates of interphase momentum and heat transfer, which adds to the complexity as disparity in velocities (inhomogeneous flow) and temperatures (thermal non-equilibrium flow) can develop, with the two phases deviating from the saturation conditions and entering the metastable states (superheated liquid or subcooled vapour). This disparity in velocities and temperatures of liquid and vapour are commonly known as non-equilibrium effects.

There have been different models proposed in the literature, which vary in complexity, depending on the treatment of non-equilibrium effects. Generally, three categories of models can be distinguished that include equilibrium, semi-equilibrium and non-equilibrium models. The equilibrium model assumes an instantaneous transfer of momentum and heat such that both phases have identical velocity and temperature; this is commonly known as the homogenous-equilibrium model. The semi-equilibrium models include inhomogeneous equilibrium and homogeneous non-equilibrium models. The former assume thermal equilibrium but account for a velocity slip, typically relying on some form of an analytical or empirical slip ratio correlation [132]. The latter assume identical velocities, but account for a finite rate of heat transfer between the phases. Some homogeneous non-equilibrium models proposed in the past include the homogenous-relaxation and delayed equilibrium models. Lastly, there is a full non-equilibrium model that accounts for both mechanical and thermal non-equilibrium. Such a model formulates in the Eulerian-Eulerian framework is referred to as a two-fluid model, which is recommended when both velocity and temperature disparity

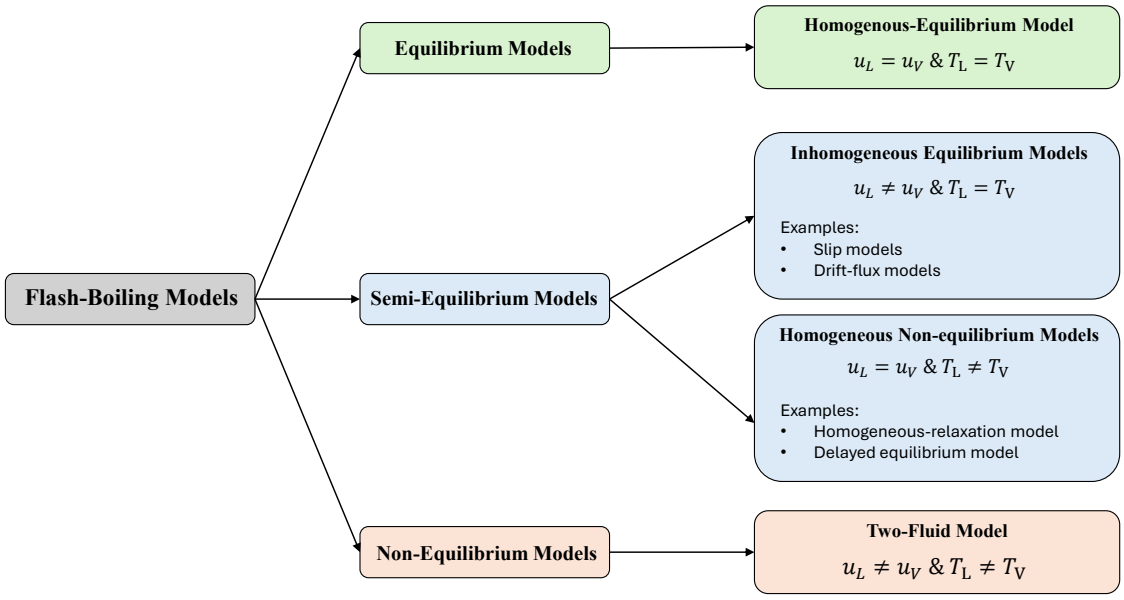


Figure 3.2: Different categories of flash-boiling models divided based on the treatment of non-equilibrium effects; u_L and u_V represent liquid and vapour velocities, while T_L and T_V denote temperatures of the two phases respectively.

effects are important [132]. These three approaches to modelling flashing flows with some proposed models under each category are shown on the tree diagram in Fig 3.2.

It is worth reiterating that the the phase change process in flash-boiling problems is commonly assumed to be dominated by the interphase heat transfer, while the effect of pressure non-equilibrium is deemed of secondary importance [132]. As such, all the flashing models discussed below assume that liquid and vapour phases have identical pressures.

3.3.1 Homogeneous-equilibrium model

The most simplistic approach to modelling flash boiling is based on the homogeneous-equilibrium approach, which assumes that the two-phase mixture behaves as a pseudo single-phase fluid with both phases having identical velocities and temperatures. The phase change is assumed to happen instantaneously according to the change in local pressure and temperature, with both phases remaining at saturation conditions. The model solves a single set of mass, momentum and energy conservation equations for the mixture:

$$\frac{\partial\left(\rho_m\right)}{\partial t} + \boldsymbol{\nabla}\cdot\left(\rho_m \vec{U}_m\right) = 0 \tag{3.1a}$$

$$\frac{\partial\left(\rho_m \vec{U}_m\right)}{\partial t} + \boldsymbol{\nabla}\cdot\left(\rho_m \vec{U}_m \vec{U}_m\right) = -\nabla P + \boldsymbol{\nabla}\cdot\tau \tag{3.1b}$$

$$\frac{\partial\left(\rho_m\, h_m\right)}{\partial t} + \boldsymbol{\nabla}\cdot\left(\rho_m\, \vec{U}_m h\right) = \frac{\partial P}{\partial t} + \boldsymbol{\nabla}\cdot\left(k\,\nabla T\right) + \boldsymbol{\nabla}\cdot\left(\vec{U}_m \tau\right) \tag{3.1c}$$

where subscript m designates mixture properties. All thermodynamic properties are determined using a suitable equation of state, and the mixture properties are interpolated between the saturated liquid and saturated vapour properties in a standard manner:

$$\phi_m = \phi_L + x_{eq}\,(\phi_V - \phi_L) \tag{3.2}$$

where ϕ_m is a mixture thermodynamic property, while subscripts L and V denote saturated liquid and saturated vapour states respectively. The equilibrium vapour quality, x_{eq}, is defined as:

$$x_{eq} = \frac{h - h_L}{h_V - h_L} \tag{3.3}$$

where h is the local enthalpy. The homogeneous-equilibrium model was applied in early studies devoted to assessing the critical mass-flow rate and pressure in flashing choked flows [148–150]. Such technical scenarios are particularly relevant to loss-of-coolant analysis in the design of nuclear reactors [30]. The loss-of-coolant accidents can take place due to certain mechanical failures in the reactor cooling system such as pipe breaks or valve failures. The main emphasis in such analysis is placed on predicting the critical flow rate, which is of paramount importance in the nuclear reactor safety analysis. The homogeneous-equilibrium model can be reasonably accurate when applied to long channels, where the expansion is relatively gradual and both phases can maintain the mechanical and thermal equilibrium. However, as pointed out by Wallis [151], the model turns out to be inadequate for short-channel analysis due to insufficient time for the phases to establish equilibrium as the expansion progresses. In fact, the survey conducted by the author [151] indicates that the homogeneous-equilibrium predictions for the critical flow rate can have an error as high as 20%. The experimental tests on flashing of subcooled water in a converging-diverging nozzle conducted by Abuaf et al. [35] indicate that the phase change is initiated with a noticeable delay with respect to the saturation conditions. Such an effect cannot be accounted for in the homogeneous-equilibrium model.

3.3.2 Inhomogeneous equilibrium models

Owing to a large difference in densities, it is expected that the liquid and vapour will accelerate differently for a given pressure gradient applied. As a result, a velocity slip may develop between the phases, affecting the characteristics of the flash-boiling process. The semi-equilibrium models that address the velocity slip issue while assuming identical temperatures are referred to as inhomogeneous equilibrium models. Some authors attempted to compensate for the velocity slip by introducing a slip factor, defined as the ratio of average vapour to liquid velocities [132]. Moody [152] extended the application of the homogenous-equilibrium model, relaxing the mechanical-equilibrium constraint by introducing a slip ratio derived based on an analysis of an isentropic two-phase flow in thermal equilibrium.

$$S = \left(\frac{\rho_L}{\rho_V}\right)^{1/3} \tag{3.4}$$

A similar slip correlation expressed as a function of density ratio was derived analytically by Fauske [153] for a non-isentropic two-phase flow.

$$S = \left(\frac{\rho_L}{\rho_V}\right)^{1/2} \tag{3.5}$$

Although the introduction of slip could compensate for an underestimation of critical mass-flow rate by the homogeneous-equilibrium model [132], some authors pointed out to unrealistically high velocity slips predicted by those models [154]. An overly simplistic nature of these correlations (only dependent on the density ratio) also casts doubts on the applicability of such slip models to a wider range of two-phase regimes that can exhibit different velocity slip for the same density ratio [155]. Elias & Lellouche [156] investigated ten different models for predicting critical mass-flow rate, using an extensive set of experimental data. The slip model based on the correlation proposed by Moody [152] did not demonstrate satisfactory agreement with the empirical trends. The applicability of the Moody slip model was also assessed by De Lorenzo et al. [157] using an experimental dataset containing over 450 operating points. Generally, the Moody slip model could predict the critical mass-flow rate in long tubes with an average accuracy of about 8.9% so long as subcooled liquid conditions were maintained at the inlet. The mean error increased to about 22.8% for short channels and was drastically higher for short slits. The Moody model could not accurately predict the critical flow rate under two-phase inlet conditions in any of the investigated channel geometry. In summary, the results suggest that such models lack generality and can only provide reasonable prediction under specific conditions.

Bilicki [158] investigated the suitability of two different slip models, Bankoff [159] and a drift-flux models, for predicting the critical mass-flow. The author found that both models significantly over-predicted the void fraction as critical conditions were approached, and emphasises that those models were only validated for low void fractions. The drift-flux model assessed by Bilicki [158] provides a more complex empirical correlation for the relative motion between the phases than the slip models discussed earlier. Wallis [151] discussed the shortcoming of the drift-flux model and advised against using the model for rapidly accelerating flows with changing void fraction. Similar to Saha [160], the author pointed to the superiority of a full non-equilibrium two-fluid model for predicting the relative motion between the phases. However, the two-fluid models requires reliable momentum closure models for the accurate prediction of the momentum exchange [30, 132].

3.3.3 Non-equilibrium phase-change

As discussed in the preceding sections, some experiments reported a visible delay in the flashing inception with respect to local saturation conditions. De Lorenzo suggested that this delay is mainly the result of thermal non-equilibrium between the phases [157]. The phase-change rate has a significant impact on the characteristics of the two-phase expansion. A delayed phase-change implies higher content of the liquid phase at the throat of the nozzle, which effectively reduces flow compressibility leading to increased choked mass-flow rates. The phase-change rate also affects the phase distribution in the diverging section

of the nozzle, which influences the pressure, velocity and temperature fields. The effect of non-equilibrium effects on the two-phase flow is further discussed in Section 3.4. This section summarises different phase-change modelling techniques applied in homogeneous non-equilibrium and two-fluid models presented in Fig. 3.2.

In non-equilibrium flashing, the phase-change does not occur instantaneously as the liquid pressure drops below the saturation level due to finite interphase heat-transfer rate. As such, the liquid phase becomes superheated (metastable), and the phases can no longer be assumed to be in thermodynamic equilibrium. Various models have been proposed to model non-equilibrium phase-change in flashing flows. Some of these models, such as the homogeneous-relaxation model has been derived assuming mechanical equilibrium, whereas others, such as the thermal phase-change model, have typically been implemented in full non-equilibrium frameworks with separate momentum and energy equations for both phases. Irrespectively of whether the mechanical equilibrium is imposed, the non-equilibrium phase-change models relax the thermal equilibrium constraint, therefore, they have been grouped and discussed in the same section.

Ortego Sampedro et al. [147] classified the non-equilibrium phase-change models based on a potential (ϕ) and a relaxation coefficient (K), where the mass-transfer rate is defined as the product of the two parameters.

$$\dot{m} = K\phi \tag{3.6}$$

The potential term describes the local flow deviation from the thermodynamic equilibrium, which is assumed to be the driving force for the phase change. The relaxation coefficient defines the rate at which the thermodynamic equilibrium is restored through phase change. In other terms, the relaxation coefficient defines how fast the thermodynamic equilibrium is restored through phase change for a given deviation from the thermodynamic equilibrium defined by the potential term. Depending on the model, the relaxation coefficient can be purely empirical or more physics-based. Due to the deviation from thermodynamic equilibrium, the key to implementing the non-equilibrium phase-change models is the ability of the employed equation of state to predict fluid thermodynamic properties under metastability (i.e. superheated liquid or subcooled vapour). Ortego Sampedro et al. [147] distinguished three main categories of phase-change models according to the type of potential applied - vapour quality, pressure and temperature difference models.

Vapour-quality based models
The most common model based on the vapour quality difference is the homogeneous-relaxation model proposed by Bilicki & Kestin [161]. Similar to the homogeneous-equilibrium model, it also treats the two-phase mixture as a pseudo single-phase fluid but complements the governing equations (Eq.3.1a-3.1c) with an additional equation for the vapour mass fraction, which is no longer assumed to be equal to the thermodynamic equilibrium vapour quality:

$$\frac{\partial x}{\partial t} + \mathbf{u} \cdot \nabla x = -\frac{1}{\theta}(x - x_{eq}) \tag{3.7}$$

where x is the instantaneous vapour mass fraction, and x_{eq} is the equilibrium vapour quality defined as:

$$x_{eq} = \frac{h_{mix} - h_{L,sat}}{h_{V,sat} - h_{L,sat}} \tag{3.8}$$

where h_{mix} is the local mixture enthalpy, while $h_{L,sat}$ and $h_{V,sat}$ are the saturation enthalpies of liquid and vapour at the corresponding pressure. The instantaneous vapour mass fraction approaches the thermodynamic equilibrium value at a rate defined by an empirically-derived time constant, θ, which constitutes the relaxation term K from Eq. 3.6. Downar-Zapolski et al. [44] derived the relaxation time constant based on experimental data for flash boiling of water in a converging-diverging nozzle.

$$\theta = \theta_0 \alpha_V^a \phi^b \tag{3.9}$$

where α_V is the vapour volume fraction, θ_0 is an empirical constant with units of a second, while a and b are fitting coefficients. Downar-Zapolski et al. [44] proposed the following non-dimensional pressure difference for low- and high-pressure expansions:

$$\phi = \begin{cases} \left| \dfrac{P_{sat} - P}{P_{sat}} \right|, & P < 10\,bar \\ \left| \dfrac{P_{sat} - P}{P_{cr} - P_{sat}} \right|, & P > 10\,bar \end{cases}$$

where P_{sat} and P_{cr} are the saturation and critical pressure, respectively. The authors found the best agreement with the experimental trends using θ_0, a and b values of 6.51×10^{-4} s, -0.257 and -2.24 for $P < 10$ bar and 3.84×10^{-7} s, -0.54 and -1.76 for $P > 10$ bar, respectively. The authors implemented the homogeneous-relaxation model within a one-dimensional code to simulate flashing of water. The relaxation model gave much better estimations for the mass-flow rate compared to the homogeneous-equilibrium model. However, the authors emphasised the fact that relaxation time derived for water may be invalid when studying different fluids. Angielczyk [162] used the relaxation time derived for water and found that it led to large deviations from the experimental data when applied to simulating flash boiling of carbon dioxide in an ejector motive nozzle. The authors modified the relaxation time to better match the experimental data, which was later used by Palacz et al. [163] in simulating two-phase expansion of carbon dioxide in an ejector nozzle designed for refrigeration systems. The homogeneous-relaxation model was found to be only slightly more accurate than the homogeneous-equilibrium model in predicting the mass-flow rate. The authors suggested that it could come from the fact that the relaxation time for carbon dioxide was derived for relatively narrow range of operating conditions. This indicates that both the fluid and operating conditions affect the validity of the relaxation time constant. Loska et al. [38] applied the homogeneous-relaxation model to simulate flash boiling of R410A through an electric expansion valve. The authors found that the model predicted the mass flow rate with a 17-25% uncertainty when the relaxation time derived for water was used, but the uncertainty fell to about 5% when the time constant was tuned to the experimental data taken for R410A.

Pressure-based models

The next category of phase-change models defines the mass-transfer rate in terms of the flow deviation from the saturation pressure. Such pressure-difference models have been widely adopted in simulating the cavitation phenomenon. Although at the macroscopic level, cavitation is a similar process to flash boiling, some of the previous studies cast doubts on the applicability of cavitation models to flashing flows. Karathanassis et al. [164] applied the Zwart et al. [165] (ZGB) cavitation model to simulate flash boiling of water in three different types of channels. The ZGB model is based on a simplified solution of the Rayleigh-Plesset equation that governs bubble dynamics in an infinite body of liquid medium. The phase-change rate estimated by the ZGB model is given as:

$$\dot{m} = \frac{3 a_{nuc} \alpha_L}{R_b} \sqrt{\frac{2}{3\rho_L} \left(P_{sat} - P\right)} \tag{3.10}$$

where F_e is an empirical coefficient, a_{nuc} is the nucleation-site volume fraction, while R_b is the bubble diameter. Values of 50 and 0.0005 for F_e and a_{nuc} have been proposed for cavitating flows [165]. Karathanassis et al. [164] found that the model had to be heavily tuned, with the F_e lowered from 50 to 3 to achieve a mass-transfer rate characteristic of flashing flows. The results of the study indicate that the cavitation model was the least capable to replicate the experimental results compared to models based on the kinetic theory of gases and the homogeneous-relaxation model. Kumar et al. [166] also applied the ZGB model along with the Schnerr and Sauer cavitation model [167] to simulate flashing of water in a converging-diverging nozzle. Similar to the findings of Karathanassis et al. [164], the cavitation models required significant tuning in order to replicate the experimental results. Although cavitation is similar in nature to flash boiling, previous studies indicate that the underlying mechanism governing the phase-change process differ, and the cavitation models may generate misleading results when directly applied to flashing flows.

Another class of models that rely on the pressure difference is based on the kinetic theory of gases. These models typically employ a variation of the Hertz-Knudsen equation [168, 169], which in its basic form, estimates the mass-transfer rate as:

$$\dot{m} = \lambda \left(P_{sat} - P_V\right) \sqrt{\frac{M}{2\pi R T}} \tag{3.11}$$

where λ is the accommodation coefficient, P_{sat} and P_v are the saturation and vapour pressures, M is the molecular mass, R is the universal gas constant and T is the liquid-vapour interface temperature. The accommodation coefficient describes the fraction of molecules impinging onto the liquid-vapour interface that contribute to the phase-change, i.e. the fraction of molecules that are not reflected off the interface. Karathanassis et al. [164] investigated three types of correlations based on the kinetic theory of gases, including a model based on the original Knudsen correlation (Eq. 3.12a) and two variations of the Hertz-Knudsen equation (Eqs. 3.12b-3.12c).

$$\dot{m} = C_{evap} A_{int} \alpha_L \rho_L \left(P_{sat} - P\right) \tag{3.12a}$$

$$\dot{m} = \frac{\lambda A_{int} \left(P_{sat} - P\right)}{\sqrt{2\pi R T_{int}}} \tag{3.12b}$$

$$\dot{m} = \frac{\lambda A_{int}}{\sqrt{2\pi R_g}} \left(\frac{P_{sat}}{\sqrt{T_L}} - \frac{P}{\sqrt{T_V}}\right) \tag{3.12c}$$

The authors assumed $C_{evap} = 0.001$, and applied two different values of 1 and 0.1 for the accommodation coefficient λ. An accommodation coefficient of unity essentially implies an instantaneous heat transfer, leading to thermodynamic equilibrium, whereas a value of 0.1 is considered to represent significant deviation from equilibrium conditions. It is worth noting that each of the correlations based on the kinetic theory of gases includes an interfacial area term A_{int}, which depends on the nucleation-site density and bubble size. The authors emphasised that due to flow contaminants, micro bubble and other impurities, the determination of the nucleation-site distribution is strongly dependent on the specific case. Based on the empirical data recorded for cavitating flows [170, 171] and numerical data generated for flashing flows [172, 173], the authors applied a constant and uniformly distributed nucleation-site density of 10^{13} bubbles per unit volume of liquid, assuming a bubble diameter of 1 µm. The authors also studied a variable bubble number density using the following relationship:

$$N_b = C_n exp\left(\frac{-5.279}{\Delta T_{L,sup}}\right) \tag{3.13}$$

where C_n is the baseline bubble number density of 10^{13} bubbles per unit volume, while $T_{L,sup}$ is the liquid superheat level. The relationship was originally proposed by Senda et al. [174] based on the available experimental data that give insight into the effect of liquid superheat level on the bubble number density. The three correlations based on the kinetic theory of gases were applied along with the ZGB cavitation and homogeneous-relaxation models to simulate flash boiling of water in a converging-diverging nozzle, a throttle nozzle with a stepwise flow contraction and a transient blow-down pipe. Among the investigated phase-change models, the correlations based on the Knudsen and Hertz-Knudsen equations demonstrated the best agreement with the experimental data and could replicate the main flow trends with satisfactory accuracy. The Hertz-Knudsen equation has also been applied to simulate flashing of cryogenic fluids [175–177] and flashing in fuel-injection systems [178, 179].

Thermal phase-change model

The last type of phase-change models distinguished by Ortego Sampedro et al. [147] is based on the temperature difference, which is also known as the thermal phase-change or thermally-driven model. It assumes that the vapourisation in flashing flows is solely a result of the heat transfer between the liquid and vapour. The model is often applied in conjunction with a so-called two-resistance approach that assumes that the liquid and vapour phases exchange heat with an interface with a temperature equal to the local saturation temperature:

$$\dot{m} = \frac{\mathfrak{H}_L A_{int} \left(T_{int} - T_L\right) + \mathfrak{H}_V A_{int} \left(T_{int} - T_V\right)}{h_{LV}} \tag{3.14}$$

where $\mathfrak{H}_L$ and $\mathfrak{H}_V$ are the heat-transfer coefficients on the liquid and vapour side of the liquid-vapour interface, T_{int} is the interface temperature equal to the local saturation temperature, while h_{LV} is the difference between vapour and liquid enthalpies. The derivation of the thermal phase-change model is discussed in detail in Chapter 4.1, alongside the estimation methods for the heat-transfer coefficients and the interfacial area. Although the implementation of the thermal phase-change does not require solving separate momentum equations for the liquid and vapour, the review of literature indicates that this phase-change model has been most frequently combined with the two-fluid model that resolves both mechanical and thermal non-equilibrium between the phases. As such, the application of the thermal phase-change model to specific flash-boiling problems is discussed in a separate section on the two-fluid model .

Delayed equilibrium model

A different less-explored phase-change model that attempts to account for the delay in the phase-change onset is the delayed equilibrium model, which assumes that the mixture is composed of three fluids: saturated liquid, saturated vapour and metastable liquid phase. Similar to other relaxation models, empirical coefficients are required to determine the rate of vapourisation of the metastable liquid phase. De Lorenzo et al. [157] compared the performance of the delayed equilibrium model and three other flashing models including the homogeneous-equilibrium model for predicting the critical mass-flow rate and critical pressure in various types of channels using a one-dimensional code. The delayed equilibrium model was found to be superior to other models in that it could more reliably estimate those parameters in both long and short tubes as well as through narrow slits. Recently, Tammone et al. [180] extended the application of the one-dimensional delayed equilibrium model to simulating flashing of refrigerant R134a in a converging-diverging nozzle. The authors found that the mass flow rate could be predicted with an average relative error of 10.3% compared to the experimental data, using coefficients derived for water. Once the coefficients were tuned based on the experimental data for R134a, the relative average error reduced to 6.1%. Overall, the delayed equilibrium model demonstrated increased capability of simulating flash-boiling problems, but also demonstrated the need for empirical coefficients tuned to the specific working fluid and operating conditions to achieve satisfactory accuracy.

3.3.4 Nucleation process

Non-equilibrium phase-change models such as those based on the kinetic theory of gases or temperature difference require an estimation of the interfacial area (A_{int}) to evaluate the interphase mass-transfer rate. The interfacial area in flash boiling of subcooled liquids depends on the number and size of nucleated bubbles. Modelling the nucleation process (the process of formation vapour bubbles in the liquid medium) is one of the most challenging tasks in simulating the flash boiling phenomenon. Liao and Lucas [132] distinguished three main approaches to modelling the nucleation process, referred to as seeding, step function and nucleation approaches, which are presented in Fig. 3.3.

The authors divided the nucleation process into four different zones. First, a sub-cooled liquid expands (Zone I), turns into superheated liquid (metastable state) (Zone II), the formation of bubbles is then initiated, which is referred to as nucleation or non-equilibrium

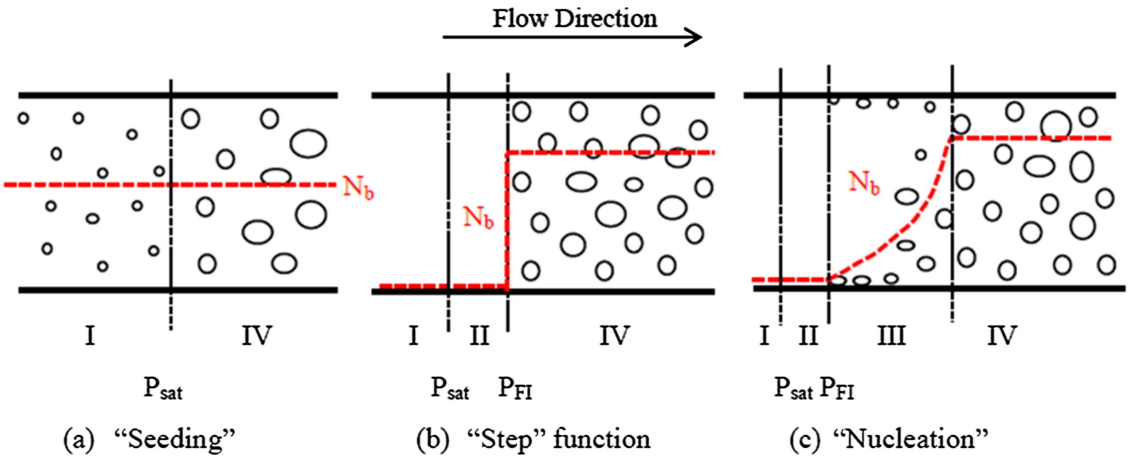


Figure 3.3: Different approaches to modelling the nucleation process in flash-boiling of subcooled liquids. The area denoted by I, II, III and IV represent subcooled liquid, superheated (metastable) liquid, nucleation and equilibrium zones (figure retrieved from Liao and Lucas [132]).

zone (Zone III), and finally once the nucleation is completed, the equilibrium zone is achieved, where a constant number of uniformly distributed bubbles is achieved (Zone IV). The term equilibrium here, does refer to equilibrium in phase velocities or temperatures, but rather signifies the completion of the nucleation process. The most simplistic approach,"seeding" (Fig. 3.3a), is based on assuming that the subcooled liquid contains a constant number of uniformly distributed vapour nuclei. The phase change occurs as soon as the local pressure (and temperature) drops below the saturation level, which cause an increase in vapour volume fraction and bubble size according to the following equation:

$$D_b = \left(\frac{6\alpha_V}{\pi N_b}\right) \tag{3.15}$$

where α_V is the vapour volume fraction and N_b is the assumed nucleation-site density. The "seeding" approach disregards the metastable and non-equilibrium nucleation regimes, as the bubbles pre-exist in the subcooled liquid. Previous numerical studies on flash boiling of subcooled water assumed N_b to lie in the range of 10^9 to 10^{11} bubbles per unit volume [155, 181, 182]. An alternative approach to assuming a constant bubble number density is to assume a constant bubble diameter, however, Laurien [183] argued that assuming a constant bubble number better reflect the physical process of flash boiling as the bubbles are allowed to increase in size in line with the increasing volume fraction of vapour (see Eq. 3.15). The main limitation of the "seeding" approach is that it does not resolve the metastable and non-equilibrium stages of nucleation. Liao and Lucas [132] emphasised that the width of the metastable regime influences the liquid superheat level prior to nucleation, which was found to have a significant effect on the intensity of the phase-change process and subsequently on the distribution of the void fraction inside the nozzle.

A slightly more advanced approach that can account for the effect of liquid metastability on the nucleation process is based on assuming that the nucleation happens in a stepwise manner, where a certain threshold expressed in terms of a minimum liquid superheat level

or pressure undershoot (the difference between the saturation and local liquid pressure) is required to trigger the nucleation process (Fig. 3.3b). Once that threshold is crossed, the nucleation is assumed to happen instantaneously, that is a pre-defined number of bubbles is formed uniformly throughout the fluid over an infinitesimally small streamwise distance. Alamgir and Lienhard [184] derived an expression for the pressure undershoot based on the homogeneous nucleation theory:

$$P_{undershoot} = \left(\frac{16\pi\sigma^3}{3k_B T_{cr}(1 - v_L/v_V)^2 \left(\frac{Gb}{\phi}\right)} \right)^{1/2} \tag{3.16}$$

where k_B, T_{cr}, v_L, v_V are the Boltzmann constant, fluid critical temperature and the specific volume of liquid and vapour, respectively. The terms Gb and ϕ denote the Gibbs number and heterogeneity factor. Liao and Lucas [132] report that the pressure undershoot model proposed by Alamgir and Lienhard has been successfully applied to transient flashing flows with high depressurisation rates and stagnation conditions [154, 185, 186]. Jones [187] and Abuaf et al. [186] subsequently adjusted the model to continuos flow systems, taking into account the convective and turbulence effects. Different variations of the Alamgir and Lienhard [184] correlation have been applied to simulate flashing inception in different types of channels [188–190]. An alternative approach to modelling the flashing inception was proposed by Elias and Chambre' [191], who derived the pressure-undershoot correlation based on an asymptotic analysis of the mass and energy equations at the flashing inception point. The model was developed for both steady and transient flashing flows, and demonstrated the capability of predicting the pressure at the inception point with an error smaller than 11 %, compared against 83 experimental points.

Finally, the most advanced approach to modelling the formation of vapour bubbles attempts to resolve all the distinct zones shown in Fig. 3.3c, using nucleation models to simulate the non-equilibrium nucleation phase. Although, the full nucleation model provides the most realistic picture of the nucleation process, Liao and Lucas [132] emphasised that it also requires reliable constitutive relations for accurate prediction of the nucleation process. In practice, the nucleation process is triggered by pre-existing nuclei, flow impurities and poorly-wetted wall cavities, which is referred to as heterogeneous nucleation because bubbles form irregularly throughout the domain [132]. Within the heterogeneous nucleation, one can distinguish between wall and bulk nucleation; the former assumes nucleation occurs at the walls of the channel, while bulk nucleation assumes that it occurs throughout the entire liquid medium.

According to Liao and Lucas [132], there are two main methods for estimating the heterogeneous bulk nucleation that area based on a modified homogeneous nucleation theory and on a probability density function. The first method assumes that the heterogeneous bulk nucleation resembles the homogeneous nucleation process, and the formation of bubbles can be estimated with the following correlation derived from the classical theory of nucleation [184]:

$$J_{het,B} = J_0 exp\left(-\frac{W_{cr}\varphi}{k_B T_0}\right) \tag{3.17}$$

where J_0 is the nucleation-site density and W_{cr} is the critical work that is needed to form a vapour bubble of the critical size [132]. The term φ is referred to as heterogeneity factor, which is always less than unity and acts to reduce the activation energy to account for the effect of channel walls on the nucleation process. The critical work combines the work that needs to be done to displace the liquid volume when a bubble is form with energy stored in the bubble surface, and can be expressed as:

$$W_{cr} = \frac{4}{3}\pi R_{cr}^2 \sigma \tag{3.18}$$

where R_{cr} is the critical bubble diameter, which for two-phase flows characterised by much lower density of the vapour phase can be approximated as:

$$R_{cr} = \frac{2\sigma T_{sat}}{(T_0 - T_{sat}) h_{LV} \rho_{V,sat}} \tag{3.19}$$

To determine the rate of heterogeneous bulk nucleation, the nucleation-site density, J_0 has to be defined. This term has been commonly modelled as a product of the number density of liquid molecules and the rate of molecular interactions [192, 193].

An alternative approach to modelling heterogeneous bulk nucleation was proposed by Kumzerova and Schmidt [194], who assumed that the size of bubbles formed during nucleation is governed by the normal distribution curve.

The second type of heterogeneous nucleation is the wall nucleation, which has often been assumed to be the dominant mechanism for the formation of bubbles in practical applications. Within the wall nucleation models, there have been models developed for smooth and non-smooth walls. For smooth walls, the Blander and Katz [195] correlation has previously been applied to flashing flows, which is based on a modified bulk homogeneous nucleation model:

$$J_{het,W} = N_s^{2/3} S \sqrt{\frac{2\sigma}{\pi m_W B \varphi}}\, exp\left(-\frac{W_{cr}\varphi}{k_B T_L}\right) \tag{3.20}$$

where S and φ are the geometrical and heterogeneity factors that both are functions of the contact angle that the vapour nuclei make with the wall. Liao and Lucas [132] emphasised that the main limitation of the model lies in the uncertainty of nucleation-site density, N_s, the heterogeneity factor, φ, and the contact angle that has been shown to be difficult to estimate even under idealised conditions [196]. Furthermore, previous studies [184, 197] indicate that the value of the heterogeneity factors is substantially smaller than unity, which points to the significant influence of wall cavities on the nucleation process. As such, majority of numerical flash-boiling studies relied on the non-smooth wall correlations for predicting the formation of bubbles at the walls. The wall nucleation models for non-smooth walls have been derived analogously to the correlations describing nucleation at the walls of a heated duct, with the main difference that the heat supplied comes from the superheated liquid rather than from the wall, which is assumed to be at the local saturation temperature [132].
Liao and Lucas [132] distinguished three wall nucleation models that have been applied to flashing flows; these include correlation proposed by Riznic et al. [198], Kolev [199], and Jones et al. [200]. Riznic et al. [198] defined the nucleation rate as a product of the activated

nucleation-site density per unit area of the wall (N_a) and the bubble departure frequency (f):

$$J_{het,W} = N_a f \tag{3.21}$$

The activated nucleation-site density was defined in terms of bubble departure diameter, the liquid superheat level and several other parameters:

$$N_a = 0.002244 D_d^{2.4} \left(\frac{\sigma T_{sat}}{(T_L - T_{sat}) \rho_V h_{LV}} \right)^{-4.4} \Psi(\rho^*) \tag{3.22}$$

where $\Psi(\rho^*)$ is a property function that depends of the ratio of phase densities. The departure frequency was defined based on the surface tension (σ), gravitational constant (g), phase densities and bubble departure (D_d):

$$f = 1.18 \left(\frac{\sigma g \Delta \rho}{\rho_L} \right)^{0.25} \frac{1}{D_d} \tag{3.23}$$

The departure diameter present in the N_a and f functions was related to the contact angle that the nuclei make with the wall cavities. Kolev [199] derived a wall nucleation rate, assuming that the formation of bubbles is proportional to the heat exchange between the superheated liquid in the bulk and the liquid in the boundary layer:

$$J_{het,W} = \frac{6 \Gamma_W}{\rho_V \pi D_d^3} \tag{3.24}$$

where Γ_W is the vapour generation rate at the wall, determined as the ratio of the heat exchange between the bulk and the boundary layer divided by the local latent heat of vapourisation: $\Gamma_W = \dot{q}/h_{LV}$. Jones et al. [200] found that the correlations formulated based on the analogy with subcooled boiling under-estimated the nucleation rate in flashing flows. The authors modified the activated nucleation-site density (N_a) and departure frequency (f) to tailor the wall nucleation model to flash-boiling problems. The nucleation-site density was expressed as a ratio of departure (R_d) to critical (R_{cr} radii:

$$N_a = 0.25 \times 10^{-7} \frac{R_d^2}{R_{cr}^4} \tag{3.25}$$

where the relationship between the departure and critical radii was evaluated based on the balance between the drag and surface tension forces. The departure frequency was defined in terms of liquid superheat level:

$$f = C_{dp} (T_L - T_{sat})^3 \tag{3.26}$$

where the constant C_{dp} was assumed to be equal to $10^4 \, [K^{-3} s^{-1}]$.

In summary, different approaches have been proposed to model the nucleation process in flashing of subcooled liquids, ranging from simple assumption of pre-existing vapour nuclei to more sophisticated nucleation models that attempt to capture the process of bubble formation. Since the two-phase mixture is partially evaporated before it enters a turboexpander

designed for the wet-to-dry cycle, the bubble nucleation process is not directly relevant to the current study. As such, this section only presented an overview of the nucleation modelling techniques. For more detailed discussion on modelling the nucleation process, the interested reader is referred to the work of Liao and Lucas [132].

3.3.5 Non-equilibrium two-fluid model

Previous sections outlined various techniques for modelling non-equilibrium phase-change process in flashing flows. One of those methods referred to as the thermal phase-change model estimates the mass-transfer rate based on the interphase heat-transfer rate. This type of phase-change model has most often been coupled with the two-fluid model, which is discussed in this section. The two-fluid model solves two separate set of governing equations for liquid and vapour, such that each phase has its own velocity and temperature field. Hence, the two-fluid model can account for both mechanical and thermal non-equilibrium effects.The mass continuity equation for the liquid and vapour phases are expressed as:

$$\frac{\partial \left(\alpha\, \rho\right)_i}{\partial t} + \boldsymbol{\nabla} \cdot \left(\alpha \rho \vec{U}\right)_i = \sigma_{M,i} \tag{3.27}$$

where subscript i represents the phase index (either liquid or vapour), ρ and $\vec{U}$ are phase density and velocity, while α is the phase volume fraction. The term $\sigma_{M,i}$ represents the interphase mass transfer rate. The momentum conservation equations are given as:

$$\frac{\partial \left(\alpha \rho \vec{U}\right)_i}{\partial t} + \boldsymbol{\nabla} \cdot \left(\alpha \rho \vec{U} \vec{U}\right)_i = -\alpha_i \nabla P + \boldsymbol{\nabla} \cdot \tau_i + \sigma_{J,i} \tag{3.28}$$

where the stress tensor τ for the given phase is expressed as:

$$\tau = \mu \left(\nabla \vec{U} + \left(\nabla \vec{U}\right)^T - \frac{2}{3} \delta\, \boldsymbol{\nabla} \cdot \vec{U} \right) \tag{3.29}$$

Since the two phases have different velocity fields, there is a momentum exchange through interfacial forces such as drag, lift forces. In addition to that, momentum will be carried from one phase to the other due to mass transfer. The resultant momentum transfer due to these two effects is represented by $\sigma_{J,i}$.The pressure vector P has no phase subscript because it is assumed that the phases have identical pressures. Energy conservation equations are expressed in terms of total enthalpy:

$$\frac{\partial \left(\alpha \rho\, h_{tot}\right)_i}{\partial t} + \boldsymbol{\nabla} \cdot \left(\alpha \rho\, \vec{U} h_{tot}\right)_i = \alpha_i \frac{\partial P}{\partial t} + \boldsymbol{\nabla} \cdot \left(\alpha k \nabla T\right)_i + \boldsymbol{\nabla} \cdot \left(\vec{U} \tau\right)_i + \sigma_{E,i} \tag{3.30}$$

where T and k are phase temperature and thermal conductivity. Energy is exchanged between the phases by mass and heat transfer, which is denoted by the term $\sigma_{E,i}$.

Contrary to single-phase flows, an additional conservation equation is solved for the volume fraction, which states that the sum of vapour and liquid volume fractions in each control volume must add up to unity.

$$\alpha_L + \alpha_V = 1 \tag{3.31}$$

To close the system of equations, interphase models that account for the exchange of mass, momentum and heat between the phases are required. It is a common practice in modelling flashing flows to assume that the phase change in flashing problems results from the interphase heat transfer, while pressure non-equilibrium effects are neglected. Therefore, liquid and vapour are assumed to share the same pressure field. As already mentioned, the two-fluid model has typically been applied in conjunction with the thermal phase-change model, where each phase is assumed to exchange heat with an interface with a temperature equal to the local saturation temperature.

The open literature contains numerous works on the implementation of the two-fluid model in numerical models to carry out multidimensional simulations. Although the studies discussed below applied different methods for estimating the nucleation process and the interfacial area, all of the studies apply the thermal phase-change model to estimate the interphase mass-transfer rate and the growth of nucleated bubbles. Most authors assumed that the primary resistance to heat transfer is on the continuous liquid side, while the vapour remains saturated throughout the expansion. Mimouni et al. [201] employed the two-fluid model to simulate the "Super Moby Dick" experiment [202], which involved flashing of sub-cooled water in a converging-diverging nozzle. Both wall and bulk nucleation modes were included to model the formation of bubbles. Overall, the model proved capable of simulating flash boiling with acceptable deviations from the experimental data. The model was also applied to simulate cavitation in a flow through an orifice plate; the numerical predictions agreed relatively well with the experimental observations. Marsh and O'Mahony [203] implemented the two-fluid model in ANSYS Fluent to simulate flash boiling of sub-cooled water in a converging-diverging nozzle referred to as the BNL nozzle. The nozzle was an object of an experimental campaign carried out by Abuaf et al. [35]. The authors considered only the drag force, neglecting other interphase forces and several BNL runs were simulated. The numerical results were in relatively good agreement with the experimental measurements in most of the investigated cases. Nevertheless, radial vapour distribution within the nozzle differed from the experimental data, which indicate that the vapour tends to form in the vicinity of the wall, where its concentration is much higher than in the nozzle centre. More uniform distribution was predicted in the simulation due to the type of nucleation model applied that simulates uniform nucleation throughout the cross-section of the nozzle. Janet et al. [204] used the two-fluid model in ANSYS CFX to test the capability of three different wall nucleation models to predict bubble-formation process in the BNL nozzle [35]. The authors also included the bubble coalescence effect. Compared to the experimental data, a modified Jones model [173, 200, 205] could predict average streamwise variations and mass flow rates with satisfactory accuracy. However, the authors found that the radial distribution of vapour visibly deviated from the experimental measurements; the model underestimated the amount of vapour generated around the centre of the nozzle. Supplementing wall nucleation with a bulk nucleation term improved the radial void-fraction profiles.

Liao and Lucas [206] also used CFX to implement the two-fluid model for simulating flashing

of water in the BNL nozzle. However, in contrast to the study of Janet et al. [204], a constant bubble number density, tuned to match experimental measurements, was assumed, which varied between 10^8 and 8×10^{10}. The authors suggest that such an approach is suitable if the nucleation zone is sufficiently narrow. Lift, wall lubrication and turbulent dispersion forces were considered alongside the drag force, while turbulence in the liquid phase was modelled with the k-ω SST model and the dispersed phase zero model was applied to estimate the eddy viscosity of vapour. Generally, it was found that the mass flow rate could be predicted with a maximum deviation not exceeding 7%. The average streamwise pressure profiles were well predicted when flash boiling was initiated close to saturation conditions, but noticeable deviations between the numerical and experimental results were observed when it was initiated at pressures significantly lower than the saturation pressure,. In most cases, the vapour volume fraction streamwise variation trends were captured by the two-fluid model, however an underestimation of vapour generation rate was often observed. The discrepancy may have been due to the inability of the thermal phase-change model to account for the pressure non-equilibrium effect on the bubble formation process. Overall, the model provided satisfactory estimations when average variations are of interest, but when radial vapour distributions are concerned, much larger deviations were found, which may be due to the assumption of a constant bubble number density. Comparing the 3D simulation to 1D analysis, the 3D approach proved more stable and provided a closer match with the experiments.

In later studies [32], the authors applied the two-fluid model to simulate several flash boiling scenarios using various approaches to modelling bubble number and size. The authors simulated flash boiling in a pipe blowdown test [207] and oscillations induced by flashing in a riser pipe [31]. A constant bubble diameter of 1 mm and a constant bubble number density of 5×10^4 were assumed for these two cases respectively. Generally, the model correctly evaluated the average trends in both cases, however, there were some visible quantitative differences, which could result from the fact that neither approach is able to account for the bubble dynamic effects such as breakup and coalescence. The authors also simulated flash boiling in the BNL nozzle, solving the bubble number density transport equation based on the wall and bulk nucleation models. Generally, it was found that wall nucleation was dominant, however, the nucleation zone was relatively short, past which the bubble number remained approximately constant. Streamwise variations of vapour volume fraction were relatively well predicted, while the pressure drop in the diverging section was visibly over-predicted. This may indicate that, in reality, flashing requires a smaller pressure undershoot to occur. In other words, the simulation may underestimate the interphase heat-transfer coefficient or interfacial area. Pressure non-equilibrium effects that were neglected may also play a role. Both numerical results and experiments show a wall peak in the vapour concentration and low values in the nozzle centre area. However, the experiment variation was more gradual, indicating that the bubble generated near the wall well better distributed toward the centre. This may be due to the coalescence of small bubbles into larger bubbles as the lift force acting on large bubbles push them toward the centre of the nozzle. Also, the turbulent dispersion effect may have been underestimated. This shows the importance of non-drag (secondary) forces on the vapour distribution and highlights the shortcoming of the mono-dispersed approach that assumes a constant bubble size within a control volume. To improve the model accuracy, the authors employed the inhomogeneous multiple size group

model (MUSIG) in CFX to simulate flash boiling of water in a vertical pipe, identical to the one available in the TOPFLOW facility dedicated to two-phase flow tests [208]. The MUSIG model divides the bubbles into a number of size and velocity groups. The effects of nucleation, breakup and coalescence are considered within each group, whereas the interaction between the groups is accounted for via source/sink terms [32]. The model accurately predicted bubble size spectrum in a high-pressure case (65 bar expansion), while accuracy was lower in the case of lower pressure expansion (10 bar). The authors suspect this may be caused by the increased relative impact of pressure non-equilibrium (neglected in the thermal phase-change model) on vapour formation at low pressures or inaccuracy in predicting the coalescence and breakup effects, which is a very challenging task. In the high-pressure expansion, pressure variation within the pipe was well captured, but some deviation appeared when radial velocity and vapour fraction profiles were compared to the experimental data. Since the bubble size variation was accurately predicted, the problem was thought to come from inaccuracy in predicting the lift force or turbulent dispersion effects.

Rane and He [41] employed the two-fluid model to simulate flash boiling of water through a curved channel of a two-phase reaction turbine designed for power generation from geothermal sources. CFX was used to perform 3D simulations, while the setup was similar to that of Liao and Lucas [206]. The authors followed the constant bubble number density approach. The results showed that both the bubble number and the selected interphase heat-transfer coefficient correlation significantly affected the results. Generally, with the bubble density number of 5×10^7 and the Wolfert Nusselt number correlation [209], the turbine power output could be predicted with a deviation smaller than 5% compared to the experimental data at the design speed. When the speed was lowered below the design level, the deviation increased to about 30-50%. On the other hand, the flow rate was well predicted within the entire operation range. The average variation of vapour mass fraction was also captured relatively well, with the model slightly underestimating the vapour generation rate. Nevertheless, the trends were well conserved. The authors later employed the model to study flash boiling in a modified turbine geometry, including a rotor-stator assembly [42].

In most of the discussed cases the dispersed phase was assumed to be vapour, although in some cases the void fraction at the outlet reached over 0.7 which may lead to inaccuracies. This issue was recognised by Ortego Sampedro et al. [147], who proposed a transitional model capable of switching from the bubbly to the droplet flow regime. The transition was modelled using two distinct values for the bubble and droplet density numbers, which were applied when the void fraction was below 0.3 and above 0.7 respectively. A linear variation of the interfacial area was assumed in between the bubbly and droplet flow regimes. Generally, it was found that the transitional model could better predict the mass flow rate and efficiency of the nozzle compared to other models due to being able to use both the bubble and droplet numbers as the calibration parameters. The authors commented that the nucleation models could be coupled with the model to predict the number of bubbles; for the droplet number, it is not clear how to predict it but it was stated a droplet breakup model could possibly be applied.

Most numerical studies on the application of the two-fluid model to simulate in-nozzle flash-

ing focused on subcooled/saturated liquid water flashing, for which suitable experimental data exist to validate numerical models such as the two-fluid model. Having said that, Zhu & Elbel [210] fairly recently published experimental results on flash boiling of refrigerant R134a in a converging-diverging nozzle with a variable-strength vortex generated at the inlet of the nozzle. The results could be used to validate the application of the two-fluid model to simulating flashing of organic fluids. In fact, Zhu & Ebel [211] applied the two-fluid model in a subsequent study to simulate flashing of R134a using a nucleation model in conjunction with a bubble number density transport equation to predict the bubble size. The model estimations of mass-flow rate and pressure distribution showed good agreement with the experimental data for various vortex strengths. With that being said, it should be noted that the nucleation model was calibrated based on the experimental results.

To summarise, the two-fluid model has been applied to perform numerical simulation of flash-boiling occurring in confined channels, mainly converging-diverging nozzles, accounting for both mechanical and thermal non-equilibrium effects. Despite some discrepancies in the cross-sectional vapour distribution, the model was found to be capable of providing relatively accurate estimates for the mass flow rate and average streamwise variations of pressure and volume fractions. The main challenge in the implementation of the two-fluid model lies in simulating the nucleation process and estimating the interfacial area, which is the main factor determining the interphase exchange of mass, momentum and energy.

3.4 Simulating wet-to-dry expansion

Section 3.3 presents an overview of different models that can be applied to simulate the phase change under flash-boiling conditions. The simplest of the models based on the homogeneous-equilibrium flow assumption was applied in first CFD studies conducted by White [8]. The governing equations of the homogeneous-equilibrium model have been outlined in Section 3.3.1 (Eqs. 3.1a-3.1c). The author applied the model to perform three-dimensional turbulent simulation of the wet-to-dry expansion of the siloxane MM in a stator of a radial-inflow turbine designed for the wet-to-dry cycle. Figure 3.4 shows the two-dimensional variation of vapour quality and Mach number for the two-phase expansion from an inlet pressure of 500 kPa and inlet vapour quality of 0.3, plotted at the mid-span of the stator vane. The thermodynamic proprieties of the siloxane MM were evaluated using so-called look-up tables generated with NIST REFPROP [212]. The results seems promising as complete mixture vapourisation was predicted to happen at about two-thirds of the streamwise distance, ensuring dry vapour flow at the stator outlet. Furthermore, the estimated efficiency of the two-phase stator was in the order of 90 %. The Mach number contours reveal a formation of an oblique shock in the vicinity of the trailing edge, which suggests the shape of the stator could be further optimised.

Although the results obtained by White [8] look promising, the application of the homogeneous-equilibrium model implies that neither velocity slip nor thermal non-equilibrium were taken into account in the simulation. Owing to the large density difference between the liquid and vapour, the phases are expected to accelerate at a different rate for a given pressure

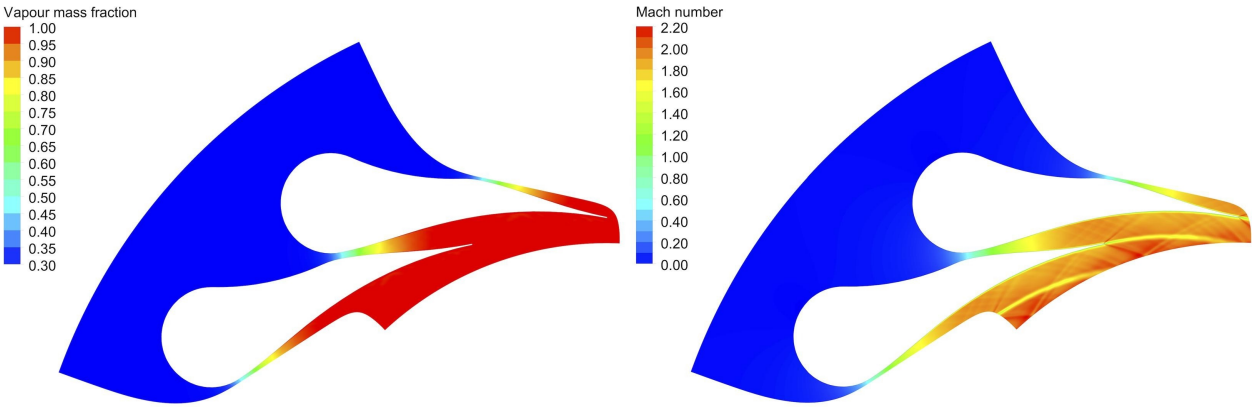


Figure 3.4: Two-dimensional variation of vapour quality and Mach number in radial-inflow turbine stator designed for the wet-to-dry cycle. The contours were obtained using a homogenous-equilibrium model applied to a two-phase expansion of the siloxane MM from an inlet pressure of 500 kPa and inlet vapour quality of 0.3 (figure retrieved from White [8]).

gradient applied in the nozzle. The velocity slip is counteracted by the drag force that tends to equalise phase velocities. Beside the increased relative mass flux of the vapour phase, the velocity slip may also affect the trajectory of the liquid droplets. Due to higher density and the associated longer relaxation times, liquid droplets take more time to adjust to the changing flow direction that is dictated by the geometry of the nozzle channel. This may lead to phase separation, where the liquid phase accumulates in the wall area in the form of a film or close to the centre of the nozzle, creating a characteristic core flow. Compared to homogeneous flows, where liquid droplets are well-mixed with the vapour, the areas of highly-concentrated liquid hinder an effective heat exchange between the phases, leading to reduced phase-change rates. The accumulation of the more viscous liquid phase at the nozzle wall may lead to elevated shear losses. The homogeneous-equilibrium model also assumes an instantaneous heat transfer between liquid and vapour, resulting in thermal equilibrium. Real two-phase flows will be characterised by a finite heat-transfer rate, giving rise to thermal non-equilibrium and thereby limited mass-transfer rate. Therefore, thermal non-equilibrium is inherently related to the phase-change rate and consequently to the variation of vapour and liquid volume fraction inside the nozzle. Since even limited vapourisation can significantly affect the flow compressibility, leading to a rapid decrease in the speed of sound, a delay in phase-change was found to cause a significant rise in the critical flow rate at the throat of the nozzles designed for flash boiling of subcooled water [44]. Since the fluid is already partially evaporated at the inlet of the wet-to-dry nozzle, the effect of phase-change delay is likely to be less pronounced compared to flashing of subcooled liquids, however, the phase change will still have a significant effect on the two-phase expansion. First of all, thermal non-equilibrium may result in incomplete vapourisation, leading to wet conditions at the turbine rotor, which raises concerns over erosion and deterioration of the machine performance. Since the phase-change rate defines the rate of decrease of droplet size along the nozzle, limited mass-transfer rate translates to larger droplets at a given streamwise location. Therefore, thermal non-equilibrium is also closely coupled with the mechanical homogeneity of the two-phase flow because larger droplets are less capable of following the mean flow direction, which as explained before, gives rise to effects such as phase separation.

Overall, mechanical and thermal non-equilibrium effects can significantly affect the distribution of phases, affecting the pressure, velocity and temperature variations inside the nozzle. Moreover, the delayed phase change is likely to affect the compressibility of the two-phase mixture, leading to different flow conditions at the nozzle throat compared to equilibrium flows. Generally, it is reasonable to assume mechanical and thermal equilibrium in long channels that feature a gradual flow expansion. When it comes to nozzles designed for the wet-to-dry turbine, such as that shown in Fig. 3.4, the two-phase flow is rapidly accelerated to supersonic speeds over a relatively short distance. As a result, the liquid and vapour phases may have insufficient time to maintain the equilibrium as the expansion advances, likely making the homogeneous-equilibrium model unsuitable for the wet-to-dry expansion studies.

Elliot [28] applied an inhomogeneous equilibrium model within a one-dimensional code to study the wet-to-dry expansion of toluene. Although, the authors did not provide a description for the numerical model, it is likely that the employed method is based on the previous study of the author [213] that is concerned with numerical modelling of two-phase expansions. For single-component two-phase mixtures, the model accounts for the velocity slip but assumes that both phases remain saturated throughout the expansion. The author applied the code to simulate an expansion of toluene from an inlet temperature of 289 °C (2847 kPa) and vapour quality of 0.01 to an outlet temperature of 70 °C (27.19 kPa) in a converging–diverging nozzle. Figure 3.5 illustrated the streamwise variation of pressure, nozzle diameter, vapour quality, and velocity of liquid and vapour predicted by the inhomogeneous equilibrium model. A successful wet-to-dry transition was predicted by the model, while the nozzle efficiency was estimated to be in the order of 98%. The figure also indicates that a considerable slip can emerge in the presence of extremely high flow velocities. Although the velocity slip was considered, the thermal non-equilibrium was neglected, which could have a significant influence on the phase change process.

In theory, the semi-equilibrium models such as the homogeneous-relaxation or delayed-equilibrium models could be employed to account for the delay in evaporation with respect to the homogeneous-equilibrium flow. These models, however, require fine-tuned empirical coefficients specific to the investigated working fluid and operating conditions for reasonably accurate predictions. Since there is currently no experimental data for the fluid and operating conditions to the wet-to-dry cycle known to the author, a more general modelling approach that accounts for the non-equilibrium effects is needed. The two-fluid model, capable of accounting for both inhomogeneity and thermal non-equilibrium appears to be a suitable model for that task. The two-fluid model can be applied in conjunction with the thermal phase-change model described in Section 3.3.3 to simulate the vapourisation of liquid droplets. Although, the thermal phase-change model does not remove all empiricism as heat-transfer coefficients for both phases have to be defined, it does not rely on fine-tuned empirical coefficients, as in the case of the homogeneous-relaxation model.

The first, and to this date, the only attempt to employ the two-fluid model in the analysis of wet-to-dry expansions was made by White [43]. The author simplified the two-fluid model governing equations (Eqs. 3.27-3.31) assuming an inviscid one-dimensional flow:

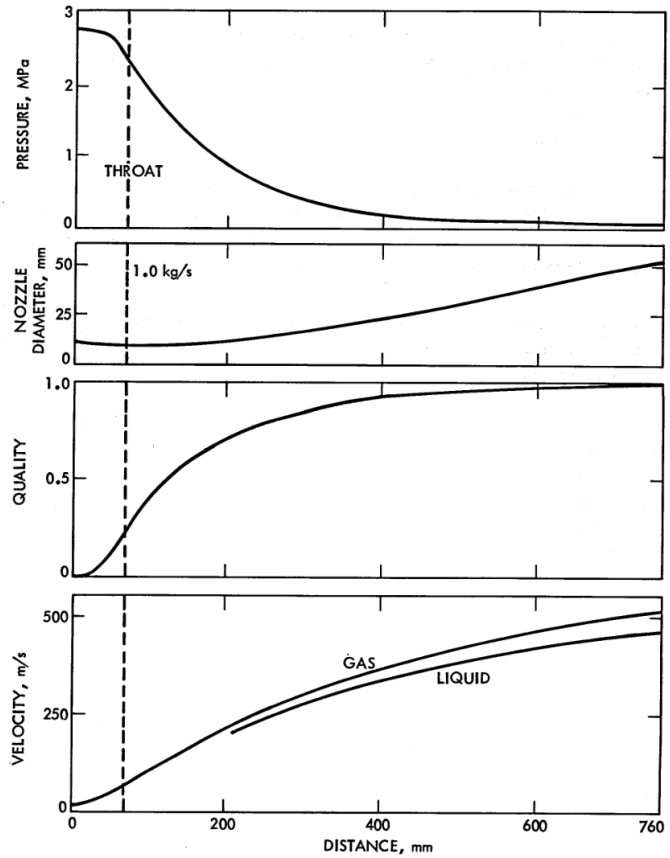


Figure 3.5: The graph illustrates the streamwise variation of pressure, nozzle diameter, vapour quality and velocity of liquid and vapour estimated with a one-dimensional inhomogeneous equilibrium model applied to a wet-to-dry expansion of toluene from an inlet pressure of 2847 kPa and inlet vapour quality of 0.01 (figure retrieved from Elliot [28]).

$$\frac{1}{A}\frac{\partial\left(\alpha\,\rho\right)_{\beta}}{\partial x} = \dot{m}_{ex} \tag{3.32a}$$

$$\frac{1}{A}\frac{\partial\left(\alpha\,\rho A u^{2}\right)_{\beta}}{\partial x} = -\alpha_{\beta}\frac{\partial p}{\partial x} + \dot{m}_{ex}u_{ex} + \vec{F}_{D} \tag{3.32b}$$

$$\frac{1}{A}\frac{\partial\left(\alpha\,\rho A u h_{tot}\right)_{\beta}}{\partial x} = \dot{m}_{ex}h_{ex} + \dot{q}_{ex} \tag{3.32c}$$

where A is the nozzle cross-sectional area, u is the streamwise velocity, h_{tot} is the total enthalpy, and β is the phase index that represents either liquid or vapour. The interphase mass-transfer and heat-transfer rates are denoted as $\dot{m}_{ex}$ and $\dot{q}_{ex}$, respectively. The terms $\dot{m}_{ex}u_{ex}$ and $\dot{m}_{ex}h_{ex}$ represent the momentum and enthalpy carried from one phase to the other during phase change, whereas $\vec{F}_D$ is the interfacial drag. The two-fluid model was coupled with the thermal phase-change models that estimates the vapourisation rate based on the interphase heat-transfer rate (see Eq. 3.14). The heat-transfer coefficient on the continuous vapour side of the liquid-vapour interface was estimated using the Ranz-Marshall correlation

(Eq. 3.33a), while a constant Nusselt number of 6 (Eq. 3.33b) was applied on the liquid side:

$$Nu_V = \frac{\mathfrak{H}_V D_d}{\lambda_V} = 2 + 0.6 Re_d^{0.5} Pr_V^{0.33} \tag{3.33a}$$

$$Nu_L = \frac{\mathfrak{H}_L D_d}{\lambda_L} = 6 \tag{3.33b}$$

where Re_d is the droplet Reynolds number defined based on velocity slip and droplet diameter, while Pr_V is the vapour Prandtl number. The drag coefficient was estimated using the Schiller-Naumann [214] correlation:

$$C_D = \begin{cases} \dfrac{24\,(1 + 0.15 Re_d^{0.687})}{Re_d}, & Re_d < 1000 \\ 0.44, & Re_d > 1000 \end{cases}$$

The author considered three approaches to estimating the interfacial area (A_{int}), which include a constant droplet diameter, a constant number of droplets per unit volume and a droplet diameter profile determined based on breakup considerations.

White [43] applied the code to design nozzle geometries and analyse the two-phase expansion, taking into account the velocity slip and thermal non-equilibrium. The code was verified against the inhomogeneous-equilibrium results obtained by Elliot (see Fig. 3.5) and against non-equilibrium CFD simulations performed for two-phase expansion of R1233zd(E). At this point, it is worth clarifying that the simulated expansion of R1233zd(E) was not a wet-to-dry process, as the fluid remained with the two-phase dome. Figure 3.6 presents the results of the one-dimensional code and the non-equilibrium CFD simulation the author obtained for the two-phase expansion of R1233zd(E). Generally speaking, the one-dimensional code predictions agreed fairly well with the non-equilibrium CFD simulations, with certain deviation in phase velocities at low droplet numbers. As far as non-equilibrium effects are concerned, extremely high difference in phase temperatures were observed at all droplet numbers. On the other hand, the velocity slip was found to be dependent on the droplet number, and was more pronounced in two-phase flows characterised by fewer number of larger droplets.

The author attempted to use the non-equilibrium CFD model to simulate wet-to-dry expansions, but encountered numerical issues related to the transition from two-phase to superheated vapour conditions. As such, further investigation on the wet-to-dry expansion was carried out only using the verified one-dimensional code. It was applied to study twelve different expansions of siloxane MM, with an inlet pressure varying between 478 and 1545 kPa and inlet vapour quality in the range of 0.1 to 0.4. The droplet diameter variation was determined based on the local value of the critical Weber number, which is commonly used in atomisation studies to determine the onset of droplet breakup.

Figure 3.7 illustrates the streamwise variation of nozzle half-length predicted by the homogeneous-equilibrium model and the non-equilibrium one-dimensional code. The streamwise

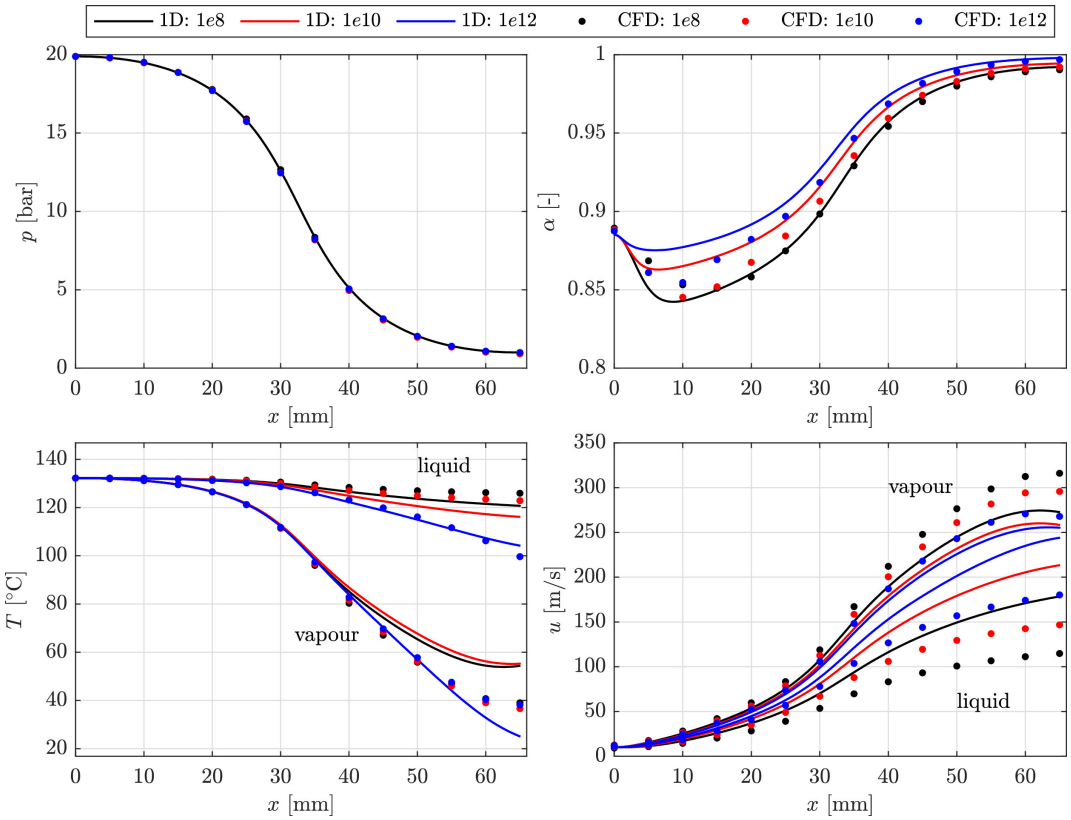


Figure 3.6: Streamwise variation of pressure, void fraction (α), temperatures and velocities of vapour and liquid obtained by White [43] using a quasi-1D inviscid two-fluid model and non-equilibrium CFD simulations for the two-phase expansion of R1233zd(E). Three different droplet numbers were considered in the study, ranging from 10^8 to 10^{12} droplets per unit volume (figure retrieved from White [43]).

location of the transition out of the two-phase regime was denoted by a dot. In case incomplete vapourisation occurred, the dot is placed at the outlet of the nozzle, and the corresponding outlet vapour quality was reported in the figure. According to the homogeneous-equilibrium model, the wet-to-dry transition was achieved under any of the considered conditions. The presence of non-equilibrium effects seem to delay the transition, and when these effects were factored in, incomplete mixture vapourisation was estimated for four out of twelve investigated expansions that correspond to the lowest inlet pressure of 478 kPa. It is worth mentioning that low-pressure conditions correlate with the greatest thermodynamic advantage of the wet-to-dry cycle, which suggests that there could be a trade-off between the feasibility of achieving complete vapourisation and maximising cycle performance. With that being said, the results provide an initial indication that the wet-to-dry transition is possible as long as the inlet pressure is high enough.

Overall, the one-dimensional code demonstrated that non-equilibrium effects can significantly delay the vapourisation process. Provided that the inlet pressure was sufficiently high, dry vapour conditions were estimated at the nozzle outlet. This seems to provide an initial indication that it is possible to achieve the wet-to-dry transition in practical nozzles. Having said that, these results were obtained under the assumption of an inviscid one-dimensional

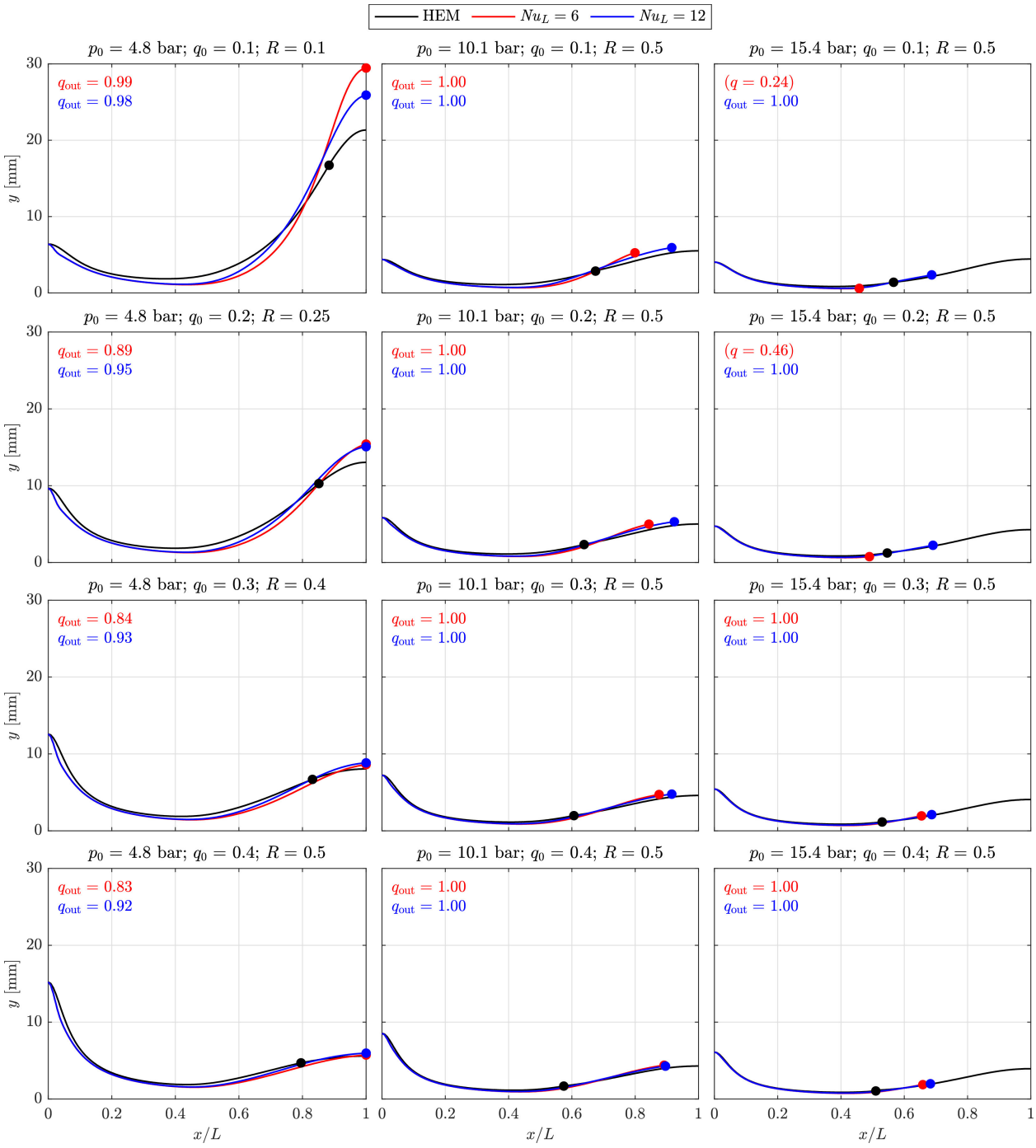


Figure 3.7: Streamwise variation in nozzle half-height obtained by White [43] using a homogeneous-equilibrium model (HEM) and a non-equilibrium one-dimensional code for liquid Nusselt number of 6 and 12. The dot represents the location of the wet-to-dry transition, while the value q_{out} gives the vapour quality at the nozzle outlet (figure retrieved from White [43]).

flow, neglecting multidimensional flow variations, viscous and turbulence effects, and the influence of non-drag forces such as lift and turbulent dispersion forces. As such, further numerical studies are deemed necessary to evaluate the concept of a two-phase turboexpander

for wet-to-dry cycles.

3.5 Scope of research

The critical component of wet-to-dry turboexpanders is the two-phase nozzle, which has to facilitate complete mixture evaporation, delivering uniform dry flow to the rotor and ensuring erosion-free operation. In the absence of relevant experimental data, the concept of achieving a complete mixture vapourisation in a nozzle is being investigated with the aid of numerical tools. Previous studies indicate that non-equilibrium effects play an important role in the phase change process under conditions relevant to the wet-to-dry cycle. To date, only one study attempted to perform non-equilibrium simulations of the wet-to-dry expansion, however, the expansion was substantially simplified by assuming an inviscid one-dimensional flow. Moreover, none of the previous studies seem to have considered the effect of nozzle shape on the phase change process. As such, further numerical efforts are justified to evaluate the concept of the wet-to-dry nozzle.

The main aim of this thesis is to assess the feasibility of designing a two-phase nozzle that would facilitate complete mixture vapourisation in an efficient manner under conditions relevant to the wet-to-dry cycle. This assessment will rely on conducting CFD simulations of the wet-to-dry expansion in a converging-diverging nozzle under a range of relevant operating conditions, simultaneously taking into account non-equilibrium effects, multidimensional flow variations, the effects of turbulence and viscosity and the influence of drag and non-drag forces. Furthermore, the study will attempt to optimise the nozzle and study the effect of nozzle shape on the two-phase expansion. This will be carried out in two stages. First, a previously developed non-equilibrium design tool will be employed to optimise the nozzle pressure profile to maximise the vapourisation rate. In the second stage of optimisation, direct CFD-based shape optimisation of the nozzle wall profile will be conducted, aiming to simultaneously maximise the vapourisation rate and nozzle efficiency. A detailed breakdown of this research work with the main aim, objectives, and specific tasks can be found in Chapter 1.1.

Chapter 4

Two-fluid model

4.1 Introduction

The previous chapter discussed different approaches to modelling flashing problems. Former numerical studies indicate that under conditions relevant to the wet-to-dry cycle, the two-phase flow can significantly deviate from the homogeneous-equilibrium conditions. This emphasises the need for suitable modelling technique that could account for the non-equilibrium effects that can significantly affect the phase change process. Among available models, the two-fluid model, being capable of accounting for both thermal and mechanical non-equilibrium effects, appears to be suitable for simulating wet-to-dry expansion. Although it does not remove all empiricism, the two-fluid model can be implemented for a wider range of applications without the need for fine-tuned empirical coefficients, which is advantageous due to lack of directly relevant experimental data for wet-to-dry expansion. This chapter provides a detailed description of the two-fluid model along with validation study results. It is worth reiterating that the phase change in flash-boiling flows is commonly assumed to be the result of interphase heat transfer, while the pressure difference between the phases is neglected. As such, the pressure field was assumed to be shared by both phases when deriving the governing equations for the two-fluid model.

4.2 Governing equations

The two-fluid model relies on the Eulerian-Eulerian framework, which means that both phases are treated as interpenetrating continua with separate conservation of mass, momentum and energy equations. These equations are formulated similarly to single-phase flows, with two main differences. Firstly, each control volume can be occupied by both phases simultaneously, which is why each term in the governing equations is multiplied by the volume fraction (fraction of the control volume occupied by the given phase) of the corresponding phase. Secondly, the phases can interact with each other by exchanging mass, momentum and energy, which requires the addition of source terms.

Mass continuity

With the above taken into account, the mass continuity equations for the liquid and vapour phases are formulated as follows:

$$\frac{\partial \left(\alpha\,\rho\right)_L}{\partial t} + \boldsymbol{\nabla}\cdot\left(\alpha\rho\vec{U}\right)_L = \sigma_{M,L} \tag{4.1a}$$

$$\frac{\partial \left(\alpha\,\rho\right)_V}{\partial t} + \boldsymbol{\nabla}\cdot\left(\alpha\rho\vec{U}\right)_V = \sigma_{M,V} \tag{4.1b}$$

where ρ and $\vec{U}$ represent phase density and velocity, while α is the phase volume fraction. The subscripts L and V correspond to liquid and vapour phases respectively, whilst $\sigma_{M,L}$ and $\sigma_{M,V}$ represent the mass transfer between the phases.

Momentum conservation
The momentum conservation equations are derived in a similar fashion, with individual terms multiplied by the volume fraction of the given phase:

$$\frac{\partial \left(\alpha\rho\vec{U}\right)_L}{\partial t} + \boldsymbol{\nabla}\cdot\left(\alpha\rho\vec{U}\vec{U}\right)_L = -\alpha_L\,\nabla P + \boldsymbol{\nabla}\cdot\tau_L + \sigma_{J,L} \tag{4.2a}$$

$$\frac{\partial \left(\alpha\rho\vec{U}\right)_V}{\partial t} + \boldsymbol{\nabla}\cdot\left(\alpha\rho\vec{U}\vec{U}\right)_V = -\alpha_V\,\nabla P + \boldsymbol{\nabla}\cdot\tau_V + \sigma_{J,V} \tag{4.2b}$$

The stress tensor, τ, for a given phase is expressed as:

$$\tau = \mu\left(\nabla\vec{U} + \left(\nabla\vec{U}\right)^T - \frac{2}{3}\delta\,\boldsymbol{\nabla}\cdot\vec{U}\right) \tag{4.3}$$

where δ is the Kronecker delta. The terms $\sigma_{J,L}$ and $\sigma_{J,V}$ represent the interphase momentum exchange, which is the result of mass transfer as well as the combined effect of interfacial forces. The role of individual interfacial forces distinguished in two-phase flows is discussed in the following sections.

Energy conservation
Equations 4.4a and 4.4b are the energy conservation equations formulated in terms of total enthalpy.

$$\frac{\partial \left(\alpha\rho\,h_{tot}\right)_L}{\partial t} + \boldsymbol{\nabla}\cdot\left(\alpha\rho\,\vec{U}h_{tot}\right)_L = \alpha_L\frac{\partial P}{\partial t} + \boldsymbol{\nabla}\cdot\left(\alpha k,\nabla T\right)_L + \boldsymbol{\nabla}\cdot\left(\vec{U}\tau\right)_L + \sigma_{E,L} \tag{4.4a}$$

$$\frac{\partial \left(\alpha\rho\,h_{tot}\right)_V}{\partial t} + \boldsymbol{\nabla}\cdot\left(\alpha\rho\,\vec{U}h_{tot}\right)_V = \alpha_V\frac{\partial P}{\partial t} + \boldsymbol{\nabla}\cdot\left(\alpha k,\nabla T\right)_V + \boldsymbol{\nabla}\cdot\left(\vec{U}\tau\right)_V + \sigma_{E,V} \tag{4.4b}$$

where phase temperature and thermal conductivity are denoted by T and λ, respectively. The energy exchange due to interphase transfer of mass and heat is accounted for by the terms $\sigma_{E,L}$ and $\sigma_{E,V}$.

Contrary to single-phase flows, an additional constraint equation is solved for the volume fraction, which states that the sum of liquid and vapour volume fraction in each control volume must add up to one.

$$\alpha_L + \alpha_V = 1 \tag{4.5}$$

4.2.1 Interphase exchange terms

The terms σ_M, σ_J and σ_E, which appear in the governing equations represent the exchange of mass, momentum and energy between the liquid and vapour phases. Since the amount of mass gained by one phase must be equal to the amount of mass lost by the other, σ_{M_L} and σ_{M_V} are equal in magnitude but have opposite signs.

$$\sigma_{M_L} = -\sigma_{M_V} \tag{4.6}$$

The momentum exchange (σ_J) is the combined effect of the interfacial forces ($\vec{F}$) and momentum exchange due to phase change ($\sigma_M \vec{U}_{ex}$).

$$\sigma_J = \vec{F} + \sigma_M \vec{U}_{ex} \tag{4.7}$$

The interfacial forces arise from unequal phase velocities, in so-called inhomogeneous two-phase flows. The force vector can be broken down into five main components that represent the drag ($\vec{F}_D$), lift ($\vec{F}_L$), turbulence dispersion ($\vec{F}_{TD}$), wall lubrication ($\vec{F}_{WL}$) and virtual mass ($\vec{F}_{VM}$) forces.

$$\vec{F} = \vec{F}_D + \vec{F}_L + \vec{F}_{TD} + \vec{F}_{WL} + \vec{F}_{VM} \tag{4.8}$$

The relevance of these mechanisms in two-phase droplet flows alongside modelling techniques are discussed in the following sections. Since the force exerted by the liquid on the vapour is equal in magnitude and opposite to the force exerted by the vapour on the liquid, it follows that $F_L = -F_V$. In addition to the effect of interfacial forces, the phase-change process itself entails some momentum transfer as the mass exchanged between the phases carries some momentum, which is represented by the term $\sigma_M \vec{U}_{ex}$. The exchange velocity, U_{ex}, is fundamentally related to the nature of the phase change process. For example, during vapourisation, it is known that the momentum of the liquid phase is transferred to the vapour phase, so U_{ex} is simply the liquid velocity. The opposite is true when condensation takes place.

The interphase energy exchange can be expressed as:

$$\sigma_E = q_{ex} + \sigma_M h_{tot,ex} \tag{4.9}$$

where q_{ex} is the exergy exchange due to heat transfer, while $\sigma_M h_{tot}$ represents the exergy exchange due to mass transfer. Similar to U_{ex}, $h_{tot,ex}$ is dependent on the nature of the phase change process.

The details concerning the evaluation of mass and heat transfer as well as the interfacial forces are provided in the following section.

4.3 Phase coupling

In the two-fluid model, conservation equations are solved for each phase separately, while the phases are coupled through several source/sink terms that determine interphase exchange of mass, momentum and energy. This section explains how these source/sink terms are determined, discussing interfacial area definition, the phase-change model and interphase models.

4.3.1 Interfacial area

The critical parameter that affects the interphase coupling is the contact area between the phases. Generally, modelling the interfacial area requires knowledge about the two-phase flow pattern, which can generally depend on the ratio of vapour to liquid flow rate, geometry and orientation of the channel as well as fluid properties. These conditions are governed by the component upstream of the turboexpander, which is the heat-exchanger that facilitates the partial evaporation of the fluid. It is assumed that the mixture leaving the heat-exchanger is well-mixed and characterised by uniform spatial distribution of phases. There is some uncertainty associated with this assumption, as phase separation could occur in the components upstream of the nozzle (e.g. in pipe bends). Wu et al. [185] studied non-equilibrium flashing of water in a converging-diverging nozzle. Based on experimental results and certain assumptions, the author proposed a transitional interfacial area model, which assumed that the transition from bubbly-slug to droplet flow begins at a void fraction of 0.7. A similar assumption was made by Ortego Sampedro et al. [147] who proposed a transitional model for the interfacial area density, and assumed that the droplet flow regime was present at void fractions above 0.7. To decide on the suitable approach to modelling the interfacial area, void fraction at the nozzle inlet was plotted for a range of relevant inlet pressures and vapour qualities (Fig. 4.1).

Considering a range of inlet vapour quality between 0.1 and 0.5, the inlet void fraction for low inlet pressures below 750 kPa is expected to remain above 0.7, justifying the assumption of the droplet flow regime. However, as the inlet pressure is raised from 750 to 1250 kPa, the minimum inlet vapour quality to maintain the void fraction above 0.7 increases from 0.15 to 0.30. Although at high inlet pressures and low vapour qualities the void fraction is not sufficiently high to assume droplet flow regime at the nozzle inlet, it is expected it will increase downstream of the inlet due to two factors. First, in comparison with the liquid phase, the density of vapour decreases at a higher rate when the pressure begins to drop in the streamwise direction. The higher relative decrease in vapour density results in an increase of the void fraction even if no vapourisation takes place. The other factor is related to phase change that naturally causes a decrease in the volume occupied by the liquid phase. It is presumed that if the combination of these two factors leads to a sufficiently high rise in the void fraction in the early stage of the expansion, the droplet flow regime may be established

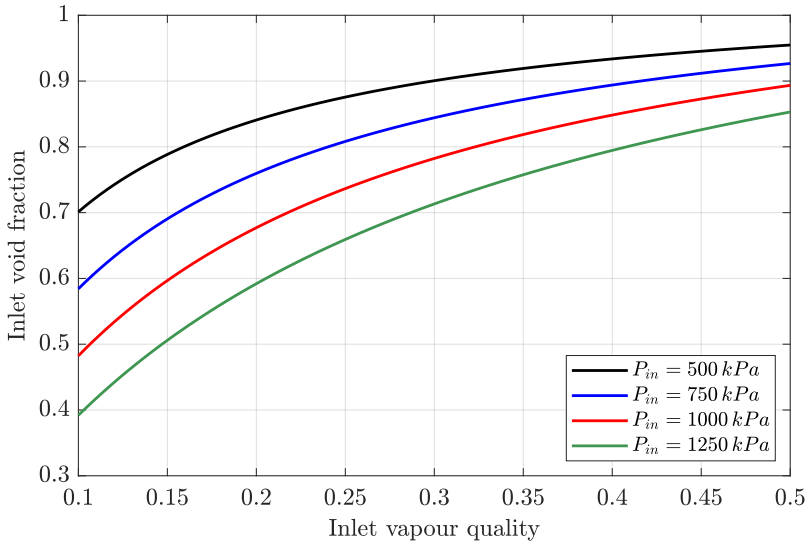


Figure 4.1: Relationship between the inlet void fraction and inlet vapour quality for different inlet pressure relevant to the wet-to-dry cycle.

relatively close to the inlet of the nozzle. In other words, even if the void fraction is too low at the inlet of the nozzle to safely assume a droplet flow regime, it increases quickly enough to make the assumption of the droplet flow regime justified when the entire expansion is concerned. To investigate this, the non-equilibrium one-dimensional code developed by White [43] was applied to simulate the wet-to-dry expansion from 1000 and 1250 kPa and an inlet vapour quality of 0.1. The author estimated the droplet diameter based on the critical Weber number that has been extensively used in atomisation studies to predict the onset of droplet breakup [215]. In essence, the author applied the critical Weber number correlation from Eq. 4.17 to estimate the maximum stable droplet diameter using Eq. 7.11 under given flow conditions. Starting with an assumed droplet diameter at the nozzle inlet, the droplet size was reduced in accordance with Eq. 7.11 whenever the Weber number exceeded the critical value, providing an approximation to the breakup process. The method is further explained in the following paragraphs. Figure 4.2 illustrates the streamwise variation of void fraction and vapour mass fraction. Generally, the results look fairly similarly for the two expansions and the void fraction reaches 0.7 within 40% of the nozzle length. This may seem like a relatively large distance to assume droplet flow regime for the entire expansion, however, the corresponding increase in vapour mass fraction over that distance is only about 0.1 to 0.15. Since the majority of the phase change occurs at a void fraction greater than 0.7, it seems reasonable to assume droplet flow to estimate the interfacial area. At this point it should be highlighted that there remains an uncertainty related to the flow pattern and interfacial area definition in the first part of the expansion. With that said, the model proposed by Wu et al. [185] suggests that the interfacial area remains relatively constant between void fraction of 0.3 and 0.7, which indicates that the expansion would not be drastically affected.

To summarise, the void fraction at the inlet of the nozzle exceeds 0.7 for most of operating conditions considered in this study. Higher inlet pressure and low inlet qualities are characterised by lower void fractions, but as indicated by a preliminary analysis, the majority of

phase change occurs at void fraction above 0.7. Therefore, this study will assume a droplet flow regime when estimating the interfacial area and modelling the interphase coupling.

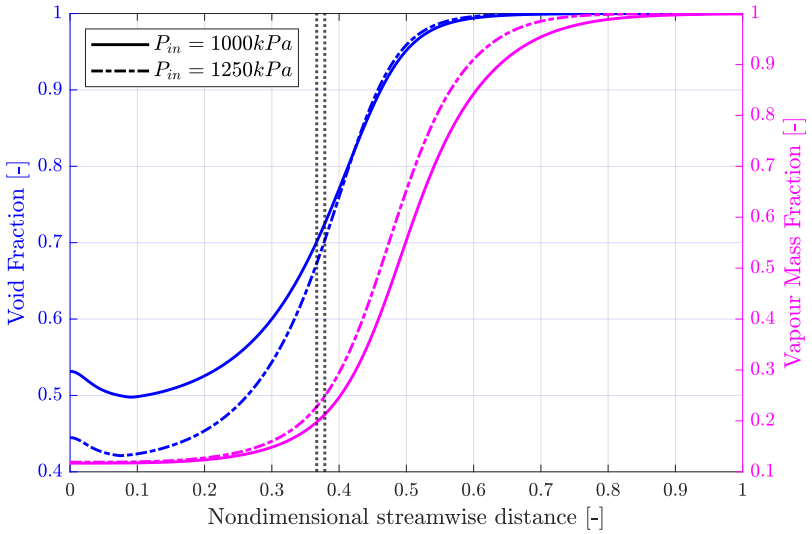


Figure 4.2: Streamwise variation of void fraction and vapour mass fraction predicted using a non-equilibrium one-dimensional code applied to the expansions from an inlet total pressure of 1000 and 1250 kPa and an inlet vapour quality of 0.1; the dotted lines denote the streamwise location where the void fraction exceeded 0.7.

Assuming that the droplets are not in contact with one another, the interfacial area will simply be the combined surface area of all the droplets in the control volume. If there is N_d droplets per unit volume, the interfacial area per unit volume A_{int} becomes:

$$A_{int} = N_d \, \pi D_d^2 \tag{4.10}$$

where D_d is droplet diameter, while N_d is often referred to as droplet number density or droplet number for simplicity. Subscript d will be used to denote droplet properties. At this point, it is worth noting that Eq. 4.10 will also be applicable to calculating the interfacial area density in flashing of subcooled liquid, so long as the dispersed phase can be assumed to be in the form of spherical bubbles. In fact, as pointed out by Liao and Lucas [132], majority of previous studies on flashing of liquid assumed spherical bubbles when calculating the interfacial area. With that being said, some authors recognised that the assumption may be invalid for void fractions greater than 0.3, and proposed transitional models for the interfacial area [147, 160, 181, 185].

Since the volume fraction of the dispersed phase is essentially the ratio of the combined volume of the droplets to the total volume of the control volume, α_L can be expressed in terms of droplet number as follows:

$$\alpha_L = N_d \, \frac{\pi D_d^3}{6} \tag{4.11}$$

Equations 4.10 and 4.11 can be combined to express the interfacial area in terms of liquid volume fraction and droplet diameter D_d.

$$A_{int} = 6\frac{\alpha_L}{D_d} \tag{4.12}$$

Since volume fraction is a dependent variable determined in the solution process, the interfacial area can be defined so long as the droplet diameter is known. The two-fluid model is an Eulerian-Eulerian description of the two-phase flow, which means that the conservation equations are formulated as if liquid and vapour were two interpenetrating continua. Consequently, the two-fluid model does resolve the droplet interface and thus the droplet diameter can be considered to be a lumped parameter that defines the interfacial area. As such, one can assume that either droplet diameter or droplet number is applied to calculate the interfacial area, both parameters can act as model tuning factors that effectively modify the phase-change rate. With that being said, if one attempts to more closely resemble the physical process of boiling, assuming a fixed number of droplets appears to be the preferred option as suggested by Laurien [183]. This is because when breakup and coalescence effects are ignored, it is expected that droplets will diminish in size during vapourisation. If the number of droplets is fixed, Eq. 4.11 can be rearranged to express the droplet diameter in terms of liquid volume fraction and droplet number as follows:

$$D_d = \left(\frac{6\alpha_L}{\pi N_d}\right)^{1/3} \tag{4.13}$$

Therefore, assuming a fixed droplet number allows the droplet size diminish in size in line with the decreasing volume fraction of liquid, which better describes the actual process of boiling. To clarify this further, let us assume that the phase-change rate is known at a certain point inside the nozzle. In theory, one could either tune the droplet diameter or the droplet number to adjust the interfacial area that would result in the known phase-change rate (see Eq. 4.21). From that point of view, it does not make a difference whether a droplet diameter or droplet number is selected as long as the correct figure for the interfacial area is obtained. Now, if the analysis is extended from a single point inside the nozzle to a continuous variation of the phase-change rate along the entire length of the channel, it is unlikely to be able to calibrate the interfacial area variation using a fixed droplet diameter to match the varying phase-change rate. On the other hand, assuming a fixed droplet number will naturally results in droplet size decrease in evaporating flows (Eq. 4.13), which should facilitate an easier calibration of the interfacial area variation. Moreover, in idealised conditions in which droplets undergo neither breakup or coalescence, a fixed droplet number has stronger physical grounding and should reflect the interfacial area variation that is in line with the actual phase-change process.

Although the droplet number assumption can provide a better approximation of the phase change process, it can be very challenging to estimate an appropriate figure for N_d without resorting to experimental data. Unlike flashing from a subcooled or saturated liquid state, wet-to-dry expansion begins from a two-phase state, and the nucleation models cannot be directly used to estimate population and size of the dispersed phase. Having said that, the expansion in the wet-to-dry nozzle is characterised by a rapid flow acceleration to supersonic

velocities. Under such conditions, large droplets are likely to break up into smaller fragments under the action of drag force. When it comes to flash boiling of subcooled liquids, breakup models have been combined with coalescence and nucleation models to solve a transport equation for the bubble number density [203, 204, 216]. Breakup models have also been adopted in polydispersed simulations of flash boiling, where the bubble size is no longer assumed to be uniform in a given computational cell, but a size spectrum is considered with the bubbles divided into a number of distinct size groups [217–219].

As far as accelerating droplet flows are concerned, breakup correlations have frequently been employed to estimate a realistic figure for the droplet size during the two-phase expansion [28, 43, 213, 220, 221]. Although this method does to directly rely on solving an additional transport equation for the droplet number density, the decrease in droplet size according to a certain breakup criterion leads to a variation in droplet number during expansion. In order to estimate a maximum stable droplet diameter, that is the largest droplet that is expected to remain intact under certain flow conditions, most authors resorted to the definition of the Weber (We) and Ohnesorge (Oh) numbers. These dimensionless number have been extensively used in atomisation studies to estimate the onset and nature of droplet breakup process [215].

$$We = \frac{\rho_V \left(u_V - u_L\right)^2 D_d}{\sigma} \tag{4.14}$$

$$Oh = \frac{\mu_L}{\sqrt{\rho_L D_d \sigma}} \tag{4.15}$$

The Weber number is a dimensionless number that relates the aerodynamic forces that act to deform and fragment the droplet to surface tension σ_{st} resisting that deformation. The Ohnesorge number describes the relative importance of viscous forces to inertial and surface tension effects. Droplet breakup is expected to be initiated once the Weber number reaches its critical value, We_{cr}. Hence, the maximum stable droplet size is given as:

$$D_{d,max} = \frac{We_{cr}\,\sigma}{\rho_V \left|u_V - u_L\right|^2} \tag{4.16}$$

Different empirical correlations have been proposed for estimating the critical Weber number such as the ones proposed by Bordkey [222] (Eq. 4.17) and Gelfand [223] (Eq. 4.18):

$$We_{cr} = We_{cr,\,Oh\to 0}\left(1 + 1.077 Oh^{1.6}\right) \tag{4.17}$$

$$We_{cr} = We_{cr,\,Oh\to 0}\left(1 + 1.5 Oh^{0.74}\right) \tag{4.18}$$

Although the two correlations differ significantly for $Oh > 3$, they closely agree at lower Oh and both indicate that the We_{cr} is around 11 as Ohnesorge number approaches zero ($Oh < 0.1$) [215]. This condition holds in both subsonic and supersonic flow regimes [215, 224]. It should be emphasised that the physical droplet breakup process is a more complex process, and the droplet breakup model described herein does not aim at resolving the process but rather uses the critical Weber number condition to estimate a realistic droplet size in given flow conditions.

4.3.2 Mass and heat transfer

A common practice in the analysis of flashing flows is to assume that the phase change occurs

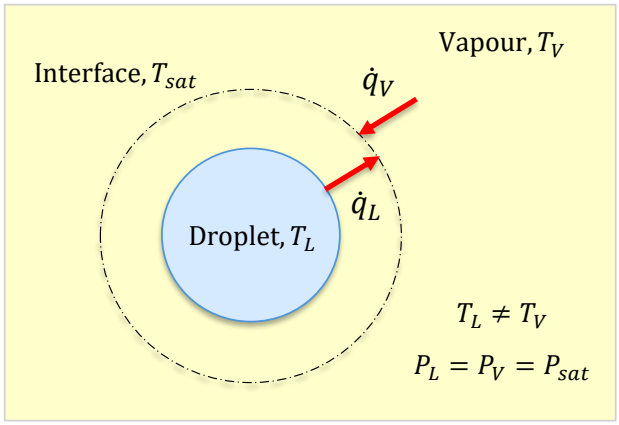


Figure 4.3: Schematic of an evaporating droplet in the wet-to-dry expansion; the phase change is assumed to occur due to interphase heat transfer which is estimated using the two-resistance model.

The heat transfer occurs separately between each phase and the interface, such that there are two distinct heat-transfer coefficients that determine the interphase heat-transfer rate:

$$\dot{q}_L = \mathfrak{H}_L \left(T_{int} - T_L\right) \tag{4.19a}$$
$$\dot{q}_V = \mathfrak{H}_V \left(T_{int} - T_V\right) \tag{4.19b}$$

where $\mathfrak{H}_L$ and $\mathfrak{H}_V$ are heat-transfer coefficients for the liquid and vapour sides respectively, while T_{int} is the interfacial temperature equal to the local saturation temperature. Assuming that the interface is not capable of storing either mass or energy, the overall energy balance applied to the interface must be zero:

$$\dot{q}_L A_{int} + \dot{m}_{LV} h_L + \dot{q}_V A_{int} + \dot{m}_{VL} h_V = 0 \tag{4.20}$$

The first two terms in Eq. 4.20 represent the energy supplied from liquid to the interface; the subscripts LV and VL denote transfer from liquid to interface and from vapour to interface respectively. The term $\dot{q}_L A_{int}$ is the energy associated with the heat transfer and $\dot{m}_{VL} h_{VL}$ is the energy associated with the mass transfer (from the interface to the liquid phase). Similarly, the last two terms in Eq. 4.20 represent the energy supplied from vapour to the interface. Substituting Eqs. 4.19a-4.19b in Eq. 4.20, and assuming that the rate of mass

gain by the vapour phase is equal to rate of mass loss by the liquid phase ($\dot{m}_{LV} = -\dot{m}_{VL}$), one can derive the following equation that determines the interphase mass transfer rate [225]:

$$\dot{m}_{LV} = \frac{\mathfrak{H}_L A_{int} \left(T_{int} - T_L\right) + \mathfrak{H}_V A_{int} \left(T_{int} - T_V\right)}{h'_V - h'_L} \tag{4.21}$$

Since negative value of $\dot{m}_{LV}$ denotes mass transfer from liquid to vapour, $\dot{m}_{LV}$ will be equal to $\sigma_{M,L}$ according to the convention followed in the governing equations (Eq. 4.1a). The enthalpies values h'_L and h'_V are dependent on the direction of mass transfer. When it comes to the phase that gives away mass, the enthalpy carried to the interface is simply the bulk fluid enthalpy. However, for the phase that receives the mass, the enthalpy incoming from the interface is the saturation enthalpy [225]. This discontinuity is simply the result of the assumption that the created phase is saturated; therefore, the enthalpy carried from the interface must be the saturation enthalpy of the corresponding created phase [226]. Therefore, in case of vapourisation, the interphase mass transfer rate becomes:

$$\sigma_{M,L} = \frac{\mathfrak{H}_L A_{int} \left(T_{int} - T_L\right) + \mathfrak{H}_V A_{int} \left(T_{int} - T_V\right)}{h_{V,sat} - h_L} \tag{4.22}$$

where $h_{V,sat}$ is the vapour saturation enthalpy. The phase-change model based on Eq. 4.21 has been applied by multiple authors to perform CFD simulations of flash boiling of subcooled liquids [32, 41, 147, 201, 204, 227]. The main difference between those previous studies and the current work is that the vapour can no longer be fixed at saturation conditions (a common assumption in flashing of subcooled liquids), which means that two separate heat-transfer coefficients have to be defined to estimate the mass-transfer rate. Compared with other phase-change models proposed in the literature, such as the homogeneous-relaxation model, the thermal-phase change model does to rely on fine-tuned empirical coefficients, which as discussed in Chapter 3.1, tend to be highly sensitive to the specific operating conditions and working fluid they have been derived for. With that being said, the model does not remove all empiricism as the heat-transfer coefficients are often determines from semi-empirical correlations [228]. However, these correlations are presumed to be applicable to a wider range of operating conditions and working fluids, which often makes the thermal-phase change model in case experimental data required for fine tuning is not available.

4.3.3 Interfacial heat-transfer rate

In order to implement the phase-change model based on the interfacial heat transfer, two heat-transfer coefficients have to be evaluated. As discussed in the previous section, the need for estimating the heat-transfer coefficients in thermally driven phase-change models adds to the empiricism, however, these heat-transfer correlations are theoretically more universal than fined-tuned empirical relaxation coefficients applied in models such as the homogeneous-relaxation model. These heat-transfer coefficients are associated with the corresponding Nusselt numbers for liquid and vapour phases, Nu_L and Nu_V, defined based on the droplet diameter D_d and corresponding thermal conductivity values:

$$Nu_L = \frac{\mathfrak{H}_L\, D_d}{k_L} \tag{4.23a}$$

$$Nu_V = \frac{\mathfrak{H}_V\, D_d}{k_V} \tag{4.23b}$$

The majority of studies on flash boiling has revolved around flashing of subcooled/saturated liquid with the dispersed phase assumed to be in form of vapour bubbles. The thermal resistance on the dispersed side of the interface has frequently been neglected (zero-resistance approach), which essentially forces the vapour phase to remain at saturation temperature throughout the expansion. The main focus lied in determining the thermal resistance on the continuous liquid side, which is a combined effect of conduction, convection and turbulence. Liao & Lucas [228] presented a comprehensive review of existing analytical and empirical correlations for predicting the heat-transfer coefficient on the continuous side of the interface. The two dimensionless numbers that were often used to derive those correlations for the interfacial heat-transfer rate are the particle Reynolds number and Prandtl number:

$$Re_d = \frac{\rho_V D_d \left|\vec{U}_V - \vec{U}_L\right|}{\mu_V} \tag{4.24}$$

$$Pr_V = \frac{c_{p,V}\mu_V}{\lambda_V} \tag{4.25}$$

where μ_V and $c_{p,V}$ are the vapour dynamic viscosity and specific heat capacity at constant pressure. Since in the wet-to-dry expansion the dispersed phase is the liquid phase , the particle Reynolds number is defined for a droplet, while Prandtl number corresponds to the continuous vapour phase. Liao & Lucas [228] evaluated a wide range of heat-transfer models for flashing flows, focusing on bubble growth in superheated liquids. The authors considered stationary, translating bubbles and bubbles in high-speed turbulent flows. Available direct numerical simulation and experimental data were used to verify the accuracy of the different correlations. The authors also implemented the two-fluid model in a commercial CFD code to simulate bubble growth with a range of heat-transfer correlations, validating the results against direct numerical simulation and experimental data. Although no correlation was found to be generally applicable, some models demonstrated high accuracy under certain flow conditions. Figure 4.4 shows the relationship between the Nusselt and Péclet (Pe) numbers estimated with several heat-transfer models and direct numerical simulations. The Péclet number is simply the product of the particle Reynolds number and the Prandtl number of the continuous phase.

$$Pe = Re_d Pr_V \tag{4.26}$$

It can be noted that for creeping flows with particle Reynolds number in the order of 0.1, the Clift model gives very good agreement with direct numerical simulations. For high-speed flows, characterised by larger Péclet numbers, the Ranz-Marshall [229] correlation demonstrated the best agreement among the tested models. The Ranz-Marshall correlation was originally derived from experimental tests of a water droplet evaporating in a hot air stream:

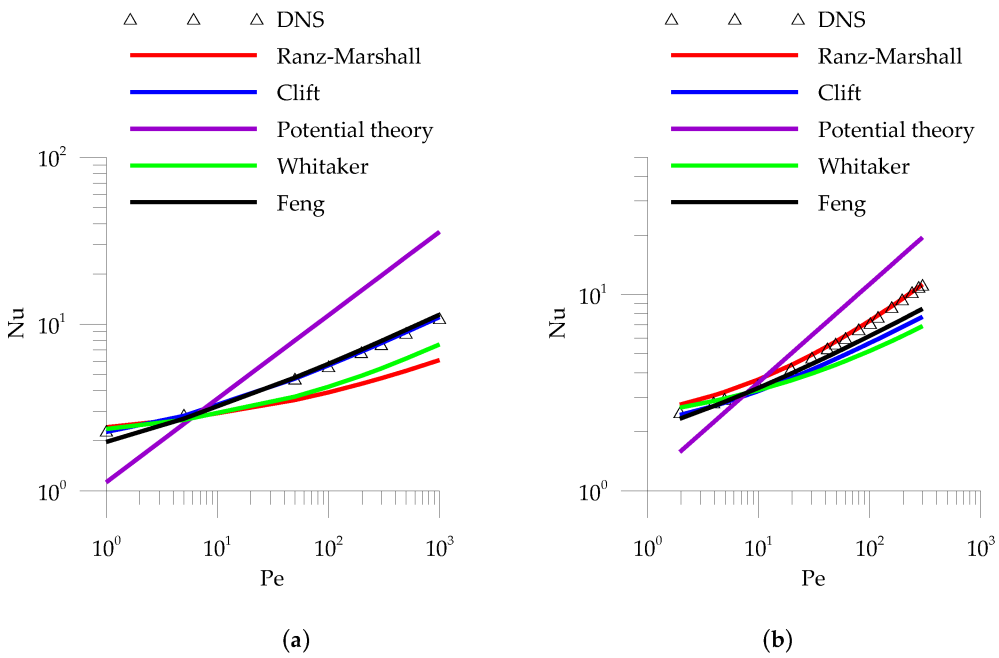


Figure 4.4: Suitability of various heat-transfer models for predicting the average Nusselt number of fully contaminated spherical bubbles: (a) $Re_b = 0.1$, $Pr_L = 1-104$. (b) $Re_b = 1-150$, $Pr_L = 2$. (figure retrieved from Liao & Lucas [228])

$$Nu_V = \frac{\mathfrak{H}_V D_d}{\lambda_V} = 2 + 0.6 Re_d^{0.5} Pr_V^{0.33} \tag{4.27}$$

Since the contaminated bubbles behave more like solid spheres, the authors suggested that the Ranz-Marshall correlation would be suitable for solid particles and liquid droplets so long as the particle Reynolds number is sufficiently high [228]. At this point it is worth noting that when it comes to the formation of bubbles in superheated liquid, an additional energy must be supplied in the nucleation process. Therefore, the application of the thermal-phase change model using heat-transfer correlations such as the Ranz-Marshall correlation carries some uncertainty as it was developed for liquid particles that are already formed. This is why some authors [204] studying flash boiling of subcooled liquids included a separate nucleation term to separately account for the bubble formation process; the thermal-phase change model was then applied to simulate the growth of the formed bubbles. Figure 4.5 shows streamwise variation of droplet Reynolds number and Péclet number obtained using a non-equilibrium one-dimensional code for four inlet pressures and a fixed inlet vapour quality of 0.3. It can be seen that the droplet Reynolds and the Péclet number are in the order of hundreds for all inlet pressures, which indicates the applicability of the Ranz-Marshall correlation.

Heat transfer modelling on the dispersed side of the interface appears to have been much less explored in the past. This is thought to be the results of negligible thermal resistance of vapour bubbles in superheated liquids, which has been the most studied flash-boiling phenomenon type. Nevertheless, a few models have been proposed in the event that the

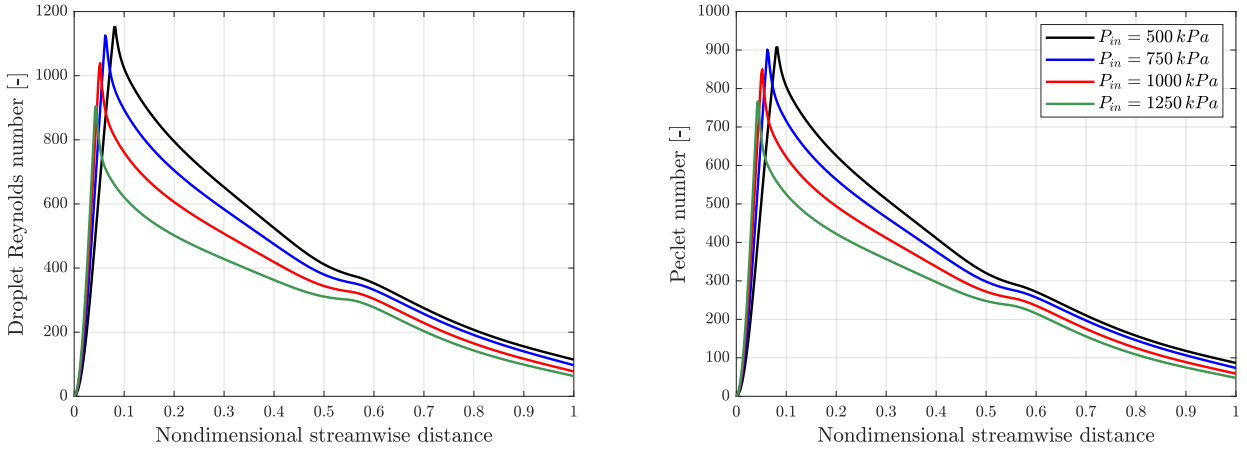


Figure 4.5: Streamwise variation of droplet Reynolds number and Péclet number obtained using a non-equilibrium one-dimensional code for four inlet pressure and an inlet vapour quality of 0.3.

thermal resistance on the dispersed side of the interface cannot be neglected. The most simplistic approach is to assume a constant Nusselt number of 6, $Nu_L = 6$, which is an approximation based on an analytical heat-transfer analysis conducted for a solid sphere. It assumes negligible advection effects and spatially-constant temperature field inside the droplet [225]. Given that the heat-transfer rate will likely be enhanced due to effects such as internal circulation, this is considered a rather conservative approach. Solbrig [230] proposed a constant Nusselt number of 16, $Nu_L = 16$, which comes from approximating the time-dependent heat conduction within a bubble with a time-independent solution. This model was also adopted by Pinhasi [231] in the work on modelling flashing flows. The authors of RELAP5/MOD3 [221], a code designed for transient simulation of flashing in light water reactor coolant systems, applied the following correlation for evaluating heat-transfer rate from the droplet to the interface:

$$Nu_L = 2 + 7 \min\left(1 + \frac{c_{p,L}\ \max(0,\ |T_{sat} - T_L|)}{h_{LV}}, 8\right) \tag{4.28}$$

The correlation is based on Brown's [232] work on condensation of water droplets and was obtained by conducting a heat-transfer analysis of a sphere suddenly immersed in a hot bath. The main difference between the Brown's correlation and the other proposed models is that it includes a direct reference to the liquid superheat level ($T_{sat} - T_L$). This is to account for the fact that a highly superheated liquid is likely to undergo a more rapid vapourisation process compared to slightly superheated conditions. As such, the heat-transfer coefficient itself depends on the superheat level. The Brown's model predicts a minimum Nusselt number of 9 in the absence of superheating, that is when phase change does not accompany the heat exchange. This value lies in the range of previously discussed model (i.e. between 6 and 16). The Nusselt number increases gradually with liquid superheating and is capped at a value of 51. However, preliminary analysis showed Nu_L estimated by the Brown's model is typically confined to the range of 9 to 16, which is not drastically different to the other available models.

As pointed out in RELAP5/MOD3 manual [221], there is some uncertainty as to how exactly the Nusselt number correlation was derived by Brown. Moreover, the effect of droplet size variation due phase change was not taken into account in the derivation process. Despite these limitations, the Brown's model is considered as the current best-estimate in the absence of more empirically-validated correlations.

4.3.4 Momentum exchange

Owing to higher density of the liquid phase, droplets, having higher inertia, are likely to accelerate to a lesser extent than the surrounding vapour for a given pressure gradient applied in the streamwise direction. In the event that the two-phase flow accelerates rapidly, the velocity difference can be significant, resulting in highly inhomogeneous two-phase flow

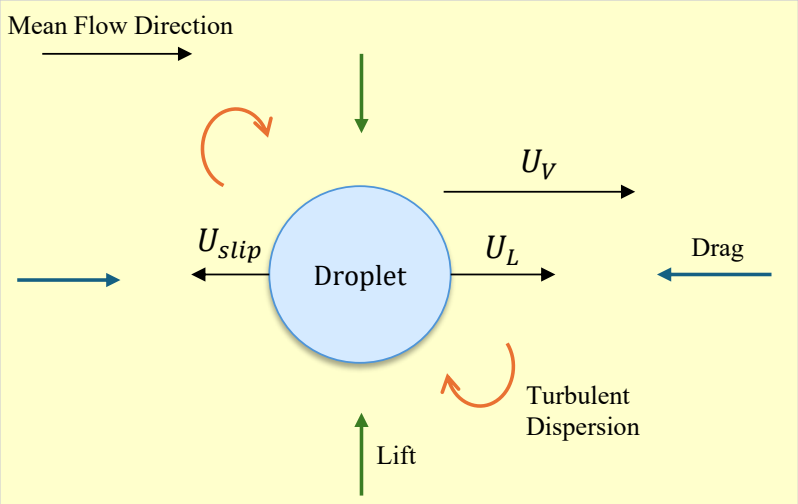


Figure 4.6: Interfacial forces relevant to two-phase droplet flows; U_{slip} represents velocity slip resulting from a difference in vapour and liquid velocities ($U_V - U_L$).

Drag

The result of two phase having non-identical velocities is the drag force that acts parallel to the mean flow direction and reduce the velocity difference. A generic expression for drag force has the following form:

$$F_D = \frac{1}{2}\,\rho_V\,A\,C_D\,(U_V - U_L)^2 \tag{4.29}$$

where A is the projected area, while C_D is the non-dimensional drag coefficient; the difference

in phase velocities, $U_V - u_U$ is frequently referred to as velocity slip (U_{slip}). For the dispersed phase in form of spherical droplets, the interfacial drag force can be expressed as:

$$F_D = \frac{3}{4}\frac{C_D}{D_d}\alpha_L \rho_V |U_L - U_V| (U_L - U_V) \tag{4.30}$$

As long as the velocity slip is relatively small, the behaviour of liquid droplets resemble the behaviour of solid particles and it may be reasonable to apply the Schiller-Naumann [214] correlation.

$$C_D = \begin{cases} \dfrac{24\left(1 + 0.15 Re_d^{0.687}\right)}{Re_d}, & Re_d < 1000 \\ 0.44, & Re_d > 1000 \end{cases}$$

For higher Re_d, when the relative velocity between the phases increases, unlike solid particles, the shape of droplets may get distorted. At first, droplet shape shifts from spherical to ellipsoidal, and as the particle Reynolds number further increases, the droplet takes a spherical cap shape [225]. Ishii-Zuber drag model is applicable to both bubbles and droplets and is capable of estimating the drag coefficient taking into account the effect of shape distortion. The Ishii-Zuber resorts to Eötvös number that describes the relative importance of gravitational forces compared to surface tension forces.

$$Eo = \frac{g\left(\rho_V - \rho_L\right) D_d^2}{\sigma} \tag{4.31}$$

For ellipsoidal droplets, drag coefficient is independent of Reynolds number and only depends on the shape of the droplet, which is determined through Eötvös number:

$$C_{D_{ellipse}} = \frac{2}{3}\sqrt{Eo} \tag{4.32}$$

For the spherical cap regime, the drag coefficient is well approximated with a constant value of 8/3.

$$C_{D_{cap}} = \frac{8}{3} \tag{4.33}$$

In the undistorted regime, the droplet behaves like a solid sphere and Schiller-Naumann can be applied.

$$C_{D_{undistorted}} \frac{24}{Re_d}\left(1 + 0.15 Re_d^{0.687}\right) \tag{4.34}$$

The distorted regime can be automatically taken into account using the following conditions:

$$C_{D_{distorted}} = \min(C_{D_{ellipse}}, C_{D_{cap}}) \tag{4.35a}$$

$$C_D = \max(C_{D_{undistorted}}, C_{D_{distorted}}) \tag{4.35b}$$

where C_D is the final value for drag coefficient.

The above correlations are applicable to two-phase flows with relatively low volume fraction of the dispersed phase. For higher volume fractions, the Ishii-Zuber model introduces correction terms to account for swarm-like behaviour of densely distributed particles [233]. Thus, the model can be applied to flows with both dilute and densely distributed droplets.

Lift Force
The lift force acts in the direction perpendicular to the mean flow direction and is responsible for lateral displacement of the dispersed particles. It is caused by shear effects and occurs in the presence of rotational movement of the continuous phase, that is when the curl of its velocity is non-zero. The lift force acting on the liquid droplets can be estimated using:

$$F_L = \alpha_L \rho_V C_L \left(U_L - U_V\right) \left(\boldsymbol{\nabla} \times U_V\right) \tag{4.36}$$

where C_L is the lift coefficient, which can be evaluated using several available models. For larger deformable fluid particles, a version of the Tomiyama [234] model slightly modified by Frank et al. can be applied to account for distorted shape regimes similar to the Ishii-Zuber drag model. The lift coefficient is defined in terms of modified Eötvös number:

$$C_L = \begin{cases} \min\left(0.288 \tanh(0.121\, Re_d),\, f(Eo')\right), & Eo' \leq 4 \\ f(Eo'), & 4 < Eo' \leq 10 \\ -0.27, & 10 < Eo' \end{cases}$$

where Eötvös number and $f(Eo')$ are given as:

$$Eo' = \frac{g\left(\rho_V - \rho_L\right) D_H^2}{\sigma} f(Eo') = 0.00105 Eo'^3 - 0.0159 Eo'^2 - 0.0204 Eo' + 0.474 \tag{4.37}$$

with D_H defined as:

$$D_H = D_d \left(1 + 0.163 Eo^{0.757}\right)^{1/3} \tag{4.38}$$

For smaller fluid particles with insignificant shape distortion, Legendre-Magnaudet [235] model can be employed. In contrast to lift correlations developed for solid particles, the Legendre-Magnaudet model accounts for the momentum transfer occurring due to the action of shear stresses on the droplet surface that cause inner circulation with the droplet. The lift coefficient is modelled as:

$$C_L = \sqrt{(C_{L,lowRe})^2 + (C_{L,highRe})^2} \tag{4.39}$$

where $C_{L,lowRe}$ and $C_{L,highRe}$ are given as:

$$C_{L,lowRe} = \frac{6}{\pi^2} (Re_d Sr)^{-0.5} \frac{2.55}{(1 + 0.2 \frac{Re_d}{Sr})^{1.5}} \tag{4.40a}$$

$$C_{L,highRe} = \frac{1}{2} \left(\frac{1 + 16 Re_d^{-1}}{1 + 29 Re_d^{-1}} \right) \tag{4.40b}$$

Sr denotes Strouhal number given as:

$$Sr = \frac{D_d \, \gamma}{\left| \vec{U}_V - \vec{U}_L \right|} \tag{4.41}$$

where γ represents shear stress.

Turbulent Dispersion Force
Turbulence enhances the distribution of the dispersed phase from regions of high concentration to regions of low concentration of the dispersed phase. The dispersed particles are caught up in turbulent eddies by means of interfacial drag force. Favre Averaged Drag is one of the available models for estimation the turbulent dispersion force F_{TD}:

$$F_{TD} = C_{TD} \, C_{VL} \, \frac{\nu_{tV}}{\sigma_{tV}} \left(\frac{\nabla \alpha_L}{\alpha_L} - \frac{\nabla \alpha_V}{\alpha_V} \right) \tag{4.42}$$

where C_{VL} is a momentum transfer coefficient for the interphase drag, ν_{tv} is the eddy viscosity of the continuous phase, while σ_{tv} is turbulent Schmidt number, which is typically set to 0.9. C_{TD} is a user-defined constant set by default to 1. It is an appropriate approximation when the dispersed phase is lighter than the continuous phase such as in bubbly flows. Since liquid droplets are significantly denser than vapour, they are not so easily caught in vapour turbulent eddies and C_{TD} may need to be lowered to take that factor into account. One way to implement it is to relate C_{TD} to turbulent Stokes number St_t, which describes the ratio of particle relaxation time to lifetime of turbulent eddies. In case the droplet relaxation time is much higher than the turbulent eddy lifetime, the droplets will be weakly affected by the eddies. Hence, the turbulent dispersion tends to zero as the turbulent Stokes number tends to infinity:

$$c_{TD} = e^{-\tau St_t} \tag{4.43}$$

where τ is a constant that determines the rate of decrease of turbulent dispersion with turbulent Stokes number. Generally, the Favre Averaged Drag model has been found suitable for a wide range of applications so long as an appropriate value for C_{TD} can be defined [236].

Additional interfacial forces
Although three types of interfacial forces have been considered for wet-to-dry expansion, there are five interfacial forces that are generally distinguished in two-phase flows. It has been previously noticed that for certain flows, such as bubbly up-flow in a vertical pipe [237], the dispersed phase tends to accumulate near the wall but is not directly adjacent to it. The repulsive force that keeps the bubbles away from the wall is called the wall lubrication force. The current work is concerned with high-speed droplet flows, with the dispersed phase density being at least an order of magnitude higher than that of the continuous phase. Due to high inertia of liquid droplets, it seems unlikely that the wall lubrication force will be sufficiently high to prevent droplets from interacting with the nozzle walls. Hence, wall lubrication effects are ignored and droplets are allowed to come in contact with the nozzle walls freely.

When a dispersed particle accelerates relative to the continuous phase, there is certain amount of the continuous phase adjacent to the particle that will be displaced in the process. Therefore, an additional force, referred to as virtual mass force, is required to displace the layer of the adjacent fluid. The force is usually only significant when the density of the continuous phase is higher or of the same order of magnitude as the density of the dispersed phase[225], which is why it has been neglected in the current study.

4.3.5 Summary of interphase models

The coupling between the phases in the two-fluid model is simulated using interphase models that are employed to estimate vapour and liquid heat-transfer coefficients ($\mathfrak{H}_L$ and $\mathfrak{H}_V$), as well as, the drag, lift and turbulent dispersion effects (C_D, C_L and C_{TD}). Each interphase transfer term is proportional to the interfacial area (A_{int}) which constitutes the sixth unknown required to model interaction between the phases. In the absence of directly relevant empirical data, one has to assess the suitability of interphase models based on available general guidelines. Such an assessment has been attempted in this section, which outlines potentially suitable interphase models for simulating the wet-to-dry expansion, which are summarised in Table 4.1.

Table 4.1: The summary of potentially suitable interphase models for simulating the wet-to-dry expansion.

Unknown Parameter	Model
A_{int}	Droplet number density, Weber number
$\mathfrak{H}_L$	$Nu_L = 6$, $Nu_L = 16$, Brown's correlation [221]
$\mathfrak{H}_V$	Ranz-Marshall [229]
C_D	Schiler-Naumann [214], Ishii-Zuber [233]
C_L	Tomiyama [234], Legendre-Magnaude [235]
C_{TD}	Favre Averaged Drag

The interphase models constitute the critical part of the two-fluid model; arguably, the two-fluid model can be less reliable than the simplified models if unsuitable models are used [132]. Recognising the importance of the interphase models, sensitivity of the solution to the type of interphase models applied was evaluated to confirm the reliability of the current setup and decide between the alternative models presented in Table 4.1. The results of the sensitivity study when applied to the wet-to-dry expansion of organic fluids are documented in the next chapter.

4.4 Turbulence modelling

In the current study, the two-fluid model has been implemented with a Reynolds-Averaged Navier Stokes solver to simulate turbulent two-phase flow. More refined models, such as the

Large Eddy Simulation (LES) method could potentially be applied to more accurately resolve the turbulent flow features and investigate the influence of turbulence on the two-phase expansion. However, the LES simulations are associated with increased modelling complexity and significantly higher computational cost. Given that the current study is the first known attempt to simulate non-equilibrium wet-to-dry expansion with the aid of computational fluid dynamics solver, which in itself carries multiple challenges, the simpler approach to modelling turbulence based on the RANS equations has been deemed suitable for the task. Furthermore, one of the objectives of this study is to characterise the two-phase expansion under a wide range of operating conditions, which requires tens of simulation runs. This would potentially require very high computational effort when applied in conjunction with the LES solvers. For those reasons, this work relies on the RANS approach for modelling the turbulence in the two-phase flow, while LES can be considered in future studies.

For inhomogeneous dispersed two-phase flows, turbulence can be modelled separately in each phase. The turbulence in the continuous phase can theoretically be modelled with well-known techniques applied to single-phase flows. Review studies performed by Liao & Lucas [30] and Ortego Sampedro [147] indicate that the most frequently selected turbulence model in numerical studies of flash boiling is the $k-\omega$ SST model, which was selected mostly on the basis of accurate treatment of the boundary layer region and reliability in the presence of adverse pressure gradients [147, 206, 227]. Dang Le [238] investigated the suitability of several RANS turbulence models for simulating flashing in converging-diverging nozzles. The authors implemented a mixture model coupled with a slip correlation in a commercial CFD code to perform two-dimensional simulations. Thermal non-equilibrium was factored in using an artificial boiling delay coefficient, while the phase change was assumed to be driven by the pressure non-equilibrium. The authors compared the numerical results with experimental results of Abuaf et al. [35] to assess the performance of the RANS turbulence models. With an error of 0.2% in the estimated mass-flow rate and well-predicted streamwise pattern of void fraction, the $k-\omega$ SST turbulence model with standard wall function was recommended for this type of problems.

As for the dispersed phase, a so-called *dispersed zero-equation model* can be applied, which correlates the dispersed and continuous eddy viscosities using the turbulent Prandtl number (P_t). Assuming liquid is the dispersed phase:

$$\mu_{t,L} = \frac{\rho_L}{\rho_V}\frac{\mu_{t,V}}{P_t} \tag{4.44}$$

where $\mu_{t,L}$ and $\mu_{t,V}$ are the eddy viscosities of liquid and vapour, while P_t is the turbulent Prandtl number. The value of P_t is dependent on the two-phase flow regime. For bubbly flows, characterised by relatively short relaxation time of the dispersed phase, P_t can be set to one [236]. For flows with the dispersed phase significantly denser than the continuous phase, such as in the wet-to-dry expansion, the droplet relaxation time can be significantly longer and P_t may have to be increased [236].

4.5 Metastability and fluid properties

Molecularly complex fluids, such as the siloxane MM considered in this study, may exhibit non-ideal behaviour close to the critical point of the fluid and in the proximity of the saturation curve [239]. Generally, the extent of non-ideal behaviour can be assessed using the fundamental derivative (Γ):

$$\Gamma = 1 + \frac{\rho}{a}\left(\frac{\partial a}{\partial \rho}\right)_s \tag{4.45}$$

where a is the speed of sound and subscript s refers to an isentropic process. For ideal fluids, the fundamental derivative is equal to one. Once the non-ideal effects arise, it falls to the range $0 < \Gamma < 1$, with smaller Γ values indicating more significant non-ideal behaviour. In cases the fundamental derivative becomes negative, non-classical effects such as expansion shock may occur [240]. White [240] extended the concept of the fundamental derivative to two-phase flows and applied it to the expansion of the siloxane MM from an inlet pressure between 500 to 1500 kPa and an inlet vapour quality between 0.1 and 0.9. A homogenous flow was assumed with both phase having identical velocity. Two different approaches were considered for modelling the thermal interaction; one assuming an instantaneous (thermal equilibrium) and the other assuming negligible (frozen model) heat transfer between the phases. Both flow models estimated the fundamental derivative to lie between 0 and 1 under all investigated conditions. Generally, non-ideal effects were most pronounced near the critical point and close to the saturated liquid curve. In summary, the results point to the need for a suitable equation of state for evaluating fluid properties when simulating two-phase e

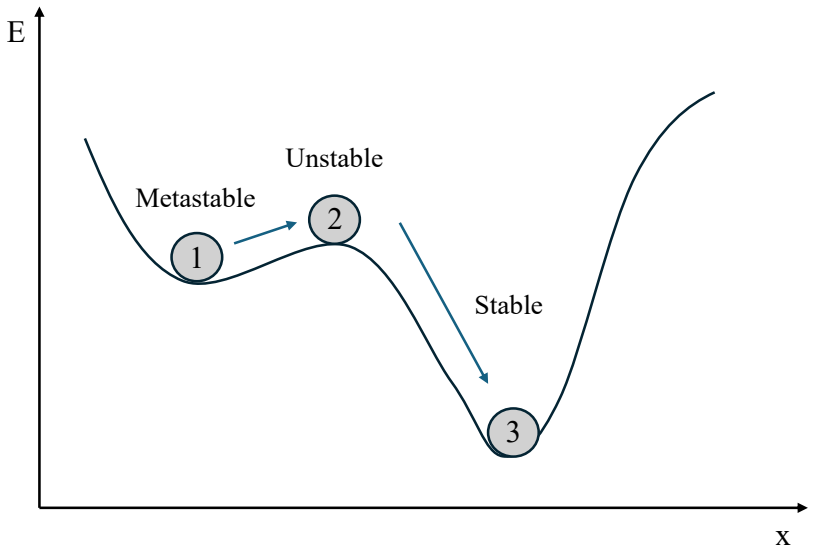


Figure 4.7: The illustration explaining metastable, unstable and stable states.

The wet-to-dry expansion is likely to be associated with rapid flow acceleration within a relatively short channel. Under such conditions, the two phases may not have sufficient time

to effectively exchange heat and remain in thermal equilibrium throughout the expansion. Under such conditions, liquid and vapour can become metastable. It is convenient to explain the metastability concept using an illustration of a sphere resting in a hollow on a slope as shown in Fig. 4.7. Metastability can be thought of as a temporary intermediate state, which will eventually transition to the stable state. Unlike the unstable state, where the system cannot sustain an infinitesimally small disturbance without changing state, the system can remain metastable for a short period of time.

In the context of flashing flows, metastable states correspond to superheated liquid and subcooled vapour states. These states are temporary and result from limited interfacial heat-transfer rates. The two phases eventually exchange heat and mass reaching their stable saturated states. Figure 4.8 shows a $T - v$ diagram of water generated by de Lorenzo [241] using the IAPWS-IF97 equation of state derived specifically for water and steam [242]. The curve composed of the blue, dotted and red curves represents an isobaric curve. The spinodal curve denotes a thermodynamic limit to the attainable metastability degree. Following the blue line from a to b, the liquid phase turns from saturated to superheated until it reaches the spinodal limit, where the liquid cannot be further superheated without changing phase. The same applies to vapour as it is subcooled from a saturated state (point d) to the spinodal limit denoted by c. Therefore, the areas enclosed by the spinodal curve and the saturated-liquid and saturated-vapour curves denote the metastable regime.

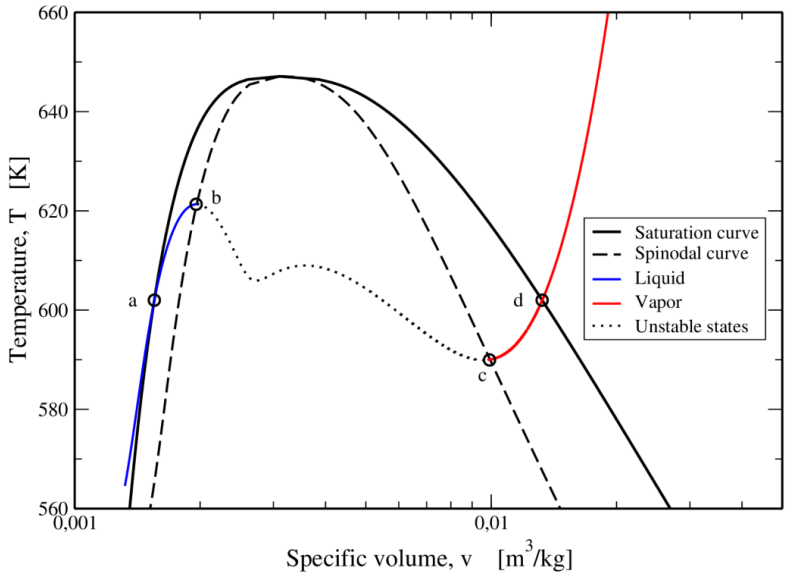


Figure 4.8: The illustration metastability of liquid and vapour phases on temperature-volume diagram (figure retrieved from de Lorenzo [241]).

Metastability plays an important role in the phase-change process in flashing flows. The non-equilibrium phase-change models presented in Chapter 3.1 assume that the phase-change rate is proportional to the deviation of the liquid phase from the local saturation state. In other words, the intensity of the phase change is defined by the degree of metastability of the liquid phase (e.g. homogeneous-relaxation model, thermally-driven models etc.). It is therefore

essential to employ a suitable equation of state that could estimate the fluid properties in the metastable regime enclosed by the saturation and spinodal curves (Fig.4.8). NIST REFPROP 10.0 [212] includes a range of up-to-date equations of state for a variety of organic fluids including siloxanes. For the siloxane MM specifically, which is the fluid of interest in this work, REFPROP 10.0 uses the Span-Wagner Helmholtz equation of state derived from empirical data and molecular simulation results [243]. The equation of state can potentially be used to predict liquid and vapour properties in metastable conditions, however, this may require further validation. In order to assess the importance of the equation of state, White [43] investigated the wet-to-dry expansion of the siloxane MM using two different equations of state, which include the Span-Wagner Helmholtz and a cubic Peng-Robinson models. The two-phase expansion was simulated with a one-dimensional code, assuming either a homogeneous-equilibrium or a non-equilibrium flow.

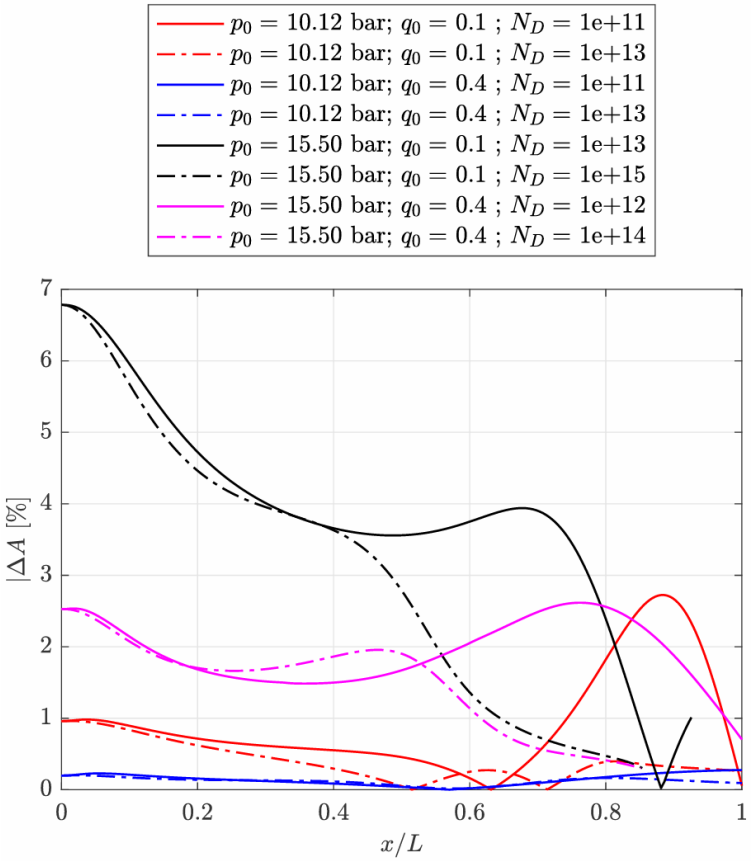


Figure 4.9: Deviation in the estimated nozzle flow area between the Span Wagner Helmholtz and the cubic Peng-Robinson equations of state; the results were obtained with a one-dimensional non-equilibrium code for various wet-to-dry expansions of the siloxane MM and the assumption of a fixed droplet number density N_D (figure retrieved from White [43]).

Figure 4.9 shows the relative deviation in the estimated nozzle flow area distribution between the two equations of state, obtained with the one-dimensional non-equilibrium code for various operating conditions and droplet number densities (N_D). The maximum percentage difference of about 7 % was observed for the higher inlet pressure (15.50 bar) and lower inlet vapour quality (0.4) in the region close to the nozzle inlet. The difference gradually

diminished downstream of the inlet. For other investigated conditions, the difference was below 3 % throughout the entire streamwise distance. Overall, the discrepancy between the two thermodynamic models was not significant, indicating that the type of equation of state employed in such simulations plays a secondary role.

4.6 Numerical implementation

The two-fluid model was implemented in a commercial CFD code, ANSYS CFX 2021 R1 [244], to carry out steady-state quasi-two-dimensional simulations of the wet-to-dry expansion. ANSYS CFX has been used by multiple authors studying non-equilibrium flash boiling in converging-diverging channels [32, 41, 147, 204, 206, 216], and has proven to be a suitable CFD platform for the implementation of the two-fluid model. Some of the interphase models, such as the drag and lift models, are built-in functions. However, other, less-conventional models such as the Brown model for estimating the heat-transfer rate were implemented using user-defined expressions in CFX. The details concerning the implementation of the user-defined expressions in CFX can be found in Appendix A.1.

The solver follows the finite-volume approach to solve Reynolds-averaged Navier-Stokes (RANS) equations. Second-order accurate schemes were applied to discretise the advection and turbulence equations. Turbulence in the continuous vapour phase was modelled using the $k-\omega$ SST model, which, as discussed before, was previously found suitable for modelling flashing in converging-diverging nozzles [238]. The dispersed zero-equation model was applied to estimate the eddy viscosity of the liquid phase. CFX uses an automatic wall function method, which automatically switches from directly resolving the boundary layer to using standard wall functions depending on the local y^+ value. Turbulence intensity at the inlet was set to 5 %. Concerning the boundary conditions, total pressure and temperature was set at the inlet, alongside volume fraction values of each phase, while static pressure was imposed at the outlet.

To evaluate the fluid properties, look-up tables were generated using NIST REFPROP 10.0 [212], and were coupled with solver. The look-up tables were generated for specified ranges of pressure and temperature. These were extended well beyond the expected minimum and maximum pressure and temperature values. This was to ensure that fluid properties can be reliably evaluated in case the fluid significantly deviates from the final steady-state during the solution process. Depending on the division of the pressure and temperature ranges, different resolution of the look-up tables could be achieved. Sensitivity study was carried out to decide on an appropriate table resolution. When generating the look-up tables, liquid and vapour properties were extended into the metastable region and calculated up until the spinodal limit so that the solver could evaluate phase properties when liquid and vapour phases became superheated and subcooled respectively.

4.7 Validation study

The wet-to-dry expansion studied in this current work differs from majority of experimental flash-boiling studies that were concerned with flashing of subcooled or saturated liquid. In flashing of subcooled liquid, vapour bubbles nucleate in the liquid medium, and therefore the dispersed phase has often been assumed to be composed of dispersed spherical bubbles [132]. One of the main research questions those previous studies attempted to answer revolved around flashing inception as it significantly affects the compressibility and thus the critical conditions at the nozzle throat. The wet-to-dry expansion begins with a partially evaporated fluid with inlet vapour volume fraction typically between 70 and 90%. Since the expansion does not involve bubble nucleation process, and the dispersed phase is in the form of liquid droplets, the modelling techniques applied to estimate the interphase transfer of mass, momentum and heat may differ from those applied in flashing of liquids. In the same vein, since it is still a flashing process, the physics of wet-to-dry expansion also differs from studies concerning condensation in steam turbines, where modelling droplet nucleation is of primary importance. Hence, there is no directly relevant experimental data available to validate the CFD model specifically for wet-to-dry expansion.For instance, it has been commonly assumed that the thermal resistance on the dispersed vapour side is negligible, which cannot be assumed in the wet-to-dry expansion due to the dispersed phase being in the liquid phase. Therefore, if one wishes to validate a two-fluid model set up for the wet-to-dry expansion using previous experimental studies, necessary changes are required to adjust the model to the assumption of dispersed vapour phase. Because of these adjustments, previous experimental studies on flashing liquids are not directly relevant to the wet-do-dry expansions and a two-fluid model set up to work with liquid droplets cannot be directly validated using those studies. Having said that, the overall two-fluid model setup for simulating flashing of subcooled/saturated liquid is fairly similar to the one described for wet-to-dry expansion, with the main difference being the dispersed phase in the form of vapour bubbles. Thus, some adjustments are required, especially in the employed interphase models (e.g. zero thermal resistance on the dispersed side). In the light of above, the purpose of the validation study is to verify correct overall implementation of the two-fluid model rather than the specific setup described earlier. Furthermore, the use of an in-house tool, used to construct look-up tables that extend into the metastable region, will be validated.

Experimental data suitable for the validation purpose come from tests conducted by Abuaf et al. [35], who investigated flash boiling of subcooled/saturated water in a converging-diverging nozzle referred to as the BNL nozzle. The schematic of the BNL nozzle is presented in Fig.4.10, which is a circular symmetric converging-diverging nozzle, 0.609 m long, with an inlet and outlet diameter of 0.051 m and throat of 0.025m. The test results include streamwise profiles of pressure and vapour volume fraction, making it particularly useful for assessing the phase change process. Another benefit of using the BNL tests as validation is the possibility of comparing the results to other existing numerical studies [41, 206]. The main difference between these previous studies is the use look-up tables generated by REFPROP rather than using a built-in equation of state; the authors applied built-in IAPWS-IF97 water property tables that are derived from the Helmholtz equation of state

[245].

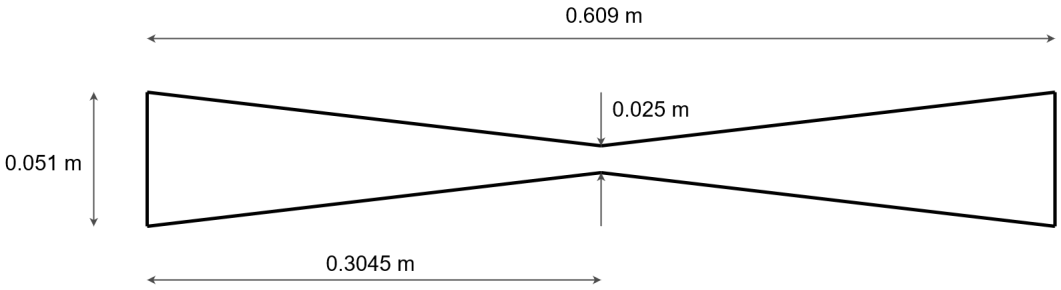


Figure 4.10: Schematic of the BNL nozzle

The experimental campaign documented by Abuaf et al. [35] involved a number of experimental runs with different boundary conditions. One particular set-up referred to as BNL309 will be taken for validation. The boundary conditions for the BNL309 run are shown in Table 4.2.

Table 4.2: BNL309 boundary conditions

Inlet State	Subcooled Water
Inlet Pressure	555.9 kPa
Inlet Temperature	422.25 K
Outlet Pressure	402.5 kPa

4.7.1 Solver setup

Several amendments were made to adjust the two-fluid model to simulate flash boiling of subcooled water. The dispersed phase was set to be in the form of vapour bubbles, while water liquid was set to be the continuous phase. Wall lubrication force, deemed inapplicable in the case of the wet-to-dry expansion, was included for vapour bubbles, using a correlation developed by Hosokawa et al. [246]. Vapour temperature was fixed to the saturation temperature, while the heat-transfer coefficient on the continuous side was evaluated with the Ranz-Marshall correlation [229]. The rest of the set-up remained unchanged from that presented for the wet-to-dry expansion. To simulate the phase change process in CFX, the *thermal phase change model* was applied in conjunction with the two-resistance model. A constant bubble density number of $N_b = 5 \times 10^9$ was assumed in the studies of Liao & Lucas[206] and Rane & He [41] based on empirical tuning to estimate interfacial area. The same bubble number was adapted in the current simulation. Overall, the set-up is similar to those used by Liao & Lucas [206] and Rane & He [41] except for the way water properties were evaluated. Both previous studies used the water/steam properties, IAPWS-IF97, published by the International Association for the Properties of Water and Steam [242]. IAPWS-IF97 water properties are approximations of IAPWS-95 properties, which are based on the Helmholtz equation of state [245]. In this simulation, water properties are evaluated by means of look-up tables generated by REFPROP 10.0 [212], which also uses the

Helmholtz equation of state. The model was implemented in ANSYS CFX 2021 R1 [244], to perform 3D steady-state turbulent viscous simulations.

4.7.2 Mesh independence study

The BNL nozzle was a fully structured mesh constructed with hexahedral elements as displayed in Figure 4.11. The mesh was refined in the proximity of the wall, and standard wall functions were applied to estimate the wall profiles. The Reynolds number was in the range of 5,000 to 10,000. Several grids, starting with a coarse 77-thousand element mesh up to a fine 527-thousand element grid. For each mesh, a converged solution was achieved with all r.m.s mass and momentum residuals below 10^{-4}, except for the liquid momentum residual in the longitudinal direction, which dropped below 5×10^{-4}. Although a converged solution was achieved, the solution was characterised by certain controlled fluctuations of flow properties. The fluctuations remained within a certain range, which was relatively small; however, the fluctuations were sufficiently large to be taken into account in the mesh independence study. The fluctuations indicate that inherent unsteady effects exist in the nozzle, which prevents the solver from reaching a fully steady solution. This was also confirmed in private communication with one of the authors of the previous numerical studies of the BNL nozzle [41], who also noticed similar oscillations that prevent achieving a fully steady solution. The inherent transient fluctuations are considered to be the cause of relatively high residual of the liquid momentum in the longitudinal direction (of the order of 5×10^{-4}), and mass imbalance that found to be in the range of 0.6-0.8 %. Because of the small fluctuations, comparing instantaneous values of flow parameters would not be reliable when assessing solution independence to the mesh resolution. Nonetheless, as pointed out before, the fluctuations exhibited a controlled and relatively regular behaviour, which allowed to take average values of relevant flow properties over a number of simulation steps. These average values have successfully converged to single values, which also indicates that the main factor preventing a fully steady solution are transient oscillations. In this study, several flow parameters averaged across a thousand simulation steps were taken to assess whether the solution is independent of further mesh refinement.

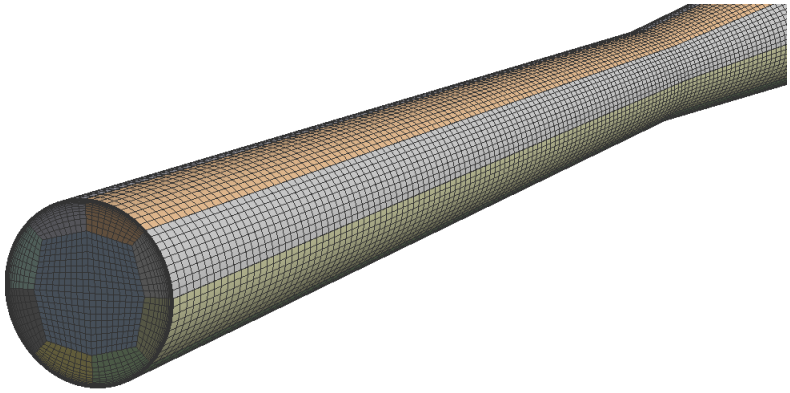


Figure 4.11: BNL309 mesh (389 thousand-elements mesh displayed)

The results of the mesh independence study are summarised in Table 4.3; y_l^+ and y_v^+ stand

for maximum y^+ values for water liquid and water vapour respectively, whereas $\dot{m}_{out}$ and α_v are the total mass flow rate and vapour volume fraction at the nozzle outlet respectively. Mass imbalance represents the percentage difference between mass entering and leaving the nozzle. As the mesh resolution increases, the average mass flow rate converges to a single value of around 8.37 kg/s. The average mass imbalance does not seem to converge to a single value; however, it remained below 0.8 % for all the grids, which was deemed acceptable. The average vapour volume fraction at the outlet practically converged to a single value of about 0.742. Based on the mesh independence study, the mesh with 389 thousand elements was selected for further studies.

Table 4.3: BNL309 mesh independence study results

Element Count $\times 10^3$	y_l^+	y_v^+	$\dot{m}_{out}$ [kg/s]	α_v	Mass Imbalance [%]
77	60.1	5.70	8.333	0.744	0.63
168	63.9	5.88	8.364	0.743	0.79
270	57.6	5.50	8.369	0.742	0.67
389	40.9	4.05	8.373	0.741	0.61
527	41.5	4.22	8.373	0.742	0.70

4.7.3 Comparison with experimental and numerical data

The main objective of the BNL309 analysis was to validate the overall two-fluid model setup and the use of look-up tables. Table 4.4 illustrates the comparison of the average water mass flow rate at the nozzle outlet. It is evident that the average mass flow rate is very close to the values obtained by Rane & He, and Liao & Lucas, with a similar discrepancy of 4.9%, compared to experimental data.

Table 4.4: Comparison of average mass outflow between the current study, other numerical studies and experimental data for the BNL309 run

	Current Model	Experimental	Liao & Lucas	Rane & He
Mass Flow Rate [kg/s]	8.37	8.80	8.40	8.38
Difference [%]	-	4.89	0.36	0.12

As discussed before, comparing the instantaneous values may not be appropriate due to certain transient fluctuations in flow properties. However, since these fluctuations are relatively small, the overall trends and values should be similar. Figure 4.12 presents the comparison of the centre-line distribution of pressure and vapour volume fraction. It is evident that the overall trends and values closely resemble the other CFD studies and the experimental results. Having said that, compared with the current study and the experimental data, the other two numerical studies estimated a more pronounced pressure recovery immediately downstream of the nozzle throat, which indicates that a shock wave may occur in that area.

This could point to the difference in the phase-change rate in that area, which would affect the compressibility of the flow close to the throat. However, both the current study and the other numerical studies model the phase-change rate in terms of interphase heat-transfer rate using an identical figure for the bubble number density. The only difference is that Liao and Lucas [206] used a different correlation for predicting the heat-transfer coefficient, but a similar trend was also observed by Rane and He [41]. It is not completely understood by the author, what is the cause of the more pronounced pressure recovery downstream of the throat. As an extra means of validation, the vapour volume fraction contour of the current model and the one obtained by Rane & He were plotted in Figure 4.13. The volume fraction distribution within the nozzle is practically identical for the two studies.

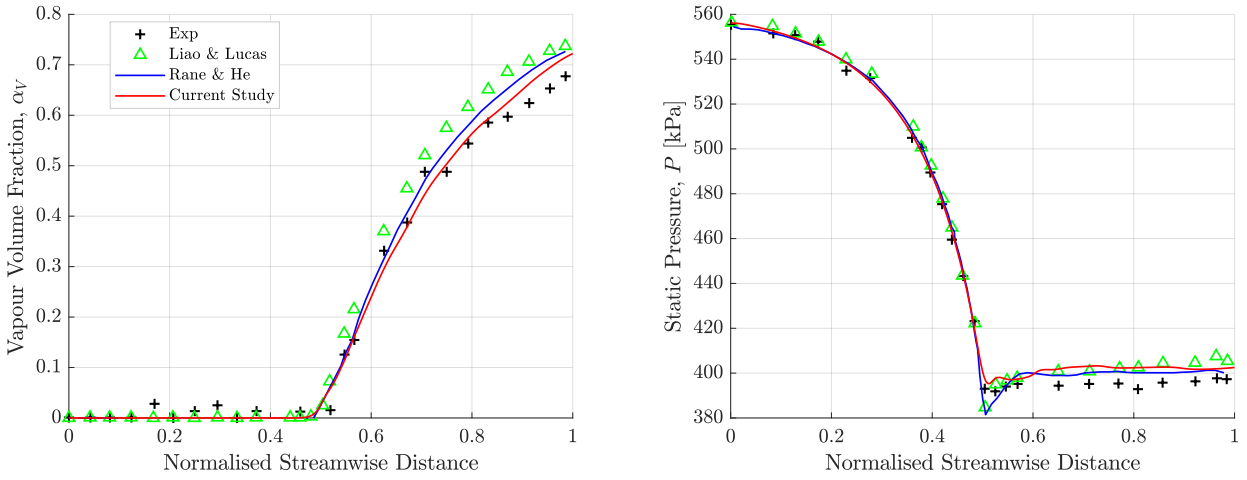


Figure 4.12: The variation of static pressure and vapour volume fraction along the centre line of the BNL nozzle; comparison between the experimental trends, current study, and the other numerical studies of Liao & Lucas [206] and Rane & He [41].

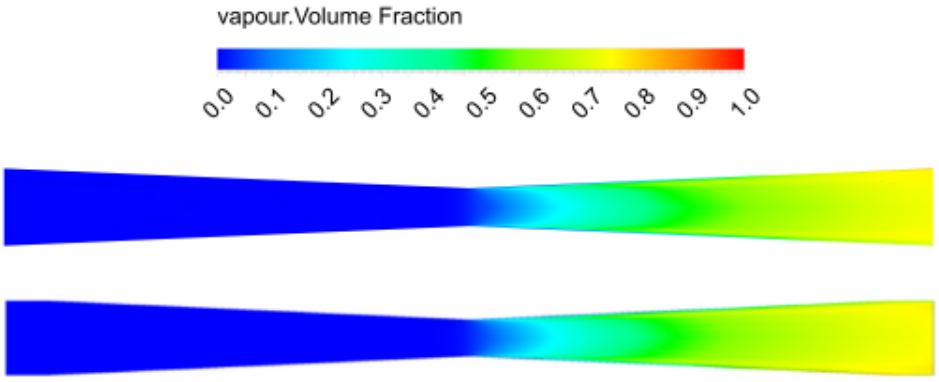


Figure 4.13: The variation of vapour volume fraction across the BNL nozzle - comparison between Rane & He [41] study (top contour) and the current study (bottom contour)

In addition to the specific operating point referred to as BNL309, four additional experimental runs were simulated to further validate the two-fluid model. The boundary conditions

of the four additional cases are shown in Table 4.5, alongside the assumed bubble number density (N_b), experimental mass-flow rate ($\dot{m}_{exp}$), and the mass-flow rates estimated by the model of Liao and Lucas [206] ($\dot{m}_{Liao}$) and the current study ($\dot{m}$). The bubble number for each was set in line with the values proposed by Liao and Lucas [206], who tuned the number based on the experimental results.

Table 4.5: Additional BNL experimental runs simulated in the validation study.

Case	P_{in} [kPa]	P_{out} [kPa]	T_{in} [°C]	N_b [m^{-3}]	$\dot{m}_{exp}$ [kg/s]	$\dot{m}_{Liao}$ [kg/s]	$\dot{m}$ [kg/s]
BNL145	305	208.7	121.2	10^9	7.5	7.7	8.0
BNL133	349	203	121.2	5×10^8	9.0	9.2	9.5
BNL278	688.6	434.1	148.8	8×10^{10}	11.7	10.9	10.5
BNL296	764.9	432.6	148.8	8×10^{10}	13.1	12.4	11.9

Overall, the estimated mass-flow rate showed slightly higher deviation from the experimental results compared with the model of Liao and Lucas [206]; the relative error was around 5-6 % for lower-pressure expansions, and about 9-10 % for the higher inlet pressures. The streamwise variations of pressure and vapour volume fraction were plotted in Figs. 4.14-4.15.

Comparing the current model to the experimental results and the model of Liao and Lucas [206], a rather systematic difference in pressure profiles was observed in the converging section. When it comes to the lower-pressure expansions (BNL145 and BNL133), both the current and Liao and Lucas models predicted similar pressure undershoot (the lowest pressure occurring just before flashing inception) and visibly lower pressure recovery rate compared to the experiments. Overall the pressure profiles simulated for BNL145 and BNL133 predicted by the two numerical models were relatively similar. As for the high-pressure expansions (BNL278 and BNL296) the pressure in the diverging section was noticeably higher than that predicted by Liao and Lucas [206], while the experimental measurements lied somewhere in between the two numerical profiles. With that being said, the model of Liao and Lucas more accurately predicted the pressure at the flashing inception point. Concerning the variation of vapour volume fraction, the current model predicted the phase-change rate with either higher or similar accuracy to the model of Liao and Lucas depending on the boundary conditions. It is known that Liao and Lucas applied a different correlation for estimating the heat-transfer coefficient between the liquid and the liquid-vapour interface compared to the current study and the model developed by Rane and He [41]. It is presumed that the bubble density number reported in Table 4.5 were tuned to match the pressure at the flashing inception (since this was accurately predicted in each simulation run by Liao and Lucas). Since the model is not identical to the one applied by the author, the bubble number reported in Table 4.5 may not be ideal in this case. This could explain higher deviation in pressure profiles and mass-flow rates. With that being said, the overall trends predicted by the two models are relatively similar, which confirms the correct overall implementation of the two-fluid model coupled with the look-up tables.

The comparison with experimental data and other existing numerical studies which confirms the correct implementation of the two-fluid model coupled with the look-up tables in ANSYS

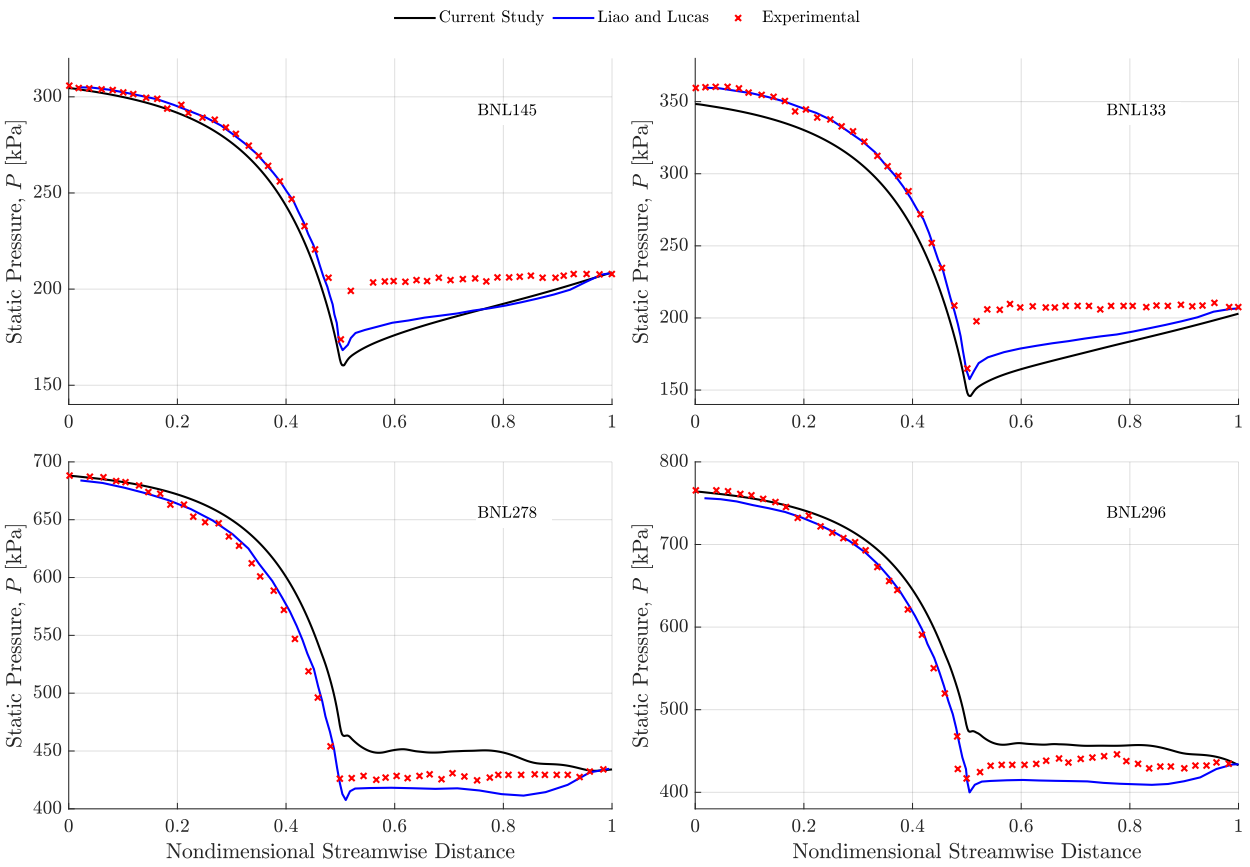


Figure 4.14: Streamwise variation of static pressure inside the BNL nozzle estimated for four experimental runs; the figure also illustrates the experimental measurements and the prediction of the Liao and Lucas [206] model.

CFX, which will be utilised to investigate the wet-to-dry expansion. It should be reiterated here that the study documented herein does not validate the specific model setup for studying wet-to-dry expansions due to significant modifications introduced to tailor the model to flashing of subcooled liquids. Having said that, the overall implementation of the two-fluid model coupled with the look-up tables in ANSYS CFX has been validated. The same CFD solver will be employed to investigate wet-to-dry expansions. Since the overall setup has been validated, it is rationalised that if appropriate correlations are used for the interphase models and interfacial area, the model can provide reasonable estimates for wet-to-dry expansions. When it comes to the interfacial area, in flashing of subcooled liquids, this is the total surface area of the dispersed vapour bubbles, whereas in the wet-to-dry expansion it is the total surface area of the dispersed liquid droplets. The challenge lies in defining an appropriate figure for the number and size of the dispersed droplets. In case of flash boiling of subcooled liquids, nucleation models can be applied to estimate the bubble number density variation; alternatively, a constant bubble number tuned based on the experimental data can be applied. In case of the wet-to-dry expansion, estimating the number and size of droplets can be challenging due to lack of suitable experimental data. Droplet breakup correlations can be potentially be applied to estimate a realistic variation of the droplet diameter as discussed

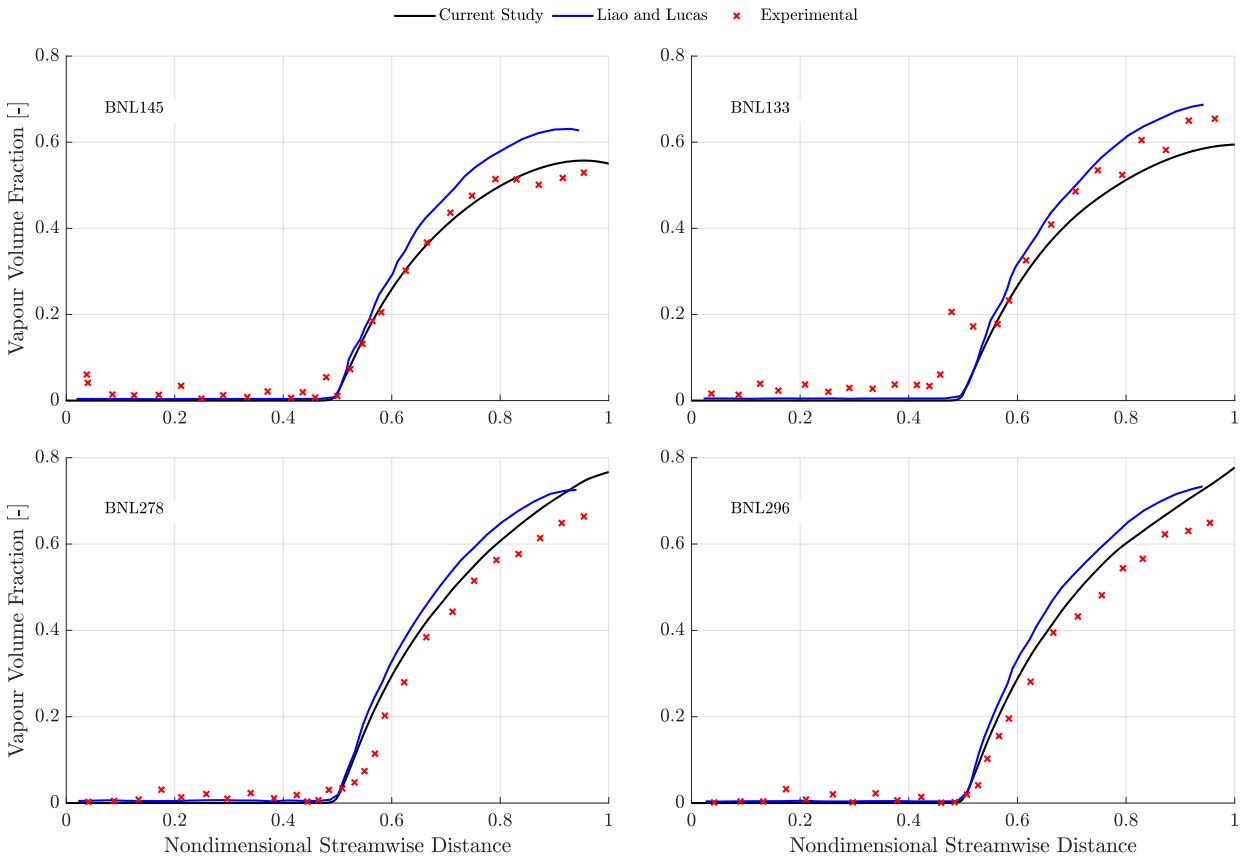


Figure 4.15: Streamwise variation of vapour volume fraction inside the BNL nozzle estimated for four experimental runs; the figure also illustrates the experimental measurements and the prediction of the Liao and Lucas [206] model.

4.3.1. As far the interphase models are concerned, some of the correlations (e.g. drag models, the heat-transfer correlation on the continuous side of the liquid-vapour interface) can be applied to both droplet and bubbles. However, some other modelling approaches applied in the study of flashing of liquids, such as zero heat-transfer resistance on the dispersed side of the interface are no longer applicable, and appropriate correlations need to be introduced to estimate the interphase heat-transfer rate. This emphasises the need for additional sensitivity study concerning the employed interphase models to ensure the model is reliable.

4.8 Conclusions

Due to rapid flow acceleration in a relatively short channel, non-equilibrium effects cannot be ignored in modelling the wet-to-dry expansion. Generally, thermal non-equilibrium affects the phase-change rate and the distribution of phases within the nozzle, which affects the compressibility of the two-phase flow, affecting the choking conditions as well as pressure, velocity and temperature fields within the nozzle. The Eulerian-Eulerian two-fluid model was identified as a suitable model for simulating the wet-to-dry expansion, taking into account mechanical and thermal non-equilibrium effects. The two-fluid model formulates two

separate sets of conservation equations for liquid and vapour, which include source terms to account for mass, momentum, and energy exchange between the phases.

The rate of interphase exchange is strongly influenced by the interfacial area, which in turn, depends on the two-phase flow pattern. Previous studies on flash boiling in converging-diverging nozzles indicate that the transition to a droplet flow regime begins at a void fraction of around 0.7. Preliminary studies demonstrated that this condition is satisfied under most operating conditions relevant to the wet-to-dry cycle. Although, it should be highlighted that it was assumed that the two-phase mixture leaving the heat-exchanger in the wet-to-dry cycle is characterised by an uniform spatial distribution of well-mixed phases, which carries some uncertainty. However, expansions characterised by high inlet pressure and low vapour qualities could have a void fraction considerably lower than 0.7. Although the inlet void fraction in those cases was below 0.7, the phase change analysis showed that the majority of vapourisation occurs at void fractions above 0.7, which justifies the assumption of the droplet flow regime.

Different approaches to estimating the interfacial area relevant to two-phase droplet flows were discussed. These include a constant droplet diameter or a constant number of droplets per unit volume. The second approach was deemed more suitable as the droplets are allowed to change size during vapourisation, which seems to better reflect the physical process of phase change. The shortcoming of this method is that droplet breakup and coalescence effects are neglected. Furthermore, experimental data may be required to select an appropriate droplet number for a given expansion. An alternative approach relies on limiting the droplet diameter based on the critical Weber number. This can be useful for estimating a realistic droplet size based on breakup considerations.

The critical part of the two-fluid setup are the interphase models that are used to evaluate the interphase transfer of mass, momentum and energy. These models are applied to evaluate drag, lift and turbulent dispersion forces as well as heat-transfer coefficients between each phase and the liquid-vapour interface. Several interphase models potentially suitable for two-phase droplet flows were discussed. Common factors affecting the applicability of the interfacial force models include droplet Reynolds number, shape distortion effects and droplet relaxation time. Schiller-Naumann and Legendre-Magnaudet can be applied to estimate drag and lift in case of insignificant droplet shape distortion, while Ishii-Zuber and Tomiyama models are suitable if these effect are important. The Favre Averaged Drag model can be used to account for the effect of turbulent dispersion, however, some uncertainty remains with regard to the dispersion coefficient due to long droplet relaxation times. The estimated droplet Reynolds number is in the order of hundreds. Previous studies indicate that under such conditions, the Ranz-Marshall can provide accurate estimations of the heat-transfer rate on the continuous vapour side of the interface. As for the heat-transfer rate on the dispersed liquid side, the Brown's correlation that relates the heat-transfer coefficient to the liquid superheat level is deemed as the current best estimate. Although these models can be selected based on available guidelines and expected characteristics of the two-phase expansion, solution sensitivity to the type of interphase models employed is viewed necessary for a reliable model setup.

The two-fluid model was implemented in ANSYS CFX, which has previously been successfully employed by other authors to simulate non-equilibrium flashing in converging-diverging nozzles. Turbulence in the continuous phase was modelled using $k-\omega$ model with standard wall functions, which showed the best agreement with experimental data obtained for flashing in a converging-diverging nozzle. Turbulence in the dispersed phase was modelled with a zero-equation model that relates the vapour and liquid eddy viscosities through the turbulent Prandtl number. Due to non-ideal fluid behaviour and metastability effects, a suitable equation of state was found necessary for evaluating fluid properties. The CFD solver was coupled with look-up tables generated using REFPROP 10.0, which uses the Span-Wagner Helmholtz equation of state for the siloxane MM. Previous studies found insignificant deviation between the Spang-Wagner Helmholtz and Peng-Robinson equations of state, which suggests that the exact type of the thermodynamic model plays a secondary role.

Finally, the two-fluid model implemented in ANSYS CFX was validated against experimental data taken for flash boiling of subcooled water in a converging-diverging nozzle. Flashing of subcooled liquid differs from the wet-to-dry expansion mainly in that the dispersed phase can no longer be assumed to be in the form of droplets but rather in vapour bubbles. As such, the two-fluid model needed some adjustments to work with vapour bubbles, and the setup used for the wet-to-dry expansion could not be validated directly. Having said that, the underlying physical principles remained the same, and the overall correct implementation of the two-fluid model could be validated alongside the use of look-up tables for predicting fluid properties. The two-fluid model could estimate the water mass-flow rate with an error below 5 % compared to the experiments, and with a deviation below 0.32 % compared to non-equilibrium simulations performed by other authors. Furthermore, the streamwise profiles of pressure and void fraction agreed reasonably well with the experimental data and the other numerical studies, confirming the correct implementation of the model and the use of look-up tables.

Chapter 5

Non-equilibrium simulation of the wet-to-dry expansion

5.1 Introduction

The two-fluid model described in detail in the previous chapter is applied in this chapter to conduct non-equilibrium CFD simulations of the wet-to-dry expansion of the siloxane MM. First, the nozzle design method is explained alongside the set of operating conditions and nozzle geometries considered in this study. Computational fluid dynamics setup and mesh independence study results are then discussed. Prior to conducting further analysis, solution sensitivity to the type of interphase models employed is assessed. Finally, a parametric study is performed, where the wet-to-dry expansion is simulated for a range of inlet pressures, inlet vapour qualities, and droplet sizes. The results give insight into the phase change characteristics, the extent of non-equilibrium effects, and the overall effect of thermodynamic conditions and droplet size on the expansion. Furthermore, flow uniformity is evaluated, while the performance of the nozzle design tool is assessed by comparing the design and simulated expansions. The chapter is concluded with a preliminary breakup study to evaluate possible breakup effects and estimate a realistic droplet size.

5.2 Nozzle design

Several types of turboexpander architecture that can be potentially integrated with the wet-to-dry cycle have been discussed in Section 2.7. These include radial-inflow, radial-outflow and impulse axial turbines. Independent of the selected turboexpander type, each turboexpander features a set of nozzles (stator) that accelerates the two-phase flow and ought to facilitate complete mixture vapourisation. To aid in understanding the function of the nozzle within a turboexpander, a simplified schematic of a radial-inflow turbine is presented in Fig. 5.1. In a wet-to-dry radial-inflow turbine, a partially evaporated mixture flows from the heat-exchanger into the volute, a spiral-shaped component with decreasing cross-sectional area, which aims to uniformly distribute the flow and admit it to the row of nozzle vanes in a tangential direction with respect to the rotor. The main purpose of the nozzle row is

to accelerate the flow in an efficient manner and facilitate complete mixture vapourisation, providing dry vapour flow to the rotor with large amount of angular momentum at a designed angle with respect to the rotor blades. The rotor consists of an encased hub with attached blades, which are shaped such that fluid can make a 90° turn and exit the rotor in the direction parallel to the rotation axis. Rotor blades form a set of flow passages in which the flow is further expanded and deflected in a way that the angular momentum of the fluid is exchanged with the rotor blades, generating mechanical power. The fluid can then either leave the turbine directly or optionally through a diffuser to recover any kinetic energy left after the expansion. It is worth to mention that the nozzle vanes shown in Fig. 5.1 only serve illustration purpose and do not reflect the actual nozzle geometry of a nozzle designed for the wet-to-dry turbine. Owing to the high volumetric expansion ratios typical of two-phase expansions and low speed of sounds characteristic of organic fluids, the nozzle vanes will require a converging-diverging architecture to accelerate the fluid to supersonic speeds in an efficient manner [8]. The main difference when it comes to the nozzle component between the three turboexpander types mentioned above, is that in case of an impulse axial turbine, the nozzle has a straight centre-line and is fully bladed (wall-bounded) all the way from the inlet to the outlet. In case of the radial-inflow and radial-outflow turbine, the flow is deflected at the inlet and outlet of the nozzle row as shown in Fig. 3.4. Furthermore, the fluid leaving the diverging section of the nozzle travels through a semi-bladed region, before it reaches the rotor. Despite these differences, each turboexpander features a wall-bounded converging-diverging channel, and therefore the subsequent analysis is focused on a simple wall-bounded converging-diverging nozzle.

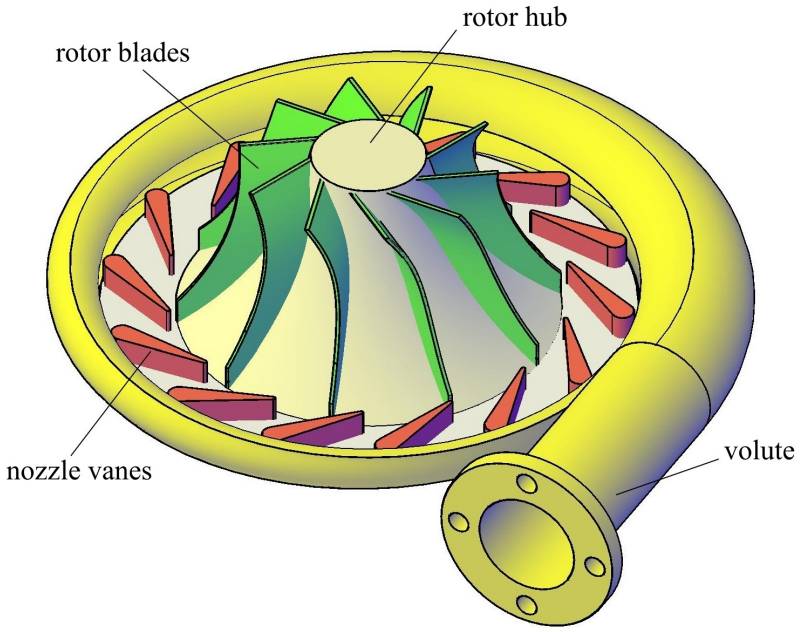


Figure 5.1: A simplified schematic of a radial-inflow turbine.

In order to conduct CFD simulations of the wet-to-dry expansion, first a nozzle geometry must be designed and imported into the solver for analysis. Depending on how non-

equilibrium effects are treated in the analysis of flashing flows, there exist various models that can be used to design two-phase nozzles. Design codes typically simplify the expansion by assuming a quasi-1D flow (often referred to as simply 1D flow), where flow properties vary only along the longitudinal axis of the nozzle. The most simplistic approach is based on the homogeneous-equilibrium flow, which assumes that both phases remain in the state of equilibrium throughout the expansion, having identical temperatures and velocities. The design framework based on the homogeneous-equilibrium model benefits from simplicity; however, it could be inaccurate if the two-phase flow is associated with significant non-equilibrium effects. The design code could be further refined by taking into account velocity slip and thermal non-equilibrium, but this also increases the complexity of the code. The main objective of the first part of this work is to perform non-equilibrium numerical simulation to assess the physics of the wet-to-dry expansion and give insight into the phase-change process under various operating conditions. As the goal is not to generate an optimal geometry, the most straightforward design approach was followed, based on the assumption of a quasi-1D isentropic homogeneous-equilibrium flow. This approach will provide suitable geometries that can be studied numerically. The main limitation is that it neglects non-equilibrium effects, and if these are significant, nozzles are likely to be associated with under- or over-expansion issues.

The nozzle design routine is initiated with the selection of the working fluid, target mass-flow rate and appropriate boundary conditions that ensure the fluid can transition from a two-phase state to a superheated vapour. The inlet conditions are defined in terms of total pressure (P_{in}), vapour quality (q_{in}) and mixture velocity (u_{in}), while static pressure is imposed at the outlet (P_{out}). Since the nozzle is studied in the context of turbomachinery, and intended as a stator of a turbine integrated within the wet-to-dry cycle, the cycle condensation temperature (T_{cond}) and the turbine degree of reaction (R) are used to determine the nozzle outlet pressure. This is also the reason why the investigated nozzles are planar converging-diverging nozzles of a rectangular cross-section. The degree of reaction is defined as the ratio of the enthalpy drop across the turbine rotor to the enthalpy drop across the turbine stage, i.e. across the stator-rotor assembly. Assuming that the enthalpy at the rotor inlet is equal to the enthalpy at the nozzle outlet (neglecting the effect of the interspace between the rotor and stator), the degree of reaction can be expressed as:

$$R = \frac{h_{out} - h_{out,turbine}}{h_{in} - h_{out,turbine}} \tag{5.1}$$

where h_{in} and $h_{out,turbine}$ are the enthalpy values at the nozzle inlet and turbine outlet, respectively, while h_{out} represents the enthalpy at the nozzle outlet. The degree of reaction is particularly important in the design of a turbine for the wet-to-dry cycle because it determines the fraction of the total expansion that takes place in the stator. Hence, this has to be sufficiently high to ensure that the fluid can escape the two-phase dome. On the other hand, a low degree of reaction can have a negative effect on the turbine performance as indicated by the preliminary turbine design performed by White [8]. More specifically, turbine performance deteriorated significantly when R was reduced below 0.4. Hence, the degree of reaction was set above that value if possible.

The design code follows an inverse design approach, where a static pressure profile is imposed and the flow equations are solved to satisfy that profile. The static pressure profile is constructed using a 4^{th} order Bezier curve with five control points (Fig.5.2), which were found to provide sufficient control over the shape of the profile. The equations describing the Bezier curve with five control points are given as:

$$x(t) = (1-t)^4 x_0 + 4(1-t)^3 t x_1 + 6(1-t)^2 t^2 x_2 + 4(1-t) t^3 x_3 + t^4 x_4 \tag{5.2a}$$

$$y(t) = (1-t)^4 y_0 + 4(1-t)^3 t y_1 + 6(1-t)^2 t^2 y_2 + 4(1-t) t^3 y_3 + t^4 y_4 \tag{5.2b}$$

where t is a nondimensional parameter varying between 0 and 1, while x_n and y_n are the normalised streamwise location and pressure. The x and y coordinates, denoted x_0 through to x_4 and y_0 through to y_4, represent the position of the five control points on the non-dimensional plane. The first and last control points are fixed with (x_0, y_0) and (x_4, y_4) at $(0, 1)$ and $(1, 0)$ to ensure that the pressure is equal to the design inlet and outlet values at the entrance and exit of the nozzle, respectively. Furthermore, the vertical position of CP_1 and CP_3 are fixed at $y_1 = 1$ and $y_3 = 0$ so that the pressure gradient is zero at the inlet and outlet of the nozzle. In summary, the shape of the pressure profile is determined by the position of the four free coordinates: x_1, x_2, y_2 and x_3.

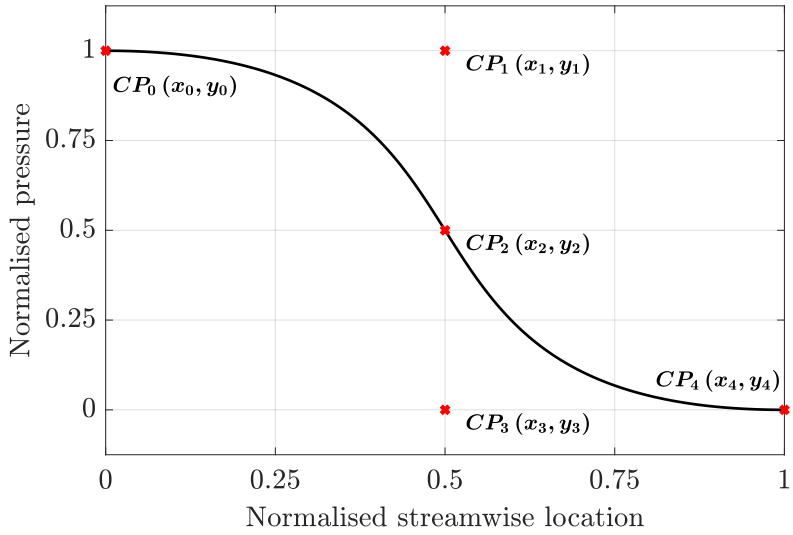


Figure 5.2: Normalised baseline nozzle pressure profile constructed using a Bezier curve with five control points; the red asterisks (*) show the location of the Bezier curve control points.

An exemplary pressure profile is illustrated in Figure 5.2. In this profile, the three movable control points, CP_1, CP_2 and CP_3 are positioned at $x_n = 0.5$, while the pressure at the middle of the nozzle is set to the average of the inlet and outlet pressures ($y_2 = 0.5$). This pressure profile was kept fixed for all the operating points considered in the parametric study.

Having defined the static pressure profile, and assuming that the flow is isentropic, pressure-entropy values will be known at any streamwise location. All other thermodynamic properties

can be determined using pressure-entropy values and a suitable equation of state. Since there is no work done in the nozzle and the flow is adiabatic, the total enthalpy will remain constant throughout the expansion.

$$h_0 = h + \frac{v^2}{2} = const. \tag{5.3}$$

Since the design tool assumes a homogeneous flow, both phases have identical velocity v, while the assumption of thermal equilibrium (phases remain saturated during expansion) results in the following expressions for mixture static enthalpy:

$$h = h_{L,sat} + (1 - x)(h_{V,sat} - h_{L,sat}) \tag{5.4}$$

where x denotes the vapour quality, while $h_{L,sat}$ and $h_{V,sat}$ are saturation enthalpies of liquid and vapour, respectively. When the fluid escapes the two-phase dome, h will simply be the enthalpy of superheated vapour determined from local pressure and entropy values. Once the velocity variation has been determined from Equation 5.3, the flow area variation can be calculated from the design mass-flow rate:

$$A = \frac{\dot{m}}{\rho v} \tag{5.5}$$

where A is the cross-sectional area of the nozzle, while ρ is the mixture density defined as:

$$\rho = \alpha_V \rho_{V,sat} + (1 - \alpha_V)\rho_{L,sat} \tag{5.6}$$

where α_V is the vapour volume fraction, while $\rho_{L,sat}$ and $\rho_{V,sat}$ are the saturation densities of the liquid and the vapour, respectively.

This study investigates nozzles that are intended as part of turbomachines designed for two-phase organic Rankine cycles. For this reason, converging-diverging nozzles of a rectangular cross section (planar nozzles) were analysed, which represent nozzle geometries of radial-inflow and radial-outflow turbines - two potentially suitable turboexpander architectures. To define the nozzle geometry, the ratios of nozzle length to throat height (L/o_{th}), and nozzle width to throat height (b/o_{th}) are set as model inputs. The throat height can be expressed in terms of the throat area and b/o_{th} ratio as follows:

$$o_{th} = \frac{A_{th}}{b/o_{th}} \tag{5.7}$$

where A_{th} is the throat area, which is the minimum flow area found from Eq. 5.5. With the throat height o_{th} known, the nozzle width b and nozzle length L can be obtained from the assumed geometrical ratios. This way, the entire nozzle geometry is determined. The schematic of the nozzle design routine is presented in Figure 5.3.

5.3 Investigated operating conditions

The current analysis focuses on the wet-to-dry expansion of the siloxane MM, which was found to be a suitable working fluid in the previous cycle optimisation studies conducted by

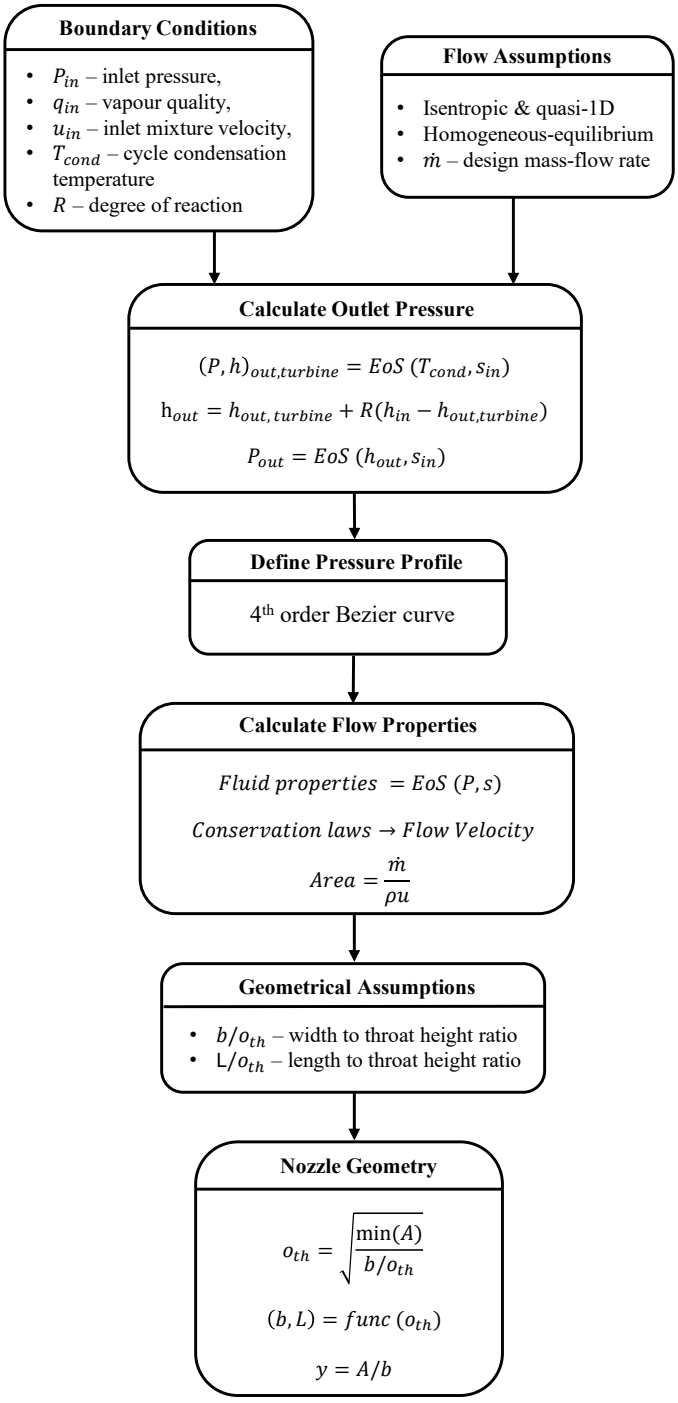


Figure 5.3: Wet-to-dry nozzle design routine based on the assumption of quasi-1D isentropic homogeneous-equilibrium flow; *EoS* stands for the equation of state, while y represents the passage height.

White [8]. Compared with working fluids, the siloxane MM could offer a relatively high thermodynamic advantage over single-phase ORC, while not causing certain technical challenges, such as extremely high expansion ratios or near-vacuum condensation conditions. To evaluate physical properties of the siloxane MM, the nozzle design code was coupled with NIST

REFPROP 10.0 [212], which used the Span-Wagner Helmholtz equation of state derived from empirical data and molecular simulation results [243]. The discussion on fluid properties and the suitability of the Span-Wagner Helmholtz thermodynamic model was provided in Section 4.5. The design mass-flow rate in a single passage was set to 0.12 kg/s, which under the investigated conditions translates to a turbine isentropic power of around 90 to 170 kW. This power output is estimated assuming that the turbine has sixteen stator vanes; each nozzle representing one stator passage. An alternative approach would be to fix the power output and vary the mass flow rate for given operating conditions. This power rating could correspond to small-scale systems designed for waste-heat recovery from low-temperature sources.

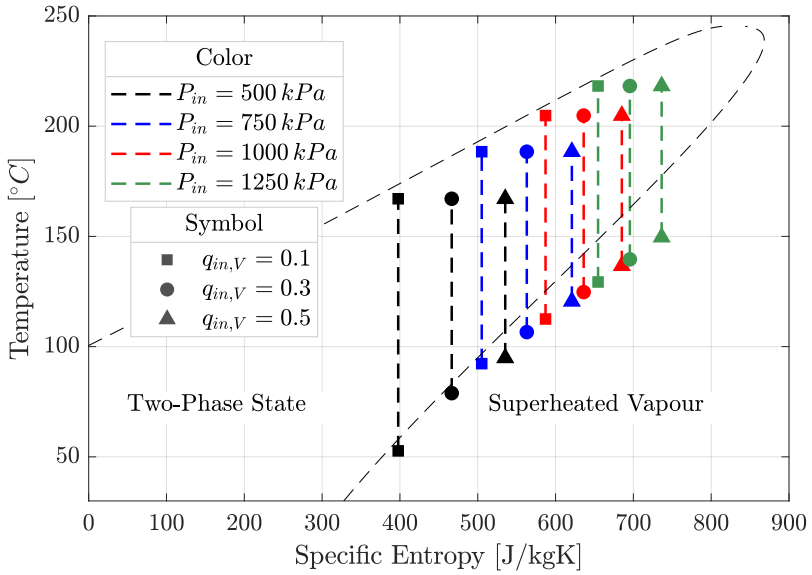


Figure 5.4: The temperature-entropy diagram of the twelve simulated expansion cases; the depicted expansions define the boundary conditions used in the nozzle design and CFD simulations, and are generated under the assumption of isentropic homogeneous-equilibrium flow.

The boundary conditions were selected such that the fluid can transition from the two-phase state to a superheated vapour under the isentropic homogeneous-equilibrium flow assumption. To provide a thorough assessment of the wet-to-dry expansion characteristics under different thermodynamic conditions, twelve expansion cases relevant to the wet-to-dry cycle were considered. These expansions were defined in terms of inlet pressure and vapour quality; four inlet pressures were investigated, 500, 750, 1000 and 1250 kPa, and three inlet qualities, 0.1, 0.3 and 0.5. The saturation temperature corresponding to the investigated pressure range varied between 167 and 220 °C, which is the temperature level originally considered for the wet-to-dry cycle [8]. At lower temperatures, the volumetric expansion ratio is typically lower, which means that volumetric expanders characterised by a limited built-in volume ratio can potentially be considered. At higher temperatures, the thermodynamic advantage of two-phase expansion diminishes and transcritical cycles may be preferred. As for the inlet vapour quality, values below 0.1 are likely to be associated with excessive volumetric expansion ratios due to a large density difference between saturated liquid at the entrance and superheated vapour at the exit of the nozzle. On the other hand, at inlet vapour

qualities greater than 0.5 the cycle performance begins to approach that of the single-phase architecture, mitigating the thermodynamic benefit of two-phase expansion. The cycle condensation temperature T_{cond} was fixed at 40 °C, while the degree of reaction R was set to 0.5 for all operating points except for the expansion from 500 kPa, for which R had to be lowered to 0.1 for the inlet quality of 0.1 and to 0.4 for the inlet quality of 0.3 and 0.5 to allow the fluid to escape the two-phase dome. The twelve expansion cases are illustrated on the temperature-entropy diagram in Figure 5.4.

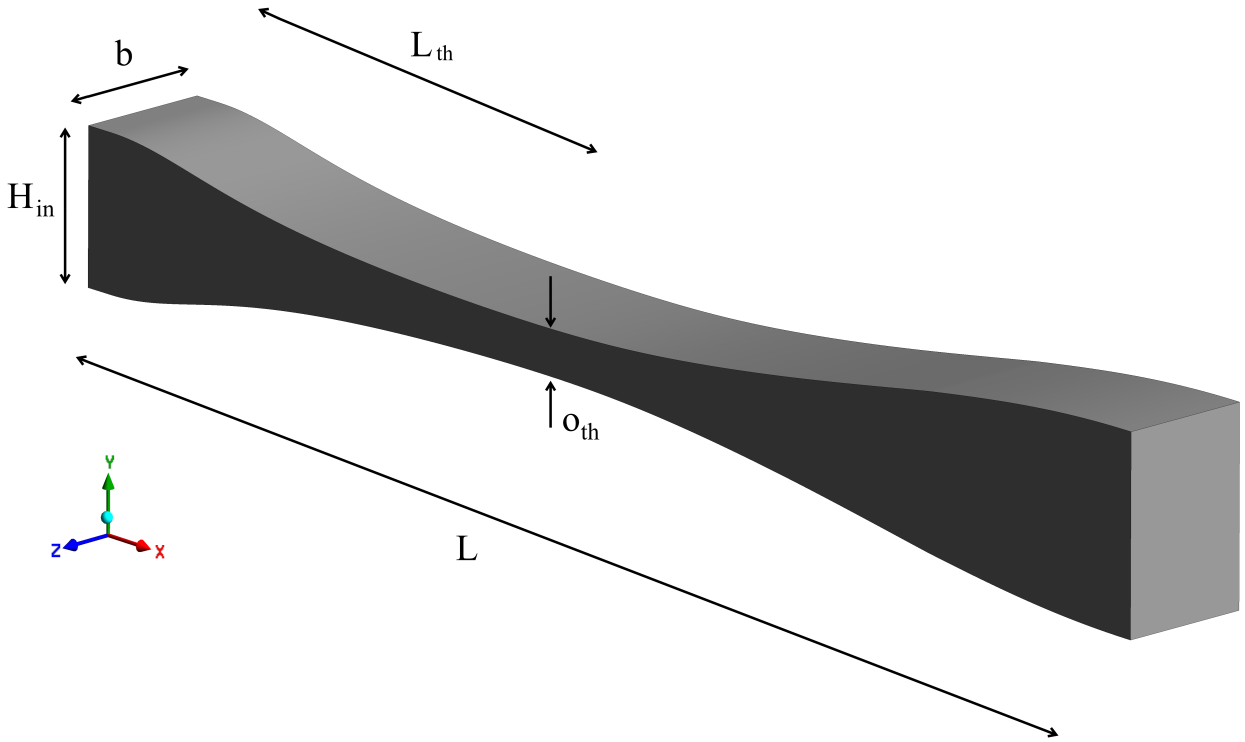


Figure 5.5: Nozzle geometry for the expansion from 500 kPa and inlet quality of 0.3; although the figure illustrates a three-dimensional geometry, the subsequent analysis used a thin slab in the z direction to perform quasi-2D simulations.

A geometry of the nozzle designed for one of the investigated cases along with relevant dimensions are illustrated in Fig. 5.5. The nozzle was generated assuming a small inlet velocity u_{in} of 10 m/s, while the geometrical ratios b/o_{th} and L/o_{th} were set to 3 and 30 respectively. The same values were used to generated nozzle geometries for all the investigated operating conditions. The geometrical ratios, b/o_{th} and L/o_{th}, were set in line with the guidelines outlined by White [8], who applied the homogenous-equilibrium model to design a nozzle vane for a radial-inflow turbine intended for wet-to-dry expansion of the siloxane MM. The author designed a number of nozzle candidates for two inlet pressures of 500 and 1000 kPa and inlet vapour quality ranging from 0.1 to 0.5; these operating conditions are therefore directly relevant to the current study. The wet-to-dry expansion was simulated in each nozzle using three-dimensional viscous CFD simulations coupled with the homogenous-equilibrium model. Although, the design mass-flow rate in the study of White [8] was lower compared to the current study, the findings of the study are deemed relevant due to similarities in the

nature of the simulated phase-change process, the identical working fluid, similar operating conditions and similar geometry of the converging-diverging channel of the turbine nozzle. The author recognised the nozzle width (denoted as b in Fig. 5.5) as the most influential parameter as far as the loss coefficient (ζ_n) was concerned, which was defined as:

$$\zeta_N = \frac{\overline{h}_{out} - \overline{h}_{out,is}}{\frac{1}{2}\overline{u}^2_{out}} \tag{5.8}$$

where $\overline{h}_{out}$, $\overline{h}_{out,is}$ and $\overline{U}_{out}$ are the averaged enthalpy, isentropic enthalpy and flow velocity at the nozzle outlet. The following relationship can be applied to convert the loss coefficient into nozzle efficiency (η_N):

$$\eta_N = \frac{1}{1 + \zeta_N} \tag{5.9}$$

Figure 5.6 illustrates the relationship between the loss coefficient and nozzle width obtained for the several candidate nozzles. A sharp decrease in nozzle performance was observed for nozzle width smaller than 3-4 mm. On the other hand, the estimated efficiency in the nozzles with width greater than 7 mm was of the order of 90 %. The ratio b/o_{th} of 3 was found suitable as it results in a nozzle width that varies between 7.26 and 12.1 mm depending on the operating conditions. When it comes to the L/o_{th} ratio, the value of 30 was found to result in geometries that were characterised by relatively gradual expansions [8]. It should be noted that the current study is concerned with two-dimensional simulations, which means that the nozzle width is not resolved in the simulations. As such, the nozzle width b is only used in the nozzle design process to define the other dimensions of the nozzle.

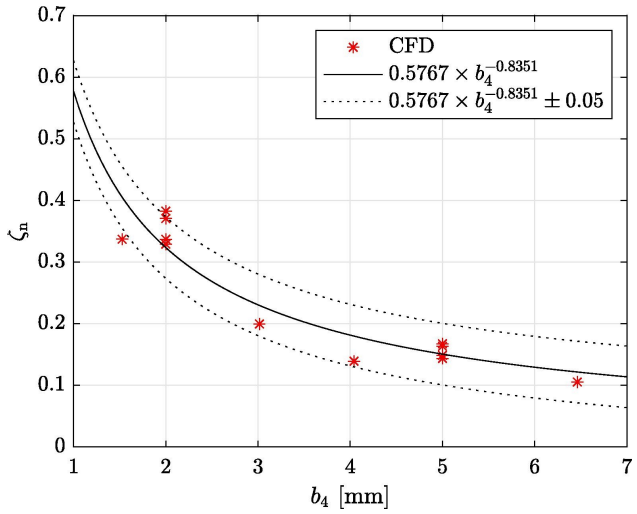


Figure 5.6: The relationship between the nozzle loss coefficient (ζ_n) and the width of of a radial-inflow turbine nozzle designed for the wet-to-dry cycle. The CFD results were obtained using a homogeneous-equilibrium model. The presented correlations were obtained using b_4 divided by the corresponding unit of length to derive the correlations presented in the figure (figure retrieved from White [8]).

Following the notation defined in Fig.5.5, Table 5.1 provides the dimensions of all the investigated nozzle geometries. Analysing the conditions at the throat, it was found that the

mixture velocity was almost independent of the inlet pressure, however mixture density, defined in Eq. 5.6, was higher at elevated pressures. Since the mass-flow rate was fixed, the resulting throat area was larger for low-pressure expansions, which is reflected in smaller o_{th} that varies between 3 and 4 mm for inlet pressures of 500 and 750 kPa, and between 2 and 3 mm for 1000 and 1250 kPa. The mixture density also decreases with inlet quality, which explains why the expansions with low $x_{V,in}$ are characterised by a larger inlet height compared to the height of the outlet. Although the dimensions vary from case to case, the overall pressure ratio was typically between 9 and 14, and the overall shape of the nozzle does not vary significantly. This is except for the expansion from P_{in} of 500 kPa and $x_{V,in}$ of 0.1, where the pressure ratio and the difference in the height of the inlet and outlet passages are considerably higher. This is caused by lower outlet pressure and associated low vapour density.

Table 5.1: Geometrical features of each investigated converging-diverging nozzle.

P_{in} $[kPa]$	$x_{V,in}$	P_{out} $[kPa]$	H_{in} [mm]	o_{th} [mm]	H_{out} [mm]	L_{th} [mm]	L [mm]
500	0.10	15.24	6.52	3.49	41.30	37.80	104.67
500	0.30	41.85	12.98	3.80	16.68	47.32	114.07
500	0.50	46.03	19.01	4.03	14.22	52.72	120.96
750	0.10	63.61	5.83	2.96	14.89	32.67	88.87
750	0.30	72.96	10.60	3.18	12.08	39.23	95.47
750	0.50	79.79	15.09	3.35	10.52	43.32	100.49
1000	0.10	76.79	5.53	2.64	13.57	29.13	79.26
1000	0.30	85.29	9.18	2.80	11.55	34.02	84.15
1000	0.50	91.55	12.66	2.93	10.33	37.18	88.00
1250	0.10	88.28	5.44	2.42	12.76	26.92	72.61
1250	0.30	95.72	8.24	2.54	11.26	30.41	76.27
1250	0.50	101.30	10.92	2.64	10.28	32.98	79.26

5.4 Computational fluid dynamics setup

To simulate the wet-to-dry expansion of the siloxane MM, the two-fluid model was implemented in a commercial CFD code, ANSYS CFX 2021 R1 [244]. The general description of the CFD solver and the implementation of the two-fluid model was provided in the previous chapter in Section 4.6. Some of the important details are reiterated here. The solver follows the finite-volume approach to solve Reynolds-averaged Navier-Stokes (RANS) equations. Second-order accurate schemes were applied to discretise the advection and turbulence equations. Turbulence in the continuous vapour phase was modelled using the $k-\omega$ SST model, while a dispersed zero equation model was used to estimate the eddy viscosity of the dispersed liquid phase. CFX uses an automatic wall function method, which automatically switches from directly resolving the boundary layer to standard wall functions according to the local y^+ value.

The analysed nozzles are planar converging-diverging nozzles with a rectangular cross-section. Although CFX only allows for three-dimensional simulations, a thin nozzle slab with a thick-

ness of 0.15 mm was imported to ANSYS and the mesh was extruded by a single element in the spanwise direction. A symmetric boundary condition was then applied to the upper and lower faces of the slab to perform steady-state quasi-2D simulations. Total inlet pressure and temperature were specified at the inlet of the nozzle alongside volume fraction of both phases. Fixed static pressure was imposed at the nozzle outlet. In contrast to former non-equilibrium simulations of the wet-to-dry expansion, the CFD results reported in this work give insight into the effect of both longitudinal as well as lateral flow variations. Moreover, the viscosity and turbulence effects were included alongside the lift and turbulent dispersion forces, which were previously neglected.

As discussed in Section 4.3.1, assuming a constant number of droplets may be a better approach to modelling droplet size, because the droplets are allowed to change size during expansion, which is considered to be more in line with the actual vapourisation process. Therefore, a constant droplet number density N_d, given as the number of droplets per unit volume, was applied to estimate the droplet diameter. The droplet number is one of the main unknowns in the simulation. In the absence of experimental data, it is difficult to state what value for N_d would be appropriate. Therefore, the subsequent analysis will examine a range of N_d, extending from 10^{11} to 10^{13} droplets per unit volume, which corresponds to an inlet droplet diameter approximately 200 to 20 µm. The higher limit of $N_d = 10^{13}$ was chosen as at this droplet number the solution begins to resemble the homogeneous-equilibrium flow; this indicates that the droplets were sufficiently small for the non-equilibrium effects to become negligible. The lower limit of $N_d = 10^{11}$ was selected based on the Weber number analysis; below $N_d = 10^{11}$ the droplets become so large that breakup is very likely to occur at the beginning of the expansion leading to an eventual increase in N_d.

The solution convergence was assessed using the standard residual plots, average flow properties at the inlet and outlet of the nozzle with three additional monitor points, one located at the throat and the other two located in the middle of the converging and diverging sections of the nozzle. To improve numerical stability in the early stages of the solution, the outlet pressure was gradually varied over the first five hundred iterations until it reached the design value. ANSYS CFX uses the pseudo-transient approach to solving steady-state problems; the transient terms eventually tend to zero as the solution approaches steady state. The timescale applied for these pseudo-transient terms was crucial for the numerical stability of the solution. It was found that a physical timescale, which represents a uniform timescale applied throughout the domain, of 20 µs provided a good balance between simulation time and numerical stability. Such a timescale was found to be approximately two orders of magnitude lower than the average fluid residence time in the nozzle. The solution was considered to be converged if the average momentum and mass residuals dropped below 10^{-6}, the percentage variation in the flow properties at the outlet and at the monitor points was below 0.25% per 1000 iterations, while the mass imbalance was below 0.5 %. Generally, simulations with higher droplet numbers converged within the first few thousands iterations. On the other hand, as the droplet number was lowered, non-equilibrium effects become more pronounced and the solution typically required between 10,000 and 30,000 iterations to fully converge.

Although ANSYS CFX does not have a built-in capability to directly couple the solver with NIST REFPROP 10.0 [212], the solver allows to use custom property tables (so-called RGP tables) provided these are created according to a specific formatting guidelines [236]). Therefore, such look-up tables were generated using NIST REFPROP 10.0 [212] and coupled with ANSYS CFX to evaluate the thermodynamic and transport properties of the siloxane MM. When generating the look-up tables, liquid and vapour properties were extended into the metastable region and calculated up to the spinodal limit so that the solver could evaluate phase properties in the event that the liquid and vapour phases became superheated and subcooled, respectively. To generate the look-up tables, a pressure range between 1 and 1800 kPa, and a temperature range between -23 °C and 277 °C were applied. These limits extend well beyond the expected minimum and maximum pressure and temperature values, ensuring that fluid properties can be calculated even if the flow significantly deviates from the final converged state in the solution process. Several look-up tables were generated with different resolution that depends on the way the pressure and temperature intervals were discretised. A look-up table with the pressure and temperature ranges divided into 500 equal intervals is referred to as 500×500 table. To assess the sensitivity of the solution to the resolution of the look-up tables, the expansion from 500 kPa and an inlet quality of 0.3 was simulated using tables with a resolution ranging from 50×50 to 1000×1000. The droplet number was assumed to be 10^{12} for this sensitivity analysis. It should be noted that the results were obtained from grid-independent solutions, which will be discussed further in the following section.

Table 5.2: Sensitivity of the solution to the resolution of the look-up tables; the simulated expansion had an inlet pressure of 500 kPa and inlet vapour quality of 0.3.

Table resolution	$\dot{m}_{out}$ [g/s]	$u_{V,out}$ [m/s]	$u_{L,out}$ [m/s]	$T_{V,out}$ [K]	$T_{L,out}$ [K]	$x_{V,out}$	η_N[%]
50×50	2.034	233.94	161.56	379.25	362.23	0.8514	72.85
100×100	2.038	234.02	161.38	379.44	363.13	0.8489	72.78
250×250	2.038	234.05	161.33	379.49	363.35	0.8482	72.76
500×500	2.039	234.05	161.31	379.48	363.38	0.8481	72.76
1000×1000	2.039	234.05	161.31	379.50	363.39	0.8481	72.76

Table 5.2 summarises several average flow properties calculated at the outlet of the nozzle alongside nozzle efficiency (η_N) for the different look-up tables resolution. The nozzle efficiency was calculated using the formula shown in Eq. 7.5. Since the study is concerned with non-equilibrium two-phase flows, where liquid and vapour can significantly deviate from thermodynamic equilibrium, the vapour mass fraction, x_V, was defined as the ratio of the vapour mass-flow rate to the total mass-flow rate:

$$x_V = \frac{\dot{m}_V}{\dot{m}_V + \dot{m}_L} \tag{5.10}$$

where $\dot{m}_L$ and $\dot{m}_V$ are the mass-flow rates of liquid and vapour. The average flow properties at the outlet of the nozzle were found to be practically identical for table resolution higher than 250×250. As such, a resolution of 500×500 was deemed sufficiently fine and applied

in the subsequent simulations. One can note that despite the mass-flow rate being fixed in the nozzle design process, the mass-flow rate estimated by the CFD solver is not constant as seen in Table 5.2. This is because the CFD solver uses the total inlet conditions and static outlet pressure as the boundary conditions, while the mass-flow rate is an output of the solution. Therefore, its value depends on the calculated flow field and may differ from the design value, which was obtained under idealised conditions (one-dimensional isentropic homogeneous-equilibrium flow).

5.5 Mesh independence study

One particular expansion case, with P_{in} of 1000 kPa, $q_{V,in}$ of 0.3 and N_d of 10^{12} was selected to carry out the mesh independence study. The mesh was generated using ANSYS Meshing tool, with predominantly hexahedral elements as shown in Fig. 5.9. A single element was applied in the spanwise direction to perform a quasi-2D simulation. Three different grids were constructed with an element size of 0.6, 0.4 and 0.25 mm. The resolution of the mesh was refined near the wall, with the width of the element adjacent to the wall kept constant at 10 µm in each grid. The width of the elements applied in the lateral direction was progressively smaller when approaching the nozzle wall, to ensure that the boundary layer is well resolved. Based on simplified estimates of the thickness of the boundary layer for a flat plate, the boundary layer was estimated to be resolved with at least 20 elements. It was found that reducing the element width below 10 µm caused solution convergence issues. At first, it was suspected that these numerical issues could occur due to increased aspect ratio of the elements, but further investigation showed that even when the aspect ratio was limited by simultaneously reducing the element size in the longitudinal direction, numerical issues persisted. With that being said, the width of 10 µm was sufficient for the average y^+ value of vapour and liquid to remain below 50 and 150 respectively, where standard wall functions can be applied.

Since the wall functions were developed for standard single-phase flows, the use of these functions in the current case may carry some uncertainty. However, the two-fluid model applied in this study simplifies the problem by treating the two-phase flow as composed of two interpenetrating continua with the velocity profile estimated for each phase separately, similar to single-phase flows. The difference lies in the addition of interfacial forces that affect the velocity of both phases in the boundary layer region. As such, even though in reality the mixture could exhibit more complex behaviour, in the context of the employed modelling framework, it seems reasonable to assume that the standard wall functions are applicable. Generally, accurate estimation of the boundary layer effects is going to be more critical when viscous losses are significant. Previous studies have demonstrated the importance of viscous losses in flash-boiling phenomena, and in particular the influence of viscous losses on the nozzle pressure distribution [180]. However, these studies typically dealt with the expansion from a subcooled or saturated liquid state, where a substantial portion of the expansion occurs at high liquid volume fractions. In contrast, in the current work the two-phase expansion begins with a liquid volume fraction close to 70 %, which further decreases

downstream. Therefore, the channel is mostly occupied by the less viscous vapour phase throughout the expansion, which is why viscous losses are expected to be less significant than in flashing of subcooled liquids. To verify this assumption, two of the simulations were re-run with the viscosity of both phases reduced by a factor of 1000. The effect of viscosity on the average streamwise variation of static pressure and mixture velocity is shown in Fig. 5.7. The mixture velocity is computed as a mass-flow averaged velocity:

$$u_{Mix} = \frac{\dot{m}_L u_L + \dot{m}_V u_V}{\dot{m}_L + \dot{m}_V} \tag{5.11}$$

where $\dot{m}_L$ and $\dot{m}_V$ represent the mass-flow rates of liquid and vapour, while u_L and u_V are the velocities of liquid and vapour.

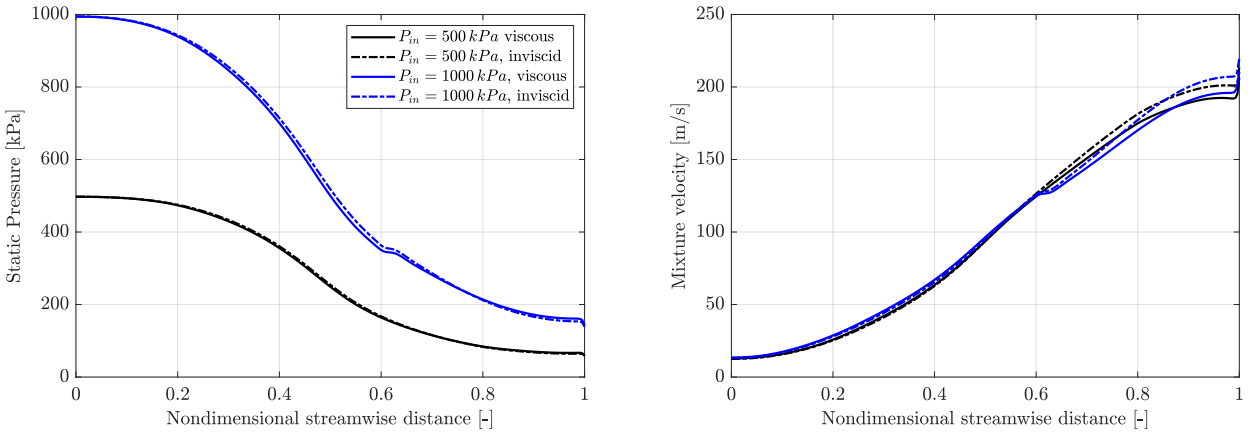


Figure 5.7: The effect of viscosity on average streamwise variation of static pressure and mixture velocity. The results were obtained for a fixed inlet vapour quality of 0.3 and a droplet density number of 10^{12}.

It appears that the pressure profile is marginally affected by the viscosity of the fluid, indicating that the viscous pressure losses in the wet-to-dry expansions are not significant. The average mixture velocity was found to be very similar in the converging section of the nozzle; however, the viscous and inviscid profiles begin to diverge at a streamwise distance of approximately 60 % of the nozzle length. The maximum relative difference in mixture velocity was about 4.6 and 5.6 % for 500 and 1000 kPa expansions, respectively. The corresponding difference in the mass-flow rate calculated at the nozzle outlet was below 1.72 and 1.69 % for the two pressure levels. With a relatively small difference in the outlet flow properties and a negligible viscous pressure drop, the viscous effects are not critically important, and the current approach to resolving the boundary layer seems justified.

As discussed earlier, the convergence of the solution was assessed based on the average residual values along with the solution mass imbalance, and various flow parameters such as mass-flow rate, average phase velocities, and vapour mass fraction measured at the outlet of the nozzle. Additionally, three monitor points, one at the throat and two in the converging and diverging sections of the nozzle, were placed to assess the convergence. The solution converged in each grid within about 10,000-20,000 iterations, with the average mass and

momentum residuals below 10^{-6}, mass imbalance less than 0.04% and various averaged and local flow parameters practically converging to single values.

Table 5.3: Mesh independence study results

Mesh	Coarse	Moderate	Fine
Element Size	0.6 mm	0.4 mm	0.25 mm
Element Count	4,426	10,332	20,517
Average Aspect Ratio	24.66	17.26	10.46
Maximum Aspect Ratio	120.22	79.96	50.08
Average Orthogonal Quality	0.997	0.997	0.998
Minimum Orthogonal Quality	0.513	0.487	0.475
Average Skewness	0.016	0.011	0.0094
Maximum Skewness	0.661	0.576	0.714
$y^+_{V,\,avg}$	45.92	45.98	45.89
$y^+_{L,\,avg}$	100.94	100.75	100.46
$q_{V,out}$ [%]	94.22	94.05 (0.18%)	94.06 (0.01%)
$u_{V,out}$ [m/s]	245.57	245.13 (0.18%)	245.36 (0.09%)
$u_{L,out}$ [m/s]	176.35	174.76 (0.90%)	174.56 (0.11%)
$T_{V,out}$ [°C]	138.19	138.12 (0.07 °C)	138.14 (0.02 °C)
$T_{L,out}$ [°C]	126.62	127.68 (1.06 °C)	127.76(0.08 °C)
$\dot{m}_{out}$ [g/s]	2.912	2.927 (0.52%)	2.920 (0.24%)
Δ_{max}	-	0.90%	0.24%

The results of the mesh independence study are summarised in Table 5.3, which includes information on mesh metrics, quality metrics, average near-wall y^+ values for both phases, various outlet flow properties, and the total mass-flow outflow ($\dot{m}_{out}$). Despite the aspect ratio being relatively high, the average values of quality metrics (aspect ratio, orthogonal quality and skewness) lie within recommended ranges, which indicates a good quality of the grids. Similarly, the quality metrics of the worst grid elements remain within recommended limits [247]. The values reported in the brackets represent percentage difference between two consecutive grids, i.e. between the moderate and coarse, and between the fine and moderate grids. Since comparing percentage difference in temperature values was deemed less meaningful, absolute temperature difference was shown in the brackets for liquid and vapour temperatures. The maximum of the percentage variations, Δ_{max}, is reported at the bottom of the table. The greatest difference between the moderate and coarse grid was around 0.90%, and it corresponded to the average liquid velocity, while the maximum temperature difference was 1.06 °C. The maximum percentage difference and temperature difference dropped to around 0.24% and 0.08 °C between the fine and moderate grids. Generally, all the grids

generated very similar results when it comes to the average outlet flow properties, with the difference becoming practically negligible as the element size is reduced below 0.4 mm.

In addition to the outlet properties, average streamwise variations were also examined, which were calculated using a custom user-defined script. The averaging routine relied on defining a number of cross-sectional planes stretching between the inlet and outlet of the nozzle and calculating the average of a phase-dependent property, ϕ, with the following expression:

$$\phi_{avg} = \frac{\sum \left(d\dot{m}_L \phi_L + d\dot{m}_V \phi_V \right)}{\dot{m}_L + \dot{m}_V} \tag{5.12}$$

where the summation is carried out over all mesh elements across the cross-sectional planes.

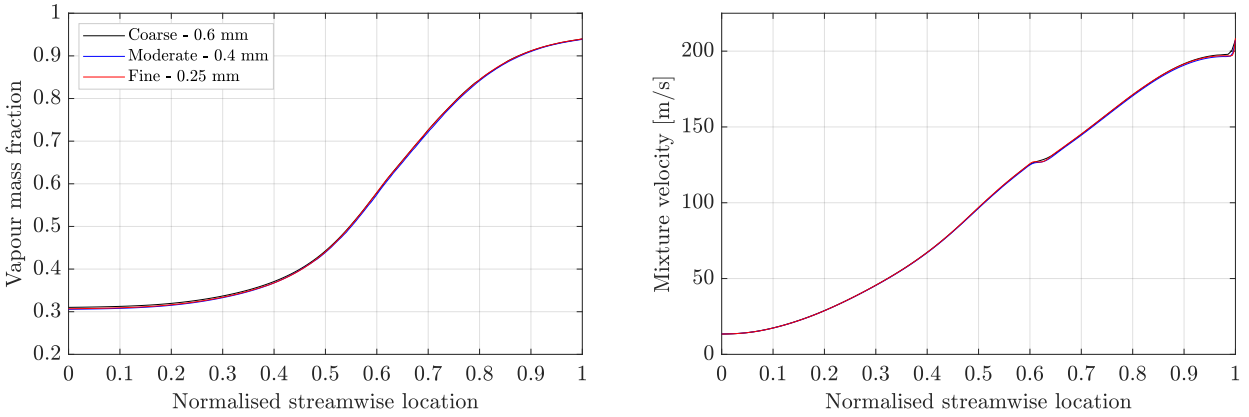


Figure 5.8: Average streamwise variation of vapour mass fraction and mixture velocity for different grid sizes.

Figure 5.8 presents the average streamwise variation of vapour mass fraction and mixture velocity for the three investigated grids. It can be observed that the average streamwise variations are nearly identical for all the considered grids. When comparing the variation of the fraction of the vapour mass, the mean and maximum deviation between the coarse and moderate grids were below 0.82% and 1.48%, respectively. These values dropped to around 0.36% and 0.85% when the mesh resolution was increased. When it comes to the profiles of mixture velocity, the mean and maximum deviation between the coarse and moderate grids were less than 0.42% and 1.51%, and less than 0.36% and 0.78% for the moderate and fine grids. To summarise, the mean deviation in the streamwise profiles between the moderate and coarse grids was below 0.36%, and the maximum value did not exceed 0.85%. Based on the assessment of outlet flow properties and the average streamwise variations, the mesh with the element size of 0.4 mm was considered sufficiently fine. The structure of the final mesh with a close-up of the throat area is shown in Fig. 5.9. This element size was applied to generate grids for all the investigated expansions in the parametric study.

5.6 Three-dimensional and transient effects

The current work simplifies the simulation of the wet-to-dry expansion by assuming that both three-dimensional and transient effects are of secondary importance. In order to assess

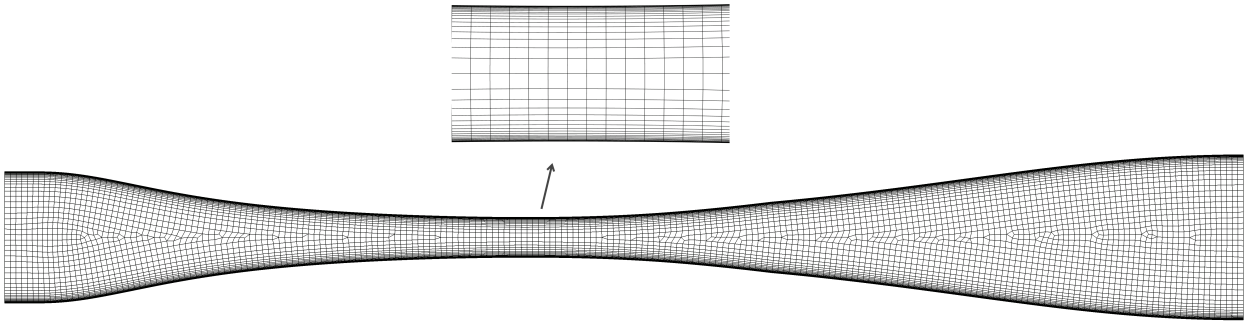


Figure 5.9: The structure of the grid generated with an element size of 0.4 mm; the enlarged section illustrates the grid topology in the throat area.

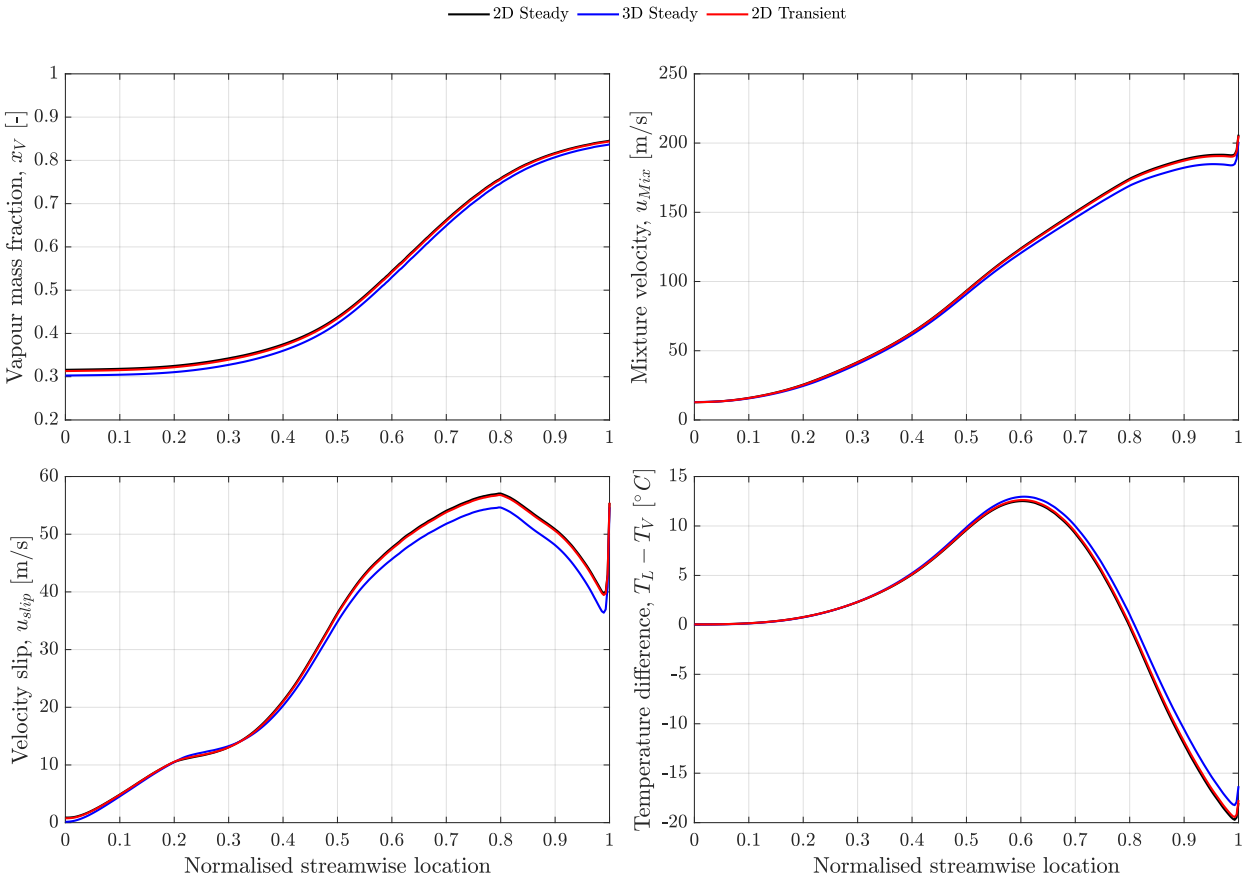


Figure 5.10: Streamwise variation of average vapour mass fraction, mixture velocity, velocity slip and temperature difference predicted by two-dimensional steady, two-dimensional transient and three-dimensional steady solvers.

the validity of this assumption, three-dimensional steady and two-dimensional transient simulations were carried out for the expansion from an inlet total pressure of 500 kPa and inlet vapour quality of 0.3. In the three-dimensional simulation, the two-phase flow was simulated in the entire nozzle geometry shown in Fig. 5.5, with no-slip wall condition set to the end walls. The mesh was constructed in line with the mesh independence study results reported in the previous section. The three-dimensional solution converged well with the average

mass and momentum residuals below 10^{-6} and relevant flow properties monitored at the inlet and outlet of the domain converged to single values. As for the transient simulation, the same thin slab of the nozzle was extracted in the z-direction (see Fig. 5.5) to perform two-dimensional simulations. Second-order backward Euler scheme was applied to discretise the transient terms. Several settings for the timestep and simulation time were tested. It was found that a timestep of 0.25 µs was sufficient for the maximum Courant number to stay below 0.48 for the vapour phase and below 0.84 for the liquid phase. The simulation time was set to 15 ms, and a fully steady solution was established after approximately 10 ms. A constant number of droplet per unit volume equal to 10^{12} was set in the three-dimensional and transient simulations.

Figure 5.10 shows the streamwise variation of average vapour mass fraction, mixture velocity, and non-equilibrium effects defined in terms of velocity slip and temperature difference. The definition of vapour mass fraction, mixture velocity and the averaging process were explained in the previous section (see Eqs. 5.10-5.12). It is apparent that the difference in results obtained by the two-dimensional steady and transient solvers was negligible. As far as the three-dimensional effects are concerned, the phase-change pattern is almost identical, however, the inlet vapour quality is slightly lower, which generally results in delayed phase change. It is not entirely clear why the inlet vapour quality is lower in the three-dimensional simulation, but the overall difference is rather small. The mixture velocity profiles are also similar, however, the profiles diverge slightly in the diverging section of the nozzle, with the three-dimensional simulation estimating lower outlet velocity. This may be attributed to the viscous effects on the end walls, which results in mixture velocity reduction. Non-equilibrium effects estimated by the three- and two-dimensional simulations are comparable, with slightly lower velocity slip and temperature difference predicted by the former. Overall, neither transient nor three-dimensional effects appear to have a significant impact on the two-phase expansion.

5.7 Sensitivity to interphase models

The interphase models determine the rate of mass, momentum and energy exchange between the phases, and are a critical part of the two-fluid model. Some authors have emphasised that the two-fluid model may be less reliable than the simplified models if unsuitable interphase models are used [132]. Knowing the importance of the interphase models, a sensitivity analysis is performed prior to the parametric study. Several interphase models, potentially applicable to simulating the wet-to-dry expansion, have been discussed in detail in Chapter 4.1. These models evaluate the interfacial forces, including drag, lift and turbulent dispersion effects, and the interfacial heat transfer for which two distinct heat-transfer coefficients on the liquid and vapour side of the interface need to be specified.

5.7.1 Baseline model

The baseline model was set up taking into account the fact that the parametric study aims to assess the wet-to-dry expansion for a range of droplet sizes. Since the shape of large droplets can be significantly distorted, the Ishii-Zuber [233] drag and Tomiyama [234] lift models were selected in the baseline setup as these take into account shape distortion effects. The Favre Averaged Drag turbulent dispersion model, applicable to a wide range of two-phase flows [225], was used with the default dispersion coefficient C_{TD} of one. The heat-transfer coefficient on the droplet side was predicted with the Brown's correlation [221, 232] that includes a direct reference to the liquid superheat level and has previously been used in codes designed for nuclear reactor safety analysis. [221]. Regarding the heat transfer rate on the continuous vapour side, the Ranz-Marshall [229] correlation, derived based on experiments of heating water droplets in a hot air stream, was deemed suitable for the wet-to-dry expansion. The interphase models applied in the baseline model are summarised in Table 5.4.

Table 5.4: The summary of interphase models employed in the baseline two-fluid model setup.

Unknown Parameter	Model
Drag	Ishii-Zuber [233]
Lift	Tomiyama [234]
Turbulent dispersion	Favre Averaged Drag
Liquid-side heat transfer	Brown's correlation [221, 232]
Vapour-side heat transfer	Ranz-Marshall [229]

5.7.2 Alternative interphase models

Alongside the baseline models discussed above, Chapter 4.1 outlined several alternative interphase models. These include the Schiller-Naumann [214] drag model applicable to solid spheres, and the Legendre-Magnaudet [235] lift correlation suited to small non-deformable fluid particles. An alternative approach to estimating turbulent dispersion was proposed with the turbulent dispersion coefficient, C_{td}, given as

$$c_{TD} = e^{-\tau St_t} \tag{5.13}$$

where St_t is the turbulent Stokes number, which describes the ratio of droplet relaxation time to the average lifetime of vapour turbulent eddies. This correlation attempts to reflect the fact that, when the turbulent Stokes number increases, the turbulent vapour eddies will have a little effect on the distribution of droplets. The user-defined constant τ was set to 0.5 in the sensitivity study. Beside the Brown's correlation, a constant Nusselt number of 6 and 16 were proposed for modelling heat-transfer rate on the liquid side, based on heat-transfer analysis in a solid sphere and in a vapour bubble, respectively.

The above are the alternative models discussed in Chapter 4.1. Several additional correlations were tested in the sensitivity study. For a smooth sphere, the drag coefficient is

expected to be between 0.4 and 0.5 as long as the Reynolds number is between 10^3 and 2×10^5 [248]. In this study a constant drag coefficient of 0.47 was be applied as an alternative drag model. The Saffman Mei correlation [249, 250] applicable to solid spheres was assessed as an alternative lift correlation. For the turbulent dispersion, the Lopez de Bertodano Model [251] turbulent dispersion model with C_{TD} set to one was considered as an alternative to the Favre Averaged Drag model. Moreover, the results were generated with lift and turbulent dispersion forces turned off to assess the overall significance of these effects.

To investigate the sensitivity of solution to the heat-transfer rate between the liquid and the interface, Nu_L of 16 was tested alongside the Brown's correlation and Nu_L of 6. When it comes to modelling heat-transfer rate on the continuous vapour side of the interface there are generally two main families of correlations [41, 228]. The first family is based on the dispersed particle Reynolds number Re_d (Eq.4.24) and the continuous phase Prandtl number Pr_V (Eq.4.25). An example of such a correlation is the Ranz-Marshall [229] applied in the baseline model. The other family of correlations is based based on the Péclet and Jakob numbers. The Péclet number is simply the product of Re_D and Pr_V, while the Jakob number represents the ratio of heat required to bring the continuous phase to the saturation conditions to the latent heat of vapourisation of the corresponding volume of the dispersed phase:

$$Ja_T = \frac{\rho_V c_{p,V}(T_V - T_{sat})}{\rho_L(h_{V,sat} - h_{L,sat})} \tag{5.14}$$

In this sensitivity study, the model representing the latter category was the Wolfert [209] correlation expressed as:

$$Nu_V = \frac{12 Ja_T}{\pi} + 2\sqrt{\frac{Pe}{\pi}} \tag{5.15}$$

The summary of all the interphase models considered for the sensitivity analysis is given in Table 5.5.

5.7.3 Sensitivity to momentum-transfer models

To assess the solution sensitivity to the interphase models under different operating conditions, two operating points with an inlet pressure of 500 and 1000 kPa and a fixed inlet vapour quality of 0.3 were considered. Three droplet numbers of 10^{11}, 10^{12} and 10^{13} were simulated to investigate the sensitivity of the solution in expansions characterised by different droplet sizes.

Figure 5.11 compares the average streamwise variation of vapour mass fraction x_V and mixture velocity u_{Mix} for the three drag correlations. The streamwise profiles appear to be hardly affected by the type of drag model and were nearly identical for most of the operating conditions. In fact, in some cases, the streamwise profiles generated using the Schiller-Naumann and Ishii-Zuber (baseline) models practically overlap and cannot be easily distinguished in Fig. 5.11. The greatest deviation from the baseline x_V profile was around 2.33 %, and corresponded to $C_D = 0.47$ and the expansion from 500 kPa and $N_d = 10^{13}$. The same operating

Table 5.5: The summary of the interphase models considered for the sensitivity study.

Transfer mechanism	Models
Drag	Ishii-Zuber [233]
	Schiller-Naumann [214]
	$C_D = 0.47$
Lift	Tomiyama [234]
	Legendre-Magnaudet [235]
	Saffman Mei [249, 250]
	No lift
Turbulent dispersion	Favre Averaged Drag - $C_{TD} = 1$
	Favre Averaged Drag - $C_{TD} = e^{-0.5St_t}$
	Lopez de Bertodano Model [251] - $C_{TD} = 1$
	No turbulent dispersion
Liquid-side heat transfer	Brown [221, 232]
	$Nu_L = 6$
	$Nu_L = 16$
Vapour-side heat transfer	Ranz-Marshall [229]
	Wolfert [209]

conditions corresponded to the maximum velocity difference, which was about 2.66%. For the remaining cases, the maximum percentage deviation from the baseline profiles of x_V and u_{Mix} was typically below 1.5%. Further investigation of two-dimensional contours of vapour quality demonstrated a negligible impact of drag models on the phase distribution within the nozzle.

Figure 5.12 shows the average streamwise variation of x_V and u_{Mix} for the three lift correlations and for the model with the lift force turned off. The x_V profiles were fairly similar for all the investigated lift models. The maximum percentage deviation from the baseline model corresponded to the simulation with the lift force turned off and was around 1.92%. It occurred in the the expansion from 500 kPa and $N_d = 10^{10}$. The maximum difference for the remaining cases was below 1.2%. Similar to x_V variations, the difference in u_{Mix} between the tested lift models was relatively small for $N_d \geq 10^{12}$, and did not exceed 2.9%. For larger droplets ($N_d = 10^{10}$), the discrepancies are more noticeable with the maximum relative deviation reaching 4.73%. Similarly to the vapour mass fraction, it corresponded to the baseline and no-lift model, and occurred for the expansion from 500 kPa.

Unlike the drag force, the lift, being responsible for the lateral displacement of droplets,

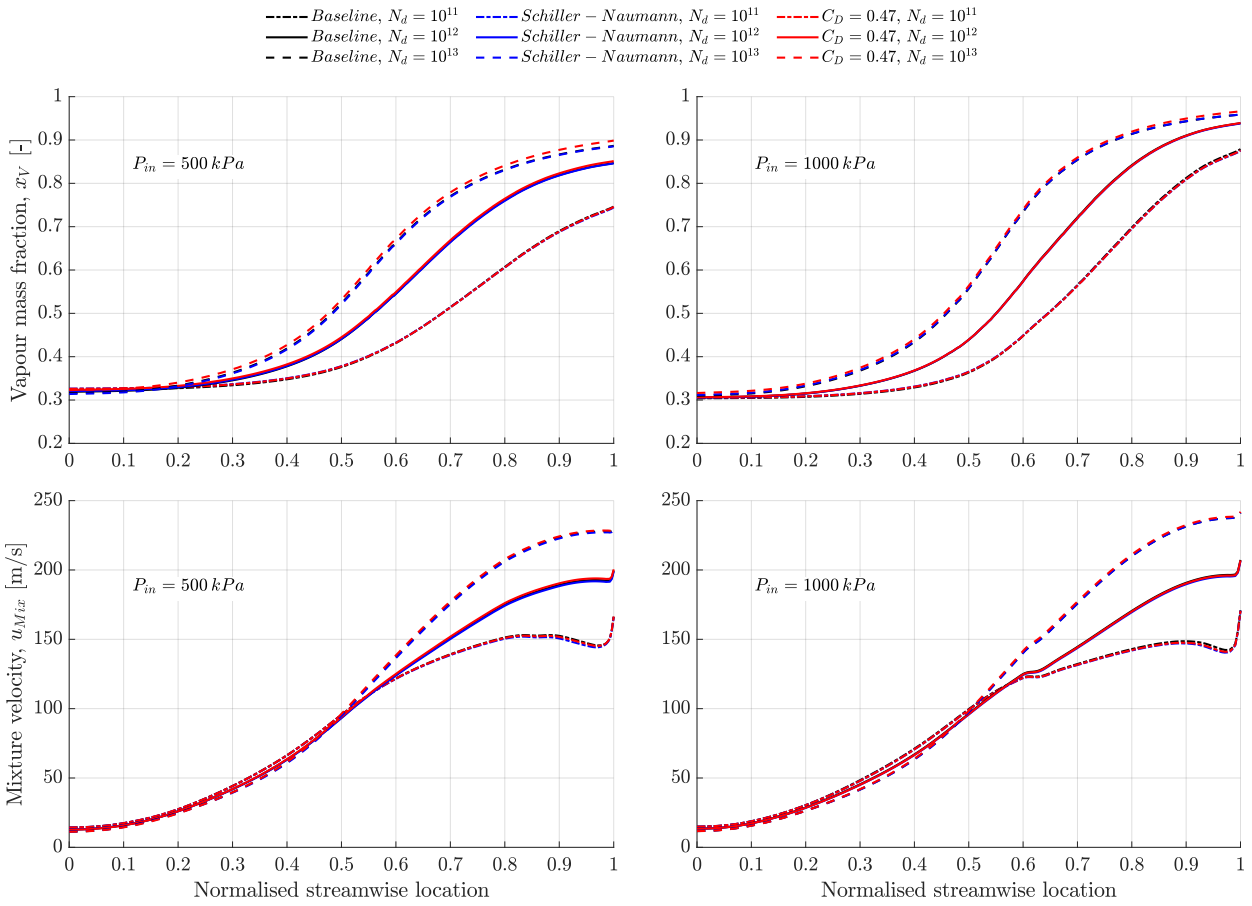


Figure 5.11: Streamwise variation of average vapour mass fraction x_V and average mixture velocity u_{Mix} obtained using alternative drag models. The plot shows two expansion cases: the expansions from 500 and 1000 kPa with a fixed inlet vapour quality of 0.3.

had a greater effect on the phase distribution within the nozzle. Figure 5.13 illustrates the two-dimensional contours of vapour quality obtained with the investigated lift models for a droplet number of 10^{11}, where the lift force had the greatest impact on the flow. It appears that the lift force acts to shift the droplets adjacent to the wall towards the centre of the nozzle in the converging section. This results in a higher concentration of liquid close to the centreline of the nozzle. A similar effect was predicted by all three lift models, albeit slightly more pronounced in the baseline and Legendre-Magnaudet correlations. When the lift force was turned off, the liquid core flow was visibly reduced and the liquid layers adjacent to the walls appeared to be attached to the walls upstream of the throat. Having said that, the liquid core flow is still evident downstream of the throat. The employed phase-change model can theoretically model condensation, which could explain the elevated liquid fraction in the core of the nozzle. However, further investigation of the solution demonstrated that the interphase mass-transfer has only occurred from the liquid to the vapour phase throughout the entire fluid domain. The temperature field of the liquid phase has also been assessed, indicating that liquid remained superheated throughout the expansion. Therefore, it is suspected that the liquid core flow is related to mechanical non-equilibrium, and it is thought to

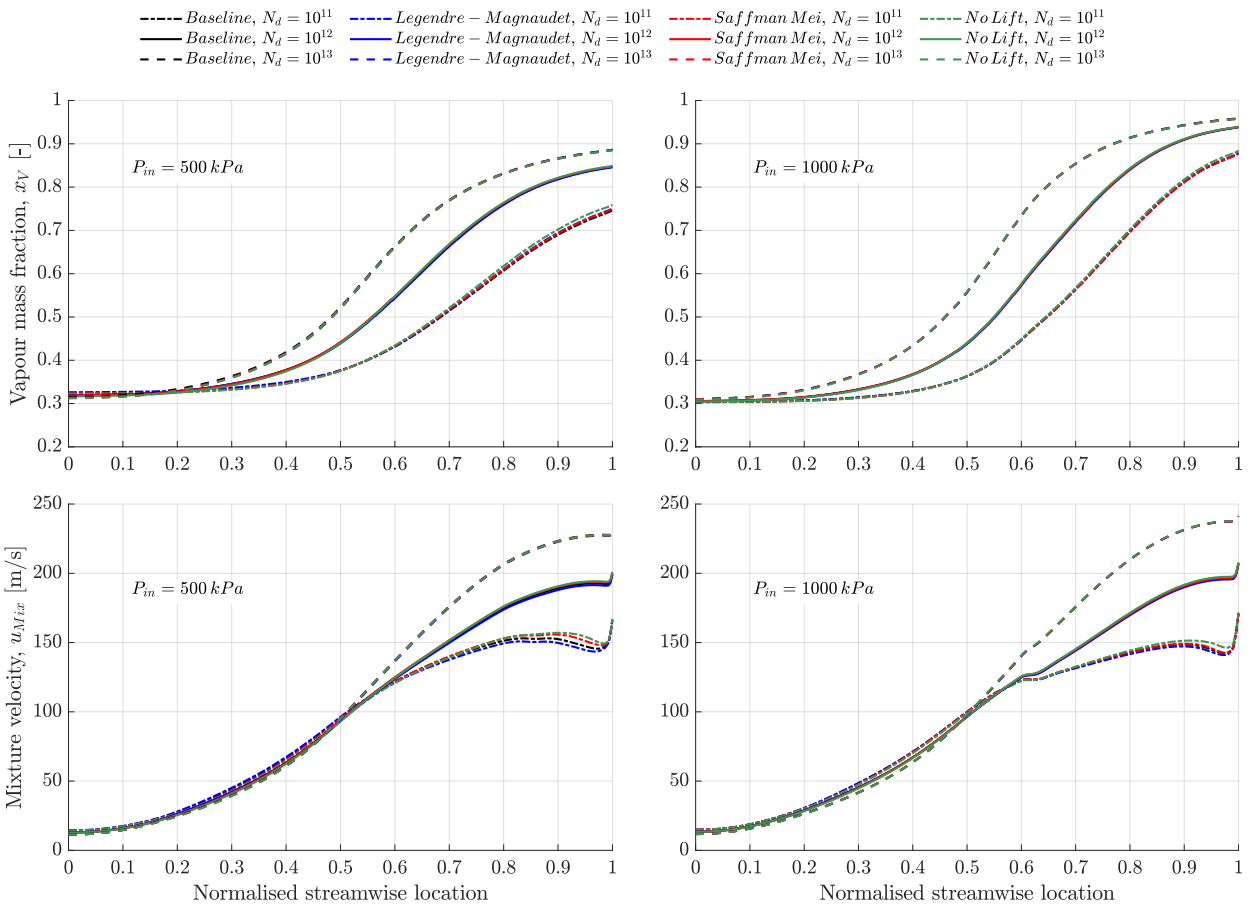


Figure 5.12: Streamwise variation of average vapour mass fraction x_V and average mixture velocity u_{Mix} obtained using alternative lift models. The plot shows two expansion cases: the expansion from 500 and 1000 kPa with inlet quality of 0.3.

be the effect of vapour adjusting its flow direction to the shape of the nozzle in the diverging section. In other words, following the throat, the vapour expands outward of the centreline, whereas liquid droplets, having much higher inertia, tend to remain on their flow path. This eventually leads to an increased liquid concentration in the centre of the nozzle despite no condensation occurring in that area. As the flow approaches the nozzle outlet, the deviation between the investigated models diminishes and the phase pattern looks fairly similar in all the cases. Generally, these observations apply to both pressure levels, but the lift effects are slightly more pronounced at low pressures. This could be related to a larger density difference between the phases at low pressures, which results in greater inhomogeneity of the two-phase flow. The observed lift effects were less significant at higher droplet numbers characterised by smaller droplets.

Figure 5.14 shows the average streamwise variation of x_V and u_{Mix} for the three turbulent dispersion correlations and for the model with the turbulent dispersion force turned off. It is observed that the streamwise profiles practically overlap with negligible discrepancy between the models. With the maximum deviation in x_V and u_{Mix} profiles of about 0.86 and 1.44%, the turbulent dispersion is considered to be of secondary importance in the

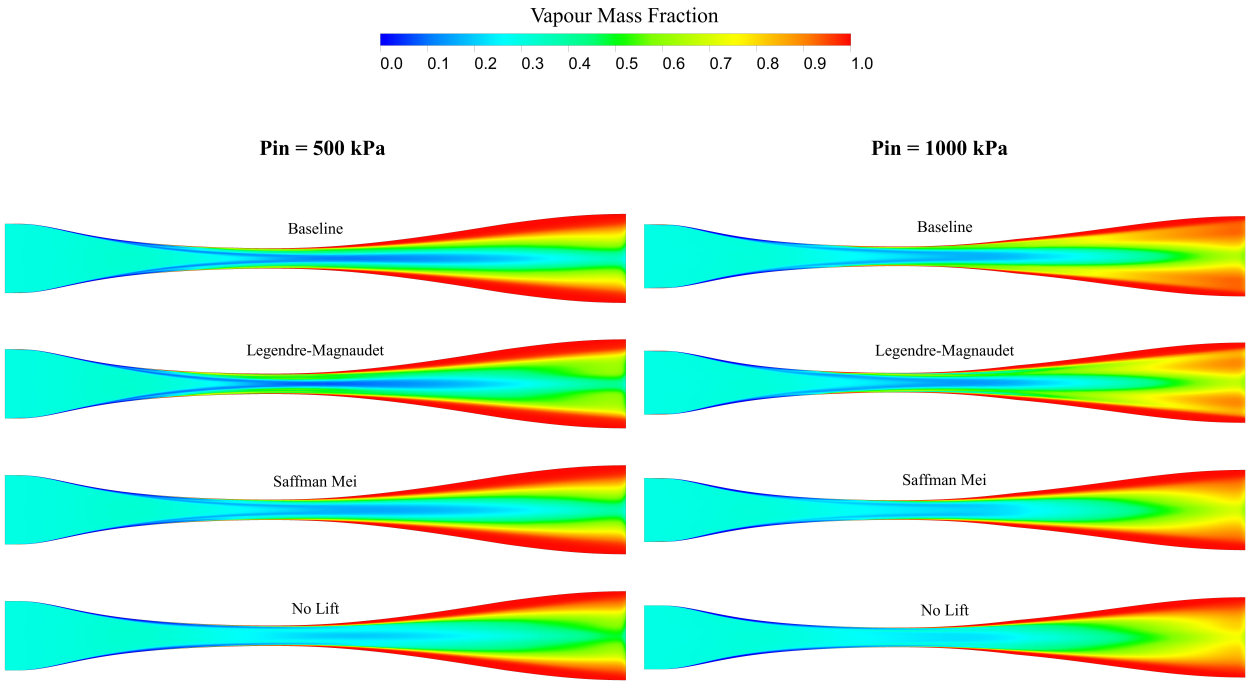


Figure 5.13: Two-dimensional contours of vapour mass fraction x_V obtained using alternative lift models. The contours illustrate the expansions from 500 kPa (left) and 1000 kPa (right), with an inlet quality of 0.3 and a droplet number of 10^{11}.

wet-to-dry expansion. The two-dimensional contours of the vapour mass fractions were also examined, but the turbulent dispersion had very little impact on the phase distribution compared to the lift models.

5.7.4 Sensitivity to heat-transfer models

To assess how the solution is affected by the type of heat-transfer models employed, average streamwise variation of vapour mass fraction and phase temperatures were investigated. Figure 5.18 shows how the average x_V varies between the three Nusselt number correlations applied to estimate the heat-transfer rate between the liquid droplets and the liquid-vapour interface. First, much higher discrepancies between the correlations can be observed compared to the momentum-transfer models. The primary resistance to heat transfer lies on the liquid side of the interface; therefore, Nu_L was expected to have a significant effect on the vapourisation rate. The difference between the Brown correlation used in the baseline setup and the assumption of constant $Nu_L = 16$ is not as significant as in the case of $Nu_L = 6$. For the expansion from 500 kPa, the Brown correlation estimates Nu_L to be between 9 and 14 at $N_d = 10^{11}$, with the highest values in the diverging section where the liquid reaches the maximum superheat level. For smaller droplets, the liquid superheating and the Nusselt number are typically lower, between 9 and 11 at $N_d = 10^{12}$, and between 9 and 10 at $N_d = 10^{13}$. Similar was observed in the 1000 kPa expansion, with the Nu_L values slightly higher, reaching approximately 15 at $N_d = 10^{11}$. This explains why the difference between the Brown model and $Nu_L = 16$ is smaller compared to $Nu_L = 6$. The constant Nusselt

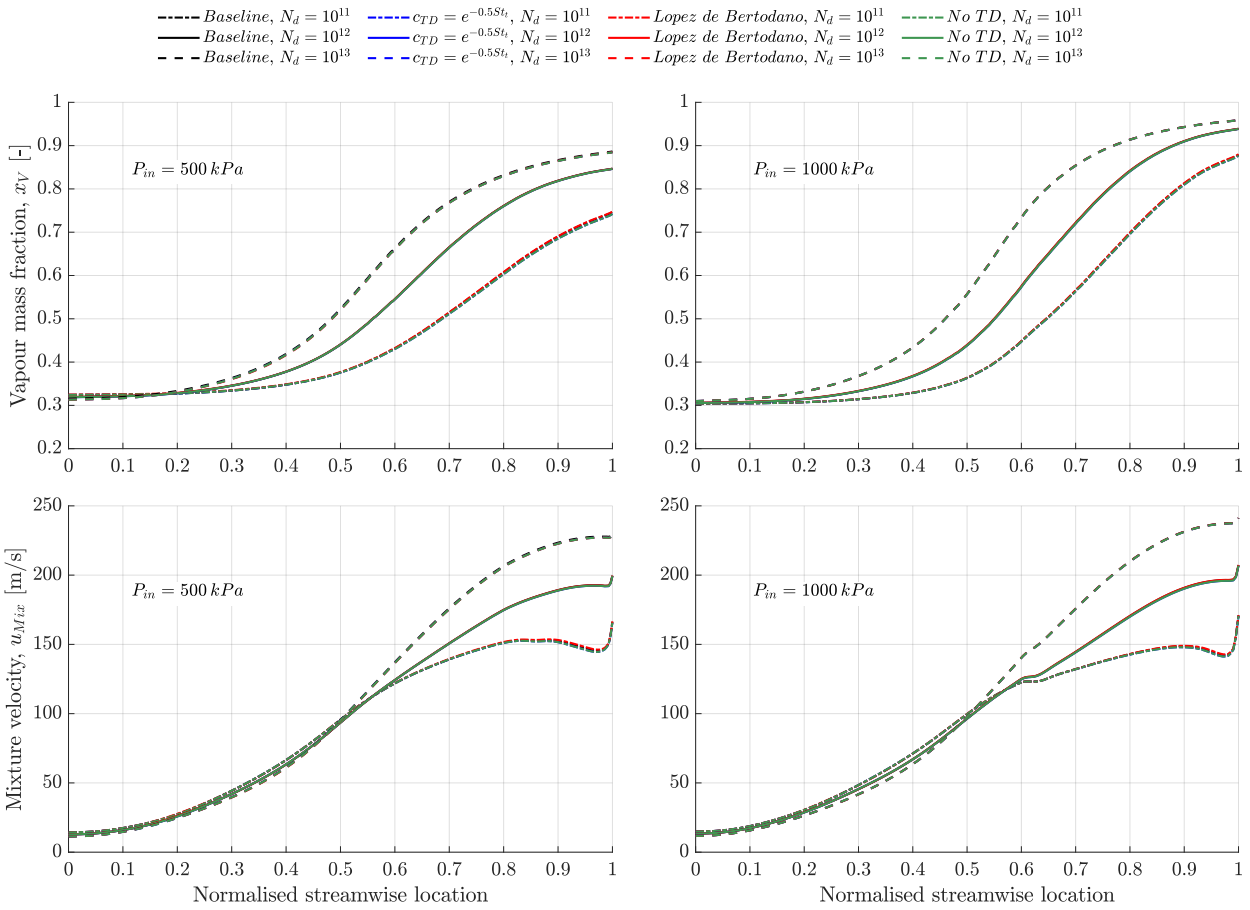


Figure 5.14: Streamwise variation of average vapour mass fraction x_V and average mixture velocity u_{Mix} obtained using alternative turbulent dispersion models. The plot shows two expansion cases: the expansion from 500 and 1000 kPa with inlet quality of 0.3.

number of 6 was derived based on a heat-transfer analysis in a solid sphere. When it comes to fluid particles, the heat-transfer rate is likely to be enhanced by effects such as inner circulation. Therefore, it is reasonable to assume that the Nusselt number would be higher than 6 for bubbles or droplets, which is in line with the predictions of the baseline Brown model.

The maximum percentage difference in x_V between the baseline model and $Nu_L = 16$ was found for $P_{in} = 500kPa$ and $N_d = 10^{12}$, and was around 5.3%. The maximum difference for the remaining expansions was typically between 3-5%. The maximum deviation increases to about 9% when Nu_L is set to 6 and corresponds to $P_{in} = 500kPa$ and $N_d = 10^{11}$. Something peculiar can be noticed in that for a droplet number of 10^{12} the outlet vapour mass fraction for $N_L = 6$ eventually reaches a value similar to those predicted by the Brown correlation and $Nu_L = 16$. One possible explanation is that smaller Nusselt numbers cause the droplets to develop a higher superheat level, which in turn accelerates the heat transfer in the diverging section of the nozzle.

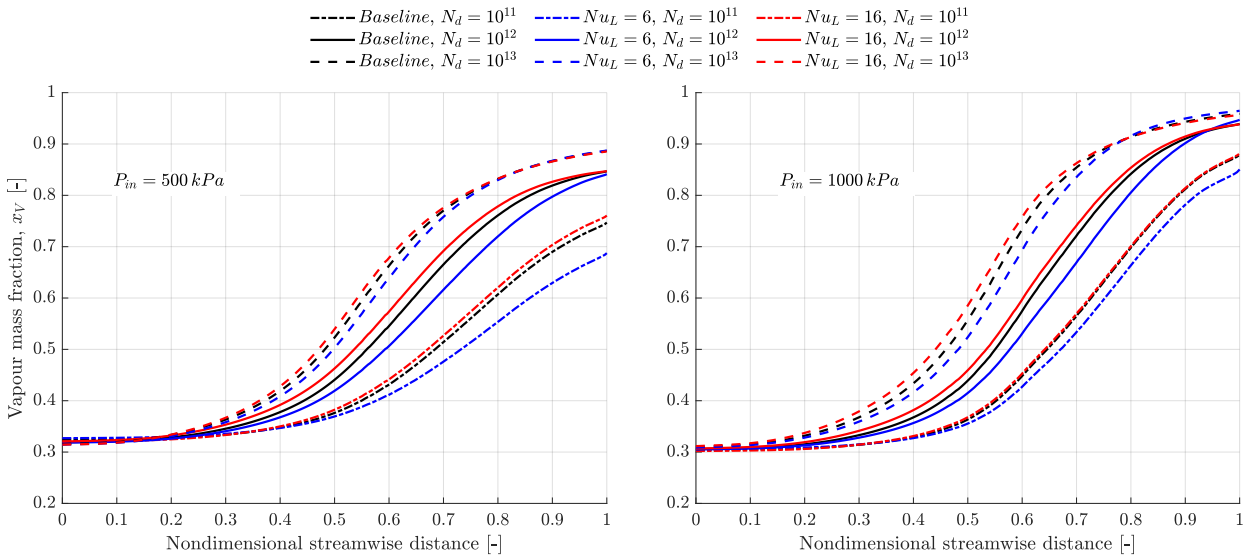


Figure 5.15: Streamwise variation of average vapour mass fraction x_V obtained using alternative models for predicting heat-transfer rate on the liquid side of the interface. The plot shows two expansion cases: the expansion from 500 and 1000 kPa with a fixed inlet vapour quality of 0.3 and a droplet number of 10^{11}.

To illustrate the effect of the liquid heat-transfer coefficient on the phase pattern, the two-dimensional contours of vapour quality are plotted in Fig. 5.16. The contours generated with the baseline model and $Nu_L = 16$ are practically identical, which is also reflected in a small difference in the average vapour quality calculated at the nozzle outlet ($x_{V,out}$) - 0.013 for $P_{in} = 500\,kPa$ and 0.001 for $P_{in} = 1000\,kPa$. The main difference between the Brown correlation and $Nu_L = 6$ is that the liquid core vapourises slightly slower at $Nu_L = 6$, which results in a decrease in outlet vapour quality from 0.751 to 0.691 for $P_{in} = 500\,kPa$, and from 0.896 to 0.874 for $P_{in} = 1000\,kPa$. Overall, the phase-change pattern is weakly affected by the type of model used to predict the heat-transfer rate between the droplets and the interface.

Lastly, the effect of the liquid heat-transfer model on the average variation of phase temperatures was plotted in Fig. 5.17. Due to the high surface area-to-volume ratio, large droplets ($Nd = 10^{11}$) have reduced capability to cool down by exchanging heat with the surrounding vapour. For such large droplets, the liquid temperature remains approximately constant within the first two-thirds of the nozzle length. Only in the late stage of the expansion does the heat-transfer model begin to play a role, where the liquid superheat level accelerates the heat transfer and the droplets drop in temperature. As the droplet number is raised to $N_d = 10^{12}$, the liquid phase cools down faster and the heat-transfer model has a greater effect on its temperature. For high droplet numbers in the order of 10^{13} liquid droplets can exchange heat more effectively with the interface, and the type of heat-transfer model is again less significant. The variation in vapour temperature is practically unaffected by the heat-transfer coefficient on the liquid side.

The last interphase models investigated in this sensitivity analysis concern the heat-transfer rate between the continuous vapour phase and the liquid-vapour interface. Figure **??** illus-

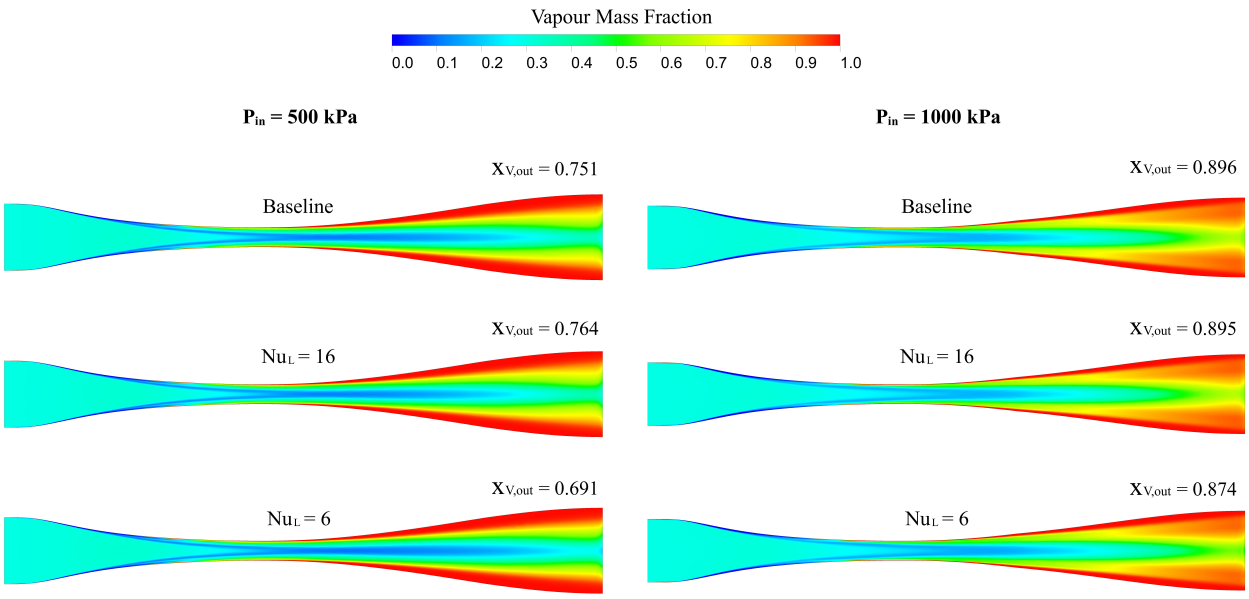


Figure 5.16: Two-dimensional contours of vapour mass fraction x_V obtained using different approach to modelling heat transfer between liquid droplets and the liquid-vapour interface. The contours illustrate the expansions from 500 kPa (left) and 1000 kPa (right), with an inlet quality of 0.3 and a droplet number of 10^{11}; Nu denotes Nusselt number on the liquid side of the interface. The values $x_{V,out}$ reported in the figure denote the average vapour quality calculated at the nozzle outlet.

trates the variation of x_V for the two investigated correlations applied to estimate the Nu_V. The Wolfert model predicts slightly higher vapourisation rates, which is considered to be the result of including the effect of vapour superheating that can be significant in the wet-to-dry expansion. The difference in the x_V profiles is relatively small, below a few percent, which is consistent between the simulated droplet numbers and the inlet pressures. Generally, this small deviation was expected since the main thermal resistance is on the liquid side. Figure 5.19 illustrates the temperature variations predicted by the two models, which indicates that the vapour heat-transfer model has a negligible impact on phase temperatures.

5.7.5 Summary of the sensitivity study

In summary, the solution was found to be relatively insensitive to the type of interphase models used to estimate the interfacial drag, lift, and turbulent dispersion forces. Among these effects, the lift appears to have the greatest influence on the average flow properties and phase distribution inside the nozzle. Having said that, any of the three investigated lift models predicted a fairly similar phase pattern near the nozzle outlet. When the average streamwise variation of vapour mass fraction and mixture velocity are concerned, the maximum relative deviation from the baseline model was typically below a few percent.

Similarly to the momentum-transfer models, the solution was weakly affected by the type of correlation applied to predict the heat-transfer rate between the vapour and the interface. The interphase model that had the greatest influence on the two-phase flow was that used to predict the heat-transfer rate between the droplets and the interface. The maximum devia-

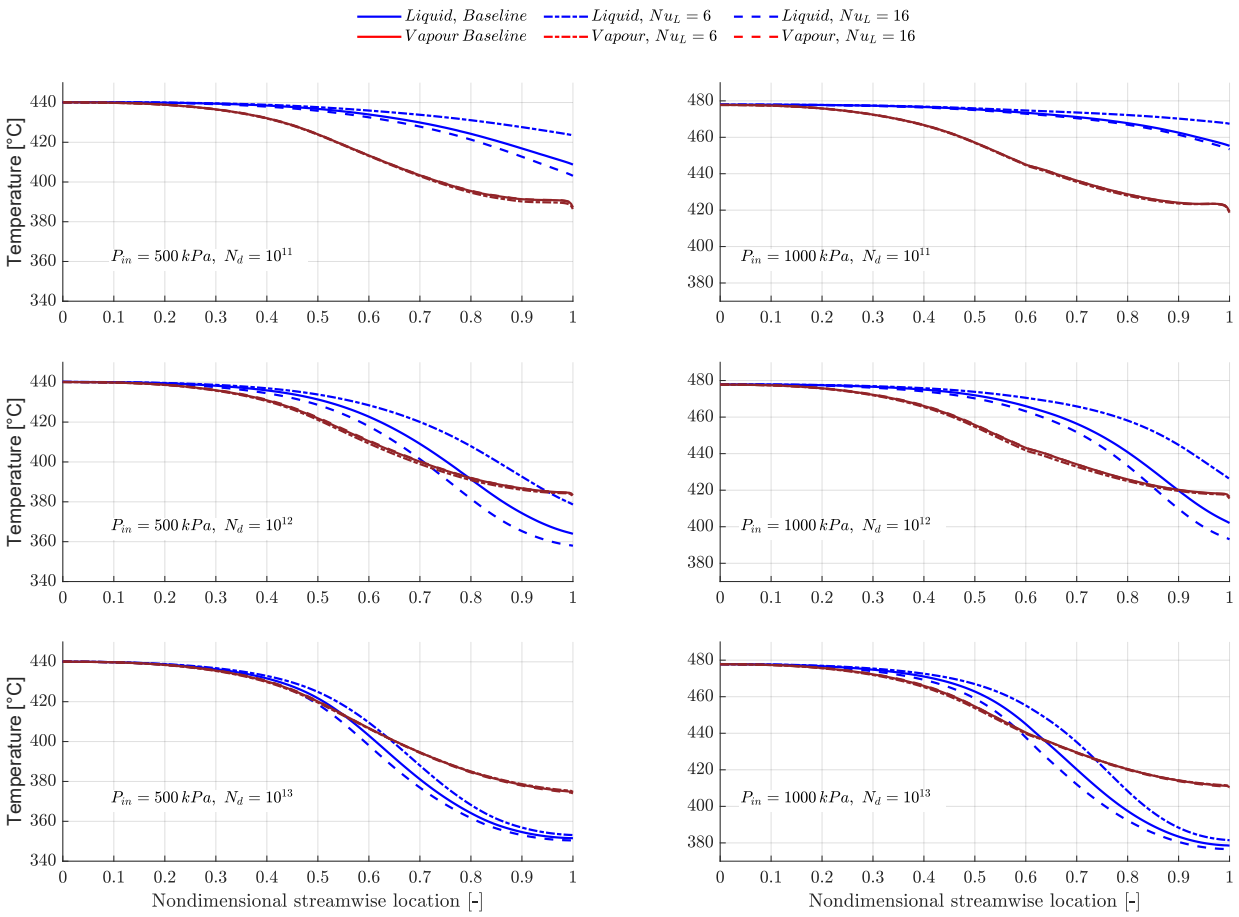


Figure 5.17: Streamwise variation of liquid and vapour temperatures obtained using alternative models for predicting heat-transfer rate on the liquid side of the interface. The plot shows two expansion cases: the expansion from 500 and 1000 kPa with a fixed inlet vapour quality of 0.3 and a droplet number of 10^{11}.

tion in vapour mass fraction relative to the baseline model corresponded to the assumption of a constant liquid Nusselt number of 6, and was around 9 %. This deviation is noticeable, but it is not considered very large. Furthermore, two-dimensional vapour mass fraction contours demonstrated that all of the liquid heat-transfer models predicted a very similar phase change pattern. The most affected parameter was the liquid temperature, especially at intermediate droplet numbers.

In conclusion, the main characteristics of the wet-to-dry expansion remained consistent across the alternative interphase models, and none of them drastically affected the phase-change process, either qualitatively or quantitatively. Therefore, the results of the sensitivity study give further assurance in the reliability of the baseline setup as far as the interphase models are concerned.

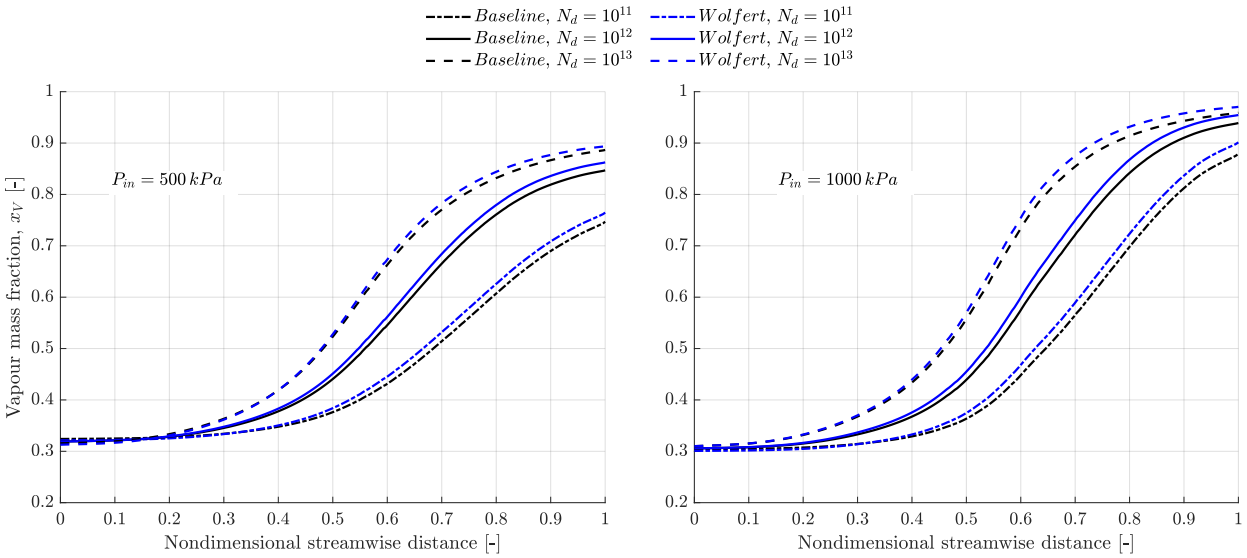


Figure 5.18: Streamwise variation of average vapour mass fraction x_V obtained using alternative models for predicting heat-transfer rate on the vapour side of the interface. The plot shows two expansion cases: the expansion from 500 and 1000 kPa with a fixed inlet vapour quality of 0.3.

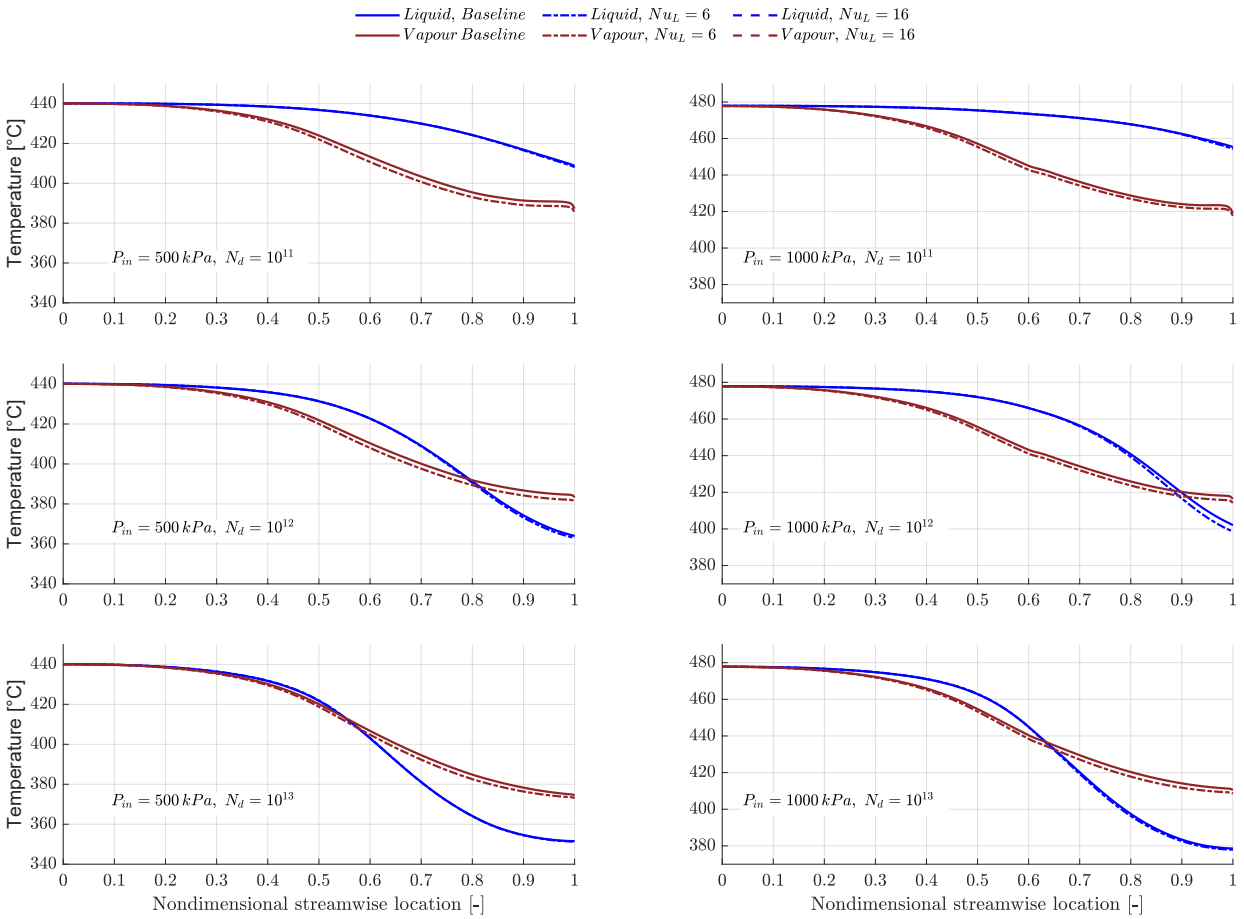


Figure 5.19: Streamwise variation of liquid and vapour temperatures obtained using alternative models for predicting heat-transfer rate on the vapour side of the interface. The plot shows two expansion cases: the expansion from 500 and 1000 kPa with a fixed inlet vapour quality of 0.3 and a droplet number of 10^{11}.

5.8 Parametric study results

This section presents the results of the numerical simulations performed for the twelve expansion cases depicted in Fig. 5.4. The influence of inlet conditions and droplet number on the vapourisation rate and the significance of non-equilibrium effects are discussed. The results also give insight into the uniformity of the flow under different operating conditions. To understand the following discussion, one should remember that higher droplet numbers are equivalent to a higher number of smaller droplets, whilst lower droplet numbers represent fewer larger droplets for a given volume fraction of liquid. Hence, the terms "high droplet number" and "small droplets" or "low droplet numbers" and "large droplets" are used interchangeably.

5.8.1 Mixture vapourisation

All the expansion cases were designed under the assumption of a homogeneous-equilibrium flow, which predicted full vapourisation in each case. Therefore, the first comparison aims to investigate whether the wet-to-dry transition can be achieved when non-equilibrium effects are considered. Figures 5.20- 5.23 illustrate the streamwise variation of the average vapour mass fraction x_V for all the investigated boundary conditions and droplet numbers.

It is clear from Figs. 5.20- 5.23 that N_d has a significant impact on the vapourisation rate, especially at low inlet vapour qualities. If $N_d \geq 10^{13}$, one can expect near-dry outlet conditions for any inlet quality above 30%, provided that the inlet pressure is above 1000 kPa. For lower inlet qualities, the model predicted a liquid mass fraction of 5 to 10 % at the outlet of the nozzle. Reducing P_{in} to 750 kPa and maintaining $N_d = 10^{13}$, a near-dry flow was predicted only for $x_{V,in} \geq 0.5$, while for $x_{V,in} \leq 0.3$ the fluid leaving the nozzle had considerable amount of liquid present, approximately 10 to 15% by mass. Bringing the inlet pressure down to 500 kPa, while maintaining $N_d = 10^{13}$, $x_{V,out}$ higher than 90% was only predicted to happen for the expansion from $q_{V,in} \geq 0.5$. With N_d reduced to 10^{12}, the phase-change pattern remains similar, but the vapour mass fraction at the nozzle outlet is typically between 4 to 8% lower than for $N_d = 10^{13}$. Near-dry conditions for N_d of 10^{12} are only expected at inlet pressures above 1000 kPa and inlet qualities above 0.3. At lower pressures, $x_{V,out}$ is approximately between 80 and 90%. The vapourisation rate decreases more significantly when N_d is lowered to 10^{11}. For lower operating pressures (with P_{in} at 500 and 750 kPa) the mixture was quite far from dry conditions at the nozzle outlet with a significant amount of liquid present for all inlet vapour qualities. For the expansion from 1000 kPa, only in the case of a sufficiently high inlet quality of 0.5 or higher, the fluid is expected to reach a vapour mass fraction greater than 95%; the expansions from lower $q_{V,in}$ were associated with significant liquid mass fraction at the outlet of the nozzle. With P_{in} fixed at 1250 kPa, reducing the droplet number to 10^{11} had a little effect on the vapour mass fraction at the nozzle exit, as long as the inlet quality was above 0.3. At such conditions, almost complete mixture vapourisation was predicted for any of the droplet numbers studied, with the liquid mass fraction in the order of 2-3%.

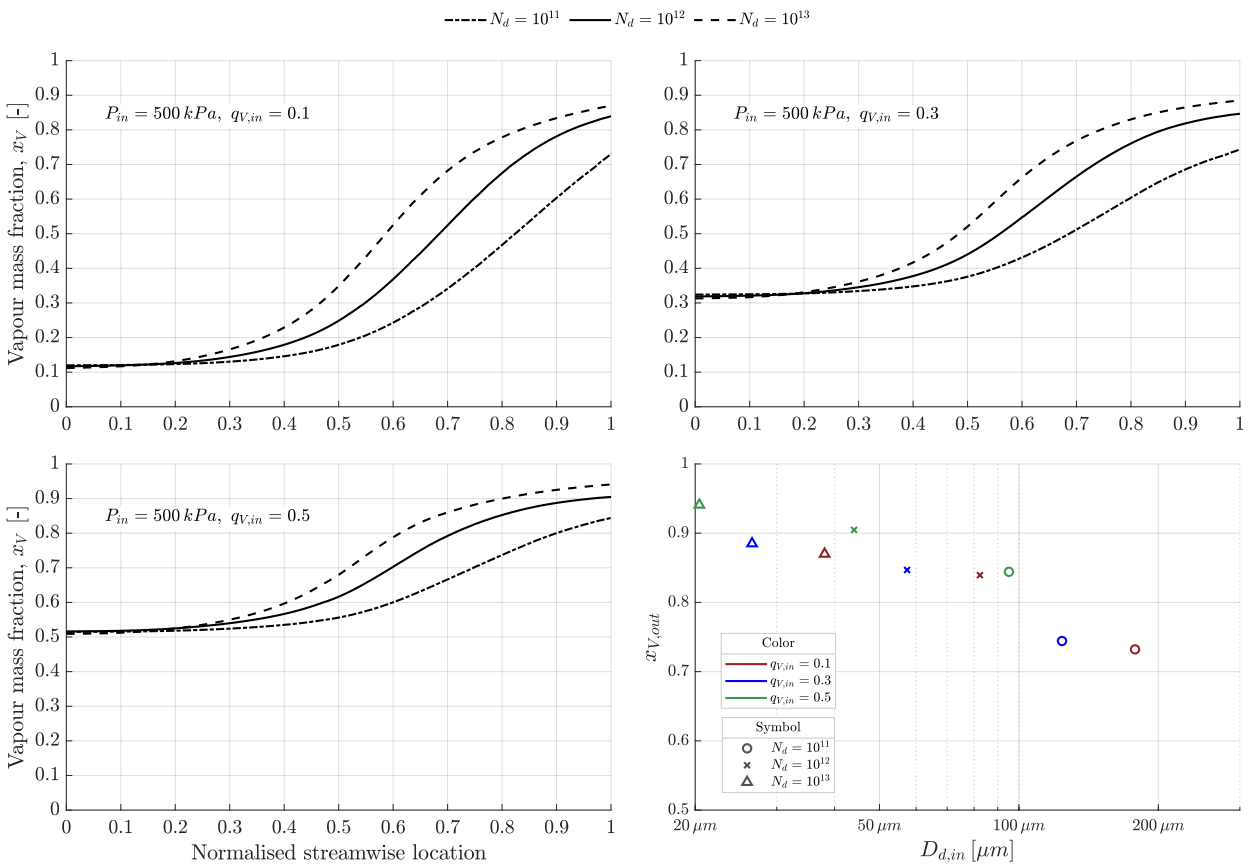


Figure 5.20: Streamwise variation of average vapour mass fraction x_V for the wet-to-dry expansion pressure from an inlet pressure of 500 kPa, and from three different vapour inlet qualities: 0.1, 0.3 and 0.5. The variation of x_V for each expansion case has been shown for three different droplet density numbers N_d: 10^{11}, 10^{12} and 10^{13}.

Referring to the droplet number, it may be difficult to visualise what sort of droplet size each simulated case corresponds to. The plot in the bottom right corner of Figs. 5.20-5.23 illustrates the relationship between the inlet droplet diameter $D_{d,in}$ and the outlet vapour mass fraction $x_{V,out}$ for all the investigated cases. First, it can be observed that the initial droplet size range corresponding to $N_d = 10^{11}$ is around 100-200 µm. Having $D_{d,in}$ in that size range results in incomplete vapourisation of the mixture with a relatively high liquid mass fraction at the outlet (except for the expansions from the highest pressure of 1250 kPa and inlet quality above 0.3). For $N_d = 10^{12}$, the initial droplet size range is reduced to around 20-50 µm and the mixture vapourises more effectively, reaching a visibly higher outlet quality between 80-95%. For $N_d = 10^{13}$, the inlet diameter is in the range of 20-50 µm. For such small droplets, the mixture transitions more easily to dry vapour with $x_{V,out}$ typically between 85-95% for P_{in} at 500 and 750 kPa, and between 95-100% for P_{in} at 1000 and 1250 kPa.

Streamwise profiles of the average vapour mass fraction have been used as a means of assessing the flow capability to reach dry conditions at the nozzle outlet. Figure 5.24 illustrates the relationship between the inlet droplet diameter Dd, in and the average void fraction calculated at the outlet of the nozzle $\alpha_{V,out}$. The void fraction is simply defined as the volume

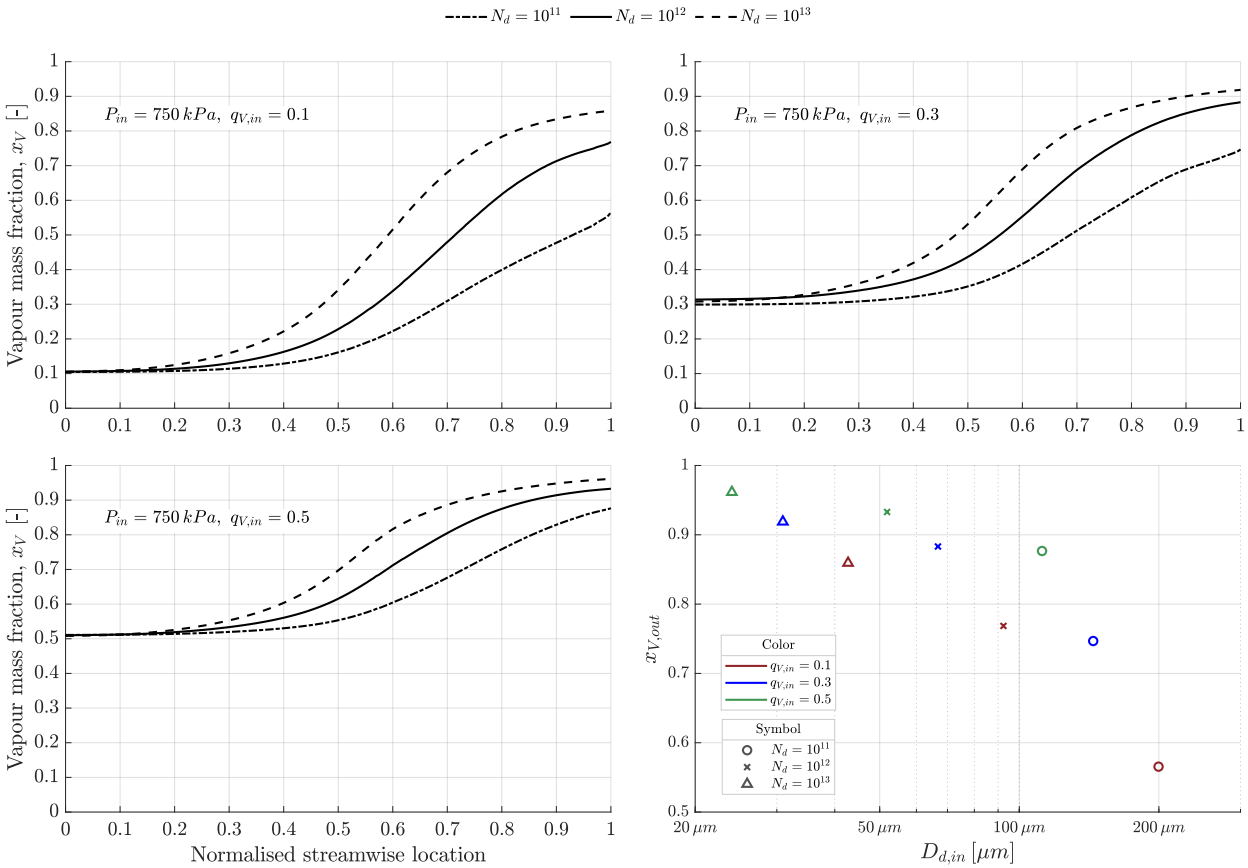


Figure 5.21: Streamwise variation of average vapour mass fraction x_V for the wet-to-dry expansion pressure from an inlet pressure of 750 kPa, and from three different vapour inlet qualities: 0.1, 0.3 and 0.5. The variation of x_V for each expansion case has been shown for three different droplet density numbers N_d: 10^{11}, 10^{12} and 10^{13}.

fraction of the vapour phase. For $D_{d,in}$ below 50 µm, the estimated void fraction was greater than 99.9 %, being very close to unity. Even for larger droplets, in the range of 50 to 180 µm, the void fraction remains above 99.5 %. Only for the largest droplets with an inlet diameter greater than 200 µm, the volume fraction of liquid exceeded 1%. Although the void fraction appears to decrease with droplet size, the trend is not as apparent as in the plots of the vapour mass fraction. This is due to a very large difference in the vapour and liquid densities at low exit pressures. Therefore, even if a significant amount of liquid is present by mass at the nozzle outlet, the void fraction remains high. For this reason, it was considered more suitable to use the variation of the vapour mass fraction when assessing whether the wet-to-dry transition can be achieved under given operating conditions.

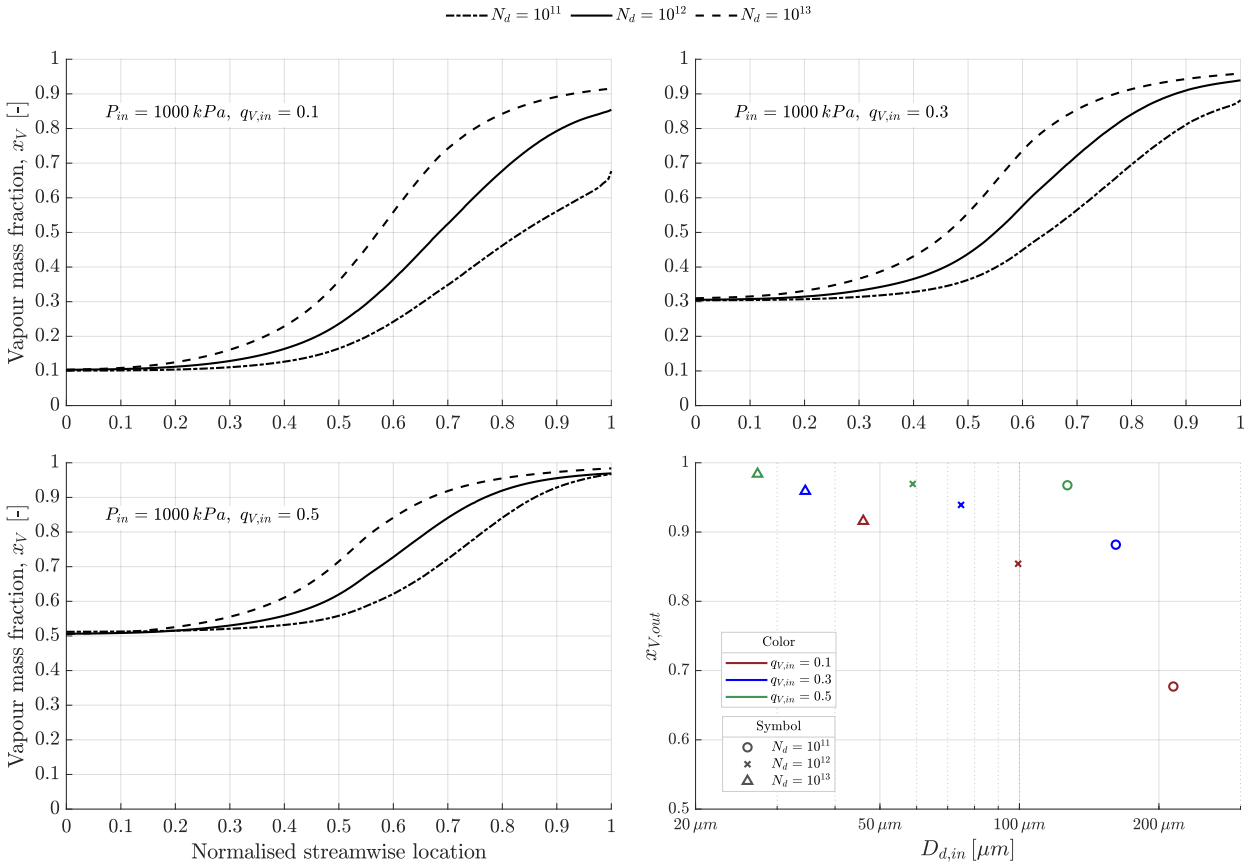


Figure 5.22: Streamwise variation of average vapour mass fraction x_V for the wet-to-dry expansion pressure from an inlet pressure of 1000 kPa, and from three different vapour inlet qualities: 0.1, 0.3 and 0.5. The variation of x_V for each expansion case has been shown for three different droplet density numbers N_d: 10^{11}, 10^{12} and 10^{13}.

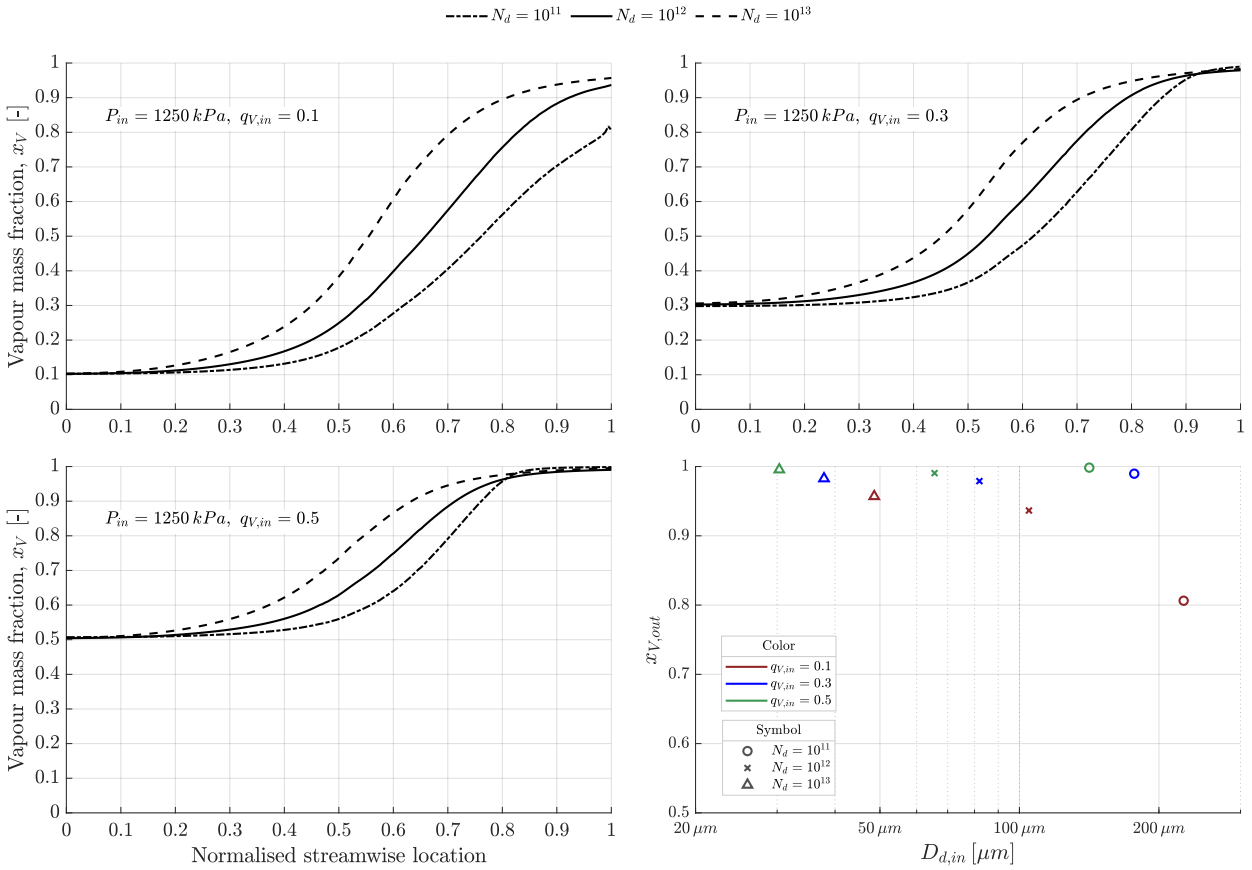


Figure 5.23: Streamwise variation of average vapour mass fraction x_V for the wet-to-dry expansion pressure from an inlet pressure of 1250 kPa, and from three different vapour inlet qualities: 0.1, 0.3 and 0.5. The variation of x_V for each expansion case has been shown for three different droplet density numbers N_d: 10^{11}, 10^{12} and 10^{13}.

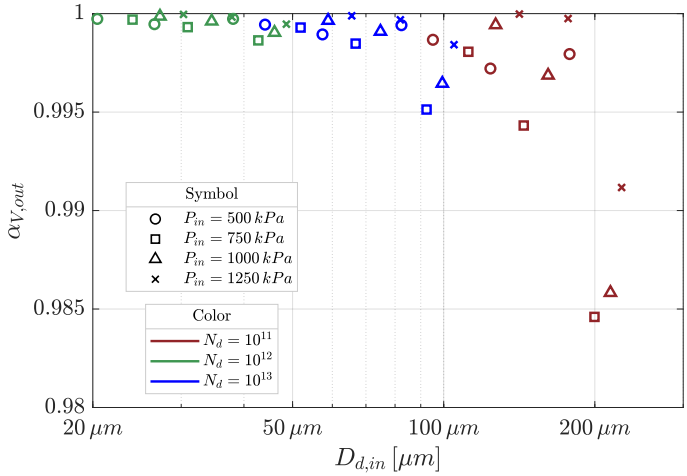


Figure 5.24: The relationship between the inlet droplet diameter $D_{d,in}$ and the outlet void fraction $\alpha_{V,out}$.

5.8.2 Significance of droplet size

This section discusses the significance of the droplet size, however, it should first be highlighted that the two-fluid model does not track the droplet interface, but rather employs a diffused interface approach, where the two phases are assumed to be interpenetrating continua. As such, the droplet diameter acts more like a tuning factor that modifies the interfacial area thereby the phase-change rate. More refined models based on the Lagrangian tracking and the volume-of-fluid approach could be applied in future studies to directly resolve the droplet interface and provide a more detailed description of the evaporation of distinct droplets in a representative flow-field. The reason for selecting the Eulerian-Eulerian approach over the Lagrangian approach for this particular study has been discussed in Section 3.2.

The results presented in Figs. 5.20-5.23 indicate that droplet size is the most dominant factor when it comes to the mixture vapourisation rate. The reason behind this becomes clear when analysing the heat-transfer rate between the droplet and the liquid-vapour interface:

$$\dot{Q}_L = \mathfrak{H}_L A_{int} \left(T_{int} - T_L\right) \tag{5.16}$$

Referring back to the definitions of the interfacial area and the Nusselt number (Chapter 4.1), the heat transfer between the droplet and the interface can be expressed as:

$$\dot{Q}_L = \frac{6 Nu_L k_L \alpha_L \left(T_{int} - T_L\right)}{D_d^2} \tag{5.17}$$

Knowing that Nu_L does not vary drastically between expansions, while the change in k_L is relatively small compared to the change in droplet diameter and liquid superheat level, the heat transfer on the liquid side $\dot{Q}_L$ for a given liquid volume fraction α_L will be proportional to the ratio of the liquid superheat to the square of droplet diameter:

$$\frac{\dot{Q}_L}{\alpha_L} \propto \frac{T_{sup,L}}{D_d^2} \tag{5.18}$$

where $T_{sup,L}$ is $T_{int} - T_L$. To visualise how the numerator and denominator of this expression vary with droplet number, these have been plotted in Fig.5.25. The plots show the ratios of these parameters obtained with $N_d = 10^{11}$ to the values obtained with $N_d = 10^{13}$ for the expansions from 500 and 1000 kPa and $x_{V,in} = 0.3$.

Looking at Fig.5.25, it becomes clear why the vapourisation enhanced when the droplet number is increased. The square of droplet diameter is at least an order of magnitude higher at $N_d = 10^{11}$, compared to $N_d = 10^{13}$. On the other hand, the liquid superheat level is only higher by a factor of 2-5 compared to $N_d = 10^{12}$ throughout most of the expansion. The heat transfer rate is therefore substantially reduced in case of $N_d = 10^{11}$ (Eq.5.18). One can notice a sudden increase in liquid superheat near the nozzle outlet; this occurs because for $N_d = 10^{13}$ liquid droplets vapourise quicker, diminish in size, and approach the saturation conditions. As the large droplets cannot effectively exchange heat in the case of $N_d = 10^{11}$,

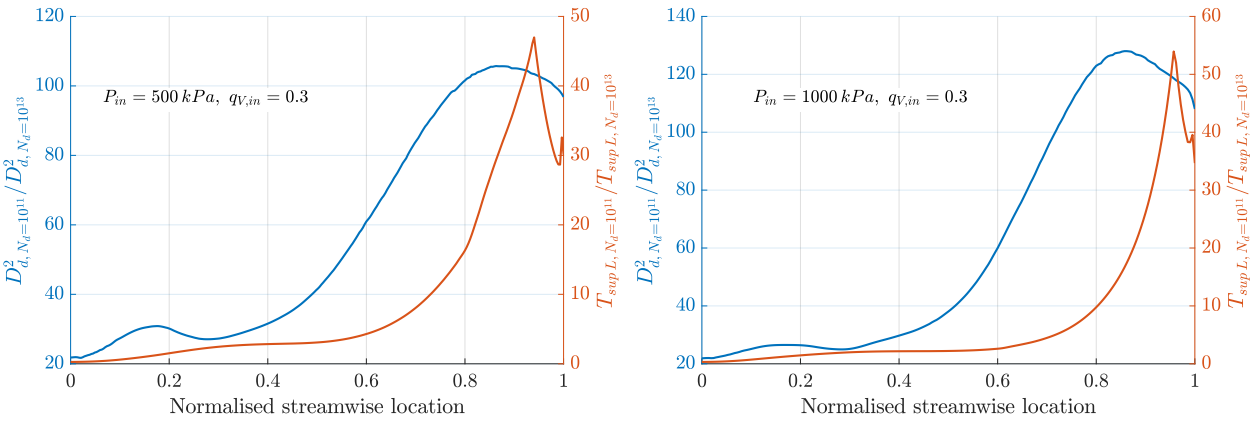


Figure 5.25: Streamwise variation of the ratios of droplet diameter square and liquid superheat; the lines represent the ratios of the values obtained with $N_d = 10^{11}$ to the values obtained with $N_d = 10^{13}$ for the expansions from 500 and 1000 kPa and inlet quality of 0.3.

they remain highly superheated throughout the expansion, causing the ratio of liquid superheat to rapidly increase near the outlet.

5.8.3 Design and simulated expansions

Figure 5.26 shows the comparison between the design and the simulated pressure and mixture profiles obtained for the expansions from 500 and 1000 kPa and an inlet vapour quality of 0.3. At both pressure levels, there is an evident underexpansion of the flow with the outlet pressure and the mixture velocity predicted by the CFD model significantly lower than the design values. This underexpansion is generally more pronounced at low droplet numbers, which is due to the increased velocity slip and thermal non-equilibrium associated with large droplets. At $N_d = 10^{11}$, the flow almost stagnates in the diverging section of the nozzle, presenting a very limited expansion in that area. This is a result of an insufficient increase in the flow area required in case non-equilibrium effects are a dominant feature of the flow. It is worth noting that for $P_{in} = 1000kPa$, there was a slight discontinuity in the pressure profile at a distance of approximately 60 %. To summarise, neglecting non-equilibrium effects in the nozzle design may potentially lead to significant flow underexpansion.

To provide a more quantitative measure of the the fluid's capability to expand to the design outlet conditions in all the investigated cases, two parameters have been introduced, namely β_p and β_u. The former is defined the ratio of the CFD-estimated pressure drop across the nozzle to the design pressure drop:

$$\beta_p = \frac{P_{in} - P_{out}}{P_{in} - P_{design,out}} \tag{5.19}$$

where $P_{design,out}$ is the design outlet pressure. The latter is defined as the ratio of the CFD-estimated mixture velocity to the design outlet velocity:

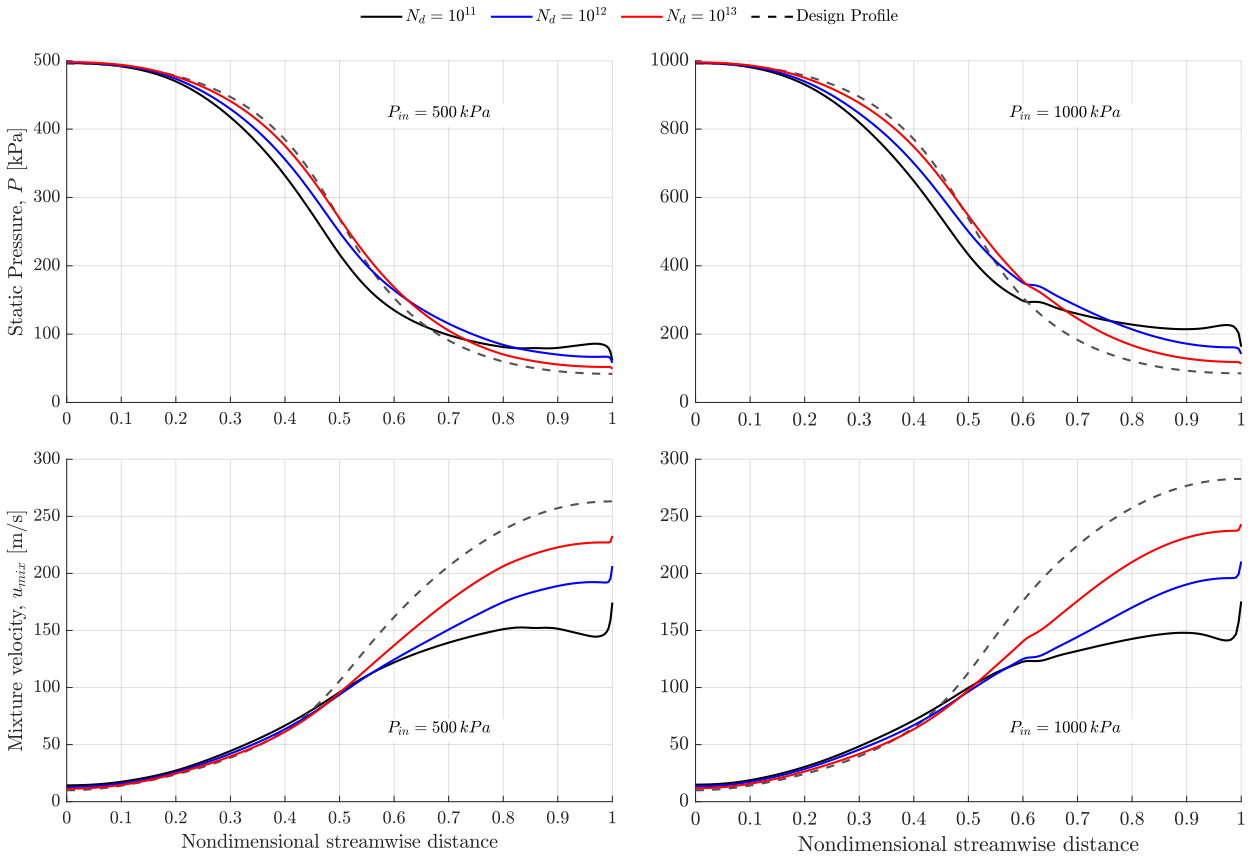


Figure 5.26: The comparison between the design and simulated pressure and mixture velocity profiles generated for the expansion from 500 and 1000 kPa and an inlet quality of 0.3.

$$\beta_u = \frac{u_{mix,out}}{u_{design,out}} \tag{5.20}$$

where $u_{design,out}$ is the design outlet velocity. Mass-averaged values of pressure and mixture velocity were used when calculating the β parameters. Referring back to Fig. 5.26, a sudden increase in mixture velocity at the nozzle outlet was observed at low droplet numbers. This sudden acceleration occurs because the flow underexpands but has to satisfy the static pressure condition imposed at the outlet. As discussed earlier, this underexpansion is due to the difference between the design outlet area and the area required to reach the design conditions if non-equilibrium effects are factored in. As will be shown in the following sections, the velocity slip can be very high in the wet-to-dry expansion. As a consequence, the average mixture velocity will be lower compared to the predictions of the homogeneous-equilibrium model used in the nozzle design tool. Therefore, non-equilibrium flows typically require larger flow area to expand to a given outlet pressure. Due to sudden acceleration at the nozzle outlet required to satisfy the imposed boundary conditions, the values for the outlet velocity and pressure were taken just before the actual nozzle outlet when assessing the flow capability to reach the design conditions.

Figure 5.27 illustrates the relationship between the inlet droplet diameter $D_{d,in}$ and the β

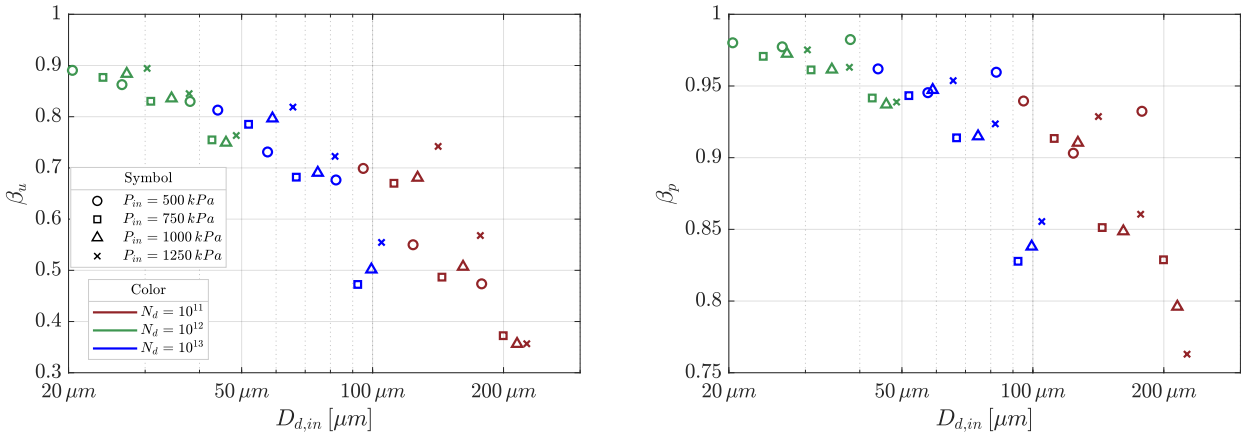


Figure 5.27: The relationship between the inlet droplet diameter $D_{d,in}$ and the β parameters; β_p is the ratio of the pressure drop to the design pressure drop, while β_u is the ratio of the mixture outlet velocity to the design outlet velocity.

parameters. As expected, the mixture velocity is significantly lower in expansions characterised by larger inlet droplets. The delayed vapourisation is associated with a higher overall mixture density and hence lower mixture velocities. For the same reason, the outlet pressure deviated from the design values. These effects gradually diminish as the droplet number increases. For $N_d = 10^{11}$ the fluid expands to approximately 40-70 % of the design outlet velocity. This increases to about 65-80% for $N_d = 10^{12}$, except for the lowest inlet quality, where the under-expansion is more severe. For the highest droplet number of 10^{13} the mixture reaches around 80-90% of the design velocity. The similar pattern in outlet pressure is observed, with about 75-95% under-expansion for larger droplets, which gradually diminishes as smaller droplets are expanded.

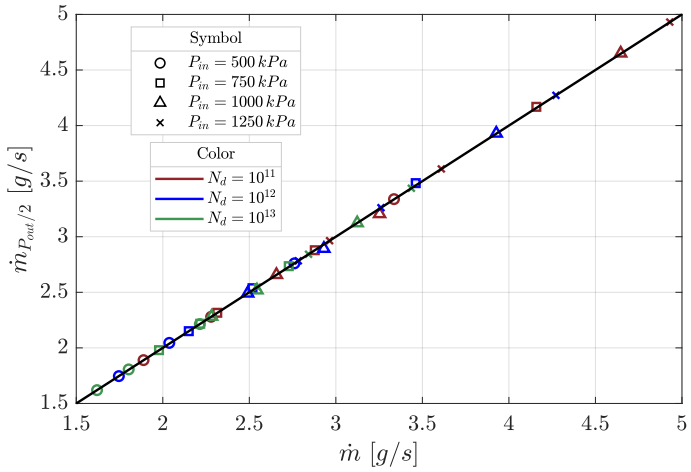


Figure 5.28: The relationship between the mass-flow rate obtained in the original CFD simulations ($\dot{m}$) and the mass-flow rate obtained with the outlet pressure reduced by a factor of 2 ($\dot{m}_{P_{out}/2}$). The black solid line represents the equality line where the mass-flow rates are identical, which indicates that the nozzle is choked.

Lastly, the effect of non-equilibrium effects on the mass-flow rate was studied by comparing the design and simulated mass-flow rate values. However, it was first investigated whether choking conditions were achieved in each of the investigated cases. Since in a choked nozzle further reduction of the outlet pressure should have no effect on the mass-flow rate, the CFD simulations were re-run with the outlet pressure reduced by a factor of 2 to investigate whether the mass-flow rate remained unchanged. Figure 5.28 shows the relationship between the mass-flow rate calculated in the original simulations ($\dot{m}$) and mass-flow rate obtained for an outlet pressure reduced by 50 % ($\dot{m}_{P_{out}/2}$). The black solid line is a line of equality between the original mass-flow rates and those obtained with the reduced outlet pressure; for choked nozzle the values obtained for the reduced outlet pressure should lie on that line. It is apparent that all the data points demonstrate a negligible deviation from the equality line, which indicates that the nozzle was choked under all of the operating conditions.

Figure 5.29 illustrates the relationship between the inlet droplet diameter and the estimated mass-flow rate by the CFD solver. The mass-flow rates estimated by the CFD solver were multiplied by the ratio of the design nozzle width (b in Fig. 5.5) to the thickness of the thin slab applied to perform two-dimensional simulations. In this way, the values were directly compared with the design mass-flow rate, which was fixed at 0.12 kg/s. It should be clarified that in a choked nozzle, the mass-flow rate depends on the inlet stagnation conditions, and therefore should vary from case to case. However, in the current study, the nozzle width was adjusted accordingly in the design process to keep the mass-flow rate constant at 0.12 kg/s. To understand the variation in the mass-flow rate, it should first be explained that for a given inlet pressure and droplet number, lower droplet diameters correspond to lower inlet vapour qualities in the plot shown in Fig. 5.29. Generally, larger droplets are associated with higher mass-flow rates. This is primarily due to the delayed phase change associated with a higher liquid content at the nozzle throat. It is in line with previous studies on the critical two-phase flow, where the authors reported that the homogeneous-equilibrium model underestimated the critical flow rate compared to the experimental observations [44, 132]. However, the mass-flow rate is also highly sensitive to the inlet vapour quality. Even if the droplets are comparable in size, expansions from lower inlet vapour qualities will be associated with significantly higher liquid content at the nozzle throat, as indicated in Figs. 5.20-5.23. This is why a sudden increase in the mass-flow rate can be observed in Fig. 5.29, which appears to be disproportional to the corresponding change in $D_{d,in}$. The percentage difference between the estimated and the design mass-flow rates for high vapour qualities or small droplets was between 10.4 and 38.3 %, whereas for lower vapour qualities the deviation could be extremely high, ranging from 44.1 to 105 %.

The discrepancy between the design and simulated outlet conditions emphasises the need for an appropriate nozzle design tool that can account for non-equilibrium effects, rather than using a homogeneous-equilibrium model to generate the nozzle, as was the case in this parametric study. However, it is worth repeating that since the main goal of this study was to provide further insight into the wet-to-dry expansion characteristics in a converging-diverging nozzle, rather than develop an optimal nozzle design technique, the nozzle design tool based on the homogeneous-equilibrium flow was deemed suitable for this study. In subsequent studies, focused on the nozzle optimisation, non-equilibrium design tools, such

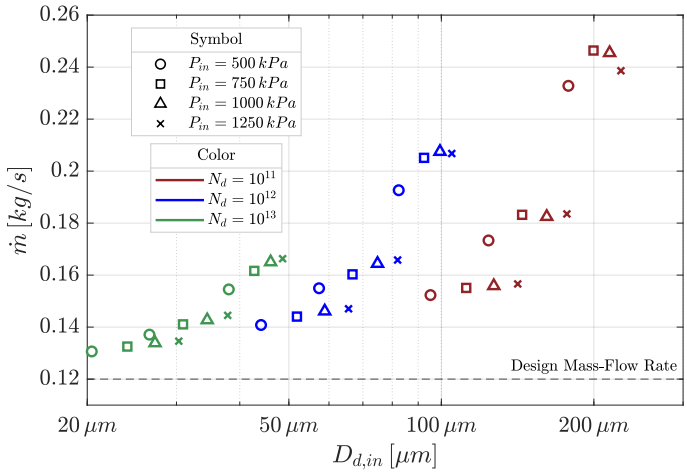


Figure 5.29: The relationship between the inlet droplet diameter $D_{d,in}$ and the mass-flow rate $\dot{m}$ obtained using the CFD model. The estimated mass-flow rate was multiplied by the ratio of the design nozzle width to the thickness of the thin slab applied to perform two-dimensional simulations. The dashed line represents the design-mass flow rate.

as the one developed by White [43], will be explored.

5.8.4 Significance of non-equilibrium effects

The results presented so far indicate that the two-fluid model predictions may seriously deviate from the homogeneous-equilibrium model results for low droplet numbers. Figure 5.30 explicitly shows the extent of mechanical and thermal non-equilibrium for the expansions from 500 kPa and 1000 kPa. The level of mechanical inhomogeneity is represented by a relative velocity slip $u_{slip,rel}$ which is the velocity slip normalised by mixture velocity: $u_{slip,rel} = (u_V - u_L)/u_{mix}$. Thermal non-equilibrium is simply expressed as the temperature difference between the liquid and vapour $(T_L - T_V)$. Looking at the average velocity slip (Fig.5.30) it is observed that the velocity slip increases significantly with the droplet number. For $N_d = 10^{13}$, $u_{slip,rel}$ the slip throughout most of the expansion is between 15-30% of the average mixture velocity. Reducing the droplet number to $N_d = 10^{12}$ and $N_d = 10^{11}$ increases the slip to about 25-45% and 45-65%, respectively. In absolute terms, the velocity difference is below 40 m/s for the highest droplet number, around 30-55 m/s for the intermediate droplet number and about 50-90 m/s for the lowest droplet number. It could therefore be concluded that mechanical non-equilibrium is significant for any droplet number and can become extremely high for $N_d \leq 10^{12}$. It should be noted that the relative slip is generally higher in the case of lower operating pressures. Looking at Figs.5.20-5.23 it can be seen that for the same droplet number, the expansion from higher pressure is associated with larger inlet droplet size. Therefore, one might expect that at the beginning of the expansion, the relative slip should be higher for the higher-pressure case. The inverse is observed, which is the effect of a smaller density difference between the vapour and liquid at elevated pressures. For example, the ratio of saturated-liquid to saturated-vapour densities at 500 kPa is about 22; this reduces to around 8 when the pressure is raised to 1000 kPa. The reduced density difference contributes to the improved mechanical homogeneity of the two-phase flow.

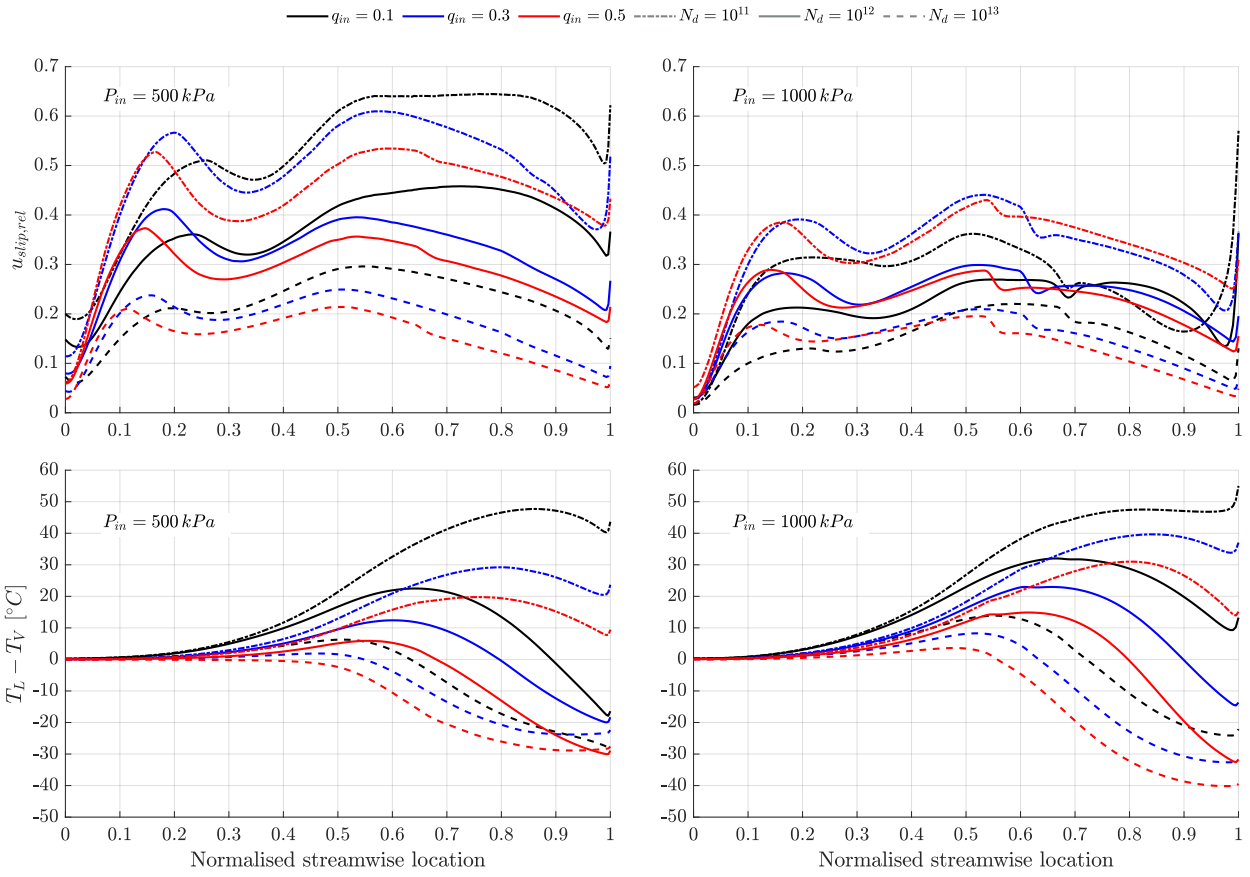


Figure 5.30: Streamwise variation of average relative velocity slip ($u_{slip,rel}$) and average thermal non-equilibrium ($T_L - T_V$) in the expansions from 500 kPa and 1000 kPa, with three inlet qualities $x_{V,in}$ of 0.1, 0.3 and 0.5 and three different droplet density number N_d of 10^{11}, 10^{12} and 10^{13}; $u_{slip,rel}$ is the velocity slip normalised by the mixture velocity, while $T_L - T_V$ is temperature difference between the liquid and vapour phases.

Concerning thermal non-equilibrium, it was expected that flows characterised by large droplets would have highly superheated liquid phase due to its reduced capability to give out heat to the interface and vaporise (see. Eq.5.18). This effect should gradually diminish as the droplet number is raised, expecting the liquid temperature to approach vapour temperature, reducing thermal non-equilibrium. This, to some extent, can be observed in Fig.5.30, where the liquid superheat for $N_d = 10^{11}$ remains relatively high throughout the expansion. On the other hand, thermal non-equilibrium becomes smaller when N_d is raised; however, one can see that in these cases, the temperature of liquid can fall below that of the vapour phase. The areas where the liquid temperature was significantly lower than that of vapour typically correspond to axial positions characterised by high vapour qualities, i.e. extremely low liquid volume fractions and very small droplets. These areas could represent superheated gas flows containing tiny droplets that did not manage to fully vapourise during expansion. Despite T_L being lower than T_V, evaporation continues as indicated by Figs.5.20 and 5.22. To better understand this phenomenon, one could refer back to Eq.4.21, and assume that vapour remains saturated throughout the expansion, i.e. $T_V = T_{int}$. Such an assumption

was made in previous numerical studies of flash boiling of water [41, 206]. As the fluid expands, the liquid is expected to become superheated before boiling initiates. This would then imply that the numerator of Eq.4.21 becomes negative when boiling takes place. In this study, T_V could not be fixed to the saturation conditions as this would prevent vapour from becoming superheated. Nevertheless, one should expect that the same rule applies to the wet-to-dry expansion, i.e. boiling is expected when the numerator of Eq.4.21 is negative. Therefore, even if $T_L < T_V$, but both phases remain superheated or the vapour develops sufficient superheat, the mixture would continue to evaporate, and the numerator of Eq.4.21 would remain negative. In summary, the regions where T_L remains above T_V can be thought of as the regions where superheated liquid droplets travel in cooler vapour, and vaporise giving off heat to the surrounding vapour. On the other hand, the regions where T_L drops below T_V can be thought of as the regions where tiny droplets travel in superheated vapour, and continue to vaporise being heated up by the surrounding hotter vapour. This explains the physical process of boiling in both conditions. It is worth to mention that in some cases both liquid and vapour phases were found to become superheated in early stages of the expansion. Since these areas would correspond to the two-phase regime under equilibrium conditions, it is expected that if the phases are given sufficient time they should reach the saturation conditions. At first, it may seem unclear how liquid and vapour could reach the saturation temperature by exchanging heat given that both are superheated with respect to the local saturation temperature. However, the interphase heat transfer will be accompanied by a simultaneous phase change, which is expected to affect the local saturation conditions. This can be easily understood when assuming that the two phases were to exchange heat under fixed volume conditions. In such a case, the mixture vapourisation accompanying the interfacial heat transfer would lead to an increase in the fluid pressure, and consequently in saturation temperature. In an open channel, like the converging-diverging nozzle, the phase change would not occur under fixed volume conditions and it would cause the fluid to expand. Nevertheless, the fact that the saturation conditions are not going to remain constant during interfacial heat exchange remains valid. As such, it is expected that if these aspects are factored in, the two phases should eventually be able to reach the saturation temperature even if both are superheated at beginning of the heat transfer process.

Given that mixture temperature at the inlet of the nozzle was approximately 167.1 and 204.8 °C for the inlet total pressure of 500 and 1000 kPa, the magnitude of thermal non-equilibrium shown in Fig. 5.30 can be considered rather large. For the lowest droplet number, $N_d = 10^{11}$, the temperature of liquid in the diverging section of the nozzle was approximately 20 to 50 °C higher compared to that of vapour. That difference dropped to around 10-30 °C for $N_d = 10^{12}$, however, liquid droplets became significantly cooler than the vapour near the outlet of the nozzle. This was further amplified in the expansion with $N_d = 10^{13}$, which presented limited liquid superheating, but displayed large negative temperature difference in the diverging section. With that being said, it should be remembered that the temperature difference is more important in the case of large droplets, as it signifies the inability of the liquid phase to give off heat and effectively vapourise. In case of small droplets, large temperature differences would typically correspond to the areas where extremely small liquid droplets travel in the superheated vapour - the areas of the void fraction approaching unity.

Overall, the results suggest that wet-to-dry expansion of the siloxane MM can be accompanied by large velocity and temperature difference, which implies that neither mechanical nor thermal non-equilibrium should be neglected in the analysis of such flows.

5.8.5 Flow uniformity

Apart from assessing average flow properties, it is also important to investigate whether the flow properties at a given streamwise location are uniform across the nozzle. Flow uniformity may be particularly important when the wet-to-dry nozzle forms a part of a turbine stator. For example, the overall vapour quality could be high, while a small amount of liquid concentrated in one area, in the form of a streak or film, could impinge on the rotor blades. This could possibly entail erosion issues, increased wear rates, and lead to performance deterioration.

Figure 5.31 shows the two-dimensional variations of vapour quality obtained for the expansions from 500 kPa and 1000 kPa, both with an inlet quality of 0.3. Although the two nozzles have different lengths, with the one designed for the 1000 kPa expansion being shorter, the longer nozzle has been scaled to facilitate easier visual assessment of the flow field. As the fluid is accelerated through the converging section of the nozzle, the flow is turned towards the nozzle core (i.e. the centre line of the nozzle). Liquid droplets, having higher density than the surrounding vapour, require more time to adjust to the changing flow direction (i.e., they are characterised by longer relaxation times), and instead of immediately adjusting to the main flow direction, droplets tend to continue along their flow path. This results in the accumulation of the liquid phase near the wall in the converging part of the nozzle. The situation is reversed past the throat; the flow is now being turned away from the nozzle core. For the same reasons described above, liquid droplets tend to continue on their path, creating a characteristic core flow region, as visible in Figure 5.31, while the area in the vicinity of the nozzle walls is mostly occupied by the vapour phase. The phase separation is more pronounced at lower N_d due to higher inertia of larger liquid droplets, which translates to longer relaxation times and reduced ability to follow the mean flow. As for the effect of the operating pressure, the separation appears to be more pronounced at lower pressures. The reason for this is two-fold; as discussed before, the density difference between the liquid and the vapour is higher at lower pressures, which enhances mechanical inhomogeneity. Moreover, the evaporation rate is higher in case of the 1000 kPa expansion, which means that droplets evaporate faster and are likely to be smaller at a given streamwise location compared to the 500 kPa expansion; smaller droplets have lower inertia, shorter relaxation times, and higher capability to follow the mean flow. In general, the lower the droplet number (or in other words the larger the droplets) and the lower the inlet pressure, the higher the flow non-uniformity in terms of the lateral separation of the two phases.

Figure 5.31 also shows the two-dimensional variations of mixture velocity. The velocity is relatively uniform in the converging section; velocity in that area is very low, and spatial uniformity is of little concern. The lateral variations in velocity become important in the diverging section; u_{mix} in the proximity of the wall is visibly higher than in the core of the nozzle. Generally, the velocity of the liquid phase is lower than that of the vapour due to

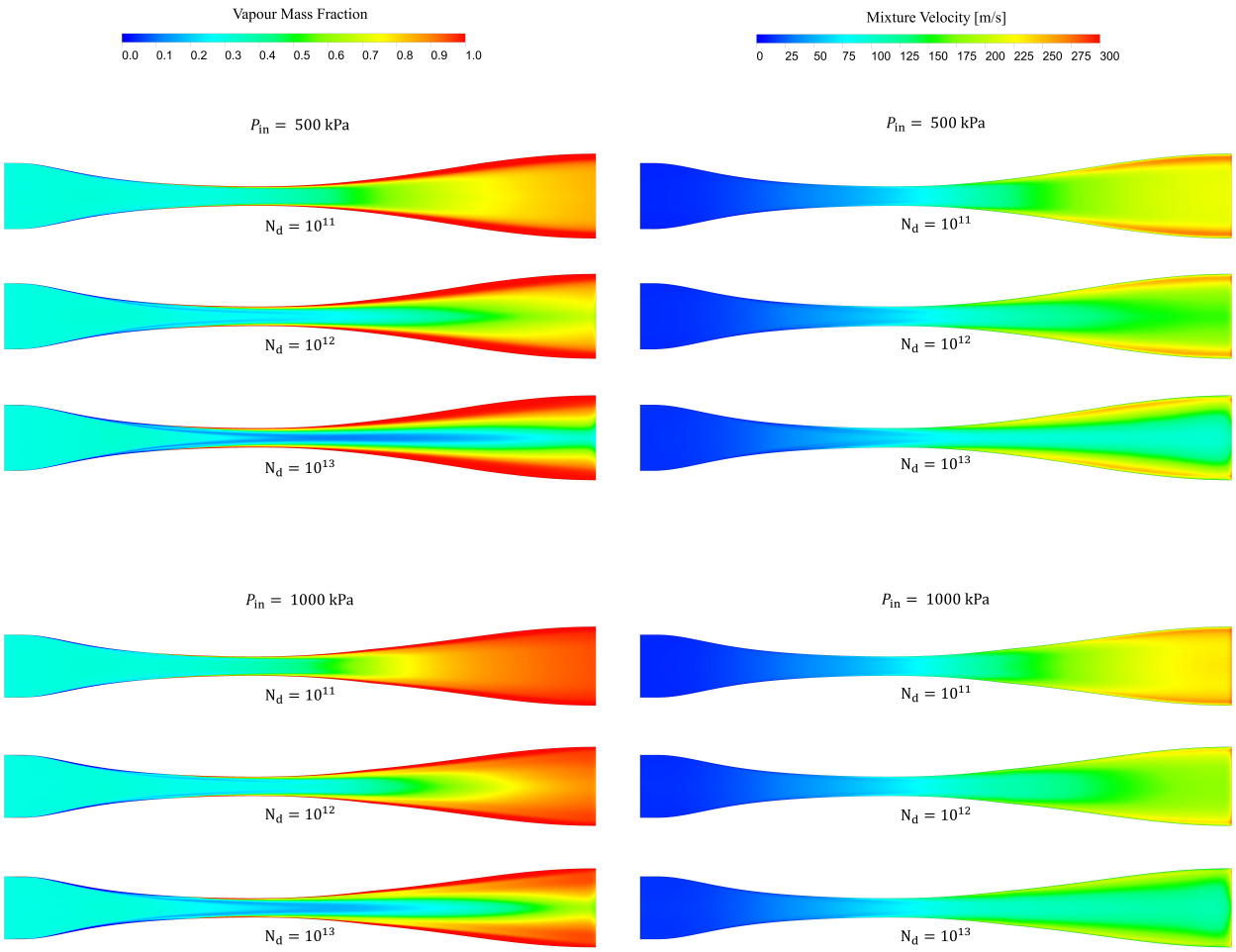


Figure 5.31: Two-dimensional variations of vapour mass fraction and mixture velocity within the nozzles designed for the expansions from 500 and 1000 kPa and inlet vapour quality of 0.3.

higher density. For a given pressure gradient applied to the control volume, the droplets develop a lower velocity. Hence, the overall velocity in a given control volume is lower when it contains more liquid in relation to the control volume with a lower liquid content. The lower liquid velocity also contributes to the development of drag between the phases such that the vapour phase is slowed down by the presence of droplets. This is why, in the region close to the wall, where there is almost pure vapour, the velocity tends to be higher than in the core of the nozzle, where there is a significant amount of liquid present. As the transverse separation of phases is higher for lower N_d and lower pressure, so is the velocity non-uniformity under these conditions.

To provide a more quantitative measure of flow uniformity at the nozzle outlet, normalised standard deviations of outlet vapour mass fraction and mixture velocity have been calculated for all the simulated expansions. In order to calculate the standard deviations, the nozzle outlet was discretised into 500 points and x_V and u_{mix} data have been retrieved at each point. In fact, the number of data points was limited by the number of grid elements at the outlet, which was below 500; therefore, the data for 500 points was obtained by interpolation.

Using this data standard deviations were calculated and normalised by the mean values of outlet vapour mass fraction and mixture velocity. Figure 5.32 presents the variation of the normalised standard deviations with the inlet droplet diameter for all the expansion cases. For all the inlet conditions, the flow leaving the nozzle appears to be highly non-uniform when the inlet droplet diameter is above 100 μ m ($N_d = 10^{11}$), with σ_{x_V} and $\sigma_{u_{Mix}}$ being typically in the range of 20-50% and 10-30% of the mean values, respectively. This is not surprising having observed how the flow behaviour changes as the droplet number decreases (see Fig.5.31). An exception here are the expansions from high pressures and inlet qualities, which are characterised by a highly uniform flow even at low droplet numbers. Once $D_{d,in}$ falls to about 50-100 microns ($N_d = 10^{12}$), the normalised standard deviation for both the outlet quality and mixture velocity drops below 15% in most cases. For inlet droplet diameter below 50 µm ($N_d = 10^{13}$), the standard deviation of x_V and u_{mix} do not exceed 10%, and are practically negligible in higher-pressure expansions. A visual assessment of the two-dimensional variation of u_{mix} and q_V presented in Fig. 5.31 suggests that the two-expansions with lower droplet numbers and lower inlet pressures tend to be less uniform; this is well reflected when assessing the standard deviations for all the studied cases, which also indicates that for a given inlet droplet diameter the flow is more uniform for higher-pressure expansions. This was also noted and explained when discussing Fig.5.31.

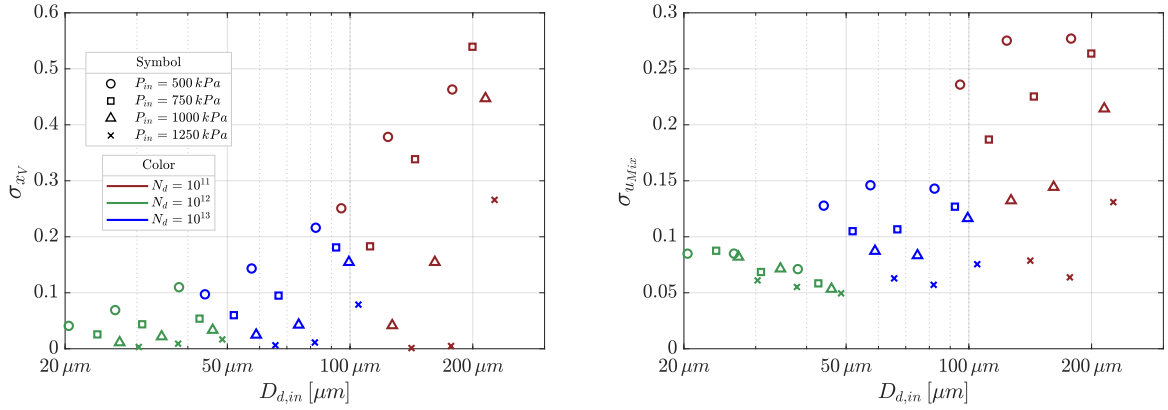


Figure 5.32: The relationship between the inlet droplet diameter and normalised standard deviations of vapour mass fraction (σ_{x_V}) and mixture velocity ($\sigma_{u_{Mix}}$) across the nozzle outlet; the standard deviations were normalised by mean outlet values of x_V and u_{mix}.

In summary, wet-to-dry expansions appear to be highly non-uniform when the mixture is characterised by droplet numbers of the order of 10^{11}. The flow uniformity increases with the droplet number such that it may be considered insignificant for inlet droplet size below 50 microns under most of the investigated operating conditions.

5.8.6 Comment on the initial conditions

It is clear that the mixture vapourisation is strongly affected by the droplet size. Other factors affecting the vapourisation rate are the inlet pressure and vapour quality. The inlet conditions have little impact on the vapour quality at the nozzle outlet as long as N_d is sufficiently high; i.e. when the droplet inlet diameter was below 50 µm. Nonetheless, when N_d is reduced and

droplets become larger, the inlet conditions begin to play an important role, which becomes evident when analysing Figs. 5.20-5.23. In general, the results show that the fluid can reach dry conditions more easily when expanding from higher pressures and higher inlet qualities. This could be anticipated when looking at Fig.5.4, which indicates that under isentropic homogeneous-equilibrium conditions, the vapour develops a higher superheat at the outlet for the expansions from higher pressures and vapour qualities. On the other hand, the fluid expanding from lower pressures are barely able to escape the two-phase dome. Hence, one can imagine that for high-pressure expansions, even if the phase change is delayed with respect to the ideal conditions shown in Fig.5.4, the fluid could still cross the saturated-vapour curve, whereas for lower-pressure expansions this would probably lead to wet outlet conditions. Therefore, from the point of view of nozzle design, it seems advisable to expand the fluid from the highest possible pressure and inlet quality. Nevertheless, from a thermodynamic point of view, the higher the inlet pressure and vapour quality, the smaller the relative advantage of two-phase expansion compared to single-phase ORC systems. White [8] found that for an open sensible heat source with inlet temperature of 150 °C a two-phase ORC could generate around 30% more power than a single-phase cycle. The power improvement reduced to around 15% and 3% when the heat source temperature was raised to 200 and 250 °C, respectively. Looking at the wet-to-dry cycle diagram in Fig.1.3, it is obvious that the heat source inlet temperature must be higher than the saturation temperature of the mixture entering the expander. The saturation temperatures corresponding to inlet pressures of 500, 750, 1000 and 1250 kPa are 167.1, 188.4, 204.8 and 218.2 °C, respectively. It then becomes clear why lower pressures are more attractive from the thermodynamic point of view. White's study [8] also showed that the relative increase in power output drops as the inlet vapour quality increases, which is simply due to the fact that as the inlet quality increases, the cycle gradually approaches the single-phase architecture and the change between these two diminishes. However, it should also be highlighted that expanding the fluid from very low qualities may lead to extremely large volumetric expansion ratios that could affect the turbine design and performance. Therefore, when designing the wet-to-dry cycle integrated with a two-phase turboexpander, there will likely be a trade-off between the thermodynamic performance and the feasibility of the turbine design.

5.8.7 Droplet breakup

As has been presented, the ability of the two-phase mixture to vapourise and turn into a uniform vapour flow is primarily dependent on the droplet size. In the absence of experimental data, it is difficult to estimate a definite number for the droplet diameter, and instead, a range of values can be studied. The upper limit of N_d is not of great concern, as the solution tends to approach the homogeneous-equilibrium model and the mixture can vapourise relatively easily during expansion. On the other hand, the maximum droplet size is critical to the vapourisation rate and flow uniformity, and estimating the lower limit of N_d is important when assessing the feasibility of achieving the wet-to-dry transition. In Chapter 4.1, an approach to estimating the maximum stable droplet size based on the critical Weber number was discussed in detail. In short, the Weber number is a non-dimensional number frequently used in atomisation studies to estimate the onset of droplet breakup. Various experimental correlations have been proposed, and these generally are consistent in that droplet breakup

is initiated at Weber number of around 11 as long as the Ohnesorge number is below 0.1, which was satisfied in almost entirety of the flow domain. With that being said, the following correlation proposed by Bordkey [222] was applied to estimate the critical Weber number in the case the Ohnesorge number was above 0.1

$$We_{cr} = We_{cr,\,Oh\to 0}\left(1 + 1.077Oh^{1.6}\right) \tag{5.21}$$

where $We_{cr,\,Oh\to 0}$ is the critical Weber number as Oh tends to zero, which as mentioned can generally be considered to be about 11.

Figure 5.33 illustrates the streamwise variation of the average ratio of the Weber number to the critical Weber number We/We_{cr}. The ratio We/We_{cr} has been shown for all investigated pressures. The inlet quality was fixed to 0.3 for each case, although similar trends were observed for other inlet qualities. The location at which We exceeds We_{cr} marks the location of the anticipated onset of droplet breakup. The average Weber number was found to exceed the critical value for all the droplet numbers and inlet pressures, which means that the breakup is anticipated in all the simulated expansions. For $N_d = 10^{13}$, We/We_{cr} is typically between 1-10 throughout much of the expansion. The ratio further increases by around an order of magnitude as the droplet number is reduced to 10^{11}. In summary, droplet breakup is expected to take place when $N_d \leqslant 10^{13}$. This means that even though incomplete mixture vapourisation was predicted in most operating conditions (especially for larger droplets) and the flow presented highly non-uniform outlet conditions, it could be anticipated that the expansion characteristics would change if the droplet breakup effects are taken into account. It was shown that delayed vapourisation is primarily caused by the inability of larger droplets to give out heat to the interface; therefore, if the larger droplets were to fragment into a number of smaller droplets, the vapourisation rate could be potentially enhanced. Therefore, the results documented in this chapter can be considered as a 'worst-case scenario' considering the average Weber number values. The effect of droplet breakup will be further investigated in the following chapters.

5.9 Effect of scale

Based on the results reported in the previous sections, certain patterns were identified with respect to the phase-change process that takes place in nozzles designed for the wet-to-dry expansion. A question may be posed whether these patterns are going to be conserved when the scale of the application changes. To answer this question, two additional nozzles with the design mass-flow rate increased from 0.12 to 0.50 kg/s were designed for two of the twelve operating points considered previously. These include the expansions from inlet pressures of 500 and 1000 kPa and the intermediate vapour quality of 0.3. The same three droplets numbers of 10^{11}, 10^{12}, and 10^{13} were applied to analyse different droplet sizes. Compared to the mass-flow rate of 0.12 kg/s that can represent an isentropic turbine power of approximately 90 to 170 kW, the mass-flow rate of 0.50 kg/s may correspond to larger power systems with a power output in the order of 400-800 kW. The nozzles were designed using the same technique described in Section 5.2. Table 5.6 summarises the main geometrical features

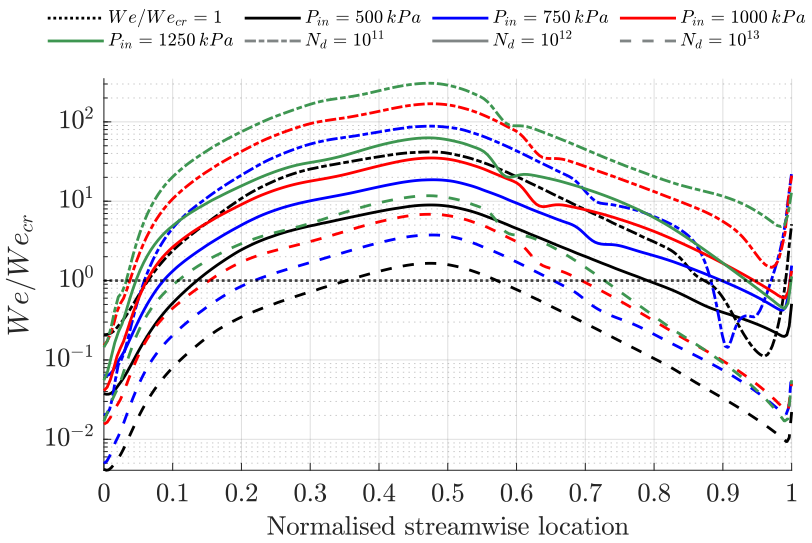


Figure 5.33: The streamwise variation of the ratio of the average Weber number to the critical Weber number; droplet breakup is expected to occur if the ratio We/We_{cr} exceeds unity (denoted by the black dotted line). The mixture was expanded from inlet quality of 0.3 for each presented case.

of the nozzles designed for the two mass-flow rates, following the notation defined in Fig. 5.5.

Apart from the difference in size, the shape of the nozzles was identical. The same solver was applied to perform non-equilibrium CFD simulations. Since the nozzles designed for the mass-flow rate of 0.50 kg/s are larger, the ratio of grid element size to respective characteristic dimensions of the nozzles (e.g. the throat height) was lower if the same mesh was to be applied. As such, it was presumed that using the same element size to mesh the flow passage would be sufficiently accurate.

Table 5.6: Geometrical features of the nozzles designed for the mass-flow rates of 0.12 and 0.50 kg/s.

P_{in} [kPa]	$x_{V,in}$	$\dot{m}$ [kg/s]	H_{in} [mm]	o_{th} [mm]	H_{out} [mm]	L_{th} [mm]	L [mm]
500	0.30	0.12	12.98	3.80	16.68	47.32	114.07
500	0.30	0.50	26.50	7.76	34.05	96.59	232.84
1000	0.30	0.12	9.18	2.80	11.55	34.02	84.15
1000	0.30	0.50	18.74	5.73	23.57	69.44	171.76

Figure 5.34 shows the streamwise profiles of the average vapour mass fraction and mixture velocity obtained in the nozzles designed for the mass-flow rates of 0.12 and 0.50 kg/s. The results indicate that the vapourisation rate is improved in the larger nozzles. For the inlet pressure of 500 kPa, the outlet vapour quality achieved in the larger nozzle was 10.65, 2.76 and 3.65 % higher at N_d of 10^{11}, 10^{12} and 10^{13}, respectively. The corresponding increase at the higher operating pressure was 6.18, 1.47 and 2.61 % for the three droplet numbers. An even more significant improvement was reported in the outlet mixture velocity, which increased by 17.34, 12.53 and 4.56 % for $P_{in} = 500kPa$, and by 25.80, 14.41 and 6.37 % in for $P_{in} = 1000kPa$ at the droplet number of 10^{11}, 10^{12} and 10^{13}, respectively. Although the

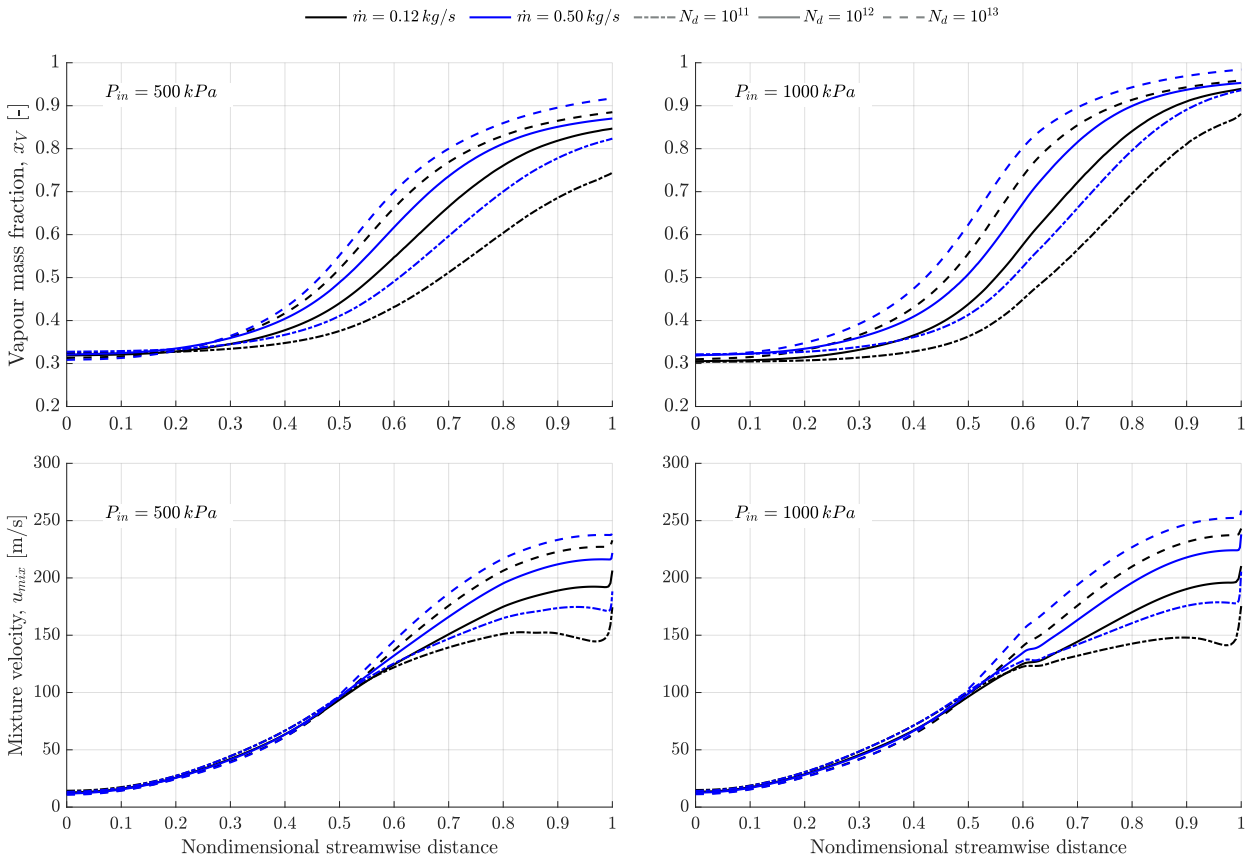


Figure 5.34: Streamwise variation of the vapour mass fraction and mixture velocity obtained in the nozzles designed for the mass-flow rates of 0.12 and 0.50 kg/s. The results were generated for the expansion from 500 and 1000 kPa and a fixed inlet vapour quality of 0.3.

phase change and mixture velocity are enhanced, the overall trends appear fairly similar.

To further investigate the effect of scale on the wet-to-dry expansion, the two-dimensional variations of vapour quality have been plotted in Fig. 5.35. When plotting the two-dimensional contours, the nozzles designed for the mass-flow rate of 0.50 kg/s were scaled down for easier comparison. It is apparent that the two-phase flow is more homogeneous in the nozzles designed for the higher mass-flow rate. By design, the flow is to be accelerated to the same outlet velocity in both nozzles, however, due to the increased length of the nozzles designed for $\dot{m} = 0.50kg/s$, the acceleration occurs more gently. As a result, liquid droplets have more time to adjust to the changing flow conditions and can better follow the mean flow. This is reflected in reduced phase separation and more homogeneous flow, which has a positive effect on the vapourisation rate and mixture velocity. Furthermore, an enlarged flow passage leads to higher average residence time of liquid droplets inside the nozzle. In case of the nozzles designed for $\dot{m} = 0.12kg/s$, the average liquid residence time was around 3 ms for $P_{in} = 500kPa$ and around 2 ms for $P_{in} = 1000kPa$. For the nozzles designed for $\dot{m} = 0.50kg/s$, the residence time increased to about 6 and 4 ms for the two operating pressures, respectively. This means that the droplets have more time to exchanges mass, momentum and heat with the surrounding vapour, which may contribute

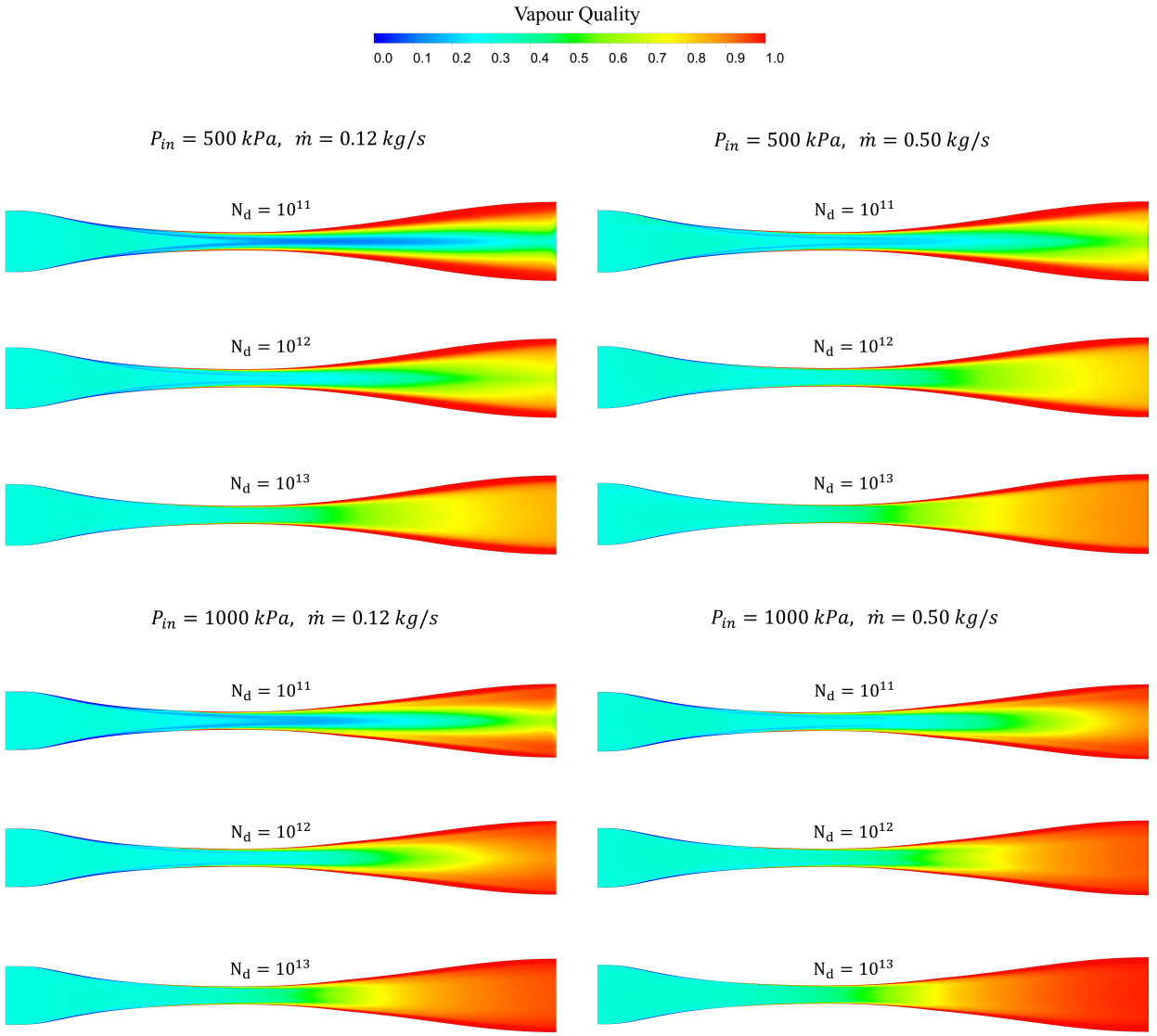


Figure 5.35: Two-dimensional variations of vapour vapour quality obtained in the nozzles designed for the mass-flow rates of 0.12 and 0.50 kg/s. The results were generated for the expansions from 500 and 1000 kPa and a fixed inlet vapour quality of 0.3. The larger nozzles were scaled down for comparison purposes.

to increased vapourisation rate and better flow homogeneity. Despite the separation effects being reduced, the overall flow pattern did not change drastically.

To summarise, the scale of application may have a significant impact on the wet-to-dry expansion and complete mixture vapourisation can be potentially more easily achieved in larger nozzles due to increased time scales available for interphase exchange of mass, momentum, and heat. The more gradual acceleration present in larger nozzles may contribute to reduced phase separation and better flow homogeneity. With that being said, the overall flow patterns appear to be consistent across different scales.

5.10 Conclusions

The two-fluid model has been applied to simulate the wet-to-dry expansion of the siloxane MM in a planar converging-diverging nozzle, where both thermal and mechanical non-equilibrium effects were considered. Various boundary conditions with an inlet pressure ranging from 500 to 1250 kPa and an inlet vapour quality from 0.1 to 0.5. The size of the droplets was modelled using a constant number of droplets per unit volume, which varied between 10^{11} and 10^{13}. The main conclusions of this study can be summarised as follows.

- A sensitivity study showed an acceptably small deviation in the solution when alternative momentum-transfer and vapour heat-transfer models were used. The expansion was more affected by the correlation used to predict the heat-transfer rate between the droplets and the liquid-vapour interface. With that being said, the maximum deviation in average vapour mass fraction relative to the baseline model was below 9%, while the overall phase-change pattern was very similar.

- The decisive factor influencing the phase change process was the droplet size; for small inlet droplet diameters, below 50 µm ($N_d = 10^{12}$), the mixture vapourises more effectively, reaching higher outlet vapour mass fraction, typically above 90%. For inlet droplet diameters between 50-100 µm ($N_d = 10^{12}$), the outlet vapour mass fraction was between 85-95% and this reduced to about 60-85% for droplet diameters higher than 100 µm ($N_d = 10^{11}$), except for the highest inlet pressure of 1250 kPa, for which near-dry conditions were predicted even at low droplet numbers.

- The significance of mechanical and thermal non-equilibrium effects predominantly depends on the droplet size. For the investigated droplet number range, the non-equilibrium effects were found significant even for relatively small droplets, and could be extremely high for larger ones. Generally, the results indicate that both mechanical and thermal non-equilibrium effects cannot be neglected in the analysis of the wet-to-dry expansion.

- Flows characterised by lower droplet numbers could not reach the design outlet velocity and pressure mainly due to delayed evaporation and high velocity slip. Significant flow under-expansion is likely to occur at lower N_d, which highlights the limitation of the nozzle design tool based on the homogeneous-equilibrium model.

- Generally, expansions from higher inlet pressures and vapour qualities can more readily accomplish complete vapourisation. However, such cases are also associated with a reduced relative advantage of two-phase cycles compared to single-phase architectures.

- Significant flow non-uniformity, measured in terms of the standard deviation of vapour quality and mixture velocity, was observed for large droplets. For $N_d = 10^{11}$ the standard deviation of the outlet quality ranged from 20 to 50% of the mean x_V, while the standard deviation of mixture velocity varied between 10 and 30% of the mean u_{Mix}. The flow non-uniformity visibly reduced as the droplet number was raised, with fairly uniform flow at $N_d = 10^{13}$ in most studied conditions. Higher pressures were

characterised by better flow uniformity, which is due to smaller interphase density differences and quicker vapourisation.

- The analysis of the average Weber number indicates that droplet breakup is likely to occur for all the investigated droplet numbers, with the average Weber number exceeding the critical value by as much as two orders of magnitude at low N_d. This suggests that the results presented in this chapter can be considered as the worst-case scenario as far the droplet size is concerned. This also underlines the need for taking into account droplet breakup effects in the analysis of wet-to-dry expansions.

- The investigation of the effect of scale revealed that larger nozzles can more easily accomplish the wet-to-dry transition due to increased residence time of liquid droplets and more gradual expansion, which translate to reduced phase separation and increased vapourisation rates. Despite the quantitative differences, the scale of application is not expected to drastically affect the main features of the two-phase flow.

Chapter 6

Importance of non-equilibrium effects in the nozzle design

6.1 Introduction

Results reported in the previous chapter indicate that the wet-to-dry expansion can significantly deviate from homogeneous-equilibrium conditions, which were assumed when designing the nozzle geometries. As a result, the average flow conditions at the nozzle outlet, expressed in terms of static pressure and mixture velocity, differed considerably from the design values. Taking into account non-equilibrium effects at the nozzle design stage can potentially reduce these deviations, allowing for a closer match between the design and simulated expansions. Moreover, accounting for non-equilibrium effects during nozzle design can potentially help generate geometries that can facilitate higher vapourisation rates.

6.2 Nozzle design methodology

White [43] has previously developed a non-equilibrium design tool based on a simplified formulation of the two-fluid model described in Chapter 4.1. Except for the difference in flow modelling, overall, the nozzle design routine was similar to the one presented in Fig. 5.3. The same set of boundary conditions and geometrical assumptions was used alongside the static pressure profile designed with the Bezier curve shown in Fig. 5.2. The flow was assumed to be steady, quasi-1D and inviscid, varying only along the longitudinal axis of the nozzle. Consequently, the lift and turbulent dispersion forces were not included, and the two-fluid model governing equations were reduced to:

$$\frac{1}{A}\frac{\partial\left(\alpha\,\rho\right)_{\beta}}{\partial x} = \dot{m}_{ex} \tag{6.1a}$$

$$\frac{1}{A}\frac{\partial\left(\alpha\,\rho A u^{2}\right)_{\beta}}{\partial x} = -\alpha_{\beta}\,\frac{\partial p}{\partial x} + F_{D} \tag{6.1b}$$

$$\frac{1}{A}\frac{\partial\left(\alpha\,\rho A u h_{tot}\right)_{\beta}}{\partial x} = \dot{m}_{ex} h_{ex} + \dot{q}_{ex} \tag{6.1c}$$

where A is the nozzle cross-sectional area, F_D is the interfacial drag force, while β is the phase index representing either the liquid or the vapour phase. As in the CFD model, the Ishii-Zuber model was applied to estimate the drag coefficient, while the heat-transfer coefficient on the liquid and vapour side of the interface were calculated using the Brown [221, 232] and Ranz-Marshall [229] correlations, respectively. Similarly to the design tool based on the homogeneous-equilibrium model, the inverse design approach was followed with a pre-defined pressure profile. The governing equations were discretised with a second-order accurate backward scheme, while fluid properties were evaluated using NIST REFPROP 10.0 [212], which allowed to evaluate fluid properties in the metastable regime. Three different methods for estimating the droplet size were incorporated in the design tool, namely a constant droplet size, a constant droplet number, or the critical Weber number approach discussed in Section 4.3.1. It is worth noting that the nozzle design tool assumes an inviscid flow. That assumption was verified in Section 5.5, where viscous and inviscid simulations were compared for two inlet pressures. In summary, viscous pressure losses were found to be insignificant in the wet-to-dry expansion, which justifies the assumption of an inviscid flow.

The main objective of this chapter is to assess the importance of including non-equilibrium effects in the nozzle design process. This is done by comparing the performance of the nozzles designed with the non-equilibrium design tool to the performance of nozzles designed with the homogeneous-equilibrium model. The numerical simulations are performed similarly to the nozzles designed with the homogeneous-equilibrium model. The nozzle geometries generated by the non-equilibrium tool are imported into ANSYS CFX 2021 R1 [244] to perform CFD simulations using the same setup as in the parametric study described in Section 5.4. Similar grids were constructed in the non-equilibrium models, while an appropriate element size was selected based on the mesh independence study documented in the previous chapter in Section 5.5. Two inlet pressures of 500 and 1000 kPa and the intermediate inlet vapour quality of 0.3 were investigated, while the droplet number varied between 10^{11} and 10^{13}.

6.3 Nozzle wall profile discontinuity

Before discussing the results, it should be explained that in the non-equilibrium design tool, once the flow reaches a vapour quality greater than 99.9%, the model automatically switches to an isentropic flow to simulate the remaining superheated vapour expansion. In the event of a rapid phase-change process and significant non-equilibrium effects, the transition out of the two-phase regime could be related to an abrupt change in the streamwise gradient of certain flow properties such as mixture density defined as:

$$\rho_{mix} = \alpha_V \rho_V + \alpha_L \rho_L \tag{6.2}$$

where α_V and α_L are the volume fractions of the vapour and liquid. Generally, an abrupt change in the streamwise gradient of ρ_{mix} is associated with a sudden change in the flow area and, thus, a sudden change in nozzle wall profile.

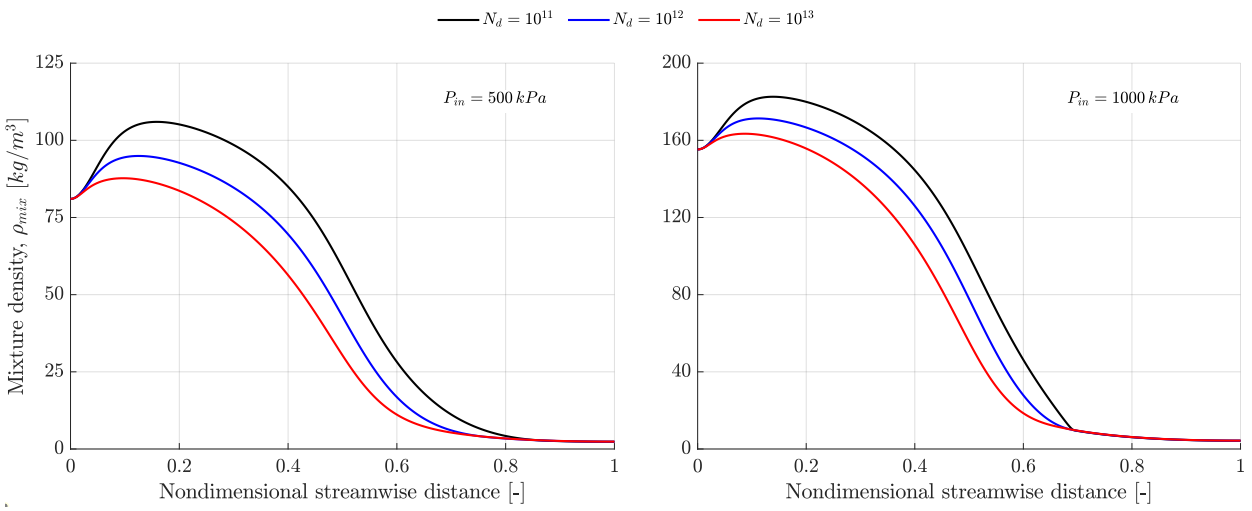


Figure 6.1: Streamwise variation of mixture density ρ_{mix} predicted by the non-equilibrium design tool two inlet pressure of 500 and 1000 kPa, and a fixed inlet vapour quality of 0.3. The droplet size was estimated using a constant droplet number density that varied between 10^{11} and 10^{13}.

Figure 6.1 shows the streamwise variation of ρ_{mix} obtained with the non-equilibrium design tool for the two inlet pressures and three droplet numbers. Analysing the mixture density variation in the expansion from 500 kPa, no discontinuity in ρ_{mix} profiles was found for any of the droplet numbers. Having said that, one can observe that the change in density was more gradual at high droplet numbers, which was related to a more gradual phase-change process near the wet-to-dry transition point. On the other hand, the two-phase expansions

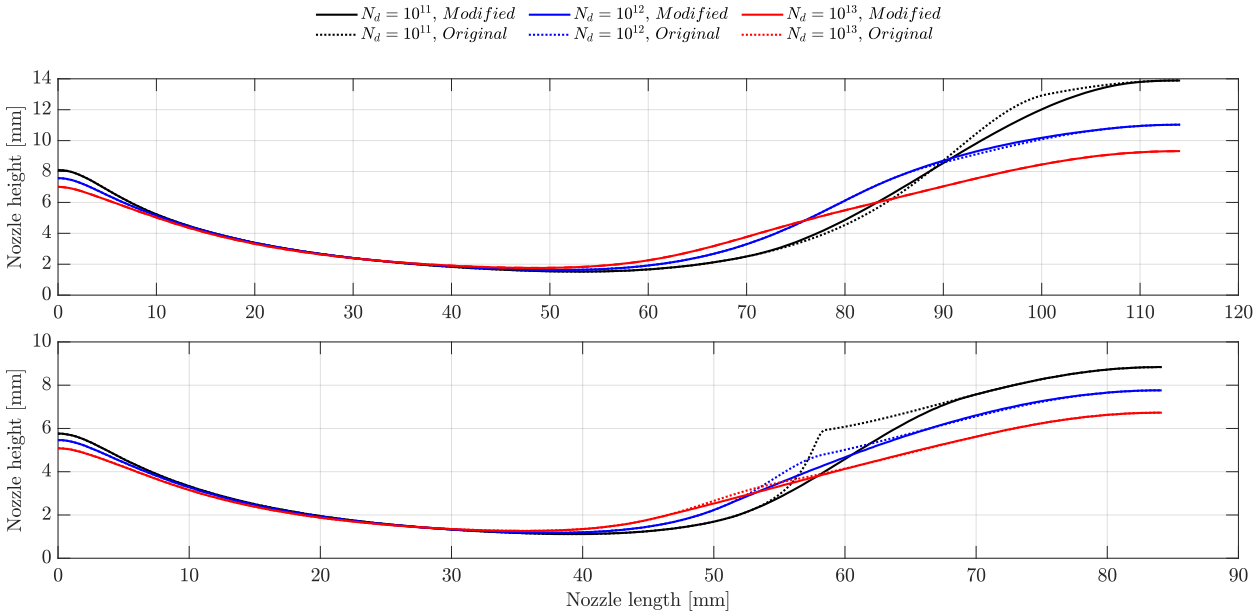


Figure 6.2: The effect of fitting a spline between the two-phase and superheated nozzle section for the expansions from an inlet total pressure of 500 (top) and 1000 (bottom) kPa and an inlet vapour quality of 0.3.

characterised by larger droplets were characterised by a delayed vapourisation with respect to the streamwise location, but the phase change occurred more rapidly when approaching dry conditions. This was associated with a more abrupt change in the flow area and wall profile at the transition point. These effects were further amplified in the expansion from 1000 kPa, where, as can be seen in Fig.6.1, there was a clear discontinuity in the gradient of mixture density at $N_d = 10^{11}$. When CFD simulations were performed for the cases with a visible abrupt change in ρ_{mix}, a relatively strong shock was found to form in the area corresponding to the location of the transition point, as predicted by the design tool.

To mitigate this issue and allow for smooth shockless expansion, the nozzle wall profile was modified during post-processing. The nozzle wall profile generated with the non-equilibrium design tool was imported into SOLIDWORKS, where a section of the wall profile characterised by an abrupt gradient change was removed and a built-in function was used to fit in a spline and replace the removed section. It was ensured that the fitted spline was tangent to the sections it connected, so that the wall profile continuity was maintained. A suitable length of the removed wall profile was determined through trial and error using the CFD solver. Generally, the goal was to mitigate the issues surrounding the abrupt change in flow area and the resulting shock, with as little modification as possible. The comparison between the original and modified wall profiles is shown in Fig. 6.2.

For the expansion from an inlet pressure of 500 kPa, moderate alteration in the wall profile was required for $N_d = 10^{11}$ to avoid the formation of shock, while little to no alteration was required at higher droplet numbers. More significant modifications had to be introduced for the expansion from 1000 kPa, especially at low droplet numbers, which is in line with the discussion around mixture density profiles. Further analysis documented in the following sections indicates that even in case the wall profile was significantly altered, the flow was only affected locally with respect to the design variations; the flow downstream of the area where the spline was fitted appeared to be unaffected. In other terms, the flow could successfully reach the design outlet conditions despite the local change in the wall profile. In summary, the nozzle geometries generated by the non-equilibrium design tool for low droplet numbers required certain post-processing modifications to avoid the adverse effects of abrupt wall profile changes in the diverging section of the nozzle.

6.4 Investigated expansions

A detailed comparison between nozzles generated with the non-equilibrium design tool and the homogeneous-equilibrium model is carried out for two operating points. These include expansions from an inlet pressure of 500 and 1000 kPa and an inlet vapour quality of 0.3. The two cases considered in this study are shown in the temperature-entropy diagram in Fig. 6.3, which illustrates an ideal isentropic expansion.

The first operating point represents the lower limit of the pressure range considered in the wet-to-dry cycle, as long as the siloxane MM is the working fluid. These conditions are most desired from the standpoint of maximising the cycle performance, however, the results

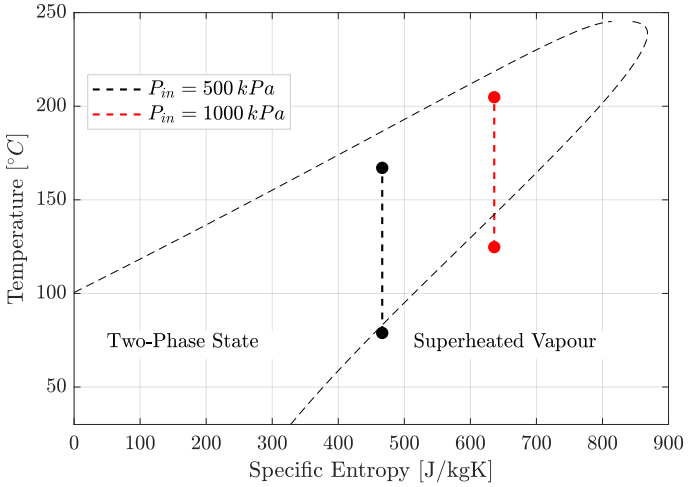


Figure 6.3: The temperature-entropy diagram of two expansion cases considered for the assessment of including non-equilibrium effects in the nozzle design process. The illustrated expansions refer to an ideal isentropic flow.

presented in the previous chapter also indicate that achieving complete mixture vapourisation at such low pressures can be challenging. On the other hand, the wet-to-dry transition appears to be more readily accomplished at an inlet pressure of 1000 kPa, but the thermodynamic advantage of two-phase expansion gradually diminishes with increasing pressure. Thus, this operating point is rather close to the upper limit of the pressure range relevant to wet-to-dry cycles that use the siloxane MM. The results presented in this chapter allow to assess whether the conclusions concerning the phase change dependence on the thermodynamic conditions hold when non-equilibrium effects are taken into account at the nozzle design stage. To evaluate the effect of droplet size, the two expansions were simulated with a droplet number ranging from 10^{11} to 10^{13}, which coincides with the droplet number range considered in the previous chapter.

6.5 Influence on vapourisation rate

First, it was assessed how including non-equilibrium effects in the nozzle design affects the vapourisation rate. Figure 6.4 shows the streamwise variation of vapour mass fraction in the nozzles generated with the homogeneous-equilibrium and non-equilibrium models. The plot presents the design and CFD x_V variations for the two investigated inlet pressures and different droplet numbers. For simplicity, the nozzles generated by the homogeneous-equilibrium model and the non-equilibrium design tool will be referred to as equilibrium and non-equilibrium nozzles, respectively. When it comes to the design x_V profiles, despite the wet-to-dry transition being slightly delayed by the presence of non-equilibrium effects, full vapourisation is predicted by both tools under any of the investigated conditions. The transition is predicted to be achieved sooner in the case of higher inlet pressures, which is in line with the temperature-entropy diagram shown in Fig.6.3, which indicates that the higher the inlet pressure, the sooner the flow can escape the two-phase dome under isentropic flow conditions.

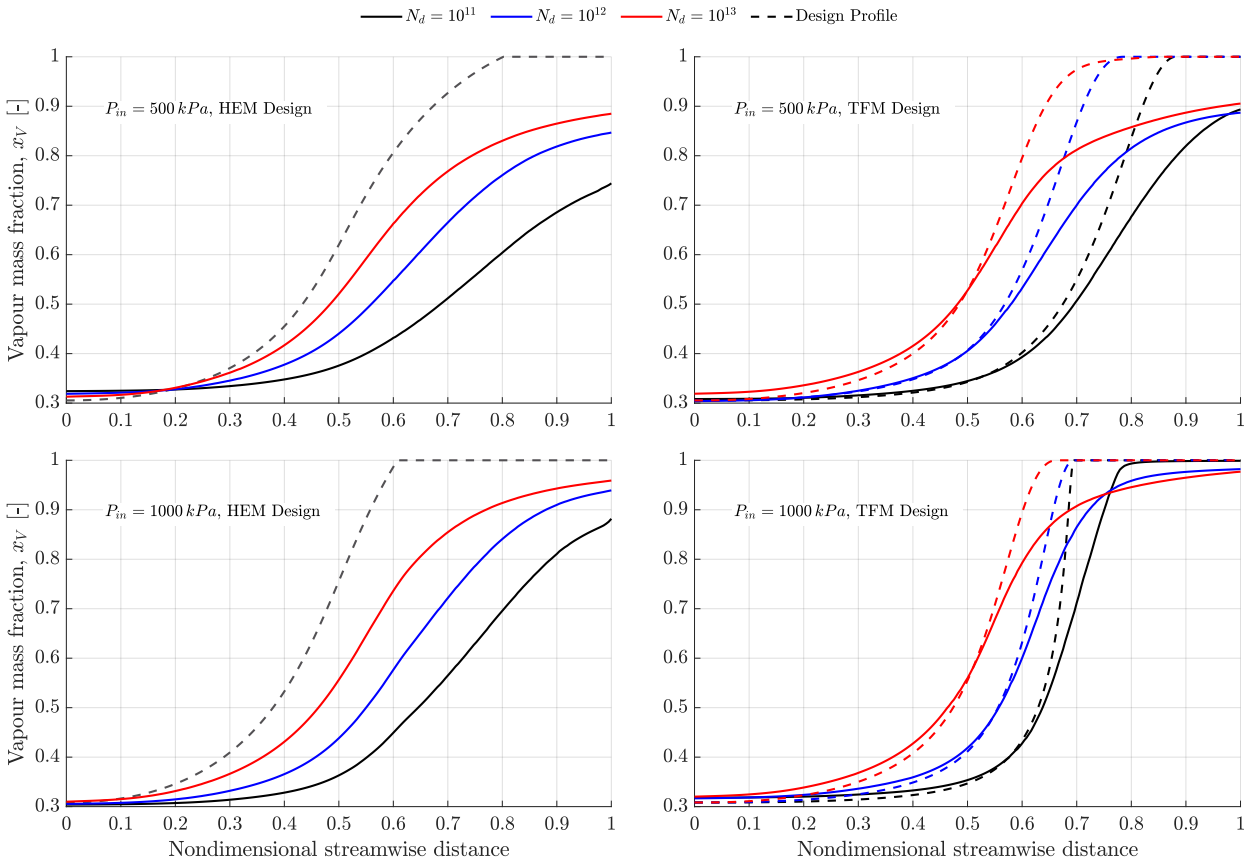


Figure 6.4: Streamwise variation of average vapour mass fraction x_V in nozzles generated by the non-equilibrium and homogeneous-equilibrium design tools; the plot illustrates the design profiles and CFD predictions for the expansion from an inlet pressure of 500 and 1000 kPa, fixed inlet vapour quality of 0.3 and three droplet density numbers N_d of 10^{11}, 10^{12} and 10^{13}.

Analysing the CFD results, it can be easily noticed that including non-equilibrium effects in the design routine can help generate geometries that facilitate significantly higher vapourisation rates at low droplet numbers. The average vapour mass fraction at the nozzle outlet, $x_{V,out}$, in the equilibrium nozzles designed for $P_{in} = 500kPa$ was around 88.5, 84.7 and 74.4% at N_d of 10^{13}, 10^{12} and 10^{11} respectively. This increased to about 90.5, 88.7, and 89. 4% in the nozzles designed with the non-equilibrium tool. The improvement in the vapourisation rate was also recorded for $P_{in} = 1000kPa$, where $x_{V,out}$ increased from 95.9, 93.9 and 88.2% to 97.7, 98.2, and 99.9% at N_d of 10^{13}, 10^{12} and 10^{13}, respectively. The increase in $x_{V,out}$ at $N_d = 10^{11}$ was as high as 15% in the lower-pressure expansion and over 12% at the inlet pressure of 1000 kPa. On the other hand, the improvement in the vapourisation rate is visibly smaller in the expansions characterised by higher droplet numbers ($N_d = 10^{13}$). This was expected since the expansions characterised by small droplets begin to resemble the homogeneous-equilibrium flow, making the difference between the two design models less significant.

Something peculiar can be observed regarding the simulated phase-change pattern in the

non-equilibrium nozzles. Namely, the CFD model predicts that the two-phase expansions characterised by lower droplet numbers eventually reach greater vapour mass fraction at the nozzle outlet compared to higher droplet numbers. This effect is particularly visible in the expansion from 1000 kPa, where the mixture at $N_d = 10^{11}$ was found to transition to a superheated vapour state at a distance of about 80% of the nozzle length, reaching $x_{V,out}$ several percent higher compared to $N_d = 10^{12}$ and $N_d = 10^{13}$. This, at first, may seem to stand in contradiction with the results reported earlier, where it was found that larger droplets significantly delay the wet-to-dry transition process. However, one should keep in mind that in the previous analysis the nozzle geometries were generated under the assumption of a homogeneous-equilibrium flow and were not adjusted to the presence of non-equilibrium effects. As a result, the flow characteristics may differ between these two models despite the identical boundary conditions and droplet number. In order to understand this peculiar phenomenon, the equation for the vapourisation rate is reiterated here:

$$\sigma_{M,L} = \frac{\mathfrak{H}_L A_{int} \left(T_{int} - T_L\right) + \mathfrak{H}_V A_{int} \left(T_{int} - T_V\right)}{h_{V,sat} - h_L} \tag{6.3}$$

where $\mathfrak{H}_L$ and $\mathfrak{H}_V$ are heat-transfer coefficients on the liquid and vapour side of the interface, A_{int} is the interfacial area defined as the combined surface area of the droplets per unit volume, while $h_{V,sat}$ and h_L are vapour saturation and liquid enthalpies. In wet-to-dry expansions, the primary thermal resistance lies on the liquid side of the interface (i.e. between the droplets and the liquid-vapour interface), which was also confirmed when studying the sensitivity of the solution to the type of heat-transfer models employed (see Section 5.7). Therefore, the term $\mathfrak{H}_L A_{int} \left(T_{int} - T_L\right)$, which represents heat-transfer rate between the droplets and the interface, is expected to have the greatest influence on the phase-change rate. The absolute value of $(T_{int} - T_L)$ is the liquid superheat level $T_{L,sup}$.

Figure 6.5 compares the interfacial area density (A_{int}), liquid heat-transfer coefficient ($\mathfrak{H}_L$) and liquid superheat level ($T_{L,sup}$) for the three droplet numbers of 10^{11}, 10^{12} and 10^{13}. The plot also shows the interphase mass-transfer rate per unit volume, which defines the vapour generation rate. The expansion from an inlet pressure of 1000 kPa was analysed as that was the pressure level for which the peculiar phenomenon was more apparent. As expected, smaller droplets in flow characterised by higher droplets numbers are associated with larger interfacial area and higher heat-transfer coefficient, which translates to enhanced heat-transfer rate and consequently higher vapourisation rates in the initial stage of the expansion. However, as the flow progresses downstream and the volume fraction of liquid decreases, the interfacial area available for heat transfer also decreases and eventually matches the interfacial area of the flow with larger droplets at a streamwise distance of about 60% of the nozzle length. From that point, both A_{int} and $T_{L,sup}$ decrease, which is reflected in a gradual fall in the interphase mass-transfer rate. This is why x_V profile depicted in Fig. 6.4 plateaus in the diverging section of the nozzle. When it comes to larger droplets, the interfacial area and heat-transfer coefficient are initially lower, which delays the phase-change process. However, larger droplets, having reduced ability to exchange heat with the surrounding vapour, develop a significantly higher superheat level, which is sustained throughout much of the diverging section as shown in Figs. 6.5-6.6.

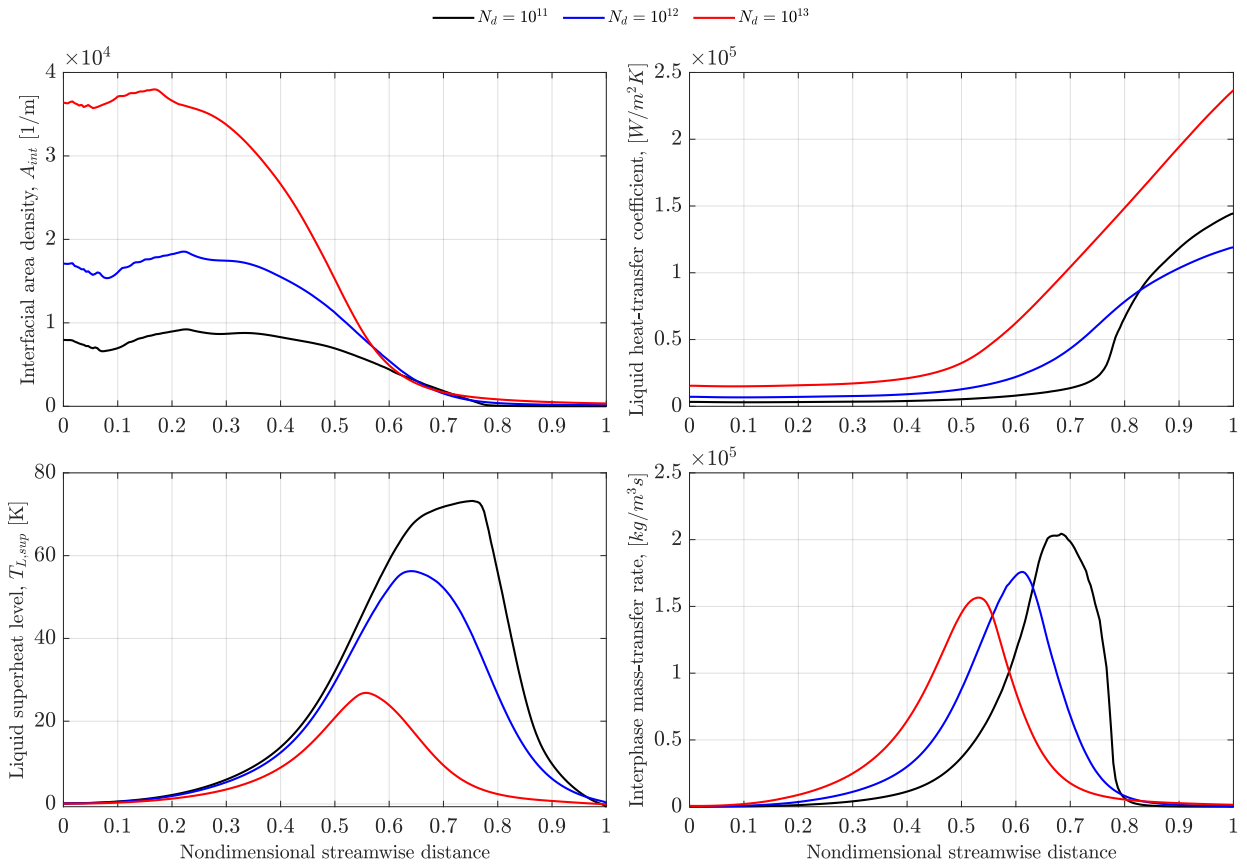


Figure 6.5: Streamwise variation of average interfacial area density, liquid heat-transfer coefficient, liquid superheat level and interphase mass-transfer rate in the nozzle designed by the non-equilibrium tool for the expansion from an inlet pressure of 1000 kPa and inlet vapour quality of 0.3; the figure shows the variations for the droplet numbers N_d of 10^{11}, 10^{12} and 10^{13}.

In order to assess the effect of the liquid superheat level on the phase-change rate, a simplified analysis is conducted under a few assumptions. As discussed earlier, the primary resistance to heat transfer (which limits the phase-change rate) lies on the liquid side of the interface. Therefore, completely ignoring the thermal resistance on the vapour side, the phase-change rate shown in Eq. 6.4 can be expressed as:

$$\sigma_{M,L} = \frac{\mathfrak{H}_L A_{int} \left(T_{int} - T_L\right)}{h_{V,sat} - h_L} \tag{6.4}$$

The heat-transfer coefficient $\mathfrak{H}_L$, has been estimated using the Brown's model, which is reiterated below:

$$Nu_L = \frac{\mathfrak{H}_L D_d}{k_L} = 2 + 7 \min\left(1 + \frac{c_{p,L}\ \max(0,\ |T_{sat} - T_L|)}{h_{LV}}, 8\right) \tag{6.5}$$

Since it was found that liquid remained superheated throughout the expansion ($\max(0,\ |T_{sat} - T_L|) = T_{L,sup}$), and that the term $(1 + c_{p,L}\ \max(0,\ |T_{sat} - T_L|)/h_{LV}$ was less than 8, Eq. 6.5, can be simplified:

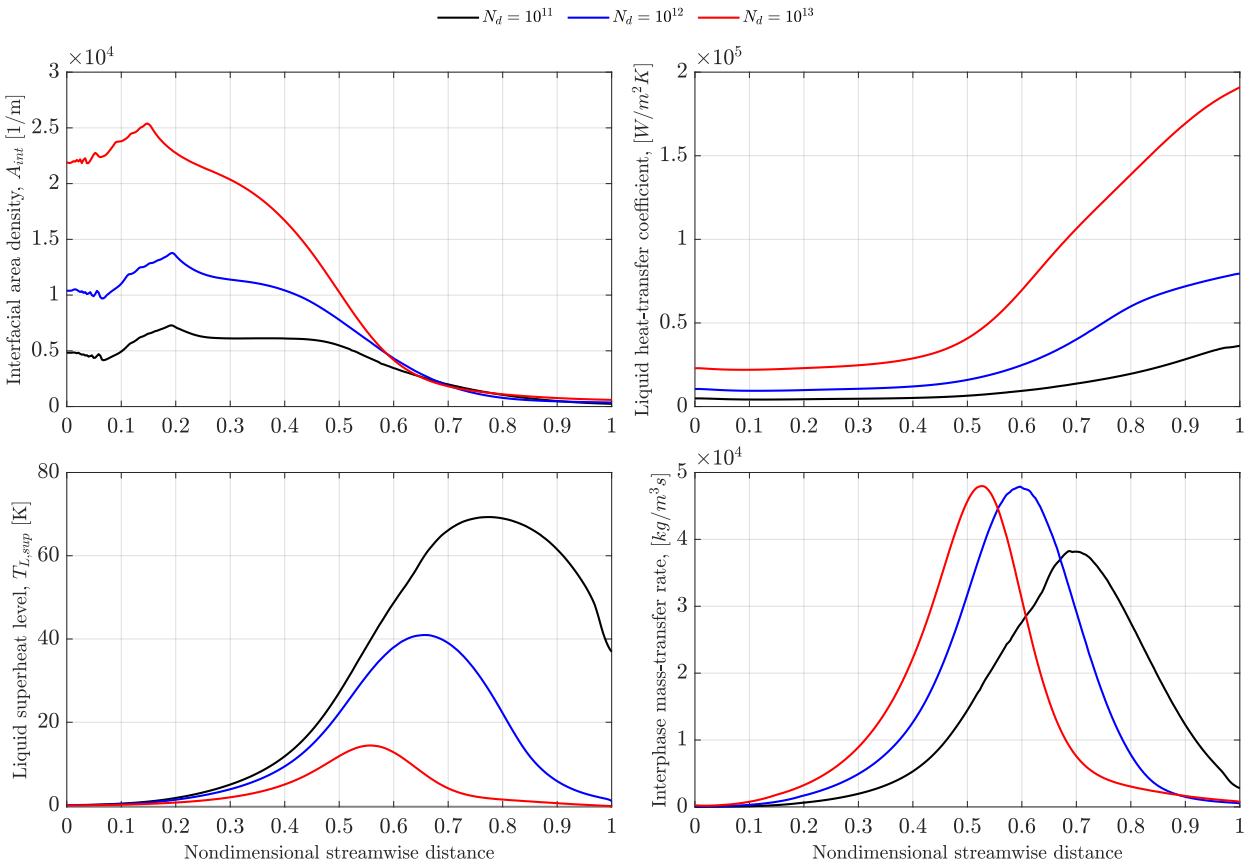


Figure 6.6: Streamwise variation of average interfacial area density, liquid heat-transfer coefficient, liquid superheat level and interphase mass-transfer rate in the nozzle designed by the non-equilibrium tool for the expansion from an inlet pressure of 500 kPa and inlet vapour quality of 0.3; the figure shows the variations for the droplet numbers N_d of 10^{11}, 10^{12} and 10^{13}.

$$Nu_L = \frac{\mathfrak{H}_L D_d}{k_L} = 2 + 7\left(1 + \frac{c_{p,L}\, T_{L,sup}}{h_{LV}}\right) \tag{6.6}$$

Rearranging Eq. 6.6 for the liquid heat-transfer coefficient and inserting it into Eq.6.4, gives:

$$\sigma_{M,L} = \frac{k_L A_{int}\left(9\, T_{sup,L} + 7\,\frac{c_{p,L} T_{sup,L}^2}{h_{LV}}\right)}{D_d(h_{V,sat} - h_L)} \tag{6.7}$$

Equation 6.7 indicates that the phase-change rate can be significantly enhanced by the liquid superheat level. Although the ratio of the liquid specific heat capacity and latent heat ($c_{p,L}/h_{LV}$) was found to lie somewhere in the range of 0.04 to 0.1 in the diverging section of the nozzle, the term becomes important at high liquid superheat levels due to the square dependency on $T_{sup,L}$. Referring back to Fig. 6.5, the maximum superheat level for $N_d = 10^{12}$ is about 40 K, while for $N_d = 10^{11}$ it reaches 70 K. Assuming $c_{p,L}/h_{LV} = 0.05\, K^{-}1$, the raise of $T_{L,sup}$ from 40 to 70 K increases the heat-transfer rate between the droplet and the interface by a factor of over 2.5, provided that other parameters in Eq. 6.7 remain the same.

The phase-change rate in the expansions characterised by lower droplet numbers is initially limited by the lower ratio of surface area to the volume of droplets. However, as the flow advances downstream, the raising liquid superheat enhanced the phase-change rate, which in turn increases the surface area to volume ratio of droplets. This eventually leads to the situation where the size of the droplets is similar to higher droplet numbers, but the superheating is considerably higher. The combination of all these factors leads to a delayed but more rapid phase-change process in the diverging section of the nozzle. Since at $N_d = 10^{11}$, higher liquid superheat level was sustained throughout much of the expansion in the diverging section, it led to higher interphase mass-transfer rates and consequently to higher vapour mass fractions at the nozzle outlet. The same parameters were plotted for the expansion from 500 kPa in Fig.6.6. There are some discrepancies in the streamwise variation of these parameters compared to the expansion from 1000 kPa. These mainly concern the peak interphase mass-transfer rate, the rate of rise and fall of $T_{L,sup}$, and the behaviour of heat-transfer coefficient near the nozzle outlet. With that being said, the main trends remain unchanged with $T_{L,sup}$ significantly higher at low droplet numbers, which is considered to be the driving factor for mixture vapourisation near the nozzle outlet. Since the nozzles designed with the homogeneous-equilibrium model experience significant underexpansion when expanding flows characterised by low droplet numbers, the liquid superheating in the diverging section was effectively suppressed and the effect was not observed in the results reported in the previous chapter.

6.6 Influence on mixture velocity

The results presented in the previous section indicate that including non-equilibrium effects in the nozzle design routine can potentially help generate geometries that facilitate higher vapourisation rates, especially in case of two-phase expansions characterised by larger droplets. To illustrate the effect on mixture velocity, average streamwise variation of u_{mix} in the nozzles generated by the two design tools is presented in Fig. 6.7. The mixture velocity is a mass-flow averaged velocity defined as:

$$u_{Mix} = \frac{\dot{m}_L u_L + \dot{m}_V u_V}{\dot{m}_L + \dot{m}_V} \tag{6.8}$$

where $\dot{m}_L$ and $\dot{m}_V$ represent the mass-flow rates of liquid and vapour, while u_L and u_V are the velocities of the two phases. Figure 6.7 indicates that the discrepancy between the design and CFD u_{mix} profiles is considerably reduced in the case of non-equilibrium nozzles. For the expansion from 500 kPa, the average mixture velocity at the nozzle outlet, $u_{mix,out}$, predicted by the CFD model in the equilibrium nozzles was 30.3 to 88.7 m/s lower than the design value. This range was reduced 15 to 26.5 m/s in the non-equilibrium nozzles, with drastic improvements at low droplet numbers. The velocity discrepancy was further reduced when the inlet pressure was raised to 1000 kPa, and was within 3.2-10.9 m/s in non-equilibrium nozzles as opposed to 39.7-107.4 m/s in the geometries designed by means of the homogeneous-equilibrium model.

Beside closer agreement with the design profiles, the non-equilibrium nozzles appear to

achieve a higher $u_{mix,out}$ compared to the equilibrium nozzles. Neglecting the effect of sudden flow acceleration at the outlet of the equilibrium nozzles, which occurs due to flow underexpansion, $u_{mix,out}$ was 13.3 to 25.2 m/s higher in the non-equilibrium nozzles designed for the inlet pressure of 500 kPa. The increase in $u_{mix,out}$ was much higher for the expansion from 1000 kPa and was between 22.2 and 90.6 m/s, being more significant at low droplet numbers.

Upon evaluating the velocity profiles, there was a certain velocity drop near the outlet of the nozzle designed for $P_{in} = 500kPa$ and at $N_d = 10^{11}$. This discontinuity occurred because of the formation of a shock in that area. It can also be noted that in the nozzle designed for $P_{in} = 1000kPa$ at $N_d = 10^{11}$, the velocity profile clearly deviated from the design one across a distance of 70 to 80 % of the nozzle length. This corresponds to the area where the spline was fitted to avoid the discontinuity in the nozzle wall profile, which is considered to be the cause of that deviation. However, the velocity profile of the mixture downstream of that area was found similar to the design profile, indicating that the spline only affected the flow locally.

Similarly to the vapourisation rate, the non-equilibrium design tool was found to be able to generate nozzle geometries that display closer agreement between the design and CFD velocity profiles and achieve higher overall mixture velocity at the nozzle outlet, especially at lower droplet numbers.

6.7 Nozzle shape and pressure distribution

The preceding sections indicate that the nozzles generated by the non-equilibrium tool can achieve higher vapour qualities and mixture velocities. This section aims to illustrate the effect of non-equilibrium effects on the nozzle shape and pressure distribution. This further insight should also help clarify why the geometries generated with the non-equilibrium tool can enhance the vapour generation rate and mixture velocity.

Figure 6.8 illustrates the effect of the assumed droplet number on the shape of nozzles generated with the non-equilibrium design tool for the expansions from an inlet pressure of 500 and 1000 kPa. Despite the fact that the inlet conditions were fixed and independent of the assumed droplet number, a slight difference in the nozzle height was observed at the inlet of the nozzle. The difference comes from a fixed ratio of the width of the nozzle to the height of the throat (b/o_{th}). Since the flow conditions were affected by the extent of the non-equilibrium effects, the throat height was slightly different depending on the droplet number. This resulted in a slightly different nozzle width in each expansion, although the difference was confined to a relatively narrow range of 9.14 to 10.57 mm at $P_{in} = 500kPa$ and 6.71 to 7.60 mm at $P_{in} = 1000kPa$. Hence, the difference in the width of the nozzles does not explain a much larger deviation in the nozzle height visible in the diverging section of the nozzle.

The nozzle wall profiles begin to diverge downstream of the throat. Initially, expansions characterised by lower droplet numbers have a smaller nozzle height, which is due to delayed vapourisation and the associated higher liquid content. However, as the flow advances down-

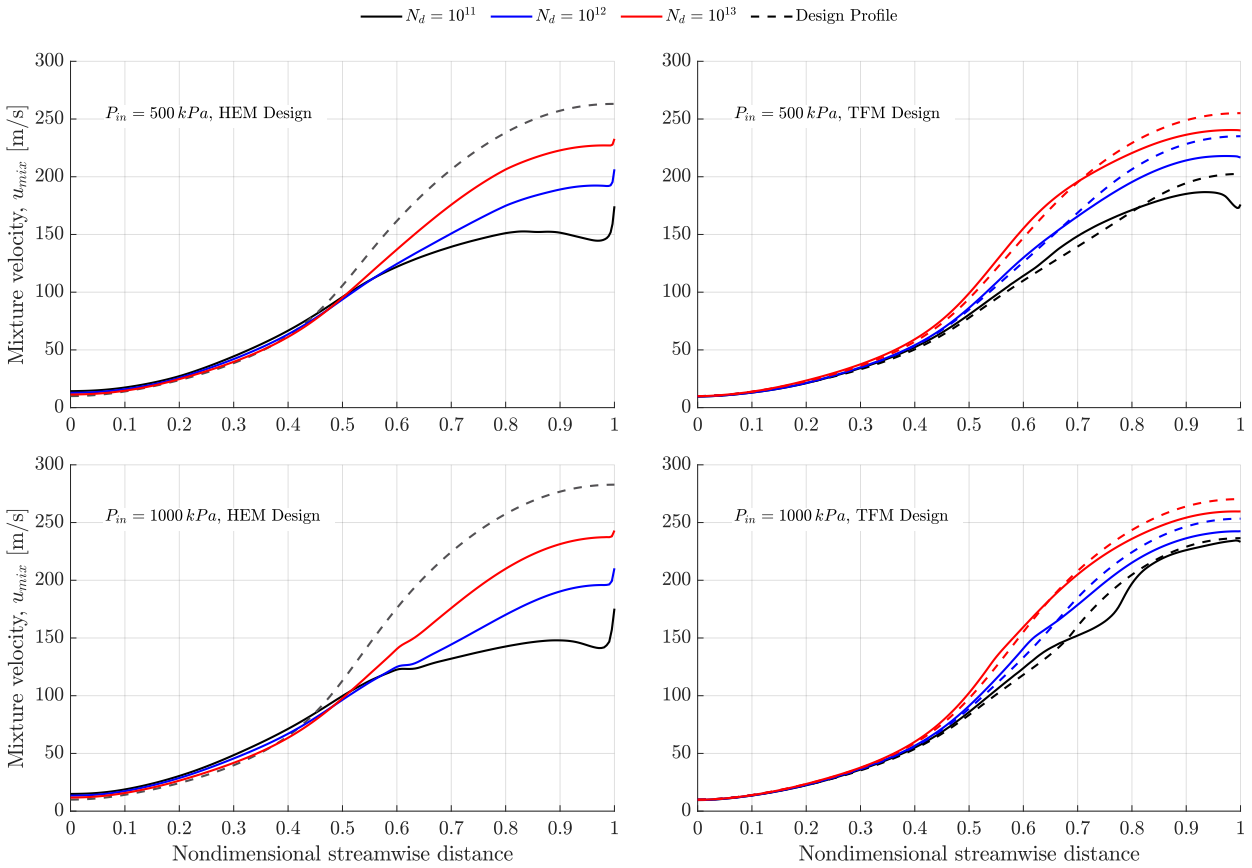


Figure 6.7: Streamwise variation of average mixture velocity u_{mix} in nozzles generated by the non-equilibrium and homogeneous-equilibrium design tools; the plot illustrates the design profiles and CFD predictions for the expansion from an inlet pressure of 500 and 1000 kPa, fixed inlet vapour quality of 0.3 and three droplet density numbers N_d of 10^{11}, 10^{12} and 10^{13}.

stream of the throat and vapourisation takes place, the flow area begins to increase. Since larger droplets are associated with higher velocity slip, the two-phase flow tends to have a lower velocity for a given volume fraction of liquid. This trend was observed in Fig. 6.7 which indicates that larger droplets are associated with a smaller mixture velocity throughout the entire diverging section, even if complete mixture vapourisation takes place. In consequence, nozzles designed for low droplet numbers need to have an increased flow area downstream of the throat to accommodate the design mass-flow rate.

The enlargement of the flow area at low droplet numbers allows the mixture to expand closer to the design outlet pressure as shown in Fig. 6.9. The comparison between the design and the CFD pressure profiles indicates that the underexpansion issues common in the equilibrium nozzles have been practically eliminated and the flow could expand to the design outlet pressure. One thing to note are certain deviations from the design pressure profiles in the diverging section, especially in the expansion from 1000 kPa and $N_d = 10^{11}$. As noted earlier, this could be due to the alteration of the original nozzle shape required to obtain a smooth shockless expansion. Overall, the agreement between the CFD and design static pressure profiles is considerably improved in relation to the equilibrium nozzles.

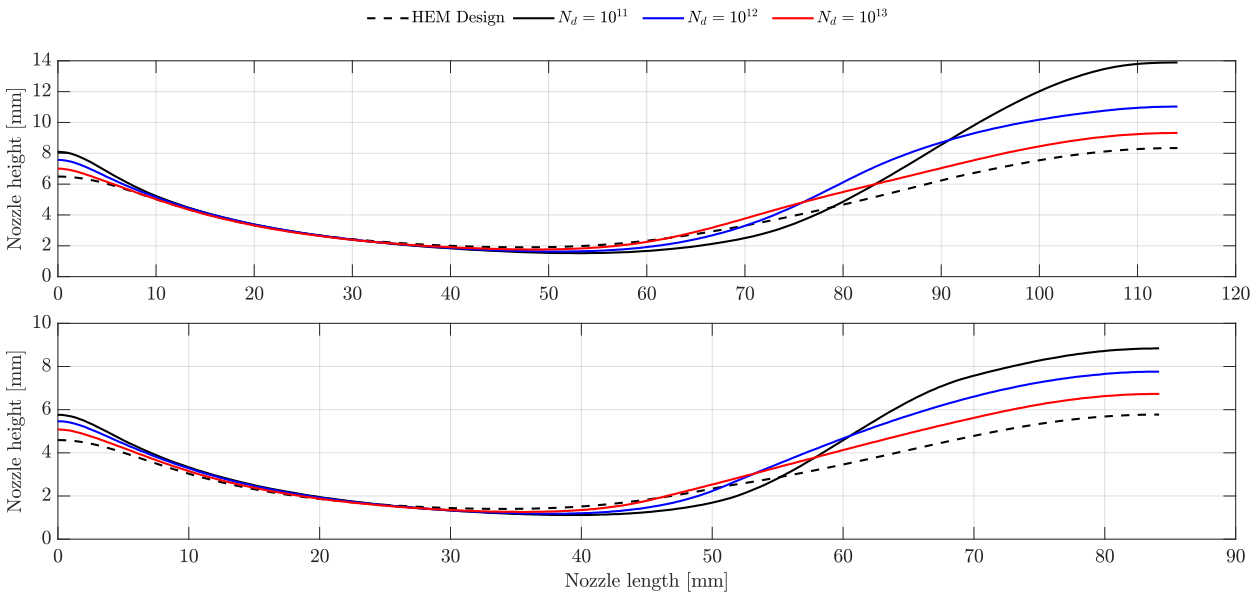


Figure 6.8: The effect of droplet density number on the shape of nozzle generated by the non-equilibrium design tool for the expansions from an inlet pressure of 500 (top) and 1000 kPa (bottom).

6.8 Non-equilibrium effects

The results of the parametric study reported in the previous chapter demonstrated that both the velocity and temperature difference between the phases was significant and mainly dependent on the droplet size. Figure 6.10 shows the streamwise variation of relative slip and thermal non-equilibrium; the relative slip is defined as the velocity slip normalised by the average mixture velocity ($u_{slip,rel} = (u_V - u_L)/u_{mix}$), whereas thermal non-equilibrium was simply defined as the difference in liquid and vapour temperatures.

Generally, the relative velocity slip profiles were fairly similar in the equilibrium and non-equilibrium nozzles, although the slip appeared to be higher in the latter due to increased expansion and related flow acceleration in the diverging section of the nozzle. The only profile significantly different was the one generated for the inlet pressure of 1000 kPa and $N_d = 10^{11}$, which indicates a sudden reduction in velocity slip near the outlet of the nozzle. This is related to abrupt vapourisation in that area and the associated decrease in droplet size, which consequently led to reduced velocity slip. As for thermal non-equilibrium, the enhanced expansion seems to bring an increase in temperature difference in the diverging section. As the phase change is accelerated in the non-equilibrium nozzles, small droplets cool down more rapidly as the flow approaches the outlet. This resulted in a similar phenomenon observed in the equilibrium nozzles with high droplet numbers, where small cooler droplets travel in hotter superheated vapour. Despite the temperature of these small droplets being lower than that of the vapour, both phases remain superheated, which is why the vapourisation continues. Overall, whether the nozzles are generated using the homogeneous-equilibrium model or the non-equilibrium tool, significant disparity in phase velocities and temperatures accompany the wet-to-dry expansion and these effects should not be neglected in such studies.

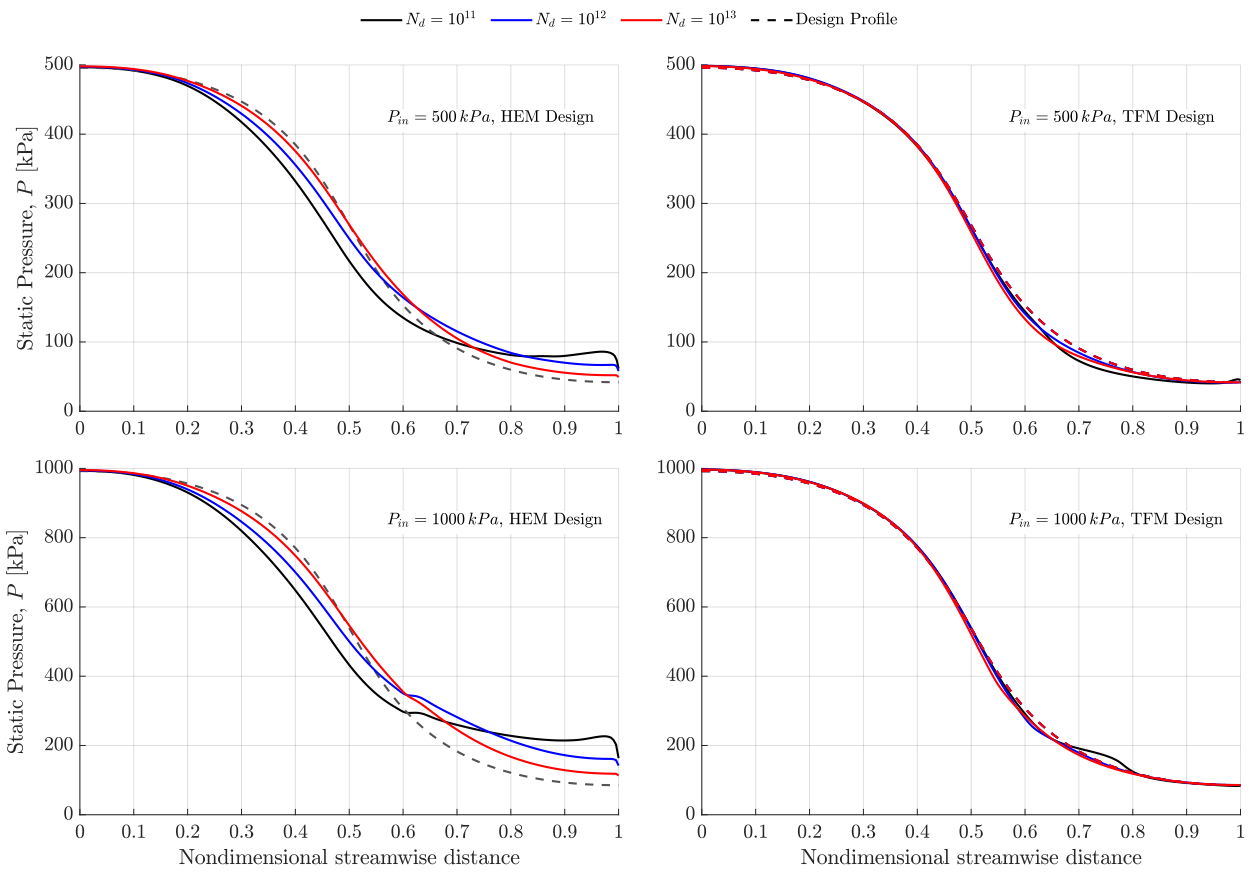


Figure 6.9: Streamwise variation of static pressure P in nozzles generated by the non-equilibrium and homogeneous-equilibrium design tools; the plot illustrates the design profiles and CFD predictions for the expansion from an inlet pressure of 500 and 1000 kPa, fixed inlet vapour quality of 0.3 and three droplet density numbers N_d: 10^{11}, 10^{12} and 10^{13}.

6.9 Two-dimensional flow patterns

Lastly, two-dimensional contours of vapour quality and mixture velocity have been plotted in Figs. 6.11 and 6.12 to demonstrate the effect of the non-equilibrium design on two-dimensional flow patterns.

Analysing the phase distribution in the equilibrium and non-equilibrium nozzles designed for the expansion from 500 kPa, a consistent improvement in the vapourisation rate is observed. Despite the enhanced vapourisation, the key flow characteristics concerning the phase distribution remain unchanged. Liquid droplets having higher inertia tend to concentrate around the centre of the nozzle, creating a characteristic core liquid flow. The lighter vapour phase, having an increased capability to adjust its direction to the nozzle shape, occupies the proximity of the nozzle walls in the diverging section. This leads to significant lateral phase separation near the nozzle outlet, and as in the equilibrium nozzles, this effect is more pronounced at low droplet numbers.

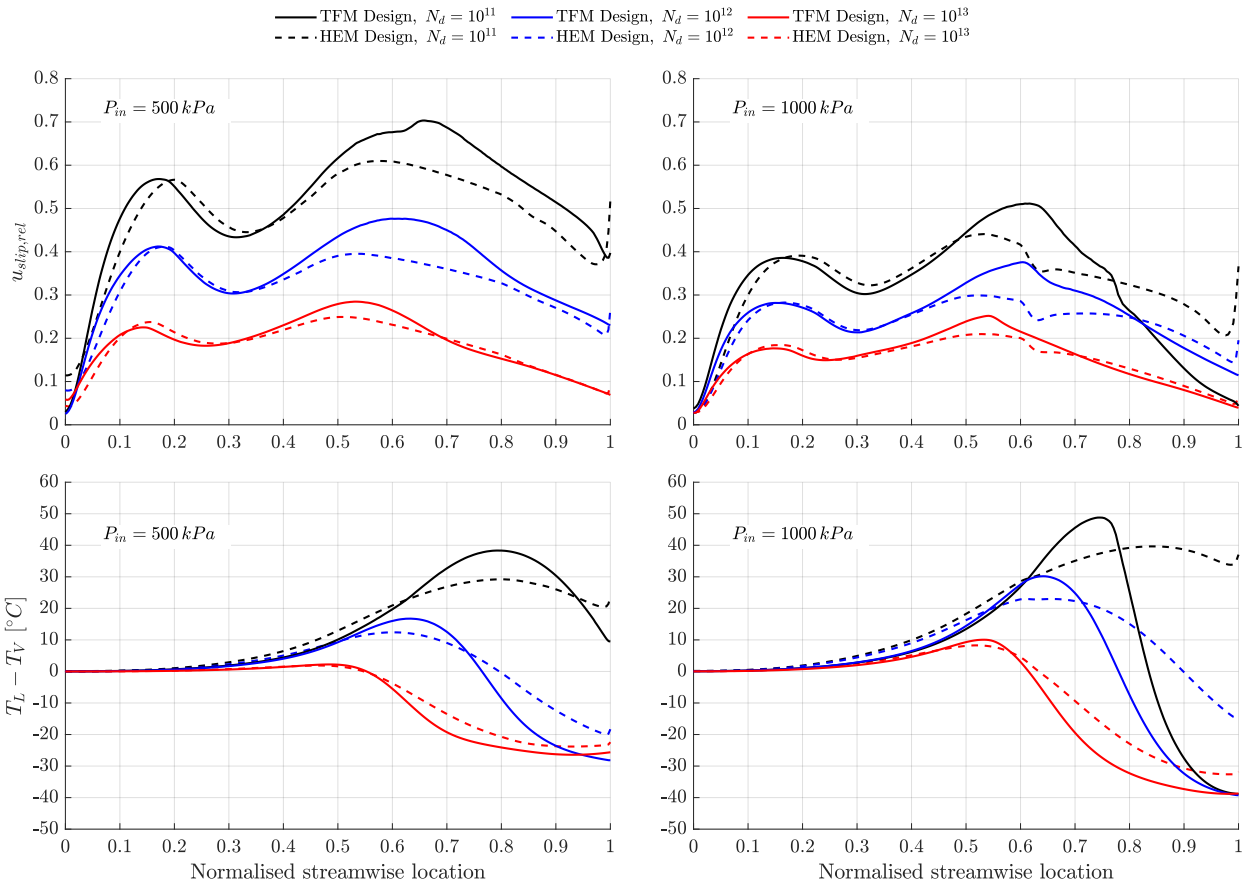


Figure 6.10: Streamwise variation of average relative velocity slip ($u_{slip,rel}$) and average thermal non-equilibrium ($T_L - T_V$) in the nozzles generated by the non-equilibrium (TFM) and homogeneous-equilibrium (HEM) design tools for the expansions from inlet pressure of 500 and 1000 kPa, a fixed inlet vapour quality of 0.3 and three droplet density numbers N_d: 10^{11}, 10^{12} and 10^{13}; $u_{slip,rel}$ is the velocity slip normalised by the mixture velocity, while $T_L - T_V$ is temperature difference between the liquid and vapour phases.

When it comes to the expansion from 1000 kPa, the flow uniformity is drastically improved at low droplet numbers, which can be attributed to the rapid vapourisation of highly superheated droplets as discussed in Section 6.5. The flow exiting the nozzle is in the form of dry or near-dry vapour with no sign of lateral non-uniformity in terms of phase distribution.

As for the two-dimensional variation of mixture velocity illustrated in Fig. 6.12, it was found that even though the overall mixture velocity at the outlet was higher in the non-equilibrium nozzles, the flow remains highly non-uniform in terms of lateral variation of velocity. In fact, the non-uniformity appears to be enhanced in the non-equilibrium nozzles, which is thought to be the effect of a more rapid increase in the flow area in the diverging section, which promotes phase separation where the nozzle begins to widen. This effect was observed even in the expansion from 1000 kPa despite the fact that complete mixture vapourisation occurred relatively early in the diverging section at $N_d = 10^{11}$. To help understand this phenomenon, the centreline variation of mixture velocity and vapour mass fraction have been plotted in Fig.6.13. The dotted vertical lines in Fig. 6.13 represent the streamwise location corre-

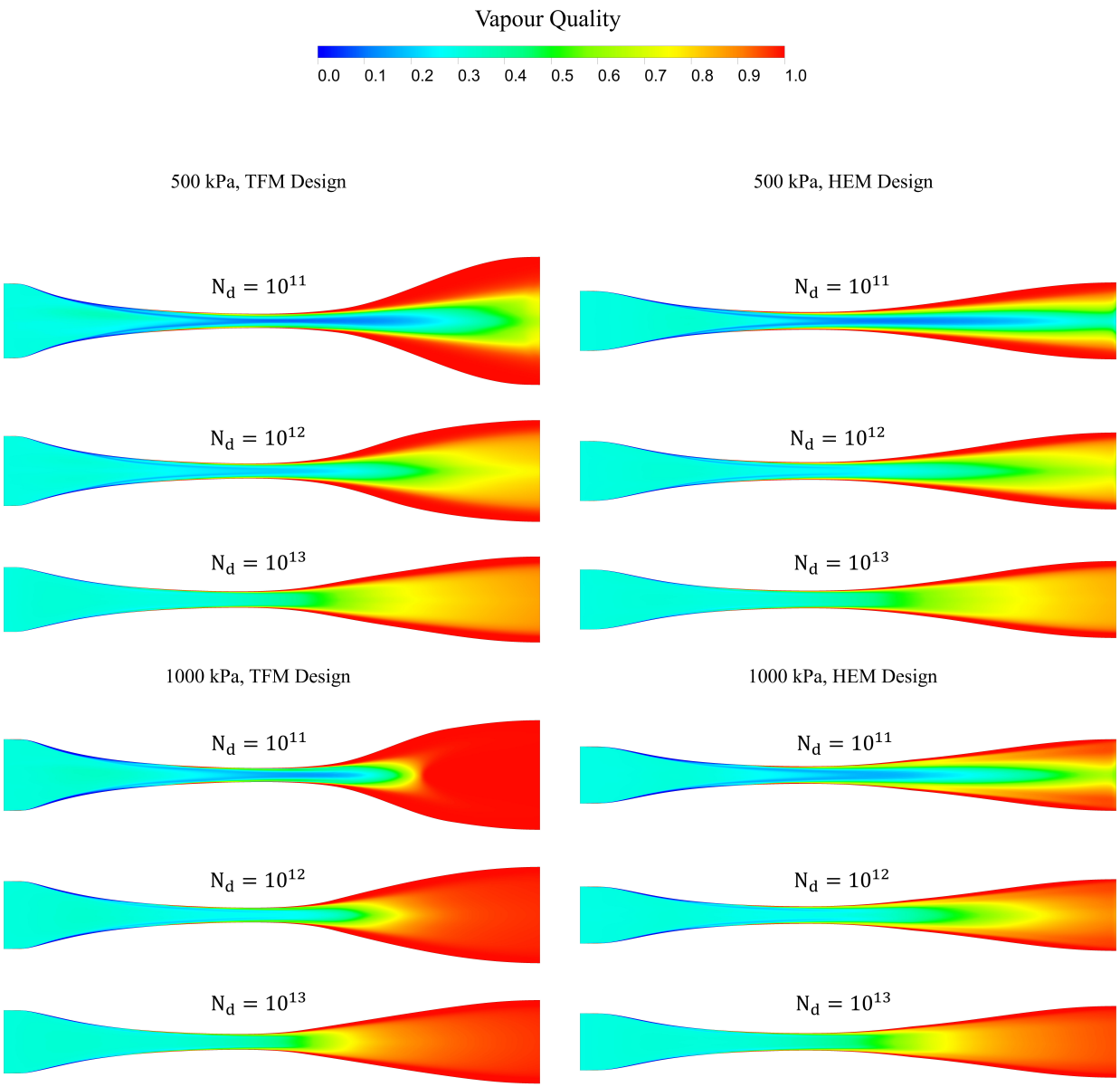


Figure 6.11: Two-dimensional variation of vapour quality in the nozzles generated by the non-equilibrium (TFM) and homogeneous-equilibrium (HEM) design tools for the expansions from inlet pressure of 500 and 1000 kPa, a fixed inlet vapour quality of 0.3 and three droplet density numbers N_d: 10^{11}, 10^{12} and 10^{13}.

sponding to a rapid flow acceleration. As can be seen, the vapour mass fraction across the distance corresponding to the rapid flow acceleration varies between 55 and 100 %. This implies that the mixture expanding across that distance had a relatively high content of the liquid phase. The presence of liquid droplets essentially reduces vapour velocity through the mechanism of interfacial drag. As such, even if the mixture fully vapourises downstream of that region, superheated vapour in the core of the nozzle can have a noticeably lower velocity. On the other hand, the mixture expanding in the proximity of the nozzle wall, having negligible amount of liquid present, reaches much higher velocities. This leads to significant non-uniformity of the velocity field near the nozzle outlet.

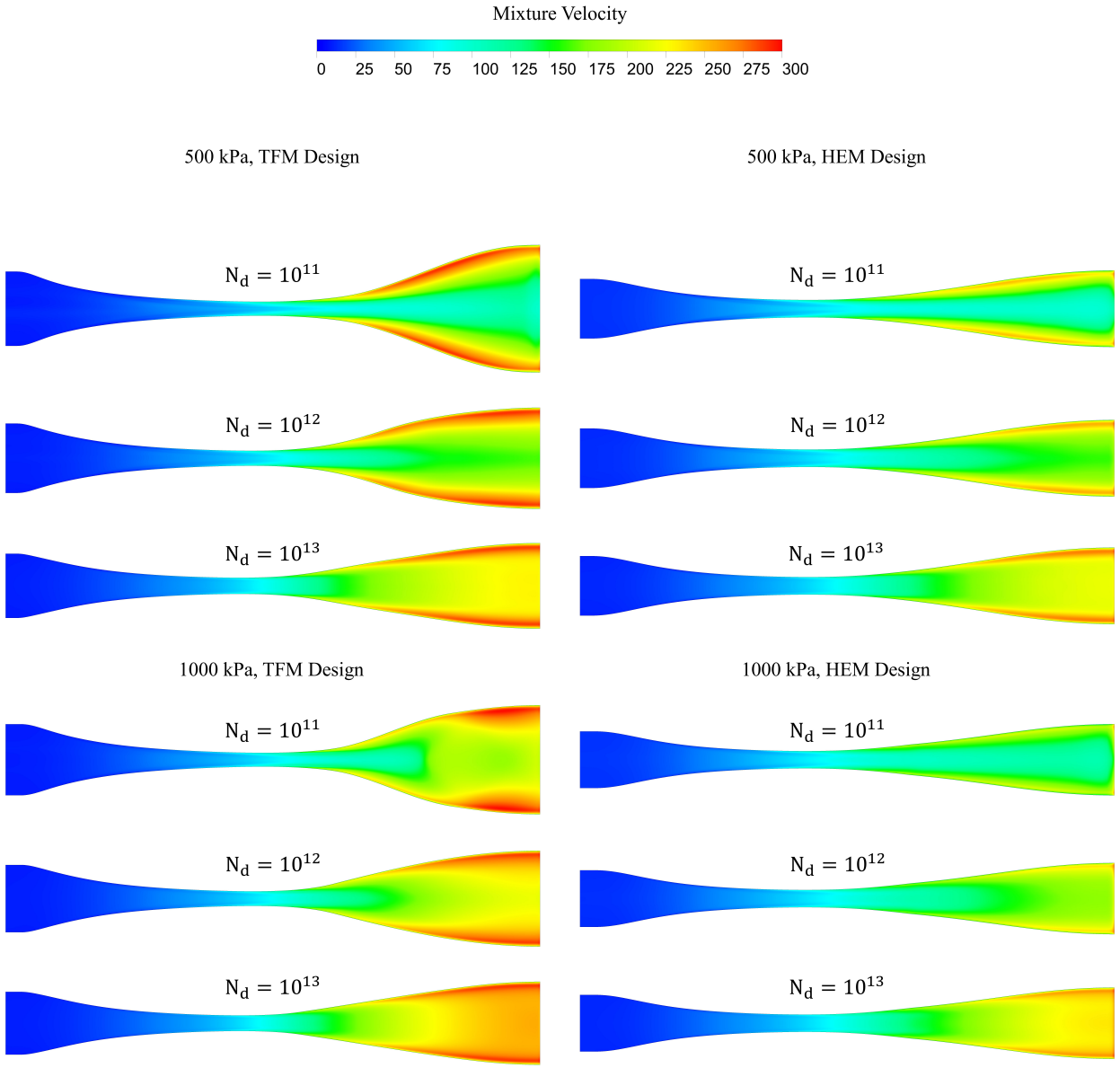


Figure 6.12: Two-dimensional variation of mixture velocity in the nozzles generated by the non-equilibrium and homogeneous-equilibrium design tools for the expansions from inlet pressure of 500 and 1000 kPa, a fixed inlet vapour quality of 0.3 and three droplet density numbers N_d: 10^{11}, 10^{12} and 10^{13}.

Finally, distinct velocity fields of the vapour and liquid phases were plotted in Fig. 6.14 for the expansions from inlet pressure of 500 and 1000 kPa, a fixed inlet vapour quality of 0.3, and a fixed droplet density number of 10^{12}. Overall, the velocity variation of vapour and liquid appear to be similar in both, equilibrium and non-equilibrium nozzles. The main difference is the noticeably lower magnitude of liquid velocity in the core of the nozzle in the diverging section. This area is characterised by higher concentration of the liquids phase, larger droplets and consequently higher velocity slip. On the other hand, the velocity slip in the proximity of the wall in the diverging section appears to be much smaller; this area is

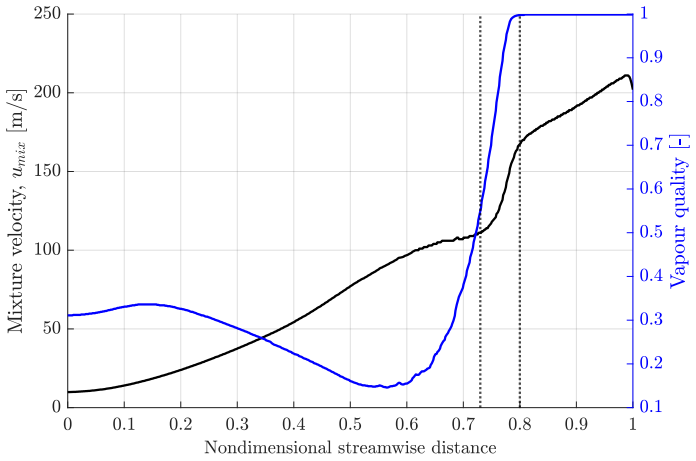


Figure 6.13: The variation of mixture velocity and vapour quality along the centreline of the non-equilibrium nozzle designed for the expansion from an inlet pressure of 1000 kPa, inlet vapour quality of 0.3 and droplet number of 10^{11}; the dotted lines represent the streamwise location corresponding to a rapid flow acceleration.

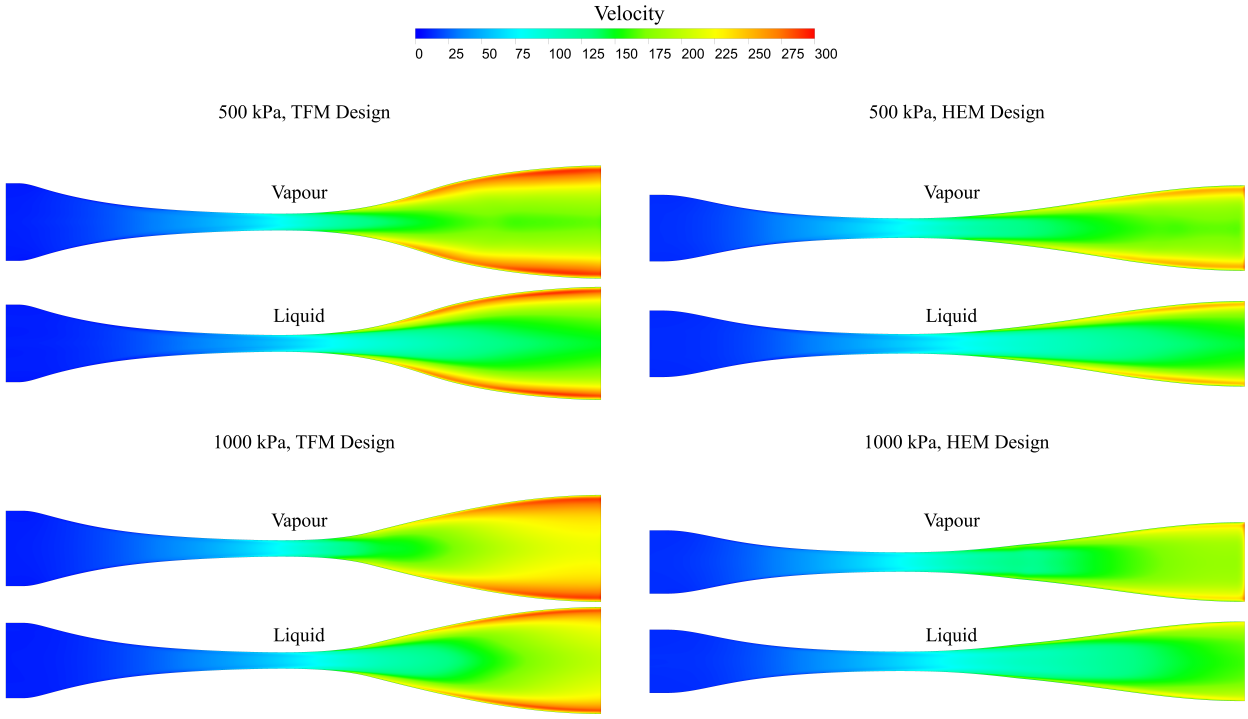


Figure 6.14: Vapour and liquid velocity fields in the nozzles generated by the non-equilibrium and homogeneous-equilibrium design tools for the expansions from inlet pressure of 500 and 1000 kPa, a fixed inlet vapour quality of 0.3, and a fixed droplet density number of 10^{12}

mostly occupied by the vapour phase, and any liquid droplets present near the wall are very small, which makes the momentum exchange more effective.

In summary, including non-equilibrium effects in the design process allowed to design nozzles that deliver dry vapour flow as long as the inlet pressure was sufficiently high. For lower op-

erating pressures the mixture exiting the nozzle had a considerable amount of liquid present at low droplet numbers, and displayed significant phase separation. As for the flow velocity, high non-uniformity was present at the nozzle outlet independently of the inlet pressure and droplet number. As for the flow velocity, high non-uniformity was present at the nozzle outlet independently of the inlet pressure and droplet number.

6.10 Summary of the performance of non-equilibrium nozzles

Although two inlet pressures of 500 and 1000 kPa were selected for in-depth analysis, the simulations were also performed in non-equilibrium nozzles designed for inlet pressures of 750 and 1250 kPa and a fixed inlet vapour quality of 0.3. This was done to provide a more comprehensive comparison between the two design tools and to assess the consistency of the observed patterns across a wider range of pressures. Figure 6.15 illustrates the relationship between the inlet droplet diameter ($D_{d,in}$) and various flow parameters relevant to this study. These include the average exit vapour mass fraction ($x_{V,out}$) and mixture velocity ($u_{mix,out}$), β parameters (Eqs. 5.19-5.20) that are used to assess the flow capability to expand to the design outlet conditions, and σ parameters that evaluate the flow uniformity at the nozzle outlet. To recall, β_p was defined as the ratio of the design pressure drop to the pressure drop predicted by the CFD model, while β_u was the ratio of the design velocity increase to the one predicted by the CFD model. The parameters σ_{x_V} and $\sigma_{u_{mix}}$ denote the standard deviation of the vapour mass fraction and mixture velocity calculated across the nozzle outlet and normalised by average $x_{V,out}$ and $u_{mix,out}$, respectively. Figure 6.15 was plotted using the CFD data obtained for both equilibrium and non-equilibrium nozzles.

In contrast to the equilibrium nozzles, $x_{V,out}$ appears to be weakly affected by the inlet droplet diameter, and the trend of $x_{V,out}$ decreasing with the droplet size is no longer apparent. Conversely, the outlet mixture velocity is visibly reduced as $D_{d,in}$ is raised, especially in the expansions characterised by lower inlet pressures. When it comes to β parameters, the flow ability to reach the design outlet conditions is significantly improved in the non-equilibrium nozzles. The difference between the design and the CFD outlet pressure was practically negligible, while $u_{mix,out}$ reached values greater than 90% of the design outlet velocity in most of the investigated cases. Including non-equilibrium effects in the design process also improved the uniformity of vapour quality at the nozzle outlet. However, the uniformity of the flow velocity at the outlet was slightly worsened, which can be attributed to a more rapid increase in the flow area downstream of the throat and the associated phase separation in that area. In summary, the results appear to be consistent across different inlet pressures and agree well with the patterns discussed in detail for P_{in} of 500 and 1000 kPa.

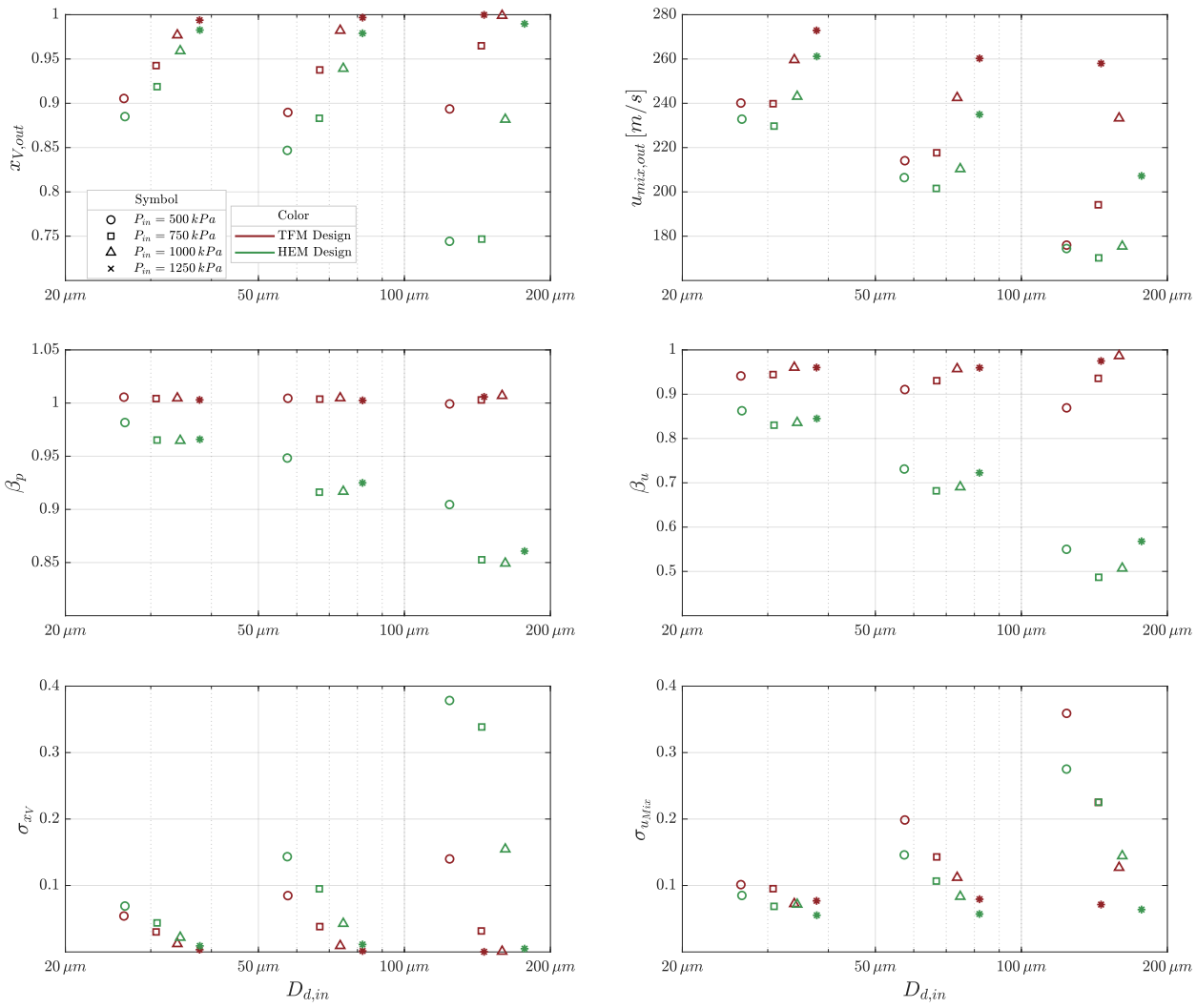


Figure 6.15: The relationship between the inlet droplet diameter $D_{d,in}$ and outlet vapour mass fraction $x_{V,out}$, outlet mixture velocity $u_{mix,out}$, β and σ parameters. The β parameters represent the flow's capability to reach the design outlet conditions, while the σ parameters represent flow's uniformity at the nozzle outlet. The plot has been generated using CFD data obtained in the equilibrium and non-equilibrium nozzles.

6.11 Droplet breakup effects

Similar to the analysis of the equilibrium nozzles, a preliminary droplet breakup analysis was conducted based on the assessment of the average Weber number. The details concerning the evaluation of the critical Weber number can be found in the previous chapter in Section 5.8.7. Figure 6.16 illustrates how the average ratio of the Weber number to the critical Weber number (We/We_{cr}) varies along the nozzle.

Generally, the streamwise profiles of We/We_{cr} appear to be fairy similar to those predicted in the equilibrium nozzles. The average Weber number begins to exceed We_{cr} close to the inlet and typically remains above the critical throughout much of the expansion. The peak ratio of We/We_{cr} for the droplet number of 10^{13} was estimated to be between 2 and 10.

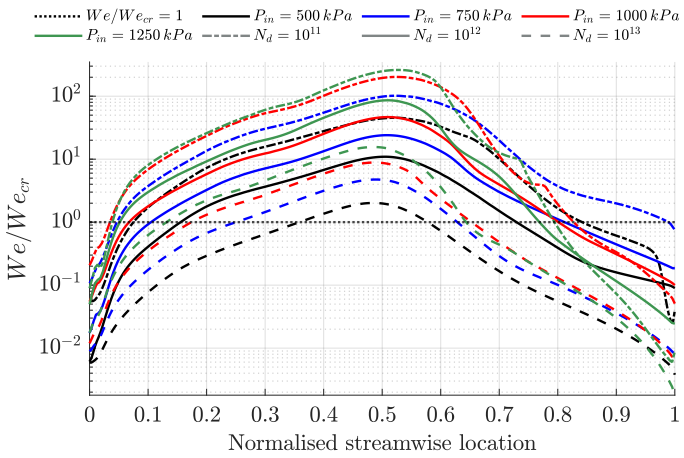


Figure 6.16: The streamwise variation of the ratio of the average Weber number to the critical Weber number in the non-equilibrium nozzles; droplet breakup is expected to occur if the ratio We/We_{cr} exceeds unity (denoted by the black dotted line). The mixture was expanded from inlet quality of 0.3 for each presented case.

As the droplet number is reduced, the ratio We/We_{cr} increases dramatically, with the maximum We reaching values two orders of magnitude greater than We_{cr}. As a result, the droplet number is unlikely to remain below 10^{13} due to the highly probable droplet breakup effects.

As already pointed out, the droplet size is one of the unknowns in the analysis of the wet-to-dry expansion, and it is difficult to estimate without directly relevant experimental data. The results presented so far have been obtained for a range of droplet numbers in order to understand the relationship between the droplet size and the physics of the wet-to-dry expansion. However, as indicated by the preliminary breakup analysis, some flow conditions may be difficult to achieve in practice. For example, the vapourisation rate in the non-equilibrium nozzles designed for low droplet numbers was estimated to be significantly enhanced due to high superheating of large droplets. Based on the preliminary droplet breakup analysis, achieving these flow conditions in practice may be difficult because of the highly probable fragmentation of such large droplets in the early stages of the expansion.

The advantage of the non-equilibrium nozzle design tool is the possibility of estimating droplet size based on the critical Weber number, which is evaluated using the Brodkey [222] correlation:

$$We_{cr} = We_{cr,\,Oh\to 0}\left(1 + 1.077Oh^{1.6}\right) \tag{6.9}$$

where $We_{cr,\,Oh\to 0}$ is the critical Weber number as Oh tends to zero, which can be assumed to be about 11 based on the available experimental data [215]. A more detailed description of breakup modelling can be found in Sections 5.8.7 and 4.3.1. The maximum droplet size $D_{d,max}$ that is not expected to undergo breakup under given flow conditions is determined based on the local value of the critical Weber number.

$$D_{d,max} = \frac{We_{cr}\,\sigma}{\rho_V\,|u_V - u_L|^2} \tag{6.10}$$

The method relies on prescribing a certain inlet droplet diameter, which remains constant as long as the Weber number remains below the critical value. The maximum stable droplet size is computed starting from the inlet. Once it becomes lower that the assumed inlet diameter, which in this case was set to 0.1 mm, the droplet size is adjusted accordingly. The droplet size is only allowed to remain constant or decrease in the streamwise direction in accordance with the local value of We_{cr}. This prevents droplets from increasing in size in the streamwise direction, which could occur only due to condensation or coalescence effects, which were neglected in this study. The non-equilibrium design tool demonstrated that the results are insensitive to the assumed inlet droplet size, as long as it was sufficiently large to induce breakup within the early stage of expansion. Given the lack of directly relevant empirical data, such a method is deemed useful for estimating a realistic droplet size in the wet-to-dry expansion. It is worth noting that the method outline above is based on two major simplifications. First of all, it is assumed that the droplets entering the nozzle have a fixed diameter. In reality, the flow is likely to have a population of droplets with a varying diameter. The other major simplification pertains to the breakup process itself. In reality, large parent droplets will fragment into a number child droplets with varying diameter. In this model, the diameter of droplets is simply reduced based on the average value of the Weber number, which is an oversimplification.

Previous studies implemented droplet breakup models within Lagrangian CFD solvers combined with the volume-of-fluid approach for droplet interface tracking [138]. A direct implementation of the breakup model described above in an Eulerian-Eulerian CFD solver is much more complex. This is because the droplet diameter at a given point in the nozzle depends not only on the local flow conditions but also on conditions directly upstream of that point. This is necessary to ensure that the droplet diameter does not begin to increase in the streamwise direction. This would most likely require access to the solver source code for node-to-node control, and cannot be easily implemented without proper expertise. For the purpose of this analysis, the droplet diameter profile predicted by the non-equilibrium nozzle design tool was imported into ANSYS CFX using a user-defined expression, thus simplifying the problem.

Figure 6.17 illustrates the streamwise variation of average vapour mass fraction, mixture velocity, droplet diameter (D_d) and the ratio of average to critical Weber number (We/We_{cr}) as predicted by the non-equilibrium design tool and the CFD model applied to the expansion from an inlet pressure between 500 and 1250 kPa and a fixed inlet vapour quality of 0.3. The method described above was used to estimate the droplet diameter variation in the design tool; the CFD solver indirectly accounted for the breakup by relying on the droplet diameter profile generated by the design tool.

First, it should be noted that the non-equilibrium design tool predicts complete vapourisation for all the inlet pressures except $P_{in} = 500kPa$, for which the outlet vapour mass fraction reached 98.9%. As expected, the corresponding CFD profiles indicate a delayed

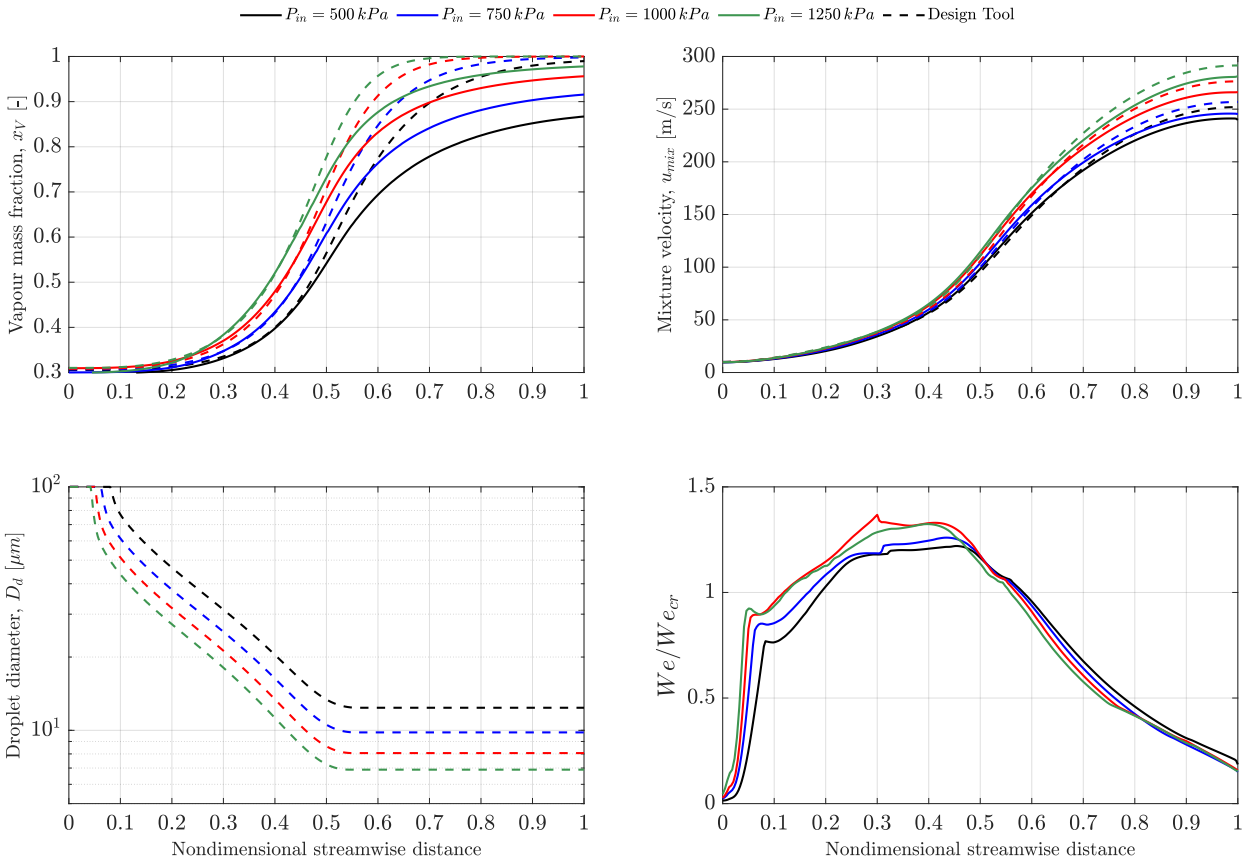


Figure 6.17: The streamwise variation of average vapour mass fraction (x_V), mixture velocity (u_{mix}), droplet diameter (D_d) and the ratio of average to critical Weber number (We/We_{cr}) in the expansion from an inlet pressure between 500 and 1250 kPa and a fixed inlet vapour quality of 0.3. The results were obtained using the non-equilibrium design tool and the CFD model. Droplet size in the non-equilibrium design tool was estimated based on the critical Weber number. The CFD model relied on the droplet diameter profile predicted by the design tool.

vapourisation with respect to the design predictions. Generally, $x_{V,out}$ greater than 95% was achieved only for inlet pressures greater than 1000 kPa; at lower pressures $x_{V,out}$ was between 85-90%. Regarding the mixture velocity, relatively good agreement is observed between the design and the CFD profiles, with a deviation in the outlet velocity below 10-11 m/s under all investigated conditions. When it comes to the droplet diameter profiles obtained with the design tool, the breakup was found to take effect very close to the inlet. The droplet size then continued to decrease up to a distance of approximately 50 % of the nozzle length. From that point on, the diameter remains constant and tends to be lower in higher-pressure expansions. Generally, the size of the droplets in the post-breakup region varied between 7 and 12 µm. The constant droplet size in the diverging section of the nozzle may explain why no complete vapourisation was achieved for any of the inlet pressures. Assuming a constant droplet allowed the droplets to continually decrease in size during the entire expansion. The smaller the droplets, the higher the interfacial area density for a given volume fraction of liquid, and the higher the heat-transfer coefficient. These effects were limited because of the fixed droplet size past the breakup zone, which highlights the main limitation of this

breakup model. The possible effect of further droplet size decrease due to phase change will be explored in the next chapter.

It is worth noting that the ratio of the average to critical Weber number predicted by the CFD model remains fairly close to unity. This suggests that the design tool provided a reasonable approximation of the critical droplet diameter, which was not significantly affected by two-dimensional flow variations and other effects neglected at the design stage.

6.12 Conclusions

The main objective of this chapter was to assess the importance of including non-equilibrium effects in the design of nozzles for wet-to-dry expansion. To this end, a previously developed non-equilibrium design tool was employed to design nozzles for the expansions from an inlet pressure of 500 and 1000 kPa, and a fixed inlet vapour quality of 0.3. The droplet size was modelled with a constant droplet number density, which was varied between 10^{11} and 10^{13}. The performance of the nozzles designed with the non-equilibrium tool was compared to the performance of the nozzles design with the homogeneous-equilibrium model for the same operating conditions.

- Including non-equilibrium effects in the design process was found to have a significant effect on the expansion, especially in two-phase flows characterised by large droplets. For the droplet number of 10^{11}, the non-equilibrium nozzles achieved 12-15 % higher vapour mass fraction and 25.7-90.6 m/s higher than the equilibrium nozzles. Generally, the difference between the non-equilibrium and equilibrium nozzles gradually diminished when the droplet number was raised, which is due to a lower relative importance of non-equilibrium effects in flows characterised by small droplets.

- The main difference in the geometry of nozzles designed with the non-equilibrium tool was an increased flow area in the diverging section of the nozzle. This allowed the mixture to expand close to the design outlet conditions, effectively eliminating the underexpansion issues prevalent in the equilibrium nozzles.

- The assessment of average velocity slip and thermal non-equilibrium demonstrated that both effects remain significant independently of the design method. In fact, the velocity slip and temperature difference increased in magnitude, which can be attributed to a more rapid expansion in the diverging section of the non-equilibrium nozzles.

- Due to the enhanced vapourisation rate, a dry uniform flow was more easily achieved at the outlet of nozzles designed for high inlet pressures. At lower pressures, the improvement in flow uniformity in terms of phase distribution was rather marginal. Regardless of the inlet pressure, the mixture velocity close to the centre of the nozzle at the outlet remained visibly lower compared to the wall area, which contributed to high non-uniformity of the flow velocity.

- The results obtained for two additional inlet pressures of 750 and 1250 kPa confirm the consistency of the observed trends over a wide range of operating pressures.

- The average Weber number was substantially higher than the critical value, indicating that droplet numbers less than 10^{13} are unlikely to be maintained throughout the expansion due to highly probable breakup effects. Droplet diameter profiles satisfying the critical Weber number conditions were generated by the design tool and imported into the CFD solver. With the inlet droplet diameter set to 0.1 mm, breakup was found to occur within the first 50 % of the nozzle length, resulting in a diameter drop to 7-12 µm. With breakup effects taken into account, complete mixture vapourisation was more difficult to achieve at pressures below 1000 kPa, which is due to the assumption of a constant droplet size in the diverging section of the nozzle, which affects the attainable vapourisation rate.

Chapter 7

Nozzle optimisation

7.1 Introduction

As far as the wet-to-dry cycle is concerned, with the siloxane MM as the working fluid, previous studies indicate that the benefit of two-phase expansion gradually diminishes as the open heat-source temperature increases from 150 to 250 °C [8]. Since, the turbine inlet temperature (equal to the saturation temperature of the working fluid in two-phase cycles) must be at least several degrees lower than the heat-source inlet temperature (see Fig. 2.18), the greatest relative of the wet-to-dry cycle using the siloxane MM over single-phase cycles is achieved at saturation temperatures of 150-200 °C. The saturation pressure of the siloxane MM corresponding to that temperature range is approximately between 350 and 900 kPa. The results reported in the preceding chapters indicate that when non-equilibrium effects are taken into account, the wet-to-dry transition is generally more difficult to achieve in nozzles with inlet pressures below 750 kPa. However, the previous analysis did not consider any form of geometry optimisation and all nozzles were constructed using a fixed pressure profile. This chapter aims to optimise the wet-to-dry nozzle to maximise the vaporisation rate and maintain an efficient expansion process. This is done in two stages; first, the non-equilibrium design tool is employed to optimise the design static pressure profile, aiming at increasing the vapourisation rate. In the second stage of optimisation, the nozzle wall profile is parametrised in the CFD solver to directly optimise the shape of the nozzle to maximise both the vapourisation rate and nozzle efficiency.

The previous chapters demonstrated the importance of including droplet breakup effects in the wet-to-dry expansion to approximate a realistic droplet size under given flow conditions. This was fairly simple to implement in the non-equilibrium design tool and was explained in Section 6.11 and is known to have been implemented by other authors studying two-phase expansion in nozzles based on one-dimensional codes [43, 213]. On the other hand, approximating the breakup process in such a manner in two- or three-dimensional CFD simulations is far more complex, and to the best of the author's knowledge, it has not yet been attempted. Therefore, in this chapter, a novel approach to approximating the breakup process in two- and three-dimensional two-phase flows is proposed, which does not require complex manipulation of the solver source code.

7.2 Overview and literature review

The optimisation of the nozzle geometry to achieve vapourisation at lower inlet pressures seems attractive. The advantage of numerical methods is the possibility to assess a variety of geometries and operating conditions at relatively low cost. Therefore, optimisation strategies have frequently been incorporated in the design and analysis of turbomachinery components designed for organic Rankine cycles. Among different optimisation techniques, gradient-free methods are particularly attractive as they do not require access to the numerical source code and perform the optimisation based on function evaluations. The drawback of these methods is the need for a large number of data points, which can imply prohibitively long computation times. This is why gradient-free optimisers are often combined with surrogate models, also known as metamodels, which aim at creating an approximate relationship between the design variables and the objective functions, thereby reducing the number of required high-fidelity evaluations. This is done through the construction of a response surface based on an initial database. The database can be created using design-of-experiments techniques, which aim to effectively resolve the design space with a minimum number of design points. The design points are evaluated with high-fidelity numerical tools, such as CFD simulations. Finally, an optimisation algorithm, such as the genetic algorithm, can be coupled with the response surface to perform optimisation studies.

Such an optimisation framework has frequently been incorporated in the design and analysis of ORC turbomachinery components, where CFD solvers were often used as a means of high-fidelity evaluations. Pasquale et al. [252] performed shape optimisation of a supersonic radial turbine nozzle vane using metamodel-assisted genetic algorithm with 8-10 design variables defining the shape of the vanes. The Latin hypercube was used to create the initial database, while the response surface was constructed using two different metamodels, namely the Kriging and feed-forward neural network. The optimised geometries facilitated a more gentle flow turn, resulting in a shock-less expansion with a more uniform flow at the stator outlet. A similar approach was followed by Persico [253], who optimised the performance of two stages of centrifugal (radial-outflow) turbine nozzles, with design variables being the control points of the B-spline defining the vanes curvature. The response surface was constructed using the Kriging model based on a database created using the Latin hypercube sampling. The optimisation resulted in a decrease in the total pressure loss coefficient from 4.4 % to 3.1 % for one of the nozzle cascades, and from 3.1 % to 2.8 % for the other. The optimised vanes were generally characterised by a reduced shock strength that appeared within the baseline geometry, facilitating a more gradual expansion. In a subsequent study [254], the authors extended the optimisation to the entire nozzle-rotor assembly, resulting in a 2 % increase in stage efficiency. Al Jubori et al. [255] used a gradient-free optimiser to improve the performance of a small-scale ORC radial-inflow turbine by optimising the entire nozzle-rotor stage. The authors applied the optimal-space filling method to uniformly distribute the design points across the design space. Second-order polynomials were used to construct the response surface, which was coupled with a multi-objective genetic algorithm.

The optimised turbine was characterised by an improved blade loading distribution, better flow guidance without flow reversal, and smaller entropy generation, which translated to an efficiency increase as high as 13.95 %. Espinosa et al. [256] also used a surrogate model-based optimisation to improve the performance of an ORC radial-inflow turbine, focusing on the rotor blades. The shape of the blades was defined by a wrap angle and two control points of a Bezier curve. Using a full factorial design and three-dimensional CFD simulations, a response surface was constructed based on radial basis functions. The optimiser was coupled with the genetic algorithm. The refined rotor passage resulted in a 1.9 % increase in total-to-total efficiency and a 3 % increase in power output. Abdeldayem et al. [257] optimised the first stage of a large-scale axial turbine operating with supercritical carbon dioxide blends. The authors used 11 design variables, defining the angle and thickness of the stator and rotor blades, and applied the central composite design as the design-of-experiments technique. A genetic algorithm coupled with the response surface created using genetic aggregation was capable of increasing the stage efficiency by 1.76 to 2.54%.

In general, the studies cited above are examples of successful incorporation of surrogate model-based optimisation techniques in the design of various turbomachinery components, which yielded significant performance improvements. In this chapter, the wet-to-dry nozzle designed for inlet pressures below 750 kPa is optimised to maximise the vapourisation rate, while maintaining an efficient expansion process. The first stage of optimisation is carried out using the non-equilibrium design tool to maximise the vapourisation rate by optimising the design static pressure profile. Since the one-dimensional code assumes inviscid flow, the effect of pressure profile on nozzle efficiency could not be directly accounted for. However, the optimised geometries were evaluated with the CFD model to verify the optimisation results and provide a better understanding of the effect of nozzle geometry on the phase change process and nozzle efficiency. In the second part of this chapter, multi-objective CFD-based shape optimisation is performed, following a surrogate model-based approach. This CFD-based shape optimisation enables the vapourisation rate and nozzle efficiency to be studied simultaneously, which were set as the objectives of the optimisation. The results of the study provide valuable insight into the effect of the nozzle profile on the flash-boiling process, whilst providing further assessment of the feasibility of designing a wet-to-dry nozzle that could operate with low inlet pressures.

7.3 Modelling breakup in the CFD solver

In the absence of relevant experimental data, the most suitable method of estimating realistic droplet size in the wet-to-dry expansion is deemed to be based on the critical Weber number. This methods assumes that liquid droplets can change size only due to breakup, while coalescence effects are neglected. This means that the droplet diameter could either remain constant if the Weber number stays below the critical value or decrease in the streamwise direction if it exceeds the critical value. Therefore, computational modelling of breakup requires not only the knowledge of flow conditions at a given streamwise position but also the knowledge of droplet size upstream of that position to ensure that the droplet diameter does not begin increasing in the streamwise direction. This was easily implemented in the non-

equilibrium design tool, where the equations were solved by marching along the longitudinal axis of the nozzle. On the other hand, simulating the breakup process in two-dimensional CFD simulations is less straight forward. Alternatively, the streamwise droplet diameter profile could be extracted from the non-equilibrium design tool as attempted in Section 6.11. However, such an approach does not allow for estimating the relationship between the nozzle shape and resulting droplet size directly in the CFD simulations, which would be necessary in CFD-based shape optimisation studies. Generally, droplet breakup models such as those proposed by Reitz & Diwakar [258] and Schmehl et al. [259] are known to have been implemented in the Lagrangian (Particle Tracking Model) simulation of secondary breakup of spray droplets. These models rely on an additional partial differential equation that describes the variation in droplet size with time based on the Weber number and estimated breakup time. Given that the current model treats both phases in the Eulerian framework, which is applied to conduct steady-state simulations, alternative approaches are required to estimate droplet breakup.

In order to estimate droplet breakup in an Eulerian-Eulerian steady-state solver, the breakup process was approximated by discretising the nozzle into a number of control volumes along the nozzle's longitudinal axis, as shown in Fig.7.1. In this way, at a single iteration within the simulation it is possible to simultaneously estimate the critical diameter in each control volume based on the average flow conditions and implement a user-defined expression in CFX that prevents the droplets from increasing in size in the streamwise direction.

The breakup process is approximated in the following manner. First, the average critical diameter is evaluated using the following equation:

$$D_{cr,avg} = \frac{\sum (\alpha_L D_{cr})}{\sum \alpha_L} \tag{7.1}$$

where the summation is carried out over all the grid cells in the specific discretised volume. The critical diameter is defined based on the local Weber number, velocity slip, vapour density and liquid surface tension coefficient:

$$D_{cr} = \frac{We_{cr}\,\sigma}{\rho_V u_{slip}^2} \tag{7.2}$$

Since in the investigated expansion the Ohnesorge number was smaller than 0.1, the critical Weber number could be approximated with a constant value of 11, as proposed by Bordkey [222] and Gelfand [223]. The purpose of weighing the critical diameter with the volume fraction of liquid is to ensure that the average critical Weber number corresponds to the area mostly occupied by the liquid phase. If the critical diameter was not weighed by the volume fraction of liquid, the areas with extremely small content of the liquid phase could inappropriately influence the average critical droplet size. Once the average critical droplet diameter was estimated in the discretised volumes indicated in Fig. 7.1, an additional set of user expressions was implemented to prevent the droplet size from increasing in the streamwise direction. This was simply implemented using the following expression:

$$D^i = min\left(D^{i-1}_{cr,avg}, D^i_{cr,avg}\right) \tag{7.3}$$

where the index i denotes the number of the discretised volume, counting from the inlet of the nozzle. Hence, the droplet diameter in a given control volume cannot start increasing in the streamwise direction. Having a droplet diameter calculated in each volume using Eq. 7.3, the following expression was use to simulate the variation of droplet size in the streamwise direction:

$$D^i(x) = D^i - \left[(D^i - D^{i+1})/(x^{i+1} - x^i)\right](x - x^i) \tag{7.4}$$

where x is the streamwise coordinate, whereas x^i and x^{i+1} are the streamwise position of the beginning and end of the i^{th} volume. In that way there is a linear variation between the estimated droplet size between the volumes i and $i+1$. In case, the droplet size is the same in these two adjacent volume, the droplet size will remain constant. Equation 7.4 is formulated for each discretised volume shown in Fig. 7.1. The details concerning the numerical implementation of the breakup method can be found in Appendix A.2.

In addition to this, an initial droplet diameter is specified at the inlet of the nozzle, which is set to 0.1 mm. The shortcoming of such an approach is that the averaged droplet diameter varies only along the longitudinal axis of the nozzle, and thus no lateral variations are considered. It should also be pointed out that, even though this study refers to this droplet size estimation routine as a breakup model, the physical breakup is a much more complicated process. As such, the model herein described should be considered as a simplified technique of estimating maximum stable droplet size under given flow conditions. With that being said, a similar approach was implemented by Elliot [213] in a one-dimensional code designed to study expansions of two-component two-phase mixtures. The design code could estimate the exit velocity and flow rate of the water-nitrogen and water-air mixtures with an error below 5 % compared to the experimental results.

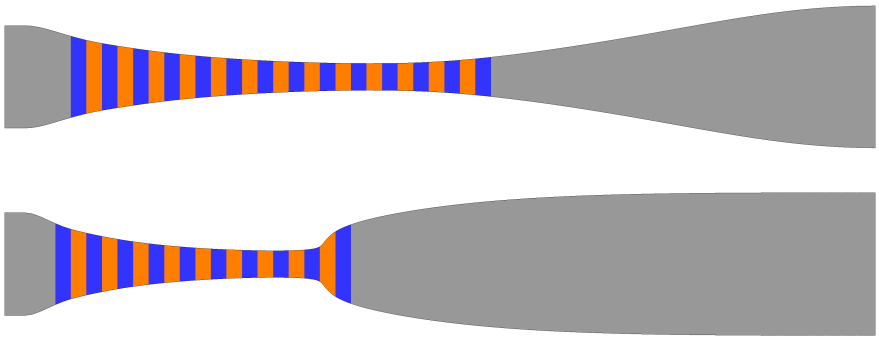


Figure 7.1: The breakup zone in the baseline (top) and 1D-optimised (bottom) nozzles expanding the two-phase mixture from 550 kPa and inlet quality of 0.3; the blue and orange stripes represent the control volumes used to approximate the breakup, which signify the location of breakup.

In theory, the nozzle could be divided into a very high number of volumes to make sure that the droplet breakup process is well resolved. However, it was found that a high number of volumes was associated with significantly longer simulation times, which is thought to be related to the additional burden of calculating average properties within each volume. In

the context of shape optimisation, which may involve a large number of simulations, it is desired to reduce the simulation time as much as possible. Therefore, calibration studies were conducted to determine where the breakup is most likely to occur and to limit the discretisation to that location. Since the breakup is closely related to the shape of the nozzle, two different geometries were tested, representing two extremes that correspond to very gradual and abrupt expansions. The first geometry was the baseline nozzle with a pressure profile illustrated in Fig.5.2, while the latter was a geometry obtained from one-dimensional optimisation described in the following sections. The length of the two nozzles was identical and equal to 109.39 mm, while the throat location differed, being at 44.5 and 32.2 mm from the inlet in the baseline and optimised nozzles, respectively. An identical expansion from 550 kPa and an inlet quality of 0.3 was simulated, and an appropriate mesh size was selected in accordance with the mesh independence study described in the next subsection. The goal of these calibration studies was to find the region where breakup occurs, as well as to determine a suitable width of the control volumes needed to accurately capture the breakup process.

The results in Figure 7.1 illustrate the location of the breakup as predicted by the CFD simulations for the two investigated geometries. The breakup was found to begin very close to the inlet in both nozzles; however, in the case of the gradual expansion, the breakup process extended over a larger length of the nozzle. More specifically, the breakup ceased at a distance of around 15 mm downstream of the throat in the baseline nozzle, compared to around 10 mm for the optimised nozzle. It was thus decided to place the control volumes between the nozzle inlet and 16 mm downstream of the throat, which should capture the breakup in both gradual and abrupt-expansion nozzles. The second part of the sensitivity analysis concerned the width of the volumes required for an accurate prediction of the droplet diameter profiles. To this end, the breakup zones shown in Fig.7.1 were discretised with volumes of a width ranging from 1 to 4 mm. The results in Figure 7.2 illustrate the relationship between the width of the volume and the streamwise variation of the average droplet diameter. It can be seen that the droplet diameter profiles are very similar for the width of 1 and 2 mm. Therefore, the width of 2 mm, which corresponds to approximately 1.8 % of the total nozzle length, was considered to be sufficiently small for approximating the breakup process. The total number of control volume required to estimate the breakup was 28 in the baseline geometry and 19 in the optimised one.

7.4 Mesh independence study

Although the mesh independence study has already been performed when conducting the parametric study (Chapter 5.1), the mesh was improved in two aspects. First, the grid was improved by constructing a fully structured hexahedral mesh, eliminating distorted elements of lower quality. Secondly, the mesh density was increased in the proximity of the throat, which helped to more accurately resolve the breakup process in the presence of high flow gradients typical of the optimised geometries. It also helped to more accurately resolve the formation of shock waves if ones occurred in the nozzles. This was not as important in the previous analyses as no shocks were estimated to form in that section of the nozzle.

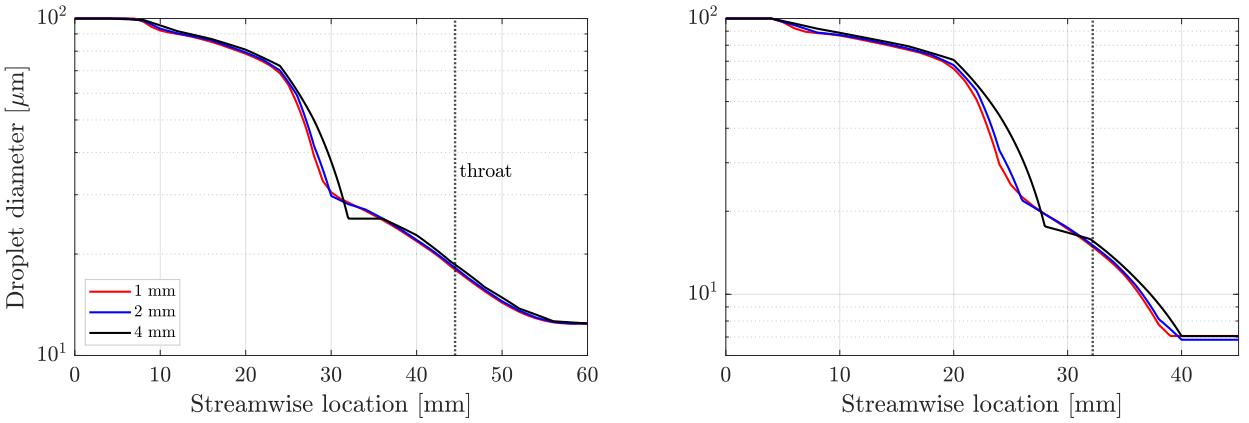


Figure 7.2: The relationship between the width of the volumes used to model the breakup and the streamwise variation of the average droplet diameter; the two plots correspond to the baseline (left) and 1D-optimised (right) nozzles expanding the two-phase mixture from 550 kPa and inlet quality of 0.3.

The mesh independence study was conducted on the 1D-optimised nozzle shown in Fig.7.1. Three different grids were constructed: a coarse mesh with approximately 7,500 elements, a moderate mesh with 15,000 elements and a fine mesh with 30,000 elements. The width of the element adjacent to the wall was kept constant at 10 µm in each grid, which was sufficient for the average y+ of vapour and liquid to remain below 50 and 150 respectively, where standard wall functions can be applied. It is worth recalling that, based on the analysis included in previous chapters, viscous losses play a secondary role in the expansion. As such, the main interest lies in predicting the free stream flow. The width of the elements applied in the lateral direction was progressively smaller when approaching the nozzle wall, to ensure that the boundary layer is well resolved. Based on simplified estimates of the thickness of the boundary layer for a flat plate, it was estimated that the boundary layer was resolved with at least 20 elements. Similar to the previous analyses, the convergence of the solution was assessed based on the average residual values along with the solution mass imbalance, and various flow parameters such as mass flow rate, averaged velocities and vapour mass fraction measured at several planes along the nozzle. Moreover, several monitor points were placed in the diverging and converging sections and at the throat to additionally examine the convergence. The solution converged well within several thousand iterations, with the average mass and momentum residuals below 10^{-6}, mass imbalance less than 0.005% and various averaged and local flow parameters converging to single values.

The results of the mesh independence study are summarised in Table 7.1, including information on mesh metrics, various outlet flow properties, nozzle efficiency (η_N) and total mass-flow rate at the outlet ($\dot{m}_{out}$). The nozzle efficiency is calculated based on the ratio of the actual to isentropic kinetic energy rise:

$$\eta_N = \frac{\left(\dot{m}_{V,out}u^2_{V,out} + \dot{m}_{L,out}u^2_{L,out}\right) - \dot{m}_{in}u^2_{in}}{\dot{m}_{out}u^2_{is,out} - \dot{m}_{in}u^2_{in}} \tag{7.5}$$

where $\dot{m}_{in}$ is the total mass-flow rate at the inlet, while $u_{is,out}$ is the isentropic outlet velocity, which was estimated with a simple code based on a quasi-1D isentropic homogeneous-

Table 7.1: Mesh independence study results performed for the 1D-optimised nozzle.

Mesh	Coarse	Moderate	Fine
Element Count	7520	15066	29988
Longitudinal Elements	188	243	357
Lateral Elements	40	62	84
$x_{V,out}$ [%]	93.31	93.43	93.39
$u_{V,out}$ [m/s]	233.25	234.06	234.31
$u_{L,out}$ [m/s]	215.00	216.67	216.75
$T_{V,out}$ [°C]	99.70	99.85	100.02
$T_{L,out}$ [°C]	76.29	76.13	76.33
$\dot{m}_{out}$ [g/s]	1.715	1.708	1.708
η_N [%]	74.12	74.69	74.84
Δ_{max} [%]	-	0.77	0.20

equilibrium expansion. Based on the results of the mesh independence study reported in Table 5.3, a percentage variation was calculated in each parameter reported between two consecutive grids, i.e., between the moderate and coarse, and between the fine and moderate grids. The maximum of these percentage variations, Δ_{max}, is reported at the bottom of the table. The greatest difference between the moderate and coarse grid was below 0.77%, and it corresponded to the outlet velocities and nozzle efficiency. The maximum difference dropped to around 0.20% between the fine and moderate grids. Generally, all the grids generated very similar results when it comes to the outlet flow properties, with the difference becoming practically negligible when the number of elements was greater than 15,000.

Alongside the outlet properties, average streamwise variations were also examined, which were calculated using a user-defined expression shown in Eq. 5.12. Several average streamwise variations were examined but no significant deviations were found except for the mass-flow averaged entropy profiles, which are plotted in Fig. 7.3.

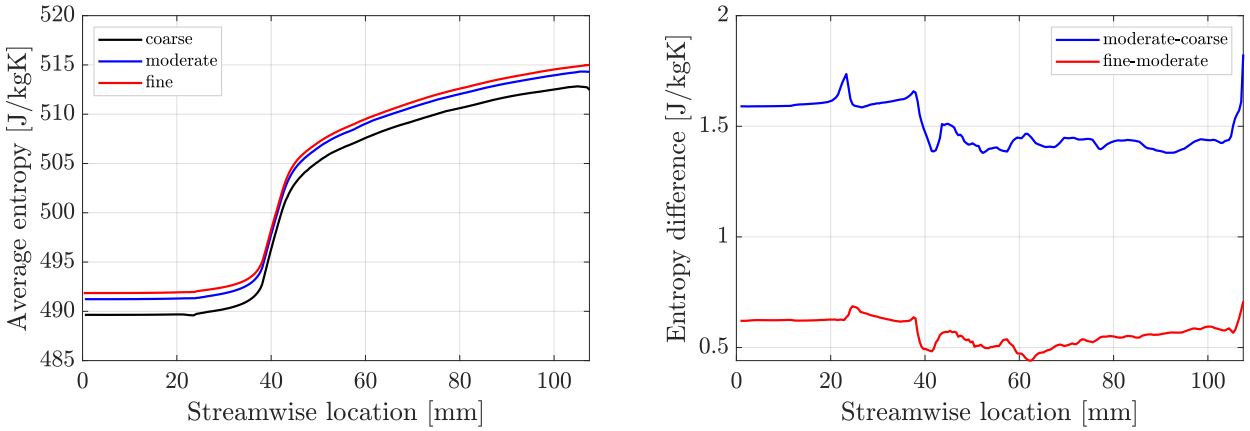


Figure 7.3: Streamwise variation of mass flow-averaged entropy for various grid sizes (left) and absolute difference in average entropy between the consecutive grids (right).

It is observed that the averaged entropy differs for the coarse mesh from the very beginning of the expansion, despite that overall trend and entropy generation being almost identical (Fig. 7.3 (right)). The vapour and liquid entropy values at the inlet were found to be identical

and the difference was found to be related to a slightly different ratio of vapour and liquid mass-flow rates, which were used in the averaging. The difference in the average streamwise entropy profiles between the moderate and coarse grids oscillates between 1.4 and 1.8 J/kgK, which drops to around 0.45-0.70 J/kgK for the fine mesh. Based on the results of the mesh independence study, it was decided that the mesh with 30,000 elements was sufficiently fine.

7.5 One-dimensional optimisation

This section first explains what operating conditions were considered for the optimisation, followed by the verification of the non-equilibrium design nozzle design tool. The one-dimensional optimisation setup and results are then presented and discussed.

The first stage of optimisation focuses on the static pressure profile imposed in the non-equilibrium design tool. In essence, an optimal nozzle pressure profile is sought that would maximise the vapourisation rate in the nozzle. The pressure profile is constructed using a Bezier curve as shown in Fig. 5.2. It influences the rate of expansion, which, in turn, affects the breakup process and the resulting droplet size. Since the droplet size is arguably the most important factor influencing the rate of mass and heat transfer, the optimisation of the pressure profile imposed in the design of the nozzle could help maximise the outlet vapour quality. The design process assumes a quasi-1D non-equilibrium flow as discussed in Section 6.2. As such, the optimisation of the pressure profile will be referred to as one-dimensional optimisation.

7.5.1 Operating points for optimisation

Previous cycle studies that focused on optimising the wet-to-dry cycle indicate that the two-phase expansion gives the greatest advantage when the heat source is at temperature between 150 and 200 °C, where the power output could be between 29% and 14% higher than in the simple ORC [8]. This temperature range corresponds to an evaporation pressure between 300 to 1000 kPa, if the siloxane MM is used. Although low operating pressures are preferred as far the cycle performance is concerned, the initial CFD analysis indicates that the successful wet-to-dry transition may be difficult to achieve when expanding from pressures lower than 750 kPa and from vapour qualities below 30%. For this reason, the optimisation was applied to three operating points with low inlet pressures, namely, 450, 550 and 650 kPa. These pressure levels could correspond to heat-source inlet temperatures in the approximate range of 170 to 190 °C, where the cycle can potentially offer a significant increase in power output [8]. The inlet vapour quality was set to 0.3, which provides the good balance between the cycle thermodynamic advantage while enabling the wet-to-dry transition. The nozzle design process was explained in detail in Sections 5.2 and 6.2.

The three expansion cases are reported in Fig. 7.4, which shows the ideal isentropic process. Although expanding from lower inlet qualities could offer a further increase in the power output, preliminary turbine design studies have shown that it would require a lower degree of reaction, which could have a detrimental effect on the turbine efficiency [8]. Similarly to

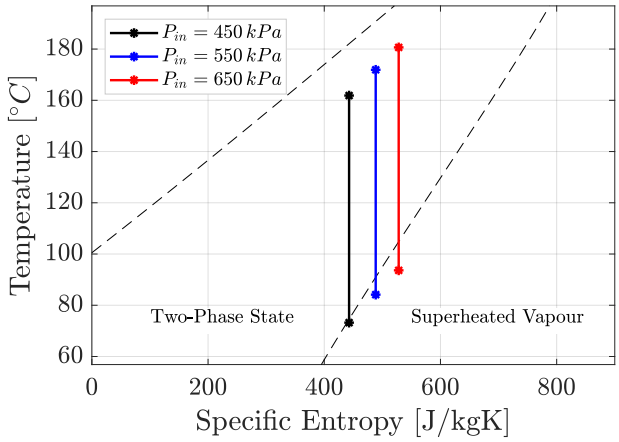


Figure 7.4: Three operating points investigated in the optimisation study; the expansions shown under the isentropic flow assumption

the previous analysis, the mass-flow rate was set to 0.12 kg/s, which translates to a turbine isentropic power of around 100 to 120 kW under the investigated operating conditions. This power rating could correspond to a small-scale system designed for waste-heat recovery from low-temperature sources. The ratios of nozzle length to throat height (L/o_{th}), and nozzle width to throat height (b/o_{th}) were set to 30 and 3 respectively, which are values in line with the former studies. Since the design code assumes a one-dimensional flow, neither the nozzle width b nor the throat height o_{th} had any effect on the expansion. The only geometrical parameter that could affect the phase change in the one-dimensional code was the nozzle length. Table 7.2 shows the vapour mass fraction at the nozzle outlet predicted by the non-equilibrium tool for the three investigated expansions, obtained with different L/o_{th} ratios, which directly affects the nozzle length.

Table 7.2: Outlet vapour mass fraction predicted by the non-equilibrium design tool for different nozzle length to throat height ratios (L/o_{th}).

P_{in} $[kPa]$	$q_{V,in}$	L/o_{th}	$q_{V,out}$	$D_{d,out}$ [µm]
450	0.30	10	0.9854	8.66
450	0.30	30	0.9821	13.09
450	0.30	60	0.9800	17.61
550	0.30	10	0.9819	7.96
550	0.30	30	0.9786	12.30
550	0.30	60	0.9766	16.37
650	0.30	10	0.9904	7.15
650	0.30	30	0.9885	11.11
650	0.30	60	0.9874	14.79

It can be seen that the length of the nozzle had very little influence on the outlet vapour mass fraction. It is worth noting that $q_{V,out}$ tends to be lower in longer nozzles. This is associated with a more gradual expansion that minimises droplet breakup. In consequence, the benefits of a longer timescale for interphase heat exchange are outweighed by higher

post-breakup droplet diameter ($D_{d,out}$) and the vapourisation rate remains approximately the same. Based on the preliminary assessment of the influence of geometrical ratios on the wet-to-dry expansion, only the nozzle pressure profile was set as a design variable in the one-dimensional optimisation.

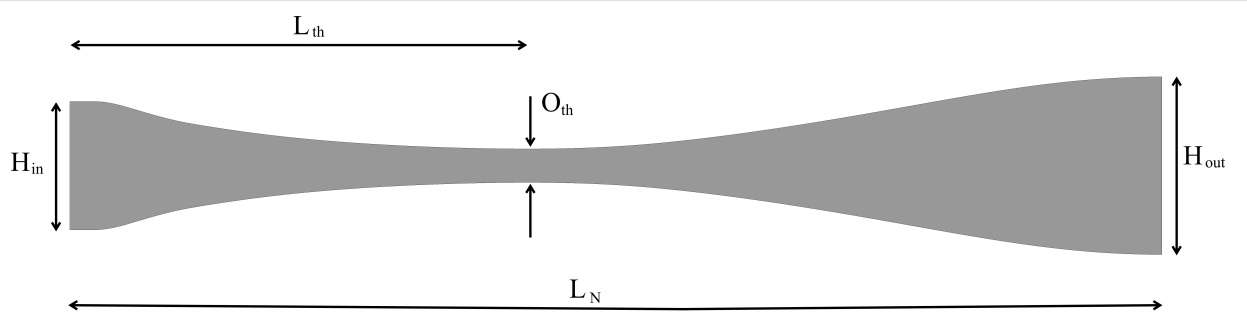


Figure 7.5: Baseline nozzle geometry for the expansion from 550 kPa.

Figure 7.5 illustrates the baseline nozzle geometry designed for the expansion from 550 kPa. The baseline nozzles for the two other investigated cases (with P_{in} at 450 and 650 kPa) had similar shapes. Using the same notation defined in Fig.7.5, Table 7.3 provides the dimensions of all the investigated nozzles. It should be pointed out that even though the baseline nozzles will undergo optimisation, all the parameters except for the streamwise location of the throat (L_{th}) will remain unchanged. This is because the design inlet and outlet conditions as well as the design mass-flow rate, which determines the throat height (o_{th}) are held constant.

Table 7.3: Geometrical features of each investigated converging-diverging nozzle.

P_{in} $[kPa]$	$q_{V,in}$	P_{out} $[kPa]$	H_{in} [mm]	o_{th} [mm]	H_{out} [mm]	L_{th} [mm]	L_N [mm]
450	0.30	39.77	14.56	3.74	18.78	49.09	119.49
550	0.30	43.78	13.14	3.43	18.20	44.50	109.39
650	0.30	47.32	12.04	3.21	17.74	40.75	101.66

7.5.2 Comparison of nozzle design tool against CFD simulations

Before proceeding with the optimisation, the performance of the baseline nozzles generated using the quasi-1D tool has been verified using the CFD model. At this point, it is worth noting that such a verification has been carried out in Section 6.11, for inlet pressures ranging from 500 to 1250 kPa. However, in the optimisation study, the CFD solver incorporates direct approximation of the droplet size based on the approach outlined in Section 7.3. Hence, the verification study is repeated for inlet pressure levels directly relevant to the optimisation study. The three nozzles for the operating points defined in Fig. 7.4 were designed using the baseline pressure profile shown in Fig. 5.2. These were assessed using the quasi-2D

steady-state CFD simulations, as described in Section 4.6.

Figure 7.6 presents the comparison of the average streamwise pressure variations between the quasi-1D design tool and the CFD model. The results indicate that the pressure distribution slightly diverged from the design profiles within the diverging section of the nozzle. A close-up of the profiles near the nozzle outlet reveals a slight overexpansion for the 550 and 650 kPa cases. However, this is rather insignificant, with the outlet pressure being approximately 2.5% lower than the design value. This effect was slightly more pronounced for the 450 kPa case, with flow reaching a pressure 7.6% lower than the design pressure. Overall, the pressure profiles estimated with CFD were fairly close to the design profiles.

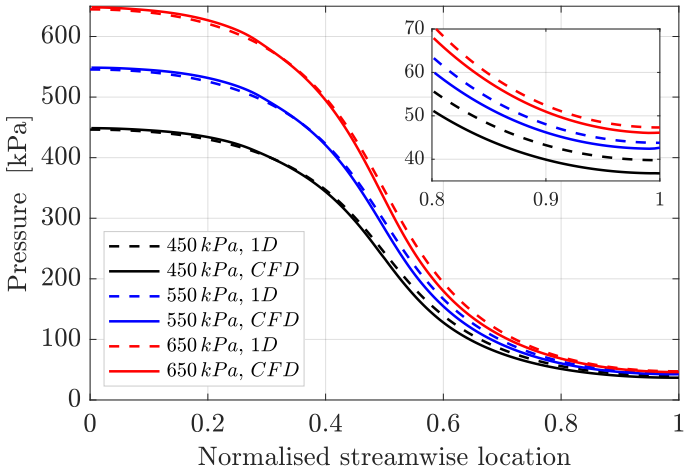


Figure 7.6: Comparison of average streamwise variation of pressure between the quasi-1D design tool and CFD; the box in the top right presents a close-up of the variations near the nozzle outlet.

The results shown in Fig. 7.7 compare the average streamwise variation of vapour mass fraction (x_V) and velocity slip for the different nozzles. The quasi-1D tool predicts near-dry conditions at the nozzle outlet with x_V ranging from 0.984 to 0.998. Most of the phase change occurs shortly past the throat in the diverging section. The curve then plateaus as the flow approaches the outlet. This trend is similar for each of the three expansions; however, the higher the pressure the quicker the evaporation and the higher the outlet vapour quality. Although the CFD model predicts a visibly lower evaporation rate compared to the quasi-1D design tool, the phase-change pattern looks similar in both cases. The discrepancy in x_V gradually increases in the diverging section, reaching a maximum of around 10 to 15% at the outlet. In summary, lateral phase separation, viscosity, and turbulence effects are likely to delay phase change and lead to an increased liquid content of the flow leaving the nozzle. Among these effects, the lateral phase separation is considered to have the greatest impact on the phase change process. This is because as the phases separate out there are areas of highly-concentrated liquid, characterised by reduced interfacial area available for the heat transfer, which drives the mass exchange according to Eq. 5.16.

When it comes to the maximum stable droplet size, the deciding factor is the velocity slip

(see Eq.6.10). Overall, the average slip variation in the streamwise direction predicted by the design tool is similar to the CFD estimates. It is worth highlighting that the maximum velocity slip reaches 40 m/s; knowing that the mixture velocity at that point in the nozzle is in the range of 230 to 250 m/s, the corresponding slip velocity is between 14 and 17% of the mean mixture velocity.

Despite the quantitative differences between the quasi-1D design tool and the CFD, the overall phase change pattern is conserved. Therefore, it seems rational to assume that enhancing the evaporation rate in the quasi-1D tool will translate to improved vapourisation in the CFD model. This justifies using the quasi-1D tool for initial optimisation purposes.

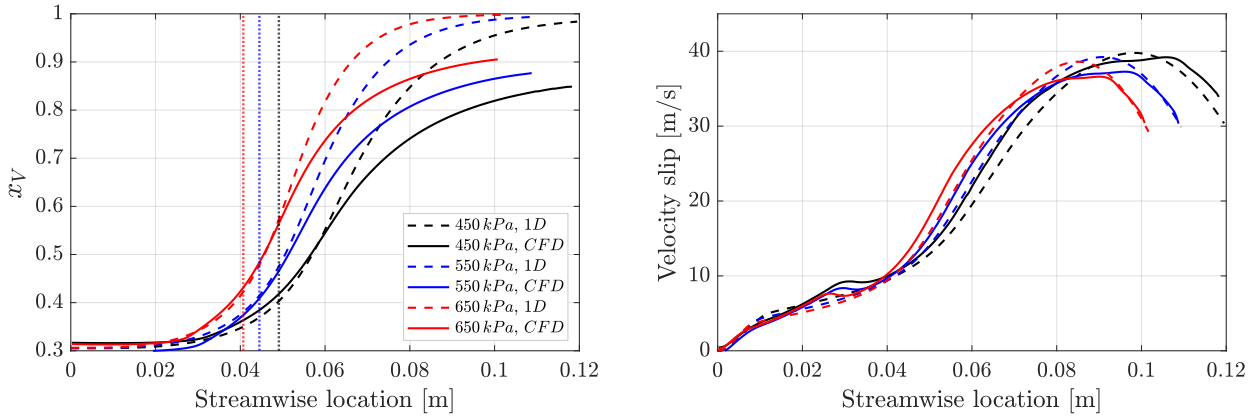


Figure 7.7: Comparison of average streamwise variation of vapour mass fraction (left) and velocity slip (right) between the quasi-1D design tool and CFD; the dotted lines represent the throat location.

7.5.3 One-dimensional optimisation results

As apparent from Fig.7.7, achieving complete mixture evaporation at pressures below 650 kPa is challenging. This study aims to enhance evaporation by optimising the nozzle pressure distribution to assess whether complete vapourisation could be achieved in low-pressure expansions. A nonlinear constrained optimisation is set up using a gradient-based *fmincon* optimiser available in MATLAB. Since multiple pressure profiles were found to result in complete vapourisation, the objective function was defined as:

$$f(\mathbf{x}) = x_{V,max} \frac{L_N}{L|_{x_{V,max}}} \tag{7.6}$$

where $x_{V,max}$ is either 1 in the case of a successful wet-to-dry transition or the maximum vapour mass fraction achieved at the nozzle outlet; L_N is the nozzle length and $L|_{x_{V,max}}$ is the streamwise distance at which the mixture turns to dry vapour or reaches the maximum quality. Maximising $f(\mathbf{x})$ ensures that a pressure profile is found that ensures the quickest wet-to-dry transition. As discussed earlier, the throat height and nozzle width had no effect on the expansion due to the assumption of a one-dimensional flow. The results summarised in Table 7.2 indicate that the length of the nozzle has a rather marginal influence on the vapour generation rate. Therefore, the one-dimensional optimisation focused only on the

nozzle pressure profile defined by the position of the five control points of a Bezier curve, as shown in Fig. 7.8.

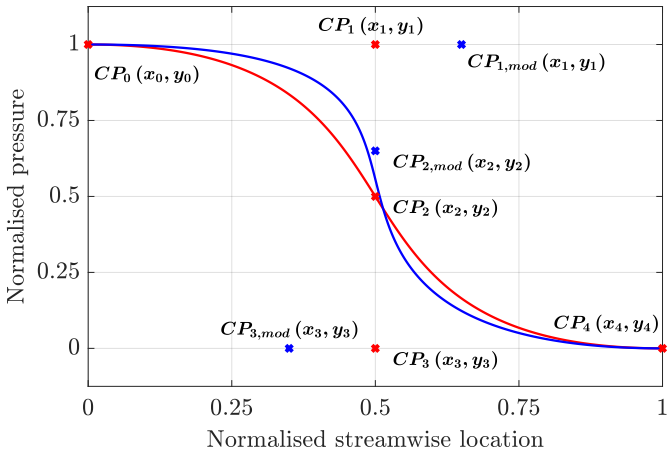


Figure 7.8: The effect of the location of the Bezier control points location on the nozzle pressure profile.

To ensure that pressure is equal to the design inlet and outlet values at the inlet and outlet, the $x-y$ coordinates of the control points CP_0 and CP_4 are fixed at (0,1) and (1,0), respectively. To avoid flow discontinuities at the beginning and end of the expansion, a zero-gradient condition is maintained at the inlet and outlet, which implies that the y-coordinate of the control points CP_1 and CP_3 is fixed at 1 and 0 as shown in Fig. 7.8. Hence, there are four design variables in total, which include the x-coordinates of the control points CP_1, CP_2 and CP_3, and the y-coordinate of CP_2. Each design variable can take any value between 0 and 1, when expressed in terms of the normalised coordinates (see Fig. 7.8). However, the resulting profile has to satisfy two constraints. First, the pressure gradient dp/dx has to remain negative throughout the expansion, i.e. the pressure must continually decrease along the nozzle. The other constraint was related to the maximum magnitude of the pressure gradient $|dp/dx|$, which could not exceed 25 (expressed in terms of non-dimensional coordinates). Pressure profiles with $|dp/dx| > 25$ were found to result in excessive curvature of the nozzle, which led to very abrupt expansions associated with flow separation and significant energy losses. To avoid ending up at a local minimum, the optimiser was run using 100 randomly generated starting points within the design space.

The results shown in Figure 7.9 provide a comparison between the baseline and optimised pressure profiles. In each case, the optimal pressure profile reached the maximum allowable gradient of 25. The profiles for 550 and 650 kPa expansions look almost identical, with most of the expansion occurring close to the inlet. This seems logical because the breakup occurs quicker, which implies that the remaining of the expansion is characterised by smaller droplets that can vapourise more effectively. It is unclear to the author why the pressure drop occurs further downstream for the 450 kPa expansion; however, dry conditions were predicted for that expansion in spite of the throat being shifted downstream. The main reason why a high pressure gradient is optimal is that it brings about a more rapid expansion that promotes a more severe droplet fragmentation and leads to smaller droplet diameters in

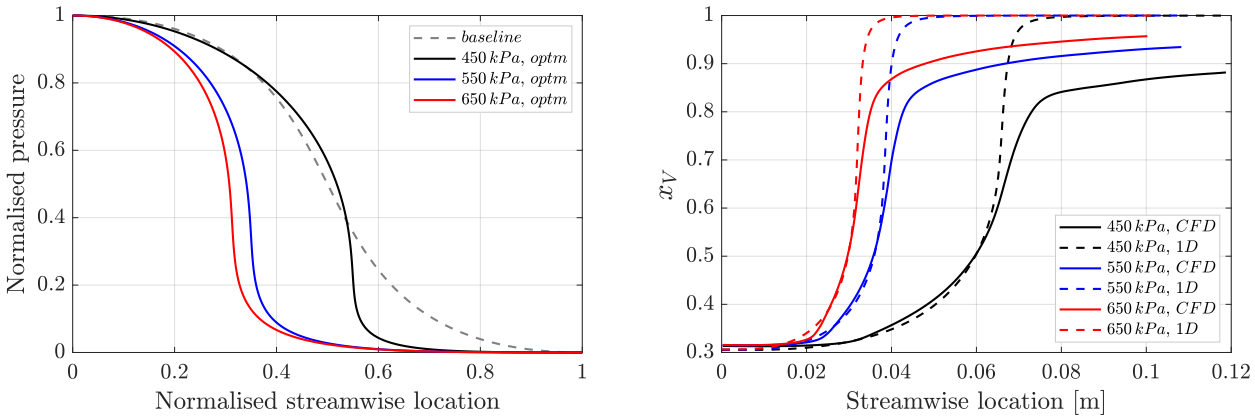


Figure 7.9: Optimised pressure profiles (left); comparison of average streamwise variation of vapour mass fraction x_V predicted by the quasi-1D tool and CFD in the optimised geometries (right).

the diverging section of the nozzle. This occurs due to high flow gradients and the associated aerodynamic disruptive forces acting on the droplet. The post-breakup droplet diameter in nozzles designed with the baseline profile varied between 10.4 and 13.2 μm. This reduced to around 4.34 to 5.57 μm in the optimised nozzles. The smaller the droplet size, the larger the interfacial area for a given volume fraction of liquid; this, in turn, directly enhances the rate of interfacial heat transfer rate and, consequently, the interphase mass transfer. The comparison between the design and the CFD pressure profiles showed a greater discrepancy near the nozzle outlet in relation to the baseline geometries. Generally, the flow was under-expanded with the outlet pressure being around 9.6% higher than the design value in each investigated case. This could be due to the formation of a shock resulting from a much more rapid expansion in the optimised nozzles, which could not be predicted with the quasi-1D design tool. When it comes to the vapourisation rate, according to the quasi-1D tool, the optimised geometries provide dry outlet conditions in each case, and the wet-to-dry transition takes place further upstream of the outlet compared to the baseline profile (compare dashed lines in Fig. 7.7 (left) and Fig. 7.9 (right)).

The optimised geometries generated with the non-equilibrium design tool were imported into the CFD solver to verify the optimisation results. Figure 7.9 (right) shows a comparison between the design and CFD predictions of the average streamwise variation of x_V for the optimised pressure profiles. First, comparing Fig. 7.7 with Fig. 7.9, it can be seen that, like in the baseline cases, the vapourisation rate estimated by the CFD model is reduced in comparison with the design tool predictions, while the overall trends are conserved. Comparing the CFD results for the baseline and optimised geometries in Fig. 7.10, a visible and consistent improvement in the outlet vapour mass fraction can be observed, which amounts to an increase of around 0.04-0.05. The outlet x_V increases from 0.849, 0.877 and 0.905 to 0.882, 0.934 and 0.957 for the 450, 550 and 650 kPa expansions, respectively. Although complete vapourisation was not achieved in any of the investigated cases, the liquid mass fraction at the outlet of the nozzle designed for the expansion from 650 kPa dropped below 5 %, which is promising. Considering the gradient of the x_V curve near the nozzle exit, it appears that the vapour mass fraction can be further increased by elongating the nozzle.

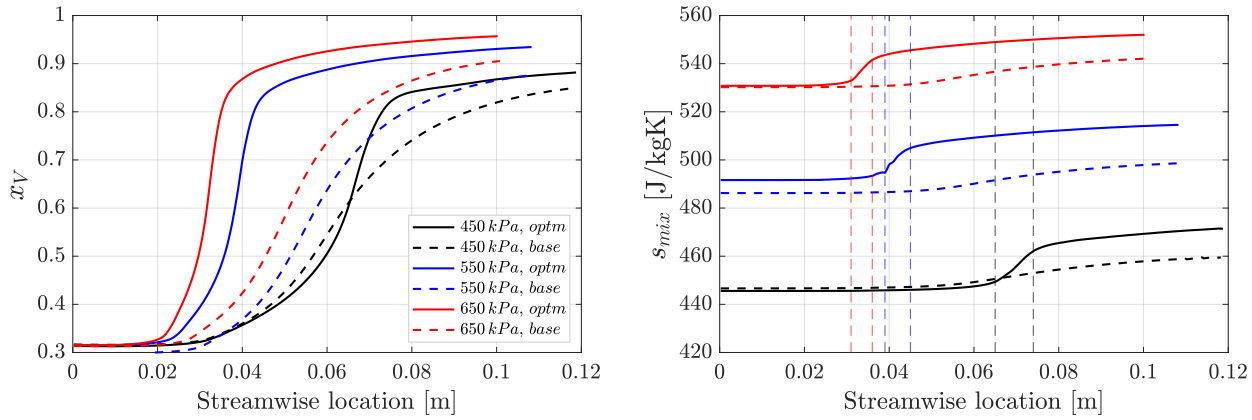


Figure 7.10: Comparison of CFD predictions of average streamwise variation of vapour mass fraction (left) and mass-flow average entropy (right) for the baseline and optimized (optm) pressure profiles; dotted lines represent nozzle sections with the most sudden entropy increase.

The influence of the pressure profile on the nozzle efficiency and flow uniformity is also important. This could not be directly accounted for in the one-dimensional optimisation due to an inviscid flow assumption, but can be assessed from the CFD results. Figure 7.10 (right) reports the average streamwise variation of mass-flow averaged entropy of the two-phase mixture (s_{mix}). Generally, the more rapid pressure change, typical of the optimised nozzles, has a negative effect on the nozzle performance as the total entropy generated increases. To provide a more explicit measure of nozzle performance, the nozzle efficiency was also estimated. The efficiency of the baseline nozzles was 81.09, 81.65 and 84.25% for the inlet pressures of 450, 550 and 650 kPa, respectively. The efficiency dropped to 67.58, 74.98 and 78.42% for the optimised geometries, which is in line with the average entropy curves shown in Fig. 7.10.

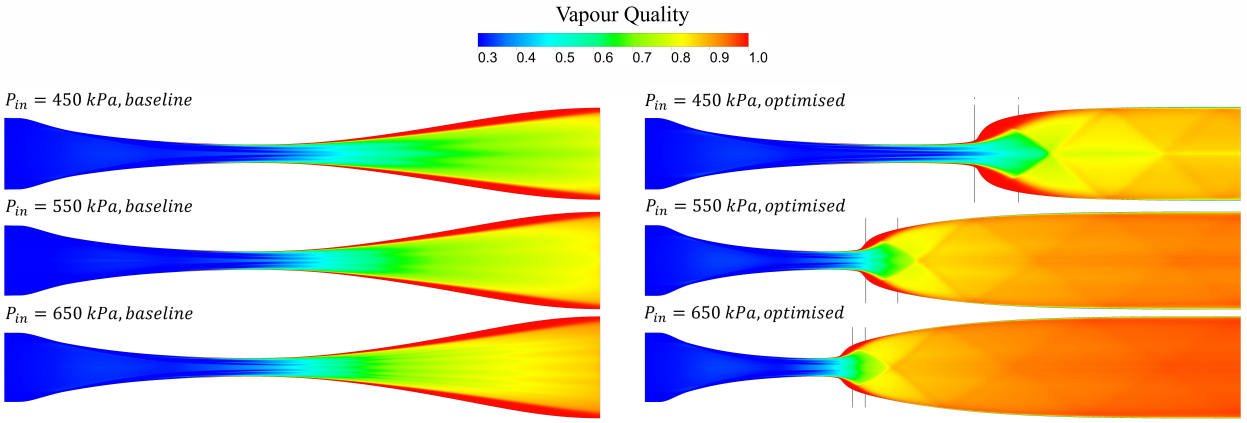


Figure 7.11: Two-dimensional contours of vapour quality in the baseline and optimised geometries; dotted lines correspond to the location of the most sudden entropy increase.

The two-dimensional contours of vapour quality predicted by the CFD simulations are reported in Figure 7.11. These contours give more insight into the spatial uniformity of the

flow and shed more light on the flow behaviour inside the nozzle and the cause of the sudden rise in entropy generation observed in Fig. 7.10. What appears to be common in each case is the phase separation in the diverging section of the nozzle. This is due to the much higher liquid density and high droplet relaxation times, which cannot immediately adjust to the changing geometry in an accelerating flow field. This becomes evident when evaluating the liquid streamlines shown in Fig. 7.12, which were plotted for the baseline nozzle designed for the expansion from an inlet pressure of 550 kPa and an inlet vapour quality of 0.3. It is clear that the droplets are not capable of immediately adjusting their flow direction to the changing nozzle geometry. This leads to accumulation of the liquid phase near the wall in the converging section of the nozzle, while it remains closer to the nozzle centre downstream of the throat, creating a characteristic core flow. As a result, the vicinity of the wall in the diverging section is occupied by the vapour phase.

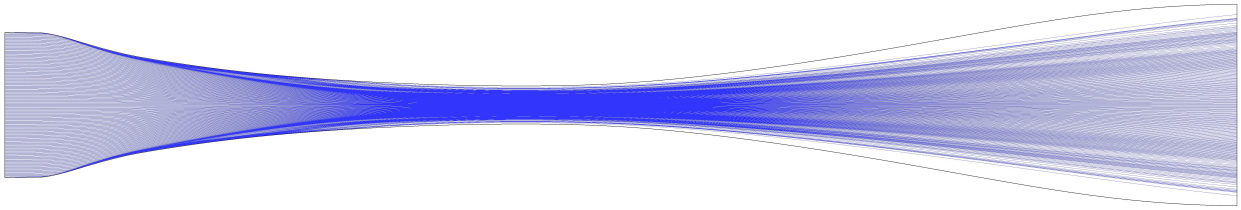


Figure 7.12: Liquid streamlines plotted for the baseline nozzle designed for the expansion from an inlet pressure of 550 kPa and an inlet vapour quality of 0.3.

Another phenomenon common to all investigated geometries is the presence of peculiar alternating strips of varying vapour quality, which is particularly visible near the throat of the nozzle. Further investigation revealed that the alternative strips are the consequence of the lift force that tends to shift the droplets in the lateral direction. Figure 7.13 illustrates the difference in the liquid streamlines in the proximity of the throat between the baseline model and the model with the lift force turned off. With the lift force turned off, the simulation predicts a layer of highly concentrated liquid at the nozzle wall, which appears to be the result of droplets impinging onto the wall in the converging section. Because of this impingement, a layer of high void fraction developed between the liquid residing at the wall and the core of the nozzle. As for the nozzle core itself, a fairly uniform liquid distribution was observed. When the lift force is introduced, a similar liquid layer was observed at the wall in the early stage of expansion. However, as the mixture advanced downstream, the droplets concentrated at the wall were repelled toward the centre of the nozzle due to lift effects. On the other hand, the droplets flowing along the centreline seemed to have been shifted toward the wall. As a result, the lift force led to multiple stratification layers which are in line with the non-uniform variations of vapour quality illustrated in Fig. 7.11. At this point it is important to mention that previous studies on flash boiling of water demonstrated difficulties in accurate prediction of vapour bubbles distribution within the studied channels [32, 204, 206]. Although polydispersed simulations were conducted with a suitable estimate of the bubble size distribution, the lateral (radial) distribution of bubbles observed experimentally could not be accurately reproduced in the CFD simulation [32]. This points to the limitations and inaccuracies of the current lift and turbulent dispersion models [32]. With

that being said, as far as the bulk flow properties are concerned, the results of the baseline model and the model with the lift force turned off did not deviate drastically. The relative difference in the vapour mass fraction at the outlet and the mass-flow rate was below 2.5%, while the difference in the estimated nozzle efficiency did not exceed 3%.

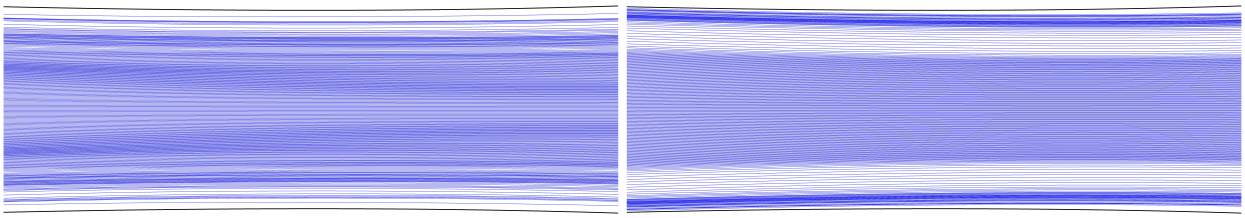


Figure 7.13: Liquid streamlines in the proximity of the nozzle throat predicted by the baseline CFD model (left) and a CFD model with the lift force turned off (right); the figure was plotted for the baseline nozzle designed for the expansion from an inlet pressure of 550 kPa and an inlet vapour quality of 0.3.

Generally, the flow-field looks very similar in each baseline geometry. When comparing the baseline and optimised nozzles, the phase separation in the diverging section appears to be alleviated to some extent. However, an oblique shock train appears to form in the optimised nozzles shortly downstream of the throat, which eventually causes an increased entropy generation and performance loss. It should be noted here that the contours illustrate the variation of vapour quality derived from the local volume fraction values multiplied by the corresponding densities of liquid and vapour. The formulation based on the ratio of mass flow rates (i.e., x_V) could not be displayed in the contours as it is calculated across planes perpendicular to the main flow direction. This also explains why there is a sudden increase in vapour quality across the shock, which is a result of the density variations of the liquid and vapour phases across the shock and is not necessarily associated with an instantaneous vapourisation taking place in that area. Essentially, the vapour phase experiences a much higher density increase across the shock relative to the liquid phase, which causes the vapour quality to increase despite the volume fraction remaining nearly constant. Although it could be more appropriate to illustrate the volume fraction contours, it was found that its value was very close to unity, and it could not illustrate the phase change process effectively. With this in mind, the vapour quality definition based on the volume fraction and density values is a useful illustration of the vapourisation process including an assessment of any occurring shocks, as long as one keeps in mind that it also reflects sudden density changes. The dotted lines in Fig.7.10 are also shown in the contours in the form of thin transverse lines. These indicate the regions characterised by the sudden increased in entropy generation. It can be observed that the location of the sudden rise in s_{mix} can be linked to the location of an abrupt geometry change and the resulting onset of the oblique shock train. The highest efficiency drop with respect to the baseline nozzles corresponded to the expansion from the lowest inlet pressure of 450 kPa and was about 13.5 %. The performance loss was not as significant at higher inlet pressures, where the efficiency drop was between 5.8 and 6.67 %.

The formation of the oblique shock train is also confirmed by analysing static pressure contours shown in Fig. 7.14, which indicate that there was no discontinuity in static pressure

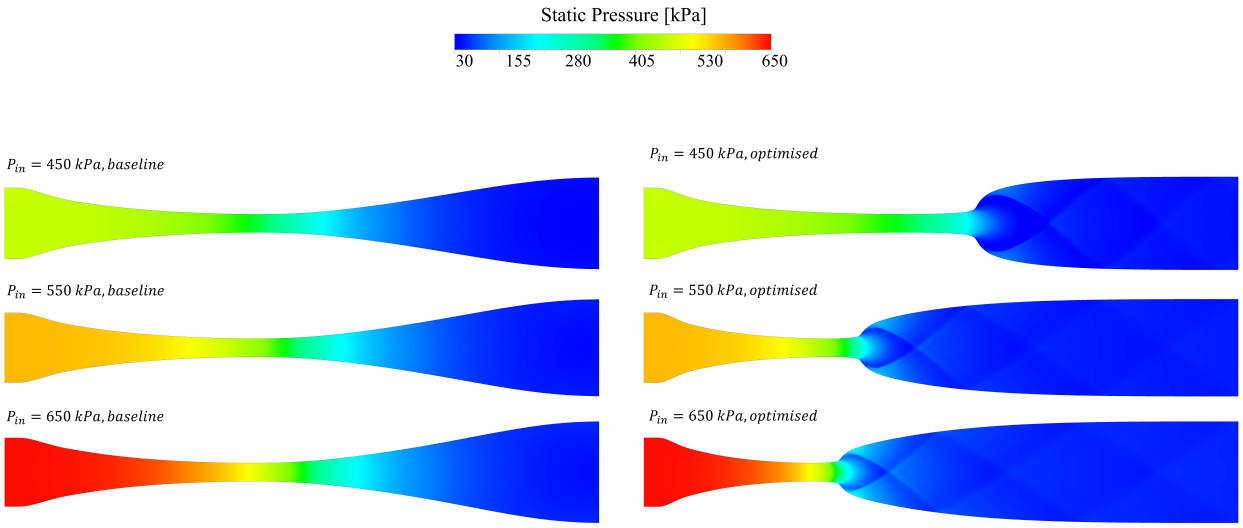


Figure 7.14: Two-dimensional contours of static pressure in the baseline and optimised geometries.

in the baseline geometries, whereas in the optimised nozzles a relatively strong shock formed shortly downstream of the throat. In summary, the optimised nozzles could increase the outlet vapour mass fraction and reduce the extent of lateral phase separation, providing a more uniform flow at the outlet, but they were also characterised by less efficient expansion due to the formation of an oblique shock.

7.6 CFD-based shape optimisation

The influence of viscosity, two-dimensional flow variations, and shock wave formation on nozzle performance highlights the limitation of using the quasi-1D nozzle design tool for optimisation purposes. In fact, the nozzle design tool was initially developed as a means of designing shock-free nozzles for wet-to-dry expansions, and as such, it is not capable of predicting or accounting for the presence of shock waves in the nozzle. Nonetheless, the optimisation study completed using this tool was considered a useful exercise to assess the influence of the pressure profile on the vaporisation rate. The results from the study also highlight the important trade-off between maximising the vapour generation rate and minimising entropy production, which are both important factors in a turbine intended for the wet-to-dry cycle. Whilst the nozzle design tool could be modified to account for shock and viscous losses, a preferred option is to carry out CFD-based shape optimisation. With this in mind, this section details a preliminary shape optimisation study for one of the expansion cases, with the aim of highlighting the potential of the technique and laying the foundations for further more detailed investigations.

7.6.1 Optimisation setup

For this preliminary shape optimisation study, only the expansion from an inlet pressure of 550 kPa and an inlet quality of 0.3 was investigated. The results of the one-dimensional

optimisation indicate that the area of the most importance is the region located directly downstream of the throat, which controls the rate of expansion and the degree of droplet breakup.

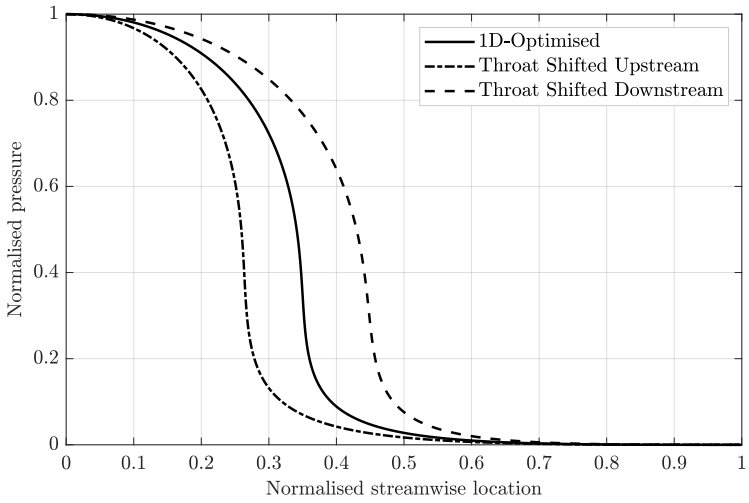


Figure 7.15: Two alternative pressure profiles with the expansion shifted upstream and downstream respectively. The profiles were obtained by horizontally shifting the control points of the 1D-optimised pressure profile for the expansion from an inlet pressure of 550 kPa and an inlet vapour quality of 0.3.

To further verify this assumption, two additional nozzle geometries with a modified axial position of the nozzle throat were investigated. In order to maintain the same wall profile downstream of the throat, these two alternative geometries were generated by horizontally shifting the control points of the optimised pressure profile obtained for the 550 kPa expansion. The two modified pressure profiles are shown in Fig. 7.15. Notably, the horizontal shift affects the shape of the profile in the converging section of the nozzle. However, the profiles are very similar downstream of the throat, which means that the wall profile in the diverging section does not change significantly. This is confirmed by observing the shape of the three nozzles shown in Fig. 7.16, which illustrates the two-dimensional variation in vapour quality. Generally, the flow pattern does not appear to be significantly affected by the position of the throat, as long as the shape of the diverging section remains similar.

Table 7.4: The influence of the throat axial position on the average vapour mass fraction at the nozzle outlet ($x_{V,out}$) and nozzle efficiency (η_N). The results were obtained for the expansion from 550 kPa and an inlet vapour quality of 0.3. The alternative throat axial positions (X_{th}) were obtained by manipulating the 1D-optimised pressure profile. Baseline geometry results were included as a reference.

Geometry	$x_{V,out}$	η_N	X_{th}
Baseline	0.877	81.66 %	44.50 mm
1D-Optimised	0.934	74.98 %	33.23 mm
Throat Shifted Upstream	0.944	75.77 %	24.99 mm
Throat Shifted Downstream	0.926	74.55 %	39.68 mm

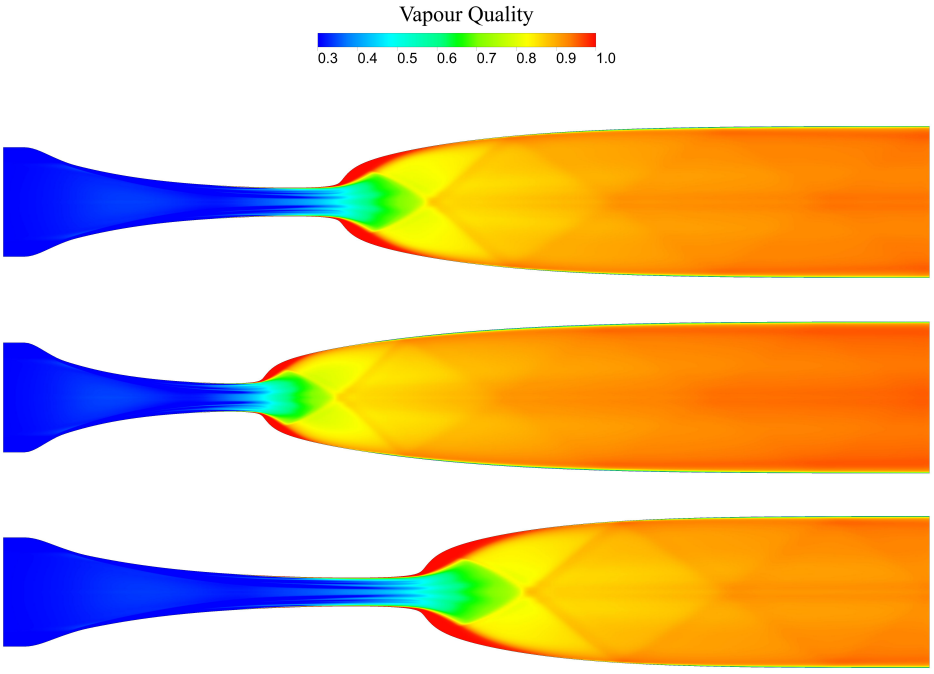


Figure 7.16: Two-dimensional variation in vapour quality predicted in the 1D-optimised nozzle (middle) and two modified nozzle geometries with the nozzle throat shifted upstream (top) and downstream (bottom). The pressure profiles used to design the nozzle were very similar which results in nearly identical wall profile downstream of the throat. The nozzles were designed for the expansion from 550 kPa and an inlet vapour quality of 0.3.

Table 7.4 shows the effect of the axial position of the throat on nozzle efficiency and average vapour mass fraction calculated at the nozzle outlet. The results for the non-optimised baseline geometry are included as a reference. When comparing the 1D optimised results with the results obtained for the modified throat position, it can be seen that the percentage difference in $x_{V,out}$ and η_N is limited to 0.934 $\pm$ 1.07 % and 74.98 % $\pm$ 1.05 %, respectively. Given that the percentage difference in $x_{V,out}$ and η_N between the 1D-optimised and baseline results was 5.7 % and 8.9 %, the axial position of the throat can be considered to be of secondary importance. As such, it was decided to simplify the problem and focus only on optimising the shape of the nozzle for a fixed throat position, using the 1D-optimised geometry as a starting point in the CFD-based optimisation.

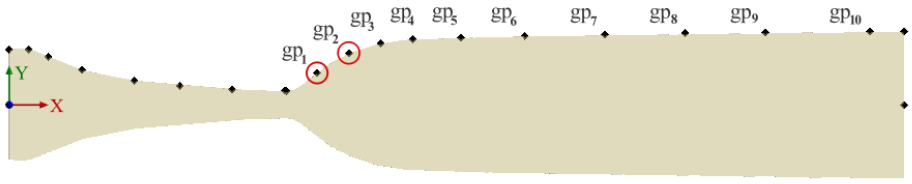


Figure 7.17: The parametrisation of the nozzle used in shape optimisation.

The optimisation was implemented within Ansys Workbench, which provides a framework that combines the geometry, meshing, solution, and optimisation modules. The wall profile

obtained from the 1D optimisation was first parameterised, using a spline with 20 geometry points, as illustrated in Fig. 7.17. The shape of the converging section was kept fixed, while the optimisation focused only on the area near the throat, which has the greatest impact on the breakup and phase-change process. As such, only two of the geometry points, gp_1 and gp_2, marked with red circles in Fig. 7.17, are set as design variables. However, the remaining geometry points in the diverging section are adjusted according to the position of the two geometry points to ensure a smooth and continuous increase in the flow area. The length of the nozzle, and the horizontal position of all the points is fixed, while the vertical position of gp_1 and gp_2 is varied during the optimisation. To ensure the mass-flow rate remains approximately the same, the throat height was fixed at 3.422 mm. Since the distance from the centreline to the wall at the throat was 1.711 mm, the range of vertical motion of the first point, y_{gp_1}, was set between 2.25 and 5.25 mm. This range was found to be sufficient to simulate nozzles with various expansion rates ranging from gradual to very rapid. The vertical position of the second point, y_{gp_2}, was controlled indirectly through the following non-dimensional parameters:

$$c_1 = 0.1 + 0.15\,(y_{gp_1} - 2) \tag{7.7a}$$

$$c_2 = \left(\frac{y_{gp_1}}{9} + \frac{4\,(y_{gp_1} - 2.25)}{45}\right) k \tag{7.7b}$$

$$c_3 = c_1 + c_2\,(0.90 - c_1) \tag{7.7c}$$

The vertical position of gp_2 is then expressed as:

$$y_{gp_2} = y_{gp_1} + c_3(y_{out} - y_{gp_1}) \tag{7.8}$$

where y_{out} is the outlet height, measured from the centreline of the nozzle. These relationships were derived based on trial and error, which involved investigating a suitable range of motion of y_{gp_2} for various positions of gp_1. Generally, the vertical position of gp_1 should control the rate of expansion within the nozzle. In other words, if y_{gp_1} was relatively small, the resulting expansion should be gradual. Therefore, y_{gp_2} had to be limited if y_{gp_1} was small in order to achieve a gradual expansion. Otherwise the expansion would only be shifted longitudinally from gp_1 to gp_2. Moreover, the maximum gradient of the wall profile was to take place between the throat and gp_1 and should gradually decrease streamwise. Therefore, the wall profile in the diverging section should feature a single inflection point between the throat and gp_2. These considerations were taken into account when developing the relationships for the vertical position of geometry points gp_2 through gp_{10}. Looking at Eq. 7.7a-7.7c, it can be seen that for any value of y_{gp_1}, y_{gp_2} depends only on the parameter k from Eq. 7.7b. This parameter was the second design variable in the optimisation, which varied between 0 and 1, controlling the range of motion of gp_2 relative to gp_1.

For a given vertical position of gp_1, a minimum height increase was necessary between gp_1 and gp_2 to avoid a double inflection in the wall profile. This minimum height increase occurs when $k = 0$ and is controlled by the constant c_1, which was derived by observing the behaviour of the wall profile for various values of y_{gp_1} between 2.25 and 5.25 mm. For example,

it was found that when $y_{gp_1} = 2.25$ mm and $k = 0$, c_1 lower than 0.1375 could cause a double inflection in the wall profile as illustrated in Fig. 7.18 (top). Whilst the constant c_1 sets the lower limit to the increase in height between gp_1 and gp_2 at $k = 0$, the constant c_2 sets the upper limit to the increase in height between those geometry points when $k = 1$. If c_2 is too high for a given y_{gp_1}, excessive wall curvature can appear as illustrated in Fig.7.18(bottom).

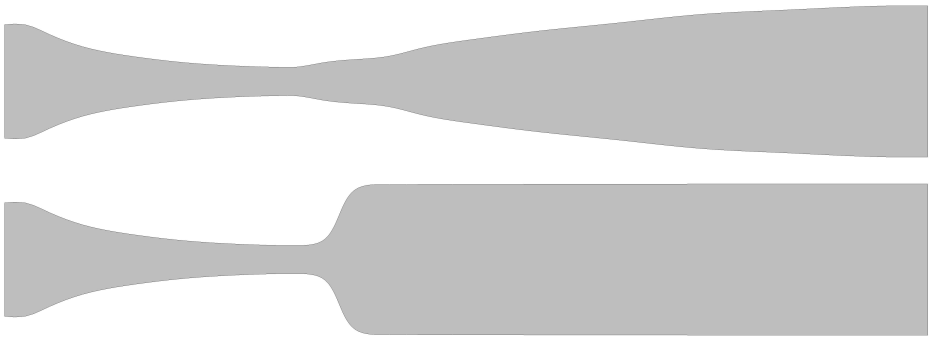


Figure 7.18: Double inflection in the nozzle wall profile (top) due to an insufficiently high c_1 constant and excessive wall curvature (bottom) due to very high value of c_2.

To summarise, the constants c_1 and c_2 control the minimum and maximum feasible increase in nozzle height between gp_1 and gp_2 for a given y_{gp_1}, while the constant k is applied to investigate different wall profiles within these limits. Although the remaining points in the diverging section were not used as optimisation inputs, a set of correlations was developed through trial and error and based on the considerations mentioned above.

$$y_{gp_3} = y_{gp_2} + c_3(y_{out} - y_{gp_2}) \tag{7.9a}$$

$$y_{gp_4} = y_{gp_3} + (0.15 + 0.1(y_{gp_3} - 2.25) + 0.1k)\,(y_{out} - y_{gp_3}) \tag{7.9b}$$

$$y_{gp_5} = y_{gp_4} + 0.2(y_{out} - y_{gp_4}) \tag{7.9c}$$

$$y_{gp_6} = y_{gp_5} + 0.25(y_{out} - y_{gp_5}) \tag{7.9d}$$

$$y_{gp_7} = y_{gp_6} + 0.2333(y_{out} - y_{gp_6}) \tag{7.9e}$$

$$y_{gp_8} = y_{gp_7} + 0.5(y_{out} - y_{gp_7}) \tag{7.9f}$$

$$y_{gp_9} = y_{gp_8} + 0.5(y_{out} - y_{gp_8}) \tag{7.9g}$$

$$y_{gp_{10}} = y_{out} \tag{7.9h}$$

The mesh with 15,000 elements, described in Section 7.4, was used in CFD evaluations, which gave a good balance between accuracy and simulation time. The CFD simulations were performed using the same setup as described previously. The construction of the initial database and the sampling of the design space was performed using optimal space filling, a variant of the Latin Hypercupe technique, which was capable of uniformly resolving the design space with 55 design points. This number of design points may seem excessively high, given that the optimisation involves only two design variables. However, because all other geometry points in the diverging section are dynamically adjusted and a relatively large range of motion of gp_1 is considered, a wide variety of geometries can be generated

with these two design variables, which justifies the high number of design points. The response surface was constructed using a genetic aggregation technique, but due to the simplicity of the problem and the smoothness of the response, other existing methods could potentially generate an equally reliable approximation. The accuracy of the response surface was assessed with 10 verification points, comparing the response surface approximations for the outlet vapour mass fraction and the nozzle efficiency against the CFD evaluations. The maximum relative difference was below 0.11% and 0.36% for the vapour mass fraction and the nozzle efficiency, respectively, which was considered sufficiently small. To carry out the optimisation of the response surface, a multi-objective genetic algorithm, non-dominated sorting genetic algorithm (NSGA-II), was used which aimed to simultaneously maximise the outlet vapour mass fraction and nozzle efficiency.

7.6.2 Shape optimisation results

Based on the evaluation of the 55 design points used to create the initial database, the range of outlet vapour mass fractions and nozzle efficiencies were assessed. The outlet vapour mass fraction varied between 0.915 and 0.951, which was considered a relatively narrow range. Comparing these values to $x_{V,out}$ of the 1D-optimised nozzle for the 550 kPa expansion, which was 0.934, the potential increase in the evaporation rate appears fairly small. Furthermore, the highest $x_{V,out}$ values corresponded to very low nozzle efficiencies. Contrary to the vapour mass fraction, the efficiency variation was substantially larger, ranging from 64.59 to 81.35%. Since the efficiency of the 1D-optimised nozzle was 74.98%, this indicates there is significant room for nozzle performance improvement. Taking into account the results obtained for the initial database, two optimisation runs were carried out. In the first run, a multi-objective optimisation was performed to simultaneously maximise both the vapourisation rate and nozzle efficiency, while in the second run a single-objective optimisation of the nozzle efficiency was carried out with a constraint set such that $x_{V,out} > 0.934$. In theory, the optimal nozzle design with an outlet vapour quality of 0.934 could have been retrieved directly from the Pareto front generated by the multi-objective optimisation, but this second run was considered to verify that there was no further room for improvement. Moreover, in this second case, the optimised geometry would at least provide the same outlet vapour mass fraction as the 1D-optimised nozzle and would enable a direct comparison. Several candidate points were generated in both runs, which were then verified with the CFD model. The results of both runs are shown in Table 7.5 alongside the one-dimensional optimisation results as a reference.

In the first optimisation run (Run 1), the optimiser was set to simultaneously enhance the evaporation rate and efficiency, while the optimal solution was generated applying equal weighting factors to both parameters. Figure 7.20 shows the Pareto front obtained in the multi-objective optimisation alongside the location of the optimal point.

The optimised nozzle achieved 0.007 higher outlet vapour mass fraction and about 1.2% higher efficiency compared to the 1D-optimised nozzle. However, when the optimiser was set to search for the maximum efficiency, while maintaining $x_{V,out} > 0.934$ (Run 2), the resulting geometry yielded a 3% increase in efficiency at the expense of a slightly lower value for $x_{V,out}$.

Table 7.5: The results of the shape optimisation study; Run 1 corresponds to the multi-objective optimisation that aims to maximise the vapour generation rate and nozzle efficiency, while Run 2 corresponds to the single-objective optimisation that aims to maximise nozzle efficiency while satisfying the constraint: $x_{V,out} \geq 0.934$.

Case	y_{gp_1}	y_{gp_2}	$x_{V,out}$	η_N
Run 1	3.973 mm	6.111 mm	0.941	76.19 %
Run 2	3.452 mm	5.261 mm	0.935	77.96 %
1D Optimal	-	-	0.934	74.98 %

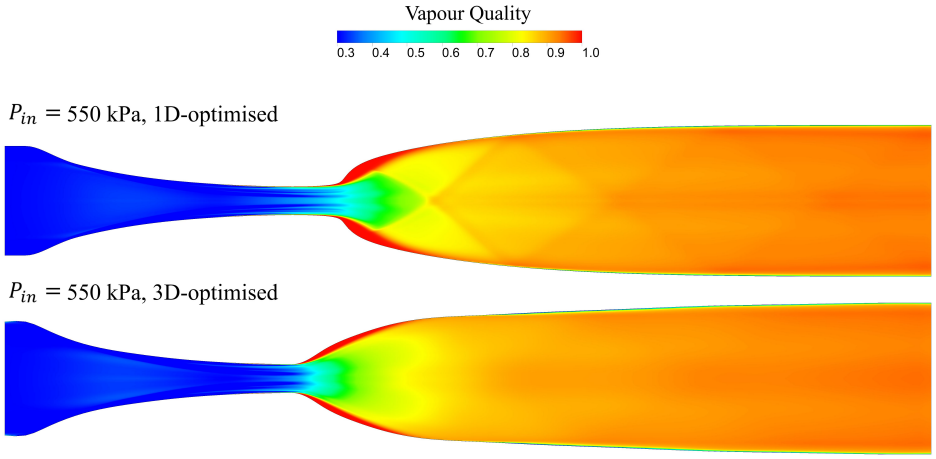


Figure 7.19: Two-dimensional contours of vapour quality in the 1D-optimised and 2D-optimised geometries.

Since $x_{V,out}$ in the second run was only marginally smaller, the geometry obtained in Run 2 was considered as the optimal nozzle design. The two-dimensional contours of the vapour quality for the 1D-optimised nozzle, and the one obtained through shape optimisation (2D-optimised) are compared in Figure 7.19. It can be observed that the 2D-optimised geometry facilitates a more gradual expansion, mitigating the negative effects of the oblique shock train that was observed in the 1D-optimised geometry. This results in reduced energy losses and a 3% increase in efficiency. In conclusion, despite being unable to significantly enhance the vapourisation rate, the shape optimisation was successful at generating a geometry that mitigated the problem of an oblique shock train, leading to a higher expansion efficiency.

7.6.3 Effect of other geometrical parameters

According to the quasi-1D design tool, the influence of the height of the passage and the length of the nozzle on the vapourisation rate is negligible. However, the design tool does not account for the viscosity effects, which could be expected to vary with geometrical parameters such as throat height and nozzle length. In order to assess the importance of the passage height and nozzle length, a preliminary analysis was conducted on the CFD-optimised geometry shown in Fig. 7.19. To vary the passage height, the vertical distance from the centreline for each geometry point shown in Fig.7.17 was multiplied by a factor of 0.5 and 2. To maintain the same wall profile and thereby the same expansion rate, the

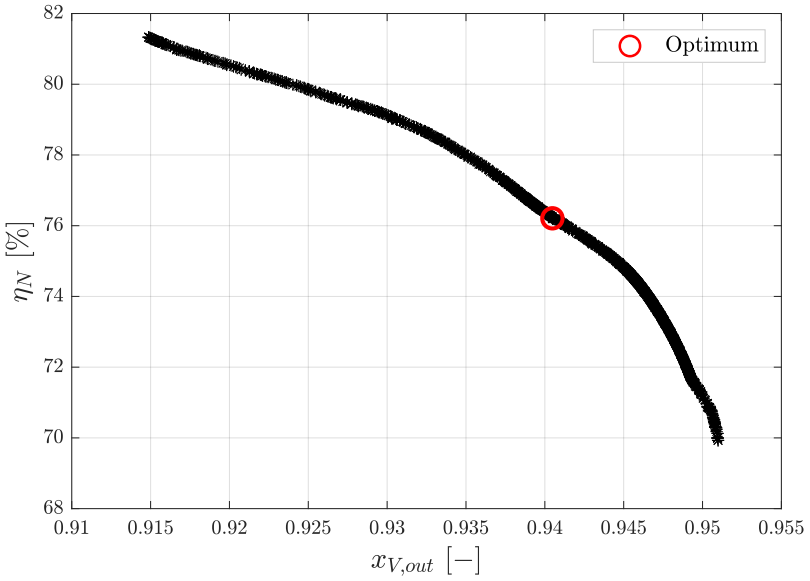


Figure 7.20: The Pareto front obtained in the multi-objective optimisation; the red circle denotes the optimal point.

horizontal distance between the consecutive geometry points was also multiplied by a factor of 0.5 or 2 accordingly. When it comes to the effect of nozzle length, the vertical position of all the geometry points was kept fixed, while the horizontal distance between the consecutive geometry points in the diverging section, starting with the 6$^{\text{th}}$ point (gp_6) downstream of the throat (Fig.7.17), was multiplied by a factor of 2 and 0.5. This ensured almost the same expansion rate, while only elongating the straight portion of the diverging section of the nozzle.

Table 7.6: The effect of nozzle width and length on the average outlet vapour mass fraction ($x_{V,out}$) and nozzle efficiency (η_N). The results were obtained by modifying the width and length of the CFD-optimised nozzle geometry, while maintaining the same wall profile in the throat area.

Geometry	$x_{V,out}$	η_N	$\dot{m}$
CFD-Optimised	0.935	77.96 %	1.768 g/s
2×Width	0.941	80.19 %	3.495 g/s
0.5×Width	0.924	74.66 %	0.919 g/s
2×Length	0.952	76.78 %	1.769 g/s
0.5×Length	0.920	78.93 %	1.766 g/s

The average vapour mass fraction at the nozzle outlet and nozzle efficiency estimated in the nozzles with modified width and length are summarised in Table 7.6. The effect of passage width on the vapourisation rate was found to be rather small with a maximum absolute difference of 0.011 compared to the original CFD-optimised geometry. In terms of efficiency, the smaller width, characterised by a narrower throat, induced a loss of efficiency of 3.3 %, which is thought to be the result of increased viscous losses in the throat area. The reverse happened for the wider passage, which was associated with an efficiency increase of about

2.2%. As expected, the mass flow rate within the nozzle with a height multiplied by a factor of 0.5 was around 51.7% lower, while for the nozzle with double throat height it was around 196% higher. The length of the nozzle had a slightly higher impact on $x_{V,out}$, which reached 0.952 and 0.912 in the longer and shorter nozzles, respectively. The difference in efficiency was around 1%, and the shorter nozzle had a higher efficiency due to reduced viscous losses. Although the channel width and nozzle length do not drastically alter the overall characteristics of the two-phase expansion (as far as the vapour quality and velocity contours are concerned), these parameters may considerably affect the vapourisation rate and efficiency if combined with the optimisation of the nozzle shape. Therefore, more comprehensive shape optimisation should be conducted in future studies, to simultaneously account for the combined effect of expansion rate, passage width, nozzle length, different operating conditions, and three-dimensional flow variations, taking into account the endwall effects.

7.7 Effect of droplet size decrease

Different approaches to modelling the interfacial area in two-phase droplet flows have been discussed in Section 4.3.1. As far as simulating phase change is concerned, assuming a fixed droplet number is arguably a more suitable approach than assuming a fixed droplet diameter as the droplets are allowed to diminish in size during vapourisation, which better reflects the physical process of flash boiling. However, following this approach, droplet breakup effects, which have been found to be important in wet-to-dry expansions, cannot be taken into account. Droplet breakup can be estimated on the basis of the average Weber number as proposed in this chapter. This allows to evaluate a realistic droplet size under given flow conditions. The limitation of this method is that once the breakup ceases, the droplet diameter is assumed to be constant, which, as discussed, may not reflect the nature of phase-change process. In this section, an approach to modelling droplet size is proposed that combines the droplet breakup model developed in this chapter with a constant droplet number approach.

Similarly to the droplet breakup model, the flow domain must be first discretised into a number of small control volumes. However, in this combined method, it is important to discretise the entire nozzle instead of only the breakup zone, as shown in Fig. 7.21.

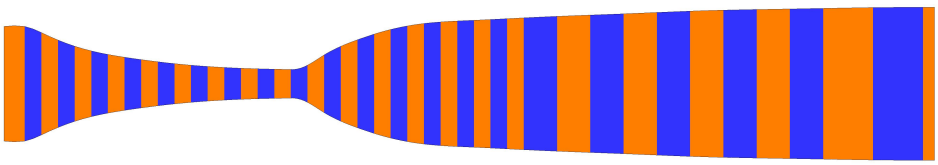


Figure 7.21: Discretisation of the flow domain for implementing the combined droplet breakup and droplet number approach; the blue and orange stripes represent the control volumes used to approximate the breakup and droplet size decrease due to vapourisation under a constant droplet number density. The nozzle represents the CFD-optimised geometry designed for the expansion from an inlet pressure of 550 kPa and an inlet vapour quality of 0.3.

The width of the control volumes in the breakup zone was set as determined suitable when developing the breakup model (Section 7.1). Since the phase change becomes much less

intensive downstream of the breakup zone, the width of the control volumes was progressively relaxed along the nozzle, as shown in Fig. 7.21. The combined droplet size evaluation method is initiated similarly to the breakup model. An inlet droplet diameter of 0.1 mm was assumed, and the droplet number was calculated based on the average volume fraction of liquid and the inlet droplet diameter:

$$N_{d,i} = \frac{6\alpha_{L,i}}{\pi D_{d,i}^3} \tag{7.10}$$

where the subscript i denotes the first control volume in the nozzle. As the flow progresses downstream to the next control volume, represented by a subscript $i+1$, the droplet size changes according to the value of the average Weber number. In general, two cases are considered, which are discussed below.

Case 1: $We_{i+1} > We_{cr,i+1}$
If the average Weber number in the control volume $i+1$ exceeds the critical Weber number, the droplets are expected to undergo a breakup, and the resulting droplet size is determined from the following equation:

$$D_{d,i+1} = \frac{We_{cr,i+1}\,\sigma}{\rho_{V,i+1}\,|u_V - u_L|_{i+1}^2} \tag{7.11}$$

where We_{cr} and $|u_V - u_L|$ are the average critical Weber number and velocity slip in the control volume $i+1$. Because breakup takes place, droplet number will change and has to be updated based on the new droplet diameter:

$$N_{d,i+1} = \frac{6\alpha_{L,i+1}}{\pi D_{d,i+1}^3} \tag{7.12}$$

Case 2: $We_{i+1} \leq We_{cr,i+1}$
In the second case, the average Weber number stays below the critical value, and because breakup is not anticipated, the droplet number is assumed to remain constant, provided that coalescence effects are negligible.

$$N_{d,i+1} = N_{d,i} \tag{7.13}$$

In that case, it is assumed that the droplet size changes due to vapourisation between control volumes i and $i+1$, which is reflected in the change of the average liquid volume fraction.

$$D_{d,i+1} = \left(\frac{6\alpha_{L,i+1}}{\pi N_{d,i+1}}\right)^{1/3} \tag{7.14}$$

Although the methodology was explained for the first two control volumes in the nozzle, it applies to any pair of adjacent control volumes i and $i+1$. In summary, in this combined approach, the droplet size is assumed to change either due to breakup or to a phase change, reflected in the decrease in the liquid volume fraction. Furthermore, the droplet number is dynamically adjusted in accordance with breakup occurring upstream of the given control volume.

To investigate the possible effect of droplet size decrease due to phase change in addition to the breakup effect, the method outlined above was applied to simulate the two-phase expansion in the CFD-optimised nozzles (Fig. 7.19). Figure 7.22 illustrates the streamwise variation of the droplet diameter and vapour mass fraction estimated with the droplet breakup model and the combined approach presented in this section.

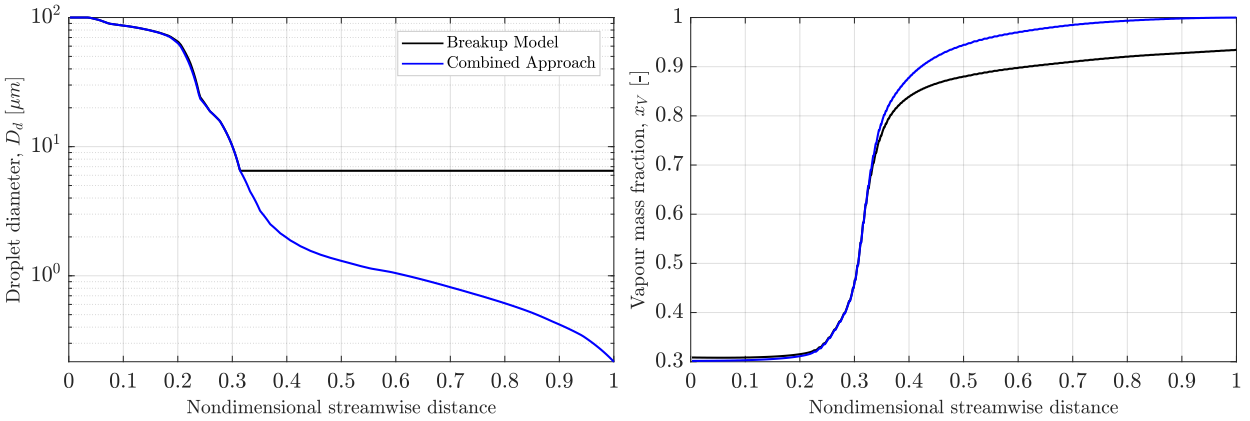


Figure 7.22: The comparison between droplet diameter and vapour mass fraction variation between the droplet breakup and a method combining droplet breakup with the droplet number approach. The results were obtained for the CFD-optimised nozzle designed for the expansion from 550 kPa and an inlet vapour quality of 0.3.

The droplet diameter profile predicted by both models is identical between the inlet and the throat. This indicates that the droplet size is mostly determined by breakup effects, and the variation in droplet size due to the phase change is of secondary importance. However, the breakup ceases shortly downstream of the throat and droplet size remains constant, whereas in the combined approach, it continually decreases as the vapourisation takes place. Because of a higher surface area-to-volume ratio of smaller droplets, the vapourisation process is accelerated as the droplet size falls. This is reflected in the variation of the vapour mass fraction of the mixture, which is predicted to reach dry conditions if the droplets are allowed to diminish in size in the diverging section. The nozzle efficiency estimated with the combined approach was approximately 83.9 %, which is about 6% higher than when the diameter of the droplet after breakup was assumed to be constant. Therefore, the results indicate that a decrease in droplet size due to phase change may have a significant effect on the the vapour generation rate and nozzle efficiency. However, it should be emphasised that the proposed method for estimating droplet size is not known to have been previously applied and requires suitable validation.

7.8 Conclusions

In this chapter, the geometry of converging-diverging nozzles for the wet-to-dry expansion of organic fluids has been studied using a combination of a quasi-1D non-equilibrium design tool and non-equilibrium quasi-2D CFD simulations. Three expansions with inlet pressure

ranging from 450 to 650 kPa and constant inlet vapour quality of 0.3 were investigated for the siloxane MM. First, pressure profile optimisation was carried out using the nozzle design tool to maximise the vapourisation rate. The optimised geometries were simulated using a CFD model that accounted for viscosity, turbulence and two-dimensional effects. In the second part of the study, CFD-based shape optimisation was carried out, focusing on optimising the near-throat area, which has the greatest impact on the expansion.

It was found that the quasi-1D nozzle design tool is capable of predicting the phase-change pattern, but the assumption of inviscid quasi-1D flow and the omission of viscous and turbulence effects leads to an over-prediction of the vapourisation rate. However, since the phase-change pattern predicted by the quasi-1D tool is similar to the non-equilibrium CFD predictions, the tool was still deemed suitable for performing initial 1D optimisation. It was found that the optimised nozzles resulted in a rapid expansion that enhanced droplet breakup and consequently the vapourisation rate. The CFD simulations conducted on the geometries generated using the optimised pressure profiles achieved 3.3 to 5.7 % higher vapour mass fraction at the nozzle outlet, which reached 88.2, 93.4 and 95.7% in the expansions from 450, 550 and 650 kPa, respectively. Although complete evaporation was achieved in none of the cases, reaching near-dry conditions at inlet pressures in the order of 650 kPa seems promising. Evaluation of the flow-field revealed that the abrupt expansion in the optimised geometries was associated with the formation of an oblique shock train downstream of the throat, which in turn contributed to elevated entropy generation. The nozzle efficiencies for the optimised geometries were in the range of 67.58 to 78.42%, approximately 5.8 to 13.5% lower compared to the baseline geometries, with more pronounced loss at low pressures. This highlights the limitation of using the quasi-1D inviscid nozzle design tool for optimisation purposes, and highlights the need for multi-objective optimisation using more advanced simulation methods.

As such, CFD-based shape optimisation studies aimed at maximising the outlet vapour mass fraction and nozzle efficiency, were conducted. The results revealed that by optimising the wall profile near the throat, it was possible to design a nozzle that achieves a similar vapourisation rate to that of the 1D-optimised geometry, while facilitating more efficient expansion. The CFD-optimised nozzle facilitated a more gradual expansion, mitigating the negative effects of the oblique shock train appearing in the 1D-optimised geometry, leading to a 3 % increase in nozzle efficiency, which reached around 78 %. A preliminary assessment of other geometrical features demonstrated that neither the nozzle width nor the length critically influenced the two-phase expansion. However, it was recognised that the combined effect of these parameters could have a considerable impact on the two-phase expansion. Therefore, it is recommended that future shape optimisation studies take nozzle width and length as optimisation variables.

The proposed droplet breakup model assumes that the droplet size remains constant after breakup. At the end of the chapter, a new approach to modelling droplet size that combines droplet breakup effects and droplet size variation due to phase change was subsequently proposed. The preliminary results indicate that the droplets can decrease in size significantly as a result of the phase change that occurs in the diverging section of the nozzle. This further

drives the vapourisation rate and can potentially help achieve the wet-to-dry transition. However, this method has not been previously applied in flash-boiling problems and requires further validation.

Chapter 8

Conclusions and recommendations for future work

8.1 Introduction

The wet-to-dry expansion of molecularly complex fluids has been proposed as a means of improving the performance of organic Rankine cycle power systems operating with open sensible heat sources. Due to a lack of experimental data, the concept had previously been assessed with the aid of numerical tools. Preliminary CFD simulations based on the homogeneous-equilibrium model indicate that the wet-to-dry transition could be successfully accomplished in a nozzle designed for a radial-inflow turbine. However, given the rapid flow acceleration in a relatively short channel, the assumption of identical velocities and temperatures of liquid and vapour phases is questionable. As a matter of fact, further studies have demonstrated that non-equilibrium effects can have a significant impact on the phase-change process and should not be neglected when simulating the wet-to-dry expansion. Although those further studies helped to understand the role of non-equilibrium effects, the problem was over-simplified by assuming and inviscid one-dimensional flow, neglecting multidimensional flow variations, effects of viscosity and turbulence, as well as the influence of non-drag forces. Therefore, further research endeavours were deemed necessary to validate the concept of the proposed two-phase turboexpander.

The primary aim of this research work was to assess the feasibility of designing a two-phase nozzle that would facilitate complete mixture vapourisation in an efficient manner under conditions relevant to the wet-to-dry cycle. To achieve this aim, two main objectives were set as follows:

1. Investigate the flash boiling in a converging-diverging nozzle under a range of operating conditions relevant to the wet-to-dry cycle and provide insight into the phase-change characteristics, taking into account non-equilibrium effects, multidimensional flow variations, and the effects of viscosity and turbulence.

2. Optimise the two-phase nozzle and investigate the influence of the nozzle shape on the phase-change process and the performance of the nozzle.

To fulfil the outlined objectives, a CFD model capable of accounting for non-equilibrium effects, multidimensional flow variations, effects of viscosity and turbulence as well as the influence of non-drag forces was set up and validated against available empirical data. The model was employed to simulate flash boiling of the siloxane MM in a converging-diverging nozzle under conditions directly relevant to the wet-to-dry cycle. The second part of this work focused on the optimisation of the converging-diverging nozzle with the aim of increasing the vapourisation rate and nozzle efficiency. The following sections summarise the main findings and conclusions of each research section completed in this work. This is followed by final remarks and recommendations for future work.

8.2 Non-equilibrium flashing model

Several flash-boiling models potentially applicable to simulating the wet-to-dry expansion of the siloxane MM were reviewed. Due to the importance of non-equilibrium effects, the homogeneous-equilibrium model was deemed adequate only for preliminary analysis purposes. Semi-equilibrium methods such as the homogeneous-relaxation and delayed-equilibrium models account for the vapourisation delay due to thermal non-equilibrium, but rely on fine-tuned empirical coefficients that have to be calibrated for specific fluid and operating conditions. Due to lack of directly relevant experimental data, the Eulerian-Eulerian two-fluid model was considered the most suitable modelling framework as it can account for both mechanical and thermal non-equilibrium effects, while not requiring fine-tuned empirical coefficients. The model treats both phases as interpenetrating continua, which are coupled via interphase models that account for the exchange of mass, momentum, and energy between the phases. The two-fluid model was applied in conjunction with the thermal phase-change model, which assumes that the phase change is solely the result of interphase heat transfer. Such a modelling framework has previously been used to study the flash boiling of subcooled liquids in converging-diverging nozzles. Despite certain difficulties in predicting the spatial distribution of vapour bubbles, the model has been found capable of accurately estimating the bulk flow properties as well as the average streamwise variation of pressure and void fraction.

In this thesis, the two-fluid model was implemented in ANSYS CFX and coupled with look-up tables generated from the Helmholtz equation of state to carry out a non-equilibrium simulation of the wet-to-dry expansion. Although the wet-to-dry expansion has not yet been studied experimentally, empirical data taken for flash boiling of subcooled water was used for validation purposes. Due to discrepancies between the two phenomena, the experimental data could not be directly used to validate the specific two-fluid model setup for the wet-to-dry expansion. However, it was rationalised that if the model was adjusted to work with the dispersed phase in the form of liquid droplets and adequate interphase models were used, it could be successfully applied to study wet-to-dry expansions. The CFD model predictions for the flashing of subcooled water were sufficiently close to the experimental results as far as the bulk flow properties and streamwise variation of pressure and void fraction were concerned, thus providing sufficient validation to proceed.

A critical part of the two-fluid model are the interphase models and additional sensitiv-

ity studies concerning the employed interphase models were deemed necessary to confirm reliability of the setup. Several alternative models for predicting interfacial forces as well as interphase heat-transfer rate were investigated. The results demonstrated a rather limited effect of drag, lift, and turbulent dispersion models on the wet-to-dry expansion. The maximum percentage deviation in average streamwise profiles of the vapour mass fraction and mixture velocity did not exceed several percent between the alternative interfacial force correlations. The solution was evidently more sensitive to the correlation used to estimate the heat-transfer rate between the droplets and the liquid-vapour interface. The maximum percentage deviation in the average streamwise profiles of the vapour mass fraction and mixture velocity could reach about 9% between various models, although the phase distribution within the nozzle seemed marginally affected. Since the quantitative deviation in the investigated streamwise profiles was confined to about 9%, while qualitative flow characteristics such as the two-dimensional phase pattern remained very similar, the model was deemed suitable for further analysis.

8.3 Numerical simulations

Following the validation and sensitivity analysis, a parametric study was conducted with the aim of investigating the wet-to-dry expansion under a range of operating conditions relevant to the wet-to-dry cycle. Twelve operating points were investigated, with an inlet pressure set at 500, 750, 1000 and 1250 kPa and an inlet vapour quality at 0.1, 0.3 and 0.5. The size of the droplets was modelled using a constant droplet density number, N_d, which ranged from 10^{11} to 10^{13} droplets per unit volume. The nozzle geometries for the twelve operating points were designed using the homogeneous-equilibrium model and assuming an isentropic one-dimensional flow. The nozzle pressure ratio varied between 9 and 14, while the mass-flow rate was set at 0.12 kg/s to represent small-scale power systems with an isentropic power output in the range of 90 to 170 kW.

The results of the CFD simulations indicate that droplet diameter has the greatest impact on the phase-change process. Because of the reduced surface area-to-volume ratio, large droplets are associated with higher thermal resistance and lower vapourisation rates. With an inlet droplet diameter in the order of 100-200 µm ($N_d = 10^{11}$), the predicted outlet vapour quality was in the range of 55 to 85 % when the inlet pressure was 500 and 750 kPa, and in the range of 70 to 100% for the expansions from 1000 and 1250 kPa. Two-phase flows characterised by such large droplets displayed significant non-equilibrium effects. The estimated velocity slip was approximately 45-65 % of the average mixture velocity, while the temperature difference between the phases could reach 60 to 90 °C. The vapour generation rate improved significantly when the inlet droplet size was reduced. With an inlet droplet diameter in the range of 40 to 100 µm ($N_d = 10^{12}$), the outlet vapour quality increased to 80 to 90% at inlet pressures below 750 kPa and to approximately 90 to 95% when the inlet pressure was higher than 1000 kPa. The vapourisation rate was further enhanced when the inlet droplet diameter was reduced to below 40 µm ($N_d = 10^{13}$), reaching 85-95 % for lower inlet pressures and approximately 95 to 100% for higher pressures. As the droplet size

was decreased to values below 40 µm, the relative velocity slip between the phases gradually decreased with a maximum value of 15 to 30% of the average mixture velocity. Similarly, the maximum temperature difference dropped to approximately 20-40 °C. Generally, non-equilibrium effects remained significant even when droplets were relatively small, which confirms the importance of including these effects when simulating the wet-to-dry expansion.

It could be inferred from the CFD results that dry vapour flow can be more readily achieved when expanding the mixture from higher inlet pressures and vapour qualities. However, lower inlet pressures and vapour qualities are preferred from the standpoint of maximising the wet-to-dry cycle performance. This suggests a trade-off will likely exist between designing a nozzle that can achieve complete vapourisation and obtaining a high thermodynamic advantage over the single-phase organic Rankine cycle.

To assess the flow ability to expand to the design outlet conditions, the ratios of the estimated pressure drop and the average outlet velocity obtained with the CFD model were compared with the design values. In all investigated cases, the flow underexpanded, reaching a pressure visibly higher than the design value. This underexpansion was proportional to the degree of departure from the homogenous-equilibrium flow, which was the basis for the nozzle design. As such, two-phase flows with small droplets achieved a pressure drop close to 95 % of the design value, while the ratio of the CFD-estimated to the design outlet velocity was between 75 and 90 %. Larger droplets that are associated with increased non-equilibrium effects displayed a much larger discrepancy between the predicted and design outlet conditions, which emphasises the need for a more suitable design method that can account for non-equilibrium effects.

Two-dimensional contours of the vapour quality and mixture velocity give insight into the phase pattern and the uniformity of the two-phase flow. Similarly to the other flow parameters, the flow pattern was mainly affected by the droplet size. Large droplets, characterised by long relaxation times could not effectively follow the mean flow. This resulted in an accumulation of the liquid phase near the nozzle walls in the converging section, whereas the droplets downstream of the throat had a tendency to accumulate close to the centreline of the nozzle, resulting in a characteristic liquid core flow. As a consequence, the flows characterised by large droplets were found to be highly non-uniform in terms of phase distribution at the nozzle outlet. Similar non-uniformity was observed in terms of mixture velocity, which appeared to be visibly lower in the core of the nozzle due to high concentration of the heavier liquid phase. Generally, these effects gradually diminished as the droplet number was raised, and to a lesser extent when the operating pressure was increased. For $N_d = 10^{11}$, the normalised standard deviation of the outlet quality ranged from 20 to 50%, while the standard deviation of mixture velocity varied between 10 and 30% of the mean velocity. The flow uniformity visibly improved as the droplet number was raised, with fairly uniform flow at $N_d = 10^{13}$ in most studied conditions. In the context of turbomachinery applications, the nozzle must deliver a uniform flow to the rotor to ensure an efficient operation of the machine. As indicated by the results, this can be difficult to achieve when droplets are too large.

Lastly, the likelihood of droplet breakup was assessed based on the streamwise profiles of

average Weber number. Generally, droplet breakup was predicted to occur under all the investigated conditions. At high droplet numbers, the average Weber number was several times higher than the local critical value at which the breakup is expected to take place. As the droplet number was lowered, the average Weber number increased sharply, exceeding the critical Weber number by approximately two orders of magnitude. Therefore, droplet numbers smaller than 10^{13} are unlikely to be sustained during expansion due to highly probable breakup effects that cause an eventual increase in the number of droplets. Therefore, the results presented indicate a worst-case scenario, and it can be hypothesised that the inclusion of breakup effects will lead to enhanced vapourisation. These results also emphasise the need to take into account these droplet breakup effects when simulating wet-to-dry expansions.

8.4 Non-equilibrium nozzle design

The results of the parametric study demonstrated the importance of non-equilibrium effects in the wet-to-dry expansion, raising a question around the importance of including these effects at the nozzle design stage. To answer this question, further CFD simulations were carried out on nozzles designed with a one-dimensional non-equilibrium tool that had previously been developed for two-phase applications. Two expansion cases from inlet pressures of 500 and 1000 kPa and an intermediate inlet quality of 0.3 were analysed in detail, while the same droplet number range of 10^{11} to 10^{13} was applied to investigate the dependence of the solution on the droplet size.

The agreement between the vapour quality profiles predicted by the non-equilibrium design tool and the CFD model was much improved compared to that of the homogeneous-equilibrium design method. However, the phase change predicted by the CFD model was still visibly delayed with respect to the design values. This suggests that certain effects such as two-dimensional flow variations neglected at the design stage played an important role in the expansion. With that being said, including non-equilibrium effects in the design process was found beneficial from the standpoint of maximising the vapourisation rate. Overall, the improvement in the vapourisation rate was more significant in flows characterised by larger droplets (11.7-15 % higher outlet vapour quality), while for smaller droplets the difference was rather marginal (1.8-2 % increase). This was expected as two-phase flows characterised by small droplets begin to resemble the homogeneous-equilibrium flow, making the difference between the two design tools less significant.

The nozzles designed with the non-equilibrium feature an enlarged flow area in the diverging section of the nozzle, which was proportional to the droplet size and compensated for higher velocity slip that translates to lower mixture velocities. Owing to the the adjustment of the flow area due to non-equilibrium effects, the mixture could expand much closer to the design outlet conditions, achieving higher velocities. At an inlet pressure of 500 kPa the outlet mixture velocity increased by 5.8 to 16.9% compared to the equilibrium nozzles. This increase was much more pronounced at the inlet pressure of 1000 kPa, where the exit velocity raised by 9.3 to 63 %, with greater improvements at low droplet numbers. Generally, the mixture could reach velocities corresponding to 90-98% of the design value. The underexpansion is-

sues were practically eliminated with the ratio of the CFD-estimated to the design pressure drop being in the range of 1 to 1.007.

Regarding the uniformity of the two-phase flow, a similar phase separation pattern was observed as previously discussed. In terms of the standard deviation of vapour mass fraction computed across the outlet and normalised by the mean value, it varied between 5.4 to 14 % for the expansion from 500 kPa and between 0.07 to 1.2 % for the expansion from 1000 kPa. The corresponding ranges computed for the equilibrium nozzles were 6.9 to 37.8 % and 2.2 to 15.4 % for the the same set of operating conditions. The phase separation occurring downstream of the throat had an effect on velocity uniformity even if complete mixture vapourisation was achieved. In most cases, the outlet mixture velocity was slightly less uniform compared to the equilibrium nozzles, which can be attributed to a more abrupt increase in the flow area downstream of the throat, which promoted phase separation. The standard deviation of mixture velocity normalised by the mean value ranged from 10.1 to 35.9 % and from 7.2 to 12.7 % for an inlet pressure of 500 and 1000 kPa respectively. These values were typically several percent higher than those reported for the equilibrium nozzles.

Similarly to the earlier results, the average Weber number exceeded the critical value in all of the cases considered. This indicates that the droplet breakup effects remain important regardless of the nozzle design methodology applied. In further analysis, a droplet diameter profile satisfying the critical Weber number condition was generated by the non-equilibrium design tool and imported into the CFD solver to simulate the two-phase expansion accounting for droplet breakup effects. Breakup was found to occur within the first 50 % of the nozzle length and resulted in a droplet diameter decrease to 7-12 µm. Although the droplet diameter limited the average Weber during expansion, complete mixture vapourisation was difficult to achieve at pressures below 1000 kPa. This was attributed to the assumption of constant droplet diameter in the post-breakup region, which limits the attainable vapourisation rate.

In summary, the results confirm the importance of including non-equilibrium effects when designing nozzles for the wet-to-dry expansion. The nozzles designed with the non-equilibrium tool could achieve higher vapour quality and mixture velocity compared to the nozzles designed with the homogenous-equilibrium model. Furthermore, the underexpansion issues were practically eliminated, and the flow could expand close to the design outlet conditions. However, the results reaffirm the importance of accounting for droplet breakup effects. Although the breakup process can be approximated with the non-equilibrium design tool, it may be desired to account for these effects directly in the CFD solver. This is particularly important when CFD-based shape optimisation studies are performed, where the relationship between the nozzle wall profile and the resulting droplet size should be evaluated during optimisation.

8.5 Nozzle optimisation

In the last chapter of the thesis, nozzle optimisation was performed, which was divided into two stages. First, a one-dimensional optimisation was conducted using the non-equilibrium design tool. As part of the design process, a static pressure profile is imposed, which had been kept constant in all previous studies. The goal of the one-dimensional optimisation is to maximise the vapourisation rate by optimising the shape of the imposed pressure profile. The results discussed previously indicate that it is more challenging to achieve dry outlet conditions if the mixture is expanded from lower pressures. However, these conditions are preferred from the standpoint of maximising the cycle performance. Therefore, three low inlet pressures of 450, 550 and 650 kPa were considered for the optimisation study to assess whether the wet-to-dry transition could be achieved under these operating conditions in the optimised nozzles. An intermediate inlet vapour quality of 0.3 was fixed in each case, while the droplet diameter was estimated based on the local Weber number, which was deemed a suitable method to predict realistic droplet size under given flow conditions. The optimised nozzles were simulated using the CFD model to verify the results of the one-dimensional optimisation. In order to account for droplet breakup effects directly in the CFD solver, a novel approach for estimating droplet breakup within two- and three-dimensional non-equilibrium simulations of two-phase flows with phase change has been proposed and incorporated in the CFD model.

The optimised pressure profiles were fairly similar and generally featured a more rapid expansion compared to the baseline profiles. More abrupt expansions resulted in enhanced droplet breakup, which consequently led to smaller droplet size and increased vapourisation rates. The CFD simulations conducted on the geometries generated using the optimised pressure profiles achieved 3.3 to 5.7% higher vapour mass fraction at the nozzle outlet, which reached 88.2, 93.4 and 95.7% for the expansions from 450, 550 and 650 kPa, respectively. Although the wet-to-dry transition was not achieved in any of the considered cases, a vapour quality of 95.7 % in the expansion from 650 kPa seemed promising. When the flow-field was assessed, an oblique shock train was found to from in each of the optimised nozzles, which was the result of a more abrupt increase in the flow area downstream of the throat. The presence of the shock resulted in an elevated entropy generation, which affected the nozzle efficiency. The nozzle efficiencies for the optimised geometries were in the range of 67.58 to 78.42%, approximately 5.8 to 13.5% lower compared to the baseline geometries, with more pronounced losses at low pressures. This indicates that more advanced optimisation methods are required to simultaneously maximise the vapourisation rate and nozzle efficiency, which could not be accomplished using the inviscid one-dimensional model.

The second stage of optimisation involved CFD-based shape optimisation of the nozzle wall profile, aimed at maximising the vapourisation rate and nozzle efficiency. The shape optimisation was carried out for the nozzle designed for the expansion of the siloxane MM from an inlet pressure of 550 kPa and an inlet vapour quality of 0.3. The geometry of the nozzle obtained from the one-dimensional optimisation was used as a starting point in the optimisation. The nozzle wall profile was parametrised using a spline with 20 geometry

points. The shape optimisation focused on the wall profile in the vicinity of the throat, which was deemed the most significant because it controlled the expansion rate and affected the breakup process and the formation of the oblique shock. The results revealed that by optimising the wall profile near the throat, it was possible to design a nozzle that achieves a similar vapourisation rate to that achieved through one-dimensional optimisation (93.4 %) but can facilitate expansion in a more efficient manner. Owing to a fine refinement of the wall profile in the throat area, the formation of the oblique shock train could be avoided, leading to a 3% increase in nozzle efficiency, which reached around 78%.

The incomplete mixture vapourisation in the optimised nozzles was attributed to the assumption of a constant droplet diameter in the post-breakup region. A new approach to modelling droplet size that combines breakup effects and droplet size variation due to phase change was subsequently proposed. The preliminary results indicate that when the droplets were allowed to decrease in size due to phase change taking place in the diverging section of the nozzle, the vapourisation rate was significantly enhanced and dry conditions were predicted at the nozzle outlet. However, this method has not been previously applied in flash-boiling problems and requires further validation.

8.6 Final remarks

The main question that this research work has attempted to answer is whether it is feasible to design a nozzle that can facilitate the wet-to-dry transition in an efficient manner. On the basis of the results of non-equilibrium simulations and optimisation study documented in this work, it can be inferred that accomplishing complete mixture vapourisation is possible but strongly depends on the operating conditions and the size of the dispersed liquid droplets. Provided that expansion begins with a droplet diameter in the order of 20-40 µm, dry conditions are likely to be achieved as long as the inlet pressure is above 1000 kPa. Flows with larger droplets or lower pressures display a visible delay in the phase change process. Furthermore, other effects come into play that include flow non-uniformity, which may affect the performance of a turboexpander intended for the wet-to-dry cycle. Using a nozzle design tool that accounts for non-equilibrium effects can potentially help design better-performing geometries that can more easily achieve the wet-to-dry transition. Furthermore, shape optimisation techniques can be applied to refine the nozzle performance. An optimised nozzle for the expansion of the siloxane MM from an inlet pressure of 550 kPa and a vapour quality of 0.3 could achieve an outlet vapour quality of 93.5 % and an efficiency of 78 %. Vapourisation rates and efficiencies are likely to be enhanced at higher operating pressures, but the thermodynamic advantage of the two-phase expansion decreases.

This work has provided a comprehensive analysis of non-equilibrium flash boiling of the siloxane MM in a converging-diverging passage representative of a turboexpander nozzle intended for the wet-to-dry cycle. The results presented in this thesis give insight into the influence of operating conditions, droplet size, and nozzle design methods on the phase-change process. Furthermore, the potential of optimisation techniques to improve the vapour generation rate and nozzle efficiency was assessed. The results revealed that achieving the

wet-to-dry transition under operating conditions that are most attractive from the standpoint of maximising cycle performance may be challenging. However, vapour qualities above 90 % and nozzle efficiencies close to 80 % seem promising. It is rational to assume that these values could be further improved by refining the design and optimisation methods. Furthermore, higher operating pressures can still offer a considerable advantage over the single-phase organic Rankine cycles, while the wet-to-dry transition can theoretically be more readily accomplished under these conditions. Therefore, the concept of a two-phase turboexpander for the wet-to-dry cycle is viewed as feasible, although further research and experimental validation are strongly recommended.

8.7 Recommendations for future work

There are several research directions that can be followed in future studies dedicated to the wet-to-dry expansion. The following recommendations are grouped into four categories that include flow modelling, design and optimisation methods, applications and experimentation.

8.7.1 Flow modelling

The numerical simulations presented in this thesis were performed within the Eulerian-Eulerian framework, which is a suitable modelling framework to simulate the phase-change process under a wide range of dispersed phase concentrations. The Eulerian-Lagrangian framework focusses on tracking the trajectory of individual droplets and can provide more detailed information on the evolution of size, temperature, and mass of each droplet, with the phase-change and breakup models applied on an individual droplet basis. As such, it can be applied in future studies to gain a better understanding of the behaviour of individual droplets under conditions relevant to the wet-to-dry expansion. Because of the discrete treatment of droplets, the Eulerian-Lagrangian model can more accurately capture the spatial distribution of droplets and predict the interaction between the droplets and the continuous vapour phase. Furthermore, higher-fidelity large-eddy or direct numerical simulations can be employed to more accurately resolve the turbulent-flow structures and their interaction with the liquid droplets. Such simulations can potentially provide a more detailed description of the interaction between turbulent vapour flow and the dispersed droplets, which affects the droplet shape, spatial distribution, the breakup process, as well as the heat transfer characteristics and consequently the vapourisation process.

The breakup modelling approach used in this study relied on simplified flow averaging in discrete control volumes, where a droplet diameter was assumed to instantaneously adjust to the average critical Weber number. The actual breakup is a more complicated process, which involves a large parent droplet undergoing a fragmentation into a number of smaller child droplets. This does not occur instantaneously and depending on the local flow conditions, a certain finite time frame is required to initiate and complete the breakup. Furthermore, the child droplets will have a non-uniform size distribution, which is also dependent on the breakup regime. On the basis of these considerations, more advanced droplet breakup models can be developed and implemented within polydispersed transient solvers.

Another area requiring further refinement is the interfacial area density modelling, which in this study was calculated based on the assumption that the dispersed phase is in the form of spherical liquid droplets. This assumption may not be valid in the early stages of high-pressure expansions, where the void fraction can be significantly lower than 30 %. Moreover, the simulation results revealed that a concentrated liquid layer may form near the wall in the converging section of the nozzle. The assumption of a dispersed droplet flow in those regions of the flow may lead to some inaccuracies, and correction to the interfacial area may be applied in a bid to improve the model.

Lastly, reduced-order relaxation models can be developed based on the results of non-equilibrium simulations. Such models are less computationally demanding and could be useful in conducting more advanced optimisation studies with a larger number of design variables.

8.7.2 Design and optimisation methods

When it comes to design and optimisation techniques, the non-equilibrium nozzle design tool can be improved by incorporating terms that account for viscous losses and shock formation. Certain correction terms could be introduced to account for the two-dimensional flow variations observed in the CFD simulations. Such an improved design tool could be applied to perform multi-objective optimisation, taking into account both the vapourisation rate and expansion efficiency. Regarding CFD-based shape optimisation, the current study focused only on the vicinity of the throat as the area of most significance and simplified the problem by assuming a two-dimensional flow. Future optimisation studies could consider three-dimensional nozzle geometries and extend the refinement beyond the throat region. A higher number of design variables could help achieve finer control over the entire wall profile. The length and width of the nozzle could also be included directly as design variables.

8.7.3 Applications

This work focused on non-equilibrium flash boiling of the siloxane MM in a converging-diverging nozzle. Certain turboexpanders, such as radial-inflow and radial-outflow turbines, are characterised by curved geometry of the nozzle vanes. This is likely to have certain implications on the phase-change process and the phase distribution within the passage because of the presence of centrifugal forces. It is suggested that the methods described in this thesis and those proposed for future research be extended to curved passages to investigate its influence on the phase-change process. Ultimately, the wet-to-dry expansion should be simulated in a nozzle vane or in an entire suitable turboexpander designed for the wet-to-dry cycle. The shape optimisation techniques applied in this study should also be applied to such nozzle vanes.

The siloxane MM was identified as a suitable working fluid for heat sources in the temperature range of 150 and 250 °C. Although other working fluids may be associated with slightly

lower cycle performance, it is worth investigating whether the same challenges are likely to be present concerning the wet-to-dry transition. Moreover, when different temperature levels are to be studied, other working fluids may be preferred.

The entire analysis conducted in this thesis focused on the performance of the nozzle at the design point. In real-world applications, the system may often operate under off-design conditions due to variation in process parameters such as temperature, pressure, and flow rates. Therefore, it is recommended that an off-design analysis is performed in future studies to investigate the two-phase flow behaviour and nozzle performance in the event that the operating conditions deviate from the design ones.

8.7.4 Experimentation

Currently, the most needed type of study in the context of the wet-to-dry expansion appears to be that of empirical nature. Although the implementation of the two-fluid model used in this work was verified using experimental data taken for flash boiling of water, the specific setup for the wet-to-dry expansion could not be validated because of the discrepancies between the two phenomena. Available guidelines and sensitivity studies were applied to confirm the reliability of the model; however, experimental tests are considered necessary for validation purposes. Blow-down and continuous test facilities such as TROVA [260], ORCHID [261] and CLOWT [262] have been designed to study high-speed flow of organic fluids in turbomachinery passages. However, to date, there have been no dedicated test facilities suitable for studying high-speed two-phase expansion of organic fluids in passages representative of turboexpander nozzles intended for the wet-to-dry cycle.

Future test facilities dedicated to studying wet-to-dry expansions should provide information on key flow characteristics required to validate the numerical models. First, appropriate flow metres and multiple pressure taps along the nozzle should be installed to measure the flow rate and pressure distribution within the nozzle. Furthermore, such facilities should allow for visual inspection of the flow to understand the two-phase flow dynamics. Backlit imaging coupled with high-speed cameras could be applied to investigate the size, shape, velocity, and spatial distribution of the dispersed droplets. Such techniques could be coupled with infrared thermography that could provide information on the variation of the temperature of both phases, giving useful insight into the heat transfer characteristics.

Bibliography

[1] International Energy Agency (IEA). *CO2 Emissions in 2022*. 2022.

[2] GOV.UK. *UK becomes first major economy to pass net zero emissions law*. 2019. URL: https://www.gov.uk/government/news/uk-becomes-first-major-economy-to-pass-net-zero-emissions-law. (Accessed: 18.10.2023).

[3] Forman, C., Muritala, I. K., Pardemann, R., and Meyer, B. "Estimating the global waste heat potential". In: *Renewable and Sustainable Energy Reviews* 57 (2016), pp. 1568–1579. DOI: 10.1016/j.rser.2015.12.192.

[4] Albert, M. D., Bennett, K. O., Adams, C. A., and Gluyas, J. G. "Waste heat mapping: A UK study". In: *Renewable and Sustainable Energy Reviews* 160 (2022), p. 112230. DOI: 10.1016/j.rser.2022.112230.

[5] Knowledge Center on Organic Rankine Cycle technology (KCORC). *Thermal Energy Harvesting - The Path to Tapping into a Large CO2-free European Power Source: Version 1.0*. 2022.

[6] Macchi, E. "Theoretical basis of the Organic Rankine Cycle". In: *Organic Rankine Cycle (ORC) Power Systems*. Ed. by E. Macchi and M. Astolfi. Woodhead Publishing, 2017, pp. 3–24. DOI: 10.1016/B978-0-08-100510-1.00001-6.

[7] Wieland, C., Dawo, F., Schifflechner, C., and Astolfi, M. "Market Report on Organic Rankine Cycle Power Systems: Recent Developments and Outlook". In: *6th International Seminar on ORC Power Systems*. Munich, Germany, Oct. 2021. DOI: 10.14459/2021mp1636584.

[8] White, M. T. "Cycle and turbine optimisation for an ORC operating with two-phase expansion". In: *Applied Thermal Engineering* 192 (2021), p. 116852. DOI: 10.1016/j.applthermaleng.2021.116852.

[9] El-Emam, R. S. and Dincer, I. "Exergy and exergoeconomic analyses and optimization of geothermal organic Rankine cycle". In: *Applied Thermal Engineering* 59.1-2 (2013), pp. 435–444. DOI: 10.1016/j.applthermaleng.2013.06.005.

[10] Safarian, S. and Aramoun, F. "Energy and exergy assessments of modified Organic Rankine Cycles (ORCs)". In: *Energy Reports* 1 (2015), pp. 1–7. DOI: 10.1016/j.egyr.2014.10.003.

[11] Chen, J., Zheng, X., Guo, G., Luo, X., Chen, Y., and Yang, Z. "A flexible and multi-functional organic Rankine cycle system: Preliminary experimental study and advanced exergy analysis". In: *Energy Conversion and Management* 187 (2019), pp. 339–355. DOI: 10.1016/j.enconman.2019.03.050.

[12] Dibazar, S. Y., Salehi, G., and Davarpanah, A. "Comparison of exergy and advanced exergy analysis in three different organic rankine cycles". In: *Processes* 8.5 (2020), p. 586. DOI: 10.3390/pr8050586.

[13] Wieland, C., Schifflechner, C., Braimakis, K., Kaufmann, F., Dawo, F., Karellas, S., Besagni, G., and Markides, C. N. "Innovations for organic Rankine cycle power systems: Current trends and future perspectives". In: *Applied Thermal Engineering* 225 (2023), p. 120201. DOI: 10.1016/j.applthermaleng.2023.120201.

[14] Astolfi, M., Romano, M. C., Bombarda, P., and Macchi, E. "Binary ORC (organic Rankine cycles) power plants for the exploitation of medium-low temperature geothermal sources - Part A: Thermodynamic optimization". In: *Energy* 66 (2014), pp. 423–434. DOI: 10.1016/j.energy.2013.11.056.

[15] Lecompte, S., Lemmens, S., Huisseune, H., Van Den Broek, M., and De Paepe, M. "Multi-objective thermo-economic optimization strategy for ORCs applied to subcritical and transcritical cycles for waste heat recovery". In: *Energies* 8.4 (2015), pp. 2714–2741. DOI: 10.3390/en8042714.

[16] Smith, I. K. "Development of the Trilateral Flash Cycle System: Part 1: Fundamental Considerations". In: *Proceedings of the Institution of Mechanical Engineers, Part A: Journal of Power and Energy* 207.3 (1993), pp. 179–194. DOI: 10.1243/PIME_PROC_1993_207_032_02.

[17] Fischer, J. "Comparison of trilateral cycles and organic Rankine cycles". In: *Energy* 36.10 (2011), pp. 6208–6219. DOI: 10.1016/j.energy.2011.07.041.

[18] Chys, M., Broek, M. van den, Vanslambrouck, B., and De Paepe, M. "Potential of zeotropic mixtures as working fluids in organic Rankine cycles". In: *Energy* 44.1 (2012), pp. 623–632. DOI: 10.1016/j.energy.2012.05.030.

[19] Lecompte, S., Ameel, B., Ziviani, D., Van Den Broek, M., and De Paepe, M. "Exergy analysis of zeotropic mixtures as working fluids in Organic Rankine Cycles". In: *Energy Conversion and Management* 85 (2014), pp. 727–739. DOI: 10.1016/j.enconman.2014.02.028.

[20] Dong, B., Xu, G., Li, T., Quan, Y., and Wen, J. "Thermodynamic and economic analysis of zeotropic mixtures as working fluids in low temperature organic Rankine cycles". In: *Applied Thermal Engineering* 132 (2018), pp. 545–553. DOI: 10.1016/j.applthermaleng.2017.12.083.

[21] Guo, T., Wang, H., and Zhang, S. "Comparative analysis of CO2-based transcritical Rankine cycle and HFC245fa-based subcritical organic Rankine cycle using low-temperature geothermal source". In: *Science China Technological Sciences* 53.6 (2010), pp. 1638–1646. DOI: 10.1007/s11431-010-3123-4.

[22] Lai, K. Y., Lee, Y. T., Lai, T. H., and Liu, Y. H. "Using a partially evaporating cycle to improve the volume ratio problem of the trilateral flash cycle for low-grade heat recovery". In: *Entropy* 23.5 (2021).

[23] Lecompte, S., Broek, M. van den, and De Paepe, M. "Thermodynamic analysis of the partially evaporating trilateral cycle". In: *2nd International Seminar on ORC Power Systems*. Rotterdam, Netherlands, Oct. 2013.

[24] Lecompte, S., Huisseune, H., Broek, M. van den, and De Paepe, M. "Methodical thermodynamic analysis and regression models of organic Rankine cycle architectures for waste heat recovery". In: *Energy* 87 (2015), pp. 60–76. DOI: 10.1016/j.energy.2015.04.094.

[25] Zhou, Y., Zhang, F., and Yu, L. "Performance analysis of the partial evaporating organic Rankine cycle (PEORC) using zeotropic mixtures". In: *Energy Conversion and Management* 129 (2016), pp. 89–99. DOI: 10.1016/j.enconman.2016.10.009.

[26] Dawo, F., Buhr, J., Wieland, C., and Spliethoff, H. "Experimental Investigation of the Partially Evaporated Organic Rankine Cycle for Various Heat Source Conditions". In: *6th International Seminar on ORC Power Systems*. Munich, Germany, Oct. 2021. DOI: 10.14459/2021mp1633102.

[27] Smith, I., Stosic, N., and Kovacevic, A. "Screw Expanders Increase Output and Decrease the Cost of Geothermal Binary Power Plant Systems". In: *Transactions of Geothermal Resource Council* 29 (2005), pp. 787–794.

[28] Elliott, D. G. *Theory and Tests of Two-Phase Turbines*. Jet Propulsion Laboratory, Institute of Technology Pasadena, California. 1982.

[29] Lhermet, G., Tauveron, N., Caney, N., Blondel, Q., and Morin, F. "A Recent Advance on Partial Evaporating Organic Rankine Cycle: Experimental Results on an Axial Turbine". In: *Energies* 15.20 (2022), p. 7559. DOI: 10.3390/en15207559.

[30] Liao, Y. and Lucas, D. "A review on numerical modelling of flashing flow with application to nuclear safety analysis". In: *Applied Thermal Engineering* 182 (2021), p. 116002. DOI: 10.1016/j.applthermaleng.2020.116002.

[31] Leyer, S. and Wich, M. "The Integral Test Facility Karlstein". In: *Science and Technology of Nuclear Installations* 2012 (2011), p. 439374. DOI: 10.1155/2012/439374.

[32] Liao, Y. and Lucas, D. "Possibilities and limitations of CFD simulation for flashing flow scenarios in nuclear applications". In: *Energies* 10.1 (2017). DOI: 10.3390/en10010139.

[33] Sallet, D. "Critical mass flow rates through pressure relief valves". In: *Wärme- und Stoffübertragung* 26.6 (1991), pp. 315–321. DOI: 10.1007/BF01591664.

[34] Henry, R. E. and Fauske, H. K. "The Two-Phase Critical Flow of One-Component Mixtures in Nozzles, Orifices, and Short Tubes". In: *Journal of Heat Transfer* 93.2 (1971), pp. 179–187. DOI: 10.1115/1.3449782.

[35] Abuaf, N., Wu, B. J., Zimmer, G. A., and Saha, P. *Study of nonequilibrium flashing of water in a converging-diverging nozzle. Volume 1: Experimental*. Brookhaven National Laboratory. 1981.

[36] Haida, M., Smolka, J., Hafner, A., Palacz, M., Banasiak, K., and Nowak, A. J. "Modified homogeneous relaxation model for the R744 trans-critical flow in a two-phase ejector". In: *International Journal of Refrigeration* 85 (2018), pp. 314–333. DOI: 10.1016/j.ijrefrig.2017.10.010.

[37] Geng, L., Liu, H., and Wei, X. "CFD analysis of the flashing flow characteristics of subcritical refrigerant R134a through converging-diverging nozzles". In: *International Journal of Thermal Sciences* 137 (2019), pp. 438–445. DOI: 10.1016/j.ijthermalsci.2018.12.011.

[38] Loska, M., Smolka, J., Haida, M., Kriezi, E. E., and Banasiak, K. "CFD modelling of R410A flow through an expansion valve using equilibrium and modified relaxation models". In: *Applied Thermal Engineering* 185 (2021), p. 116442. DOI: 10.1016/j.applthermaleng.2020.116442.

[39] Date, A., Khaghani, A., Andrews, J., and Akbarzadeh, A. "Performance of a rotating two-phase turbine for combined power generation and desalination". In: *Applied Thermal Engineering* 76 (2015), pp. 9–17. DOI: 10.1016/j.applthermaleng.2014.08.074.

[40] Date, A., Vahaji, S., Andrews, J., and Akbarzadeh, A. "Experimental performance of a rotating two-phase reaction turbine". In: *Applied Thermal Engineering* 76 (2015), pp. 475–483. DOI: 10.1016/j.applthermaleng.2014.11.039.

[41] Rane, S. and He, L. "CFD analysis of flashing flow in two-phase geothermal turbine design". In: *Journal of Computational Design and Engineering* 7.2 (2020), pp. 238–250. DOI: 10.1093/jcde/qwaa020.

[42] Rane, S. and He, L. "Numerical analysis of a novel two-phase turbine using thermal non-equilibrium, homogeneous nucleation phase change". In: *Thermal Science and Engineering Progress* 22 (2021), p. 100827. DOI: 10.1016/j.tsep.2020.100827.

[43] White, M. T. "Investigating the wet-to-dry expansion of organic fluids for power generation". In: *International Journal of Heat and Mass Transfer* 192 (2022), p. 122921. DOI: 10.1016/j.ijheatmasstransfer.2022.122921.

[44] Downar-Zapolski, P., Bilicki, Z., Bolle, L., and Franco, J. "The non-equilibrium relaxation model for one-dimensional flashing liquid flow". In: *International Journal of Multiphase Flow* 22.3 (1996), pp. 473–483. DOI: 10.1016/0301-9322(95)00078-X.

[45] UNFCCC. *The Paris Agreement*. 2019. URL: https://unfccc.int/process-and-meetings/the-paris-agreement. (Accessed: 18.10.2023).

[46] Quoilin, S., Broek, M. V. D., Declaye, S., Dewallef, P., and Lemort, V. "Techno-economic survey of organic rankine cycle (ORC) systems". In: *Renewable and Sustainable Energy Reviews* 22 (2013), pp. 168–186.

[47] Colonna, P., Casati, E., Trapp, C., Mathijssen, T., Larjola, J., Turunen-Saaresti, T., and Uusitalo, A. "Organic Rankine Cycle Power Systems : From the Concept to Current Technology , Applications , and an Outlook to the Future". In: *Journal of Engineering for Gas Turbines and Power* 137.10 (2015), pp. 1–19.

[48] Persico, G. and Pini, M. "8 - Fluid dynamic design of Organic Rankine Cycle turbines". In: *Organic Rankine Cycle (ORC) Power Systems*. Ed. by E. Macchi and M. Astolfi. Woodhead Publishing, 2017, pp. 253–297.

[49] Bronicki, L. Y. "History of organic rankine cycle systems". In: *Organic Rankine Cycle (ORC) Power Systems: Technologies and Applications*. Elsevier Ltd, 2017, pp. 25–66.

[50] Nicholas P. Cheremisinoff. "Air Pollution". In: *Clean Electricity Through Advanced Coal Technologies*. Ed. by Nicholas P. Cheremisinoff. William Andrew Publishing, 2012. Chap. 1, pp. 1–30.

[51] Read, M. G., Smith, I. K., and Stosic, N. "Multi-Variable Optimisation of Wet Vapour Organic Rankine Cycles with Twin-Screw Expanders". In: *Proceedings of the 22nd International Compressor Engineering Conference*. Purdue, France, July 2014.

[52] Papapetrou, M., Kosmadakis, G., Cipollina, A., La Commare, U., and Micale, G. "Industrial waste heat: Estimation of the technically available resource in the EU per industrial sector, temperature level and country". In: *Applied Thermal Engineering* 138 (2018), pp. 207–216. DOI: 10.1016/j.applthermaleng.2018.04.043.

[53] Tocci, L., Pal, T., Pesmazoglou, I., and Franchetti, B. "Small scale Organic Rankine Cycle (ORC): A techno-economic review". In: *Energies* 10.4 (2017), pp. 1–27.

[54] Smith, I., Stosic, N., and Kovacevic, A. "An Improved System for Power Recovery from Higher Enthalpy Liquid-Dominated Fields". In: *World Geothermal Congress 2005*. Antalya, Turkey, Apr. 2005.

[55] Li, J., Pei, G., Li, Y., Wang, D., and Ji, J. "Energetic and exergetic investigation of an organic Rankine cycle at different heat source temperatures". In: *Energy* 38.1 (2012), pp. 85–95. DOI: 10.1016/j.energy.2011.12.032.

[56] Mago, P., Srinivasan, K., Chamra, L., and Somayaji, C. "An examination of exergy destruction in organic Rankine cycles". In: *International Journal of Energy Research* 32 (2008), pp. 926–938. DOI: 10.1002/er.1406.

[57] Astolfi, M. "Technical options for organic rankine cycle systems". In: *Organic Rankine Cycle (ORC) Power Systems: Technologies and Applications*. 2017, pp. 67–89.

[58] Shengjun, Z., Huaixin, W., and Tao, G. "Performance comparison and parametric optimization of subcritical Organic Rankine Cycle (ORC) and transcritical power cycle system for low-temperature geothermal power generation". In: *Applied Energy* 88.8 (2011), pp. 2740–2754. DOI: 10.1016/j.apenergy.2011.02.034.

[59] Li, J., Liu, Q., Ge, Z., Duan, Y., and Yang, Z. "Thermodynamic performance analyses and optimization of subcritical and transcritical organic Rankine cycles using R1234ze(E) for 100–200 °C heat sources". In: *Energy Conversion and Management* 149 (2017), pp. 140–154. DOI: 10.1016/j.enconman.2017.06.060.

[60] Oyewunmi, O. A., Ferré-Serres, S., Lecompte, S., Van Den Broek, M., De Paepe, M., and Markides, C. N. "An Assessment of Subcritical and Trans-critical Organic Rankine Cycles for Waste-heat Recovery". In: *Energy Procedia* 105 (2017), pp. 1870–1876. DOI: 10.1016/j.egypro.2017.03.548.

[61] Bamorovat Abadi, G. and Kim, K. C. "Investigation of organic Rankine cycles with zeotropic mixtures as a working fluid: Advantages and issues". In: *Renewable and Sustainable Energy Reviews* 73 (2017), pp. 1000–1013. DOI: 10.1016/j.rser.2017.02.020.

[62] Xu, W., Zhao, R., Deng, S., Zhao, L., and Mao, S. S. "Is zeotropic working fluid a promising option for organic Rankine cycle: A quantitative evaluation based on literature data". In: *Renewable and Sustainable Energy Reviews* 148 (2021), p. 111267. DOI: 10.1016/j.rser.2021.111267.

[63] Lai, K. Y., Lee, Y. T., Chen, M. R., and Liu, Y. H. "Comparison of the trilateral flash cycle and Rankine cycle with organic fluid using the pinch point temperature". In: *Entropy* 21.12 (2019), p. 1197. DOI: 10.3390/e21121197.

[64] Iqbal, M. A., Rana, S., Ahmadi, M., Date, A., and Akbarzadeh, A. "Trilateral Flash Cycle (TFC): a promising thermodynamic cycle for low grade heat to power generation". In: *Energy Procedia* 160 (2019). 2nd International Conference on Energy and Power, ICEP2018, 13–15 December 2018, Sydney, Australia, pp. 208–214. DOI: 10.1016/j.egypro.2019.02.138.

[65] Dixon, S. L. and Hall, C. A. *Fluid Mechanics and Thermodynamics of Turbomachinery*. 6th. Burlington, MA: Butterworth-Heinemann/Elsevier, 2010.

[66] Rahbar, K., Mahmoud, S., Al-Dadah, R. K., Moazami, N., and Mirhadizadeh, S. A. "Review of organic Rankine cycle for small-scale applications". In: *Energy Conversion and Management* 134 (2017), pp. 135–155.

[67] Alshammari, F., Usman, M., and Pesyridis, A. "Expanders for Organic Rankine Cycle Technology". In: *Organic Rankine Cycle Technology for Heat Recovery*. Ed. by E. Wang. Rijeka: IntechOpen, 2018. Chap. 3. URL: https://doi.org/10.5772/intechopen.78720.

[68] Sauret, E. and Rowlands, A. S. "Candidate radial-inflow turbines and high-density working fluids for geothermal power systems". In: *Energy* 36.7 (2011), pp. 4460–4467.

[69] Bao, J. and Zhao, L. "A review of working fluid and expander selections for organic Rankine cycle". In: *Renewable and Sustainable Energy Reviews* 24 (2013), pp. 325–342.

[70] Pethurajan, V., Sivan, S., and Joy, G. C. "Issues, comparisons, turbine selections and applications – An overview in organic Rankine cycle". In: *Energy Conversion and Management* 166.April (2018), pp. 474–488.

[71] Maksiuta, D., Moroz, L., Burlaka, M., and Govoruschenko, Y. "Study on applicability of radial-outflow turbine type for 3 MW WHR organic Rankine cycle". In: *Energy Procedia* 129 (2017), pp. 293–300.

[72] Spadacini, C., Xodo, L., Quaia, M., Frassinetti, M., and Rizzi, D. "The geothermal radial outflow turbine". In: *Transactions - Geothermal Resources Council* 38 (2014), pp. 755–757.

[73] EXERGY. *Exergy's Radial Outflow Turbine*. 2022. URL: https://www.exergy-orc.com/technology/radial-outflow-turbine/. (Accessed: 04.10.2024).

[74] Spadacini, C., Centemeri, L., Rizzi, D., Sanvito, M., and Serafino, A. "Fluid-Dynamics of the ORC Radial Outflow Turbine". In: *Proceedings of the 3rd International Seminar on ORC Power Systems. ASME ORC 2015*. Brussels, Belgium, Oct. 2015.

[75] Spadacini, C. and Rizzi, D. "Radial outflow turbines for Organic Rankine Cycle expanders". In: *Organic Rankine Cycle (ORC) Power Systems: Technologies and Applications*. Elsevier Ltd, 2017, pp. 335–359.

[76] Zhao, Y., Liu, G., Li, L., Yang, Q., Tang, B., and Liu, Y. "Expansion devices for organic Rankine cycle (ORC) using in low temperature heat recovery: A review". In: *Energy Conversion and Management* 199 (2019).

[77] Lemort, V. and Legros, A. "Positive displacement expanders for Organic Rankine Cycle systems". In: *Organic Rankine Cycle (ORC) Power Systems: Technologies and Applications*. Elsevier Ltd, 2017, pp. 361–396.

[78] Imran, M., Usman, M., Park, B. S., and Lee, D. H. "Volumetric expanders for low grade heat and waste heat recovery applications". In: *Renewable and Sustainable Energy Reviews* 57 (2016), pp. 1090–1109.

[79] Murthy, A. A., Subiantoro, A., Norris, S., and Fukuta, M. "A review on expanders and their performance in vapour compression refrigeration systems". In: *International Journal of Refrigeration* 106 (2019), pp. 427–446. DOI: 10.1016/j.ijrefrig.2019.06.019.

[80] Smith, I. K., Stošić, N., and Aldis, C. A. "Development of the trilateral flash cycle system. Part 3: The design of high-efficiency two-phase screw expanders". In: *Proceedings of the Institution of Mechanical Engineers, Part A: Journal of Power and Energy* 210.1 (1996), pp. 75–92. DOI: 10.1243/PIME_PROC_1996_210_010_02.

[81] Smith, I. K., Stosic, N., Aldis, C. A., and Kovacevic, A. "Twin screw expanders in large chiller units". In: *1st International Conference on Compressors and their Systems*. London, United Kingdom, Sept. 1999.

[82] Smith, I. K., Stosic, N., and Kovacevic, A. "Power Recovery From Low Cost Two-Phase Expanders". In: *Transactions of Geothermal Resource Council* (2001), pp. 601–605.

[83] Smith, I., Stosic, N., Kovacevic, A., and Langson, R. "Cost effective small scale ORC systems for power recovery from low enthalpy geothermal resources". In: *Transactions - Geothermal Resources Council* 31 (2007).

[84] Read, M., Stosic, N., and Smith, I. K. "Optimization of Screw Expanders for Power Recovery From Low-Grade Heat Sources". In: *Energy Technology & Policy* 1.1 (2014), pp. 131–142. DOI: 10.1080/23317000.2014.969454.

[85] Bianchi, G., Kennedy, S., Zaher, O., Tassou, S. A., Miller, J., and Jouhara, H. "Two-phase chamber modeling of a twin-screw expander for Trilateral Flash Cycle applications". In: *Energy Procedia* 129 (2017). IV International Seminar on ORC Power Systems, ORC2017 IV International Seminar on ORC Power Systems, ORC2017 13-15 September 2017, Milano, Italy, pp. 347–354. DOI: 10.1016/j.egypro.2017.09.208.

[86] Bianchi, G., Kennedy, S., Zaher, O., Tassou, S. A., Miller, J., and Jouhara, H. "Numerical modeling of a two-phase twin-screw expander for Trilateral Flash Cycle applications". In: *International Journal of Refrigeration* 88 (2018), pp. 248–259. DOI: 10.1016/j.ijrefrig.2018.02.001.

[87] Bianchi, G., Marchionni, M., Kennedy, S., Miller, J., and Tassou, S. "One-Dimensional Modelling of a Trilateral Flash Cycle System with Two-Phase Twin-Screw Expanders for Industrial Low-Grade Heat to Power Conversion". In: *Designs* 3.3 (2019), p. 41. DOI: 10.3390/designs3030041.

[88] Bianchi, G., Marchionni, M., Miller, J., and Tassou, S. A. "Modelling and off-design performance optimisation of a trilateral flash cycle system using two-phase twin-screw expanders with variable built-in volume ratio". In: *Applied Thermal Engineering* 179 (2020), p. 115671. DOI: 10.1016/j.applthermaleng.2020.115671.

[89] Fukuta, M., Yanagisawa, T., Kosuda, O., and Ogi, Y. "Performance of Scroll Expander for CO2 Refrigeration Cycle". In: *International Compressor Engineering Conference*. Purdue, France, July 2006.

[90] Kohsokabe, H., Koyama, M., Tojo, K., Mutsunori, M., and Susumu, N. "Performance Characteristics of Scroll Expander for CO2 Refrigeration Cycles". In: *International Compressor Engineering Conference*. Purdue, France, July 2008.

[91] Kim, H. J., Ahn, J. M., Park, I., and Rha, P. C. "Scroll expander for power generation from a low-grade steam source". In: *Proceedings of the Institution of Mechanical Engineers, Part A: Journal of Power and Energy* 221.5 (2007), pp. 705–711. DOI: 10.1243/09576509JPE392.

[92] Mayer, K. *Research, Development and Demonstration of Micro-CHP System for Residential Applications*. Tech. rep. DOE/NT/42216. ECR International, Incorporated, 2010. DOI: 10.2172/1011855.

[93] Fukuta, M., Higasiyama, M., Yanagisawa, T., and Ogi, Y. "Observation of CO2 Trans-Critical Expansion Process". In: *International Refrigeration and Air Conditioning Conference*. Purdue, France, July 2008.

[94] Yang, B., Peng, X., He, Z., Guo, B., and Xing, Z. "Experimental investigation on the internal working process of a CO2 rotary vane expander". In: *Applied Thermal Engineering* 29.11-12 (2009), pp. 2289–2296. DOI: 10.1016/j.applthermaleng.2008.11.023.

[95] Jia, X., Zhang, B., Pu, L., Guo, B., and Peng, X. "Improved rotary vane expander for trans-critical CO2 cycle by introducing high-pressure gas into the vane slots". In: *International Journal of Refrigeration* 34.3 (2011), pp. 732–741. DOI: 10.1016/j.ijrefrig.2010.12.005.

[96] Dumont, O., Dickes, R., and Lemort, V. "Experimental investigation of four volumetric expanders". In: *Energy Procedia* 129 (2017). IV International Seminar on ORC Power Systems, ORC2017 13-15 September 2017, Milano, Italy, pp. 859–866. DOI: 10.1016/j.egypro.2017.09.206.

[97] Dumont, O., Dickes, R., De Rosa, M., Douglas, R., and Lemort, V. "Technical and economic optimization of subcritical, wet expansion and transcritical Organic Rankine Cycle (ORC) systems coupled with a biogas power plant". In: *Energy Conversion and Management* 157 (2018), pp. 294–306.

[98] Hays, L. "History and overview of two-phase flow turbines". In: *International Conference on Compressors and their Systems*. London, United Kingdom, 1999.

[99] Hughes, E. E. *Summart Report: Rotary Separator Turbine*. Tech. rep. RP1196. Palo Alto: Electric Power Research Institute, 1986.

[100] Studhalter, W., Cerini, D., and Hays, L. "Demonstration of an advanced biphase turbine at Coso Hot Springs". In: *Transactions - Geothermal Resources Council* 19 (1995), pp. 475–482.

[101] Welch, P. and Boyle, P. "New Turbines to Enable Efficient Geothermal Power Plants". In: *Geothermal Resources Council Transactions* 33 (2009), pp. 765–772.

[102] Energent. URL: http://www.energent.net/technology/variable-phase-turbine.html. (Accessed: 10.11.2023).

[103] Hays, L. and Brasz, J. J. "A Transcritical CO2 Turbine-Compressor". In: *International Compressor Engineering Conference*. Paper 1628. 2004. URL: https://docs.lib.purdue.edu/icec/1628.

[104] Hays, L. "Flashing Liquid Expander Energy Reduction in Refrigeration Systems". In: *17th International Refrigeration and Air Conditioning*. Purdue, France, July 2018.

[105] Li, H., Rane, S., Yu, Z., and Yu, G. "An inverse mean-line design method for optimizing radial outflow two-phase turbines in geothermal systems". In: *Renewable Energy* 168 (2021), pp. 463–490. DOI: 10.1016/j.renene.2020.12.079.

[106] Hays, L. G. and Brasz, J. J. "Two-Phase Turbines for Compressor Energy Recovery". In: *International Compressor Engineering Conference*. London, United Kingdom, 1996.

[107] Hays, L. G. *Demonstration of a Variable Phase Turbine Power System for Low Temperature Geothermal Resources*. Tech. rep. DOE-Energent-GO15153, 1136547. Energent Corporation, 2014. DOI: 10.2172/1136547.

[108] Prodanovic, M., Miltenović, A., and Nikodijević, M. "Determination of operating parameters of turbines for micro hydroelectric power plants for optimal use of hydropower". In: *IOP Conference Series: Materials Science and Engineering* 659.1 (2019).

[109] Elliot Group. *Impulse-Type, Two-Phase Cryogenic Expander*. 2022. URL: https://www.elliott-turbo.com/impulse-type-two-phase-cryogenic-expander. (Accessed: 13.11.2023).

[110] Iqbal, M. A., Rana, S., Ahmadi, M., Date, A., and Akbarzadeh, A. "Experimental study on the prospect of low-temperature heat to power generation using Trilateral Flash Cycle (TFC)". In: *Applied Thermal Engineering* 172 (2020), p. 115139. DOI: 10.1016/j.applthermaleng.2020.115139.

[111] He, T., Xia, C., Zhao, Y., Li, L., and Shu, P. "An experimental study on energy recovery by a pelton-type expander in a domestic refrigeration system". In: *HVAC&R Research* 15.4 (2009), pp. 785–799. DOI: 10.1080/10789669.2009.10390864.

[112] Elliot Group. URL: https://www.elliott-turbo.com/. (Accessed: 12.11.2023).

[113] Karakas, E. S. and Stasenko, D. "Two-Phase Cryogenic Expander for Nitrogen Rejection and Cooling Process in Natural Gas Applications". In: *Volume 9: Microturbines, Turbochargers, and Small Turbomachines; Oil and Gas Applications*. 2023. DOI: 10.1115/GT2023-101990.

[114] Patel, V. U. and Kimmel, H. "Fifteen Years of Field Experience in LNG Expander Technology". In: *Proceedings of the First Middle East Turbomachinery Symposium*. Doha, Qatar, Feb. 2011. DOI: 10.21423/R1HK96.

[115] Niu, L., Hou, Y., Sun, W., and Chen, S. "The measurement of thermodynamic performance in cryogenic two-phase turbo-expander". In: *Cryogenics* 70 (2015), pp. 76–84. DOI: 10.1016/j.cryogenics.2015.06.002.

[116] Zhang, Z., Li, M., Ma, Y., and Gong, X. "Experimental investigation on a turbo expander substituted for throttle valve in the subcritical refrigeration system". In: *Energy* 79 (2015), pp. 195–202. DOI: https://doi.org/10.1016/j.energy.2014.11.007.

[117] Tesla, N. *Turbine, Patent no: 1, 061, 206US1061206A*. 1913.

[118] Renuke, A., Vannoni, A., Pascenti, M., and Traverso, A. "Experimental and numerical investigation of small-scale tesla turbines". In: *Journal of Engineering for Gas Turbines and Power* 141.12 (2019), pp. 1–14. DOI: 10.1115/1.4044999.

[119] Talluri, L., Dumont, O., Manfrida, G., Lemort, V., and Fiaschi, D. "Experimental investigation of an Organic Rankine Cycle Tesla turbine working with R1233zd(E)". In: *Applied Thermal Engineering* 174 (2020), p. 115293. DOI: 10.1016/j.applthermaleng.2020.115293.

[120] Talluri, L., Niknam, P., Copeta, A., Amato, M., Iora, P., Uberti, S., Invernizzi, C., Di Marcoberardino, G., Pacini, L., Manfrida, G., and Fiaschi, D. "A revised Tesla Turbine concept for 2-phase applications". In: *E3S Web of Conferences* 238 (Jan. 2021), p. 10006. DOI: 10.1051/e3sconf/202123810006.

[121] Elliot Group. *Cryodynamics: Submerged Cryogenic Pumps & Expanders*. 2020. URL: https://www.elliott-turbo.com/Files/Admin/Cryodynamics/CP.7004.0622%2D%2D%2DSubmerged%2DCryogenic%2DPumps%2D%2D%2DExpanders.pdf. (Accessed: 12.11.2023).

[122] U.S. Environmental Protection Agency. *Protection of Stratospheric Ozone: Determination 37—Listing of HCFO-1233zd(E) as a Substitute*. Tech. rep. 87(13): 3037–3040. Federal Register, 2022. URL: https://www.epa.gov/system/files/documents/2022-01/snap-notice-37-1-20-22-87-fr-3037.pdf.

[123] Intergovernmental Panel on Climate Change. *AR6 WG I, Chapter 7—Supplementary Material: Table 7.SM.7 (Greenhouse-gas Metrics)*. IPCC, Geneva. 2021. URL: https://www.ipcc.ch/report/ar6/wg1/downloads/report/IPCC_AR6_WGI_Chapter07_SM.pdf.

[124] UK Department for Energy Security and Net Zero. *Greenhouse-gas Reporting: Conversion Factors 2022 — Flat-file Dataset*. 2022. URL: https://assets.publishing.service.gov.uk/media/6329dcf2e90e073725585d5c/ghg-conversion-factors-2022-flat-format.xls.

[125] Carless, H. *Pentanes — The Smart Choice for Energy-Efficient Innovation*. Tech. rep. 2015. URL: https://cms.chempoint.com/ChemPointSiteMedia/Haltermann-Carless-Pentanes-Brochure.pdf.

[126] 3M Company. *3M™ Novec™ 649 Engineered Fluid — Technical Data Sheet*. Tech. rep. 2019. URL: https://multimedia.3m.com/mws/media/5698650/3m-novec-engineered-fluid-649.pdf.

[127] 3M Company. *3M™ Novec™ 774 Engineered Fluid — Technical Data Sheet*. Tech. rep. 2014. URL: https://multimedia.3m.com/mws/media/8151680/3mtm-novectm-774-engineered-fluid.pdf.

[128] Intergovernmental Panel on Climate Change. *AR6 WG I, Chapter 7—Supplementary Material: Table 7.SM.7 (entry "Hexamethyldisiloxane")*. 2021. URL: https://www.ipcc.ch/report/ar6/wg1/downloads/report/IPCC_AR6_WGI_Chapter07_SM.pdf.

[129] OSPAR Commission. *Hexamethyldisiloxane (HMDS) — Environmental Assessment Report*. Tech. rep. 2004. URL: https://www.ospar.org/documents?v=6992.

[130] Intergovernmental Panel on Climate Change. *AR6 WG I, Chapter 7—Supplementary Material: Table 7.SM.7 (entry "Octamethyltrisiloxane")*. 2021. URL: https://www.ipcc.ch/report/ar6/wg1/downloads/report/IPCC_AR6_WGI_Chapter07_SM.pdf.

[131] Gelest, I. *Safety Data Sheet — Octamethyltrisiloxane (SIO6703.0)*. Tech. rep. 2015. URL: https://www.gelest.com/wp-content/uploads/SIO6703.0_OCTAMETHYLTRISILOXANE.pdf.

[132] Liao, Y. and Lucas, D. "Computational modelling of flash boiling flows: A literature survey". In: *International Journal of Heat and Mass Transfer* 111 (2017), pp. 246–265. DOI: 10.1016/j.ijheatmasstransfer.2017.03.121.

[133] Sher, E., Bar-Kohany, T., and Rashkovan, A. "Flash-boiling atomization". In: *Progress in Energy and Combustion Science* 34.4 (2008), pp. 417–439. DOI: 10.1016/j.pecs.2007.05.001.

[134] Bar-Kohany, T. and Levy, M. "State of the art review of flash-boiling atomization". In: *Atomization and Sprays* 26.12 (2016), pp. 1259–1305. DOI: 10.1615/AtomizSpr.2016015626.

[135] Price, C., Hamzehloo, A., Aleiferis, P., and Richardson, D. "Aspects of Numerical Modelling of Flash-Boiling Fuel Sprays". In: 2015. DOI: 10.4271/2015-24-2463.

[136] Price, C., Hamzehloo, A., Aleiferis, P., and Richardson, D. "Numerical modelling of fuel spray formation and collapse from multi-hole injectors under flash-boiling conditions". In: *Fuel* 221 (2018), pp. 518–541. DOI: 10.1016/j.fuel.2018.01.088.

[137] Price, C., Hamzehloo, A., Aleiferis, P., and Richardson, D. "An Approach to Modelling Flash-Boiling Fuel Sprays for Direct-Injection Spark-Ignition Engines". In: *Atomization and Sprays* 26.12 (2016), pp. 1197–1239. DOI: 10.1615/AtomizSpr.2016015807.

[138] Price, C., Hamzehloo, A., Aleiferis, P., and Richardson, D. "Numerical modelling of droplet breakup for flash-boiling fuel spray predictions". In: *International Journal of Multiphase Flow* 125 (2020), p. 103183. DOI: 10.1016/j.ijmultiphaseflow.2019.103183.

[139] Duronio, F., Vita, A., Allocca, L., Montanaro, A., Ranieri, S., and Villante, C. "CFD Numerical Reconstruction of the Flash Boiling Gasoline Spray Morphology". In: 2020. DOI: 10.4271/2020-24-0010.

[140] Duronio, F., Di Mascio, A., Villante, C., Anatone, M., and De Vita, A. "ECN Spray G: Coupled Eulerian internal nozzle flow and Lagrangian spray simulation in flash boiling conditions". In: *International Journal of Engine Research* 24.4 (2023), pp. 1530–1544. DOI: 10.1177/14680874221090732.

[141] Gopalakrishnan, S. and Schmidt, D. P. "A Computational Study of Flashing Flow in Fuel Injector Nozzles". In: *SAE International Journal of Engines* 1.1 (2008), pp. 160–170. DOI: 10.4271/2008-01-0141.

[142] Bi, R., Chen, C., Li, J., Tan, X., and Xiang, S. "Research on the CFD numerical simulation of flash boiling atomization". In: *Energy* 165 (2018), pp. 768–781. DOI: 10.1016/j.energy.2018.09.143.

[143] Peng, C., Xu, X., and Liang, X. "Experimental study on temperature variation patterns and deterioration of spray cooling with R21". In: *International Journal of Heat and Mass Transfer* 121 (3028), pp. 1159–1167. DOI: 10.1016/j.ijheatmasstransfer.2018.01.071.

[144] Chen, M., Xie, Y., Gong, M., Zhang, X., and Ren, Y. "Numerical study of spray cooling with flash evaporation". In: *Journal of Physics: Conference Series* 2454.1 (2023), p. 012012. DOI: 10.1088/1742-6596/2454/1/012012.

[145] Panchal, A. and Menon, S. "A hybrid Eulerian-Eulerian/Eulerian-Lagrangian method for dense-to-dilute dispersed phase flows". In: *Journal of Computational Physics* 439 (2021), p. 110339.

[146] Hajian, C. S. S., Zieringer, J., and Takors, R. "Euler-Lagrangian Simulations: A Proper Tool for Predicting Cellular Performance in Industrial Scale Bioreactors". In: *Digital Twins: Applications to the Design and Optimization of Bioprocesses*. Ed. by C. Herwig, R. Pörtner, and J. Möller. Cham: Springer International Publishing, 2021, pp. 229–254. DOI: 10.1007/10_2020_133.

[147] Ortego Sampedro, E., Breque, F., and Nemer, M. "Two-phase nozzles performances CFD modeling for low-grade heat to power generation: Mass transfer models assessment and a novel transitional formulation". In: *Thermal Science and Engineering Progress* 27 (2022), p. 101139. DOI: 10.1016/j.tsep.2021.101139. URL: https://doi.org/10.1016/j.tsep.2021.101139.

[148] Starkman, E. S., Schrock, V. E., Neusen, K. F., and Maneely, D. J. "Expansion of a Very Low Quality Two-Phase Fluid Through a Convergent-Divergent Nozzle". In: *Journal of Basic Engineering* 86.2 (1964), pp. 247–254. DOI: 10.1115/1.3653047.

[149] Leung, J. C. "A generalized correlation for one-component homogeneous equilibrium flashing choked flow". In: *AIChE Journal* 32.10 (1986), pp. 1743–1746. DOI: 10.1002/aic.690321019.

[150] Barret, M. "New Generalized Correlations for One-Component Two-Phase Critical Flow: Homogeneous Equilibrium Model". In: *Journal of Pressure Vessel Technology* 113.4 (1991), pp. 596–599. DOI: 10.1115/1.2928801.

[151] Wallis, G. B. "Critical two-phase flow". In: *International Journal of Multiphase Flow* 6.1 (1980), pp. 97–112. DOI: 10.1016/0301-9322(80)90041-5.

[152] Moody, F. J. "Maximum Flow Rate of a Single Component, Two-Phase Mixture". In: *Journal of Heat Transfer* 87.1 (1965), pp. 134–141. DOI: 10.1115/1.3689029.

[153] Fauske, H. *Contribution to the Theory of Two-Phase, One-Component Critical Flow*. Tech. rep. ANL-6633. 1962. DOI: 10.2172/4749073.

[154] Schröder, J. J. and Vuxuan, N. "Homogeneous non-equilibrium two-phase critical flow model". In: *Chemical Engineering & Technology* 10.1 (1987), pp. 420–426. DOI: 10.1002/ceat.270100152.

[155] Richter, H. "Separated two-phase flow model: application to critical two-phase flow". In: *International Journal of Multiphase Flow* 9.5 (1983), pp. 511–530. DOI: 10.1016/0301-9322(83)90015-0.

[156] Elias, E. and Lellouche, G. "Two-Phase Critical Flow". In: *International Journal of Multiphase Flow* 20 (1994), pp. 91–168.

[157] De Lorenzo, M., Lafon, P., Seynhaeve, J.-M., and Bartosiewicz, Y. "Benchmark of Delayed Equilibrium Model (DEM) and classic two-phase critical flow models against experimental data". In: *International Journal of Multiphase Flow* 92 (2017), pp. 112–130. DOI: 10.1016/j.ijmultiphaseflow.2017.03.004.

[158] Bilicki, Z., Kestin, J., and Pratt, M. "The effect of three closures on critical conditions in two-phase flow with unequal phase velocities". In: *International Journal of Multiphase Flow* 14.4 (1988), pp. 507–517. DOI: 10.1016/0301-9322(88)90025-0.

[159] Bankoff, S. G. "A Variable Density Single-Fluid Model for Two-Phase Flow With Particular Reference to Steam-Water Flow". In: *Journal of Heat Transfer* 82.4 (1960), pp. 265–272. DOI: 10.1115/1.3679930.

[160] Saha, P., Abuaf, N., and Wu, B. J. C. "A Nonequilibrium Vapor Generation Model for Flashing Flows". In: *Journal of Heat Transfer* 106.1 (1984), pp. 198–203. DOI: 10.1115/1.3246634.

[161] Blicki, Z. and Kestin, J. "Physical aspects of the relaxation model in two-phase flow". In: *Proceedings of the Royal Society of London. A. Mathematical and Physical Sciences* 428 (1990), pp. 379–397. DOI: 10.1098/rspa.1990.0040.

[162] Angielczyk, W., Bartosiewicz, Y., Butrymowicz, D., and Seynhaeve, J.-M. "1-D Modeling Of Supersonic Carbon Dioxide Two-Phase Flow Through Ejector Motive Nozzle". In: *International Refrigeration and Air Conditioning Conference*. Purdue, France, July 2010.

[163] Palacz, M., Haida, M., Smolka, J., Nowak, A. J., Banasiak, K., and Hafner, A. "HEM and HRM accuracy comparison for the simulation of CO2 expansion in two-phase ejectors for supermarket refrigeration systems". In: *Applied Thermal Engineering* 115 (2017), pp. 160–169. DOI: 10.1016/j.applthermaleng.2016.12.122.

[164] Karathanassis, I., Koukouvinis, P., and Gavaises, M. "Comparative evaluation of phase-change mechanisms for the prediction of flashing flows". In: *International Journal of Multiphase Flow* 95 (2017), pp. 257–270. DOI: 10.1016/j.ijmultiphaseflow.2017.06.006.

[165] Zwart, P. J., Gerber, A. G., and Belamri, T. "A Two-Phase Flow Model for Predicting Cavitation Dynamics". In: *ICMF 2004 International Conference on Multiphase Flow*. Yokohama, Japan, June 2004.

[166] Kumar, A., Tammone, C., and Haglind, F. "Numerical Investigation of Flashing Flow in a Convergent-Divergent Nozzle". In: *Volume 6: Education; Electric Power; Energy Storage; Fans and Blowers*. Boston, Massachusetts, USA: American Society of Mechanical Engineers, June 2023, V006T09A009. DOI: 10.1115/GT2023-103483.

[167] Sauer, J. and Schnerr, G. H. "Unsteady cavitating flow-a new cavitation model based on a modified front capturing method and bubble dynamics". In: *Proceedings of 2000 ASME fluid engineering summer conference*. Vol. 251. ASME. 2000, pp. 1073–1079.

[168] Hertz, H. "Ueber die Verdunstung der Flüssigkeiten, insbesondere des Quecksilbers, im luftleeren Raume". In: *Annalen der Physik* 253.10 (1882), pp. 177–193. DOI: 10.1002/andp.18822531002.

[169] Knudsen, M. "Die maximale Verdampfungsgeschwindigkeit des Quecksilbers". In: *Annalen der Physik* 352.13 (1915), pp. 697–708. DOI: https://doi.org/10.1002/andp.19153521306.

[170] Ceccio, S. L. and Brennen, C. E. "Observations of the dynamics and acoustics of travelling bubble cavitation". In: *Journal of Fluid Mechanics* 233 (1991), pp. 633–660. DOI: 10.1017/S0022112091000630.

[171] Brennen, C. E. *Cavitation and Bubble Dynamics*. 1st ed. Cambridge University Press, 2013. DOI: 10.1017/CBO9781107338760.

[172] Riznic, J. R. and Ishii, M. "Bubble number density and vapor generation in flashing flow". In: *International Journal of Heat and Mass Transfer* 32.10 (1989), pp. 1821–1833. DOI: 10.1016/0017-9310(89)90154-3.

[173] Shin, T. and Jones, O. "Nucleation and flashing in nozzles—1. A distributed nucleation model". In: *International Journal of Multiphase Flow* 19.6 (1993), pp. 943–964. DOI: 10.1016/0301-9322(93)90071-2.

[174] Senda, J., Hojyo, Y., and Fujimoto, H. "Modeling on atomization and vaporization process in flash boiling spray". In: *JSAE Review* 15.4 (1994), pp. 291–296. DOI: 10.1016/0389-4304(94)90209-7.

[175] Dietzel, D., Hitz, T., Munz, C.-D., and Kronenburg, A. "Numerical simulation of the growth and interaction of vapour bubbles in superheated liquid jets". In: *International Journal of Multiphase Flow* 121 (2019), p. 103112. DOI: 10.1016/j.ijmultiphaseflow.2019.103112.

[176] Gärtner, J. W., Loureiro, D. D., and Kronenburg, A. "Modelling and Simulation of Flash Evaporation of Cryogenic Liquids". In: *Droplet Dynamics Under Extreme Ambient Conditions*. Ed. by K. Schulte, C. Tropea, and B. Weigand. Vol. 124. Cham: Springer International Publishing, 2022, pp. 233–250. DOI: 10.1007/978-3-031-09008-0_12.

[177] Lyras, T., Karathanassis, I., Kyriazis, N., Koukouvinis, P., and Gavaises, M. "Modelling of liquid oxygen and nitrogen injection under flashing conditions". In: *Applied Thermal Engineering* 237 (2024), p. 121773. DOI: 10.1016/j.applthermaleng.2023.121773.

[178] Mandumpala Devassy, B., Petranovic, Z., and Edelbauer, W. "Numerical Investigation and Experimental Comparison of ECN Spray G at Flash Boiling Conditions". In: SAE Technical Paper 2020-01-0827. 2020, pp. 2020–01–0827. DOI: 10.4271/2020-01-0827.

[179] Devassy, B. M., Zhang, Y., Zhang, E., and Zhou, L. "Complete Workflow of Internal Nozzle Flow and Engine Simulation Using Multi-Component Fuel at Flash Boiling Conditions". In: *International Journal of Automotive Manufacturing and Materials* (2023). DOI: 10.53941/ijamm.2023.100008.

[180] Tammone, C., Romei, A., Persico, G., and Haglind, F. "Extension of the delayed equilibrium model to flashing flows of organic fluids in converging-diverging nozzles". In: *International Journal of Multiphase Flow* 171 (2024), p. 104661. DOI: 10.1016/j.ijmultiphaseflow.2023.104661.

[181] Dobran, F. "Nonequilibrium Modeling of Two-Phase Critical Flows in Tubes". In: *Journal of Heat Transfer* 109.3 (1987), pp. 731–738. DOI: 10.1115/1.3248151.

[182] Valero, E. and Parra, I. "Reactor pressure analysis at the initial stage ofa loss of coolant accident". In: *Annals of Nuclear Energy* 30.5 (2003), pp. 585–601. DOI: 10.1016/S0306-4549(02)00093-2.

[183] Laurien, E. "Influence of the model bubble diameter on three-dimensional numerical simulations of thermal cavitation in pipe elbows". In: *Proceedings of the 3rd International Symposium on Two-Phase Flow Modelling and Experimentation*. Pisa, Italy, Sept. 2004.

[184] Alamgir, M. and Lienhard, J. H. "Correlation of Pressure Undershoot During Hot-Water Depressurization". In: *Journal of Heat Transfer* 103.1 (1981), pp. 52–55. DOI: 10.1115/1.3244429.

[185] Wu, B. J. C., Abuaf, N., and Saha, P. *Study of nonequilibrium flashing of water in a converging-diverging nozzle: Volume 2 - Modeling*. Tech. rep. NUREG/CR·1864. Upton, New York: Brookhaven National Laboratory, 1981.

[186] Abuaf, N., Jones, O. C., and Wu, B. J. C. "Critical Flashing Flows in Nozzles With Subcooled Inlet Conditions". In: *Journal of Heat Transfer* 105.2 (1983), pp. 379–383. DOI: 10.1115/1.3245589.

[187] Jones, O. C. "Flashing Inception in Flowing Liquids". In: *Journal of Heat Transfer* 102.3 (1980), pp. 439–444. DOI: 10.1115/1.3244319.

[188] Levy, S. and Abdollahian, D. "Homogeneous non-equilibrium critical flow model". In: *International Journal of Heat and Mass Transfer* 25.6 (1982), pp. 759–770. DOI: 10.1016/0017-9310(82)90088-6.

[189] Lee, S. Y. and Schrock, V. E. "Critical Two-Phase Flow in Pipes for Subcooled Stagnation States With a Cavity Flooding Incipient Flashing Model". In: *Journal of Heat Transfer* 112.4 (1990), pp. 1032–1040. DOI: 10.1115/1.2910475.

[190] Barták, J. "A study of the rapid depressurization of hot water and the dynamics of vapour bubble generation in superheated water". In: *International Journal of Multiphase Flow* 16.5 (1990), pp. 789–798. DOI: 10.1016/0301-9322(90)90004-3.

[191] Elias, E. and Chambre´, P. L. "Flashing Inception in Water During Rapid Decompression". In: *Journal of Heat Transfer* 115.1 (1993), pp. 231–238. DOI: 10.1115/1.2910654.

[192] Elias, E. and Chambré, P. "Bubble transport in flashing flow". In: *International Journal of Multiphase Flow* 26.2 (2000), pp. 191–206. DOI: 10.1016/S0301-9322(99)00011-7.

[193] Valero, E. and Parra, I. "The role of thermal disequilibrium in critical two-phase flow". In: *International Journal of Multiphase Flow* 28.1 (2002), pp. 21–50. DOI: 10.1016/S0301-9322(01)00064-7.

[194] Kumzerova, E. Y. and Schmidt, A. "Effect of bubble nucleation mechanisms on flashing flow structure (Numerical Simulation)". In: *Computational Fluid Dynamics Journal* 11.4 (2003), pp. 507–512.

[195] Blander, M. and Katz, J. L. "Bubble nucleation in liquids". In: *AIChE Journal* 21.5 (1975), pp. 833–848. DOI: 10.1002/aic.690210502.

[196] Deligiannis, P. and Cleaver, J. "The role of nucleation in the initial phases of a rapid depressurization of a subcooled liquid". In: *International Journal of Multiphase Flow* 16.6 (1990), pp. 975–984. DOI: 10.1016/0301-9322(90)90102-0.

[197] Rohatgi, U. and Reshotko, E. "Non-equilibrium one-dimensional two-phase flow in variable area channels". In: *Proceedings of the Winter Annual Meeting*. Houston, Massachusetts, USA, Dec. 1975.

[198] Riznic, J. R., Ishii, M., and Afgan, N. "Mechanistic model for void distribution in flashing flow". In: *Proceedings of Transient Phenomena in Multiphase Flow, ICHMT Seminar*. Dubrovnik, Yugoslavia, May 1987.

[199] Kolev, N. I. "Thermal and Mechanical Interactions". In: *Multiphase Flow Dynamics 2*. 2nd. New York: Springer, Berlin Heidelberg, 2005.

[200] Blinkov, V. N., Jones, O. C., and Nigmatulin, B. I. "Nucleation and flashing in nozzles-2. Comparison with experiments using a five-equation model for vapor void development". In: *International Journal of Multiphase Flow* 19.6 (1993), pp. 965–986. DOI: 10.1016/0301-9322(93)90072-3.

[201] Mimouni, S., Boucker, M., Laviéville, J., Guelfi, A., and Bestion, D. "Modelling and computation of cavitation and boiling bubbly flows with the NEPTUNE_CFD code". In: *Nuclear Engineering and Design* 238.3 (2008), pp. 680–692. DOI: 10.1016/j.nucengdes.2007.02.052.

[202] Robert, M., Farvacque, M., Parent, M., and Faydide, B. "CATHARE 2 V2.5 : a fully validated CATHARE version for various applications". In: *Proceedings of the 10th International Topical Meeting on Nuclear Reactor Thermal-Hydraulics (NURETH 10)*. Seoul, Korea, 2003.

[203] Marsh, C. and O'Mahony, A. "Three-dimensional modelling of industrial flashing flows". In: *Progress in Computational Fluid Dynamics, An International Journal* 9.6/7 (2009), p. 393. DOI: 10.1504/PCFD.2009.027370.

[204] Janet, J. P., Liao, Y., and Lucas, D. "Heterogeneous nucleation in CFD simulation of flashing flows in converging-diverging nozzles". In: *International Journal of Multiphase Flow* 74 (2015), pp. 106–117.

[205] Shin, T. S. and Jones, O. C. "An active cavity model for flashing". In: *Nuclear Engineering and Design* 95 (1986), pp. 185–196. DOI: 10.1016/0029-5493(86)90046-4.

[206] Liao, Y. and Lucas, D. "3D CFD simulation of flashing flows in a converging-diverging nozzle". In: *Nuclear Engineering and Design* 292 (2015), pp. 149–163. DOI: 10.1016/j.nucengdes.2015.06.015.

[207] Edwards, A. and O'Brian, T. "Studies of phenomena connected with the depressurization of water reactors". In: *J. Br. Nucl. Enery Soc.* 9.2 (1970), pp. 125–135.

[208] Schaffrath, A., Krüssenberg, A.-K., Weiss, F.-P., Hicken, E., Beyer, M., Carl, H., Prasser, H.-M., Schuster, J., Schütz, P., Tamme, M., and Zimmermann, W. "TOPFLOW - A new multipurpose thermalhydraulic test facility for the investigation of steady state and transient two phase flow phenomena". In: *Kerntechnik* 66 (2001), pp. 209–213. DOI: 10.1515/kern-2001-0086.

[209] Wolfert, K. "The simulation of blowdown processes with consideration of thermodynamic nonequilibrium phenomena". In: *Proceedings of the Specialists Meeting of Transient Two-Phase Flow*. Toronto, ON, Canada: OECD/Nuclear Energy Agency, Aug. 1976.

[210] Zhu, J. and Elbel, S. "Measurement of static pressure profiles of vortex flashing R134a flow expanded through convergent–divergent nozzles". In: *International Journal of Refrigeration* 108 (2019), pp. 258–270. DOI: 10.1016/j.ijrefrig.2019.08.023.

[211] Zhu, J. and Elbel, S. "CFD simulation of vortex flashing R134a flow expanded through convergent-divergent nozzles". In: *International Journal of Refrigeration* 112 (2020), pp. 56–68. DOI: 10.1016/j.ijrefrig.2019.12.005.

[212] Lemmon, E. W., Bell, I. H., Huber, M. L., and McLinden, M. O. *NIST Standard Reference Database 23: Reference Fluid Thermodynamic and Transport Properties-REFPROP, Version 10.0, National Institute of Standards and Technology*. https://www.nist.gov/srd/refprop. 2018.

[213] Elliott, D. G. and Weinberg, E. *Acceleration of Liquids in Two-Phase Nozzles*. Tech. rep. Jet Propulsion Laboratory, California Institute Of Technology, 1968.

[214] Schiller, L. and Naumann, A. "A drag coefficient correlation". In: *Vdi Zeitung* 77 (1935), pp. 318–320.

[215] Guildenbecher, D. R., López-Rivera, C., and Sojka, P. E. "Secondary atomization". In: *Experiments in Fluids* 46.3 (2009), pp. 371–402. DOI: 10.1007/s00348-008-0593-2.

[216] Maksic, S. and Mewes, D. "CFD-Calculation of the Flashing Flow in Pipes and Nozzles". In: *Volume 1: Fora, Parts A and B*. Montreal, Quebec, Canada: ASMEDC, 2002, pp. 511–516. DOI: 10.1115/FEDSM2002-31033.

[217] Liao, Y. and Lucas, D. "Poly-disperse simulation of condensing steam-water flow inside a large vertical pipe". In: *International Journal of Thermal Sciences* 104 (2016), pp. 194–207. DOI: 10.1016/j.ijthermalsci.2016.01.016.

[218] Liao, Y. and Lucas, D. "Numerical analysis of flashing pipe flow using a population balance approach". In: *International Journal of Heat and Fluid Flow* 77 (2019), pp. 299–313. DOI: 10.1016/j.ijheatfluidflow.2019.05.005.

[219] Li, J., Liao, Y., Zhou, P., Lucas, D., and Li, Q. "Numerical study of flashing pipe flow using a TFM-PBM coupled method: Effect of interfacial heat transfer and bubble coalescence and breakup". In: *International Journal of Thermal Sciences* 193 (2023), p. 108504. DOI: 10.1016/j.ijthermalsci.2023.108504.

[220] Pilch, M. and Erdman, C. "Use of breakup time data and velocity history data to predict the maximum size of stable fragments for acceleration-induced breakup of a liquid drop". In: *International Journal of Multiphase Flow* 13.6 (1987), pp. 741–757. DOI: 10.1016/0301-9322(87)90063-2.

[221] *RELAP5/MOD3 Code Manual Volume: Models and Correlations*. Tech. rep. NUREG/CR–5535-VOL.4. Idaho National Engineering Laboratory, 1995.

[222] Brodkey, R. "Formation of drops and bubbles". In: *The phenomena of fluid motions*. Reading: Addison-Wesley, 1967.

[223] Gelfand, B. "Droplet breakup phenomena in flows with velocity lag". In: *Progress in Energy and Combustion Science* 22.3 (1996), pp. 201–265. DOI: 10.1016/S0360-1285(96)00005-6.

[224] Gobyzov, O. A., Ryabov, M. N., and Bilsky, A. V. "Study of Deformation and Breakup of Submillimeter Droplets' Spray in a Supersonic Nozzle Flow". In: *Applied Sciences* 10.18 (2020), p. 6149. DOI: 10.3390/app10186149.

[225] ANSYS, Inc. *CFX-Solver Theory Guide, Release 2021 R1.*

[226] Prakash, C. "TWO-PHASE MODEL FOR BINARY SOLID-LIQUID PHASE CHANGE, PART I: GOVERNING EQUATIONS". In: *Numerical Heat Transfer, Part B: Fundamentals* 18.2 (1990), pp. 131–145. DOI: 10.1080/10407799008944946.

[227] Jo, J. C., Jeong, J. J., Yun, B. J., and Moody, F. J. "Numerical prediction of a flashing flow of saturated water at high pressure". In: *Nuclear Engineering and Technology* 50.7 (2018), pp. 1173–1183. DOI: 10.1016/j.net.2018.06.002.

[228] Liao, Y. and Lucas, D. "Evaluation of interfacial heat transfer models for flashing flow with two-fluid CFD". In: *Fluids* 3.2 (2018).

[229] Ranz, W. E. and Marshall Jr., W. R. "Evaporation from Drops: Part 1". In: *Chemical Engineering Progress* 48.3 (1952), pp. 141–146.

[230] Solbrig, C.W., McFadden, J.H., Lyczkowski, R.W., and Hughes, E.D. *Heat transfer and friction correlations required to describe steam-water behavior in nuclear safety studies.* Tech. rep. CONF-750804–3. Idaho Falls, Idaho (USA): Aerojet Nuclear Co., 1975.

[231] Pinhasi, G., Ullmann, A., and Dayan, A. "Modeling of Flashing Two-Phase Flow". In: *Reviews in Chemical Engineering* 21 (2005), pp. 133–264.

[232] Brown, G. "Heat transmission by condensation of steam on a spray of water drops". PhD thesis. University of London (Imperial College of Science and Technology), 1948.

[233] Ishii, M. and Zuber, N. "Drag coefficient and relative velocity in bubbly, droplet or particulate flows". In: *AIChE Journal* 25.5 (1979), pp. 843–855.

[234] Tomiyama, A. "Struggle with computational bubble dynamics". In: *Proceedings of Third International Conference on Multiphase Flow.* Lyon, France, June 1998.

[235] LEGENDRE, D. and MAGNAUDET, J. "The lift force on a spherical bubble in a viscous linear shear flow". In: *Journal of Fluid Mechanics* 368 (1998), pp. 81–126.

[236] ANSYS, Inc. *CFX-Solver Modelling Guide, Release 2021 R1.*

[237] Nakoryakov, V. E. "Study of upward bubbly flow at low liquid velocities". In: *Izv. sib. Otdel Akad. Nauk SSSR* 16 (1986), pp. 15–20.

[238] Dang Le, Q., Mereu, R., Besagni, G., Dossena, V., and Inzoli, F. "Computational Fluid Dynamics Modeling of Flashing Flow in Convergent-Divergent Nozzle". In: *Journal of Fluids Engineering* 140.10 (2018), p. 101102. DOI: 10.1115/1.4039908.

[239] Spinelli, A., Cammi, G., Gallarini, S., Zocca, M., Cozzi, F., Gaetani, P., Dossena, V., and Guardone, A. "Experimental evidence of non-ideal compressible effects in expanding flow of a high molecular complexity vapor". In: *Experiments in Fluids* 59.8 (2018), p. 126. DOI: 10.1007/s00348-018-2578-0.

[240] White, M. T. "Investigating the Validity of the Fundamental Derivative in the Equilibrium and Non-equilibrium Two-Phase Expansion of MM". In: *Proceedings of the 3rd International Seminar on Non-Ideal Compressible Fluid Dynamics for Propulsion and Power*. Ed. by M. Pini, C. De Servi, A. Spinelli, F. Di Mare, and A. Guardone. Vol. 28. Cham: Springer International Publishing, 2021, pp. 3–11. DOI: 10.1007/978-3-030-69306-0_1.

[241] de Lorenzo, M. "Modelling and numerical simulation of metastable two-phase flows". PhD thesis. Université Paris-Saclay, 2018.

[242] The International Association for the Properties of Water and Steam. *Revised Release on the IAPWS Industrial Formulation 1997 for the Thermodynamic Properties of Water and Steam*. 2018. (Last Accessed: 08.02.2022).

[243] Thol, M., Dubberke, F., Rutkai, G., Windmann, T., Köster, A., Span, R., and Vrabec, J. "Fundamental equation of state correlation for hexamethyldisiloxane based on experimental and molecular simulation data". In: *Fluid Phase Equilibria* 418 (2016), pp. 133–151. DOI: 10.1016/j.fluid.2015.09.047.

[244] ANSYS Inc. *ANSYS CFX, Release 2021 R1*.

[245] Lemmon, E. W. and Tillner-Roth, R. "A Helmholtz energy equation of state for calculating the thermodynamic properties of fluid mixtures". In: *Fluid Phase Equilibria* 165.1 (1999), pp. 1–21. DOI: 10.1016/S0378-3812(99)00262-9.

[246] Hosokawa, S., Tomiyama, A., Misaki, S., and Hamada, T. "Lateral Migration of Single Bubbles Due to the Presence of Wall". In: *Proceedings of the ASME 2002 Joint U.S.-European Fluids Engineering Division Conference. Volume 1: Fora, Parts A and B*. Montreal, Quebec, Canada. July 14–18, 2002. pp.855-860., pp. 855–860. DOI: 10.1115/FEDSM2002-31148.

[247] ANSYS, Inc. *Meshing User's Guide, Release 2021 R1*.

[248] Morrison, F. A. *Data Correlation for Drag Coefficient for Sphere*. Department of Chemical Engineering, Michigan Technological University. URL: ww.chem.mtu.edu/~fmorriso/DataCorrelationForSphereDrag2016.pdf.. (Accessed: 10.10.2024).

[249] Saffman, P. G. "The lift on a small sphere in a slow shear flow". In: *Journal of Fluid Mechanics* 22.2 (1965), pp. 385–400. DOI: 10.1017/S0022112065000824.

[250] Mei, R. and Klausner, J. "Shear lift force on spherical bubbles". In: *International Journal of Heat and Fluid Flow* 15.1 (1994), pp. 62–65. DOI: 10.1016/0142-727X(94)90031-0.

[251] Lopez de Bertodano, M. "Turbulent Bubbly Flow in a Triangular Duct". PhD thesis. Rensselaer Polytechnic Institute, Troy New York, 1991.

[252] Pasquale, D., Ghidoni, A., and Rebay, S. "Shape Optimization of an Organic Rankine Cycle Radial Turbine Nozzle". In: *Journal of Engineering for Gas Turbines and Power* 135.4 (2013), p. 042308.

[253] Persico, G. "Evolutionary Optimization of Centrifugal Nozzles for Organic Vapours". In: *Journal of Physics: Conference Series* 821 (2017), p. 012015. DOI: 10.1088/1742-6596/821/1/012015.

[254] Persico, G., Romei, A., Dossena, V., and Gaetani, P. "Impact of shape-optimization on the unsteady aerodynamics and performance of a centrifugal turbine for ORC applications". In: *Energy* 165 (2018), pp. 2–11. DOI: 10.1016/j.energy.2018.09.044.

[255] Al Jubori, A. M., Al-Dadah, R., and Mahmoud, S. "Performance enhancement of a small-scale organic Rankine cycle radial-inflow turbine through multi-objective optimization algorithm". In: *Energy* 131 (2017), pp. 297–311.

[256] Espinosa Sarmiento, A. L., Ramirez Camacho, R. G., Oliveira, W. de, Gutiérrez Velásquez, E. I., Murthi, M., and Diaz Gautier, N. J. "Design and off-design performance improvement of a radial-inflow turbine for ORC applications using metamodels and genetic algorithm optimization". In: *Applied Thermal Engineering* 183.2020 (2021).

[257] Abdeldayem, A. S., White, M. T., Paggini, A., Ruggiero, M., and Sayma, A. I. "Integrated Aerodynamic and Structural Blade Shape Optimization of Axial Turbines Operating With Supercritical Carbon Dioxide Blended With Dopants". In: *Journal of Engineering for Gas Turbines and Power* 144.10 (2022), p. 101016. DOI: 10.1115/1.4055232.

[258] Reitz, R. D. and Diwakar, R. "Structure of High-Pressure Fuel Sprays". In: 1987, p. 870598. DOI: 10.4271/870598.

[259] Schmehl, R., Maier, G., and Wittig, S. "CFD Analysis of Fuel Atomization, Secondary Droplet Breakup and Spray Dispersion in the Premix Duct of a LPP Combustor". In: 2000.

[260] Manfredi, M., Persico, G., Spinelli, A., Gaetani, P., and Dossena, V. "Design and commissioning of experiments for supersonic ORC nozzles in linear cascade configuration". In: *Applied Thermal Engineering* 224 (2023), p. 119996. DOI: https://doi.org/10.1016/j.applthermaleng.2023.119996.

[261] Head, A. "Novel Experiments for the Investigation of Non-Ideal Compressible Fluid Dynamics: The ORCHID and First Results of Optical Measurements". Dissertation (TU Delft). Delft University of Technology, 2021. DOI: 10.4233/uuid:a3b03976-2df6-435c-b7df-1505718fcd3a.

[262] Reinker, F., Wagner, R., Hake, L., and Der Wiesche, S. A. "High subsonic flow of an organic vapor past a circular cylinder". In: *Experiments in Fluids* 62.3 (2021), p. 54. DOI: 10.1007/s00348-021-03158-y.

Appendix A

Implementation of custom interphase models

A.1 User-defined expressions implemented in the CFD solver

ANSYS CFX R21 [244] was employed to simulate the wet-to-dry expansion in a converging-diverging nozzle. The CFD solver provides a framework for the implementation of the two-fluid model, which solves separate mass, momentum and energy conservation for the liquid and vapour phases. The coupling between the phases, which defines the interphase exchange of mass, momentum and energy is accounted for using interphase models. CFX contains an array of built-in functions to estimate the relevant interfacial forces, which in case of the wet-to-dry expansion, include drag, lift and turbulent dispersion forces. The solver also includes built-in models for estimating the heat-transfer coefficient on both sides of the liquid-vapour interface. Provided that the solver contains the required interphase models, the user is only required to define the droplet size for interfacial area estimation. In case of this study, most of the required interphase models were available as built-in functions, some of the less-conventional correlations were not available and were implemented using user-defined expressions in CFX. The summary of the user-defined expressions implemented in this work is shown in Table A.1.

The parameters *NuL Brown* and *NuV Wolfert* represent the Brown [232] and Wolfret [209] Nusselt number correlations that were not available as built-in models in CFX, and were used to predict the heat-transfer coefficient on the liquid and vapour sides of the interface. The parameter *cTD* was the turbulent dispersion coefficient shown in Eq. 5.13 that was also a custom parameter, defined in terms of the droplet relaxation time (*dropRelaxtime*) and average lifetime of vapour turbulent eddies (*timeTurb*). With these three parameters, all the interphase models described in the baseline model as well as in the sensitivity study could be fully defined. The droplet diameter was also defined with a user-defined expression (*Dd*) based on a specific droplet number density (*Nd*), which defines the interfacial area. The parameter *PoutLIN* was introduced to gradually vary the outlet pressure over the first

500 iterations (*aitern*), which helped to obtain a converged solution.

Table A.1: The summary of user-defined expressions implemented in the simulation of the wet-to-dry expansion.

Parameter	**CFX Expression**
Dd	(6*liquid.Volume Fraction/(pi*Nd))ˆ(1/3)
JaT	(vapour.Density*vapour.Specific Heat Capacity at Constant Pressure* abs((vapour.Temperature - liquid — vapour.Saturation Temperature)))/ (liquid.Density*(vapour.Saturation Enthalpy-liquid.Saturation Enthalpy))
Nd	1e11 [mˆ-3]
NuL Brown	2 + 7*min(tn1, 8)
NuV Wolfert	(12*JaT/pi) + ((2/sqrt(pi))*Peˆ0.5)
Pe	ReD*PrV
PoutLIN	if(aitern<500, P0in - ((P0in-Pout)/500)*aitern, Pout)
PrV	(vapour.Specific Heat Capacity at Constant Pressure*vapour.Dynamic Viscosity)/vapour.Thermal Conductivity
ReD	(vapour.Density*uSlip*Dd capped)/vapour.Dynamic Viscosity
St	dropRelaxtime/timeTurb
cTD	exp(-0.5*St)
dropRelaxtime	(liquid.Density*liquid.Mean Particle Diameterˆ2)/(18*vapour.Dynamic Viscosity)
magUL	sqrt(liquid.Velocity uˆ2 + liquid.Velocity vˆ2 + liquid.Velocity wˆ2)
magUV	sqrt(vapour.Velocity uˆ2 + vapour.Velocity vˆ2 + vapour.Velocity wˆ2)
timeTurb	0.3*vapour.Turbulence Kinetic Energy/vapour.Turbulence Eddy Dissipation
tn1	1 +((liquid.Specific Heat Capacity at Constant Pressure*max(0[K],abs(liquid — vapour.Saturation Temperature -liquid.Temperature)))/(vapour.Saturation Enthalpy-liquid.Saturation Enthalpy))
uSlip	abs(magUV- magUL)

A.2 Droplet breakup implementation

The method for approximating the droplet breakup process in the CFD solver has been applied in the optimisation of the converging-diverging nozzle reported in Chapter 7.1. The method relies on discretising the section of the nozzle where the breakup is anticipated into a number of small volumes as shown in Fig. 7.1. The division of the breakup zone into discrete volume was performed in ANSYS DesignModeler, a three-dimensional geometry modelling application available within ANSYS Workbench. The geometry was simply divided into a number of separate volumes and then combined into a single solid part with a shared topology such that the nozzle composed of discrete volumes was treated as a single domain during mesh generation. This division allowed to formulate user-defined expression in CFX, and perform calculations inside the discrete volumes.

The method of simulating the breakup process was outlined in Section 7.3. In essence, approximating the breakup process is based on the following three correlations:

$$D_{cr,avg} = \frac{\sum (\alpha_L D_{cr})}{\sum \alpha_L} \tag{A.1a}$$

$$D^i = min\left(D^{i-1}_{cr,avg}, D^i_{cr,avg}\right) \tag{A.1b}$$

$$D^i(x) = D^i - \left[(D^i - D^{i+1})/(x^{i+1} - x^i)\right](x - x^i) \tag{A.1c}$$

The first equation (Eq. A.2) estimated the average critical droplet size, i.e. the maximum stable droplet diameter under given flow conditions. The critical diameter is weighed by the liquid volume fraction to more accurately represent the average droplet diameter corresponding to the volume occupied by the liquid phase. The second equation (Eq. A.1b) prevents droplets from increasing in size in the streamwise direction, which could happen when the critical droplet size raises along the nozzle. The final equation (Eq. A.1c) is applied to construct a droplet diameter profile based on the variation of critical droplet size. The droplet diameter profile is applied in such a manner that the diameter changes linearly between two adjacent discrete volumes, avoiding a stepwise droplet size change. The following paragraphs explain how the droplet breakup approximation has been implemented in ANSYS CFX.

The average critical diameter in each control volume was determined using the following expression:

$$D_{cr,avg} = max((sum(liquid.DcrWeighed)@CV/sum(liquid.Volume\ Fraction)@CV), \\ 5e-7[m]) \tag{A.2}$$

where the operator $@CV$ is applied to perform the summation over an indicated control volume (named CV) inside the nozzle (one of the discrete volume shown in Fig. 7.1). The term $liquid.DcrWeighed$ essentially represents the product of the local critical droplet diameter and the liquid volume fraction, however, an additional variable had to be defined for that product because it could not be directly inserted into the sum in the equation above.

$$liquid.DcrWeighed = Dcr * liquid.Volume\ Fraction \tag{A.3}$$

where Dcr is the local critical diameter defined as:

$$\begin{aligned} Dcr = min(((11 * liquid \mid vapour.Surface\ Tension\ Coefficient)/ \\ (vapour.Density * uSlip\hat{}2)), Din) \end{aligned} \tag{A.4}$$

The local critical diameter is simply the definition of the maximum stable droplet size based on the critical Weber number, formulated in line with the CFX expression syntax. The only difference is that the critical Weber number has been replaced with a constant value of 11. This is because preliminary analysis showed that under conditions relevant to the wet-to-dry expansion, the Ohnesorge number was close to zero (¡ 0.1), which implies a constant critical Weber number of 11. One can note that Eq. A.4 takes the minimum value between the local critical droplet size and inlet droplet diameter (Din). This is to ensure that the droplet size does not exceed the inlet droplet size, which in vapourising two-phase flows could occur due to coalescence, which was neglected in the current study. Having defined the average critical diameter in each discretised volume, Eq. A.1b has to be implemented within the CFD solver to ensure that the droplet diameter does not begin to rise along the longitudinal axis of the nozzle. This was implemented using a set of user-defined expressions formulated for each discretised volume.

$$\begin{aligned} D_d^{01} &= min(D_{in}, D_{cr,avg}^{01}) \\ D_d^{02} &= min(D^{01}, D_{cr,avg}^{02}) \\ D_d^{03} &= min(D^{02}, D_{cr,avg}^{03}) \\ &\vdots \\ D^N &= min(D^{N-1}, D_{cr,avg}^{N}) \end{aligned}$$

where $D_{cr,avg}$ is determined using Eq. A.2. The superscript of the terms D and $D_{cr,avg}$ denotes the number of the discrete volume, counting from the inlet of the nozzle. It is worth noting that the set of correlations for D shown above are not formulated in accordance with the CFX syntax, but have been shown in this form to facilitate easier understanding of the implemented correlations. An example of the correlations implemented in one of the studied cases formulated in the correct syntax is shown in Table X. The set of expressions D^{01} through D^N provide the variation of droplet size in the discrete volumes, with the constraint of no droplet size increase in the streamwise direction. Finally, Eq. A.1c was implemented in the CFD solver, to linearise the droplet size variation across the adjacent discrete volumes and avoid stepwise droplet size decrease. This was achieved with the following set of expressions:

$$
\begin{aligned}
D^{01}_{d,lin} &= Din - ((Din - D^{01}_{d})/(x^{01} - x_{in})) * (x - x_{in}) \\
D^{02}_{d,lin} &= D^{01}_{d} - ((D^{01}_{d} - D^{02}_{d})/(x^{02} - x^{01})) * (x - x^{01}) \\
D^{03}_{d,lin} &= D^{02}_{d} - ((D^{02}_{d} - D^{03}_{d})/(x^{03} - x^{02})) * (x - x^{02}) \\
&\vdots \\
D^{N}_{d,lin} &= D^{N-1}_{d} - ((D^{N-1}_{d} - D^{N}_{d})/(x^{N} - x^{N-1})) * (x - x^{N-1})
\end{aligned}
$$

where $D_{d,lin}$ is the linearised diameter profile between to adjacent discrete volumes, x is the streamwise coordinate, while x^{N-1} and x^{N} represent the streamwise location of the beginning and end of the N^{th} discrete volume. In order to convert the set of the above correlations into a single droplet diameter profile that can serve as an input parameter for the droplet size, the following conditional statement was applied:

$$
D_{d,prof} = if(x < x^{in},\ D_{in},\ if(x < x^{01},\ D^{01}_{d,lin},\ if(x < x^{02},\ D^{02}_{d,lin}, ...if(x < x^{N},\ D^{N}_{d,lin})))) \tag{A.5}
$$

The conditional statement shown in Eq. A.5, was the final user-defined expression implemented in CFX to estimate the droplet size variation within the breakup zone shown in Fig. 7.1. As mentioned earlier, the correlations for D_d, $D_{d,lin}$ and $D_{d,prof}$ shown above were not formulated in line with the CFX expression syntax. Table X shows a set of actual user-defined expressions implemented in CFX to approximate the breakup process. The expressions were formulated for 24 discrete volumes, each having a width of 2 mm. The first of these discrete volume was placed at a streamwise position of $x = 0$ $[mm]$.

Table A.2: The summary of user-defined expressions implemented in the simulation of the breakup process in the the wet-to-dry expansion.

Parameter	CFX Expression
Dcr	min(((11*liquid — vapour.Surface Tension Coefficient)/ (vapour.Density*uSlip2)), Din)
DcrAvg01	max((sum(liquid.DcrWeighed)@CV01/sum(liquid.Volume Fraction)@CV01), 5e-7[m])
DcrAvg02	max((sum(liquid.DcrWeighed)@CV02/sum(liquid.Volume Fraction)@CV02), 5e-7[m])
DcrAvg03	max((sum(liquid.DcrWeighed)@CV03/sum(liquid.Volume Fraction)@CV03), 5e-7[m])
	⋮
DcrAvg24	max((sum(liquid.DcrWeighed)@CV24/sum(liquid.Volume Fraction)@CV24), 5e-7[m])
Dd01	min(Din,DcrAvg01)
Dd02	min(Dd01,DcrAvg02)
Dd03	min(Dd02,DcrAvg03)
	⋮
Dd24	min(Dd23,DcrAvg24)
ReD	(vapour.Density*uSlip*Dd capped)/vapour.Dynamic Viscosity
St	dropRelaxtime/timeTurb
cTD	exp(-0.5*St)
dropRelaxtime	(liquid.Density*liquid.Mean Particle Diameterˆ2)/(18*vapour.Dynamic Viscosity)
magUL	sqrt(liquid.Velocity uˆ2 + liquid.Velocity vˆ2 + liquid.Velocity wˆ2)
magUV	sqrt(vapour.Velocity uˆ2 + vapour.Velocity vˆ2 + vapour.Velocity wˆ2)
timeTurb	0.3*vapour.Turbulence Kinetic Energy/vapour.Turbulence Eddy Dissipation
tn1	1 +((liquid.Specific Heat Capacity at Constant Pressure*max(0[K],abs(liquid — vapour.Saturation Temperature -liquid.Temperature)))/(vapour.Saturation Enthalpy-liquid.Saturation Enthalpy))
uSlip	abs(magUV- magUL)